Investigation of Positively Charged Supramolecular Cages Towards Guest-Uptake and Catalysis

Inauguraldissertation

Zur Erlangung der Würde eines Doktors der Philosophie

vorgelegt der

Philosophisch-Naturwissenschaftlichen Fakultät

der Universität Basel

von

Mattias Zenka

2023

Genehmigt von der Philosophisch-Naturwissenschaftlichen Fakultät

auf Antrag von

Erstbetreuer: Prof. Dr. Konrad Tiefenbacher

Zweitbetreuerin: Prof. Dr. Catherine Housecroft

Externe Expertin: Jun.-Prof. Dr. Anna McConnell

Basel, den 20.06.2023

Prof. Dr. Marcel Mayor

(Dekan)

Für meine Eltern und meine Schwester,

weil ohne euch nichts möglich gewesen wäre.

Die vorliegende Arbeit wurde von Oktober 2018 bis September 2022 an der Universität Basel unter der Betreuung von Prof. Dr. Konrad Tiefenbacher angefertigt.

Teile dieser Arbeit wurden veröffentlicht:

Zenka, M.;[†] Preinl, J.; Pertermann, E.; Lützen, A.; Tiefenbacher, K. A Water- and Base-Stable Iminopyridine-Based Cage That Can Bind Larger Organic Anions, *Eur. J. Inorg. Chem.* **2023**, e202300110. doi.org/10.1002/ejic.202300110.

[†]Erstautor

Acknowledgements

First, I wish to express my deepest gratitude to *Prof. Dr. Konrad Tiefenbacher* for giving me the opportunity to work in his group. I am truly thankful for his excellent guidance throughout these years. Without his support, his trust, his remarkable knowledge within the fields of chemistry and constant availability, this dissertation would not have been possible. Especially during difficult times and when I struggled the most with motivation, he built me up again and set me on a new route to find my passion for chemistry again. I am very thankful that he gave me many chances to improve myself professionally.

I would like to thank *Prof. Dr. Catherine Housecroft* for her continous support, sympathy, and the uplifting feedback on my first yearly talk as my second supervisor. Also, I want to thank *Jun.-Prof. Dr. Anna McConnell* for accepting to be the external expert.

Moreover, I would like to thank *Prof. Dr. Arne Lützen* and *Dr. Eric Pertermann* who provided a key compound for a collaboration project which proved fruitful and *Joachim Preinl* for his early contributions to this work. Similarly, I want to thank *Dr. Tomáš Šolomek* and *Dr. Hsin-Hua Huang* for their contributions to another project.

Furthermore, I want to thank all my colleagues from the TIEFENBACHER group and part-time visitors for the amazing working atmosphere during this journey. I want to thank *Fabian Huck*, *Severin Merget*, *Tian-Ren Li* and *Suren Nemat* for welcoming me into their lab. I am especially grateful for my former labmates *Ivana Némethová*, *Giacomo Persiani*, *Tommaso Lorenzetto*, *Ricard López-Coll*, and *Miroslava Čonková* as well as *Dario Schmid* and *Yiheng Lu* for sharing similar interests and transforming the time in the lab into a true joy. I would also like to thank *Leonidas-Dimitrios Syntrivanis*, *Melina Knezevic*, *Iris Martyn*, *Ivan Cornu*, *Jonathan Pfeuffer-Rooschüz*, *Daria Sokolova*, *Jesper Köster*, and *Fabian Bissegger* for their help and discussions. Moreover, I would like to acknowledge *Marina Schneider*, who was a formidable student to supervise.

I want to thank the entire staff of the chemistry department for their dedicated support. Special thanks go to *Michael Pfeffer* for HR-MS analysis and great conversations during our train travels, *Jonas Zurflüh* for support concerning analytical issues with poorly soluble compounds, *Sylvie Mittelheisser* for HR-MS and elemental analysis and *Alessandro Prescimone* for the X-ray analysis. I am also grateful for the whole Werkstatt team (*Markus Ast*, *Pascal Andrek*, *Andreas Sohler*, and *Isny Meha*), the IT support, especially *Bernhard Jung*, and the technical staff consisting of *Markus Hauri* and *Susanne Foley*. I also want to greatly acknowledge *Isa Worni* for taking care of administrative work and welcoming me so warm-heartedly.

I would like to thank the many friends I made along the way, both those directly around me and those I met from around the globe, who always were up for a great time or even helped on some aspects of this thesis, namely: *Aaron*, *Andreas*, *Andrej*, *Daniel*, *Felix*, *Jannik*, *Martin*, *Oliver* and *Ruben*. Especially noteworthy are those closest to me and helped shaping me into the person I am today, namely: *Arnaldo*, *Bettina*, *Eli*, *Haosu*, *Ilda*, *Jakob*, *Jonas*, *Laura*, *León*, *Liri*, *Niklas*, *Sachin*, *Samira*, and *Tabea* as well as my wonderful partner *Franziska*.

Last, but not least, I want to thank my parents, *Arben* and *Pranvera*, as well as my sister, *Sindi*, for their unconditional love and support throughout my life. Without you, I would not have been able to reach this milestone.

Deutsche Zusammenfassung

In den letzten Jahrzehnten hat das Interesse an Anion-π-Wechselwirkungen schnell zugenommen. Naphthalindiimid (NDI) Verbindungen haben sich als nützliche π-acide Plattformen erwiesen. Während offene, nicht-kapselartige Systeme mit NDI-Einheiten als Anion-π-Katalysatoren für verschiedene Reaktionen Einsatz fanden, wurden sie bisher nicht in supramolekulare Käfige für explizite Anion-π-Katalyse integriert. In dieser Arbeit wurden zwei Strategien untersucht, um positiv geladene supramolekulare Käfige zu synthetisieren, die Untereinheiten mit π-aciden Oberflächen aufweisen und somit mehrere Bindungsstellen für Anion-π-Wechselwirkungen bieten sollen. Diese Käfige könnten als potenzielle Katalysatoren für anionische Reaktionen dienen.

Als Erstes wurde die *dynamisch-kovalente Chemie* unter Verwendung der reversiblen Imin-Kondensation zwischen dem in vier Schritten synthetisierten NDI-Dialdehyd **175** und entweder TREN (**128a**), TRPN (**128b**) oder dem Triamin (**128c**) als Untereinheiten im Verhältnis 3:2 untersucht. Es bildeten sich in jedem Fall die Imin-Käfige **XXIIIa-c** mit **Tri^{2}Di^3** Topologie. Der TREN-basierte Imin-Käfig **XXIIIa** wurde erfolgreich zum entsprechenden Ammoniumchlorid-Käfig **XVIIa** reduziert. Anionenaustausch ermöglichte Zugang zu seinem Ammoniumtrifluoracetat-Käfig **XXVa**. Experimente zur Gastaufnahme wurden mit anionischen Gästen durchgeführt, wobei moderate Bindungskonstanten zwischen 75 und 460 M^{-1} bestimmt wurden. Die Bindungskonstanten waren nicht überzeugend genug und der Käfig wurde als zu klein für unsere Zwecke angesehen. Interessanterweise bildeten sich während des imin-bildenden Schritts vier weitere, augenscheinlich hochsymmetrische, Imin-Spezies mit zunehmender TREN-Konzentration. Getrieben vom Wunsch, Käfige mit größeren Hohlräumen wie solche mit **Tri^{4}Di^6** Topologie zu erhalten, wurden die Imin-Spezies als Mischungen auf ihre entsprechenden Ammoniumchlorid-Spezies reduziert. Leider wurden zwei nach umfangreicher Aufarbeitung als Ammoniumspezies **204a** und **205a** niedrigerer Molmasse identifiziert. Die anderen beiden Spezies blieben unbekannt, wobei Anzeichen für zersetzte Produkte erst nach teilweiser Aufreinigung sichtbar waren.

Im zweiten Teil dieser Arbeit wurden Koordinationskäfige über *koordinationsgetriebene Selbstassemblierung* synthetisiert. Hierfür wurde NDI-Dialdehyd **176** in zwei Schritten synthetisiert. Die Reaktion dieser Untereinheit mit TREN oder TRPN und diversen Metallvorläufern wurde untersucht. Die **$Zn_2L_3(NTf_2)_4$** Helix **XXXII** wurde erhalten. Seine Kristallstruktur wurde aufgeklärt, die keinen Hohlraum aufgrund von π-π-Wechselwirkungen zwischen den Liganden aufzeigte. Ein kantenverknüpfter tetraedischer **M_4L_6** Käfig war nicht zugänglich. Der literaturbekannte **$Fe_4L_6(NTf_2)_8$** Tetraeder **XXIX** erwies sich als instabil gegenüber Wasser und Basen. Der Trialdehyd-Ligand **177**, basierend auf dem π-aciden Triphenylen-Triimid (TPTI)-Gerüst, wurde als nächstes untersucht. Eine sechsstufige Synthese war geplant, aber das TPTI-Gerüst erwies sich als instabil gegenüber Wasser bei wässrigen Aufarbeitungen und die Synthese scheiterte beim letzten Schritt. Stattdessen wurde dann der Trialdehyd **178**, der keine π-acide Einheit aufweist, in drei Schritten dargestellt. Durch Kombination aus dem Liganden **178**, TREN und $Zn(NTf_2)_2$ entstand der flächenverknüpfte, tetraedrische **$Zn_4L_4(NTf_2)_8$** Käfig **Zn-XLIII**. Ein wasserlösliches Derivat war nicht zugänglich. Der Käfig erwies sich jedoch als stabil gegenüber Wasser und Basen bei hohen Temperaturen und konnte anionische Gäste mit Bindungskonstanten zwischen 40 und 850 M^{-1}in MeCN-d_3/H_2O = 9:1 binden. Neutrale Gäste zeigten keine Bindung. Trotz einer Gesamtladung von +8 konnte der Käfig Reaktionen mit anionischen Übergangszuständen nicht katalysieren. Stattdessen trat in allen untersuchten Fällen eine Verlangsamung der Reaktionsgeschwindigkeit auf. Der Grund dafür bleibt unbekannt.

English Abstract

Over the recent decades, interest in anion-π interactions has grown rapidly. Naphthalene diimide (NDI) compounds were found to offer a useful π-acidic platform. While open, non-capsular systems with NDI moieties have been used as anion-π catalysts for various reactions, they have not yet been incorporated into supramolecular cages for explicit anion-π catalysis. This thesis investigated two strategies for the synthesis of positively charged, supramolecular cages with subcomponents featuring π-acidic surfaces offering multiple binding sites for anion-π interactions, which could serve as potential catalysts for anionic reactions.

First, *dynamic covalent chemistry* was applied using reversible imine condensation between NDI dialdehyde **175**, which was synthesized in four steps, and either TREN (**128a**), TRPN (**128b**) or the more rigid triamine **128c** as subcomponents in a 3:2 ratio. Imine cages **XXIIIa-c** formed preferentially with **Tri^{2}Di^3** topology in every case. TREN-based imine cage **XXIIIa** was reduced to its corresponding ammonium chloride cage **XVIIa**. Anion exchange gave access to its ammonium trifluoroactetate cage **XXVa**. Guest-uptake experiments were conducted with anionic guests showing rather moderate binding constants between 75 and 460 M^{-1}. The cage was considered too small for our endeavours and the binding constants not convincing enough. Intriguingly, four more highly symmetric imine species formed with increasing TREN (**128a**) concentration during the first step. Driven by the desire to obtain cages with bigger cavities, such as those with **Tri^{4}Di^6** topology, the imine species mixtures have been reduced to their corresponding ammonium species. Unfortunately, two were identified as ammonium species **204a** and **205a** of lower molecular weight after an extensive workup procedure. The other two remained unknown with evidence for decomposition being visible only after partial purification.

In the second part of this thesis, *coordination driven self-assembly* was used as a strategy for the construction of novel coordination cages. For this, NDI dialdehyde **176** was synthesized in two steps. The reaction between subcomponent **176** and TREN or TRPN with various metal precursors was investigated. **$Zn_2L_3(NTf_2)_4$** helicate **XXXII** was obtained. Its crystal structure was elucidated, showing no cavity due to π-π stacking between the NDI ligands. An edge-linked tetrahedral **M_4L_6** cage could not be accessed with NDI dialdehyde **176**. The literature known **$Fe_4L_6(NTf_2)_8$** tetrahedron **XXIX** proved to be unstable against water and bases. Trialdehyde ligand **177**, based on the π-acidic triphenylene triimide (TPTI) scaffold, was pursued next. Six steps were envisioned for the synthesis of ligand **177**, but the TPTI scaffold was found to be unstable towards water during aqueous workups. The last step of its synthesis failed. Therefore, trialdehyde **178**, bearing no π-acidic moiety, was synthesized in three steps instead. Subcomponent self-assembly between tritopic ligand **178** with TREN and $Zn(NTf_2)_2$ gave face-capped **$Zn_4L_4(NTf_2)_8$** tetrahedron **Zn-XLIII**. No water-soluble derivative was accessible. However, the cage proved to be stable against water and various bases at elevated temperatures. It was able to bind anionic guests with binding constants between 40 and 850 M^{-1} in MeCN-d_3/H_2O = 9:1. Neutral guests were not bound by cage **Zn-XLIII**. Despite its net positive charge of +8, the cage was not able to accelerate reactions with anionic transition states. Deceleration occurred instead in every single case investigated and the exact reason for this remains unknown.

Table of Contents

1 Introduction

One of nature`s greatest inventions and prerequisites for life are molecular machines known as enzymes. Enzymes are large assemblies made of covalently linked amino acids *via* peptide bonds. They act as biological catalysts to accelerate reactions selectively and efficiently within cells. With twenty-two proteinogenic amino acids being naturally incorporated, the sheer amount of possible sequence iterations in the polypeptide chain leads to an impressive diversity with many different enzymes being able to catalyse individual reactions within the metabolic pathways. Enzymes bind their substrates with very high specificity within binding pockets utilizing a range of attractive intermolecular forces. In 1894, EMIL FISCHER used the "lock & key" analogy as a first model to describe how complementary geometries between substrate and enzyme lead to the high specificity (Figure 1a).[1] While geometric shapes certainly play an important role, this model still failed to explain the catalytic properties of enzymes. Later, DANIEL KOSHLAND suggested the „induced fit" model as an extension to the previous one. It further explains that the enzyme`s binding pocket is not rigid, but dynamic in nature. Therefore, the surrounding amino acid sidechains which construct the active site as well as the substrate may conformationally adjust to each other to allow for better binding (Figure 1b). When the substrate reacts, the transition state may then be stabilized effectively.[2,3] This dynamic adjustment occurs due to favourable non-covalent interactions such as hydrogen bonds, ion-ion interactions, π-π interactions or even cation-π interactions to name a few.

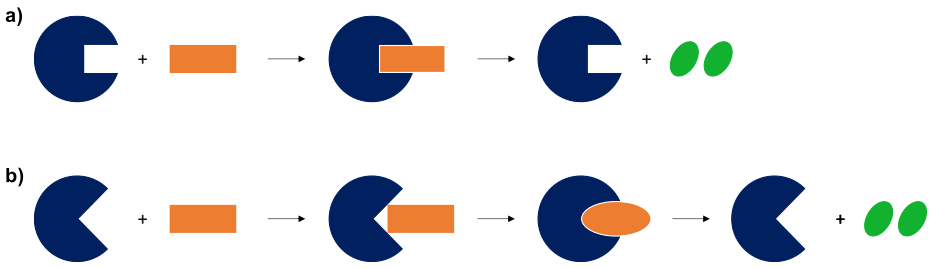

Figure 1. a) Schematic depiction of the "lock & key" model. The substrate (orange) binds to a matching enzyme (blue) to initiate a catalytic reaction. The products (green) are released, and the enzyme is recovered without any change. b) Schematic depiction of the "induced fit" model. After initial formation of a weakly binding complex between enzyme and substrate, dynamic conformational adjustments lead to a strong binding complex with geometries close to the transition state of the reaction. The products are released, and the enzyme is recovered in its original state.

Supramolecular chemistry, also known as *chemistry beyond the molecule*, focuses on the study of molecular recognition and high-order assemblies formed by these non-covalent interactions.[4] During the last few decades, a variety of purely synthetic enzyme mimics have been developed which exhibit this ability of molecular recognition. This field of supramolecular chemistry has evolved significantly over the recent decades making use of either reversible bond-forming reactions to build cages or subcomponents which self-assemble *via* molecular recognition into structures of high complexity. This work will focus on the synthesis of positively charged supramolecular cage compounds which should be able to stabilize anionic substrates and intermediates over ion-ion interactions. Additionally, the subcomponents chosen for cage formation will ideally be able to assist in this endeavour by providing aromatic moieties suited for anion-π interactions.

1.1 Anion-π Interactions

1.1.1 A Brief History on Anion-π Interactions

Among non-covalent interactions based on aromatic rings, π-π[5–9] stacking and cation-π interactions[10–13] have been studied intensively in the past. The latter describes the attractive forces between an electron-rich (π-basic) aromatic ring and cations and has been successfully applied in organocatalysis.[14–20] In sharp contrast to this, interest in anion-π interactions has only recently developed due to its counterintuitive nature. Anions were expected to only show repulsive behaviour against an aromatic π-system as they would only be able to donate even more electron density to an already electron-rich system. This was thought to be true in general for a long time. One of the earliest experimental observations for anion-π interactions was reported by HIRAOKA *et al*. in 1987.[21,22] They conducted pulsed electron-beam high-pressure mass spectrometry experiments for complexes between hexafluorobenzene and halide anions (F^-, Cl^-, Br^-, I^-) in the gas phase. The MEISENHEIMER type complex **1** was reported for the fluoride (Figure 2a),[23] while the other halides were only weakly bound by non-covalent interactions.[21] The C_{6v}-symmetric anion-π complex **2** was postulated with the help of theoretical calculations, suggesting that the halides were located above the center of the aromatic ring (Figure 2b).[22]

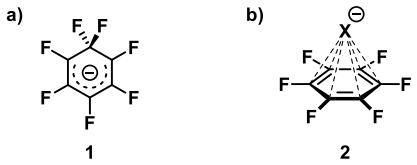

Figure 2: a) MEISENHEIMER type complex **1** (also called σ-complex) between fluoride (F^-) and hexafluorobenzene. b) Schematic representation of the electrostatic attractive interaction between halides (Cl^-, Br^-, I^-) and hexafluorobenzene.

A few years later SCHNEIDER *et al*. also observed weak interactions between negatively charged groups and polarisable arenes in solution.[24,25] In the late 1990s, several reports then documented theoretical evidence of electrostatic bonding between hexafluorobenzene and the heteroatom in small molecules such as H_2O, HCN and HF with the negative end of the dipole being directed towards the C_6 axis of the aromatic ring.[26–28] In 2002, three pioneering studies by MASCAL *et al*., ALKORTA *et al*. and DEYÀ *et al*. further confirmed the presence of attractive non-covalent interactions between electron poor aromatic systems and anions exhibiting binding energies similar to hydrogen bonds (20-50 kJ mol^{-1}).[29–31] The term 'anion-π interaction' was coined by DEYÀ *et al*. during this time. With the first explicit study published in 2013,[32] MATILE and co-workers laid the foundation for anion-π catalysis as a new concept for catalysis of reactions with anionic transition states and its applications have expanded ever since.[33]

1.1.2 Physical Properties of Anion-π Interactions

A series of computational studies investigated the very nature of the interaction between anions and aromatic π-systems.[29–31,34–38] These are mainly dominated by two effects: (1) an electrostatic term and (2) an anion-induced polarisation of the π-system. The electrostatic term is correlated with the quadrupole moment Q_{zz} of the aromatic species which describes the charge distribution perpendicular to the aromatic plane along the *z*-axis. For instance, the quadrupole moment of benzene (**3**) is negative ($Q_{zz}(C_6H_6) = -8.7$ B; 1 B (Buckingham) = $3.336 \cdot 10^{-40}$ C m²) and positive for hexafluorobenzene (**5**) ($Q_{zz}(C_6F_6) = +9.5$ B) due to the strong electronegativity of the fluorine atoms (Figure 3a).[39] A large and negative quadrupole moment leads to repulsion of negatively charged species whereas π-systems with large positive values, e.g. 1,3,5-trinitrobenzene (**6**) and naphthalene diimide (NDI) compounds of the type **7** and **8**, interact attractively with anions (Figure 3a). The resulting anion-π interaction is then strongly dominated by the electrostatic term. A schematic representation of the quadrupole moment for aromatic rings is shown in figure 3b. Studies showed that a strong correlation exists between the magnitude of the quadrupole moment Q_{zz} of an aromatic ring and the electrostatic contribution to the anion-π interaction.[34]

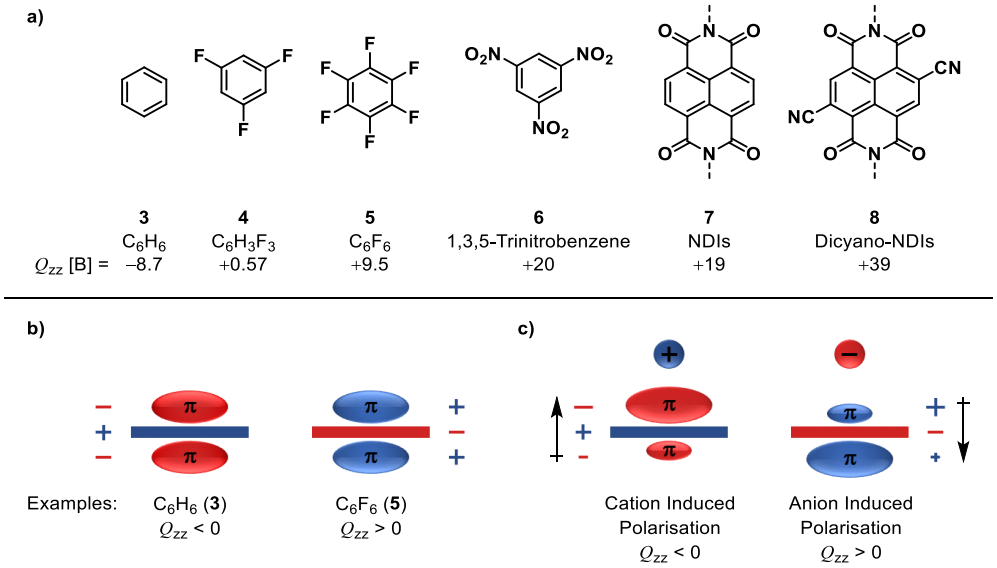

Figure 3: a) Representative π-base (**3**) and π-acids (**4**-**8**) with values for their corresponding quadrupole moments according to literature.[33,40–42] b) Representation of the quadrupole moment for benzene (**3**, left) and hexafluorobenzene (**5**, right). c) Cation induced polarisation of the aromatic π-electron density (left) and anion induced polarisation of the aromatic π-electron density (right).

The second effect is the ion induced polarisation of the π-cloud on each side of the aromatic plane. If a cation approaches an aromatic system, preferably but not necessarily, with a negative Q_{zz} value, it induces a shift in electron density within the π-system (Figure 3c, left). This polarisation leads to a dipole moment, resulting in an energetic stabilization of this cation-π complex. Similarly, the same is true for anions approaching an aromatic system with, preferably, a positive Q_{zz} value (Figure 3c, right) inducing a dipole moment which further stabilizes the anion-π interaction. For systems with large and positive Q_{zz} values, the electrostatic term dominates. However, molecules with small magnitudes in their Q_{zz} values such as 1,3,5-trifluorobenzene (**4**, $Q_{zz} = +0.57$ B)[42] are capable of interacting favourably with either cations or anions since the polarisation term of the interaction prevails and its contribution correlates with the molecular polarisability $\alpha_{||}$ of the aromatic system ($\alpha_{||}$(**4**) = 38.8 a.u.).[43]

FRONTERA *et al*. systematically probed the influence of these two effects by successively substituting oxygen atoms with sulfur in cyanuric acid (**9**) to compare the resulting binding energies and equilibrium distances in complexes formed between halides and the sulfur derivatives (**10**-**12**) of this model system (Figure 4a).[44] The consecutive exchange of oxygen for sulfur leads to a decrease in the magnitude of the quadrupole moments (from 6.96 B to 5.15 B) and an increase of the molecular polarisability of the system (from 35.52 a.u. to 63.76 a.u.). The study shows how both effects balance each other out: the binding energies for cyanuric acid (**9**) or its derivatives **10**-**12** remained almost constant at 15 kcal mol^{-1} for their chloride complexes **13**-**16** (Figure 4b).

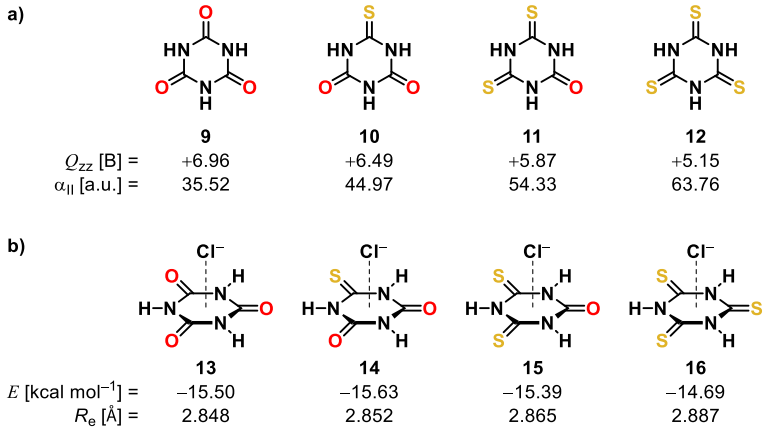

Figure 4: a) Influence of the successive substitution of oxygen with sulfur on the quadrupole moments (Q_{zz}) and molecular polarisabilities ($\alpha_{||}$) for cyanuric acid (**9**) towards its thioderivatives **10**-**12**. b) Influence on the binding energies (E) and equilibrium distances (R_e) for the complexes between a chloride anion and cyanuric acid (**13**) and its thioderivatives **14**-**16**.[44,45]

Further computational investigations performed by KIM *et al*. revealed that the electrostatic and induction terms dominate anion-π interactions in complexes with small halide anions as they are more polarising, especially fluoride (F^-), while partial contributions from dispersion interactions increase when looking at planar anions as they are higher in magnitude for anions like nitrate (NO_3^-) and carbonate (CO_3^{2-}) coupled with their ability to exhibit π-π stacking.[35] FRONTERA *et al*. reported interaction energies for these anions and various aromatic compounds such as hexafluorobenzene for a direct comparison (Table 1).[45]

Table 1: Interaction energies (E) with basis set superposition error correction and zero-point corrections together with equilibrium distances (R_e) measured from the anion to the center of the ring at the MP2/6-31++G** level of theory for complexes between hexafluorobenzene (**5**) and various anions according to FRONTERA *et al*.[45]

Anion	E [kcal mol^{-1}]	R_e [Å]
H^-	−12.1	2.69
F^-	−18.2	2.57
Cl^-	−12.6	3.15
Br^-	−11.6	3.20
NO_3^-	−12.2	2.92
CO_3^{2-}	−34.7	2.72

Fluoride (F^-) exhibits stronger interaction energies than its higher analogues due to its smaller ionic radius and its stronger polarisation while the stabilization in nitrate (NO_3^-) complexes were comparable to bromide (Br^-) and chloride (Cl^-) complexes. The carbonate (CO_3^{2-}) complex does experience the highest interaction energies, most likely due to its higher charge state of –2.

High level *ab initio* calculations to study the additivity of anion-π interactions were conducted as well. Several interaction energies (E) and equilibrium distances (R_e) for 1:1 (**19**-**22**), 1:2 (anion-π_2, **23**-**26**) and 1:3 (anion-π_3, **27**-**30**) complexes between chloride or bromide anions with either *s*-triazine (TAZ, **17**) or trifluoro-*s*-triazine (TFZ, **18**) were calculated (Figure 5, Table 2 and 3) revealing additivity in both binding energies and geometries.[46]

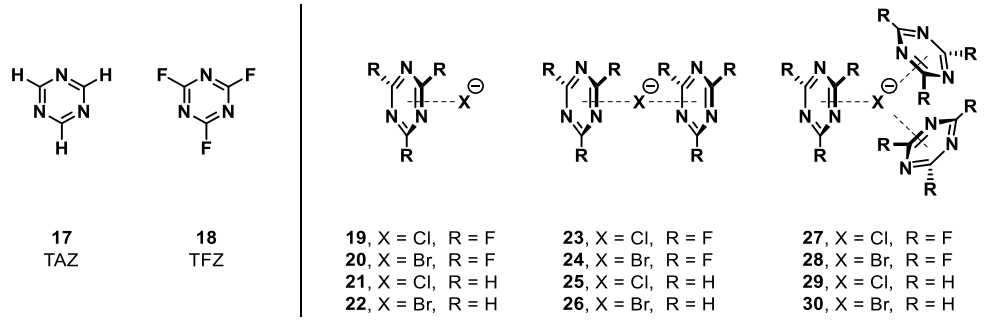

Figure 5: Schematic representation of binary (anion-π), ternary (anion-π_2) and quaternary (anion-π_3) complexes between chlorides or bromides and *s*-triazine (**17**) or trifluoro-*s*-triazine (**18**).[46]

Thus, the interaction energies for ternary anion-π_2 complexes **23-26** were calculated to be roughly twice as big in magnitude than for the corresponding binary anion-π complexes **19-22**. The quaternary anion-π_3 complexes with TFZ (**27** and **28**) exhibit binding energies which are almost three times as big as the corresponding binary ones (**23** and **24**, respectively). For the quaternary anion-π_3 complexes of TAZ (**29** and **30**), the binding energies even exceed the expected values relative to the binary complexes (**25** and **26**, respectively) with a factor that is significantly higher than 3. By analysing the molecular models of the quaternary TAZ_3-X complexes **29** and **30**, this anomaly was attributed to extra hydrogen bonds between the N atoms and the C-H bonds of the *s*-triazines, leading to binding energies that were calculated to be more negative than expected.

Table 2 (left) and Table 3 (right): Binding energies (E) for the complexes **19**-**30** with the basis set superposition error (BSSE) correction and equilibrium distances (R_e) at the MP2//RI-MP2 level of theory.[46]

Complex	E [kcal mol^{-1}]	R_e [Å]
21 (TAZ-Cl^-)	–5.2	3.220
25 (TAZ_2-Cl^-)	–10.4	3.213
29 (TAZ_3-Cl^-)	–22.2	3.015
22 (TAZ-Br^-)	–5.1	3.338
26 (TAZ_2-Br^-)	–10.0	3.370
30 (TAZ_3-Br^-)	–21.7	3.372

Complex	E [kcal mol^{-1}]	R_e [Å]
19 (TFZ-Cl^-)	–15.0	3.008
23 (TFZ_2-Cl^-)	–28.5	3.006
27 (TFZ_3-Cl^-)	–41.0	3.019
20 (TFZ-Br^-)	–14.2	3.176
24 (TFZ_2-Br^-)	–26.8	3.170
28 (TFZ_3-Br^-)	–38.6	3.172

In reality, the interaction geometries between anions and arenes are generally quite diverse as was both predicted and observed experimentally.[47,48] For example, the anion can interact with the arene from the side (Figure 6a) to participate in either non-classical C_{Aryl}-H hydrogen bonding (complexes **31** and **32**) or classical hydrogen bonding interactions (complex **33**), but halogen bonding with the arene (complex **34**) is also possible. As far as anion-π complexes are concerned, in which the anion is located on top of the arenes plane (Figure 6b), the crystallographic studies[47,48] revealed that the theoretically predicted anion-π complex **35** with η^6 hapticity is rarely found. Instead, anions generally showed close anion-π contacts with certain parts of the π-system, which were defined over their hapticity. The anion can form complexes of the type **36** (η^1), **37** (η^2) and **38** (η^3) as depicted in figure 6b in which it is not located directly above the center of the ring. Aromatic rings are often electronically asymmetric resulting in this variety. To complete the list, anions can also covalently bind to the arene to create MEISENHEIMER type complexes **39** (Figure 6c).[23]

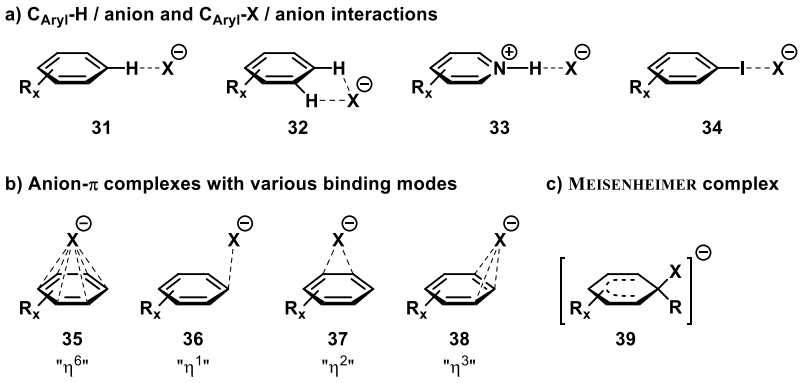

Figure 6: a) Interactions from the side: non-classical (**31**-**32**) and classical (**33**) hydrogen bonding and halogen bonding (**34**). b) Geometries for various anion-π interactions with different hapticities (**35**-**38**). c) MEISENHEIMER type complex **39**.

In other words, the equilibrium position of anions in anion-π complexes is often shifted away from the center of the ring, whereas cations show a stronger preference to align to the ring axis. For an effective comparison, further calculations were carried out to show how the interaction energy is affected by incrementally shifting the position of an anion or a cation from the center to the edge of the ring. The chloride-hexafluorobenzene anion-π complex and the sodium-benzene cation-π complex were chosen as the two model complexes for this comparison.[49] Figure 7a (left) shows the interaction energies for the chloride-hexafluorobenzene complex as the anion is moved along the *x* and *y* axes with its potential energy minimum point being at the centroid of the ring and $z = 3.05$ Å above the aromatic plane. Only a small change (less than 1 kcal mol^{-1}, ca. 5%) for the interaction energy was calculated when the anion is moved all the way to the edge in either direction. In conclusion, the anion can be located at any point over the aromatic ring without losing too much of the interaction energy relative to the minimum (−14.1 kcal mol^{-1}). The analogous results for the sodium-benzene cation-π complex (Figure 7a, right) show that the energy loss during displacement in both directions is substantially higher (ca. 20%). This theoretical result explains the experimental observations in an analysis of the crystal structures in the CSD (crystal structure database) which shows more spreading in the location of the ion in anion-π versus cation-π complexes.[50]

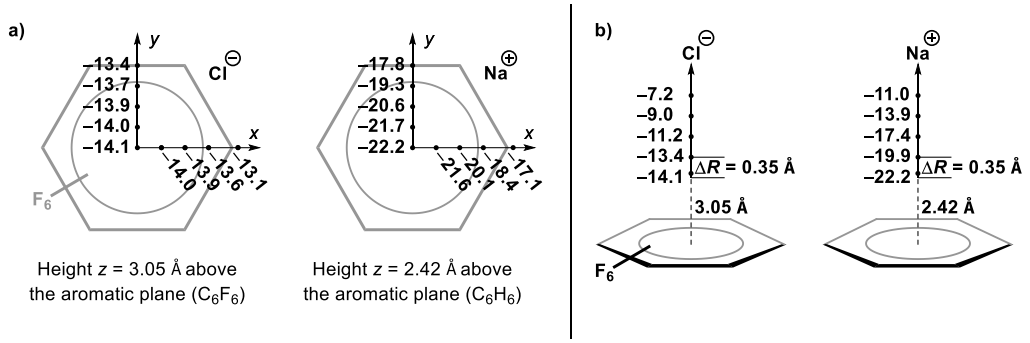

Figure 7: a) Left: Calculated interaction energies for the different positions of a chloride anion in the plane parallel to the C_6F_6 ring at z = 3.05 Å above the aromatic plane. Right: Calculated interaction energies for the different positions of a sodium cation in the plane parallel to the C_6H_6 ring at z = 2.42 Å above the aromatic plane. b) Schematic representation of the points along the main axis of symmetry (C_6, z-axis) in C_6F_6 (left) and C_6H_6 (right) where the interaction energies with Cl^- and Na^+, respectively, have been calculated. All energies were calculated with basis set superposition correction given in kcal mol^{-1}.

Additionally, figure 7b shows the interaction energies for both complexes with the corresponding ions at several points above the aromatic plane. As both electrostatic and polarisation effects dominate both types of interactions and depend on the distance between the ion and the aromatic plane, the interaction energies decrease considerably as the ion moves further away.

Strong experimental evidence for the existence of anion-π interactions in the gas phase[22,51–53], in solution[32,41,54–58] and in the solid state[52,53,59–63] was published as well, supporting the theoretical findings. The driving force behind all these recent developments targeting the concept of anion-π interactions is the vision to expand our repertoire of intermolecular interactions to create molecular functional materials of all sorts making use of this phenomenon. The following chapter will focus on the application of anion-π interactions in the context of organocatalysis and its advancements within the last decade by presenting a few selected examples to underline its importance.

1.1.3 Applications of Anion-π Interactions in Catalysis

1.1.3a Laying the Groundwork: Catalysing the KEMP Elimination

In 2013, MATILE *et al*. reported the first explicit example of anion-π catalysis from their pioneering studies.[32] The KEMP elimination was chosen as this reaction type has previously been used to develop conceptually innovative catalysts.[64–67] The reaction mechanism is rather simple with the rate-limiting step being the deprotonation of a carbon atom in benzisoxazole (**40**) with a generic base leading over one single anionic transition state to furnish nitrophenolate **41**, giving nitrophenole **42** after protonation during aqueous workup (Scheme 1a). MATILE and co-workers showed that π-acidic naphthalene diimide (NDI) systems catalyse the KEMP elimination by transition state stabilization (Scheme 1b). The key to sucessful anion-π catalysis was the covalent attachment of a carboxylate functional group on one side of the NDI moiety coupled with a solubilizing group on the other side (**43** in Scheme 1b).

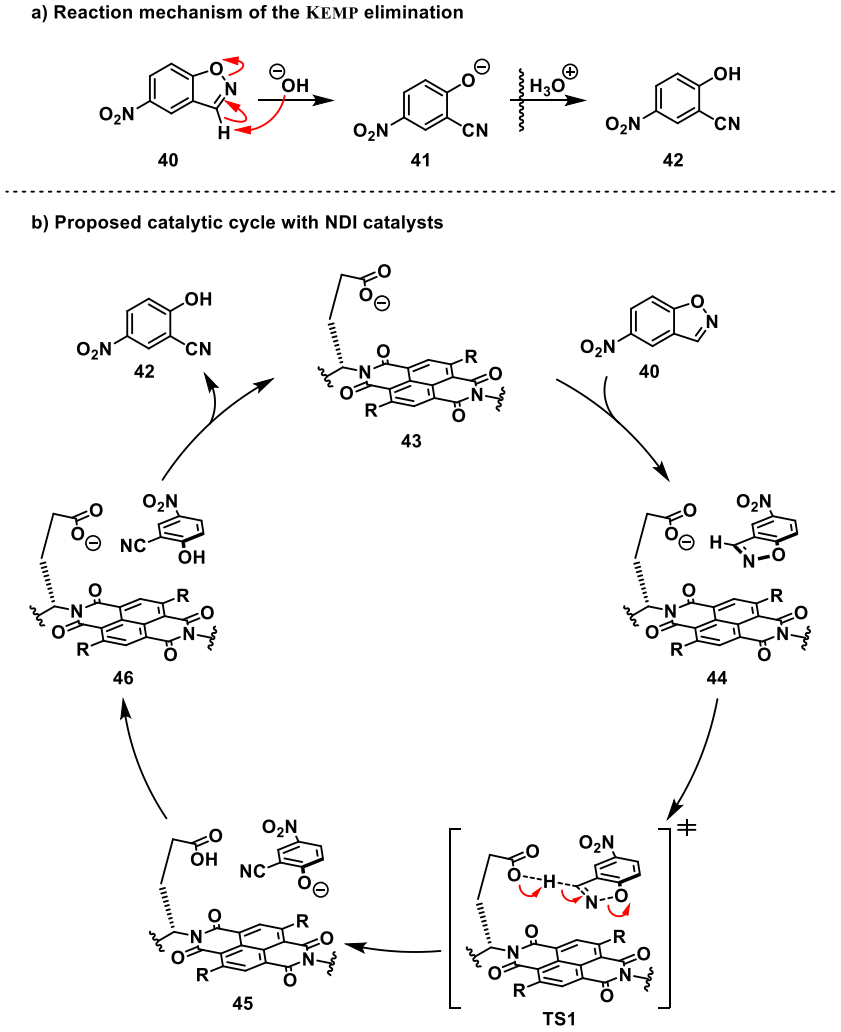

Scheme 1: Proposed catalytic cycle of the NDI-supported KEMP elimination with anion-π interactions. A carboxylate functional group is positioned on top of the NDI surface giving the general catalysts **43** to: (1) couple the deprotonation of substrate **40** with the onset of anion-π interactions for effective stabilization of the transition state **TS1** and (2) protonate the nitrophenolate in **45** to avoid product inhibition.

Once the substrate comes close to the π-surface area to form the catalyst-substrate complex **44** the carboxylate group detracts the proton of benzisoazole (**40**) leading over transition state **TS1** in which the negative charge is

translocated over five atoms from the oxygen of the carboxylate to the oxygen in benzisoxazole. This transition state is being stabilized *via* anion-π interactions with the NDI system. The forming electron-deficient nitrophenolate in **45** should still experience stabilization by anion-π interactions but is quickly protonated by the carboxylic acid in direct proximity giving the catalyst-product complex **46**. However, the neutral nitrophenole in **46** is now expelled since it is no longer electron deficient enough and the catalyst is retrieved in its initial state **43**.

The authors also reported that an increase in π-acidity of the NDI system correlates with transition state stabilization.[32] NDIs **47** and **48** (Figure 8a) were selected for their study because their π-acidity is very high. Unsubstituted NDI systems (such as **47** and **49**) already have a quadrupole moment near $Q_{zz} \approx +20$ B whereas similar NDIs with two cyano substituents in the core (**48**, $Q_{zz} \approx +39$ B) were amongst the strongest organic π-acids known so far.[52] The transition state stabilization by catalyst **47** was estimated from MICHAELIS-MENTEN analysis giving a rate enhancement of $k_{cat}/k_{non} = 7606$, a catalytic efficiency of $k_{cat}/K_M = 6.5 \cdot 10^{-3}$ $M^{-1}s^{-1}$ and a catalytic proficiency of $(k_{cat}/K_M)/k_{non} = 9.2 \cdot 10^4$ M^{-1}, which more than doubled for dicyano substituted NDI catalyst **48** to $(k_{cat}/K_M)/k_{non} = 2.0 \cdot 10^5$ M^{-1}, stabilizing the transition state by an extra 2.0 kJ mol^{-1}.

NDI **49** (Figure 8b) with its rigidified bridge between the carboxylate and the NDI system and pyrenebutyrate **50** (Figure 8b) featuring a negative quadrupole moment of $Q_{zz} \approx -14$ B both showed much slower product formation in control experiments. It was concluded that **49** is too rigid to attain the optimum geometry in the catalyst-substrate complex **44** and transition state stabilization with π-basic **50** is simply too ineffective showing that an electron deficient aromatic system is crucial for catalysis.[32] This was further solidified with control molecule **51** showing no catalytic activity.

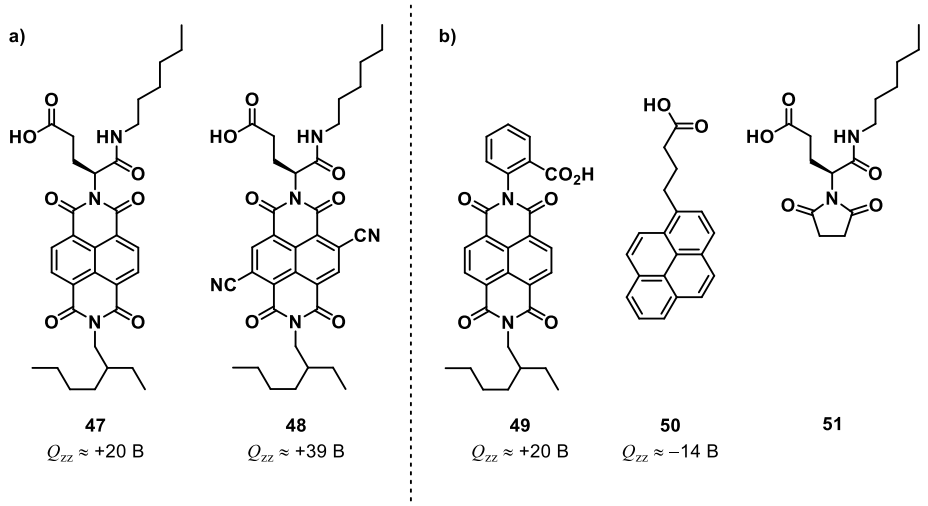

Figure 8: Chemical structures of the operational catalysts **47** and **48** together with control molecules **49**-**51**.

1.1.3b Anion-π Interactions for the Selective Acceleration of Enolate Addition Reactions

Shortly after, MATILE *et al*. targeted a biologically more relevant reaction with an anionic transition state: the addition of malonic acid half thioester (MAHT) **52** in its deprotonated form as malonate half thioesters (MHTs) to nitroolefins such as **53** as enolate acceptors (Scheme 2).[68] In solution, the (favoured) decarboxylation product dominates in the absence of any catalyst (Table 4, Entry 1) going over the non-planar transition state **TS2** (Pathway 1) with a rather localized negative charge. However, the tautomeric transition states **TS3** and **TS4** are planar featuring a delocalized negative charge by resonance and can undergo enolate addition before decarboxylation (Pathway 2).

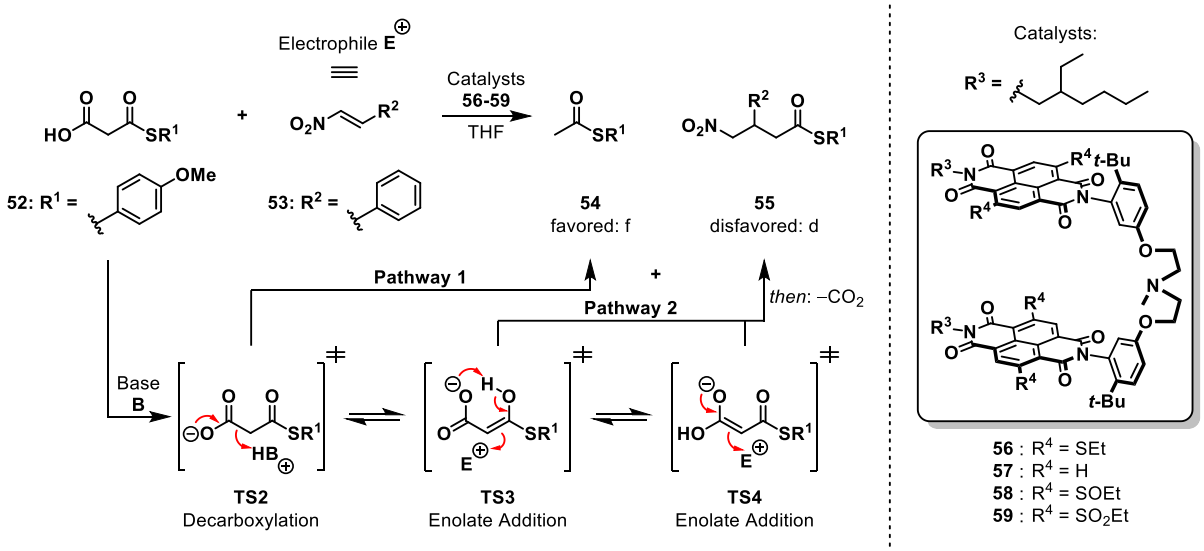

Scheme 2: Depiction of the possible reaction pathways for MAHT **52** with nitroolefin **53** under basic conditions in solution. Without any of the catalysts **56-59**, the decarboxylation product **54** dominates the product mixture. When catalysts **56-59** are introduced, the enolate addition precedes the decarboxylation and the enolate addition product **55** prevails.

MATILE and co-workers designed NDI-tweezer compounds **56-59**, in which both π-acidic surfaces are connected by an amine linker, able to replace triethylamine to deprotonate substrate **52**. Anion recognition *via* anion-π interactions (and π-π stacking interactions) were thought to influence the reaction outcome, heavily benefiting the enolate addition product **55** due to its planar transition states **TS3**/**TS4**. Thus, a systematic assessment of the contribution from anion-π interactions was envisioned. Catalyst **57** features an unsubstituted NDI moiety, whereas the aromatic core in catalysts **56, 58** and **59** was equipped with either sulfide donors or sulfoxide and sulfone acceptors to alter the catalysts π-acidity, expressed in their LUMO (lowest unoccupied molecular orbital) energies (Table 4). An increased π-acidity correlates with lower LUMO energies and table 4 shows how the product distribution $\eta^{d/f}$ (yield of naturally disfavoured product **55** divided by yield of favoured product **54**) shifts towards the disfavoured enolate addition product **55** with higher π-acidity of the catalyst (Table 4, Entries 2-5) accelerating this pathway while deceleration was observed for the direct decarboxylation towards normally favoured product **54**. This effect is even more pronounced at lower reaction temperatures (Table 4, Entries 6-9) where selectivity perfectly followed the π-acidity established: the product distribution increased from $\eta^{d/f} = 3.1$ for NDI tweezer **56** with electron donating sulfide groups to $\eta^{d/f} = 3.8$ for unsubstituted tweezer **57** and $\eta^{d/f} = 5.7$ and $\eta^{d/f} = 7.3$ for the catalysts **58** and **59** with electron-withdrawing sulfoxide and sulfone groups, respectively.[68]

Table 4: Selected conditions for the reaction shown in scheme 2. Concentration used for substrate **52**: 200 mM; concentration used for substrate **53**: 2.00 M. η^f: Yield of favoured product **54**; η^d: Yield of disfavoured product **55**. The product distribution $\eta^{d/f} = \eta^d/\eta^f$ shows how the equilibrium shifts towards the disfavoured enolate addition product **55** with increasing π-acidity ($E_{LUMO,C}$) of the catalyst used.

Entry	Catalyst (10 mol-%)[a]	$E_{LUMO,C}$ [eV]	T [°C]	t [h]	η^d [%]	η^f [%]	$\eta^{d/f}$ [%]
1	-[b]	-	23	1.5	36	62	0.6
2	**56**	–3.9	23	12	50	48	1.0
3	**57**	–4.2	23	15	48	51	0.9
4	**58**	–4.4	23	12	59	36	1.6
5	**59**	–4.6	23	12	59	31	1.9
6	**60**	**-**	**20**	-[c]	**80**	**18**	**4.4**
7	**56**	–3.9	5	40	71	23	3.1
8	**57**	–4.2	5	40	77	20	3.8
9	**58**	–4.4	5	40	80	14	5.7
10	**59**	–4.6	5	40	80	11	7.3
11	**60**	**-**	**7**	-[c]	**86**	**9**	**9.6**

[a] Relative to substrate **52**. [b] NEt_3 (10 mol-%) was added instead of a catalyst. [c] Reaction was run until full conversion was achieved. No detailed information on the reaction time was given.

Even though NDI tweezer catalysts **56**-**59** showed great potential, the amine linker between the π-acidic surfaces allows for too much flexibility. Deprotonation of the substrate **52** can lead to an ion pair with the conjugate ammonium cation, positioning the malonate half thioester rather far away from the π-acidic surfaces. To harvest the full potential of anion-π interactions, MATILE *et al*. designed NDI catalyst **60** with a rigid LEONARD turn as part of the amine linker (Figure 9a).[69] A LEONARD turn consists of three tetrahedral atoms in a half-chair constitution which are attached to an aromatic surface on one end, forcing the atom on the other end to be positioned directly on top of the *ipso* atom of the aromatic ring.[69,70] This was meant to guarantee that the deprotonated substrate is located very closely and directly on top of the aromatic system leading to enhanced stabilization of the transition state **TS5** *via* maximized anion-π interactions (Figure 9b). In fact, NDI catalyst **60**, equipped with sulfone groups, showed remarkable selectivity for the intrinsically disfavoured enolate addition product **55** with $\eta^{d/f} = 4.4$ at 20 °C and $\eta^{d/f} = 9.6$ at 7 °C (Table 4, Entries 6 and 11).[69]

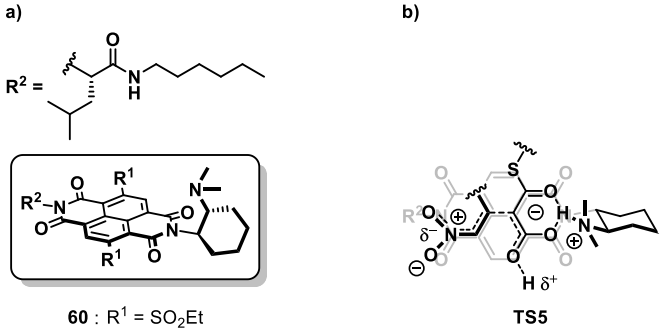

Figure 9: a) Structure of catalyst **60** featuring an amine linker with integrated LEONARD turn. b) Proposed transition state **TS5** for the enolate addition of malonate half thioester to nitroolefin **53**. The LEONARD turn should place the malonate close to the π-surface.

1.1.3c Asymmetric Anion-π Catalysis: Stereoselective Enamine Addition to Nitroolefins

The first application of asymmetric anion-π catalysis targeted the proline catalysed addition of enamines (originating from aldehyde **61**) to nitroolefin **53** (Scheme 3a). The influence of anion-π interactions on the stereochemistry of the product **62** was investigated.[71,72] Originally, the JØRGENSEN-HAYASHI catalyst **63** was used for this reaction (Scheme 3b).[73–76] However, WENNEMERS *et al*. showed that a strategically positioned carboxylic acid in bifunctional catalyst **64** changed the rate-limiting step from nitronate protonation with the JØRGENSEN-HAYASHI catalyst **63** to the preceding formation of the C–C bond.[77,78] Based on this, MATILE *et al*. once again installed NDI moieties as π-acidic surfaces in between the proline (blue) and the carboxylic acid (orange) in WENNEMERS **64** to generate new anion-π catalysts **65-67** (Scheme 3b).[71,72] The proline derivative was placed at one side for enamine formation, a bit far away from the NDI to leave space for the nitroolefin to intercalate and keep the iminium intermediate in **TS7** away from the repulsive π-acidic surface. The carboxylic acid on the other side is connected to the NDI unit using a LEONARD turn to lead nitroolefin **53** as close as possible to the π-acidic surface *via* hydrogen bonds for additional anion-π stabilization. Proposed transition state geometries for the C–C bond formation (**TS6**) and the nitronate protonation (**TS7**) above these π-acidic NDIs are shown as well (Scheme 3a). The former is believed to be part of the rate-limiting step due to the carboxylic acid in the right distance stabilizing the nitronate intermediate in **TS7**.

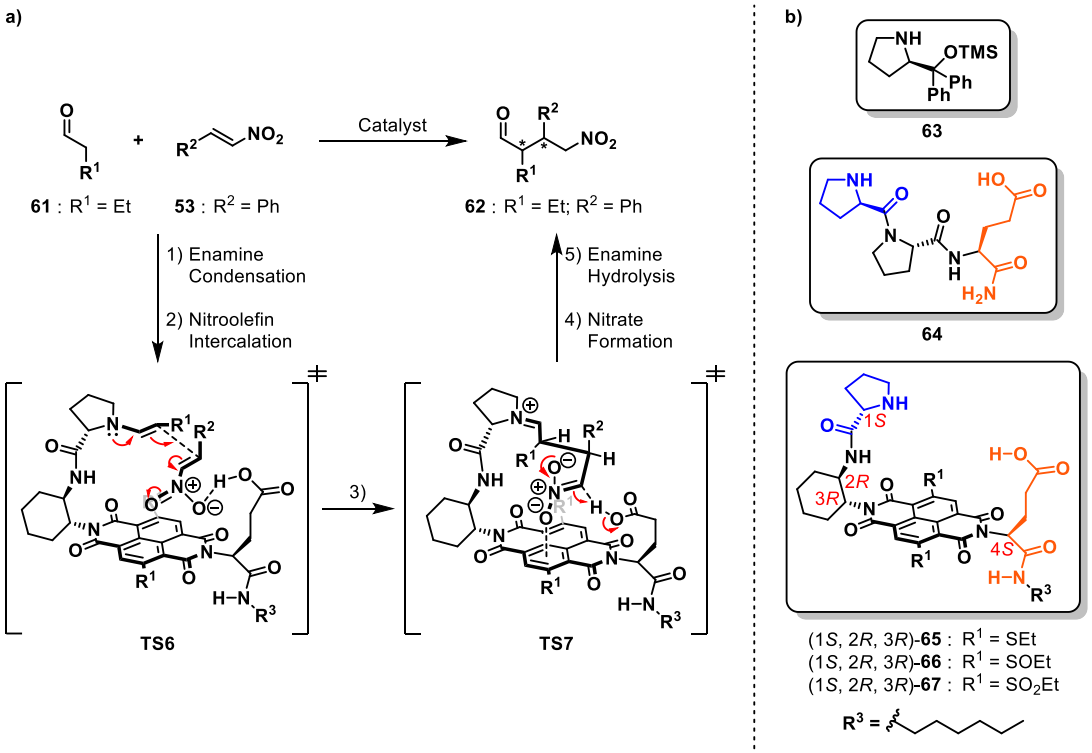

Scheme 3: a) Depiction of the enamine addition reaction of aldehyde **61** to nitroolefin **53** with anion-π catalysts **65-67**. Possible transition state geometries for the enamine addition (**TS6**) and the nitronate protonation (**TS7**) are shown. b) Structures of JØRGENSEN-HAYASHI and WENNEMERS catalysts **63** and **64**, respectively, and the general structure of the catalysts **65-67** developed by MATILE and co-workers. The fourth stereogenic center (4*S*) never changes. The following deviations on stereogenic centers have been tested: (1*S*, 2*R*, 3*R*)-, (1*R*, 2*R*, 3*R*)-, (1*S*, 2*S*, 3*S*)- and (1*R*, 2*S*, 3*S*)-configuration for **65-67**. Sulfide catalysts of the type **65** feature two extra stereogenic centers on the sulfur due to the lone-pair electrons. Their configuration remained unknown beyond circular dichroism (CD) measurements indicating *syn* or *anti* configuration.

The following conclusions were made: (1) the reaction rate increased with increasing π-acidity of the catalyst used, that is going from sulfides in **65** *via* oxidation to their electron withdrawing sulfoxides in **66** and sulfones in **67**,[71,72] an already mentioned strategy that has evolved as a unique approach to investigate the importance of π-acidity with minimal changes to the global structure. (2) Increasing π-acidity of the catalyst (from **65** to **67**) led to increased enantioselectivities. (3) "Matched" geometries around the π-acidic surface were important for diastereoselectivity but no trend in its relationship with the π-acidity of stereoisomeric catalysts could be observed.

In this series of catalysts, *anti*-(1*R*, 2*S*, 3*S*, 4*S*, 5*S*, 6*R*)-**65** (Figure 10, left) showed the best results overall with the most significant rate enhancement coupled with a diastereomeric ratio of *dr* = 10.9:1 and an enantiomeric excess of *ee* = 82% for the *syn* product of **62**.[71] In a separate study, the phenylsulfoxide derivatives of the catalysts were investigated and *syn*-(1*R*, 2*S*, 3*S*, 4*S*, 5*R*, 6*R*)-**68** (Figure 10, middle) reached even better results (*dr* = 26:1, *ee* = 91%).[72]

The enantioselectivity could be improved even further by utilizing the expanded surface of perylene diimide (PDI) compounds which were found to be of suitable length to accommodate extended anionic transition states. The quadrupole moment of simple PDIs with *N*-phenyl substituents was calculated to be Q_{zz} = +23.2 B[79], which is slightly higher in magnitude than similar NDIs with Q_{zz} = +20 B.[52] However, PDIs were of special interest because their 2,5,8,11- or "ortho"-substituted tetracyano derivatives are not only synthetically accessible compared to tetracyano-substituted NDIs (Q_{zz} = +55.5 B),[41] but they also surpass their quadrupole moments heavily with Q_{zz} = +70.9 B.[79] The enantioselectivity obtained for the *syn* product of **62** with PDI catalyst **69** (Figure 10, right) was with *ee* = 96% the highest observed thus far with a diastereomeric ratio of *dr* = 25:1.[79]

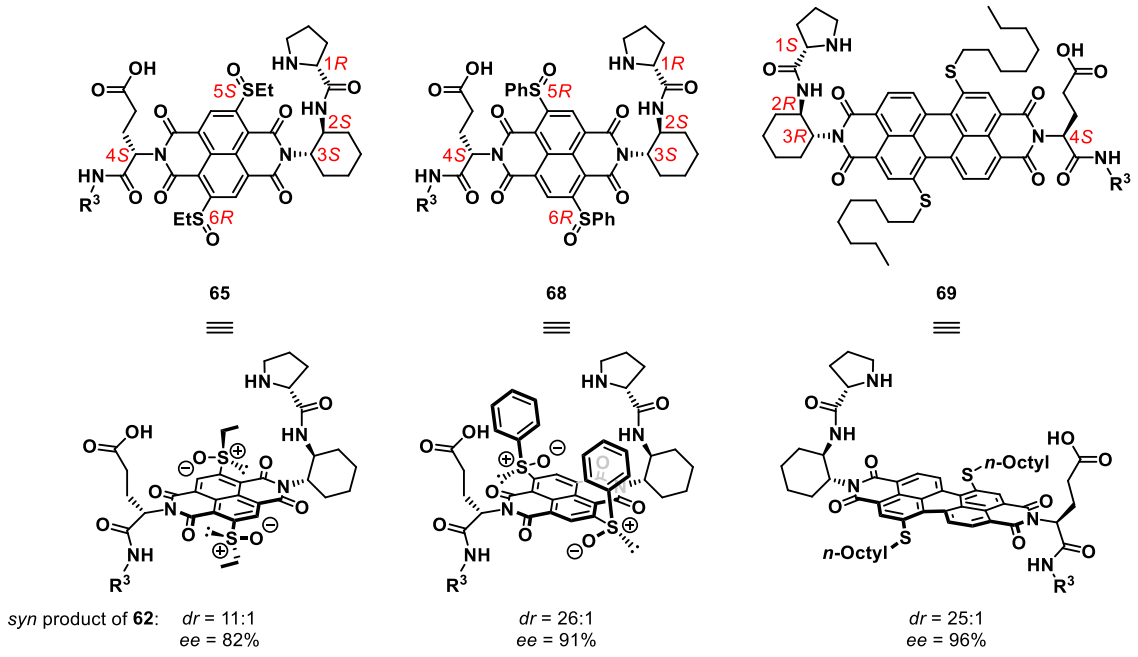

Figure 10: Examples for NDI (**65** and **68**) and PDI (**69**) catalysts investigated for enamine addition to nitroolefins.

1.1.3d Anion-π Catalysis in Epoxide-Opening Ether Cyclizations and Autocatalysis

All examples for anion-π catalysis so far featured multifunctional π-acidic catalysts with additional activating groups. MATILE *et al*. were interested in showcasing anion-π interactions as the primary driving forces. Thus, anion-π catalysis was explored on intramolecular epoxide-opening ether cyclizations with 4,5-epoxyalcohols such as **70** (Scheme 4a).[80] The selectivity for the possible tetrahydrofuran (THF) and tetrahydropyran (THP) derived products **71** and **72**, respectively, is described by the BALDWIN rules. These predict that the 5-*exo-tet* transition state **TS8** should be favoured over the 6-*endo-tet* transition state **TS9**, leading to preferential formation of THF product **71** when catalysed by conventional BRØNSTED acids.[81]

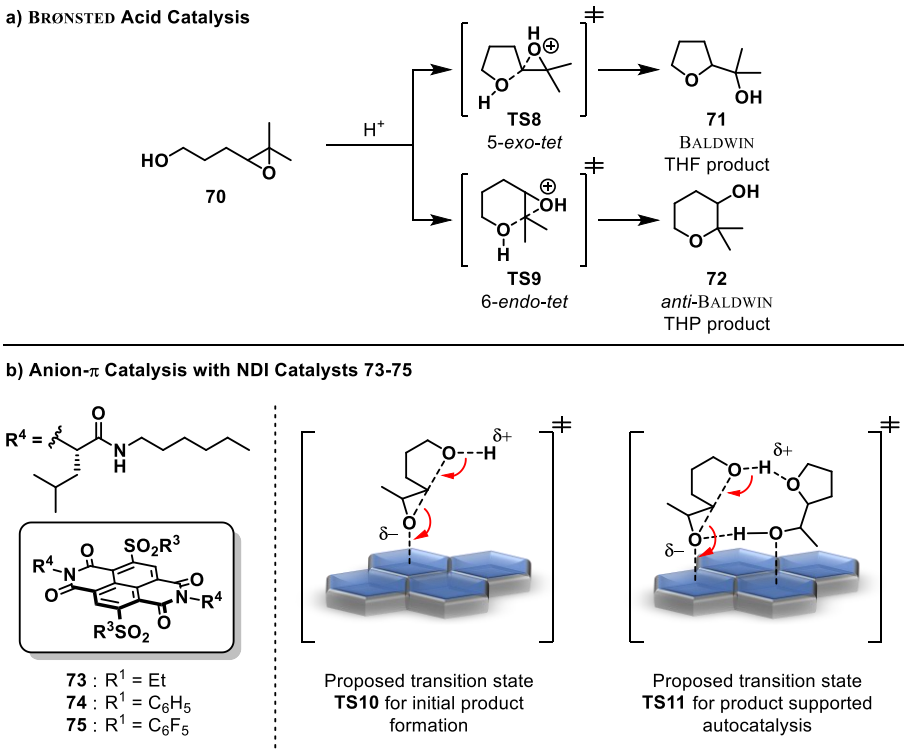

Scheme 4: a) BRØNSTED acid catalysed epoxide-opening ether cyclisation with 5-*exo-tet* transition state **TS8** leading to THF product **71** (BALDWIN product) and with the disfavoured 6-*endo-tet* transition state **TS9** leading to THP product **72** (*anti*-BALDWIN product). b) Proposed transition state **TS10** for anion-π catalysis of the same reaction with NDI catalysts **73-75** and proposed transition state **TS11** for the experimentally observed autocatalysis.

The MATILE group was interested in uncovering new selectivities by introducing anion-π catalysts such as NDI compounds **73-75** to the reaction. However, the BALDWIN product still prevailed: At 20 mol-% **73** in CD_2Cl_2, they reported full conversion after 8 days with the THF derivative **71** as the sole product in 78% yield. The rate enhancement was calculated to be $k_{cat}/k_{non} = 256$ following the proposed initial transition state **TS10** (Scheme 4b). Using the same catalyst, autocatalysis was observed. This hypothesis was supported by the increased initial rates of the substrate conversion with increasing concentration of the product at the start of the reaction. A control experiment confirmed that product **71** by itself did not accelerate the reaction. However, the addition of nitrate (NO_3^-) anions inhibited the anion-π autocatalysis, arguably due to interference from strong anion-π interactions between nitrate and the catalysts. Both controls supported the idea that anion-π interactions were indeed crucial for catalysis. A computed transition state for the autocatalytic process was provided as well (Scheme 4b, **TS11**) in which the substrate **70** and product **71** form a noncovalent macrocycle *via* hydrogen bonds while both are

exhibiting anion-π contacts with the π-acidic surface. The rate enhancement for the autocatalytic process with catalyst **73** was also determined to be k_{ac}/k_{non} = 1764 (k_{ac} = reaction rate of autocatalysis). Catalyst **74** with phenyl groups on the side and similar π-acidity gave slightly worse results: k_{cat}/k_{non} = 220; k_{ac}/k_{non} = 1514 and 69% yield for the BALDWIN product **71**. The best result was obtained with pentafluorophenyl groups attached on the sulfones (NDI catalyst **75**): k_{cat}/k_{non} = 229; k_{ac}/k_{non} = 5100 and quantitative yield for the BALDWIN product **71**.

While being difficult to achieve, a separate study two years later revealed that complete *anti*-BALDWIN selectivity was realized in just a few cases as well using NDI catalyst **75** (Scheme 4b), but this seemed quite dependent on substrate preorganization.[82] 3,4-Epoxyalcohols such as **76** and **80** with two geminal methyl groups in C-4 position were used for the formation of smaller rings with *anti*-BALDWIN selectivity (Scheme 5). Similar substrates without methyl groups showed no conversion at all. This result indicated contributions from an S_N1-type reaction pathway.

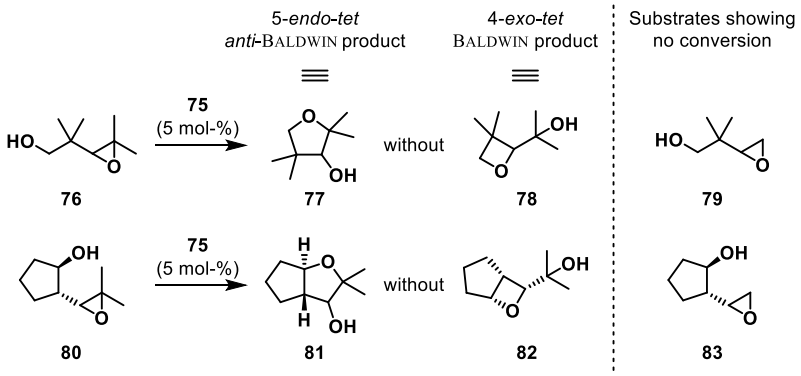

Scheme 5: 3,4-Epoxyalcohols with geminal methyl groups in C-4 position gave *anti*-BALDWIN products **77** and **81**. Substrates **79** and **83** showed no conversion with NDI catalyst **75**.

Furthermore, anion-π catalysis with NDI catalyst **75** was also applied to epoxide-opening polyether cascade cyclizations forming up to tetramers (Scheme 6).[83]

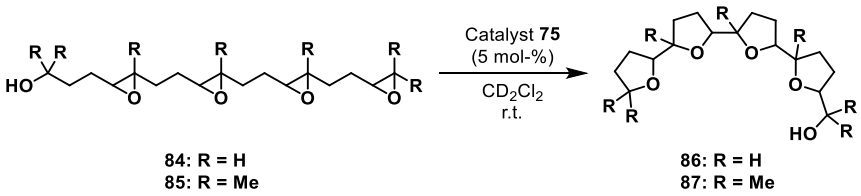

Scheme 6: Epoxide-opening polyether cascade cyclization of **84** and **85** into **86** and **87**, respectively, realized by anion-π catalysis using NDI catalyst **75**.

The examples given in this chapter for the application of anion-π catalysis in synthetic organic chemistry represent only a fraction of the developed methods so far and other reactions and catalysts have been explored.[79,84–96] However, the incorporation of functional π-acidic scaffolds, like the NDI system, in supramolecular cage compounds remains scarce and explicit anion-π catalysis has not been reported within them so far.[97–101] Building up molecular cage compounds with cavities exhibiting multiple binding sites for anion-π interactions as potential enzyme mimics is a promising field left to be explored to uncover new reactivities. The following chapters will focus on how scaffolds for anion-π interactions can be integrated in positively charged supramolecular cage compounds of either fully covalent nature or as part of coordination cages.

1.2 Fully Covalent Organic Cages

1.2.1 Early Macrocycles: Coronands, Cryptands and Spherands

The significance of synthetically constructed enzyme mimics has been acknowledged in 1987 with the Nobel Prize of Chemistry being awarded to CRAM, LEHN and PEDERSEN for the "syntheses of molecules that mimic important biological processes". PEDERSEN described methods for the construction of cyclic polyethers of varying sizes, which he named crown ethers, also known as *coronands*. Their complexes are named *coronates*. These compounds showed selectivity for the binding of potassium cations. The complexes are being formed due to multiple and cooperative ion-dipole interactions between the cation and the negatively charged oxygen atoms of the polyether.[102,103] With the most prominent crown ether being 18-crown-6 (**88,** Scheme 7a), which is able to bind potassium cations with a binding constant of $K_a = 1.1 \bullet 10^6$ M^{-1} in MeOH.[104] Inorganic salts could be solubilized in hydrophobic solvents by this complexation making **88** an ideal phase transfer catalyst.[105] The complexation leads to suppression of ion-pairing which means that the anions become "naked" nucleophiles and, therefore, more reactive. Because of these two effects, the presence of **88** accelerates various substitution reactions in organic media and is still used in modern organic chemistry.[106,107]

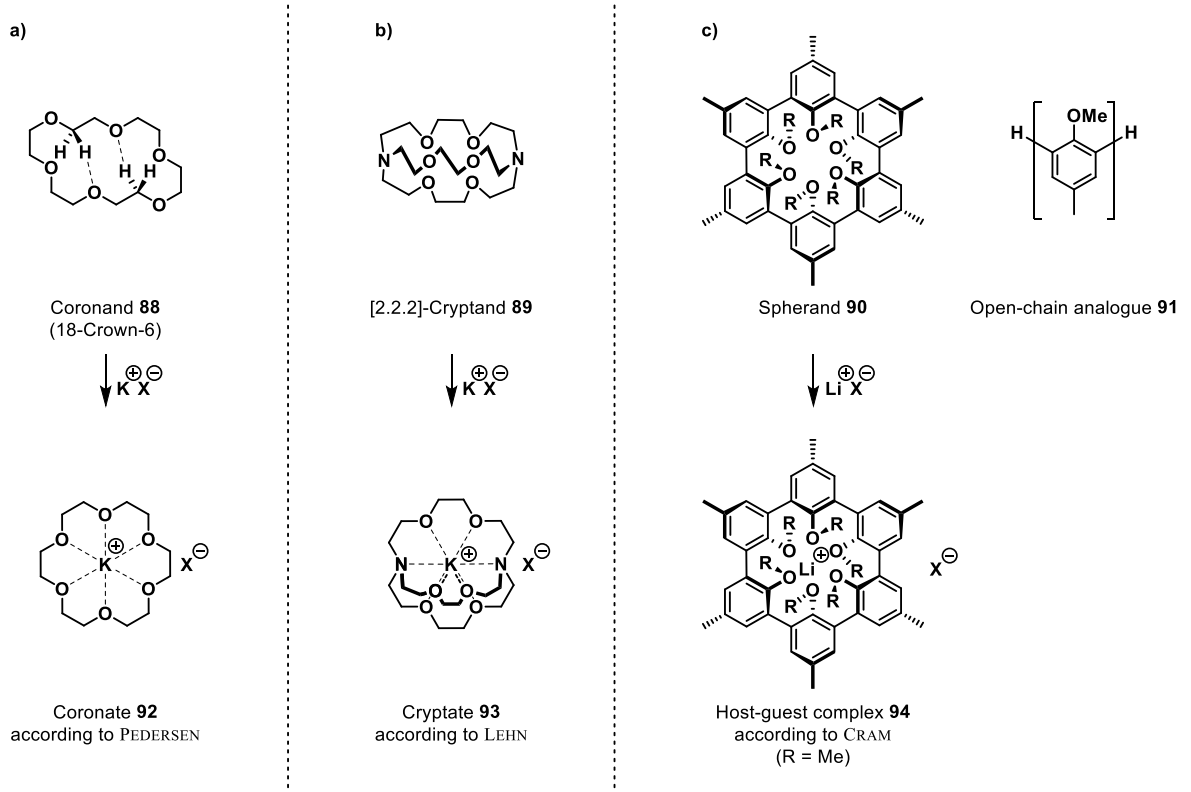

Scheme 7: a) 18-Crown-6 (**88**) and its potassium cation complex **92** as examples for coronands and coronates according to PEDERSEN. b) [2.2.2]-Cryptand (**89**) and its potassium cation complex **93** as examples for cryptands and cryptates according to LEHN. c) Spherand **90** and its lithium cation host-guest complex **94** according to CRAM.

Inspired by this, LEHN designed bicyclic compounds of this type to further increase the number of binding sites and increase preorganization.[108] These *cryptands*, as he termed them, allow for even higher affinity than their *coronand* counterparts. He named their complexes *cryptates*.[109] A well-known example is the [2.2.2]-cryptand **89** (Scheme 7b) which exhibits a binding constant of $K_a = 2.6 \bullet 10^{10}$ M^{-1} in MeOH for potassium cations rendering it an even better binder than **88**.[110]

Later, CRAM coined the term *Principle of Complementarity* which states that "in complexes of substantial stability, the binding sites of host and guest components must simultaneously contact and attract one another."[111] For strong binding, this effect must outweigh the solvation of guests by solvent molecules which, for example, is the case for the potassium complexes of coronand **88** and cryptand **89** which both display *induced fit* behaviour as shown in scheme 7. Prior to complexation, both compounds tend to fill their own cavities with the methylene groups of the ether chains. This is shown in their respective crystal structures as well.[112–115] In solution, many more conformers will be able to coexist beside each other and upon complexation the most stable conformation is going to prevail. In any case, CRAM argued that this degree of freedom would result in an entropic barrier that needs to be overcome for the complexation of cations, rendering the potential binding constants lower than for hosts that are more rigid by themselves. He introduced the *Principle of Preorganization* at the same time which states that "the more highly hosts and guests are organized for binding and for low solvation *prior* to their complexation, the more stable will be their complexes." To prove the hypothesis that binding constants would increase with this higher order of preorganization, CRAM *et al*. synthesized specific molecules which they termed *spherands*. For instance, spherand **90** (Scheme 7c) binds Li^+ and Na^+ much better than its open-chain analogue **91**. The difference in Gibbs free energy ΔG is more than 17 kcal mol^{-1} for the Li^+ and more than 13 kcal mol^{-1} for the Na^+ complexes.[111] The binding constants of Li^+ and Na^+ with spherand **90** in D_2O saturated $CDCl_3$ were determined to be $K_a = >7 \bullet 10^{16}$ M^{-1} and $K_a = 1.2 \bullet 10^{14}$ M^{-1}, respectively, while there was no binding observed for potassium cations due to their increased size and the very rigid binding pocket not being able to adjust.[116] For comparison, the binding constants for the open-chain analogue **91** and either of the cations was determined to be $K_a = <2.5 \bullet 10^4$ M^{-1}. Even though high rigidity leads to very good selectivities and strong binding, it also makes these hosts less responsive to environmental stimuli. In contrast, the binding pockets of enzymes rely on their flexibility and *induced fit* behaviour for efficient catalysis.

1.2.2 Dynamic Covalent Chemistry (DCvC)

The coronands, cryptands and spherands discussed so far were synthesized using classic, kinetically controlled substitution reactions to form robust bonds. Those reactions ideally provide the irreversible formation of one single product in high yield. A more recent strategy for the construction of complex molecular scaffolds involves thermodynamically controlled and, therefore, reversible reactions. Now, while *supramolecular chemistry* is based on multiple weak noncovalent intermolecular forces which enable systems to adjust to each other relatively fast, *dynamic covalent chemistry* (**DCvC**) introduces dynamic features by making use of strong, but reversible, bond-forming reactions which enables error correction during equilibration between multiple possible products.[117] Both of these fields are part of *constitutional dynamic chemistry* (**CDC**) as it was defined by LEHN.[118]

DCvC should not be considered a synonym to *dynamic combinatorial chemistry* (**DCC**). This is a term that was defined as "combinatorial chemistry under thermodynamic control; that is, in a *dynamic combinatorial library* (**DCL**) all constituents are in equilibrium".[119] The requirement for this is that library members (products in equilibrium) are enabled to transform into each other by reversible chemical processes. Reversible and covalent bond-forming reactions are used in **DCvC**, whereas *supramolecular chemistry* utilizes noncovalent interactions for this, including metal-ligand coordination. Both are sub-categories of *dynamic combinatorial chemistry* (**DCC**).

The reversible nature of the reactions used in **DCvC** allows for the system to reach thermodynamic minima at equilibrium under certain reaction conditions. The reaction types, however, also need to meet a few requirements:

(1) the lifetime of the reversible bond should be within 1 ms < τ < 1 min. This will make sure that the bonds are stable enough to detect and possibly isolate complex molecular structures while still exhibiting dynamic behaviour.[120] (2) Mild reaction conditions are generally preferred for the situation when derivatization by introducing other functional groups becomes interesting. (3) The reversible bond-forming reaction should give an easy option to stop the process. Common methods involve pH control, catalyst removal or simply the removal of the product mixture from the equilibrium *via* kinetic trapping, for example through reduction of reversible imine bonds to kinetically trapped amine bonds.[117]

A diverse range of reaction types is known that can be applied to **DCvC** to form fully covalent supramolecular cages with only a few being mentioned in the following section.[117,121] Those reactions can usually be assigned to one of the two following types: (1) exchange reactions which involve interchanging substituents between substrates while forming identical types of bonds and (2) reversible formation of new covalent bonds. Representative examples with dynamic covalent bonds feature alkyne metathesis for C≡C bonds in the presence of a catalyst (Scheme 8a)[122–127] and acetal exchange for C–O bonds (Scheme 8b).[128,129] Disulfide exchange for S–S bonds belongs to one of the earliest examples of reactions that have been investigated towards **DCvC** (Scheme 8c).[130,131] Moreover, boronic acid self-condensation and condensation with diols to boronic esters (Scheme 8d) has been applied in the development of 2-D macrocycles as well as 3-D cages and organic frameworks.[132] And there are many more reactions that are worth discussing and being investigated in more detail.[117] However, for this work we will focus more on the developments in regards to imine condensation (Scheme 8e).

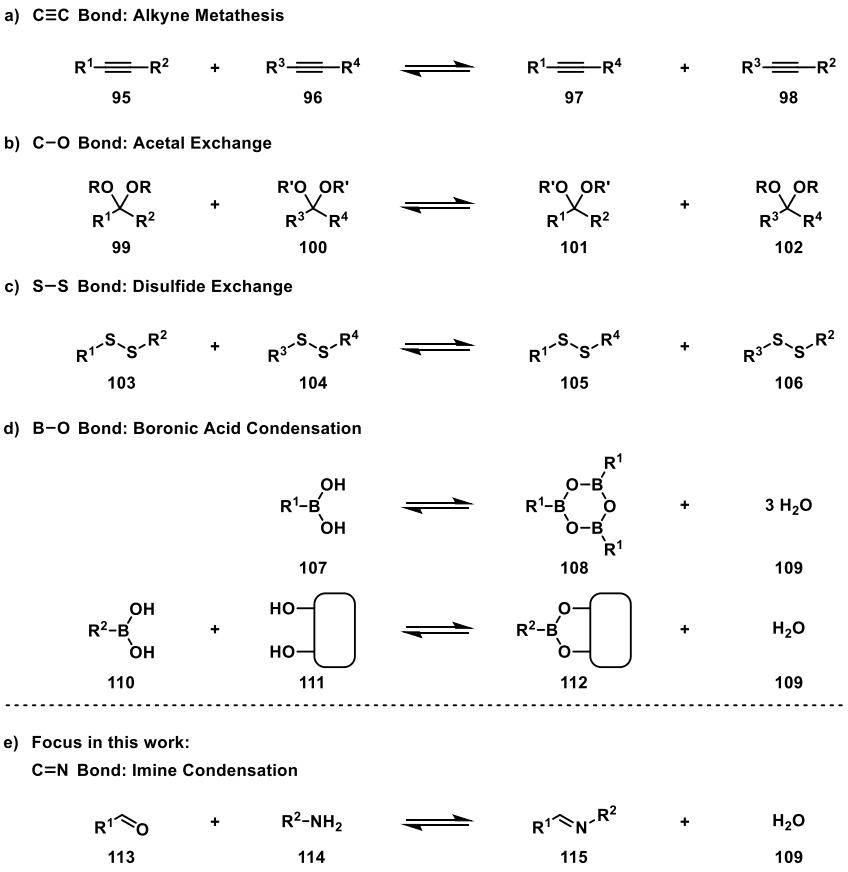

Scheme 8: Reaction type examples for **DCvC**. (1) Exchange reactions: a) Alkyne metathesis, b) acetal exchange and c) disulfide exchange. (2) Reversible formation of new covalent bonds: d) Boronic acid condensation and e) imine condensation.

1.2.3 Organic Cages Based on Imine Bonds

1.2.3a The Imine Condensation

The reversible reaction between carbonyl groups **116** ($R^1R^2C{=}O$; aldehydes or ketones) and amines **118** (R^3-NH_2) generates condensation products with the general formula $R^1R^2C{=}NR^3$ (**123**, Scheme 9). These are known as imines or "SCHIFF bases" (for R^3 = alkyl or aryl, but not hydrogen), named after the german chemist HUGO SCHIFF who discovered this reaction in 1864.[133] A general mechanism under acidic conditions with catalytic amounts of acid is depicted in scheme 9.[134–139] After protonation of the carbonyl **116**, the nucleophilic amine **118** attacks the newly generated carboxonium intermediate **117** at its electrophilic carbon atom. After deprotonation, hemiaminal **120** is formed. Protonation of its hydroxyl group leads to the oxonium intermediate **121**. Removal of water with the help of the lone-pair electrons of the amine group in **121** followed by deprotonation furnishes the imine condensation product **123**.

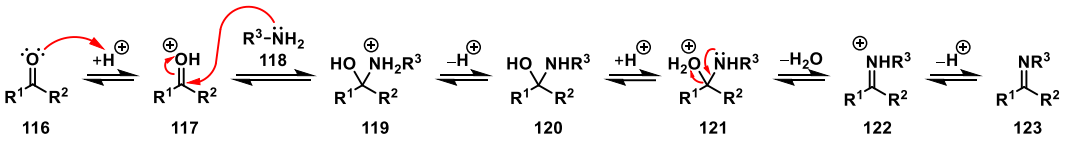

Scheme 9: Imine condensation mechanism under acidic conditions.

The equilibrium can be driven forwards or backwards. For example, removal of water as it is formed can be achieved physically as an azeotrope using a DEAN-STARK apparatus or chemically with the addition of a drying agent such as $MgSO_4$ or molecular sieves to drive the reaction forward. Adding excess water to an imine, however, results in hydrolysis of the imine to give the corresponding precursor amine and carbonyl compounds. Reductive amination, that is the reduction of the reversible and labile C=N bond, is used to remove imines from the equilibrium by kinetically trapping them as substituted amines. However, it would eliminate the reversibility that allows for the imine bond to be formed and cleaved repeatedly. The reversibility is what makes imines so useful in the context of *dynamic covalent chemistry* (**DCvC**) as it enables elements of "proof-reading" and "error-checking" within a system with multiple possible products.[140] When given enough time, the thermodynamically most stable product will prevail, after initial formation of kinetic products.

Imine condensation with all its facets has allowed for the formation of many different cage structures and molecular capsules *via* molecular self-assembly.[141–148] Molecular self-assembly, as originally defined by LEHN in 1995, is "a special type of synthetic procedure where several reactions between several reagents occur in one experimental operation to yield the final covalent structure; it is subject to control by the intramolecular conformational features of intermediates and by the stereochemistry of the reaction(s); the efficient assembly of a covalent structure may require that the connecting reaction(s) be reversible so as to allow searching for the final structure."[149]

The next section will introduce the nomenclature of fully covalent organic cages.

1.2.3b Nomenclature for Fully Covalent Organic Cages

The JELFS group has defined a nomenclature for the classification of fully covalent organic cages in 2017 to enumerate 20 of the most probable topologies with 12 having been synthetically accessed thus far.[150] For the context of this work, the most prevalent two will be discussed. For the nomenclature, the following criteria have been applied: (1) The topology must be a polycyclic cage molecule with the potential for a 3D internal cavity which excludes simple macrocycles. (2) It must be possible to form the topology from two different components in certain ratios through *dynamic covalent chemistry* (**DCvC**). (3) The components can only be ditopic (**Di**), tritopic (**Tri**) or tetratopic (**Tet**). Examples for common building blocks for imine condensation (Figure 11a) have been classified as such based on how many amine or aldehyde functional groups are present in those structures. (4) It is presumed that the building blocks exhibit a C_n symmetry axis with n being the number of reactive end groups and (5) only higher symmetry structures are included which are relatable to Platonic or Archimedean solids.[150–152]

According to JELFS *et al*., each structure is then labeled as $\mathbf{X}_p^m\mathbf{Y}^n$ where **X** and **Y** are the two different building blocks. **X** and **Y** are labelled as **Di** for ditopic, **Tri** for tritopic and **Tet** for tetratopic. The first building block mentioned (**X**) is the one with the highest amount of reactive end groups. If the underlying topology relates to a polyhedron, this building block will construct its vertices. The second building block (**Y**) can have a number of reactive end groups less than or equal to the first building block (**X**). If they are equal for **X** and **Y**, it is arbitrary which compound is denoted as **X** or **Y**. The superscripts m and n stand for the number of each building block within the structure for **X** and **Y**, respectively. The subscript p stands for the number of building blocks **Y** through which two building blocks of **X** are connected and is not written out if $p = 1$.[150]

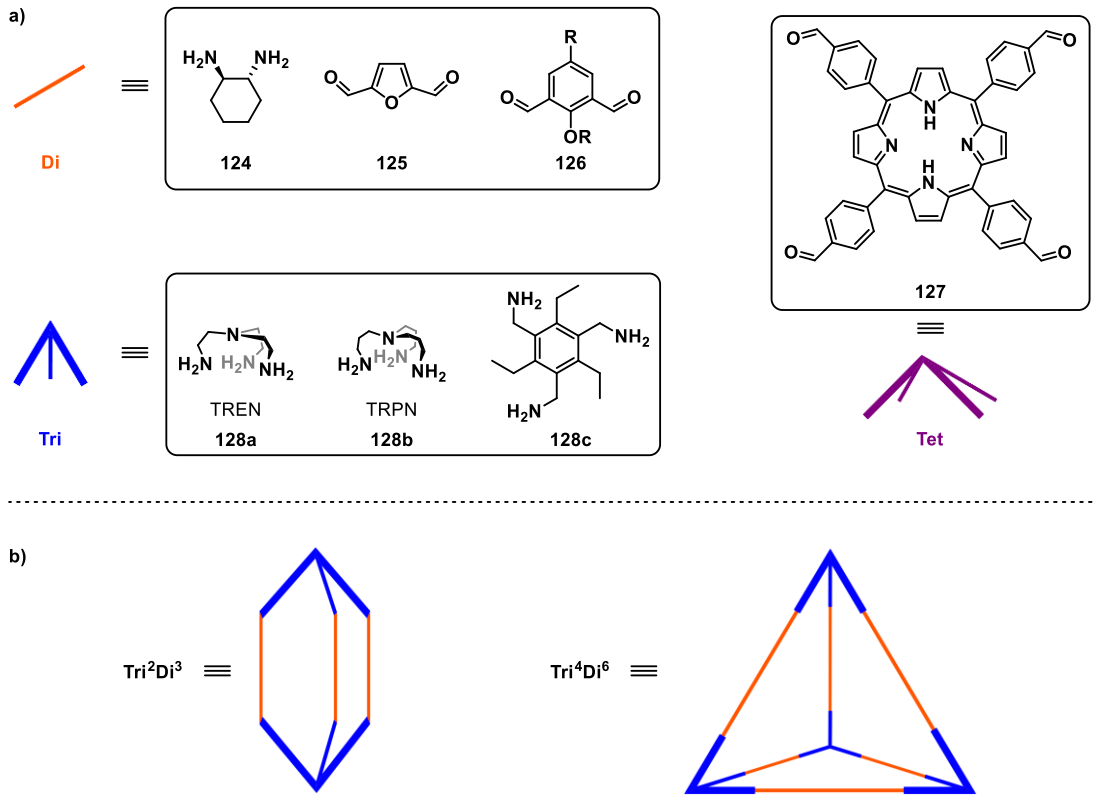

Figure 11: a) Examples for ditopic (**Di**), tritopic (**Tri**) and tetratopic (**Tet**) amine and aldehyde building blocks for the synthesis of organic cages *via* imine condensation. b) Examples for the tritopic + ditopic topology family.

For example, the combination between triamines and dialdehydes in a 2:3 (or 4:6) ratio can either lead to cryptand-type **Tri^{2}Di^3** cages or **Tri^{4}Di^6** cages of pseudo-tetrahedral geometry (Figure 11b). This nomenclature can be applied to other building blocks with different functional groups, suitable for the construction of covalent cage compounds *via* **DCvC**. The next section will show a few self-assembled covalent organic cages based on imine condensation between subcomponents such as triamines and dialdehydes.

1.2.3c Recent Developments of Cages Formed by Imine Condensation

Several **Tri^{2}Di^3** type cages, also known as cryptands, and their cryptate complexes with different cations and anions, were investigated relatively early on and obtained by formation of multiple imine bonds.[153–162] In the last two decades, more cages of the type **Tri^{4}Di^6** have been reported, which have also been categorized as *porous organic cages* (**POCs**), a class of self-assembled molecules with bigger cavities than **Tri^{2}Di^3** cages and permanent porosity. They showed potential for molecular separation,[163] molecular sensing[164,165] and as new materials, such as porous liquids.[166] However, new structures often were generated by making small changes to precursors of already existing cages (Scheme 10).[167–171]

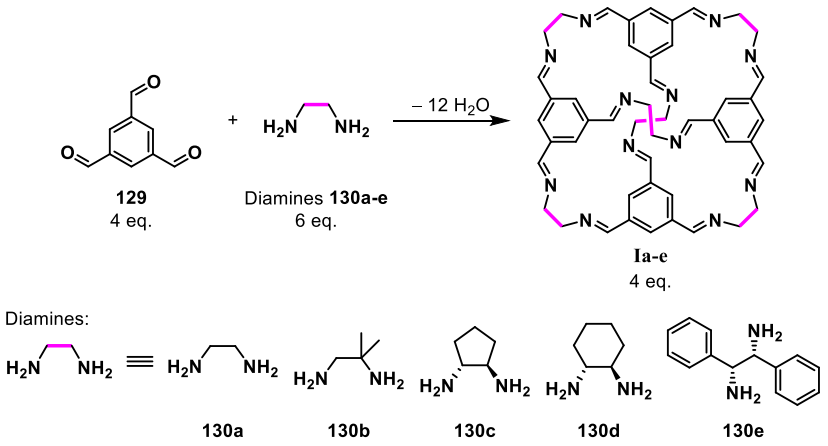

Scheme 10: Tri^{4}D^6 cage **Ia** and its derivatives **Ib-Ie** that were reported over the years as an example for new cage compounds that were synthesized by making small changes to building blocks of already existing cage **Ia**.

In an attempt to fight the slow progress on the discovery of new organic cages, the groups of COOPER and JELFS developed a new methodology which combines computational screening with automated robotic synthesis to create a high-throughput screening method.[143] In their study, they investigated 78 precursor combinations, computationally predicting the energetically most favoured topology for each, and 33 cages formed cleanly on a robot synthesizer out of which 32 were new. During screening, three triamines and 26 dialdehydes including *meta*- and *para*-dialdehydes (**Di**) as well as trialdehydes (**Tri**) were used. Scheme 11 shows some examples of triamine (**128c** and **128d**) and aldehyde precursor (**131**-**140**) combinations for which the topology of the cage was predicted correctly. In general, **Tri^{2}Di^3** type cages were calculated to be energetically preferred for *meta*-dialdehydes and **Tri^{4}Di^6** tetrahedral cages were likely to form with *para*-dialdehydes.

However, these predictions were not perfectly accurate because, according to the authors, the calculations could not include all factors that may have an influence on the reaction outcome. For instance, of 33 reactions predicted to form **Tri^{4}Di^6** type tetrahedral cages, only 9 were correct and formed cleanly. In 8 cases, **Tri^{2}Di^3** topologies formed and in 16 reactions, no cage formed at all. This is a testament to how difficult and time consuming it can be to not only design new organic cages but also form the desired topology.

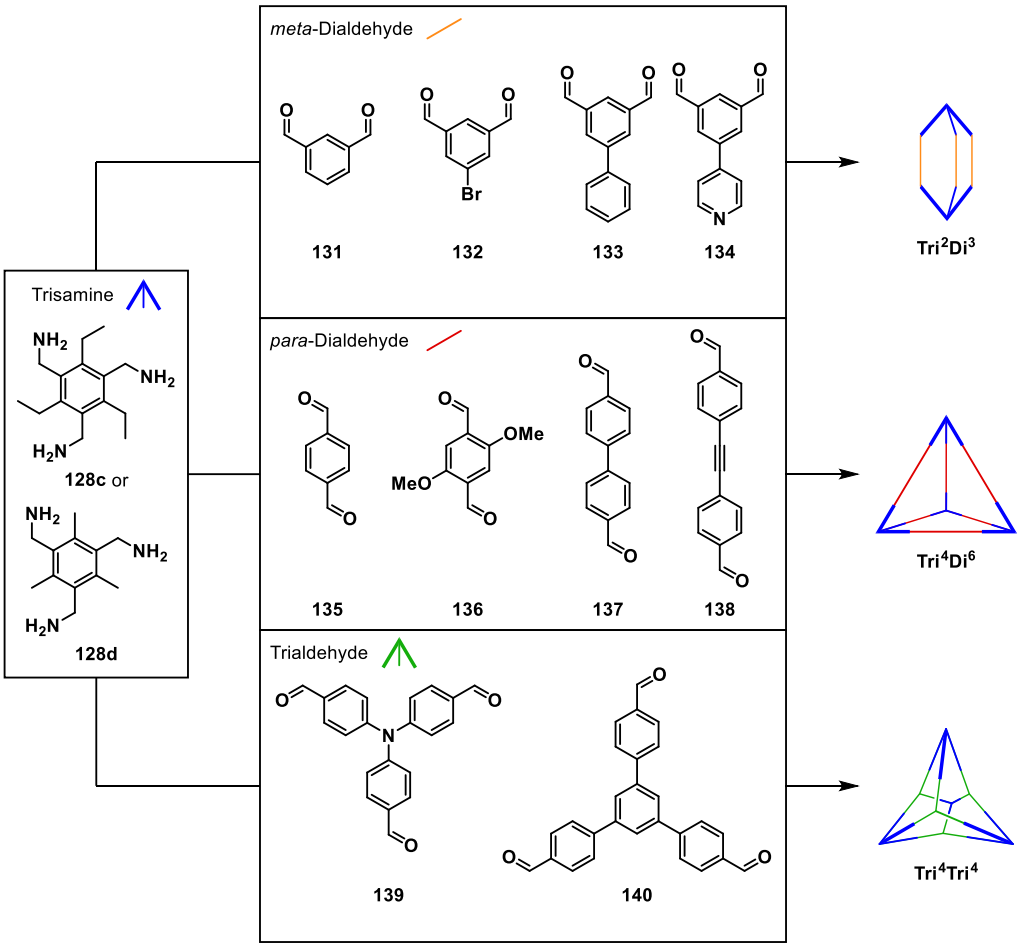

Scheme 11: Building block combinations for which the resulting cage topology was correctly predicted by computations. Either of the triamines **128c** or **128d** was combined in an appropriate ratio with one of each of the depicted aldehydes. Top: *meta*-Dialdehydes to form **Tri^{2}Di^3** type cages. Middle: *para*-Dialdehydes to form **Tri^{4}Di^6** type cages. Bottom: Trigonal trialdehydes to form **Tri^{4}Tri^4** type cages.

Trialdehydes **139** and **140** formed the predicted **Tri^{4}Tri^4** topology with triamines **128c** and **128d**.

Many more imine-based covalent organic cages and their reduced amine or ammonium cage derivatives have been reported within the last decade with different sizes and topologies.[148] However, explicit host-guest chemistry with inorganic or organic anions remains rare for cages with big cavities. Investigations towards the uptake of anions have been reported within cryptand-type cages with **Tri^{2}Di^3** topology, but mostly before *dynamic covalent chemistry* (**DCvC**) was applied as a synthetic strategy for cage formation.[172,173] Fully covalent cages can be very flexible so that anion encapsulation can promote substantial conformational rearrangements of the cage for optimal binding, mimicking the *induced fit* behaviours of enzymes which can potentially lead to interesting cages suitable for the binding of a wide variety of anions instead of a select few.[173] Some examples will be discussed next.

1.2.3d Cryptands for the Encapsulation of Anionic Guests

As early as 1986, aromatic scaffolds were introduced as spacers for the construction of oligocyclic polyamines and for the inclusion of larger, polyatomic anions.[174,175] In 1991, cryptand **II** was the first example of a cryptand-type cage with aromatic moieties (*meta*-xylyl groups) in between two tris-(2-aminoethyl)amine (**128a**, TREN) units (Figure 12a).[176] Cryptand **II** has been investigated extensively ever since and its hexaprotonated form was reported multiple times to form inclusion complexes in the solid state with a wide variety of oxoanions such as perrhenate (ReO_4^{2-}),[177] thiosulfate ($S_2O_3^{2-}$),[178] chromate (CrO_4^{2-}),[178] and selenate (SeO_4^{2-}).[178] Moreover, the inclusion of two nitrate (NO_3^-) anions in one cryptand cavity[179,180] and the encapsulation of an oxalate as an organic dianion[181] were reported as was shown in their respective crystal structures (Figure 12a) with hexaprotonated **II**•H_6^{6+} as host. For the oxalate complex, the crystal structure revealed that only one oxygen of each carboxylate group is bound *via* three hydrogen bonds with three N*H*$^+$ at each end of the cavity.

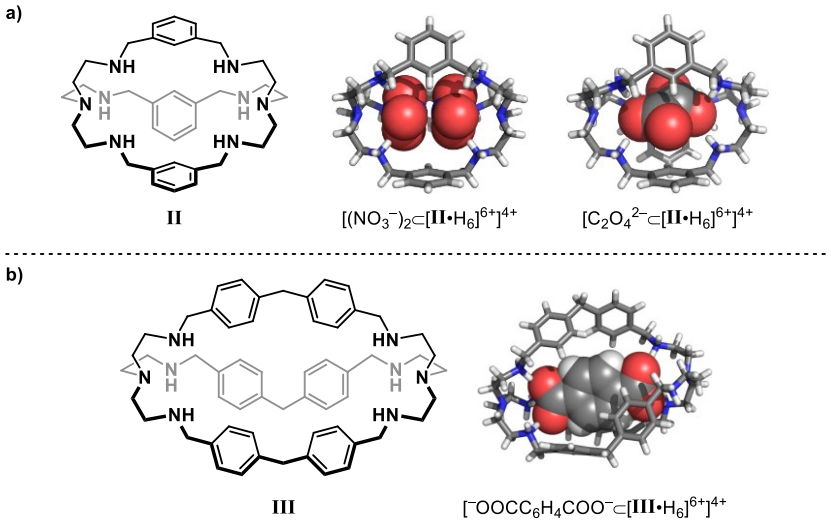

Figure 12: a) The chemical structure of cryptand **II** and the X-ray crystal structures of its hexaprotonated form **II**•H_6^{6+} as an inclusion complex with two nitrates or an oxalate dianion. b) The chemical structure of cryptand **III** and the X-ray crystal structure of its hexaprotonated form **III**•H_6^{6+} as an inclusion complex with a terephthalate dianion.

In 1991, LEHN *et al*. investigated the elongated azacyclophane **III** towards guest-uptake of a series of dicarboxylates such as terephthalate (Figure 12b), once again in its hexaprotonated form **III**•H_6^{6+}.[182] The binding constant of its 1:1 complex was determined to be $K_a = 2.5 \cdot 10^4$ M^{-1} through ^{1}H-NMR titration experiments in D_2O at 20 °C, buffered at pH = 6. The ^{1}H-NMR peaks of the anionic guest experienced an upfield shift in the presence of cryptand **III**•H_6^{6+}, indicating complexation. The binding constants were determined for a series of linear dicarboxylates of the type $^-OOC(CH_2)_nCOO^-$ with $n = 2–8$ as well (Table 5), ranging from K_a = 1400 to 2600 M^{-1}. The binding constants in this series start at the lowest point at $n = 2$ (succinate), peak at $n = 4$ (adipate) and diminish again with increasing chain length, indicating that the length of adipate is the most suitable for the cavity of hexaprotonated cryptand **III**•H_6^{6+} in this series of aliphatic dicarboxylates.[182]

Table 5: Binding constants K_a (M^{-1}) and Log K_a values for the equilibria of the inclusion complexes between aliphatic dicarboxylates with the general formula $^{-}OOC(CH_2)_nCOO^{-}$ with n = 2–8 or the positional isomers of phthalate with either hexaprotonated azacylophane **III**•H_6^{6+} in D_2O (left) or dicopper(II) cryptate $[Cu^{II}_2(\mathbf{III})]^{4+}$ in D_2O/EtOH = 1:1 (right) as hosts.

	III•H_6^{6+} in D_2O		$[Cu^{II}_2(\mathbf{III})]^{4+}$ in D_2O/EtOH = 1:1	
$^{-}OOC(CH_2)_nCOO^{-}$; n = …	**K_a (M^{-1})**	**Log K_a**	**K_a (M^{-1})**	**Log K_a**
2 (succinate)	1400	3.15	$5.62 \cdot 10^7$	7.75
3 (glutarate)	2300	3.36	$3.16 \cdot 10^8$	8.50
4 (adipate)	2600	3.41	$1.02 \cdot 10^{10}$	10.01
5 (pimelate)	2100	3.32	$2.19 \cdot 10^7$	7.34
6 (suberate)	1900	3.28	–	–
7 (azelate)	1400	3.15	–	–
8 (sebacate)	1500	3.18	–	–
Terephthalate (1,4-)	25000	4.40	$6.17 \cdot 10^9$	9.79
Isophthalate (1,3-)	–	–	$3.71 \cdot 10^8$	8.57
Phthalate (1,2-)	–	–	$5.01 \cdot 10^7$	7.70

The binding constants of the corresponding dicopper(II) cryptate complex $[Cu^{II}_2(\mathbf{III})]^{4+}$ to some of the medium sized and linear aliphatic dicarboxylates $^{-}OOC(CH_2)_nCOO^{-}$ (n = 2–5) and phthalate, isophthalate and terephthalate have also been determined in H_2O/EtOH = 1:1 at 25 °C (Table 5) by DUARTE *et al.*[183] The crystal structures of the inclusion complexes with terephthalate and adipate have also been obtained and are shown in Figure 13. The cryptate is suitably elongated for the rigid terephthalate to fit in and adjusts to the folded structure of the adipate for optimal binding, leading to short $N_{tert.}$–$N_{tert.}$ distances (from 1488 pm in the terephthalate complex to 964 pm in the adipate complex) and displaying the cryptates flexibility due to the methylene linker in between the phenyl units.[173]

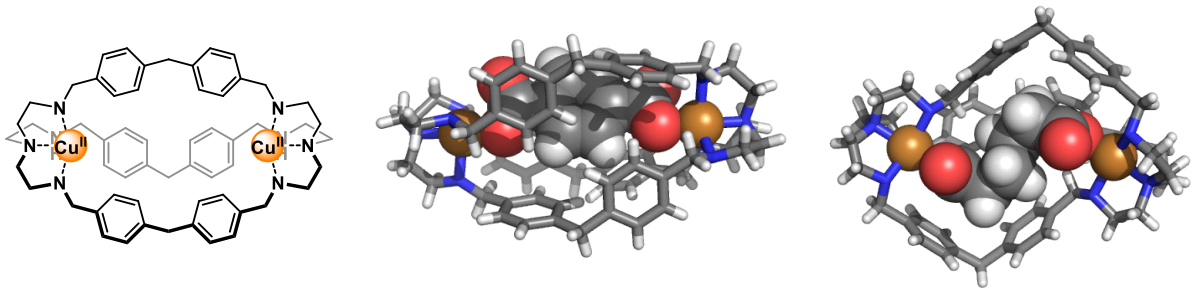

$[Cu^{II}_2(\mathbf{III})]^{4+}$ $[Terephthalate\subset[Cu^{II}_2(\mathbf{III})]^{4+}]^{2+}$ $[Adipate\subset[Cu^{II}_2(\mathbf{III})]^{4+}]^{2+}$

Figure 13: The chemical structure of the dicopper(II) cryptate complex $[Cu^{II}_2(\mathbf{III})]^{4+}$ (left) and the X-ray crystal structures of its inclusion complexes with terephthalate and adipate (right).

Table 5 summarizes the binding constants determined for the above-mentioned guests. The data show that despite the complexation of two Cu^{2+} taking up space within the cavity, it is again the adipate dianion that forms the most stable complex with dicopper(II) cryptate $[Cu^{II}_2(\mathbf{III})]^{4+}$ with a binding constant 2-3 orders of magnitude higher than similar dianions of shorter (succinate, glutarate) or longer (pimelate) chain lengths. Despite their different conformational arrangements, terephthalate and adipate show similarly high binding constants in solution.

In conclusion, bis-TREN cryptands and cryptate metal complexes are versatile and attractive cage-shaped systems which can bind anions efficiently for different reasons: (1) they can be synthesized easily in two steps including initial [2+3] imine condensation of commercially available TREN (**128a**) with dialdehydes, followed by reduction of the imine groups to amines or ammonium groups. (2) Bis-TREN cryptands can exhibit anion binding either as their corresponding and fully covalent hexaammonium species or as a dimetallic complex. (3) Both cage types can be water-soluble, providing the means for recognition and sequestering of anions in aqueous media.[173] However, the latter can also be classified as a metal-organic coordination cage.

1.3 Metal-Organic Coordination Cages

1.3.1 A Brief Introduction to Metal-Organic Coordination Cages

Metal-organic coordination cages are discrete three-dimensional supramolecular architectures consisting of organic ligands and metal ions that self-assemble in solution.[184] This class of compounds has been investigated extensively over the last three decades.[185]

Reversible ligand → metal dative bonds are responsible for the spontaneous self-assembly between organic ligands and metal ions and is thus also called *coordination-driven self-assembly*.[186,187] The binding energies of metal-ligand bonds (15-50 kcal mol^{-1}) fall in between covalent bonds (60-120 kcal mol^{-1}) and dispersive interactions (0.5-10 kcal mol^{-1}) in terms of strength, enabling reversibility and, therefore, a self-repair and correction mechanism that allows for the thermodynamic product to prevail over possible kinetic products if given enough time for the reaction to equilibrate.[186] Many different metal cations can be employed. For instance, they can favour the formation of octahedral coordination geometries such as Co^{II}, Fe^{II} or Ga^{III} and square-planar coordination geometries usually form with Pd^{II} or Pt^{II}.[184] The organic ligands can feature mono- or multidentate coordination sites for chelation to enhance the stability of the complexes. The polyhedra acquired this way often resemble Platonic or Archimedean solids and are often abbreviated $M_xL_y^{z+/-}$ (M = Metal, L = Ligand) with the subscripts x = 1, 2, 3… and y = 1, 2, 3… indicating the number of metal ions M and the number of ligands L that are incorporated within the cage structure and the superscript z = 1, 2, 3… indicating the total charge of the cage. For example, ditopic pyridyl-pyrazole ligands and a Co^{II} precursor form cationic $\mathbf{[Co_8L_{12}]^{16+}}$ cube **IV** according to WARD *et al* (Figure 14a).[188]

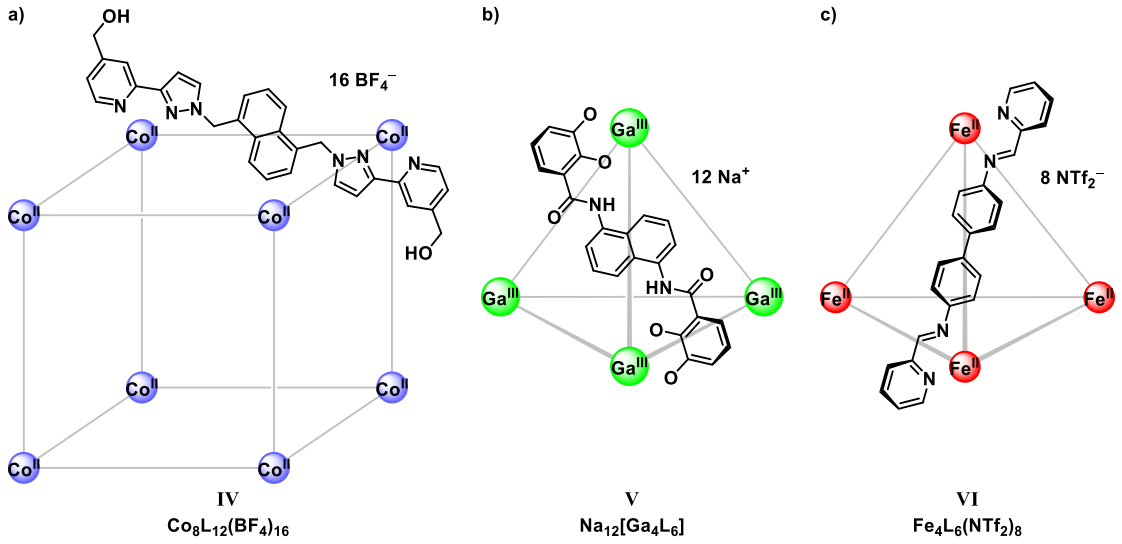

Figure 14: a) Co^{II}-based $\mathbf{M_8L_{12}}$ cube **IV** as reported by WARD *et al.* b) Ga^{III}-based $\mathbf{M_4L_6}$ tetrahedron **V** as reported by RAYMOND *et al.* c) Fe^{II}-based $\mathbf{M_4L_6}$ tetrahedron **VI** as reported by NITSCHKE *et al.*

Anionic $\mathbf{[Ga_4L_6]^{12-}}$ tetrahedron **V** from the RAYMOND group is based on bis-catecholamide naphthalene ligands forming complexes with Ga^{III} (Figure 14b),[189] and iminopyridine-based assemblies with various metals were reported by NITSCHKE *et al.* forming many different polyhedra such as $\mathbf{[Fe_4L_6]^{8+}}$ tetrahedron **VI** (Figure 14c).[190] This work will focus mostly on the latter complexes and give an insight on the structural diversity and chemistry of iminopyridine-based metal-organic coordination cages.

1.3.2 Iminopyridine-Based Metal-Organic Coordination Cages

1.3.2a General Subcomponent Combinations for Self-Assembly

Subcomponent self-assembly towards iminopyridine complexes typically require at least two different organic building blocks. One main subcomponent, equipped with either amines (**141**, Scheme 12a) or aldehydes (**144**, Scheme 12b/c), is usually modified to feature diverse organic scaffolds giving access to either ditopic, tritopic or tetratopic ligands, able to occupy the edges or faces of polyhedra. The second subcomponent is usually a complementary and simple 2-formylpyridine (**142**, Scheme 12a) or a primary amine (**145**, Scheme 12b), but it can also serve as a second subcomponent of tritopic nature, such as triamine **128a** (TREN, Scheme 12c), to covalently interconnect three pyridine-2-carbaldehyde ligands **144** with each other and create hexadentate octahedral coordination complexes **147**. $\mathbf{Fe_4L_6(NTf_2)_8}$ tetrahedron **VI** (Figure 14c) is a prime example for the first type of subcomponent self-assembly to form coordination complexes of the type **143** (Scheme 12a). In the following sections, many more examples of iminopyridine-based cages reported so far will be given, mainly for the types **143** and **147**. First, however, an introduction to the *fac*/*mer* isomerism for octahedral complexes will follow to explain the diversity these cages can achieve.

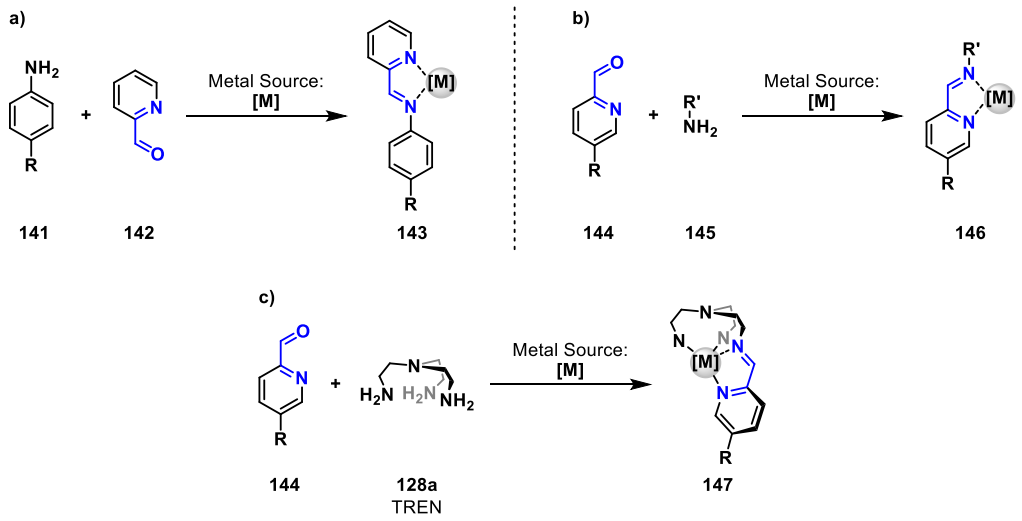

Scheme 12: a) General iminopyridine metal complexation starting from amine ligands **141** and 2-formylpyridine **142**. b) General iminopyridine metal complexation starting from pyridine-2-carbaldehyde ligands **144** and primary amines **145**. c) General iminopyridine metal complexation starting from pyridine-2-carbaldehyde ligands **144** and TREN (**128a**).

1.3.2b *fac* and *mer* Isomerism and the Consequences for Coordination Cages

Standard iminopyridine ligands offer bidentate coordination sites and the coordination cages shown herein predominantly feature octahedral complexes around the metal vertices of the type **M(A–B)$_3$]$^{z+}$**.[191] These complexes can potentially form as two configurational isomers: facial (*fac*), in which the same three ligand atoms are located on the same face of the octahedral complex (Figure 15, left), and meridional (*mer*), in which the same three ligand atoms and the metal center span a plane (Figure 15, right). For *fac* or *mer* configuration each, two enantiomers can form depending on the handedness of the complex (Δ = right-handed and Λ = left-handed), leading to four possible variants: *fac*-Δ or *fac*-Λ and *mer*-Δ or *mer*-Λ.[191,192]

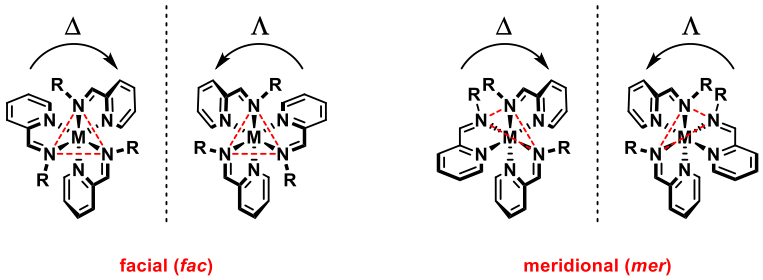

Figure 15: The possible facial (*fac*) and meridional (*mer*) configurations for bidentate octahedral complexes of the type **[M(A–B)$_3$]$^{z+}$**. Left: Right-handed *fac*-Δ and left-handed *fac*-Λ isomers. Right: Right-handed *mer*-Δ and left-handed *mer*-Λ isomers.

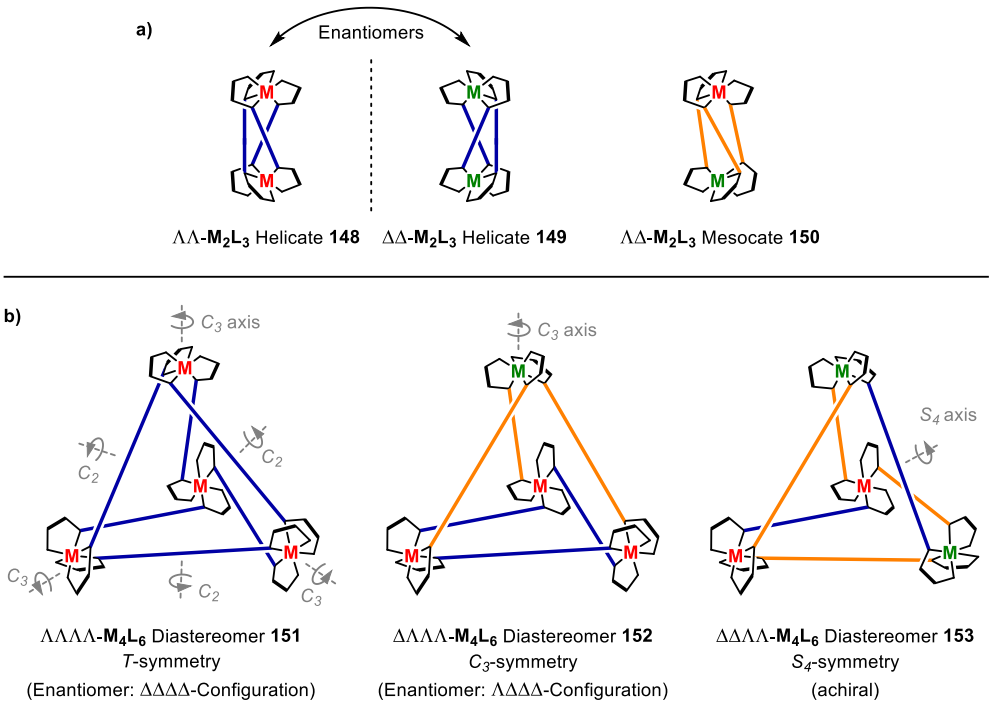

Figure 16: Red and green metal centers are of opposite stereochemical configuration. Blue lines represent *anti*-linkages between homochiral metal centers. Orange lines represent *syn*-linkages between heterochiral metal centers. a) Schematic representation of homochiral ΛΛ- and ΔΔ-**M$_2$L$_3$** helicates **148** and **149**, respectively, based on bidentate ligands (left). Achiral ΛΔ-**M$_2$L$_3$** mesocate **150** is depicted on the right. b) Schematic representation of the three different diastereomers for **M$_4$L$_6$** tetrahedral cages with bidentate ligands. Left: *T*-symmetric ΛΛΛΛ-diastereomer **151**. Middle: C_3-symmetric ΔΛΛΛ-diastereomer **152**. Right: S_4-symmetric ΔΔΛΛ-diastereomer **153**.[190]

The simplest coordination cages able to form from ditopic bidentate ligands **L** and metal cations **M** are triple helicates of $\mathbf{M_2L_3}$ stoichiometry *via* bridging of the ligands between two octahedral metal centers. When there is mechanical coupling like this between the two centers *via* rigid enough ligands, three different isomers can usually form. The enantiomeric ΛΛ- and ΔΔ-helicates **148** and **149**, respectively (Figure 15a, left) and the achiral ΛΔ-*meso*-helicate **150**, which is also called ΛΔ-mesocate (Figure 15a, right). All three ligands need to point in the same direction for helicate formation and, therefore, only *fac* configured metal centers are usually observed for helicates.[193–197] *mer* configured metal centers within helicates also can exist when using ligands which are flexible enough, but these remain scarce in literature.[198]

Ditopic (edge-linking) bidentate ligands can also form $\mathbf{M_4L_6}$ tetrahedral cages. With all-*fac* configured metal centers, three different diastereomers are possible: (1) ΛΛΛΛ-$\mathbf{M_4L_6}$ diastereomer **151** with *T* point symmetry exhibiting one set of ^{1}H-NMR signals for each proton to which a ΔΔΔΔ-$\mathbf{M_4L_6}$ enantiomer exists (Figure 16b, left), (2) ΔΔΛΛ-$\mathbf{M_4L_6}$ diastereomer **152** with C_3-symmetry exhibiting four sets of ^{1}H-NMR signals for each proton to which a ΛΛΔΔ-$\mathbf{M_4L_6}$ enantiomer exists (Figure 16b, middle) and (3) an achiral ΔΔΛΛ-$\mathbf{M_4L_6}$ diastereomer **153** with S_4-symmetry exhibiting three sets of ^{1}H-NMR signals for each proton (Figure 16b, right). For instance, the ratio of these diastereomers for $\mathbf{Fe_4L_6(NTf_2)_8}$ tetrahedron **VI** (Figure 14c) was found to be T / C_3 / S_4 = 32 : 19 : 49 in MeCN-d_3.[190] Tetrahedral cages with *mer* configured metal centers are known as well but require more flexible bidentate ligands.[199,200] These will not be discussed herein as they do not play an important role for this work.

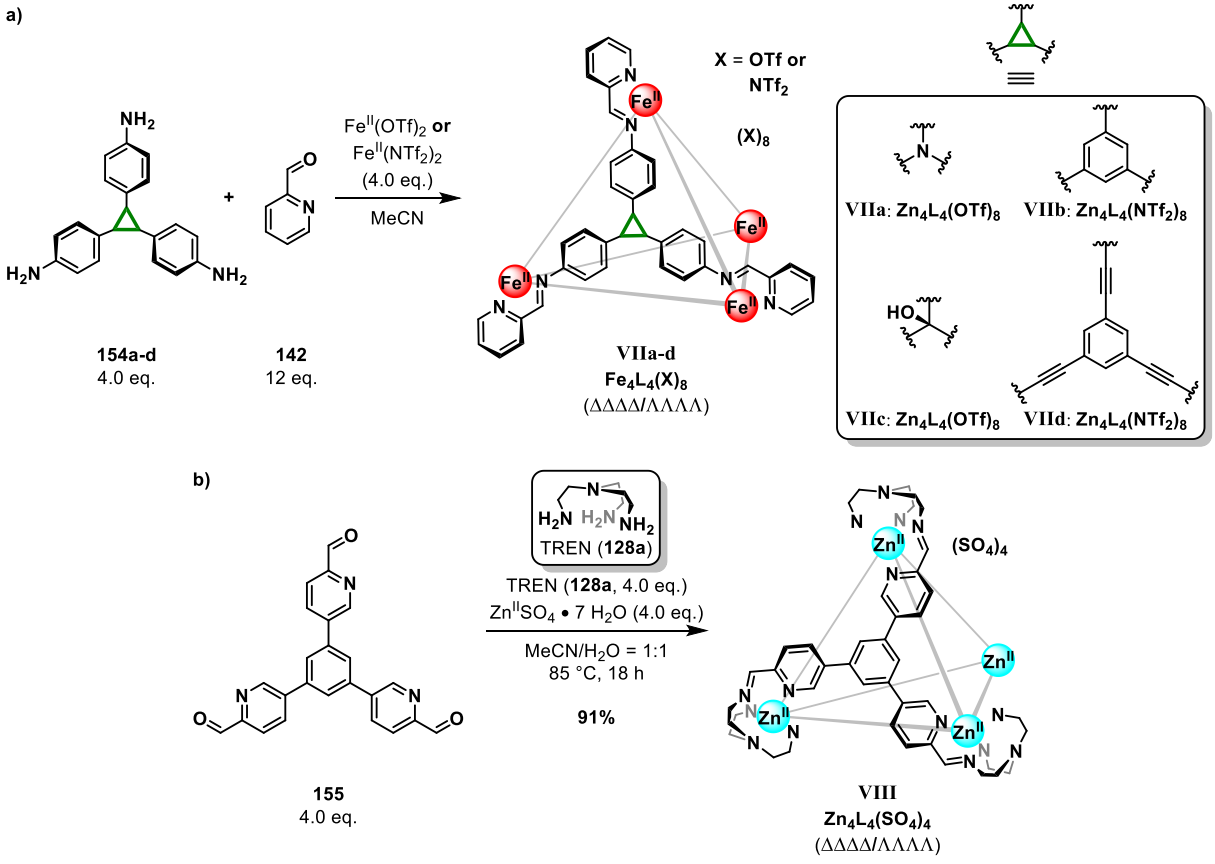

Scheme 13: a) Synthesis of face-capped $\mathbf{Fe_4L_4}$ tetrahedral cages **VIIa-d** from ligands **154a-d** and 2-formylpyridine (**142**) in MeCN with either triflate or triflimide counter anions. b) Synthesis of face-capped $\mathbf{Zn_4L_4(SO_4)_4}$ tetrahedral cage **VIII** from ligand **155** and tris(2-aminoethyl)amine (**128a**, TREN).

Tritopic bidentate ligands allow for a panelling approach to form face-capped tetrahedral cages spanning across three metal centers instead. The increased connectivity between the metal centers with rigid enough ligands can impose the same handedness on each metal center to an extent to where only one single diastereomer is observed to form which is of *T* point symmetry. Scheme 13a shows a series of acetonitrile-soluble, face-capped $\mathbf{M_4L_6}$ tetrahedra **VIIa-d** based on tritopic amine ligands **154a-d** combined with picolinaldehyde (**142**). TREN (**128a**), as a triamine subcomponent, provides a higher degree of chelation and interconnects the trialdehyde ligand **155** on each face of the water-soluble, face-capped $\mathbf{Zn_4L_4(SO_4)_4}$ tetrahedron **VIII** over covalent bonds around the metal centers at the vertices (Scheme 13b).[201,202]

1.3.2c Water-Soluble Iminopyridine-Based Coordination Cages

Most coordination cages have been synthesized and studied in organic solvent systems. Access to water-soluble and water-stable cages can be difficult due to a few key challenges: (1) Many ligands employed in cage formation are poorly soluble in aqueous solution because they typically feature nonpolar aromatic backbones.[203] Subcomponent self-assembly in water will then not be possible because the poorly soluble ligand can not enter the imine forming equilibrium. NITSCHKE *et al*. argued that employing hydrophilic glycerol groups into an otherwise hydrophobic diamine precursor would render the resulting cage water-soluble.[204]

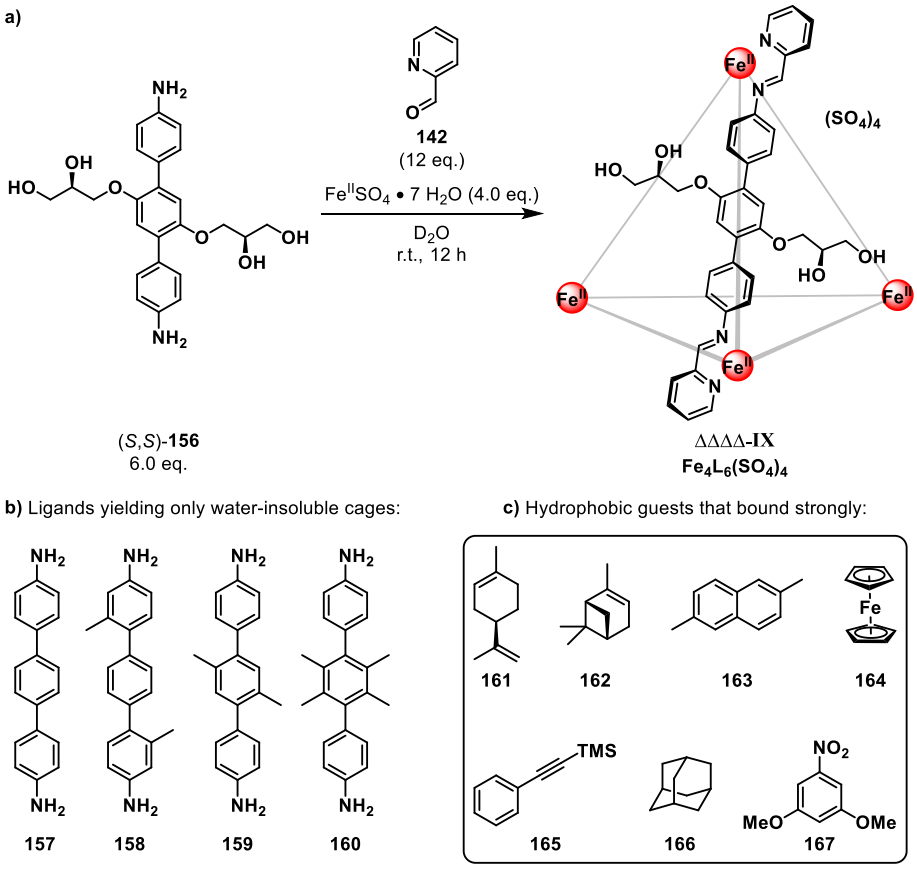

Scheme 14: a) Enantioselective synthesis of water-soluble $\mathbf{Fe_4L_6(SO_4)_4}$ tetrahedron ΔΔΔΔ-**IX** from (S,S)-**156**, picolinaldehyde (**142**) and $Fe^{II}SO_4$ by subcomponent self-assembly. b) 4,4´´-Diamino-*para*-terphenyls **157**-**160** formed water-insoluble cages as the triflimide or tetrafluoroborate salts. c) Hydrophobic guests for which guest-uptake was observed with host ΔΔΔΔ-**IX** in D_2O (slow exchange as determined by ^{1}H-NMR spectroscopy).

Thus, they synthesized the enantiomerically pure 4,4′′-diamino-*para*-terphenyl ligand (*S*,*S*)-**156** and combined it with picolinaldehyde (**142**) and $Fe^{II}SO_4$ for the enantioselective formation of water-soluble ΔΔΔΔ-**Fe$_4$L$_6$** cage **IX** (Scheme 14a).[204] Its ΛΛΛΛ-**Fe$_4$L$_6$** enantiomer was accessible with enantiopure (*R*,*R*)-**156** as well with high enantioselectivity. The ligand derivatives **157**-**160** (Scheme 14b) only formed acetonitrile-soluble cages with triflimide or tetrafluoroborate salts instead, arguably due to the absence of hydrophilic glyerol groups.[205]

(2) The hydrophobic effect may promote stacking of hydrophobic aromatic ligands instead of the formation of cage structures with cavities.[203] The hydrophobic effect describes the tendency for nonpolar molecules to aggregate in aqueous solution and exclude water molecules.[206–210] However, there is also the interest for water-soluble coordination cages featuring hydrophobic cavities because neutral and hydrophobic organic guest molecules in an aqueous environment would be driven into the cage interior by this effect, leading to stronger binding. For instance, the ΔΔΔΔ-**Fe$_4$L$_6$** cage **IX** was able to bind a series of hydrophobic guest molecules effectively in D_2O due to the hydrophobic effect. Scheme 14c shows a few examples for which slow exchange was observed with guests that were suitably sized for the cavity of the host to form 1:1 host-guest complexes.[204] The proton shifts of the guests experienced an upfield shift due to the shielding effect of the aromatic ring current in the ^{1}H-NMR upon encapsulation and only one species was observed in the presence of an equimolar amount of host which was assigned to guest⊂ΔΔΔΔ-**IX**.

(3) Water itself is a competitive ligand able to coordinate to metal complexes and disturb metal→ligand dative bonds, preventing cage formation.[203,211] Additionally, the imine bonds in iminopyridine complexes form in a reversible equilibrium with water as the condensation product. Thus, they can be labile in aqueous solution, especially at higher temperatures.

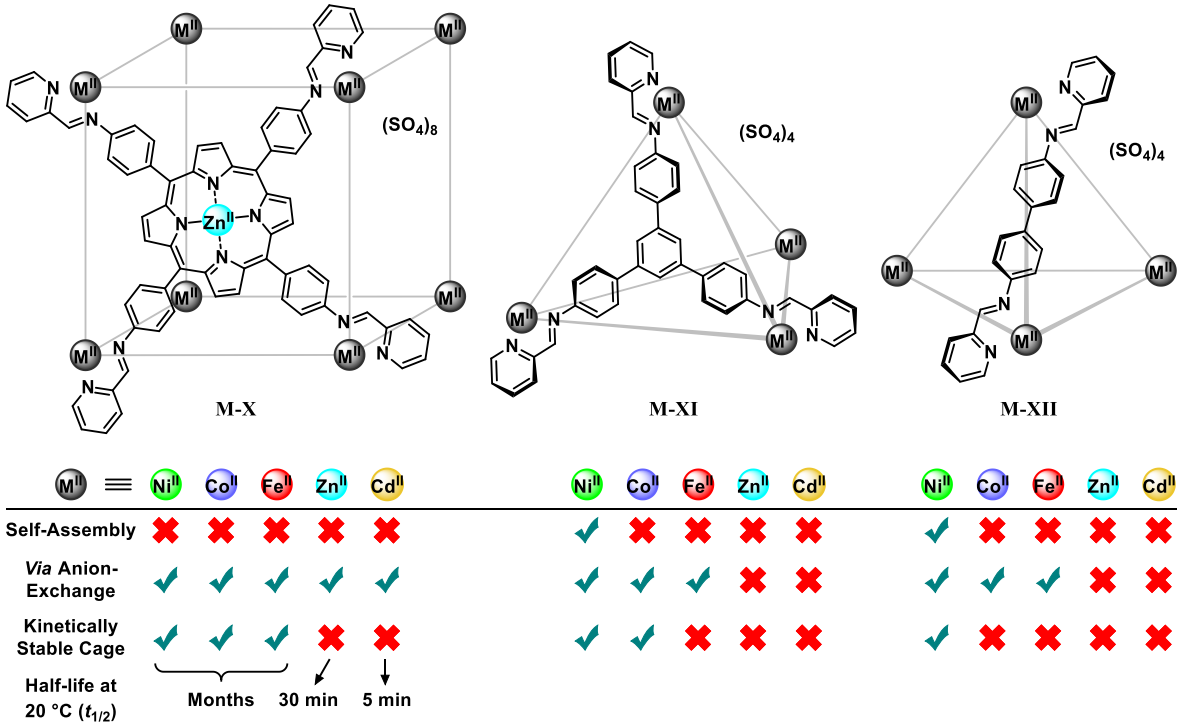

Figure 17: Overview of the face-capped **M$_8$L$_6$** cubes **M-X**, **M$_4$L$_4$** tetrahedra **M-XI** and edge-linked **M$_4$L$_6$** tetrahedra **M-XII** with **M** = Ni^{II}, Co^{II}, Fe^{II}, Zn^{II} or Cd^{II} that were accessible as sulfate salts, either from direct subcomponent self-assembly or anion exchange by addition of aq. $(TBA)_2SO_4$ (12 eq.) into an acetonitrile solution of the corresponding triflimide (NTf_2^-), triflate (OTf^-) or tetrafluoroborate (BF_4^-) cage according to NITSCHKE *et al.*[202,212]

To expand upon this topic, NITSCHKE *et al*. investigated the influence of different metal precursors to the stability of various iminopyridine cages. Specific combinations of water-insoluble ligands with metal sulfates ($M^{II}SO_4$) provided access to kinetically robust, water-soluble cages *via* subcomponent self-assembly (Figure 17). However, most water-soluble sulfate cages displayed herein were instead accessible through anion exchange reactions of preformed acetonitrile-soluble triflimide (NTf_2^-), triflate (OTf^-) or tetrafluoroborate (BF_4^-) cage derivatives, but they were not always stable for long periods of time in aqueous solution. The half-lives of cubic sulfate cages **M-X** with **M** = Ni^{II}, Fe^{II}, Co^{II}, Zn^{II} or Cd^{II} were investigated (Figure 17). While the Ni^{II}, Co^{II} and Fe^{II} cubic cages were stable for months in D_2O at room temperature, their Zn^{II} and Cd^{II} derivatives disassembled in aqueous solution with half-lives $t_{1/2}$ of 30 min and 5 min, respectively. Overall, the metal ions employed stabilized the cages into which they were incorporated following the series $Ni^{II} > Fe^{II} > Co^{II} > Zn^{II} > Cd^{II}$.[202] This was consistent with the relative stabilities given by the IRVING-WILLIAMS series: $Fe^{II} < Co^{II} < Ni^{II} > Zn^{II}$.[213] NITSCHKE *et al*. argued that the inversion for Co^{II} and Fe^{II} can be attributed to the low-spin character of Fe^{II} in their structures. On the contrary, the original IRVING-WILLIAMS series only considered high-spin Fe^{II}, which is known to form weaker metal-ligand bonds.[214]

Accordingly, the Ni^{II} structures **Ni-X**, **Ni-XI** and **Ni-XII** proved to be the most stable in aqueous solution at low temperatures. They may not be considered thermodynamically stable though since disassembly of the cage was observed in water at elevated temperatures. Higher temperatures were needed for the decomposition of cubic cage **Ni-X** (85 °C) which is based on a tetratopic ligand, followed by **Ni-XI** (75 °C) which was formed with a tritopic ligand. **Ni-XII** already started decomposing at 60 °C and is based on a ditopic dianiline compound.[202] The authors deduced that an increased topicity results in more stable iminopyridine cages due to the higher degree of binding cooperativity.[215,216] The dissociation of a single ligand arm from the tetratopic ligand of **Ni-X** would require three more imine bonds to be opened by water before the broken imine bond forms back for the ligand to precipitate. For the ditopic ligand in **Ni-XII**, only one more end needs to dissociate from the cage.

The more labile Zn^{II} and Cd^{II} metal ions did not lead to water-stable cages with edge-linking or face-capping multitopic amine ligands and a different strategy had to be employed. For this, an increased chelating effect[217–219] was introduced with the triamines tris(2-aminoethyl)amine (TREN, **128a**) or tris(3-aminopropyl)amine (TRPN, **128b**). TREN (**128a**) was successfully combined with $Zn^{II}SO_4$ to produce a series of water-stable helicates **Zn-XIIIa-d** and TRPN (**128b**) with $Cd^{II}SO_4$ to access water-stable tetrahedra **Cd-XIVa-d**, both in combination with edge-linking, ditopic aldeyhde subcomponents **168a-d** (Scheme 15), representing the first water-soluble subcomponent self-assembled cages with the labile Zn^{II} and Cd^{II} ions.[202] The improved binding cooperativity[215,216] due to the chelating triamines leads to much more stable and water-soluble cages. If an imine bond hydrolyzes, a free TREN (**128a**) or TRPN (**128b**) amine group would not be able to dissociate from the cage since it is still bound to other subcomponents holding the cage together. Thus, this amine group will remain near the free aldehyde, experiencing a high effective molarity for fast imine re-condensation. In contrast, effective disassembly of the cage would require the other imine bonds to be cleaved before this happens, which becomes less likely.[202]

The preferential formation of helicates with Zn^{II} and TREN (**128a**) or tetrahedra with Cd^{II} and TRPN (**128b**) required an explanation. Based on crystal structures, the authors deduced that TRPN (**128b**), built into a cadmium vertex, would be able to cantilever the dialdehyde ligands out into a splayed configuration since the apical nitrogen is also bound to cadmium (coordination number CN = 7), favouring tetrahedra over helicates.[202] In contrast to that, the tighter wrapping of TREN (**128a**) around the smaller Zn^{II} centers involves no coordination of the apical

nitrogen and brings the aldehyde ligands closer together, predominantly forming helicates instead. Additionally, it was found that, when $Zn^{II}SO_4$ was combined with TRPN (**128b**) or $Cd^{II}SO_4$ with TREN (**128a**), complex mixtures formed with no detectable cages.[202]

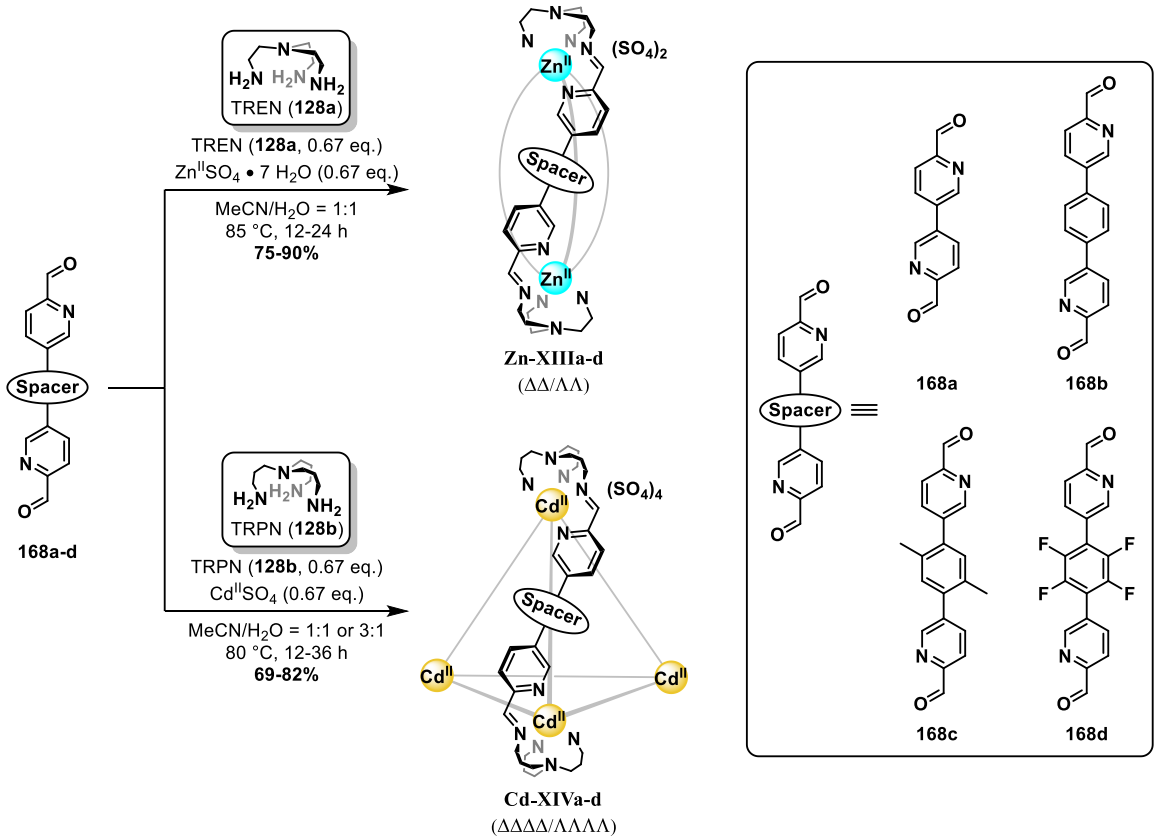

Scheme 15: Water-soluble Zn^{II}-based helicates **Zn-XIIIa-d** and Cd^{II}-based tetrahedral cages **Cd-XIVa-d** were accessed through subcomponent self-assembly with each of the ditopic ligands **168a-d** and the corresponding metal sulfate salt. Chelating tris-(2-aminoethyl)amine (TREN, **128a**) was combined with $Zn^{II}SO_4$ to create helicates and tris(3-aminopropyl)amine (TRPN, **128b**) was combined with $Cd^{II}SO_4$ to create tetrahedral structures.

A panelling approach, using tritopic aldehyde **155** (Scheme 16a), was chosen to prevent the formation of helicates even with Zn^{II}. NITSCHKE *et al.* envisioned the threefold connectivity and rigidity of the ligand to enforce the construction of a tetrahedral assembly as the simplest possible framework with a tritopic face-capping subcomponent.[202] Water-soluble $\mathbf{Zn_4L_4(SO_4)_4}$ tetrahedron **VIII** formed as the only product from TREN (**128a**), $Zn^{II}SO_4$ and trialdehyde **155** (Scheme 16a). Similarly, the combination of TRPN (**128b**), $Cd^{II}SO_4$ and ligand **155** furnished water-soluble $\mathbf{Cd_4L_4(SO_4)_4}$ tetrahedron **XV** exclusively as well. Both cages showed only one set of resonances in their corresponding ^{1}H-NMR experiments, indicating the formation of a single diastereomer each with *T* point symmetry. Both cages proved to be stable for months in D_2O at room temperature and only started decomposing at 80 °C in aqueous solution, reflecting the stability increase with increasing connectivity between the subcomponents in iminopyridine cages.[202]

It was also possible to generate the acetonitrile-soluble $\mathbf{Zn_4L_4(NTf_2)_8}$ cage **XVI** *via* subcomponent self-assembly with TREN (**128a**), $Zn(NTf_2)_2$ and trialdehyde **155** (Scheme 16a). Host-guest studies revealed that this cage was able to bind small anionic guests like PF_6^-, SbF_6^- and ReO_4^- in MeCN-d_3 in the slow binding regime on the ^{1}H chemical shift timescale (Scheme 16c).[220] However, other anions like NO_3^-, BF_4^-, ClO_4^- and TfO^- and a series of neutral organic molecules showed no binding at all (Scheme 16d).

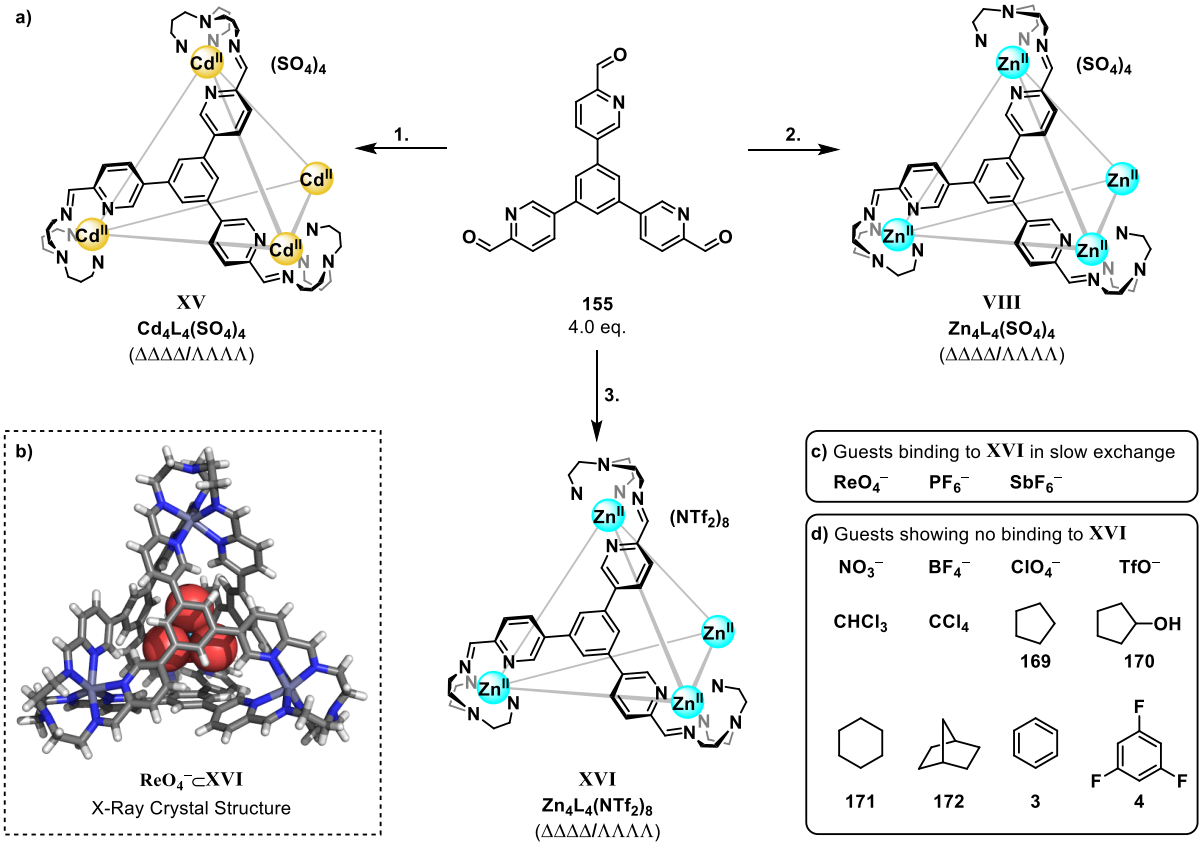

Scheme 16: a) Conditions for **1.** Synthesis of $\mathbf{Cd_4L_4(SO_4)_4}$ tetrahedron **XV**: TRPN (4.0 eq.), $CdSO_4$ (4.0 eq.), MeCN/H_2O = 1:1, 80 °C, 18 h. **2.** Synthesis of $\mathbf{Zn_4L_4(SO_4)_4}$ tetrahedron **VIII**: TREN (4.0 eq.), $ZnSO_4 \cdot 7\ H_2O$ (4.0 eq.), MeCN/H_2O = 1:1, 85 °C, 18 h. **3.** Synthesis of $\mathbf{Zn_4L_4(NTf_2)_8}$ tetrahedron **XVI**: TREN (4.6 eq.), $Zn(NTf_2)_2$ (4.0 eq.), MeCN/MeOH = 1:1, 70 °C, 24 h. b) X-ray crystal structure of $\mathbf{ReO_4^-\subset XVI}$. Solvent molecules and counter anions are omitted for clarity. c) Anionic guests binding to **XVI** in slow exchange in MeCN-d_3. d) Anionic and neutral guests showing no binding to **XVI** in MeCN-d_3.

Two guest-uptake mechanisms were considered: (1) The diffusion of guests through one of the cages portals on each edge. However, cage **XVI** may simply be too small for the larger organic guests investigated with its rather rigid and enclosed structure. (2) Partial disassembly of the cage to create larger portals has also been suggested and was considered to be more likely,[220,221] but covalent bonds in cage **XVI** would need to be distorted considerably or cleaved in order for the cage to open. They argued that the exchange of any guest would at least require N→Zn bonds to break, which would explain that some anions were bound in the slow exchange regime on the ^{1}H-NMR timescale while a through-portal mechanism may have allowed for the fast exchange of guests.[220]

1.3.3 Catalysis within Metal-Organic Coordination Cages

Metal-organic coordination cages possess different, but well-defined, central cavities due to their structural diversity[186,187] leading to many different applications ranging from chemical transport or separation[220,222–230] and molecular sensing[231–236] to the stabilization of reactive guests[237–242] and catalysis.[200,243–260] The reactions catalysed mostly feature cationic intermediates and transition states. Only a few examples of catalysis of reactions with anionic transition states in metal-organic coordination cages are known,[188,261–266] which may be surprising when considering that these cages often possess a high net positive charge for strong ion-ion interactions with anions.

1.3.3a The Anionic KEMP Elimination is Catalysed by a Cubic Coordination Cage

As a proof of principle that anionic reactions can indeed be catalysed by coordination cages, WARD *et al.* introduced the water-soluble **$Co_8L_{12}(BF_4)_{16}$** cube **IV** (Figure 18a) to catalysis,[188] which is based on ditopic pyridyl-pyrazole ligands. The hydrophobic inner cavity in aqueous solution allows for effective binding of neutral organic guests with binding constants of up to $K_a = 1 \cdot 10^8$ M^{-1} due to the hydrophobic effect.[267–269] In contrast to that, cationic and anionic guests bound only weakly since they are preferentially solvated by water.[270,271] The windows in each face of the cage were occupied by anions in several crystal structures.[267,268,270,272] The authors argued that desolvated hydroxide anions also surround the surface of the highly positively charged cage (+16), effectively increasing their local concentration.[188]

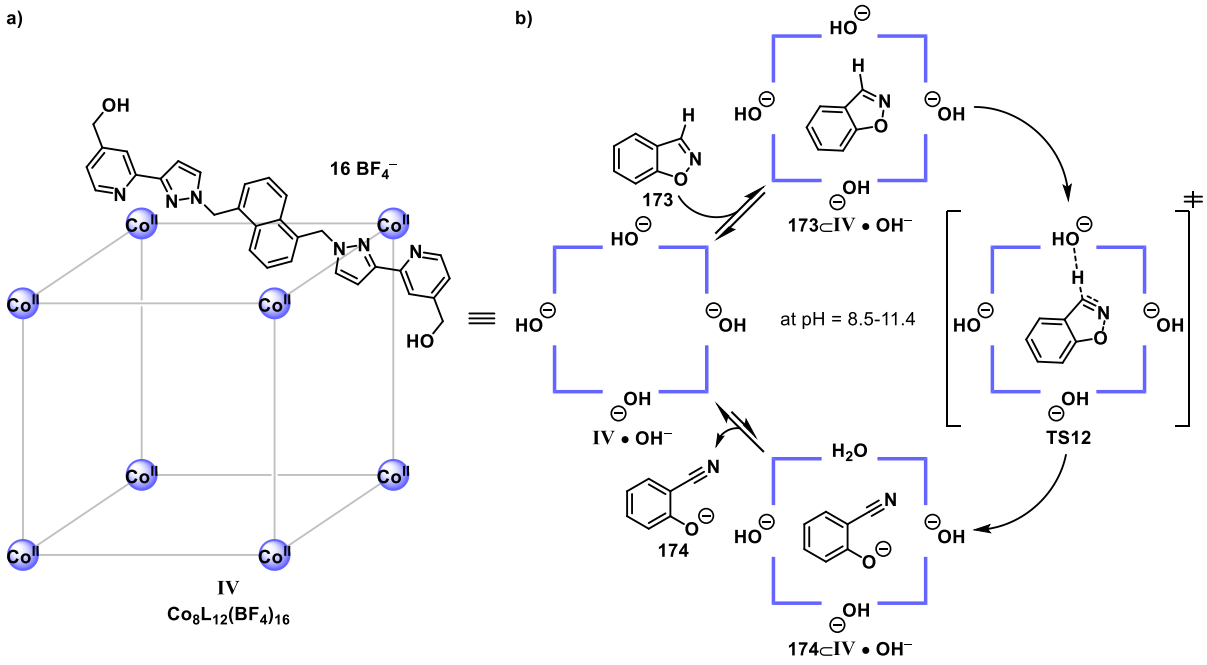

Figure 18: a) The chemical structure of **$Co_8L_{12}(BF_4)_{16}$** cube **IV**. b) Proposed catalytic cycle of the KEMP elimination reaction with cage **IV·OH⁻** as catalyst at pH = 8.5-11.4 starting with the cartoon on the left, schematically representing the cage surrounded by hydroxide anions. Benzisoxazole (**173**) binds to **IV·OH⁻** to form host-guest complex **173⊂IV·OH⁻**, leading to transition state **TS12** in which the proton in 3-position of benzisoxazole (**173**) is attacked by surface-bound hydroxide. The elimination reaction produces 2-cyanophenolate (**174**) which is expelled from the cage cavity as a weakly binding charged species, enabling catalytic turnover. The hydroxide-surrounded catalyst **IV·OH⁻** is recovered.

The cage was able to catalyse the KEMP elimination reaction of neutral, strongly binding benzisoxazole (**173**, $K_a = 4 \cdot 10^3$ M^{-1})[269] in the presence of hydroxide anions to form 2-cyanophenolate (**174**). The proposed catalytic cycle[188] is depicted in figure 18b and starts on the left with a cartoon representing the cube **IV·OH⁻** with a surface saturated with hydroxide anions at basic pH = 8.5-11.4. In a first step, the host-guest complex **173⊂ IV·OH⁻** forms between benzisoxazole (**173**) and cage catalyst **IV·OH⁻**. As benzisoxazole (**173**) gets close to the surface-bound hydroxide anions through windows at the center of each face of the cube, the elimination is initiated and goes over transition state **TS12** to give 2-cyanophenolate (**174**) in a single step. This weakly binding anionic product is then expelled from the cage cavity, enabling catalytic turnover. The water molecule is replaced with a hydroxide, and the catalyst is recovered in its initial state **IV·OH⁻**.[188]

The cage would decompose at pH = 12, setting an upper limit for catalysis. Within pH = 8.5-11.4, the rate of the catalysed reaction did not change. Above this range, the rate of the uncatalysed reaction dropped by an order of magnitude for every decrease in pH of one unit. At pH = 6, the reaction rate of the uncatalysed reaction reaches a minimum when water rather than hydroxide acts as a base. The authors chose to run the catalysed reaction under at least slightly basic conditions (pH = 8.5-11.4) to guarantee that the alcoholate product remains deprotonated and is expelled from the cage cavity as a weakly binding anionic species. The rate enhancement of the reaction at pH = 8.5 was determined to be $k_{cat}/k_{non} = 2 \cdot 10^5$. An experiment with 100 eq. of benzisoxazole (**173**) added to a 0.1 mM solution of the cage at pH = 9.9 resulted in the value for k_{cat}/k_{non} to drop to ~8800 because the background reaction becomes more likely. At the same time, the local hydroxide concentration on the cage surface would not change with increasing pH as saturation is reached at pH = 8.5.[188]

So far, examples of iminopyridine cages able to catalyse reactions remain scarce[100,273–275] and none of them feature anionic transition states. The imine groups surrounding the metal centers in iminopyridine cages may be the limiting factor. They can be prone to nucleophilic attack by aggressive anions since they are already susceptible to water alone as discussed in chapter 4.2.3 which can lead to rapid decomposition of the cages if they are not stable enough. This can also limit the use of nucleophilic bases, such as hydroxide, to initiate anionic reactions. However, design strategies for the construction of water-soluble and water-stable iminopyridine cages were shown. An extension of the research done so far towards the identification of base-stable iminopyridine cages for the catalysis of anionic reactions does seem within reach.

2 Objective of this Thesis

Research concerning anion-π interactions is a relatively young field and interest only picked up in the last two decades.[29–31] The MATILE group pioneered the application of anion-π interactions in the context of catalysis using aromatic naphthalene diimide (NDI) moieties in open, non-capsular systems.[32,33,80,83] Although NDI-based supramolecular cages have been reported,[97–101] anion-π catalysis has not yet been investigated within them to our knowledge. Thus, we envisioned that novel, positively charged supramolecular cages equipped with multiple π-acidic NDI walls would offer an interesting way to discover new reactivities and selectivites for the catalysis of anionic reactions. Two strategies for the incorporation of NDI units into cage structures were pursued.

First, imine formation between NDI dialdehyde **175** and one of the triamines **128a-c** in a 3:2 ratio was envisioned, followed by direct reduction to give access to fully covalent ammonium cages **XVIIa-c** or **XVIIIa-c** (Scheme 17). Their fully covalent nature should allow for the cages to be very flexible and encapsulate a variety of anionic guests. Cages with **Tri^{2}Di^3** or, preferentially, **Tri^{4}Di^6** topology were expected to form during the imine condensation in one step through *dynamic covalent chemistry* as was demonstrated for a variety of subcomponents.[143]

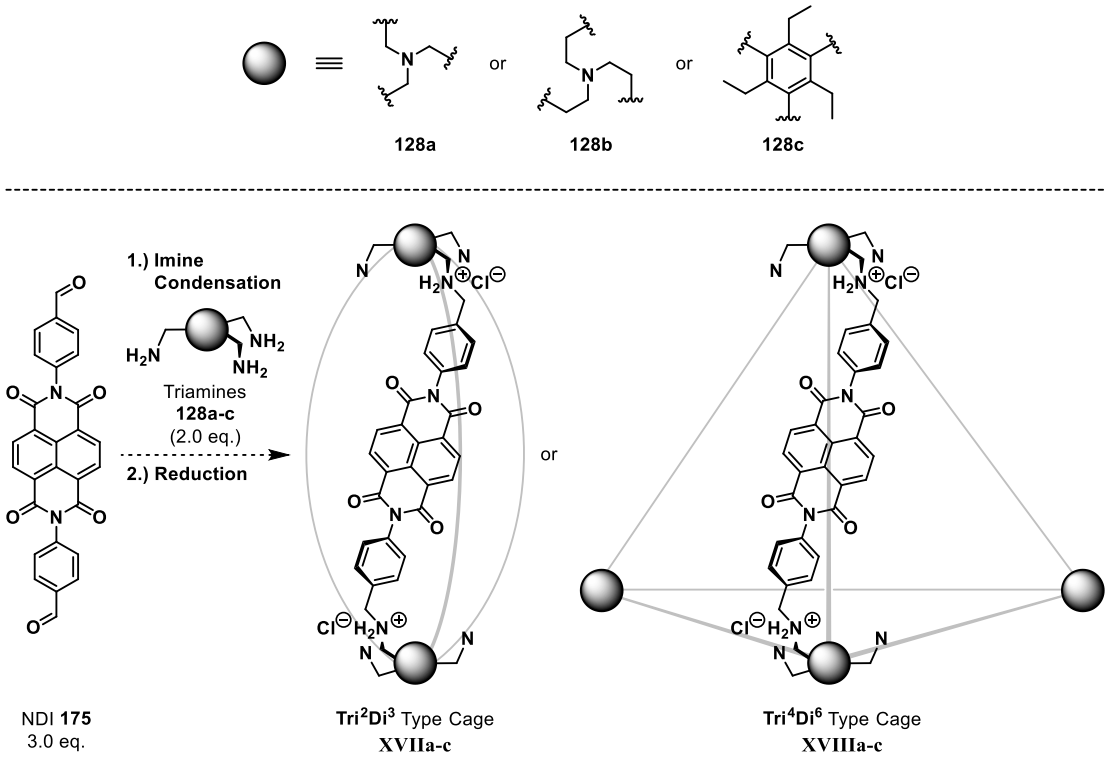

Scheme 17: Planned strategy towards positively charged and fully covalent organic ammonium cages: **Tri$_2$Di$_3$** and **Tri$_4$Di$_6$** type cages **XVIIa-c** and **XVIIIa-c**, respectively, based on NDI dialdehyde **175**.

In a second strategy to access positively charged supramolecular cages with built-in NDI moieties and sizeable cavities, we wanted to investigate the subcomponent self-assembly between the NDI dialdehyde **176** and TREN (**128a**) or TRPN (**128b**) with a variety of metal ion precursors, introduced either as sulfate salts to generate water-soluble coordination cages or as triflimide or triflate salts for acetonitrile-soluble analogues (Scheme 18). A TREN-based helicate has already been synthesized previously by Joachim Preinl in a master thesis internship in our group using NDI dialdehyde **176**. The helicate was accompanied by oligomeric side-products. In this work, we wanted

to show that no cavity was available within it for guest-uptake due to π-π stacking between the NDI units. We wanted to underline this hypothesis by obtaining its X-ray crystal structure and establish a general purification procedure using this helicate as a model coordination cage for future cages of this type.

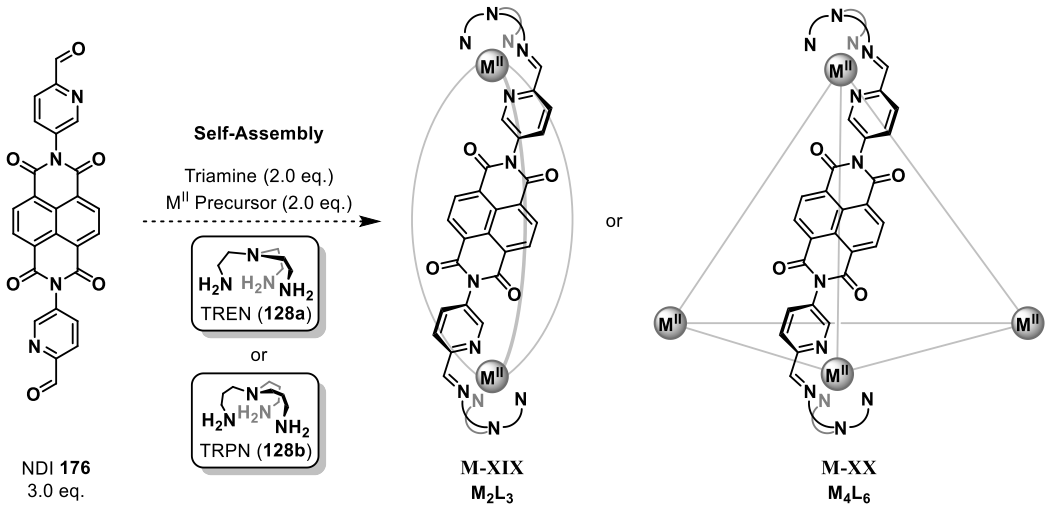

Scheme 18: Planned strategy towards edge-linked metal-organic cages: $\mathbf{M_2L_3}$ helicates **M-XIX** and $\mathbf{M_4L_6}$ tetrahedra **M-XX** based on NDI dialdehyde **176**.

Generally, we would prefer tetrahedral coordination cages because they possess a larger cavity. In case the selectivity problem of forming helicates persists with ditopic NDI dialdehyde **176** and different metals, we will set out to synthesize triiphenylene triimide (TPTI) **177** as an alternative subcomponent (Scheme 19). We figured that this tritopic ligand should selectively form face-capped tetrahedral $\mathbf{M_4L_4}$ cages **M-XXI** when combined with TREN (**128a**) or TRPN (**128b**) and metal precursors whilst still providing an electronically similarly polarised and π-acidic aromatic surface for anion-π interactions.

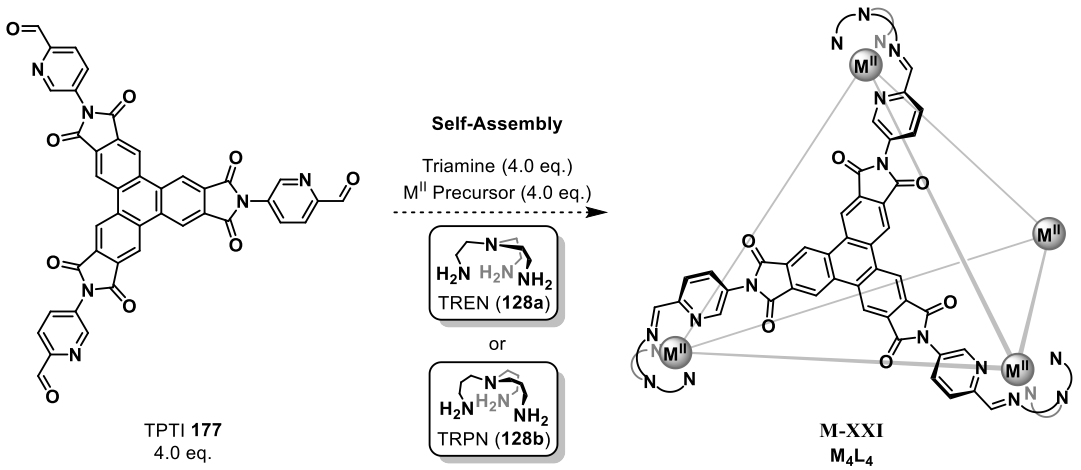

Scheme 19: Strategy towards face-capped metal-organic cages: $\mathbf{M_4L_4}$ tetrahedra **M-XXI** based on TPTI trialdehyde **177**.

If none of these strategies prove fruitful, we will pursue the synthesis of trialdehyde **178** to use it as a subcomponent for coordination cage formation together with TREN (**128a**) and metal precursors (Scheme 20). Tritopic ligand **178** should be able to provide access to water-stable tetrahedral $\mathbf{M_4L_4}$ cages as they constitute an alkyne-extended analogue to an already existing water-soluble and water-stable $\mathbf{M_4L_4}$ cage.[202] Even though anion-π interactions will not be possible with this cage, it will still possess a net charge of +8 and, therefore, should be able to bind

anionic guests and stabilize anionic intermediates and transition states in the context of catalysis *via* strong ion-ion interactions. Its increased cavity size should enable it to bind larger guests than its predecessor, which was only able to bind small anions.[220]

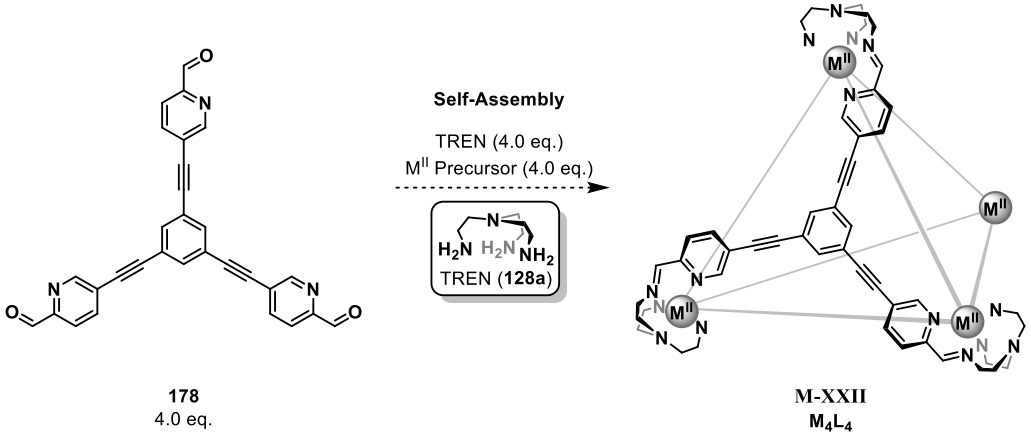

Scheme 20: Planned strategy towards face-capped metal-organic cages: **M$_4$L$_4$** tetrahedra **M-XXII** based on trialdehyde **178**.

3 Results and Discussion

3.1 Synthesis of Fully Covalent Ammonium Cages

3.1.1 Synthesis of the Subcomponents for Imine Cage Formation

For this work, investigations towards positively charged supramolecular cages started with the synthesis of naphthalene diimide (NDI) dialdehyde compound **175** as the main subcomponent. In a first attempt, NDI compound **180** was easily prepared *via* imide condensation between *p*-toluidine (**181**) and 1,4,5,8-naphthalenetetracarboxylic dianhydride (NDA, **179**) in DMF at 150 °C using microwave irradiation in 69% yield (Scheme 21).

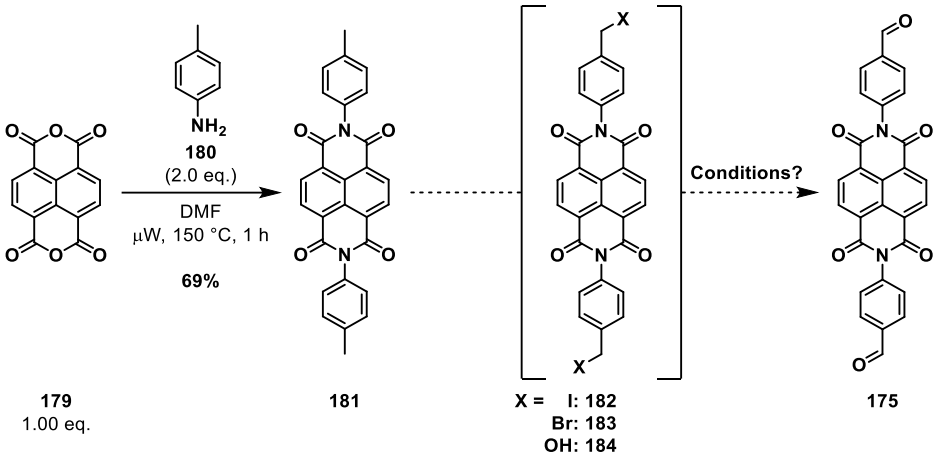

Scheme 21: First synthetic pathway investigated for the construction of NDI dialdehyde **175**.

However, oxidation of the terminal methyl groups proved to be difficult. A variety of strategies failed to deliver the desired dialdehyde **175**. Direct methods tested include a slightly modified procedure for the radical iodination and KORNBLUM oxidation in one step (Table 6, Entry 1) as reported by NITSCHKE *et al*. for 2-methylpyridines[276] and benzylic oxidation using 2-iodobenzoic acid (IBX, **186**) at various temperatures and reaction times (Table 6, Entries 2-5).[277] A stepwise approach over the WOHL-ZIEGLER bromination[278] (Table 6, Entries 6-11) was investigated as well. In all these attempts, conversion rates were quite low. For instance, the substrate was recovered after the KORNBLUM oxidation in 82% yield and would otherwise be the major component left in the crude ^{1}H-NMR spectra of the other reactions listed in table 6. Only traces of the desired products were detected, accompanied by side-products. Besides the selectivity issues, purification would be exceedingly difficult to achieve as all compounds bearing NDI moieties in a mixture of products would exhibit low solubility in most organic solvents without solubilizing groups attached to them, making the approach over NDI compound **181** not suitable for the construction of the desired subcomponent **175**. The cause for the low conversion rates may have been the very low solubility displayed by NDI compound **181**.

Table 6: Reaction conditions tested for the transformation of NDI compound **181** to dibromide **183** or dialdehyde **175**.

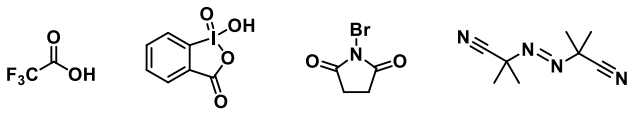

185 TFA **186** IBX **187** NBS **188** AIBN

Entry	Solvent	T [°C]	t [h]	Reagents	Yield (183)	Yield (175)
1	DMSO	150	20	I_2 (3.0 eq.), TFA (4.5 eq.)	-	Traces
2	DMSO	90	16	IBX (6.0 eq.)	-	Traces
3	DMSO	120	3	IBX (6.0 eq.)	-	Traces
4	DMSO	120	72	IBX (6.0 eq.)	-	Traces
5	PhF/DMSO (2:1)	120	72	IBX (6.0 eq.)	-	Traces
6	CCl_4	Reflux	16	NBS (2.2 eq.), AIBN (10 mol-%)	Traces	-
7	CCl_4	Reflux	40	NBS (2.2 eq.), AIBN (10 mol-%)	Traces	-
8	CCl_4	Reflux	72	NBS (2.2 eq.), AIBN (10 mol-%)	Traces	-
10	CCl_4	Reflux	96	NBS (2.2 eq.), AIBN (10 mol-%)	Traces	-
11	MeCN	Reflux	16	NBS (2.2 eq.), AIBN (10 mol-%)	Traces	-

In a second strategy, protecting group functionalized anilines were prepared for the imide condensation with NDA (**179**) to directly employ an oxygen heteroatom in benzylic position. Using 4-aminobenzyl alcohol (**189**) for the imide condensation with NDA (**179**) led to an insoluble black solid. Broad resonances in the ^{1}H-NMR spectrum suggested the presence of oligomeric side-products. Therefore, the alcohol **189** was masked using an equimolar amount of TIPS-chloride and imidazole in DMF (Scheme 22a). Concurrently, acetal protection of 4-nitrobenzaldehyde (**191**) with 2,2-dimethylpropane-1,3-diol and catalytic amounts of *p*-TsOH followed by hydrogenation of the nitro group gave access to acetal protected 4-aminobenzaldehyde (**193**) over two steps in 63% combined yield (Scheme 22b).[279]

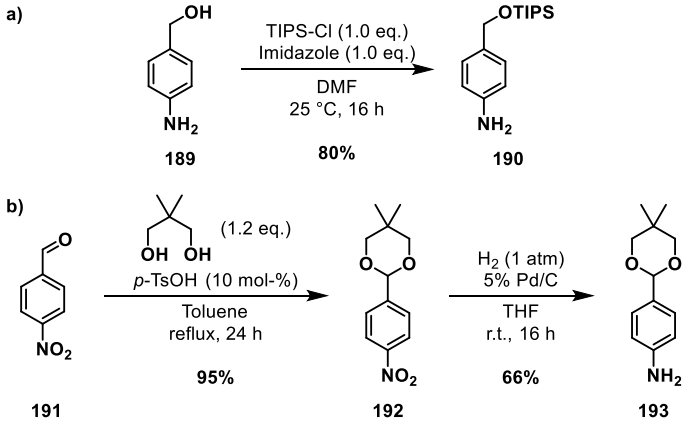

Scheme 22: Preparation of a) TIPS protected 4-aminobenzyl alcohol (**189**) in one step and b) acetal protected 4-aminobenzaldehyde (**193**) in two steps.

Imide condensation between TIPS protected amine **190** and NDA (**179**) proceeded smoothly with an excess of amine at 100 °C using microwave irradiation in 78% yield (Scheme 23). Deprotection to the free alcohol **195** and subsequent oxidation were envisioned to access dialdehyde **175**. However, treatment of NDI compound **194** with

tetrabutylammonium fluoride (TBAF) in THF/DCM at 25 °C to remove the triisopropylsilyl group according to a general literature procedure[280] led to decomposition of the material in this case. Napthalene diimides represent electron-deficient aromatic systems with electron withdrawing groups in four positions. Therefore, they may be prone to react with nucleophiles such as fluoride generating a complex mixture.

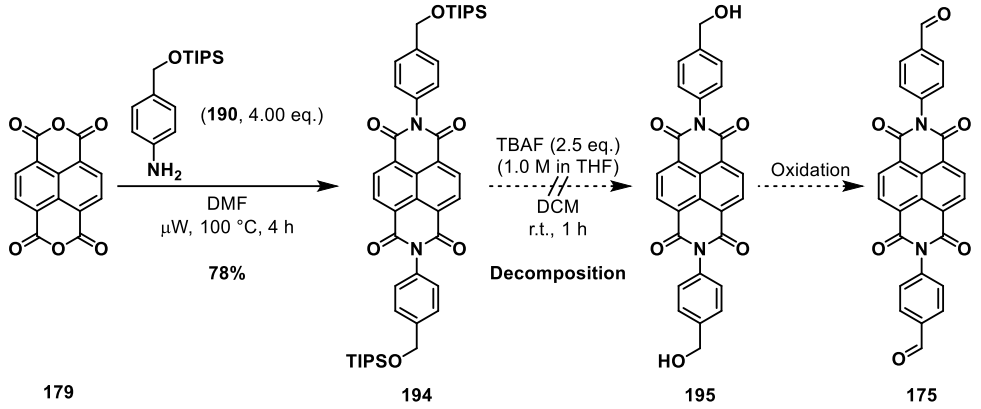

Scheme 23: Preparation of TIPS protected NDI **194** and planned synthesis route towards NDI dialdehyde **175**.

Running the reaction at lower temperatures may have been able to control this issue and still enable TIPS deprotection but a different synthetic route was chosen. Imide condensation of NDA (**179**) with acetal protected amine **193** in the presence of excess triethylamine furnished NDI compound **196** in 80% yield (Scheme 24). The base was necessary here to prevent removal of the acetal because of the following issue.

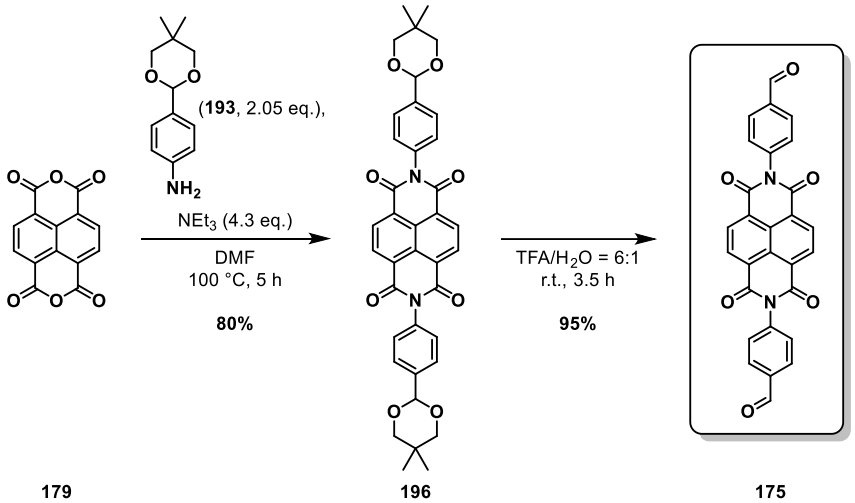

Scheme 24: Successful synthesis route towards NDI dialdehyde **175**.

It was found that one anhydride moiety in NDA (**179**) would readily get hydrolyzed in solution at ambient temperature to form dicarboxylic acid **197** as was seen in its ^{1}H-NMR spectrum in DMSO-d_6 (Figure 19). This may also explain why commercially available batches are only listed in 85% purity in assays as the dianhydride **179** seems to be unstable towards traces of water (from air moisture for example). While the TIPS protecting group was able to withstand these acidic conditions under high temperatures during imide condensation, deprotection of the acetal was not prevented and a complex mixture formed in the absence of base as the amine in **193** would now be able to react with the free aldehyde of another molecule of **193** to form imines as side-products.

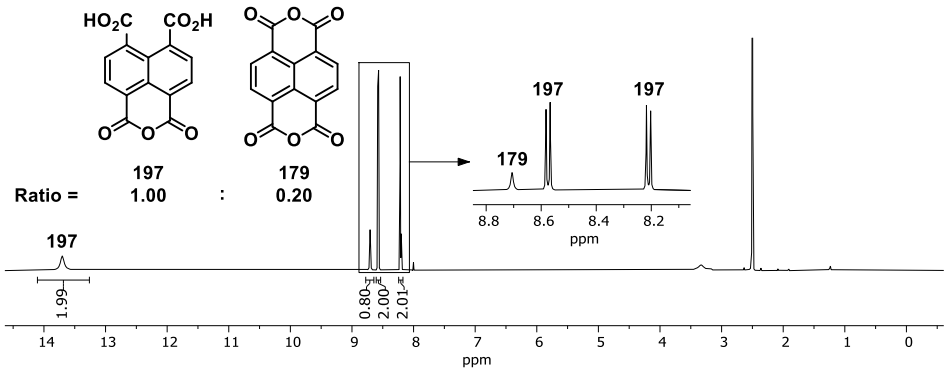

Figure 19: ^{1}H-NMR spectrum of commercially available NDA (**179**) in DMSO-d_6.

With acetal protected NDI compound **196** in hand, controlled deprotection proceeded smoothly in a TFA/H_2O = 6:1 mixture at room temperature over 3.5 h in 95% yield to furnish NDI dialdehyde **175** as the desired subcomponent for imine cage formation (Scheme 24) after aqueous workup with K_2CO_3 to neutralize the acid. The methodology also worked on gram scale. Therefore, further experiments towards the deprotection of TIPS-NDI compound **194** (Scheme 23) were not conducted.

To convert NDI dialdehyde **175** into imine cages, three different triamines were considered (Scheme 25a). Tris(2-aminoethyl)amine (**128a**), furthermore abbreviated as TREN, tris(3-aminopropyl)amine (**128b**), furthermore abbreviated as TRPN, and the more rigid triamine **128c**. While TREN (**128a**) and TRPN (**128b**) were commercially available, the literature-known GABRIEL synthesis was applied for the construction of triamine **128c** in two steps and 74% combined yield (Scheme 25b).[281]

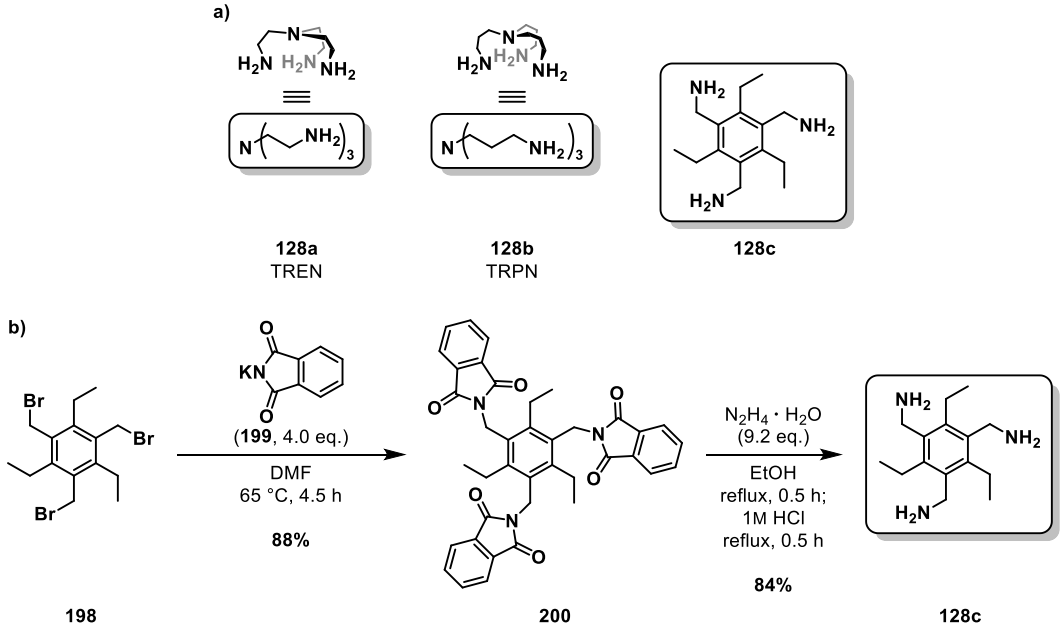

Scheme 25: a) The chemical structures of the triamine subcomponents for imine cage formation: Tris(2-aminoethyl)amine (**128a**, TREN), tris(3-aminopropyl)amine (**128b**, TRPN) and triamine **128c**. b) The GABRIEL synthesis of triamine **128c**.

Scheme 26 shows the expected outcome for when NDI dialdehyde **175** and one of the triamines **128a-c** are combined in a 3:2 ratio under high dilution, respectively, after full conversion is achieved. Imine formation is a dynamic reaction equilibrium which takes time until it reaches a local thermodynamic minimum at a given temperature. It was expected that kinetic products, monomers bearing only one NDI unit and oligomers, will form

first and disappear over time to furnish large amounts of either **Tri^{2}Di^3** type imine cages **XXIIIa-c** or **Tri^{4}Di^6** type imine cages **XXIVa-c**, if either of which constitutes the systems thermodynamic product. The screening experiments towards the formation of these novel imine cages will be the focus in chapter 3.1.2.

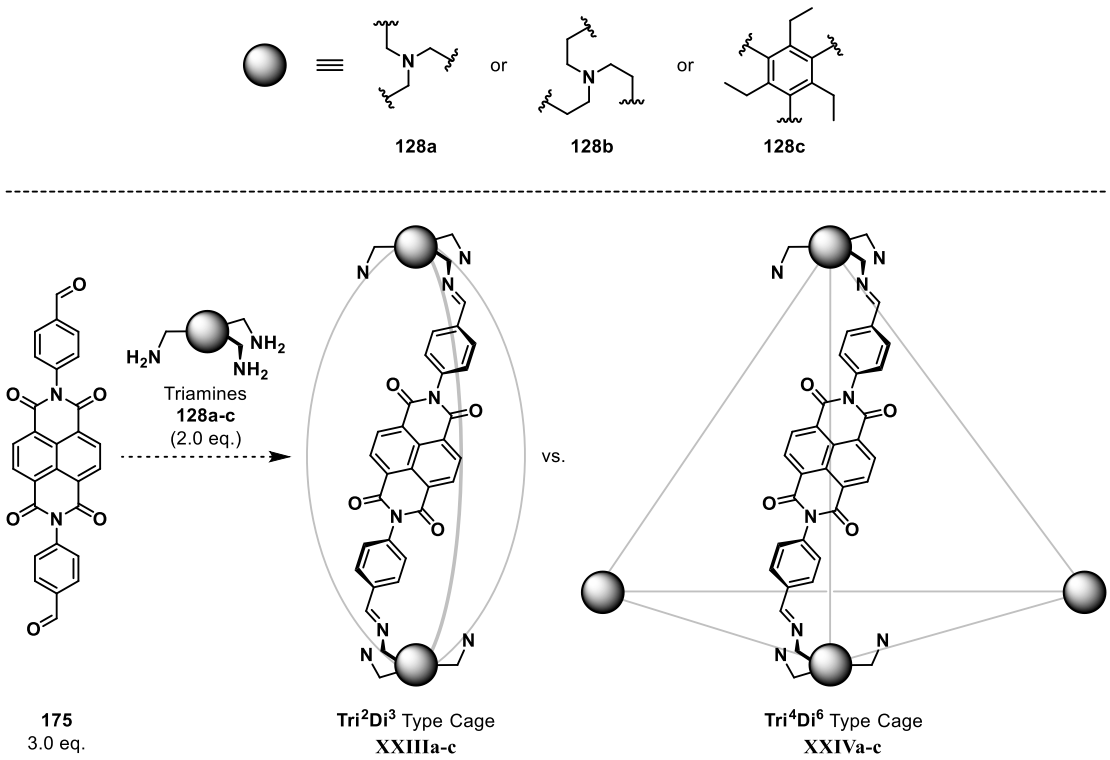

Scheme 26: Expected geometries for the imine cage formation reactions between NDI dialdehyde **175** and triamines **128a-c**.

3.1.2 Screening Experiments for Imine Cage Formation with TREN (128a)

The solubility properties of NDI dialdehyde **175** have been investigated before screening experiments were conducted. For this, about 1 mg of subcomponent **175** was diluted with 0.2-0.3 mL of each solvent tested. The compound was completely insoluble in H_2O, alkanes and benzene while at least suspensions formed in most other solvents, including toluene, chlorinated solvents such as DCM, $CHCl_3$ and 1,2-DCE as well as alcohols like MeOH and EtOH. The compound formed suspensions as well in Et_2O, THF and aprotic polar solvents like acetone, EtOAc and MeCN. Dissolution of the compound was only achieved in hot DMSO or DMF with precipitation occuring when cooling down in DMSO while the compound stayed dissolved in DMF back at room temperature for a prolonged period before precipitating as well.

Table 7: The influence of the solvent for imine cage formation between NDI dialdehyde **175** and TREN (**128a**).

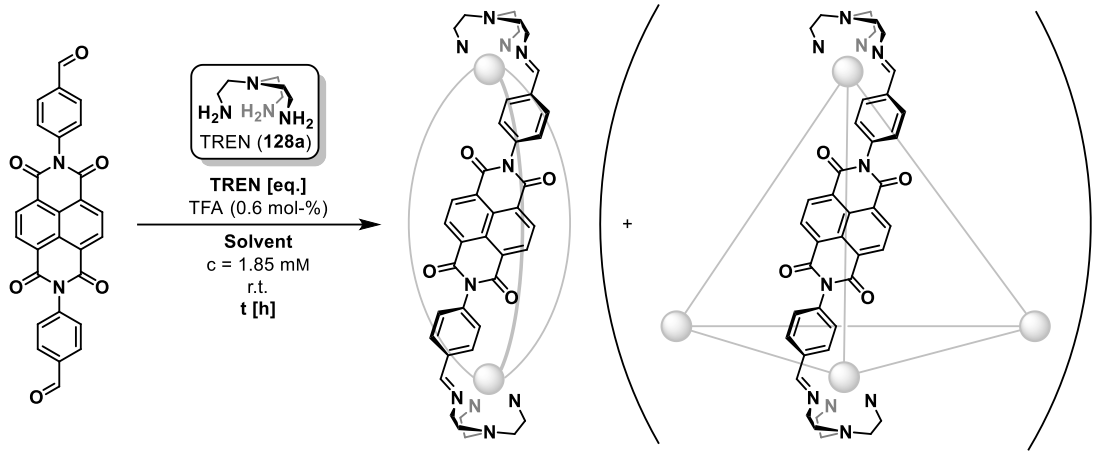

Entry	Solvent	t [h]	TREN [eq.]	Yield [%]	Ratio XXIIIa:175	Main species
1	$CHCl_3$	42	2.0	n.d.	1.00:1.69	**XXIIIa***
2	**$CHCl_3$**	**42**	**3.0**	**n.d.**	**Full Conversion**	**XXIIIa***
3	**DCM**	**18**	**3.0**	**28**	**Full Conversion**	**XXIIIa***
4	**1,2-DCE**	**18**	**3.0**	**Traces**	**Full Conversion**	**XXIIIa***
5	Et_2O	72	3.0	n.d.	n.d.	n.d.
6	THF	72	3.0	n.d.	1.00:1.50	**XXIIIa***
7	MeOH	72	3.0	n.d.	No reaction	n.d.
8	MeCN	72	3.0	n.d.	1.00:2.75	**XXIIIa***

*As interpreted from the isotopic distribution in the corresponding HR-MS experiment.

Imine formation is reversible as it constitutes a dynamic reaction equilibrium between aldehydes and amines in a condensation reaction (see chapter 1.2.3a). Once a cage formed, removal of solvent under reduced pressure at too high temperatures can shift the equilibrium again towards side-products. Therefore, the first screening experiments to find conditions suitable for imine cage formation revolved around finding an appropriate solvent with a low boiling point as it can be removed more easily, preferably one in which full conversion is achieved towards a single product (Table 7). Separation of a product mixture would be quite challenging at the imine forming step as the equilibrium would shift during any standard workup manipulation.

The first reactions tested were run at room temperature at high dilution with a concentration of [**175**] = 1.85 mM using 0.6 mol-% of trifluoroacetic acid as a catalyst. It is worth mentioning again that dialdehyde **175** did not fully dissolve in any solvent and only formed a suspension, reaching saturation quite fast. Reaction progress was monitored by diluting 0.2 mL samples of the reaction mixtures with DMSO-d_6 for mild and direct ^{1}H-NMR measurement at specific times. This was supposed to ensure that the reaction equilibrium would not change drastically during that time frame and DMSO-d_6 was chosen as the NMR solvent of choice because it proved to be the best solvent for the starting material amongst the affordable ones for NMR experiments. It was assumed that the cages forming would display similar solubility properties. However, it was found that during the reactions in chlorinated solvents, the suspension would slowly turn into a yellow solution upon completion as the slowly forming species were soluble under these high dilution conditions.

The appearance of a new imine species was already observed in $CHCl_3$ after 18 h but the reaction did not run to completion with 2.0 equivalents of TREN (**128a**) with barely any change even after 42 h (Table 7, Entry 1). Increasing the amount of TREN (**128a**) to 3.0 equivalents led to full consumption of the starting material in 42 h (Table 7, Entry 2). Low conversion of starting material was observed in THF, MeOH and MeCN even after 72 h (Table 7, Entries 6-8) while broad resonances were dominant in Et_2O hinting at oligomeric species.

However, the reaction rate increased when running the reaction in DCM or 1,2-DCE and full conversion was achieved overnight with a crude yield of 28% for the reaction in DCM (Table 7, Entries 3-4, respectively). A highly symmetrical imine species with all necessary peaks for either **Tri^{2}Di^3** cage **XXIIIa** or **Tri^{4}Di^6** cage **XXIVa** was observed as the main product in the ^{1}H-NMR spectrum accompanied by low amounts of impurities (Figure 20). For this NMR, a 0.2 mL sample of the reaction mixture was dried using a gentle nitrogen stream and the residue was diluted with DMSO-d_6 (0.5 mL) to lower the intensity of the DCM peak at 5.74 ppm.

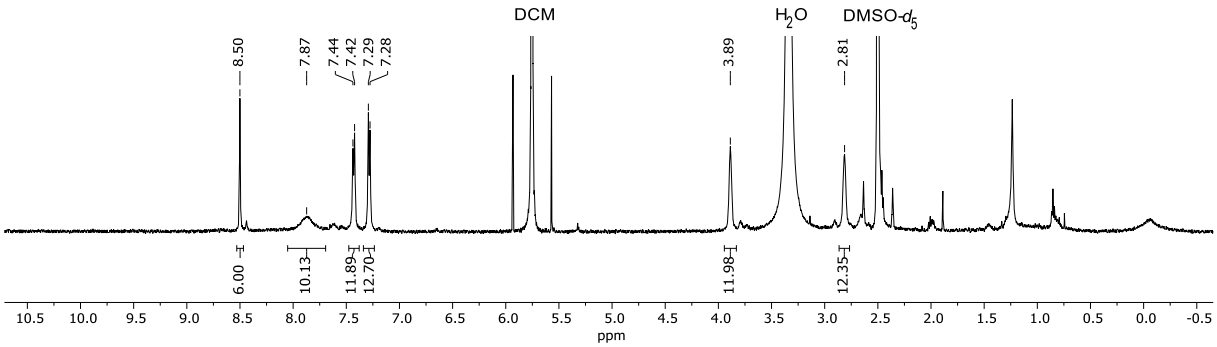

Figure 20: ^{1}H-NMR spectrum of the reaction mixture in the experiment of table 7, entry 4 after 18 h.

The high-resolution ESI-MS data gave evidence for the formation of the **Tri^{2}Di^3** imine cage **XXIIIa** as the main compound. The peak with an observed mass of 1607.5038 matched the one calculated for that species in the form of its proton adduct $[M+H]^+$ (Figure 21). Simultaneously, smaller peaks in between the main ones in an interval of about 0.5 were observed hinting at the existence of a species with a charge of +2. These peaks were much smaller in intensity compared to the main peaks. As such, the presence of **Tri^{4}Di^6** cage **XXIVa** in trace amounts could not be ruled out here as well because the smaller peaks could belong to either trace amounts of the **Tri^{4}Di^6** cage **XXIVa** in the form of its proton adduct $[M+2H]^{2+}$ or the bis-adduct $[2M+2H]^{2+}$ of **Tri^{2}Di^3** cage **XXIIIa**.

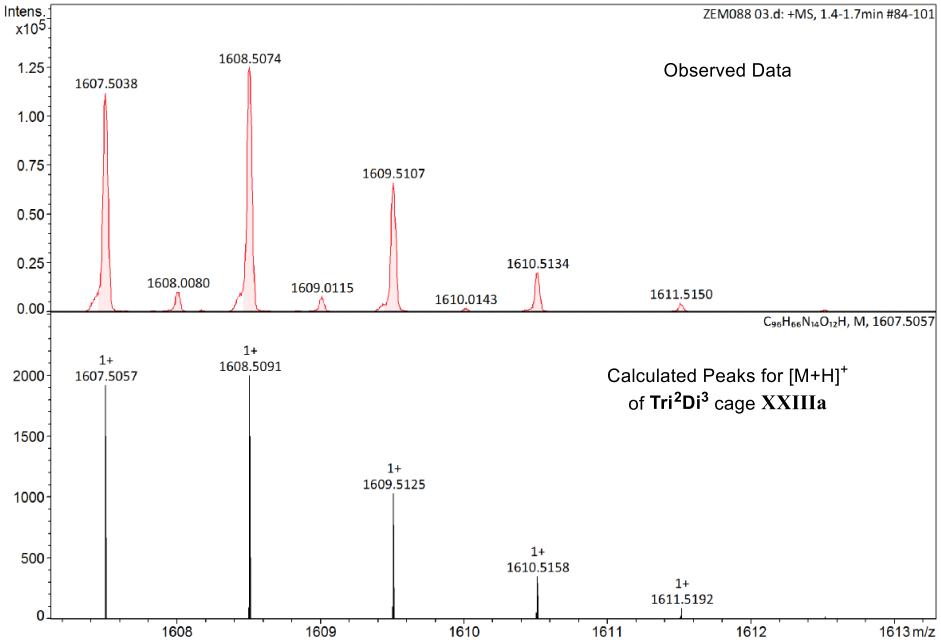

Figure 21: Relevant HR-MS peak of the reaction mixture in the experiment of table 7 (Entry 4) after 18 h.

The crude product from the experiment in entry 3 of table 7 was obtained by cooling of the reaction mixture at –20 °C for a few hours for precipitation of the product to occur. The precipitate was filtered off and washed with a small amount of cold DCM. However, a large part of the desired cage compound remained in solution and, therefore, in the filtrate. More experiments were performed because of this. First, the amount of acid catalyst was increased by a factor of 3 to try and reduce the time needed to reach full conversion within the same day of setting up the reaction (Table 8, Entry 1). However, running the reaction overnight was still necessary to reach full conversion. Increasing the temperature to 50 °C led to decomposition of the material with undefined broad resonances showing up in the ^{1}H-NMR for the experiments performed in DCM and 1,2-DCE (Table 8, Entries 2, 5 and 6).

Doubling the concentration promoted precipitation of the product and increased the yield to 25% in 1,2-DCE (Table 8, Entry 4) almost matching the yield achieved with DCM in entry 1. Based on this finding, another theory was tested to further facilitate product precipitation to increase the crude yield. In combination with a higher concentration of [**175**] = 3.70 mM, a mixture of DCM/*n*-Pentane = 10:1 was used (Table 8, Entry 7). The yield increased to 56% because the solvent mixture would allow for better precipitation of the product as it is insoluble in pure *n*-pentane.

Table 8: Optimization of reaction conditions for imine cage formation between dialdehyde **175** and TREN (**128a**).

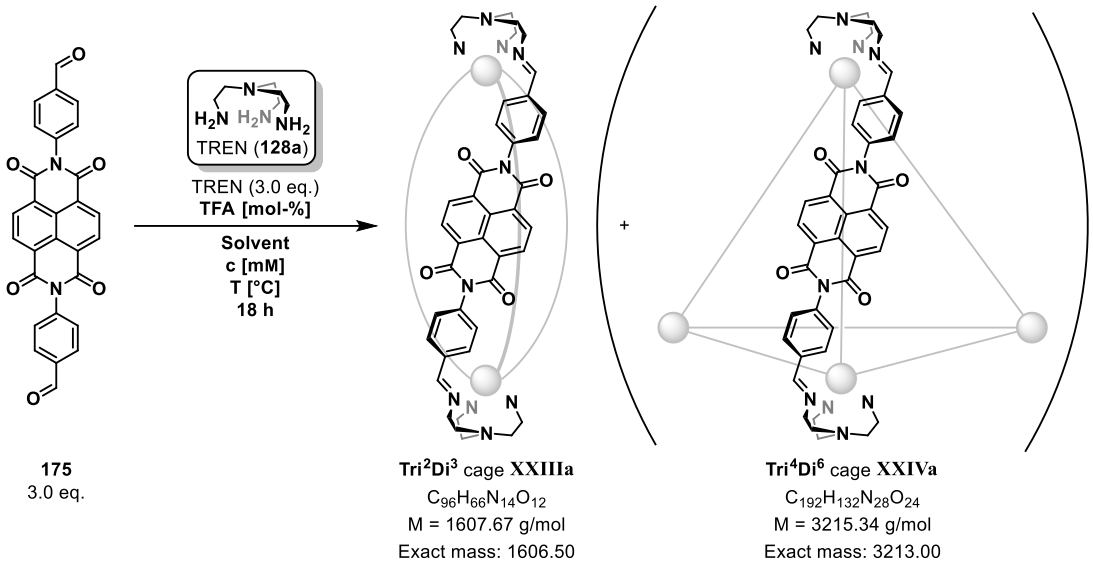

Entry	Solvent	T [°C]	c(175) [mM]	TFA [mol-%]	Yield [%]	Product
1	DCM	23	1.85	1.8	28	**XXIIIa**
2	DCM	50	1.85	1.8	n.d.	Decomposition
3	1,2-DCE	23	1.85	1.8	Traces	**XXIIIa**
4	1,2-DCE	23	3.70	1.8	25	**XXIIIa**
5	1,2-DCE	50	1.85	1.8	n.d.	Decomposition
6	1,2-DCE	50	3.70	1.8	n.d.	Decomposition
7	DCM/Pentane = 10:1	23	3.70	1.8	56	**XXIIIa**
8	**DCM**	**23**	**3.70**	**2.0**	**87***	**XXIIIa**
9**	**DCM**	**23**	**3.70**	**2.0**	**90***	**XXIIIa**

*Upon completion of the reaction, *n*-Pentane was added to give a solvent system of DCM/*n*-Pentane = 1:1 and the mixture was cooled at −20 °C for 3 h before filtration, increasing the yield drastically.

Scale-up from 15 mg to 100 mg of dialdehyde **175 with 2.5 eq. of TREN (**128a**, new batch).

Further investigations revealed that the reaction can be run in DCM and upon completion of the reaction an equal amount of *n*-pentane was added, and the reaction mixture was cooled at −20 °C for 3 h for precipitation to occur in a DCM/*n*-Pentane = 1:1 mixture (Table 8, Entry 8) to give **Tri^{2}Di^3** imine cage **XXIIIa** in 87% yield. Scale-up of the reaction from 15 mg to 100 mg of dialdehyde **175** was possible as well following the same workup procedure without any problems increasing the yield to 90% (Table 8, Entry 9). With a fresh batch, 2.0 equivalents of TREN (**128a**) were not sufficient. 2.5 equivalents of the triamine were necessary for full conversion under these conditions. The screening experiments regarding this will be the focus of chapter 3.1.5 as well as the experiments with TRPN (**128b**).

3.1.3 Experiments for Imine Cage Formation with Triamine 128c

Table 9: Optimization of reaction conditions for imine cage formation between dialdehyde **175** and triamine **128c**.

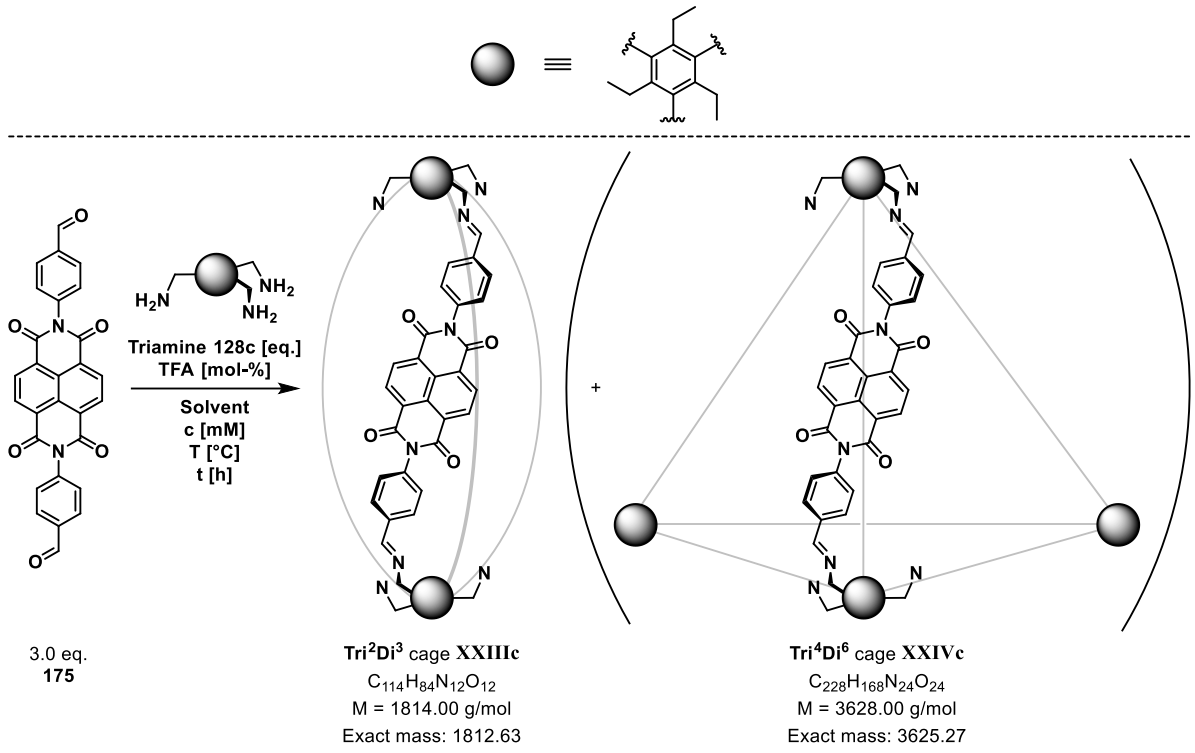

Entry	Solvent	T [°C]	t [h]	c(175) [mM]	128c [eq.]	TFA [mol-%]	Ratio XXIIIc:175	Main Species
1	Et_2O	25	18	1.85	2.3	0	No reaction	n.d.
2	Et_2O	25	96	1.85	2.3	3	No reaction	n.d.
3	MeCN	25	18	1.85	2.4	3	No reaction	n.d.
4	MeCN	25	18	3.70	2.4	3	1.00:24.8	n.d.
5	MeCN	50	18	1.85	2.4	3	1.00:44.0	n.d.
6	MeCN	50	18	3.70	2.4	3	1.00:14.1	**XXIIIc***
7	**MeCN**	**50**	**132**	**3.70**	**2.4**	**3**	**1.00:0.45**	**XXIIIc***
8	$CHCl_3$	25	18	1.85	2.4	3	No reaction	n.d.
9	$CHCl_3$	25	18	3.70	2.4	3	No reaction	n.d.
10	$CHCl_3$	50	18	1.85	2.4	3	1.00:3.80	n.d.
11	$CHCl_3$	50	18	3.70	2.4	3	1.00:5.96	n.d.
12	**$CHCl_3$**	**50**	**132**	**3.70**	**2.4**	**3**	**1.00:0.34**	**XXIIIc***
13	DCM	25	18	1.85	2.3	0	1.00:17.3	n.d.
14	**DCM**	**25**	**96**	**1.85**	**2.3**	**3**	**1.00:0.31**	**XXIIIc***
15	1,2-DCE	25	18	1.85	2.4	3	No reaction	n.d.
16	1,2-DCE	25	18	3.70	2.4	3	1.00:18.4	n.d.
17	**1,2-DCE**	**50**	**18**	**1.85**	**2.4**	**3**	**Full conversion**	**XXIIIc***
18	**1,2-DCE**	**50**	**18**	**3.70**	**2.4**	**3**	**Full conversion**	**XXIIIc***

*As interpreted from the isotopic distribution in the corresponding HR-MS experiment.

Again, several experiments with triamine **128c** in Et_2O, MeCN, $CHCl_3$, DCM and 1,2-DCE have been performed simultaneously at varying temperatures and concentrations. No reaction was observed in Et_2O (Table 9, Entries 1-2). In MeCN, the reaction progressed very slowly at room temperature. Even at 50 °C it took 5.5 days for the ratio between supposed **Tri^{2}Di^3** cage **XXIIIc** and dialdehyde **175** to reach 1.00:0.45 (Table 9, Entry 7). A similar result was obtained in $CHCl_3$ (Table 9, Entries 8-12) and DCM (Table 9, Entries 13-14). In 1,2-dichloroethane (1,2-DCE) low conversion was observed at room temperature (Table 9, Entries 15 and 16). However, at 50 °C full conversion of dialdeyhde **175** was achieved overnight (Table 9, Entries 17 and 18). At [**175**] = 1.85 mM, the ^{1}H-NMR spectrum showed the least number of residual side-products with all necessary peaks being present which may correspond to either **Tri^{2}Di^3** cage **XXIIIc** or **Tri^{4}Di^6** cage **XXIVc** (Figure 22).

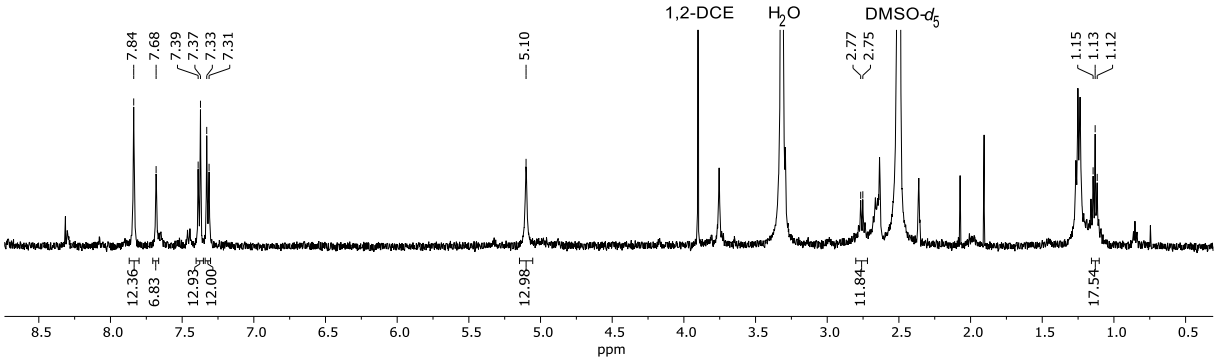

Figure 22: ^{1}H-NMR spectrum of the reaction mixture in the experiment of table 9, entry 17 after 18 h.

The rigidity of triamine **128c** may serve as an explanation for its lower reactivity compared to TREN (**128a**). The ethyl and aminomethyl groups attached to the benzene core are so close in proximity that the least amount of steric hindrance is achieved when the ethyl groups align themselves towards one side of the plane spanned by the aromatic benzene core while the aminomethyl chains face towards the other side. At the same time, the decreased reactivity also seems to prevent oligomer and/or polymer formation at 50 °C in comparison to experiments performed with TREN (**128a**, Table 8, chapter 3.1.2) at this temperature.

The corresponding high-resolution ESI-MS experiment gave evidence for the formation of **Tri^{2}Di^3** cage **XXIIIc** as the main compound with an observed mass of 1813.6396 matching the one calculated for that species in the form of its proton adduct $[M+H]^+$ (Figure 23). Smaller peaks in between the main ones in an interval of about 0.5 were observed as well hinting at the existence of a species with a charge of +2. These peaks were much smaller in intensity compared to the main peaks. As such, the presence of **Tri^{4}Di^6** cage **XXIVc** in trace amounts could not be ruled out here because the smaller peaks could belong to either the **Tri^{4}Di^6** cage **XXIVc** in the form of its proton adduct $[M+2H]^{2+}$ or the bis-adduct $[2M+2H]^{2+}$ of **Tri^{2}Di^3** cage **XXIIIc**.

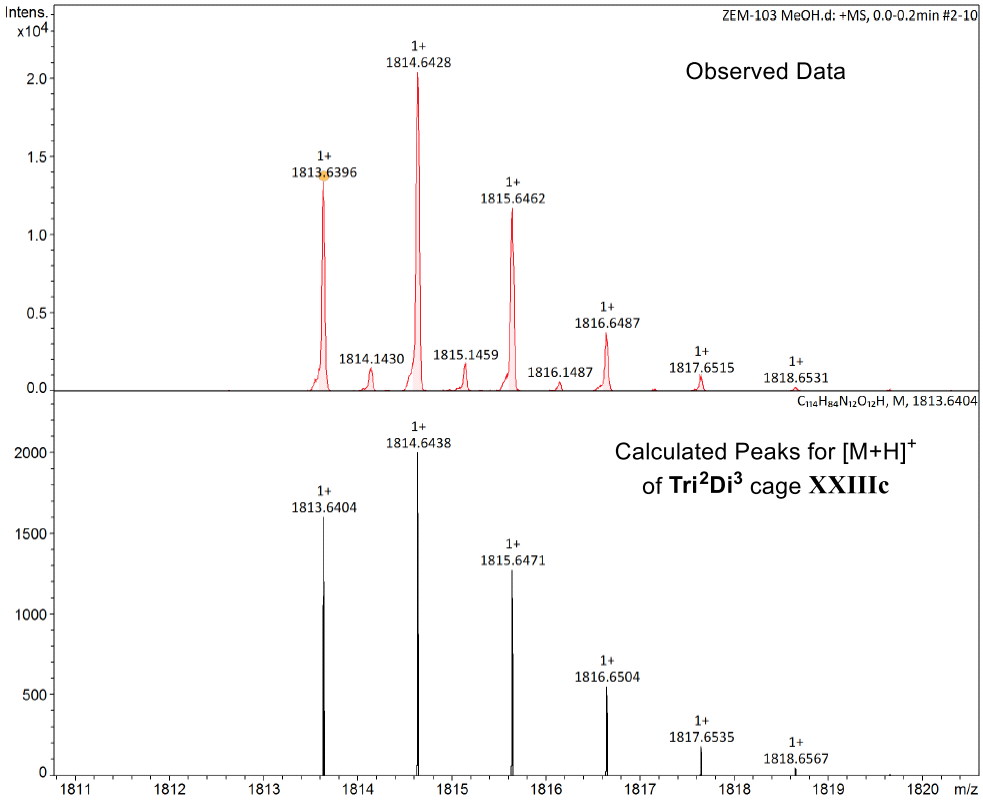

Figure 23: Relevant HR-MS peaks of the reaction mixture in the experiment of table 9, entry 17 after 18 h.

Both TREN derived **Tri^{2}Di^3** cage **XXIIIa** and **Tri^{2}Di^3** cage **XXIIIc** were not the desired cage compounds. In fact, the goal of this study was to synthesize cages large enough for guest encapsulation and catalysis. As such, pseudo tetrahedral cages **XXIVa** and **XXIVc** would have been the preferred choice as they should possess a larger potential cavity than their smaller alternatives **XXIIIa** and **XXIIIc**. Regardless, the next chapter will focus on finding suitable conditions for the reduction of imine cage **XXIIIa** to its corresponding ammonium derivative because its guest-uptake abilities may be exceptional nonetheless based on the fact that a fully covalent cage might be flexible enough for its subcomponents to rearrange around a given guest, leading to strong binding. However, more time was not invested into the isolation of imine cage **XXIIIc** as it did not seem to provide any meaningful advantage over cage **XXIIIa**.

3.1.4 Synthesis of Ammonium Cages XVIIa and XXVa

Imine formation was the first step within a two-step process called reductive amination in which a carbonyl is converted into an amine over an intermediate imine group. The second step involves the reduction of the imine functionality to an amine. In a first attempt to reduce **Tri^{2}Di^3** cage **XXIIIa** directly after its formation in DCM as described in chapter 3.1.2 (Table 8, Entry 9), an excess of sodium borohydride ($NaBH_4$, 48 eq. per imine group) was added to the same reaction flask, but this led to a complex mixture after aqueous workup showing only broad resonances in the aromatic region of the ^{1}H-NMR in DMSO-d_6, D_2O and MeOH-d_4. Because of this, control experiments were performed to find out if the NDI moiety itself is stable enough towards common reducing agents employed in the second step of reductive amination reactions. For this, previously synthesized acetal-protected NDI compound **196** (Table 10) was chosen because it dissolved readily, and the acetal group should not get attacked by nucleophiles introduced with the reducing agents tested. The NDI moiety, as an electron-deficient construct, should provide the only electrophilic positions which may be prone to nucleophilic attack.

Table 10: Stability tests with NDI compound **196** against different hydride sources as reducing agents.

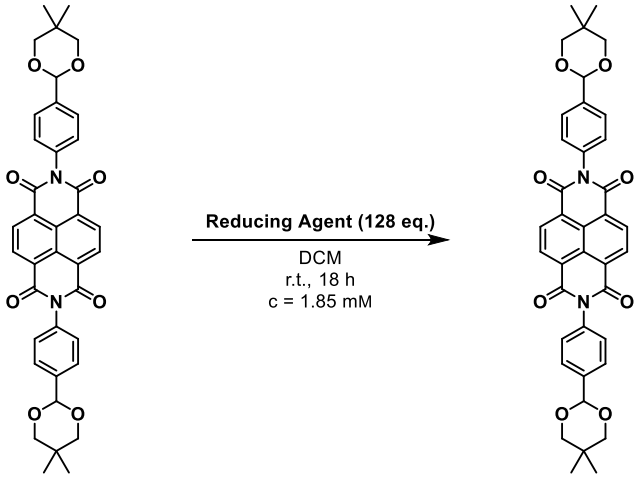

196 196

Entry	Reducing Agent	Note
1	$NaBH_4$	Decomposition
2	$NaBH(OAc)_3$	No reaction / Substrate recovered
3	$NaBH_3CN$	No reaction / Substrate recovered

NDI compound **196** was dissolved in DCM (c = 1.85 mM) and an excess (128 eq.) of either $NaBH_4$, $NaBH(OAc)_3$ or $NaBH_3CN$ was added (Table 10). The reaction mixtures have been stirred for 18 h at room temperature. The material decomposed in the presence of $NaBH_4$ (Table 10, Entry 1) and was successfully recovered after treatment with $NaBH(OAc)_3$ or $NaBH_3CN$ (Table 10, Entries 2-3). This was expected as the two latter ones are known as mild and effective alternatives to $NaBH_4$.[282,283] Since $NaBH_3CN$ can produce cyanides upon workup as toxic side-products, $NaBH(OAc)_3$ was investigated for the reduction of TREN-based **Tri^{2}Di^3** imine cage **XXIIIa** (Scheme 27).

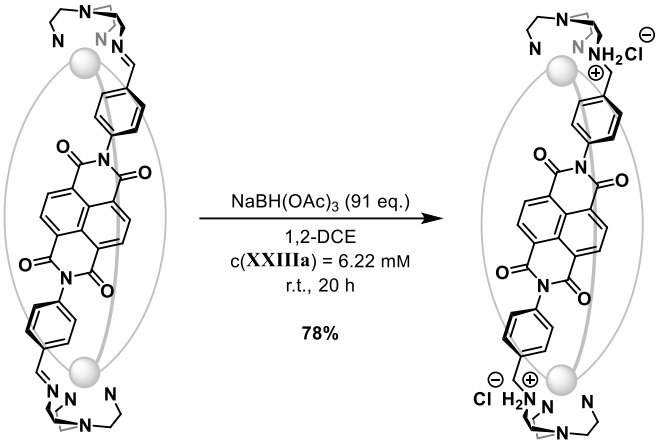

Scheme 27: Reduction of imine cage **XXIIIa** to ammonium chloride cage **XVIIa**.

Scheme 27 illustrates the scaled up and optimized reaction conditions found for the reduction of imine cage **XXIIIa** to the ammonium chloride cage **XVIIa**. According to a standard literature procedure[284] the reaction was first tested with 8.4 equivalents of $NaBH(OAc)_3$ (1.4 equivalents per imine group) in 1,2-DCE at a concentration of [**XXIIIa**] = 6.22 mM. The reaction progress was monitored *via* ^{1}H-NMR as both the substrate **XXIIIa** and the product **XVIIa** have shown a retention factor of 0.00 on TLC (either coated with normal SiO_2 or with SiO_2 deactivated with NEt_3). The NMR experiments showed a set of new signals forming which correlated well with the desired structure **XVIIa,** but the reaction was incomplete. It was found that full conversion was achieved by simply adding a huge excess of $NaBH(OAc)_3$ (up to 91 eq.). Acidic workup then furnished ammonium chloride cage **XVIIa** in 78% yield, presumably as the **Tri^{2}Di^3** cage **XVIIa** depicted in Scheme 27 with evidence for this structure gathered by NMR experiments and especially through the isotopic distribution shown in the corresponding high-resolution ESI-MS experiment (see experimental section, chapter 5.2.1).

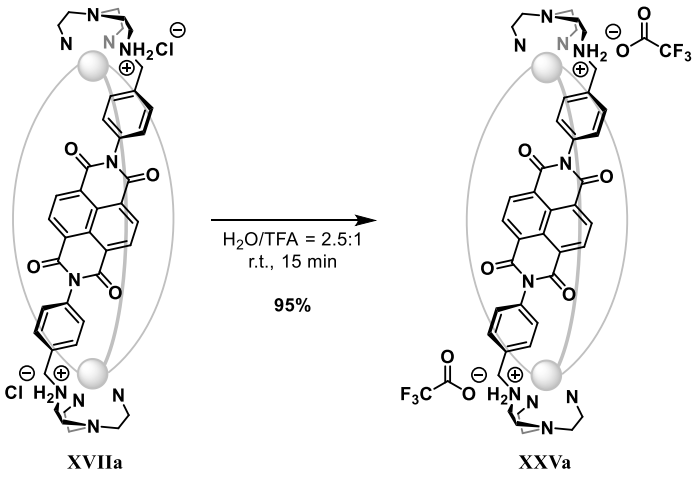

Scheme 28: Synthesis of ammonium trifluoroacetate cage **XXVa** *via* anion exchange from ammonium chloride cage **XVIIa**.

Ammonium chloride cage **XVIIa** exhibited poor solubility properties in any organic solvent and showed moderate solubility in H_2O. For this reason, anion exchange with an excess of TFA in H_2O was envisioned (Scheme 28). The aqueous solution quickly turned into a white suspension upon addition of TFA and was stirred for 15 minutes at room temperature before workup to give access to ammonium trifluoroacetate cage **XXVa** as a white solid. The

material was much better soluble in MeCN and DMSO now whilst maintaining a mediocre, yet slightly worse, solubility in water. Additonally, the TFA salt **XXVa** remained stable for months at –20 °C while the chloride derivative **XVIIa** already decomposed over 4 weeks at the same temperature. Guest-uptake experiments with anionic guests have been performed in MeCN-d_3 with the TFA salt and this will be discussed in chapter 3.1.8.

First, however, a few more experiments regarding the initial imine forming step will be presented. In chapter 3.1.2 it was mentioned that it took an excess of the triamine (TREN, **128a**) for NDI dialdehyde **175** to be fully converted into products. The batch of TREN used was an old one which seemed to have decomposed to some degree. As a fresh batch of TREN has been delivered, the amount of triamine needed had to be investigated once again. During these experiments a closer look at the reactions revealed the formation of other imine species and this will be discussed in the next chapter.

3.1.5 Influence of the TREN Concentration on the Imine Forming Step

In the following section, a new terminology for different hypothetical imine species will be introduced in which TREN (**128a**) and dialdehyde **175** are defined as subcomponents **A** and **B**, respectively (Figure 24) to make it easier to understand how many equivalents of each are present in the theoretically possible structures mentioned. For instance, the **Tri^{2}Di^3** type cage **XXIIIa** can also be written as **A_2B_3** since it is formed with 2 equivalents of TREN (**128a; A**) and 3 equivalents of dialdehyde **175 (B)**. **A_2B_2** refers to the highly symmetrical oligomer **201a**; **A_2B** refers to the simplest compound **202a** with 1 equivalent of dialdehyde **175** (**B**) being connected to 2 equivalents of TREN (**128a, A**) over imine bonds. The nomenclature for organic cages presented in chapter 1.2.3b, as it was defined, can not be applied to **A_2B_2** and **A_2B** because they are not polycyclic. Therefore, this arbitrary terminology is used for simplicity. **A_4B_6** refers to **Tri^{4}Di^6** type cage **XXIVa** and **A_8B_{12}** refers to **Tri^{8}Di^{12}** cage **XXVIa** in which dialdehyde **175** (**B**) and TREN (**128a; A**) constitute the edges and vertices, respectively.

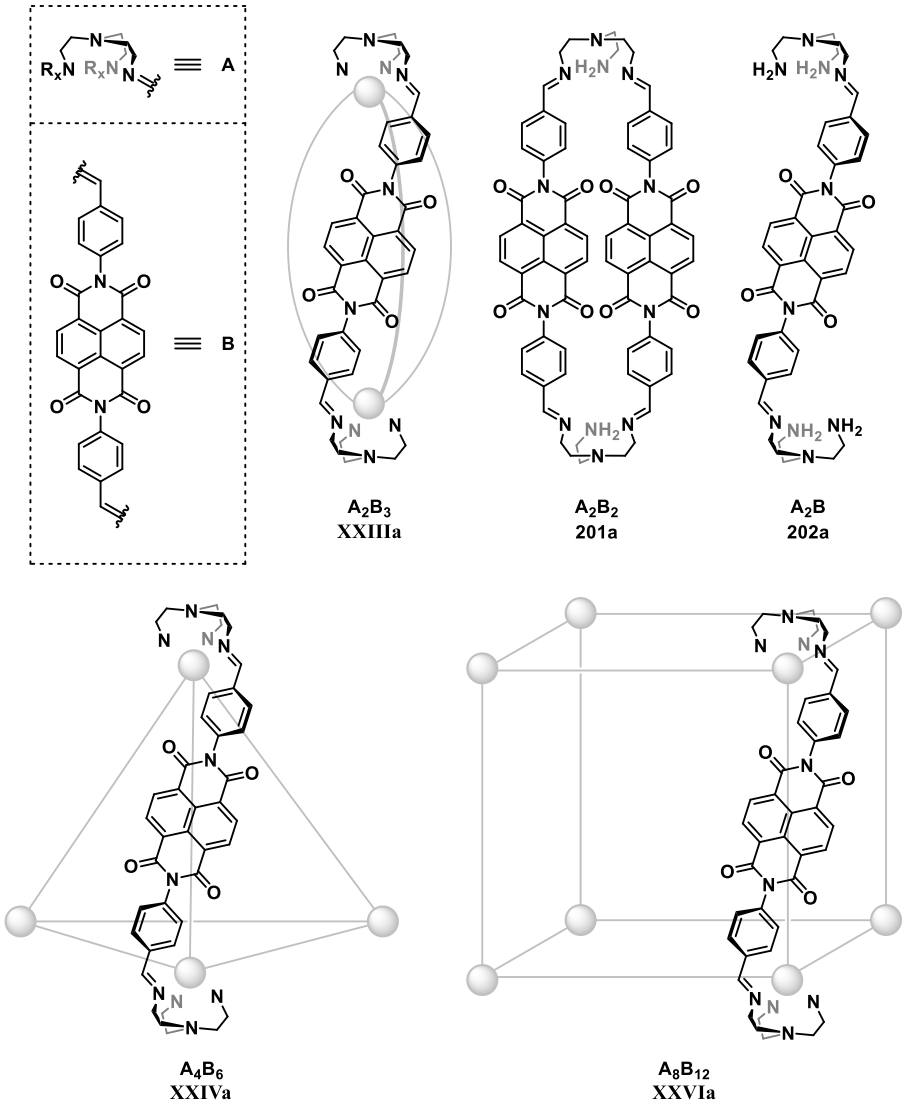

Figure 24: Hypothetical and highly symmetric structures from imine formation between dialdehyde **175** and TREN (**128a**).

As described in chapter 3.1.2, combining dialdehyde **175** with 2.5 equivalents of TREN (**128a**) at room temperature in DCM with 2 mol-% of TFA gave **A_2B_3** cage **XXIIIa** in 90% yield (Table 8, Entry 9) after 18 h. During screening experiments, samples were taken from the reactions at earlier stages to analyse them *via* ^{1}H-

NMR measurements. At least two other imine compounds formed in the first few hours being accompanied by starting material and low amounts of **A_2B_3** type cage **XXIIIa**. These other imine compounds appeared to be highly symmetrical as well based on the new ^{1}H-NMR peaks. However, their quantity decreased over time to the point where **A_2B_3** cage **XXIIIa** remained as the only product with the other two unknown imine species being left in residual amounts at best. In theory, the thermodynamic product should prevail, given enough time under certain conditions for the reaction to equilibrate. The time needed to reach this state can drastically be reduced by an increase of temperature, but this only led to broad resonances in the ^{1}H-NMR when using TREN (**128a**) at 50 °C in this case, as was discussed in chapter 3.1.2 (Table 8, marked as "Decomposition"). This hinted at the preferential formation of complex oligomers or polymers which most likely represent the systems true thermodynamic products.

Driven by the desire to find conditions for the possible formation of larger organic cages, such as **A_4B_6** type cage **XXIVa** (Figure 24), the effects of a higher triamine concentration on this reaction were explored. An increase of the reaction rate was expected with increasing TREN (**128a**) concentration. Thus, the reactions were run at lower temperatures and without the addition of an acidic catalyst to be able to follow the reaction progress over time. But technically, introducing greater amounts of TREN (**128a**) to the reaction should favour fast accumulation of kinetic products with lower molecular weight because at high enough TREN (**128a**) concentration, a molecule of dialdehyde **175** should almost only encounter molecules of TREN (**128a**) next to it. Out of curiosity, this has been investigated regardless and initial results were found to be quite intriguing.

First, the reaction was set up again at 0 °C using 10 equivalents of TREN (**128a**) without using an acidic catalyst (Scheme 29).

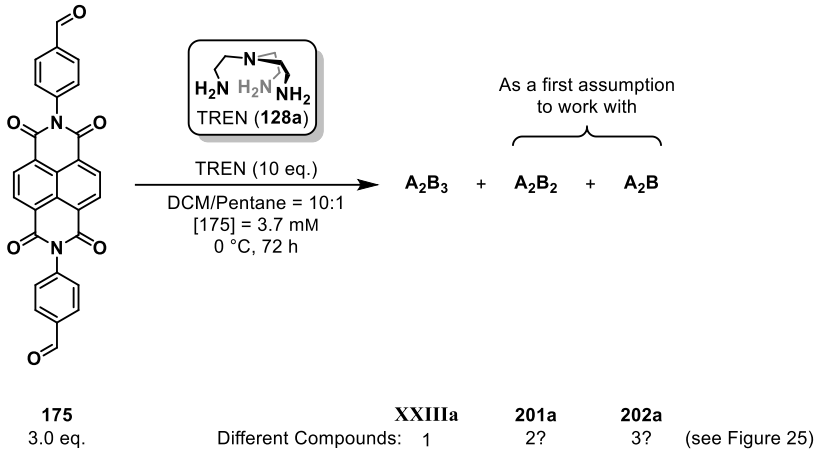

Scheme 29: Conditions used to monitor the reaction progress of imine formation between dialdehyde **175** and TREN (**128a**) over time which is shown in Figure 25.

In this early test reaction, the lower temperature and the absence of catalyst were meant to slow down the reaction for a more reliable analysis *via* ^{1}H-NMR. 0.2 mL samples of the reaction mixture were taken after each time interval. The solvent was removed with a gentle argon stream and the residue was diluted with DMSO-d_6 (0.5 mL) to compare the new signals with the ones given by isolated starting material and isolated **A_2B_3** type cage **XXIIIa**. It is worth noting that the reaction mixtures form a suspension and become solutions upon full conversion since dialdehyde **175** is less soluble than the products. The resulting spectra are shown in Figure 25. Interestingly, the peaks belonging to the NDI protons of dialdehyde **175** and **A_2B_3** type cage **XXIIIa** show up as very broad

resonances in the NMR spectra of the reaction mixtures and seem to disappear in the baseline. This may have been caused by enhanced π-π stacking of the naphthalene diimide moieties under these circumstances but this remained speculation at best.

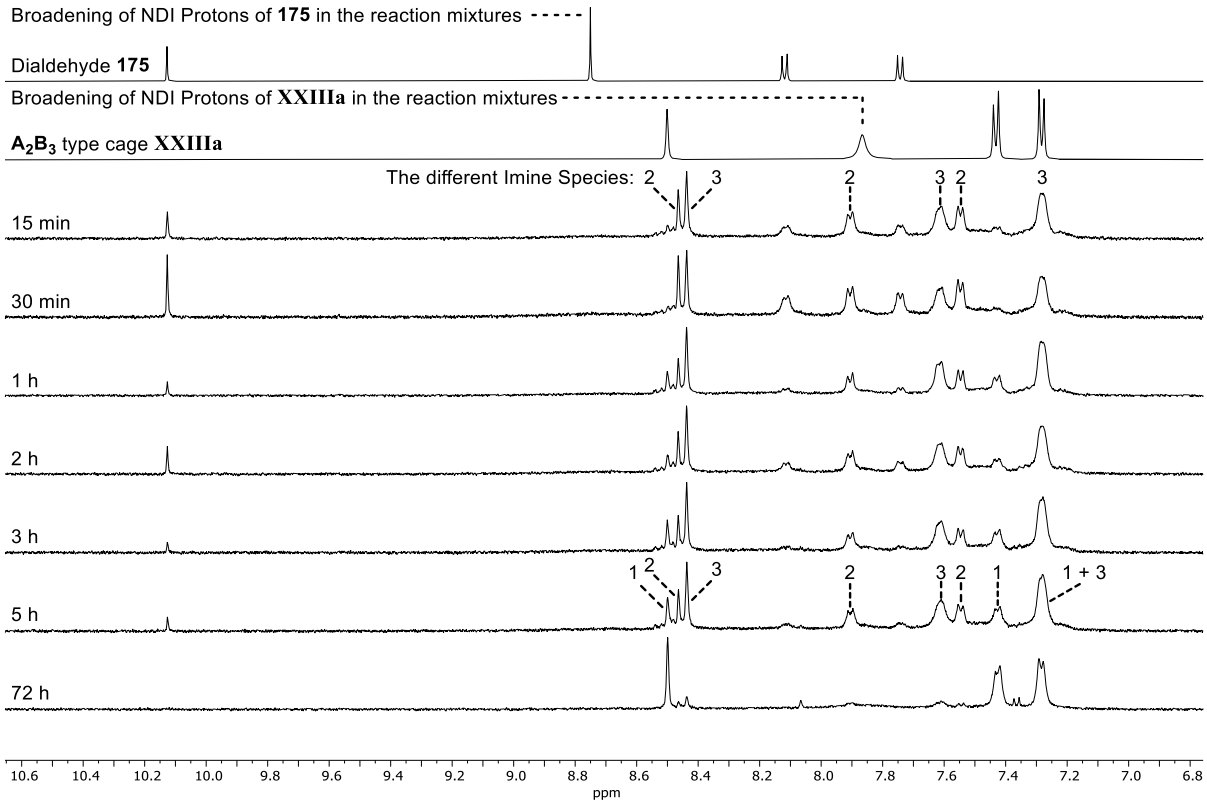

Figure 25: ^{1}H-NMR spectra of the reaction depicted in Scheme 29 showing its progress over time. Peaks for $\mathbf{A_2B_3}$ type cage **XXIIIa** have been assigned based on previously isolated material; Peaks for imine compounds 2 and 3 have been assigned here and are meant to create a basis for the NMR yield analysis in the following part (Table 11).

It was assumed that the unknown imine compounds 2 and 3 were low molecular weight kinetic products (of the type $\mathbf{A_2B_2}$ or $\mathbf{A_2B}$ for example, see figure 24) because they formed immediately at the start of the reaction (Figure 25, t = 15 min) and almost vanished after a prolonged period of time (Figure 25, t = 72 h) but their true nature was to be determined as the high-resolution ESI-MS experiments shown in chapter 3.1.2 also hinted at trace amounts of what could have been $\mathbf{A_4B_6}$ type cage **XXIVa**, which arguably is more interesting for guest-uptake and catalysis due its bigger potential cavity. The experiments have been extended to gain more insight on the influence of the TREN (**128a**) concentration. This time, the reactions were run at room temperature without TFA as they were still slow enough to easily see a difference on the distribution of imine species formed. 1,2,4,5-Tetramethylbenzene (Scheme 30, **203**) was used as an internal standard. The amount of TREN (**128a**) ranged from 5 to 60 equivalents. Table 11 summarizes the most important data obtained throughout this screening. Interestingly, the formation of at least two more highly symmetric imine species has been observed when reactions with an excess of amine (60 eq., Table 11, Entries 22-28) were given enough time to equilibrate. This was a surprising result because the simplest structure **202a** ($\mathbf{A_2B}$) was expected to dominate the reaction mixture as the main product with an excess of TREN (**128a**) which it seemed to in the first few hours (Table 11, Entries 22-24). However, the equilibrium changed over time, favouring a different product according to NMR (Table 11, Entries 25-28).

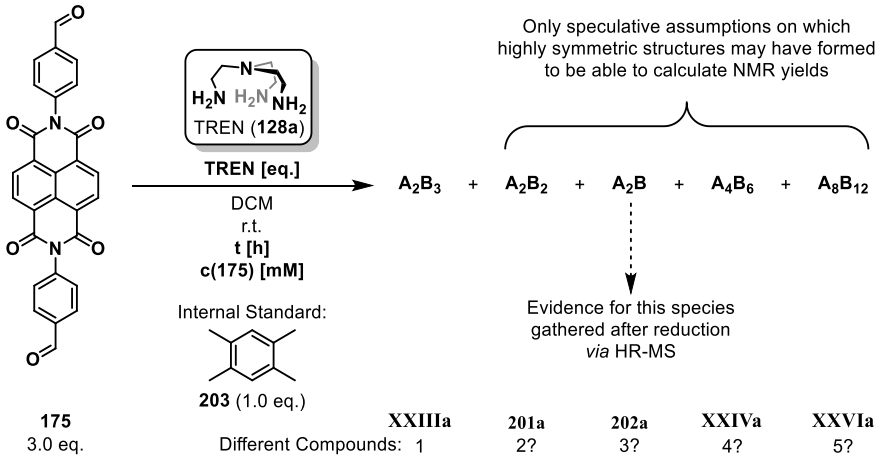

Scheme 30: Reaction conditions used to monitor the reaction progress of the imine formation between dialdehyde **175** and TREN (**128a**) over time according to table 11. 1,2,4,5-Tetramethylbenzene (**203**) was added as an internal standard.

Table 11: Reaction conditions and NMR yields for the theoretical imine species formed according to scheme 30.

Entry	TREN [eq.]	c [mM]	t [h]	XXIIIa [%]*	201a [%]*	202a [%]*	XXIVa [%]*	XXVIa [%]*
1	5.0	3.70	2.5	20	20	15	0	0
2	5.0	3.70	3.0	25	25	15	0	0
3	5.0	3.70	4.0	45	25	15	0	0
4	**5.0**	**3.70**	**5.0****	**55**	**25**	**10**	**0**	**0**
5	5.0	3.70	6.0**	55	25	10	0	0
6	5.0	3.70	24**	50	20	5	0	0
7	5.0	3.70	48**	30	15	5	0	0
8	15	3.70	2.5	10	30	40	0	0
9	15	3.70	3.0	20	40	40	0	0
10	**15**	**3.70**	**4.0****	**20**	**40**	**40**	**0**	**0**
11	15	3.70	5.0**	20	40	35	5	Traces
12	15	3.70	6.0**	20	40	35	5	Traces
13	15	3.70	24**	15	30	25	15	10
14	15	3.70	48**	10	20	15	20	20
15	30	3.70	0.25	0	Traces	35	0	0
16	30	3.70	0.50	0	15	60	0	0
17	30	3.70	1.0	0	15	65	0	0
18	30	3.70	1.5**	Traces	25	75	Traces	Traces
19	**30**	**3.70**	**2.0****	**5**	**25**	**70**	**Traces**	**Traces**
20	30	3.70	3.0**	5	30	65	Traces	Traces
21	30	3.70	24**	0	5	35	25	35
22	60	7.40	1.5**	0	5	95	Traces	Traces
23	60	7.40	2.0**	0	5	85	5	5
24	60	7.40	3.0**	0	5	70	10	15
25	**60**	**7.40**	**18****	**0**	**0**	**15**	**35**	**50**
26	60	7.40	24**	0	0	10	30	60
27	60	7.40	42**	0	0	5	20	75
28	**60**	**7.40**	**66****	**0**	**0**	**0**	**15**	**80**

*NMR yields determined with 1,2,4,5-tetramethylbenzene (**203**, 1.0 eq.) as internal standard. A reasonable margin of error of ± 2.5% has been assumed due to the presence of very broad resonances and partial overlaps between signals.

Full Conversion of dialdehyde **175 observed.

The NMR yields of the different imine species have been calculated at different reaction times by making speculative assumptions on the structure of the four new imine compounds 2, 3, 4 and 5 which have been assigned to **201a**, **202a**, **XXIVa** and **XXVIa**, respectively (Scheme 30, Figure 24). The NMR yields are not the most accurate due to some peaks overlapping and broader resonances undermining the main peaks, but they were good enough to see the change in imine compound distribution.

The general trends observed are the following: (1) with increasing TREN (**128a**) concentration the product distribution shifts from $\mathbf{A_2B_3}$ type cage **XXIIIa** to the observed new and highly symmetric imine species, which were given the numbers 2, then 3, 4 and finally 5 in this order and (2) the conversion rate of the NDI substrate (**175**) increased with higher TREN (**128a**) concentration.

Interested in the structural identity of the unknown imine compounds 2-5, the best reaction conditions in table 11 were chosen for their respective formation and a new general reduction protocol had to be established. Isolation of the different imine compounds was not possible because the crude mixtures would keep reacting due to the increased amount of TREN (**128a**) and an easy separation was not possible either, making it necessary to combine two steps in one. The following reaction mixtures, shown in table 11, have been chosen to be used for direct reduction: entry 4 for imine compound 2 (as an unavoidable mixture with compounds 1 and 3); entry 10 for imine compound 3 (as an unavoidable mixture with 1 and 2); entry 19 for compound 3 (with low amounts of 2); entry 25 for compound 4 (as an unavoidable mixture with compounds 5 and 3) and entry 28 for compound 5 (with low amounts of compound 4). In summary, the following mixtures were chosen: Entries 4, 10, 19, 25, and 28.

For the imine reductions, the conditions used in entry 19 of table 11 were chosen as a model reaction mixture for first investigations. The mild reducing agents $NaBH(OAc)_3$ (9 eq./30 eq./50 eq.) or $NaBH_3CN$ (9 eq./30 eq./50 eq.) were added in separate experiments by simple addition to an aliquot of the reaction mixture in DCM and the mixtures were stirred for 18 h at room temperature before aqueous workup with 1 M HCl. These conditions were also tested after adding an excess of 1,2-DCE or THF, creating a solvent mixture of 1,2-DCE/DCM = 4:1 or THF/DCM = 4:1, respectively. Despite all these efforts, the crude NMRs all showed complex mixtures with broad resonances, occasional sharp peaks which may have belonged to desired products and even aldehyde peaks at around 10 ppm.

$NaBH_4$ as a more potent reducing agent was investigated once again because of this. In chapter 3.1.4 it was shown that $NaBH_4$ is most likely able to attack the NDI moiety at room temperature (Table 10). This time the reaction mixture with the imine species was added dropwise to a solution of $NaBH_4$ (1.5 eq. per imine bond) in MeOH (so that DCM/MeOH = 1:1 upon complete addition) at −78 °C. The mixture was then stirred at −78 °C for 3 h before workup with aqueous 1 M HCl (see Scheme 31). It was envisioned that the low temperature would prevent an attack of the NDI moiety whilst still enabling reduction of the imines to amines and this seemed to work well right away for all previously mentioned and relevant reaction mixtures generated in the first step (Table 11, Entries 4, 10, 19, 25, 28). Figure 26 shows the crude ^{1}H-NMR spectra (in D_2O) of these relevant reactions after their reduction. In theory, the corresponding ammonium chloride compounds have formed which is why the spectrum of isolated $\mathbf{A_2B_3}$ type cage **XVIIa** is shown as well for comparison (Figure 26a). Some peaks show a slight shift change across different samples. At this stage no buffer has been used and the acidity of the different ammonium salts at different concentrations most likely caused these shift changes. But in accordance with the previously mentioned NMR yields on the imine step and by comparing the new set of singlets and centered multiplets

corresponding to the NDI protons and phenylene protons originating from dialdehyde **175**, respectively, it seemed that crude mixture b (Figure 26b) contained not only $\mathbf{A_2B_3}$ type cage **XVIIa** but also the unknown ammonium species 2 and 3 (belonging to the imine species 2 and 3 mentioned in scheme 30). Crude mixture c (Figure 26c) and crude mixture d (Figure 26d) seemed to contain a higher amount of ammonium species 2 and 3 than crude mixture b. Crude mixture e (Figure 26e) showed the first appearance of unknown ammonium compounds 4 and 5 still being accompanied by ammonium compound 3. And crude mixture f (Figure 26f) seemed to contain an excess of ammonium compound 5 with small amounts of compound 4 being left.

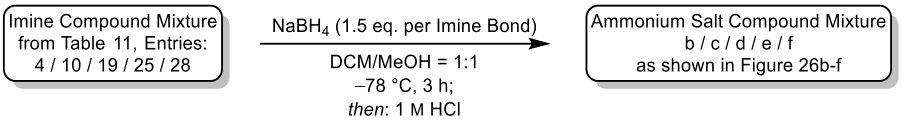

Scheme 31: General reduction method used to reduce imine mixtures from table 11 to ammonium salt compounds.

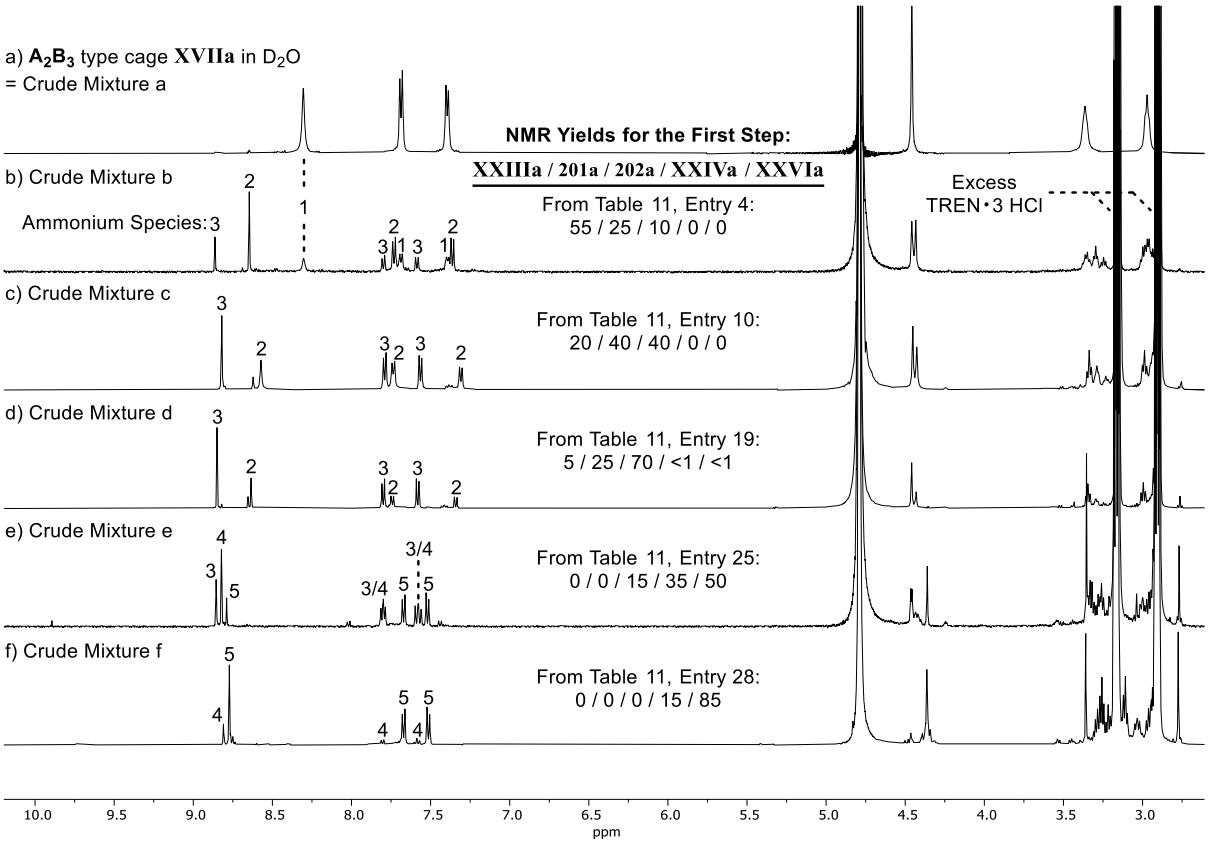

Figure 26: ^{1}H-NMR spectra in D_2O of isolated $\mathbf{A_2B_3}$ type cage **XVIIa** and the crude mixtures obtained after direct reduction of the imine mixtures mentioned in table 11, entries 4, 10, 19, 25 and 28 giving the crude mixtures b, c, d, e and f, respectively.

Direct high-resolution ESI-MS experiments as well as MALDI-TOF experiments were conducted to gather evidence for any kind of cage formation (for example the ammonium chloride species of $\mathbf{A_4B_6}$ type cage **XXIVa** or $\mathbf{A_8B_{12}}$ type cage **XXVIa**) that would seem promising to isolate. However, the excess amount of TREN hydrochloride in these mixtures seemed to make it impossible to measure anything of value at this stage. A workup procedure for the removal of TREN hydrochloride had to be found which proved to be a difficult task considering all ammonium species exhibit very similar chemical behavior. Workup methods investigated include chromatography columns over deactivated SiO_2, reversed phase chromatography and HILIC columns (**h**ydrophilic

interaction **li**quid **c**hromatography) in various solvent systems. All fractions had to be analysed by ^{1}H-NMR. However, none of these methods was able to separate the desired ammonium species from TREN hydrochloride.

Size-exclusion chromatography with Sephadex G10 resin (fractionation range < 700 Da) in H_2O (+ 0.1% formic acid) gave good enough separation under the application of compressed air. Gravity flow was not enough for effective separation and the reason for this may be that elution under gravity flow takes longer and the increased amount of time may allow for more diffusion of the analyte mixture during the column. A few drops of 1 M HCl was added to all collected fractions before the solvent was removed under reduced pressure in case anion exchange occurred on the desired ammonium species from chloride to formate counter anions. The ^{1}H-NMR spectra of the best fractions were recorded in a 50 mM ammonium formate buffer in D_2O at pD = 3.7 and they are shown in Figure 27.

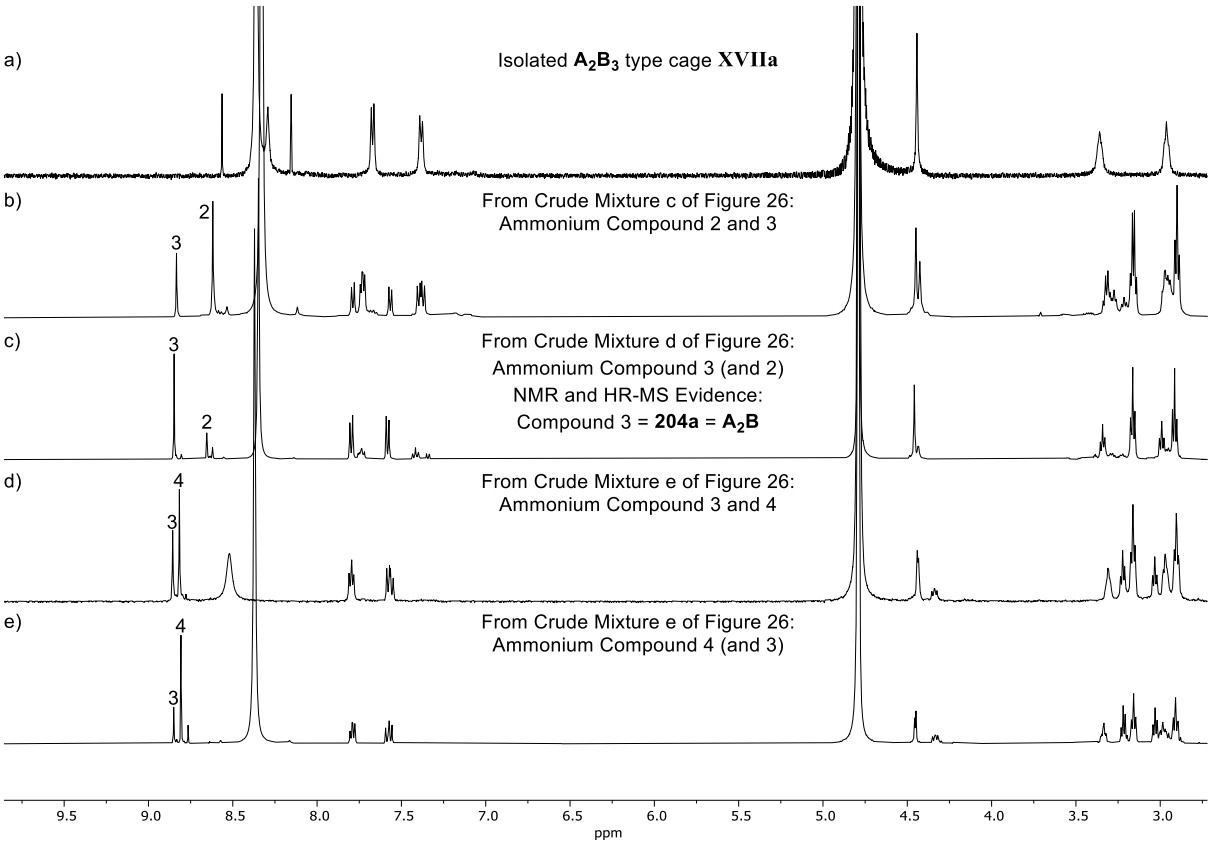

Figure 27: ^{1}H-NMR spectra obtained from different fractions after removal of TREN (**128a**) from crude mixtures c, d and e *via* size-exclusion chromatography.

The samples measured to generate the spectra in figure 27b-e were also analysed by high-resolution ESI-MS and MALDI-TOF to see if further workup efforts were worth it. The main peaks corresponding to ammonium compound **204a** of the type $\mathbf{A_2B}$ (see structure below in figure 28) were found in all of them, being the most dominant compound observed in the sample used to measure the spectrum shown in figure 27c. This sample was also analysed by ^{13}C- and 2D-NMR techniques to further confirm the structure (see experimental section, chapter 5.8). For the same sample, a peak of much lower intensity was found, which may correspond to compound **205a** of the type $\mathbf{A_3B_2}$ (Figure 28), but this was only speculation as the information given by NMR was not sufficient to support this evidence and the peaks observed almost vanished in the baseline. It may only have been present in trace amounts. The other samples, which were used to measure the spectra of figure 27d and figure 27e, did not

show any peaks corresponding to desired cages of higher mass. Only peaks of way too low molecular weight with a charge of +1 have been observed which could not be assigned. Crude mixture f from figure 26f was supposed to give a concentrated sample of unknown compound 5 after workup. However, all fractions from this crude mixture collected after size-exclusion chromatography showed that the integrals of the singlet, corresponding to NDI protons, originating from dialdehyde **175**, and the two centered multiplets, corresponding to the phenylene protons, were not consistent across all fractions. The relative integrals between those peaks inconsistently changed from 1.0:1.0:1.0 all the way to 1.0:0.3:0.3 across the eluted fractions suggesting that some form of decomposition took place which may have already been the case during imine formation in the first step.

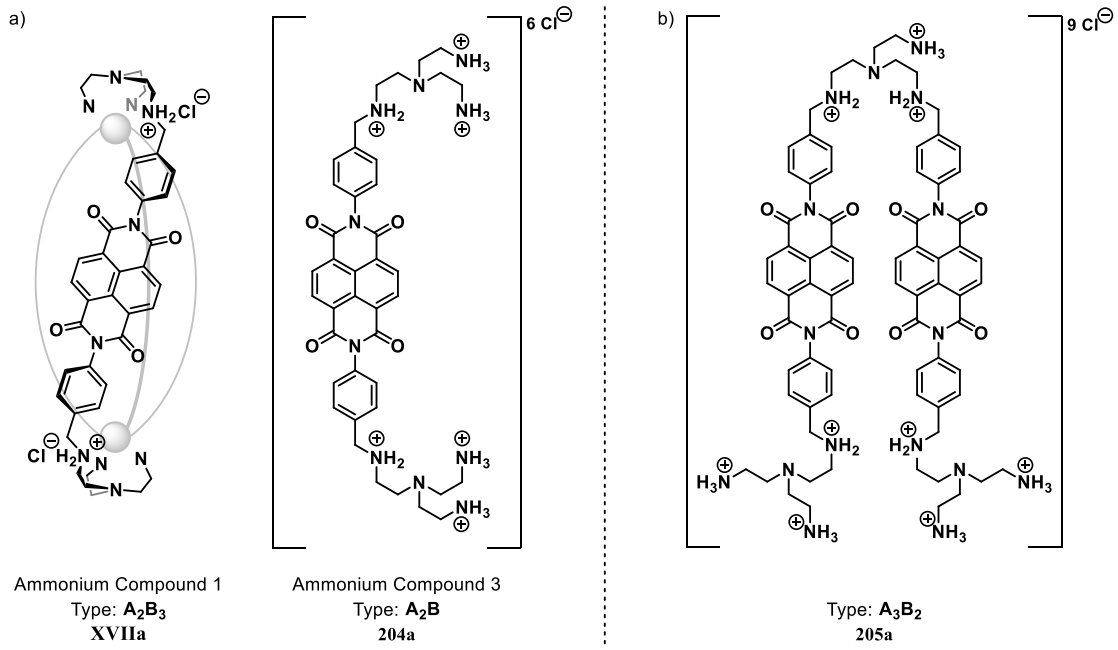

Figure 28: a) Chemical structures **XVIIa** and **204a** of ammonium salts 1 and 3, respectively. Evidence was gathered for their formation *via* NMR and HR-MS data. b) Ammonium salt **205a** for which insufficient evidence was gathered through HR-MS analysis and none through NMR.

In conclusion for this chapter, $\mathbf{A_2B_3}$ type cage **XVIIa** and compound **204a** of the type $\mathbf{A_2B}$ (Figure 28a) have been identified as ammonium compounds 1 and 3, respectively. Evidence for their formation was gathered through NMR and HR-MS data. Insufficient data was found for compound **205a** of the type $\mathbf{A_3B_2}$ (Figure 28b) and it could not be assigned to any of the other ammonium compounds 2 and 4 observed throughout the experiments shown in this chapter. Supposed imine compound 5 gave the illusion of a fifth compound of high symmetry after the imine forming step but the peaks observed in the ^{1}H-NMR spectra most likely belong to disconnected moieties of the NDI and phenylene units as unknown and decomposed material.

The next chapter will briefly discuss similar experiments conducted with TRPN (**128b**) and dialdehyde **175**.

3.1.6 Influence of the TRPN Concentration on the Imine Forming Step

Concurrently, just like for TREN (**128a**) in chapter 3.1.5, similar experiments for imine formation were performed with TRPN (**128b**) and dialdehyde **175** (Scheme 32, Table 12).

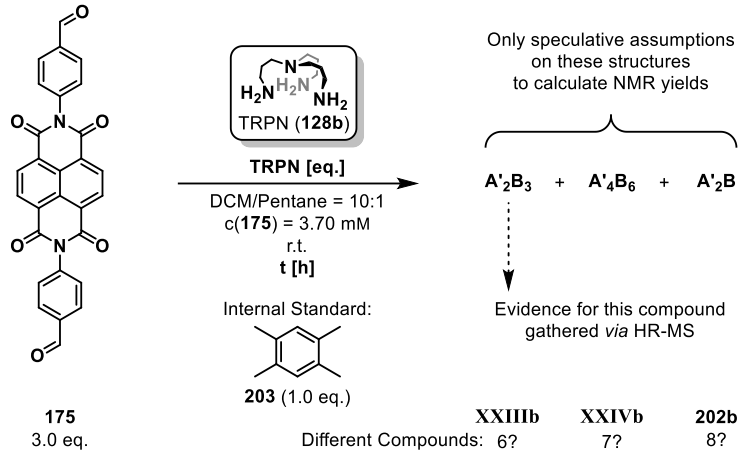

Scheme 32: Reaction conditions used to monitor the reaction progress of the imine formation between dialdehyde **175** and TRPN (**128b**) over time according to table 12. 1,2,4,5-Tetramethylbenzene (**203**) was added as an internal standard.

Table 12: Reaction conditions and NMR yields for the hypothetical imine species formed according to scheme 32.

Entry	TRPN [eq.]	t [h]	XXIIIb [%]*	XXIVb [%]*	202b [%]*	Full Conversion?
1	2.5	0.25	Traces	0	0	No
2	2.5	0.50	5	0	0	No
3	2.5	1.0	5	0	0	No
4	2.5	3.0	5	5	0	No
5	2.5	6.0	10	20	0	No
6	2.5	24	15	30	0	Yes
7	5.0	0.25	5	0	0	No
8	5.0	0.50	5	0	0	No
9	5.0	1.0	10	Traces	0	No
10	5.0	3.0	15	10	0	No
11	5.0	6.0	15	20	0	No
12	5.0	24	15	65	5	Yes
13	10	0.25	10	0	0	No
14	10	0.50	15	0	0	No
15	10	1.0	15	0	0	No
16	10	3.0	20	5	0	No
17	10	6.0	35	30	Traces	No
18	10	24	25	70	5	Yes
19	20	0.25	20	0	0	No
20	20	0.50	20	0	0	No
21	20	1.0	25	Traces	0	No
22	20	3.0	45	10	0	No
23	20	6.0	45	30	Traces	No
24	20	24	40	60	Traces	Yes
25	**18**	**18**	**40**	**60**	**0**	**Yes**

*NMR yields determined with 1,2,4,5-tetramethylbenzene (**203**, 1.0 eq.) as internal standard. A reasonable margin of error of ± 2.5% has been assumed due to the presence of very broad resonances and partial overlaps between signals.

Once again, hypothetical structures for the imine compounds 6, 7 and 8 are shown in figure 29. The ones used to calculate NMR yields for table 12 were **XXIIIb** (of the type **A'$_2$B$_3$**), **XXIVb** (of the type **A'$_4$B$_6$**) and **202b** (of the type **A'$_2$B**), respectively.

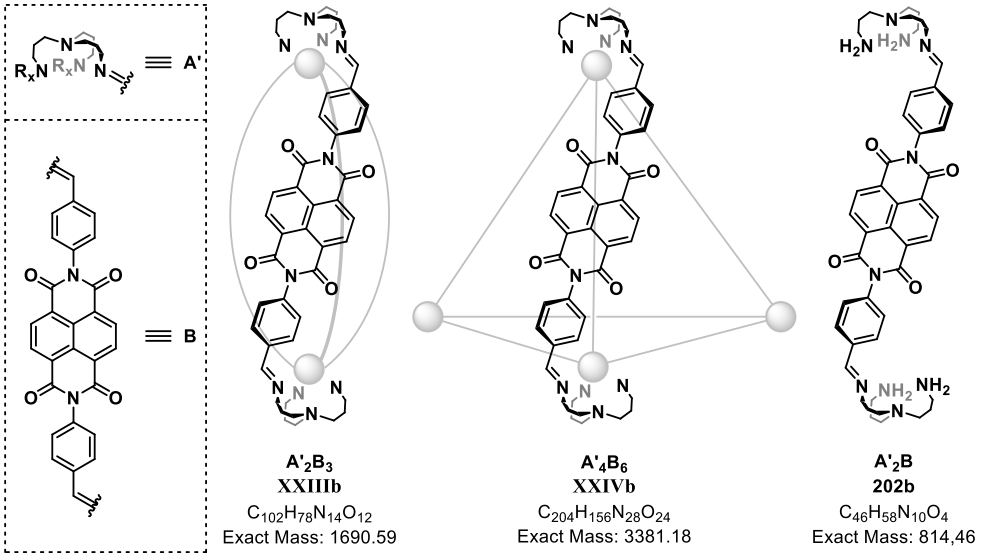

Figure 29: Hypothetical and highly symmetric structures during imine formation between dialdehyde **175** and TRPN (**128b**).

The reactions with TRPN (**128b**) seemed to progress a bit slower but a similar observation was made as with TREN (**128a**). When the reactions were run overnight, at least two distinct imine compounds of high symmetry formed according to NMR (Table 12, Entries 6, 12, 18, 24, 25) with a third one sometimes forming in very low amounts (Table 12, Entries 12, 17-18, 23-24). The reaction mixture generated by using 18 equivalents of TRPN (**128b**) over 18 h only contained the first two imine species observed and the mixture was analysed *via* high-resolution ESI-MS (Table 12, Entry 25). The data showed evidence for the formation of **A'$_2$B$_3$** type cage **XXIIIb** (Figure 29) with the corresponding peak at 1691.5969 (Figure 30a). Interestingly, more peaks were found with an isotopic distribution that could belong to **A'$_4$B$_6$** type cage **XXIVb** (Figure 29) with the main peak at 3382.1828 (Figure 30b). However, this was not sufficient enough as evidence for this cage because the peak intensity was very low and they may be assigned to either the desired **A'$_4$B$_6$** type cage **XXIVb** as the proton adduct $[M+H]^+$ or to a possible bis-adduct of **A'$_2$B$_3$** type cage **XXIIIb**, namely $[2M+H]^+$.

The imine compounds in this reaction mixture have not been isolated unlike the TREN-derived **A$_2$B$_3$** type cage **XXIIIa** (see chapter 3.1.5) which formed as a single product under optimized conditions making isolation easier, With TRPN (**128b**), the crude mixtures would have kept reacting due to the increased amount of TRPN (**128b**) needed to reach full conversion and even with low amounts only a product mixture was observed. However, complete dissolution of the material was also achieved due to full conversion of dialdehyde **175,** and the reaction mixture (Table 12, Entry 25) could easily be added dropwise to a solution of $NaBH_4$ (1.5 eq. per imine bond) in MeOH at −78 °C for direct reduction of the imine species. The same reduction protocol was applied which was used in the reduction of the TREN-derived imine species mentioned in chapter 3.1.5. This time a crude mixture was obtained that contained an excess of TRPN hydrochloride, an aldehyde species in little amounts (most likely dialdehyde **175**) and one main product, most likely the hexaammonium chloride cage derivative of **A'$_2$B$_3$** type cage **XXIIIb**. However, since these experiments were performed alongside the ones with TREN (**128a**), mentioned in chapter 3.1.5, and the mixtures generated with TREN (**128a**) did not contain any aldehyde side-products after

reduction, no time was invested into the purification of the mixture obtained with TRPN (**128b**) because there was no promising advantage to be gained from it.

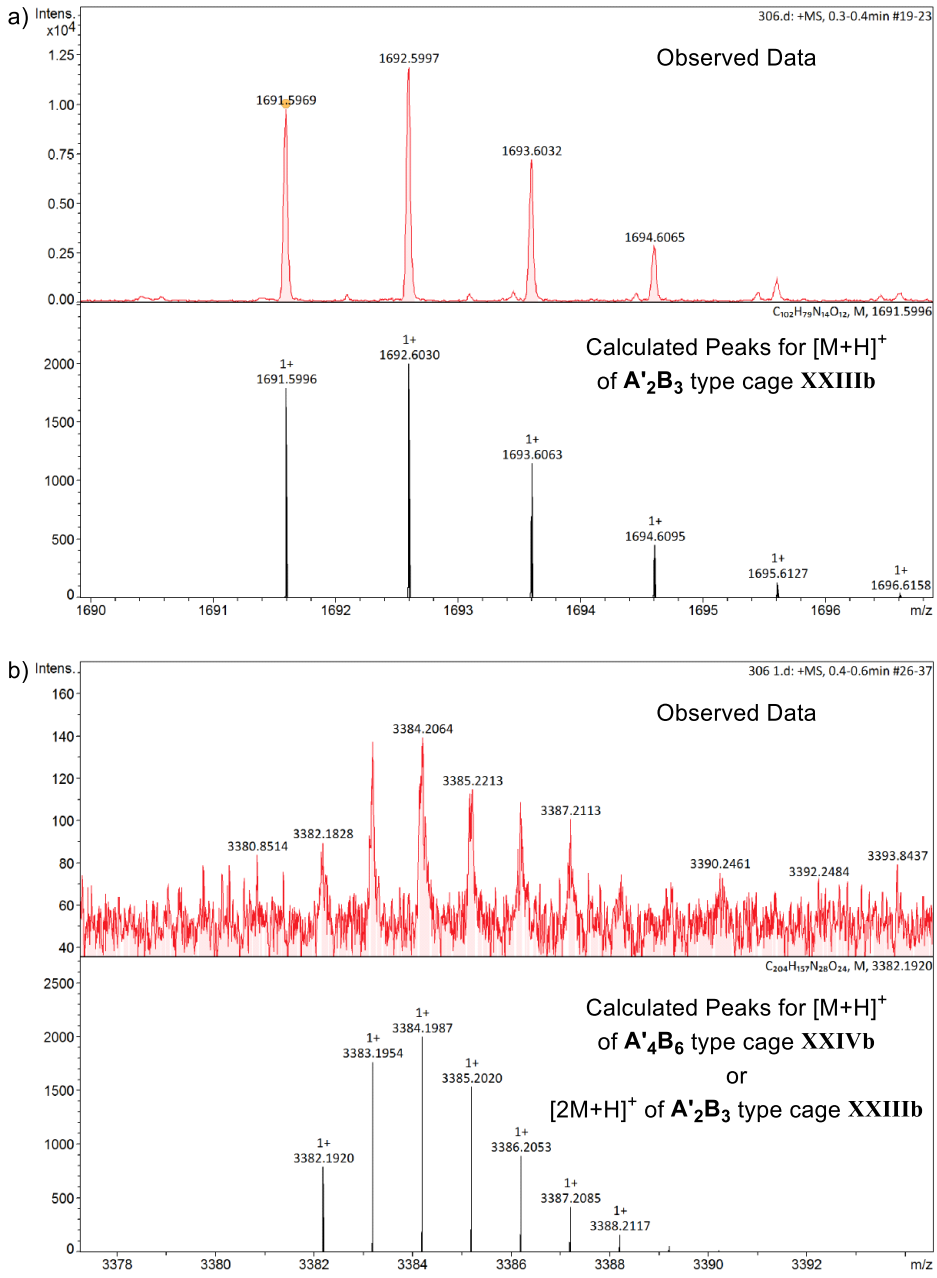

Figure 30: Relevant HR-MS data gathered from the reaction mixture in the experiment of table 12, entry 25 after 18 h.

3.1.7 Attempted Reductions of the ŠOLOMEK Imine Cage (*SSS*)-XXVII

The ŠOLOMEK group provided a sample of their **Tri²Di³** type imine cage (*S*,*S*,*S*,*S*,*S*,*S*,*S*,*S*,*S*,*S*,*S*,*S*)-**XXVII**, from now abbreviated as (*SSS*)-**XXVII** for simplicity's sake, for further investigations towards its reduction and possible guest-uptake experiments thereafter. They synthesized imine cage (*SSS*)-**XXVII**, starting with mono-Boc protected and enantiomerically pure (*S*,*S*)-*trans*-1,2-cyclohexanediamine (compound **206**, Scheme 33).[285] Condensation of the protected amine **206** with NDA (**179**) gave NDI **207** as a 1:1 mixture of diastereomers in 91% yield with the two carbamate groups on the same (*syn*) or opposite (*anti*) face of the NDI core on the NMR timescale at room temperature according to ŠOLOMEK *et al*. Deprotection of NDI **207** with TFA furnished the free enantiomerically pure NDI diamine **208** in 82% yield, again as a pair of *syn* and *anti* diastereomers. Imine condensation of **208** with triformylbenzene (**129**) in toluene under DEAN-STARK conditions gave **Tri²Di³** type imine cage (*SSS*)-**XXVII** in 79% yield.

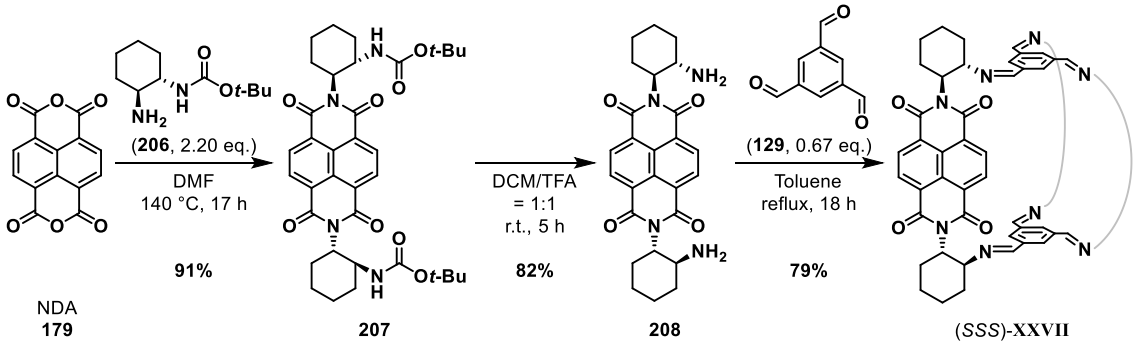

Scheme 33: Synthesis of **Tri²Di³** type imine cage (*SSS*)-**XXVII** according to ŠOLOMEK *et al*.[285]

Imine cage (*SSS*)-**XXVII** is very rigid and shape-persistent since it was made from three NDI cores, six cyclohexane skeletons and two benzene units. The subcomponents used for the synthesis of TREN-derived ammonium cage **XXIIIa** presented in chapter 3.1.4 in theory allowed for much more flexibility, which made (*SSS*)-**XXVII**, once reduced, an interesting alternative for guest-uptake investigations for direct comparison of their respective binding strengths of anionic guests.

Scheme 34 and table 13 summarize all attempts to reduce (*SSS*)-**XXVII** to its corresponding ammonium chloride cage (*SSS*)-**XXVIII**.

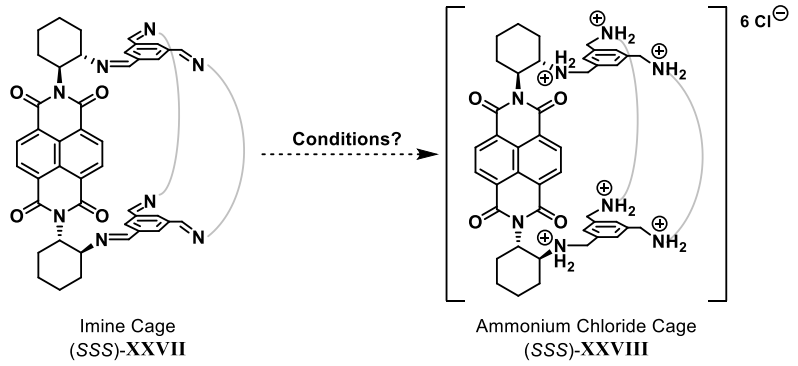

Scheme 34: General reaction equation for the conditions listed in table 13.

Table 13: Conditions investigated for the reduction of imine cage (*SSS*)-**XXVII** to ammonium chloride cage (*SSS*)-**XXVIII**.

Entry	Reagent	Solvent	T [°C]	t [h]	Note
1	$NaBH_4$ (9 eq.)	MeOH/DCM = 1:1	–40	3	Complex Mixture
2	$NaBH_4$ (9 eq.)	MeOH/DCM = 1:1	–40	6	Complex Mixture
3	$NaBH_4$ (9 eq.)	MeOH/DCM = 1:1	–78	3	Complex Mixture
4	$NaBH_4$ (9 eq.)	MeOH/DCM = 1:1	–78	6	Complex Mixture
5	$NaBH_4$ (23 eq.)	MeOH/DCM = 1:1	–78	3	Complex Mixture
6	$NaBH(OAc)_3$ (40 eq.)	1,2-DCE	25	20	Decomposition
7	$NaBH(OAc)_3$ (40 eq.)	1,2-DCE	50	20	Decomposition
8	$NaBH(OAc)_3$ (40 eq.)	1,2-DCE/MeOH = 9:1	25	20	Decomposition
9	$NaBH(OAc)_3$ (40 eq.)	1,2-DCE/MeOH = 9:1	50	20	Decomposition
10	$NaBH(OAc)_3$ (40 eq.)	1,2-DCE/TFE = 9:1	25	20	Complex Mixture
11	$NaBH(OAc)_3$ (40 eq.)	1,2-DCE/TFE = 9:1	50	20	Complex Mixture
12	$NaBH(OAc)_3$ (40 eq.)	1,2-DCE/HFIP = 9:1	25	20	Complex Mixture
13	$NaBH(OAc)_3$ (40 eq.)	1,2-DCE/HFIP = 9:1	50	20	Complex Mixture

For the reductions, $NaBH_4$ and $NaBH(OAc)_3$ were chosen as reducing agents because they gave the best results for the reduction of the imine compounds shown in previous chapters. The crude mixture after using 9 equivalents of $NaBH_4$ at –40 °C for 3-6 h in DCM/MeOH = 1:1 (Table 13, Entries 1-2) showed a complex mixture with broad resonances in the aliphatic and too many signals in the aromatic region. Therefore, the reactions were repeated at –78 °C (Table 13, Entries 3-4) but the same result was observed. Adding even more $NaBH_4$ (23 eq., Table 13, Entry 5) to supposedly drive the reaction to completion did not help either. Running the reaction with an excess of $NaBH(OAc)_3$ (40 eq., Table 13, Entry 6-7) as a milder reducing agent in 1,2-DCE at 25 °C or 50 °C led to similar problems but this time even aldehyde peaks at 10.1 ppm and 10.7 ppm have been observed. Adding MeOH (Table 13, Entries 8-9) as a proton source for the reduction with borohydrides did not help. Instead of MeOH, more acidic alcohols with strong electron withdrawing groups auch as trifluoroethanol (TFE) and hexafluoroisopropanol (HFIP) were investigated (Table 13, Entries 10-13). The idea here was twofold: (1) the higher acidity of TFE and HFIP might increase the reaction rate by protonation of the imine functions in equilibrium, activating them for the nucleophilic attack by borohydrides. (2) At the same time, TFE and HFIP are themselves less nucleophilic than methanol because of the electron withdrawing fluorine atoms, potentially eliminating the formation of side-products. However, even though the decomposition of the cage back towards aldehyde species stopped, even broader resonances were observed in the ^{1}H-NMR spectra of these experiments in D_2O as well as DMSO-d_6, this time in both the aliphatic and aromatic region.

The reduction of imine cage (*SSS*)-**XXVII** proved to be quite difficult even with the methods developed for other imine cages in this study. Therefore, no more time was invested into this as it did not seem promising.

3.1.8 Guest-Uptake Experiments with Ammonium Cage XXVa

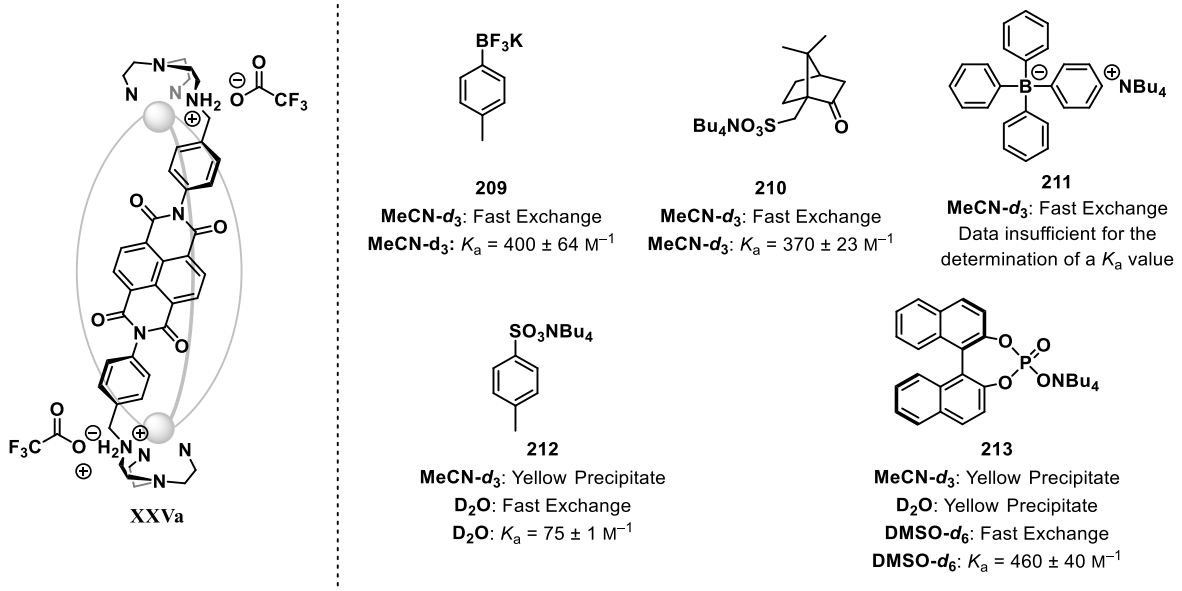

Figure 31: Results of the guest-uptake experiments with ammonium trifluoroacetate cage **XXVa** and guests **209**-**213**.

Since a larger cage was not accessible, cage **XXVa** was briefly studied in guest-uptake experiments (Figure 31). Even though the naphthalene diimide moieties of its subcomponents were most likely closing off a potential cavity due to effective π-π stacking, several anionic guests showed uptake in the fast-binding regime of the ^{1}H chemical shift time scale at 298 K. However, there was no conclusion on how the binding around host **XXVa** occurred as the data was not sufficient for this kind of information. Theoretically it is possible for the anionic parts of guests **209**-**213** to either accumulate around host **XXVa**, especially near the positive charges, or bind in between the NDI moieties. Especially for aromatic guests **209**, **212** and **213**, intercalation should be possible, but guest molecules would have to overcome the attractive π-π interactions between the NDI moieties. On top of that, these were the first guest-uptake experiments conducted in this study and a lot has been learned concerning the solubility properties of all compounds (salts) employed, explaining some inconsistencies across the different experiments such as the change of the solvent for guests **212** and **213**. All experimental details can be found in chapter 5.3. Nevertheless, binding constants K_a were determined for most guests shown in figure 31.

MeCN-d_3 was used as the solvent for the titration of guests **209**-**211**. Moderate binding constants were calculated for **209** (K_a = 400 ± 64 M^{-1}) and **210** (K_a = 370 ± 23 M^{-1}) but none for **211** because the data gathered (titration range: 0-10 eq.) seemed to be insufficient for its determination. An interaction was observed regardless, which manifested in relatively small changes of the chemical shifts for the peaks corresponding to host **XXVa** throughout the titration. For the tetrabutylammonium salts of sulfonate **212** and phosphate **213**, a yellow precipitate formed upon addition of their respective stock solutions to host **XXVa** in MeCN-d_3 for **212** and MeCN-d_3 or D_2O for **213**, making it impossible to determine binding constants in these solvents. However, the mixture remained soluble in D_2O for guest **212**, showing a binding constant of K_a = 75 ± 1 M^{-1}. This value was much smaller compared to the ones calculated for guests **209** and **210** and the reason may be that D_2O was better at solubilizing the anions than MeCN-d_3 and, therefore, may have formed more stable solvation shells which were in direct competition with binding by the positively charged host compound **XXVa**. DMSO-d_6 was used for the titration of guest **213** to host **XXVa**, giving a moderate binding constant of K_a = 460 ± 40 M^{-1} in this solvent.

The overall goal in this study was to find positively charged cages with a sizeable cavity, suitable for the encapsulation of either neutral or anionic guests for the catalysis of reactions with anionic transition states and intermediates. Including the NDI moiety for possible anion-π interactions should further stabilize those intermediates. Host **XXVa** (of the type **Tri^{2}Di^3**) was still considered too small for our endeavors and the binding constants with several anionic guests were not convincing enough. Chapter 3.2 will focus on iminopyridine-based coordination cages as a different approach, offering cages with a more rigid structure and persistent cavity.

3.2 Iminopyridine-Based Metal-Organic Coordination Cages

3.2.1 Iminopyridine-Based $Fe_4L_6(NTf_2)_8$ Tetrahedron XXIX

The LÜTZEN group from the university of Bonn prepared and provided a sample of literature-known **Fe_4L_6** tetrahedron **XXIX** (Scheme 35) for guest-uptake and stability studies as these have not been reported so far for this cage. The synthesis proceeded according to slightly modified literature procedures starting with the imide condensation between NDA (**179**) and diamine **214** which gave NDI compound **215** in 47% yield (Scheme 35).[286] The edge-linked **Fe_4L_6** cage **XXIX** was then obtained as a mixture of the *T*-, C_3- and the dominating S_4-symmetric diastereomers through subcomponent self-assembly between 6 equivalents of NDI ligand **215**, 12 equivalents of picolinaldehyde (**142**) and 4 equivalents of $Fe^{II}(NTf_2)_2$ at 50 °C in MeCN/$CHCl_3$ = 1:1 within 48 h.[98]

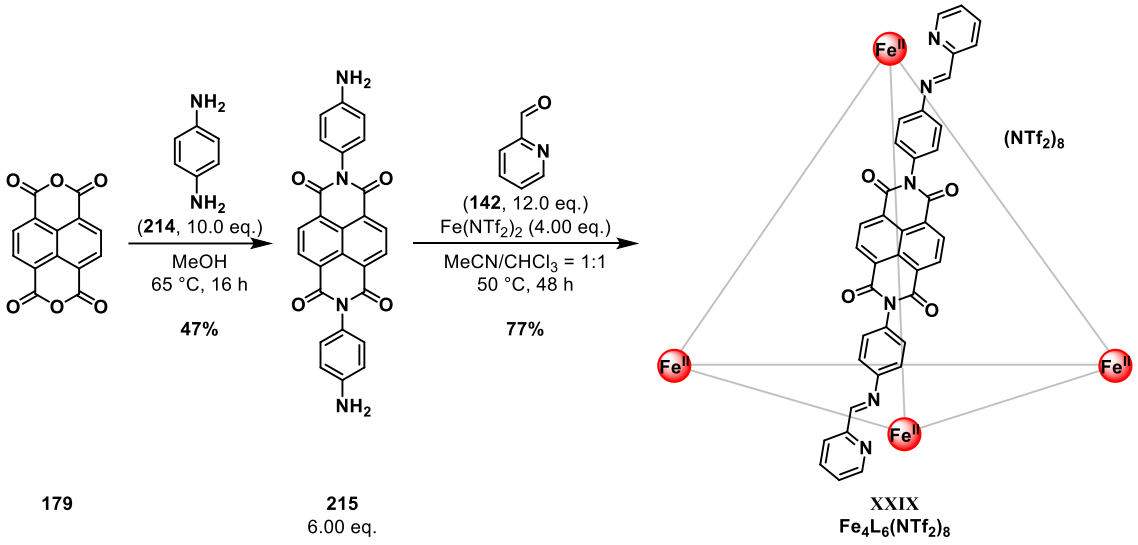

Scheme 35: Synthesis of **Fe_4L_6** tetrahedron **XXIX**.

Fe_4L_6 tetrahedron **XXIX** should be suitable for anion-π catalysis since its edges consist of naphthalene diimide (NDI) ligands, surrounding the cavity with multiple π-acidic surfaces. On top of that, the cage features a high net positive charge of +8, which should additionally stabilize anionic intermediates and transition states *via* strong ion-ion interactions. Guest-uptake experiments with **Fe_4L_6** tetrahedron **XXIX** were carried out (Figure 32) to find out if the cage was suitable for the binding of various anions in MeCN-d_3. Tetrabutylammonium tetraphenylborate (**211**) showed binding in fast exchange with a binding constant of $K_a = 140 \pm 5.9\ M^{-1}$. All the other organic salts shown in figure 32 induced partial disassembly of the cage and/or broadening of its peaks in the ^{1}H-NMR upon addition. Because of this, binding constants could not be calculated for these guests. Allylphenylether (**217**) as a neutral compound showed no binding at all. All experimental details are documented in chapter 5.3.1 and 5.3.4. **Fe_4L_6** cage **XXIX** seemed not to be stable enough for catalysis experiments such as the hydrolysis of carboxylic esters or phophates under basic conditions. Hence, further investigations towards its stability were carried out.

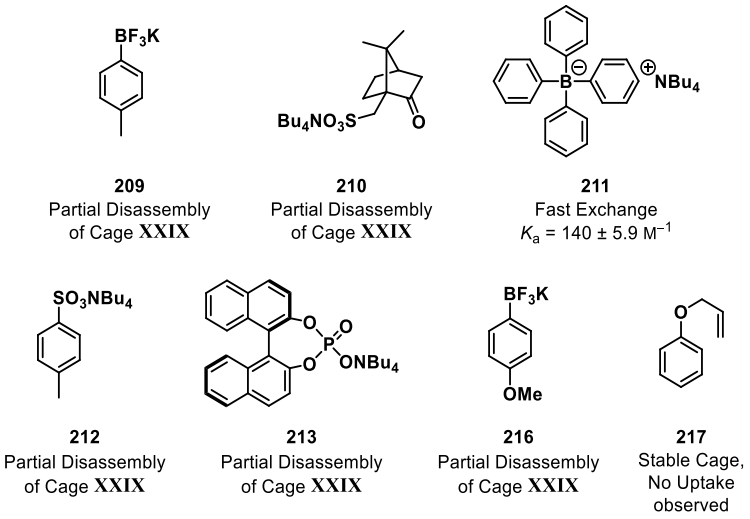

Figure 32: Results of the guest-uptake experiments with **Fe_4L_6** cage **XXIX** and guests **209**-**213** and **216**-**217**.

The stability of iminopyridine metal complexes such as **Fe_4L_6** cage **XXIX** towards bases or even water is not necessarily guaranteed since the imine bonds were formed by reversible condensation of diamine **215** with picolinaldehyde (**142**). All imine bonds in **Fe_4L_6** cage **XXIX** are interconnected over metal coordination bonds and not over stable and fully covalent bonds. Therefore, stability investigations with **Fe_4L_6** cage **XXIX** towards water and a base such as $KHCO_3$ were conducted as follows.

An NMR tube was charged with 500 µL of a stock solution of **Fe_4L_6** cage **XXIX** in MeCN-d_3 at a concentration of c = 1.00 mM. A ^{1}H-NMR spectrum was measured before and after each addition of distilled H_2O (c = 55.5 M). After each addition the NMR tube was shaken manually. The resulting spectra are shown in figure 33. The spectra showed that, at this cage concentration, an aldehyde peak at 9.94 ppm appeared which indicated partial decomposition of the cage at an increased water content of 26% or more. Overall, the cage remained mostly stable even after 18 h at 52% water content.

Next, the effect of $KHCO_3$ as a base was explored. For this experiment, an NMR tube was charged with 500 µL of a stock solution of **Fe_4L_6** cage **XXIX** in MeCN-d_3:H_2O = 6:4 at a concentration of c = 0.125 mM. This solvent mixture was necessary to ensure solubility of the base. And again, a ^{1}H-NMR spectrum was measured before and after each addition of a $KHCO_3$ stock solution in MeCN-d_3:H_2O = 6:4 at a concentration of c = 62.5 mM corresponding to 1.0 eq./µL titrated. After each addition the NMR tube was shaken manually. The resulting spectra are shown in figure 34. The cage partially disassembled prior to the addition of base due to the high water content as the aldeyhde peak at 9.94 ppm suggested once again. Further disassembly (or decomposition) of cage **XXIX** can be observed after the addition of 6 equivalents of $KHCO_3$ and onwards, demonstrated by the continous broadening of all its corresponding peaks and precipitation of the material.

$KHCO_3$ most likely generated hydroxide ions by reacting with water which were able to attack the imine bonds as nucleophiles. Hydroxide anions will be needed in catalysis experiments of some reactions leading over anionic transition states such as phosphate hydrolysis. Therefore, **$Fe_4L_6(NTf_2)_8$** cage **XXIX** was considered not stable enough for the aim of this work.

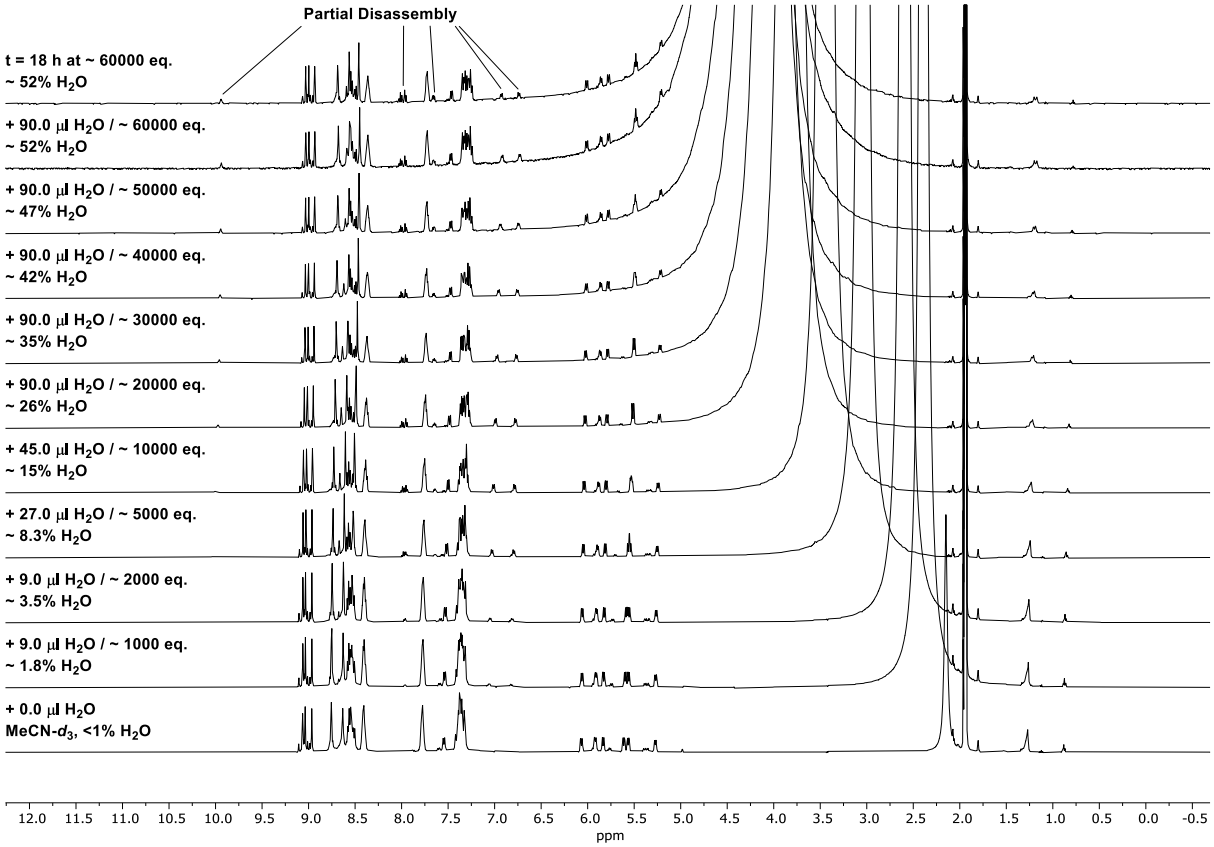

Figure 33: Titration of water to a solution of **Fe_4L_6** cage **XXIX** (c = 1.00 mM) in MeCN-d_3 at 298 K.

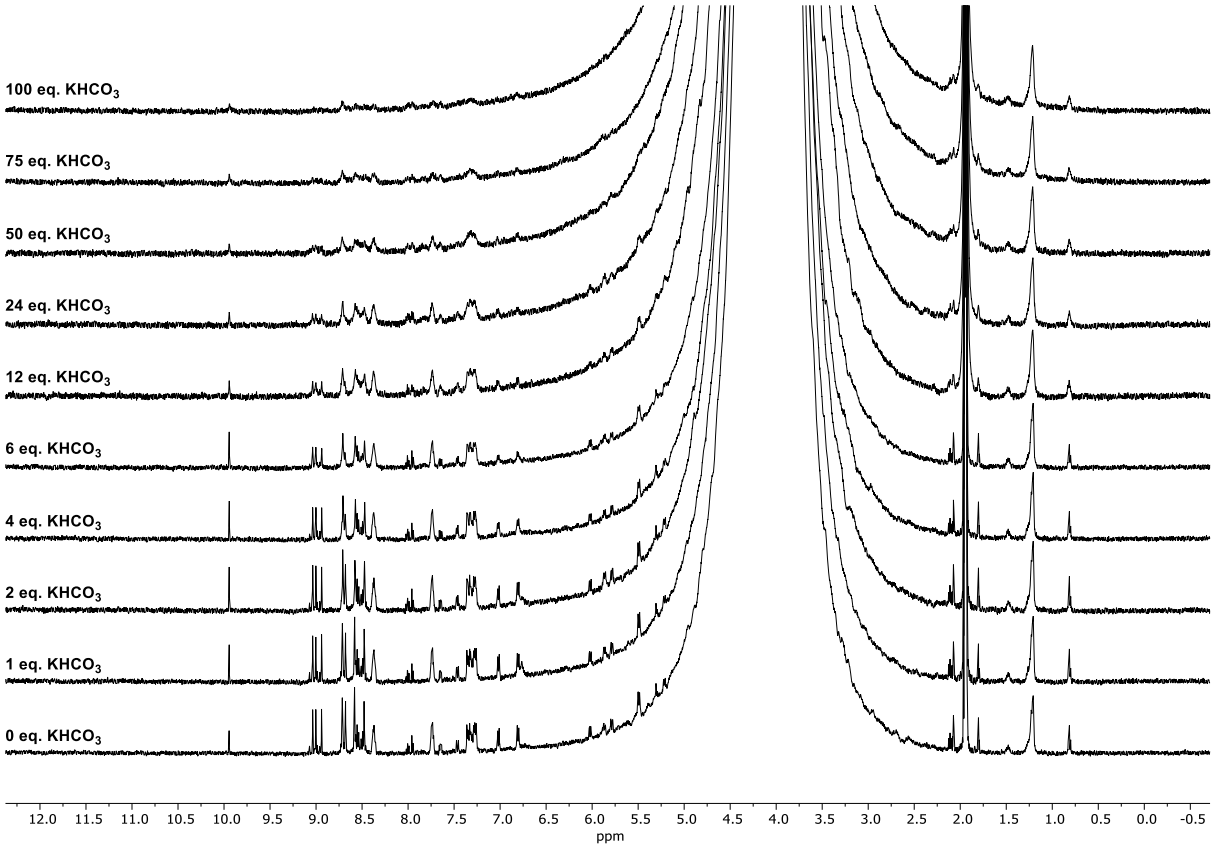

Figure 34: Titration of $KHCO_3$ to a solution of **Fe_4L_6** cage **XXIX** (c = 0.125 mM) in MeCN-d_3/H_2O = 6:4 at 298 K.

The solubility properties of iminopyridine-based metal complexes (in the form of cages in this discussion) mainly depend on the counter anion employed. For example, cages with triflimide (NTf_2^-) counter anions have been reported to exhibit high solubility in MeCN and are completely insoluble in H_2O.[202] In contrast, sulfate (SO_4^-) counter anions render them water-soluble instead, provided the cages form with metal sulfate precursors to begin with. NITSCHKE *et al.* reported the post-assembly anion exchange of iminopyridine-based cages from triflimide to sulfate counter anions *via* the addition of an excess of aqueous tetrabutylammonium sulfate (TBA_2SO_4) to an acetonitrile solution of the corresponding triflimide or triflate (OTf^-) cage.[202] Even though many examples were reported, many cages also diassembled at room temperature instead. The main reason for this could be the low water solubility of the subcomponents. Once they disassemble in H_2O, even trace amounts of the subcomponents in this equilibrium between aldehydes and amines and their corresponding imines can reach saturation and precipitate out of solution and, therefore, get removed from the equilibrium. **Fe_4L_6** cage **XXIX** was subjected to the reported anion exchange protocol from NITSCHKE *et al*. (Scheme 36) because the sulfate derivative **XXX**, which should be soluble in water, could be able to profit from the hydrophobic effect which promotes guest binding and encapsulation of neutral guests in aqueous media into hydrophobic cavities.

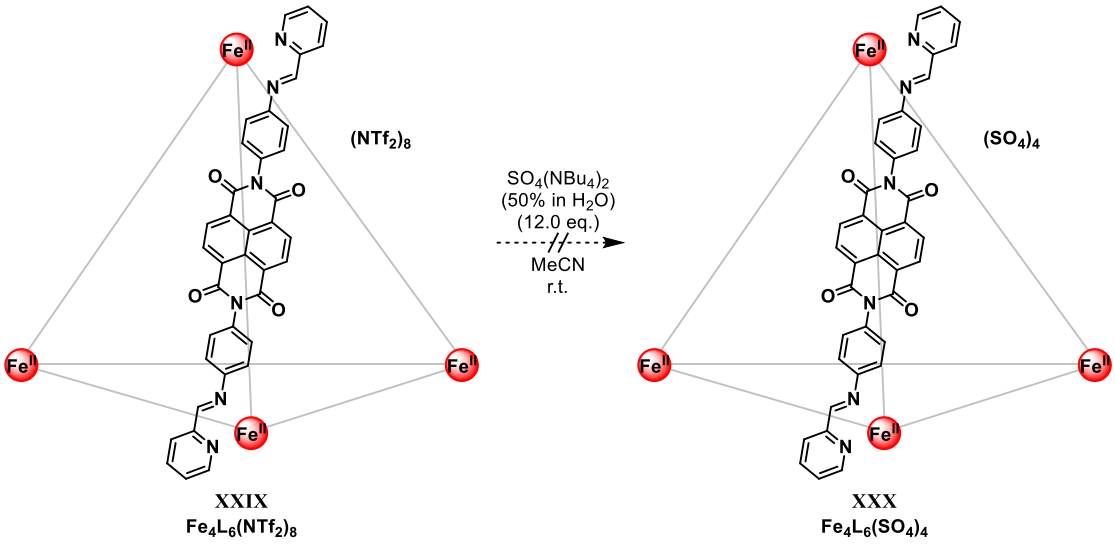

Scheme 36: Conditions for the anion exchange reaction from **$Fe_4L_6(NTf_2)_8$** cage **XXIX** to **$Fe_4L_6(SO_4)_4$** cage **XXX**.

Upon addition of aqueous TBA_2SO_4 (12 eq.) into a purple acetonitrile solution of triflimide cage **XXIX** a black precipitate formed. However, after centrifugation and removal of the supernatant, the residual black solid remained insoluble in H_2O and even in MeCN. ^{1}H-NMR measurements in either D_2O or MeCN-d_3 revealed the formation of aldehyde species in trace amounts, hinting at the disassembly of the cage in this case. Not even trace amounts of either triflimide cage **XXIX** or sulfate cage **XXX** were detected.

3.2.2 Iminopyridine-Based $Zn_2L_3(NTf_2)_4$ Helicate XXXII

To improve the stability of the iminopyridine metal complex a change of functionalities in the subcomponents employed was necessary. So far, **$Fe_4L_6(NTf_2)_8$** cage **XXIX** was the only iminopyridine-based cage discussed and the metal complexes at its vertices were constructed following the general approach of combining an amine building block **141** with 2-formylpyridine (**142**) (Scheme 37a). This leads to relatively loose and open complexes **143** for the vertices of the resulting cages in comparison to other literature-known iminopyridine-based complexes which utilized multidentate TREN (**128a**) as a triamine subcomponent providing a higher degree of chelation (Scheme 37b). All imine bonds of the complex would then be interconnected by fully covalent bonds over triamine capping units which require a suitable pyridine-2-carbaldehyde building block **144** for the formation of imine bonds. In combination with a metal source, hexadentate iminopyridine metal complexes of the type **147** are accessible which should display higher overall stability, even towards water and bases, due to the increased binding cooperativity around the metal centers and connectivity between the ligands. **$Zn_4L_6(NTf_2)_8$** cage **XXXI** was a target compound within this study and represents an example of such cages.

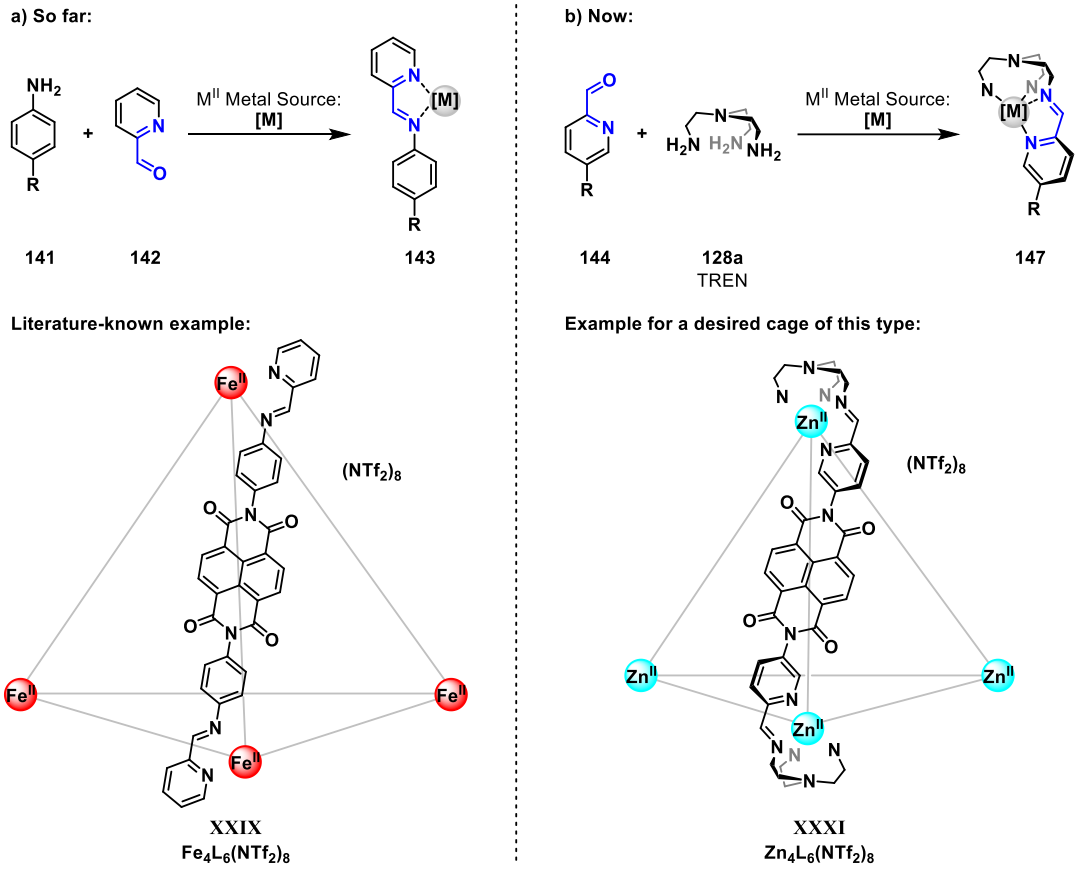

Scheme 37: a) General iminopyridine metal complexation starting from amines **141** and 2-formylpyridine (**142**). **$Fe_4L_6(NTf_2)_8$** tetrahedron **XXIX** is shown as an example. b) General iminopyridine metal complexation starting from pyridine-2-carbaldehydes **144** and TREN (**128a**). Desired target cage **$Zn_4L_6(NTf_2)_8$** tetrahedron **XXXI** is shown as an example.

Initial work on this subject was performed by Joachim Preinl during his master thesis in the TIEFENBACHER group. His work has never been published but needed to be mentioned as it laid the foundation for the upcoming chapters. His main contribution to this work was the development of a synthetic route towards **$Zn_2L_3(NTf_2)_4$** helicate **XXXII** (Scheme 38). Initially, the construction of **$Zn_4L_6(NTf_2)_8$** tetrahedron **XXXI** was envisioned but the isotopic distribution of observed peaks in HR-MS experiments gave evidence for the formation of helicate **XXXII** instead.

Dialdehyde NDI building block **176**, featuring pyridine-2-carbaldehyde moieties on either side, was accessed in two steps starting with the imide condensation between NDA (**179**) and amine **218** to furnish NDI compound **219** in 75% yield (Scheme 38). Radical iodination in benzyl position, followed by KORNBLUM oxidation in one step gave dialdehyde subcomponent **176** in 65% crude yield. In this work, the workup was further optimized increasing its purity with a final yield of 56%. **$Zn_2L_3(NTf_2)_4$** helicate **XXXII** was then synthesized *via* self-assembly from subcomponent **176** (3.0 eq.), TREN (**128a**, 2.0 eq.) and $Zn(NTf_2)_2$ (2.0 eq.) in MeCN/$CHCl_3$ = 1:1 at 150 °C for 1.5 h. It was found by Joachim Preinl (and confirmed within this study) that **$Zn_2L_3(NTf_2)_4$** helicate **XXXII** would only form at high temperatures (120-150 °C), indicated by the characteristic splitting observed for the protons of the ethylene bridges from TREN (**128a**) in a symmetric coordination cage. Only broad resonances dominated the crude mixtures at temperatures below 120 °C. Microwave irradiation was used initially to potentially reduce the reaction time significantly based on previous work from WÜRTHNER *et al.*[287] In this work, it was found that the reaction can also be run in pressure vials using conventional heating *via* oilbaths. However, **Zn_2L_3** helicate **XXXII** was still accompanied by an excess of oligomeric side-products as very broad resonances in the ^{1}H-NMR of the crude product suggested. The intensity of the peaks corresponding to helicate **XXXII** seemed to maximize at 150 °C. Higher temperatures led to a decline of those peaks.

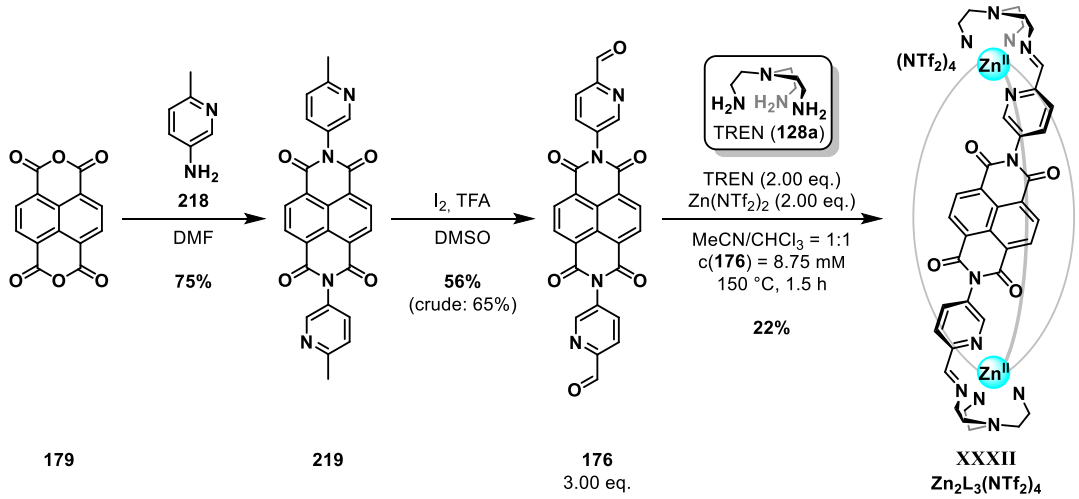

Scheme 38: Synthesis of dialdehyde NDI building block **176** and self-assembly of **$Zn_2L_3(NTf_2)_4$** helicate **XXXII.**

In this work, the helicate **XXXII** was isolated and purified once under the conditions shown in scheme 38 since the workup was time consuming and no evidence for the formation of **$Zn_4L_6(NTf_2)_8$** tetrahedron **XXXI** was observed. A method to isolate and purify **$Zn_2L_3(NTf_2)_4$** helicate **XXXII** was developed. The crude product was first subjected to size-exclusion chromatography to remove oligomers and possible polymers, followed by recrystallization *via* slow diffusion of Et_2O into an acetonitrile solution of helicate **XXXII**. Leftover residual polymers and oligomers formed a thin film that did not readily dissolve again in MeCN but the single crystals of **$Zn_2L_3(NTf_2)_4$** helicate **XXXII** dissolved quite easily. After trituration with MeCN, helicate **XXXII** was obtained in 22% yield and high purity. The single crystals obtained this way also were suitable for X-ray crystallographic analysis, giving access to its crystal structure (Figure 35). The crystal structure revealed that the three NDI moieties of the subcomponent **176** present in helicate **XXXII** stacked on top of each other *via* π-π interactions. A possible cavity was completely occupied by one of the ligands and the ^{1}H-NMR experiment of helicate **XXXII** in MeCN-d_3 showed a broad singlet for the NDI protons, suggesting that this stacking behaviour was also present in solution. Therefore, no guest-binding studies were performed with helicate **XXXII**.

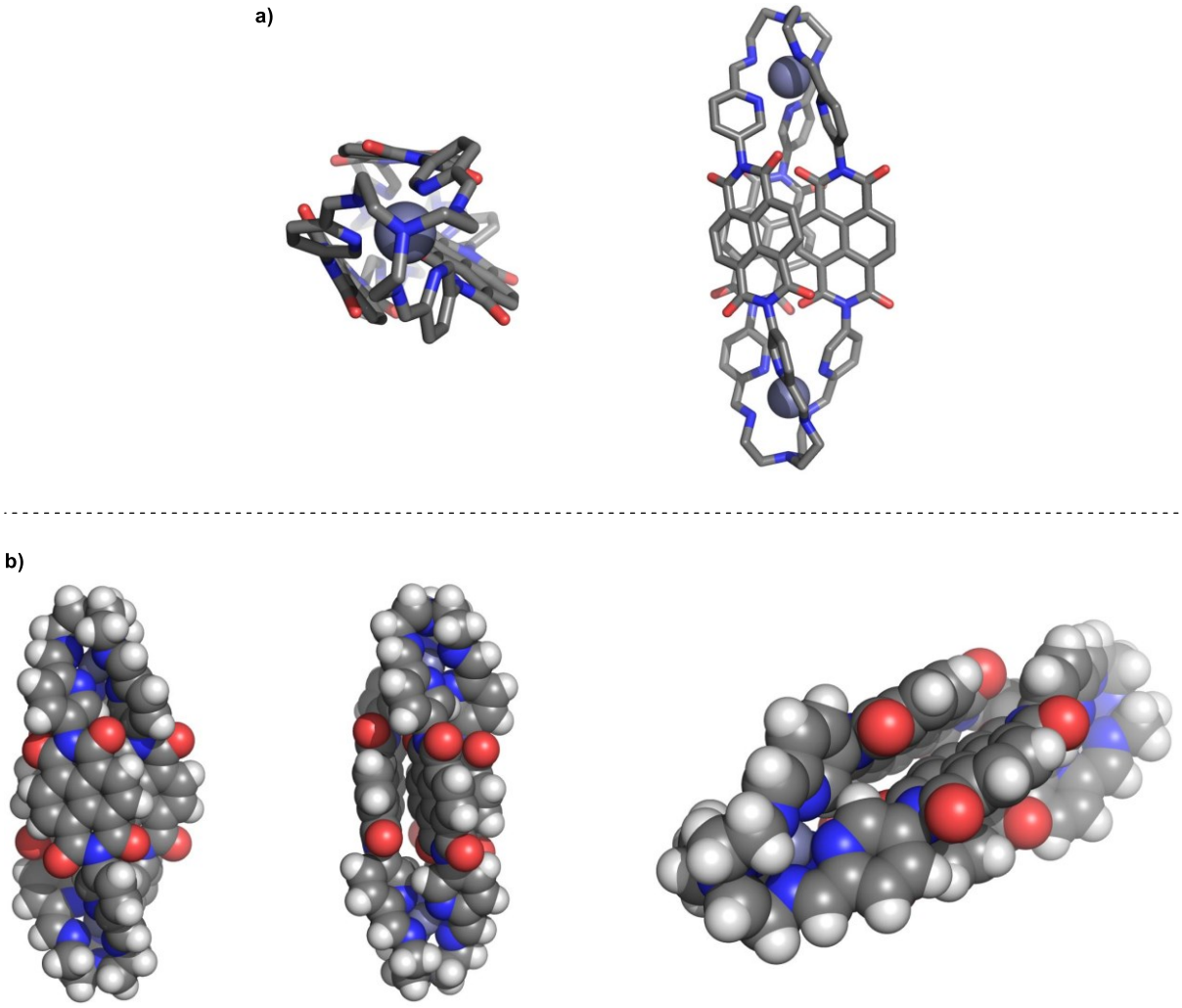

Figure 35: X-ray crystal structure of **Zn_2L_3** helicate **XXXII**. Solvent molecules were omitted for clarity. Carbon atoms are shown in grey, hydrogen atoms in white, nitrogen atoms in blue and oxygen atoms in red. a) Stick model showing helicate **XXXII** from the top and from the side. Hydrogen atoms were omitted for clarity b) Space-filling model showing helicate **XXXII** from the side and different angles. CCDC Deposition number: 222812.

No tetrahedral cage was obtained and the reason for this remained unclear, but the following key factors might have influenced the outcome: (1) ligand **176** features a reduced aspect ratio (length-to-width ratio) compared to the ligand used in the construction of **Fe_4L_6** cage **XXIX** (Scheme 37). The aspect ratio of ligands was reported to have an influence on the outcome of self-assembly processes.[288] (2) π-π-stacking was observed to influence the outcome of self-assembly processes as well.[98] Having no bulky substituents on the NDI unit might have enabled π-π-stacking between the ligands even further for preorganization. (3) The multidentate TREN (**128a**) subcomponent might have additionally influenced the outcome of the reaction when compared to the monodentate pyridine subcomponent used for **$Fe_4L_6(NTf_2)_8$** cage **XXIX**, leading to a more flexible metal complexation.

3.2.3 Screening for Additional Cages using Subcomponent 176

This chapter will focus on other metal salts used in this study in combination with subcomponent **176**. The metal salts investigated included $Fe^{II}(NTf_2)_2$ and $Cd^{II}(NTf_2)_2$ to further increase the scope of the investigations towards acetonitrile-soluble triflimide cages including other metal ions than Zn^{2+} with different ionic radii. The effective ionic radii published by SHANNON during a major review of crystallographic data for each metal ion in complexes with coordination numbers of CN = 6 were reported as follows: $r_{ion}(Fe^{2+}{}_{low\ spin})$ = 61 pm; $r_{ion}(Zn^{2+})$ = 74 pm and $r_{ion}(Cd^{2+})$ = 95 pm.[289] The influence of various ionic radii of the metal on the outcome of the self-assembly including ligand **176** was to be investigated for the potential formation of tetrahedral cages.

Other metal salts explored herein also included $Zn^{II}SO_4$ and $Cd^{II}SO_4$ to potentially get access to water-soluble coordination cages with sulfate counter anions. NITSCHKE *et al*. reported the formation of water-soluble helicates with various dialdehyde ligands when $Zn^{II}SO_4$ was used in combination with TREN (**128a**) with a coordination number (CN) of CN = 6 for each Zn^{2+} metal center.[202] Tetrahedral structures formed instead when $Cd^{II}SO_4$ was utilized together with TRPN (**128b**) as the triamine subcomponent. The explanation was that Cd^{2+}, as a larger analogue of Zn^{2+}, was able to further increase its coordination number to CN = 7 by also binding to the apical nitrogen in TRPN (**128b**), enabled by the larger ionic radius of Cd^{2+}. The bond lengths in the crystallographic data published by NITSCHKE *et al*. and other examples of heptacoordinated Cd^{2+} supported this hypothesis.[202,290] This would then help to cantilever the dialdehyde ligands out into a splayed configuration favouring tetrahedron formation. In contrast to that, the tighter wrapping of a TREN (**128a**) around the smaller Zn^{2+} centers, involving no apical coordination, seemed to promote helicate formation by preorganization of the ligands.[202]

Therefore, subcomponent **176** (3.0 eq.), TREN (**128a**, 2.0 eq.) and $Zn^{II}SO_4$ monohydrate (2.0 eq.) were combined at a set concentration of c(**176**) = 23.5 mM in different solvent systems at various temperatures and reaction times (Scheme 39, Table 14). The mixtures were cooled down to room temperature at the end of the reaction, giving suspensions in every single case. After filtration, the solid residue and the filtrate were both analysed *via* ^{1}H-NMR in different solvents (DMSO-d_6, D_2O, MeCN-d_3) when applicable to gain as much information as possible. Potential sulfate cages should be soluble in water according to many examples in literature,[202] any other solubility properties were not known. Subcomponent **176**, however, displayed very poor solubility in water and most other solvents. The best solvents for the substrate were MeCN, DMF and DMSO. High enough solubility of the substrate should be necessary for it to enter the reaction equilibrium of the reversible imine condensation. In the case of substrate insolubility in a given solvent, the equilibrium would shift entirely towards dialdeyhde **176**. Therefore, the reaction was tested in DMF at 80 °C or 120 °C (Table 14, Entries 1-2), in MeCN at 80 °C (Table 14, Entry 3) and in DMSO-d_6 at 80 °C and 120 °C (Table 14, Entries 4-5) for 18 h each. In all cases, the solid residue showed signs of decomposition as it sometimes appeared as an insoluble black solid which only showed starting material in the ^{1}H-NMR or the formation of side-products in the form of broad resonances on top of subcomponent **176**. No other interesting signals were found across all experiments. In the filtrate of the reactions at 80 °C with either DMF or DMSO-d_6, discrete resonances have been observed but none that would fit either cage **XXXIII** or **XXXIV**. All other attempts gave complex mixtures at best and even when either DMSO-d_6 was combined with D_2O (Table 14, Entry 6) or MeCN with H_2O (Table 14, Entry 7) in a 1:1 ratio to ensure solubility of a possible cage, only complex mixtures were obtained with incomplete conversion of the starting material and formation of broad resonances hinting at oligomers at best. Using microwave irradiation for the reaction in MeCN/H_2O = 1:1 for 2 h led to similar issues (Table 14, Entry 8). The filtrate in this case gave a set of discrete resonances but none which

could belong to a helicate **XXXIII** or tetrahedron **XXXIV** as the relative integrals of the aromatic peaks did not correlate to any of the desired cages and no characteristic splitting of the ethylene bridges from TREN was detected.

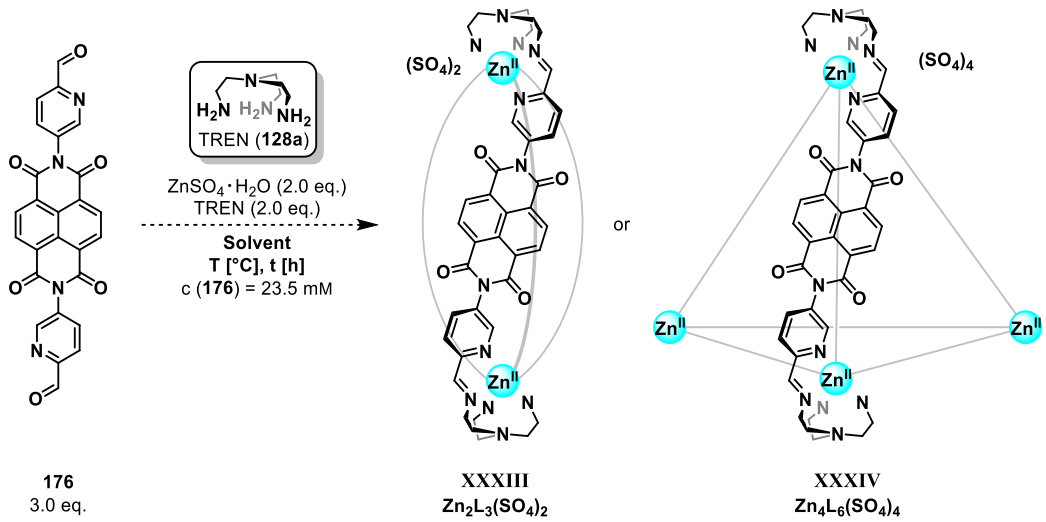

Scheme 39: General reaction conditions used for table 14.

Table 14: Conditions tested for the reaction shown in scheme 39 towards sulfate cages **XXXIII** or **XXXIV**.

Entry	Solvent	T [°C]	t [h]	Solid	Filtrate
1	DMF	80	18	Decomposition, SM*	Discrete resonances but no cage
2	DMF	120	18	Decomposition, SM*	Complex mixture
3	MeCN	80	18	Decomposition, SM*	Complex mixture
4	DMSO-d_6	80	18	Decomposition, SM*	Discrete resonances but no cage
5	DMSO-d_6	120	18	Decomposition, SM*	Complex mixture
6	D_2O/DMSO-d_6 = 1:1	80	18	Decomposition, SM*	Complex mixture
7	H_2O/MeCN = 1:1	80	18	Decomposition, SM*	Complex mixture
8**	H_2O/MeCN = 1:1	150	2	Decomposition, SM*	Discrete resonances but inconclusive

*SM: Starting Material.
**Heat source: microwave irradiation.

Simultanously, the same reaction conditions were tested for the combination of subcomponent **176** (3.0 eq.) with TRPN (**128b**, 2.0 eq.) and $Cd^{II}SO_4$ (2.0 eq.) at c(**176**) = 23.5 mM (Scheme 40, Table 15). Only complex mixtures were observed in the filtrate after workup and in half the experiments only TRPN (**128b**) and solvent peaks. The solid residues mostly only showed starting material or broad resonances, again hinting at oligomers.

In conclusion, no cage was obtained with either $Zn^{II}SO_4$ or $Cd^{II}SO_4$ as the metal source. This approach seemed not to be suitable for the construction of a water-soluble cage using highly insoluble subcomponent **176** as starting material. Next, $Fe(NTf_2)_2$ and $Cd(NTf_2)_2$ were explored which could possibly give access to acetonitrile-soluble cages with geometries other than helicates due to the different ionic radii exhibited by Fe^{2+} and Cd^{2+}.

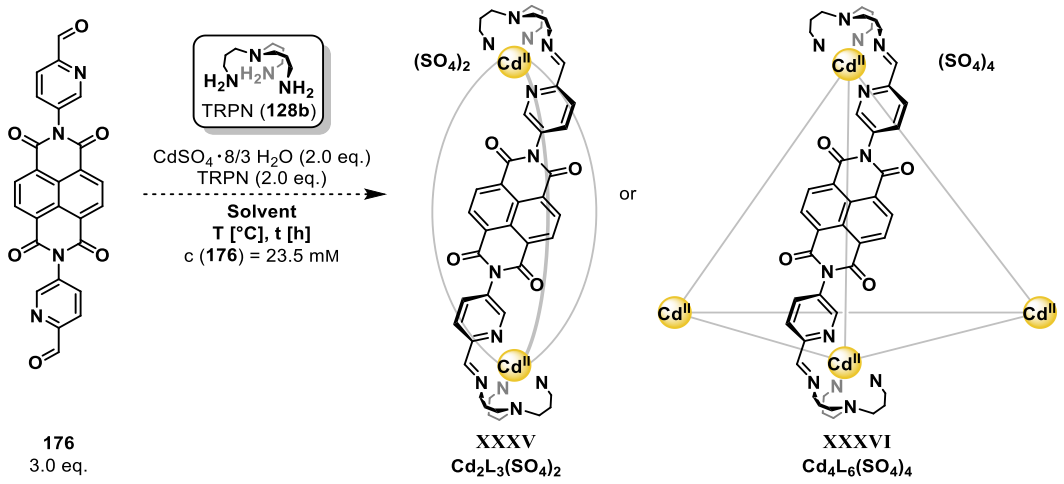

Scheme 40 General reaction conditions used for table 15.

Table 15: Conditions tested for the reaction shown in scheme 40 towards sulfate cages **XXXV** or **XXXVI**.

Entry	Solvent	T [°C]	t [h]	Solid	Filtrate
1	DMF	80	18	Only SM*	Complex mixture
2	DMF	120	18	Only SM*	Complex mixture
3	MeCN	80	18	Only SM*	TRPN and solvent peaks only
4	DMSO-d_6	80	18	Only SM*	TRPN and solvent peaks only
5	DMSO-d_6	120	18	Decomposition, SM*	Complex mixture
6	D_2O/DMSO-d_6 = 1:1	80	18	Only SM*	TRPN and solvent peaks only
7	H_2O/MeCN = 1:1	80	18	Decomposition, SM*	TRPN and solvent peaks only
8**	H_2O/MeCN = 1:1	150	2	Decomposition, SM*	Complex mixture

*SM: Starting Material.
**Heat source: microwave irradiation.

Reactions with subcomponent **176** (3.0 eq.), $Fe(NTf_2)_2$ (2.0 eq.) and TREN (**128a**, 2.0 eq.) were carried out in either MeCN or MeCN/$CHCl_3$ = 1:1 as this solvent system already proved to be successful in the construction of $\mathbf{Zn_2L_3(NTf_2)_4}$ helicate **XXXII** (see chapter 3.2.2). First test reactions were run at room temperature in either solvent system and at a concentration of c(**176**) = 8.75 mM or 17.5 mM (Table 16, Entries 1-4) for 18 h. The reaction mixtures were filtered off and the filtrates were analysed *via* ^{1}H-NMR in MeCN-d_3. In all these experiments, relatively sharp and discrete resonances were observed which set themselves apart from broader resonances which were usually associated with oligomeric side-products. However, the number of peaks in the aliphatic region did not quite fit the number of peaks expected for $\mathbf{Fe_2L_3(NTf_2)_4}$ helicate **XXXVII** or $\mathbf{Fe_4L_6(NTf_2)_8}$ tetrahedron **XXXVIII** (Scheme 41) and the corresponding HR-MS experiments also did not show any evidence for cage formation. Any other structure could not be derived from the data with certainty. The reactions also seemed to not have run to completion as free TREN (**128a**) peaks were observed as well in the filtrate after the reactions. Therefore, the reaction time was prolonged to 72 h (Table 16, Entry 5) and a different reaction was run at 75 °C for 4 h (Table 16, Entry 6) but both reaction conditions only favoured oligomer formation (broad resonances) instead.

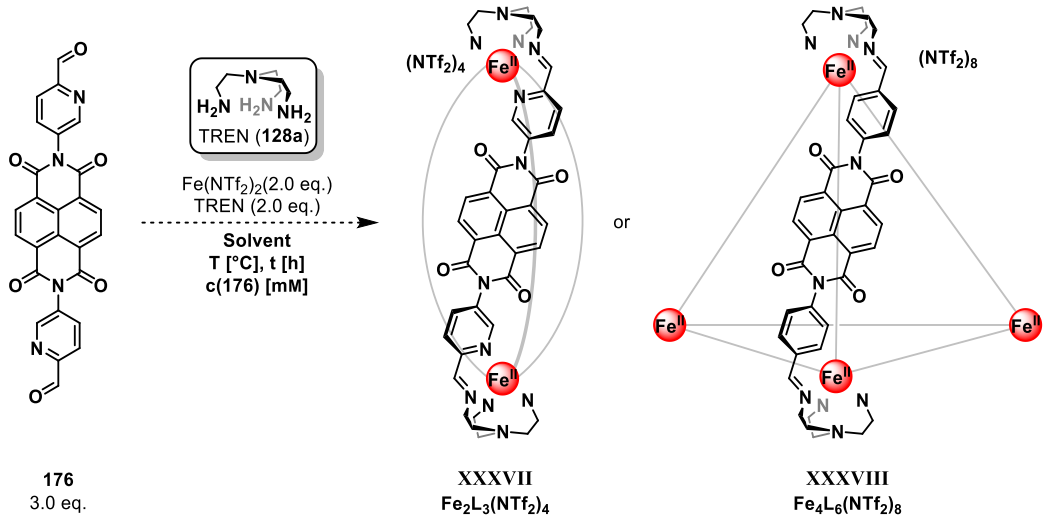

Scheme 41: General reaction conditions used for table 16.

Table 16: Conditions tested for the reaction shown in scheme 41 towards triflimide cages **XXXVII** or **XXXVIII**.

Entry	Solvent	T [°C]	t [h]	c(176) [mM]	Observation
1	MeCN	23	18	8.75	Discrete Resonances (No Cage*) + Oligomers
2	MeCN	23	18	17.5	Discrete Resonances (No Cage*) + Oligomers
3	MeCN/$CHCl_3$ = 1:1	23	18	8.75	Discrete Resonances (No Cage*) + Oligomers
4	MeCN/$CHCl_3$ = 1:1	23	18	17.5	Discrete Resonances (No Cage*) + Oligomers
5	MeCN/$CHCl_3$ = 1:1	23	72	8.75	Promoted Oligomer Formation
6	MeCN/$CHCl_3$ = 1:1	75	4	8.75	Promoted Oligomer Formation
7**	MeCN/$CHCl_3$ = 1:1	60	1	8.75	Discrete Resonances (No Cage*) + Oligomers
8**	MeCN/$CHCl_3$ = 1:1	80	1	8.75	Oligomers
9**	MeCN/$CHCl_3$ = 1:1	100	1	8.75	Oligomers
10**	MeCN/$CHCl_3$ = 1:1	110	1	8.75	Oligomers
11**	MeCN/$CHCl_3$ = 1:1	120	1	8.75	Oligomers
12**	MeCN/$CHCl_3$ = 1:1	130	1	8.75	Oligomers
13**	MeCN/$CHCl_3$ = 1:1	140	1	8.75	Oligomers
14**	MeCN/$CHCl_3$ = 1:1	150	1	8.75	Oligomers

*The same peaks were observed in the ^{1}H-NMR in all these experiments. HR-MS data did not support formation of an interesting cage.

**Heat source: microwave irradiation.

Next microwave irradiation was used, hoping for a reaction rate increase. Using microwave irradiation for the reaction at 60 °C for 1 h (Table 16, Entry 7) gave a similar result as the reactions at room temperature in entries 1-4. However, increasing the temperature even further to 80-150 °C for 1 h (Table 16, Entries 8-14) only led to very broad resonances which were associated with oligomers unlike the reaction with $Zn(NTf_2)_2$. No new signal set corresponding to a defined cage structure was observed.

Having failed to acquire a coordinaton cage with $Fe(NTf_2)_2$ as well, $Cd(NTf_2)_2$ (2.0 eq.) was explored next despite its high toxicity in combination with TRPN (**128b**) in various amounts and subcomponent **176** (3.0 eq.) in MeCN/$CHCl_3$ = 1:1 at c(**176**) = 8.75 mM and different temperatures (Scheme 42, Table 17). The reaction mixtures were again filtered at the end of the reaction and the filtrate was analysed *via* ^{1}H-NMR in MeCN-d_3.

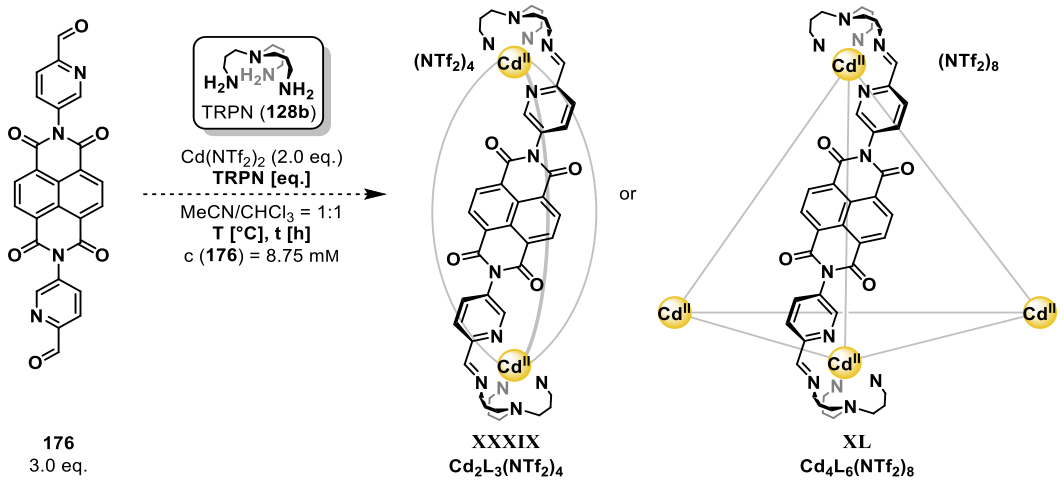

Scheme 42: General reaction conditions used for table 17.

Table 17: Conditions tested for the reaction shown in scheme 42 towards triflimide cages **XXXIX** or **XL**.

Entry	TRPN [eq.]	T [°C]	t [h]	Observation
1	2.0	23	18	Very Low Conversion
2	2.0	80	24	Oligomers only
3	2.0	80	48	Oligomers only
4*	2.0	80	2	Low Conversion / Complex Mixture
5*	2.0	90	2	Complex Mixture
6*	2.0	100	2	Complex mixture / Oligomers
7*	2.0	110	1	Oligomers only
8*	2.0	120	1	Oligomers only
9*	2.0	150	1	Oligomers only
10*	1.5	120	1	Oligomers only
11*	1.5	150	1	Oligomers only

*Heat source: microwave irradiation.

Almost no conversion of starting material was observed at room temperature after 18 h (Table 17, Entry 1). An increase of temperature to 80 °C using an oilbath gave broad resonances after 24 h and 48 h (Table 17, Entries 2-3). Switching from conventional heating methods to microwave irradiation showed low conversion again at 80 °C for 2 h (Table 17, Entry 4). The reaction did not necessarily seem to proceed faster due to the microwaves. A complex mixture was observed with some relatively sharp peaks, but the ^{1}H-NMR once again was dominated by supposed oligomers. Increasing the temperature to 90-150 °C (Table 17, Entries 5-9) only promoted oligomer formation even further with no sharp peaks being visible anymore. In a final attempt, the amount of TRPN (**128b**) was decreased from 2.0 eq. to 1.5 eq. and the reaction temperature was set to either 120 °C or 150 °C for 1 h (Table 17, Entries 10-11). The underlying idea was to reduce the concentration of TRPN (**128b**) in the mixture to make it less likely for a molecule of dialdehyde **176** to encounter another equivalent of TRPN (**128b**) after initital imine formation with a first equivalent. However, this did not change the outcome at all, and only broad resonances were observed. In conclusion, no cage other than **$Zn_2L_3(NTf_2)_4$** helicate **XXXII** (see chapter 3.2.2) could be accessed by combining NDI dialdehyde **176** with either $Zn(NTf_2)_2$, $Fe(NTf_2)_2$, $Cd(NTf_2)_2$, $ZnSO_4$ or $CdSO_4$ and TREN (**128a**) or TRPN (**128b**) within this study. Only undefined oligomeric products dominated the reaction mixtures and no other promising defined structure formed.

3.2.4 Coordination Cages based on Triphenylene Triimide (TPTI) Ligands

As the synthesis of C_2-symmetric ligands like NDI dialdehyde **176** would always lead to an unpredictable outcome as both edge-linked helicates or tetrahedral structures could form, it was decided to explore a panelling approach. The use of a C_3-symmetric (tritopic) ligand would most likely exclude helicate formation and should form a face-capped tetrahedron instead, eliminating this selectivity problem. Ligands with NDI units are not amenable for the formation of such ligands. Therefore, the π-acidic NDI surface was replaced with an electronically similarly polarised triphenylene triimide (TPTI) scaffold to potentially form $\mathbf{M_4L_4}$ tetrahedral cages **M-XXI**. The retrosynthesis pathway is shown in scheme 43.

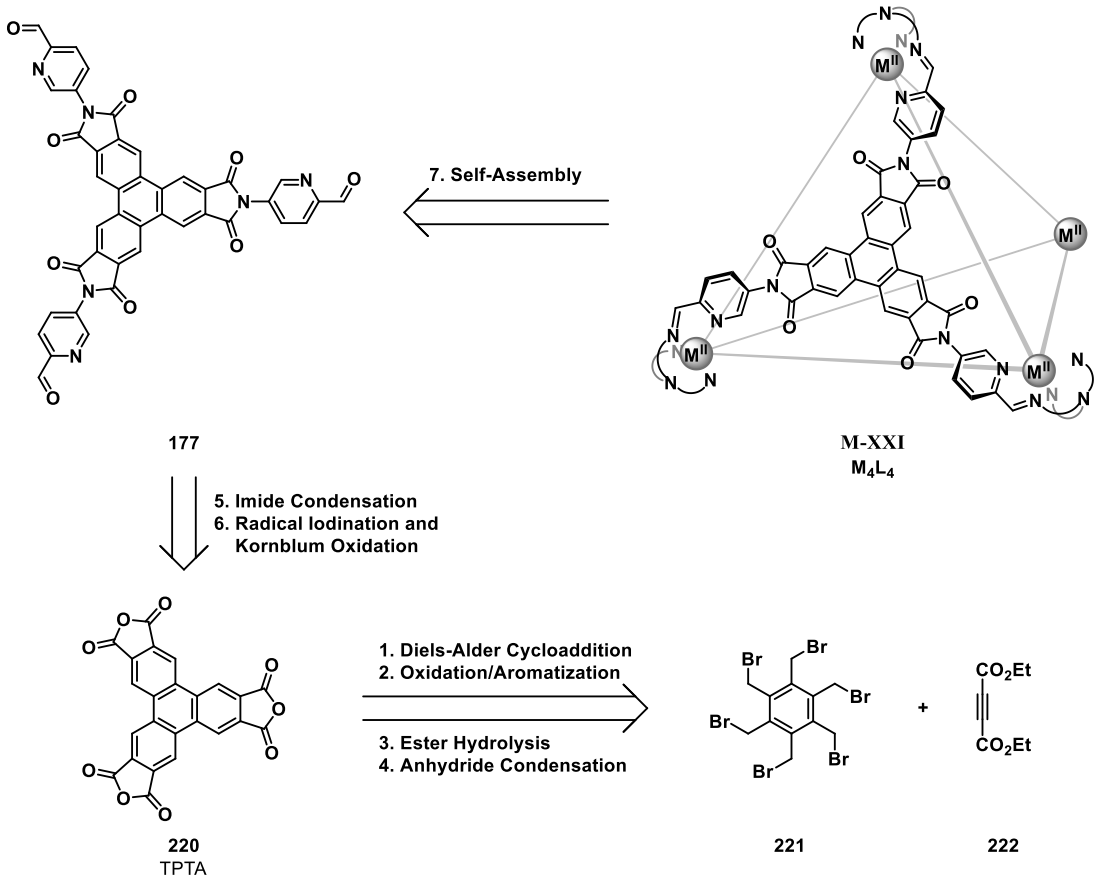

Scheme 43: Retrosynthetic plan towards face-capped $\mathbf{M_4L_4}$ tetrahedra **M-XXI** based on TPTI ligand **177**.

Trialdehyde ligand **177** was envisioned to be accessible in six steps of which the first three were literature-known. The core carbon skeleton of ligand **177** was built in two steps starting with *in-situ* radialene generation from commercially available hexakis(bromomethyl)benzene (**221**) and direct DIELS-ALDER cycloaddition with diethyl acetylenedicarboxylate (**222**) in one pot to furnish hexaethyl hexacarboxylate **223** in 17% yield (Scheme 44). Aromatization *via* oxidation with MnO_2, followed by basic ester hydrolysis gave triphenylene hexacarboxylic acid **225** in 93% combined yield. Hexacarboxylic acid **225** was then exposed to neat thionyl chloride yielding triphenylene trianhydride (TPTA, **220**) quantitatively. The material was very poorly soluble across all organic solvents to the point where a mixture of MeCN-d_3 and HCl-saturated $CDCl_3$ (1:1) was needed to record a useful ^{13}C-NMR spectrum at room temperature.

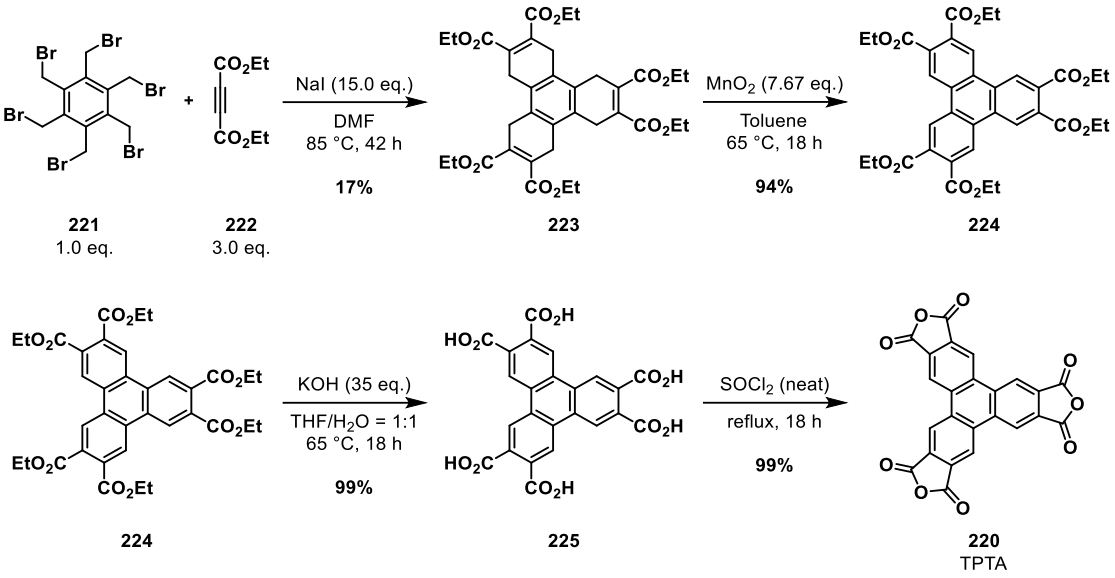

Scheme 44: Synthesis of triphenylene trianhydride (TPTA) in 4 steps.

From here, synthesis of ligand **177** was planned to proceed in an analogous manner to the synthesis of NDI dialdehyde **176** from napthalene dianhydride (NDA, **179**) as shown in chapter 3.2.2 (Scheme 38): threefold imide condensation of amine **218** to trianhydride **220** in DMF was explored next (Scheme 45b) but proved to be more difficult to achieve than expected. Test reactions between commercially available phthalic anhydride (**226**) and amine **218** (1.0 eq.) were performed for comparison (Scheme 45a) using the same reaction conditions. The results are shown in table 18. Imide condensation must be performed twice in total per amine: the first nucleophilic attack of an amine on an electrophilic carbon atom of a carboxylic anhydride opens the anhydride to form a monoamide monocarboxylic acid species as an intermediate. **227** is a simple example for these intermediates (Scheme 45a). The second imide condensation between this new amide and the free carboxylic acid in close proximity releases an equivalent of H_2O while closing the structure to form imide compound **228**. The reactions tested showed full conversion and confirmed quantitative formation of imide compound **228** at 150 °C overnight within 20 h (Table 18, Entry 2, Reaction 1) with a yield of 61% after recrystallization from EtOH. Only a portion of the intermediate monoamide monocarboxylic acid **227** converted to the final product **228** at lower temperatures such as 100 °C or 80 °C after 20 h each (Table 18, Entries 4 and 6, Reaction 1). Selective formation of intermediate **227** was achieved at 80 °C after 2 h without any traces of imide **228** or starting material in 55% yield after recrystallization from DMF.

In contrast to phthalic anhydride, the reactions with TPTA (**220**, Scheme 45b) showed decomposition at either 150 °C after 1 h or at 100 °C but longer reaction times were necessary for the material to decompose at this temperature (Table 18, Entries 1-4, Reaction 2). At 80 °C, however, a product mixture with defined peaks was observed in the ^{1}H-NMR in DMSO-d_6 after 2 h. The reaction time was extended to 4 h during scale-up without any change observed in the ^{1}H-NMR because the reaction mixture formed a jelly-like suspension which was difficult to stir properly. The desired TPTI product **229** should exhibit high symmetry and show one single peak for the aromatic triphenylene protons, but multiple peaks were observed indicating the formation of more than just a single product (Figure 36a).

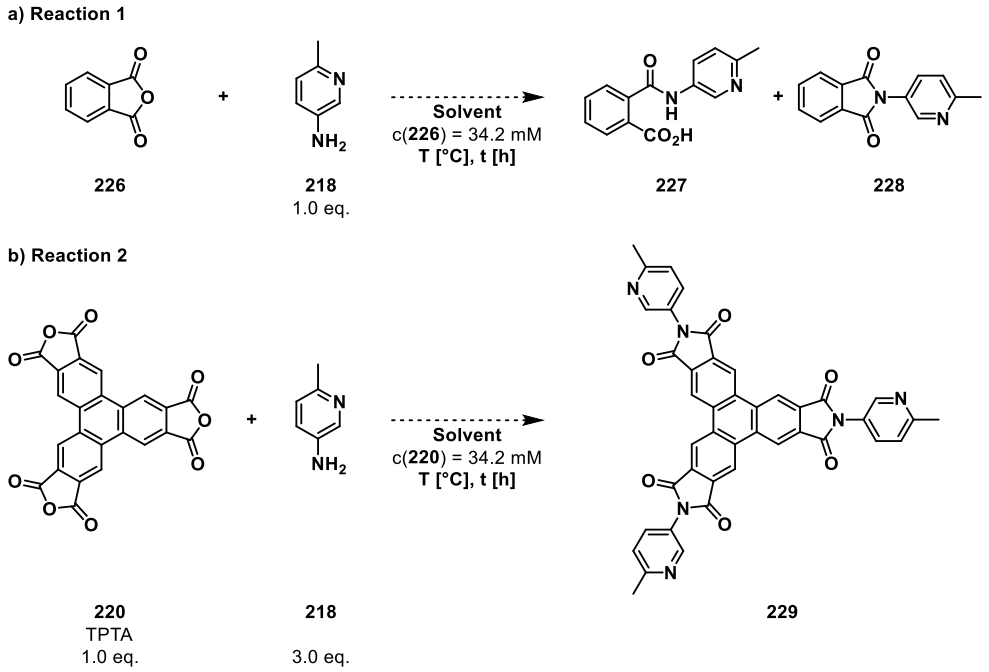

Scheme 45: General reaction conditions used for table 18.

Table 18: Experimental results for the reactions shown in scheme 45.

				Reaction 1		Reaction 2
Entry	**Solvent**	**T [°C]**	**t [h]**	**Ratio 227:228**	**Yield [%]**	**Observation in the crude ^{1}H-NMR**
1	DMF	150	1	1.00:0.26	n.d.	Decomposition
2	DMF	150	20	0.00:1.00	61	Decomposition
3	DMF	100	2	1.00:0.01	n.d.	Defined Peaks / Product Mixture
4	DMF	100	20	1.00:0.28	n.d.	Decomposition
5	DMF	80	2	1.00:0.00	55	Defined Peaks / Product Mixture
6	DMF	80	20	1.00:0.04	n.d.	Defined Peaks / Product Mixture
7	AcOH	140	18	0.00:1.00	63	Complex mixture

In accordance with the experiments using phthalic anhydride (**226**), an educated guess was made suggesting the formation of triamide tricarboxylic acid compounds **230** with C_3 symmetry and **231** with C_S symmetry (Scheme 46). The peaks in the ^{1}H-NMR could not be assigned fully with certainty as the poor solubility of this crude product mixture prevented the measurement of a useful ^{13}C-NMR spectrum and related 2D-NMR experiments in deuterated solvents including acetone-d_6, DCM-d_2, $CDCl_3$, DMSO-d_6 and MeCN-d_3 or mixtures of those with HCl-saturated $CDCl_3$. The high-resolution ESI-MS experiment showed traces of either compound **230** or **231** as well with a peak of low intensity, presumably due to the low solubility, at 763.2157 belonging to the mass of a proton adduct of **230** or **231** of the type $[M+H]^+$ (Figure 36b). When this crude product mixture was again exposed to 150 °C for 1 h in DMF to try and access TPTI **229** stepwise, decomposition was observed once again. A different methodology seemed necessary.

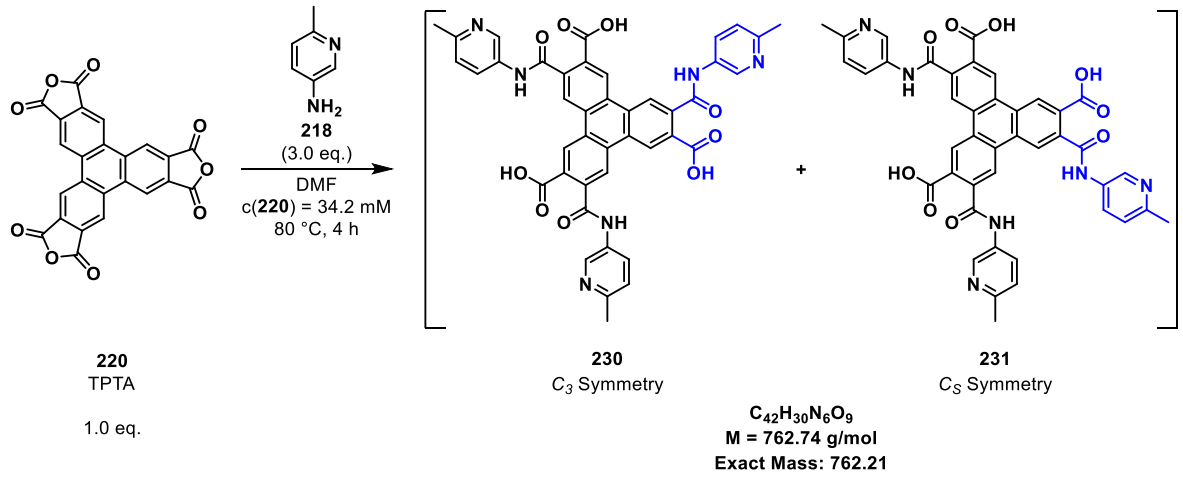

Scheme 46: Reaction conditions presumably leading to a crude mixture between products **230** and **231**.

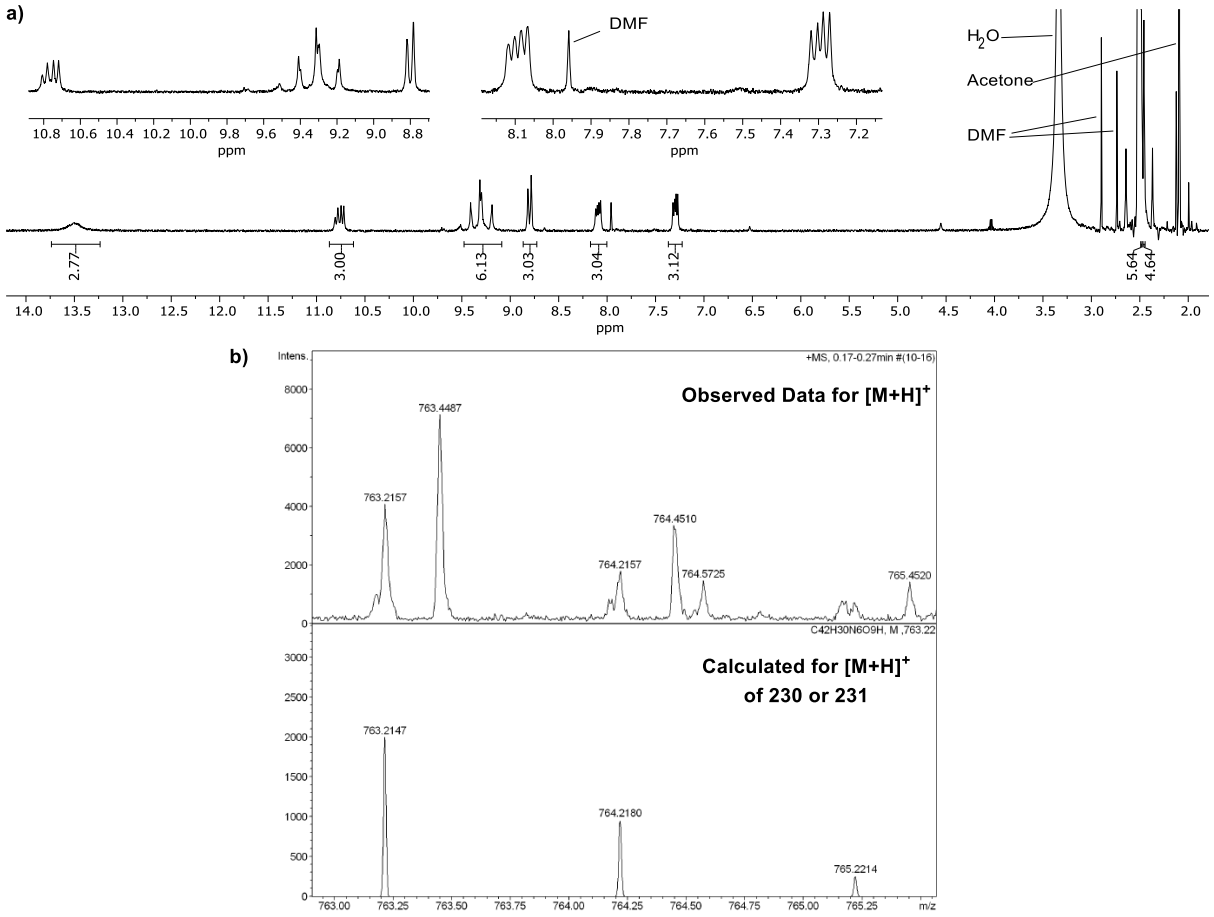

Figure 36: a) Crude ^{1}H-NMR (500 MHz, DMSO-d_6) of the reaction shown in scheme 46. b) High-resolution ESI-MS data gathered from the crude product of the reaction shown in scheme 46.

Phthalic anhydride (**226**) and amine **218** were used again as simple compounds to test the imide condensation reaction under acidic conditions. Exchanging DMF as solvent with glacial acetic acid and refluxing the reaction mixture overnight gave target product **228** in 63% yield after recrystallization from EtOH. However, the same reaction conditions once again gave a complex mixture with TPTA (**220**) as substrate (see Table 18, Entry 7, Reactions 1 and 2). Undefined and undesired side-products formed at too high temperatures in general. Therefore, the crude product mixture obtained through the reaction shown in scheme 46 was instead exposed to neat thionyl

chloride at reflux for 18 h. The underlying idea was to generate more electrophilic acyl chlorides from the carboxylic acids in **230** and **231** which in turn should further react more easily, even at lower temperatures, such as reflux at 90 °C oilbath temperature, with the amide groups in close proximity to form HCl and imides whilst preventing side-product formation. TPTI **229** was obtained this way in 47% crude yield over two steps (Scheme 47) and was fully characterized. A solvent mixture of DMSO-d_6/MeOH-d_4 = 1:1 was necessary to measure a ^{13}C-NMR spectrum and related 2D-NMR experiments because the solubility of TPTI **229** was otherwise not sufficient in any other solvent by its own. To obtain the crude material, the solvent was only removed under reduced pressure at the end of the reaction and the solid residue was washed with acetone. Workup attempts including washing steps with water to remove residual HCl or $SOCl_2$ surprisingly led to decomposition of the material. In conclusion, triphenylene triimide compounds seemed to display lower stability towards high temperatures compared to simple phthalic anhydride (**226**) and seemed to be susceptible to water.

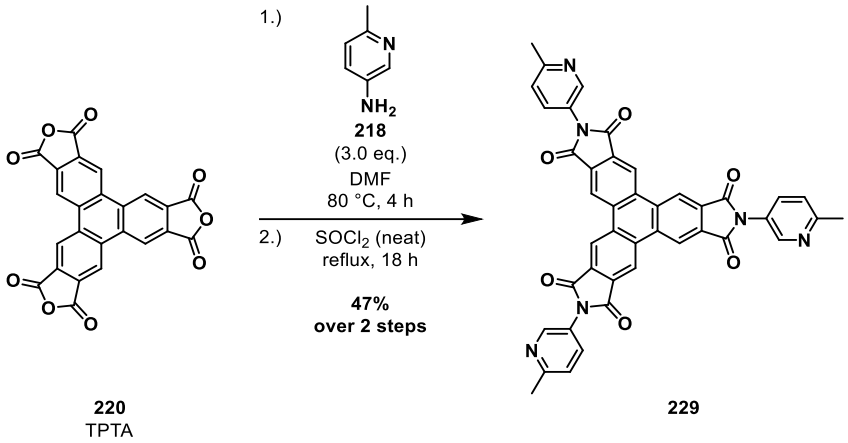

Scheme 47: Finalized reaction conditions for the synthesis of TPTI **229** in two steps from TPTA (**220**).

With TPTI **229** being fully characterized and available, the final step towards TPTI ligand **177** needed to be investigated which included radical iodination in benzyl position followed by KORNBLUM oxidation in one pot (Scheme 48). The standard protocol for the analogous NDI compound **219** (Chapter 3.2.2, Scheme 38) required the following workup: after 20 h at 150 °C in DMSO, the reaction mixture was cooled down to room temperature and poured into ice-cold H_2O for full precipitation of the material. The dark brown slurry was then filtered and the solid was washed in several steps with aqueous Na_2SO_3 to remove residual iodine, saturated aqueous $NaHCO_3$ to neutralize TFA, then H_2O and, finally, acetone. However, the solid material did react almost completely after exposure to aqueous base and no material was left on the filter after the washing step with H_2O except for a very thin film of a black tar-like residue. ^{1}H-NMR in DMSO-d_6 showed one single peak at 9.6 ppm, which could not be assigned to anything of interest. Neither TPTI **229** nor the target product TPTI **177** should display good solubility in water. Analysis of the separately collected filtrates *via* ^{1}H-NMR revealed that no starting material was left, and the material seemed to have decomposed completely.

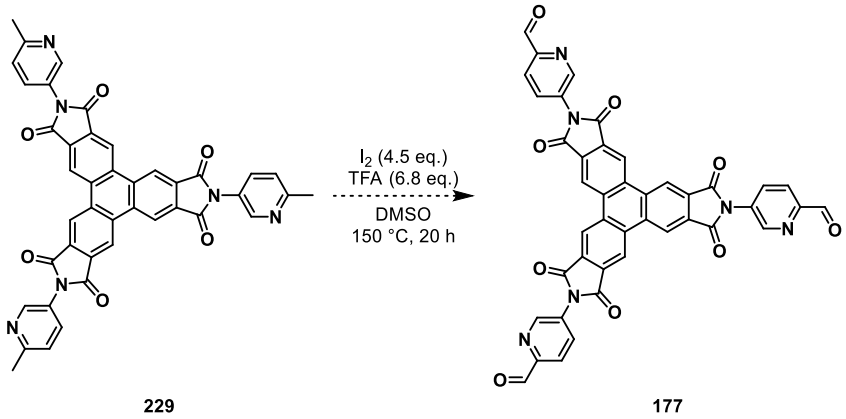

Scheme 48: Conditions for the radical iodination and KORNBLUM oxidation in benzyl position for 2-methylpyridines.

In a second attempt, the slurry obtained after pouring the mixture into ice-cold water was split in two aliquots of the same size, centrifuged and the solid residue was washed once *via* centrifugation with acetone only and the other aliquot was washed with aqueous Na_2SO_3 and acetone but the result was the same as before in either case and one single peak in the aromatic region of the ^{1}H-NMR of the solid black residue was observed. Direct measurement of a ^{1}H-NMR in DMSO-d_6 of a sample of the reaction mixture before any workup showed interesting peaks in the chemical shift range for aromatic and aldehyde compounds but after contact with water in any form during workup, only one peak was left, suggesting that decomposition occurred already upon contact with water alone. It was concluded that TPTI constructs were not stable enough, making the approach not suitable for the synthesis of a stable coordination cage.

3.2.5 Triphenylene Triimide (TPTI) Based Tweezers and Cyclophanes

As highlighted in chapter 1.1.3b, NDI-based tweezers have been used sucessfully in anion-π catalysis. While this sideproject did stir away from the overarching topic of this work, which was the construction of novel positively charged supramolecular cage compounds, non-charged TPTI cyclophanes **233** and TPTI tweezers **234** (Scheme 49a) were considered herein as they could be easily accessible through the same intermediate compound TPTA (**220**) that was already synthesized to access potential coordination cages as shown in chapter 3.2.4.

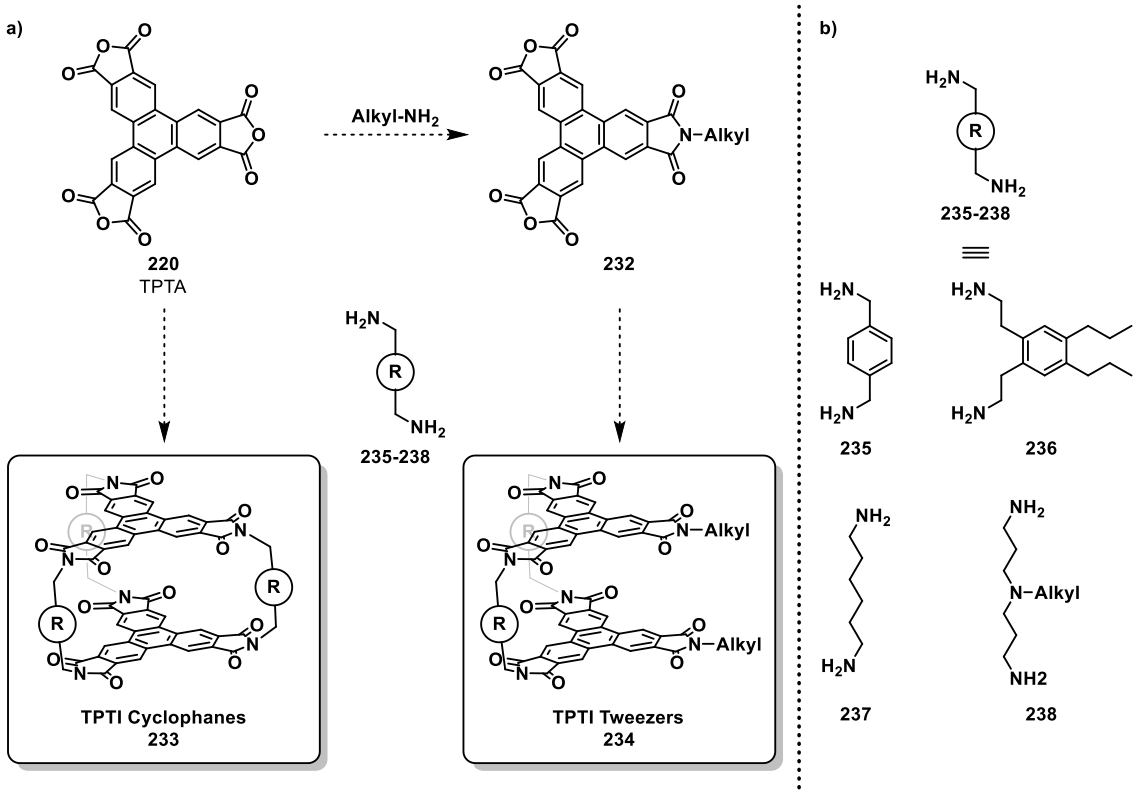

Scheme 49: a) Simplified synthetic pathways towards TPTI cyclophanes **233** and TPTI tweezers **234**. b) Possible diamine linkers **235**-**238**.

TPTA (**220**) was envisioned to form TPTI cyclophanes **233** as dimeric hosts which are linked three times in combination with potential diamine linkers **235**-**238** (Scheme 49b) or TPTI tweezers **234** which are linked only twice and, therefore, offer one open side (Scheme 49a). The latter approach offered the advantage that two imide sites could be equipped with highly solubilizing alkyl chains. Solublizing groups could turn out to be very important since TPTIs are very poorly soluble in organic solvents.[291] The solubilizing group was planned to be attached first to generate **232**, followed by twofold imide condensation with a monoprotected diamine linker and dimerization with a second equivalent of **220** under high dilution conditions. As for the length of the diamine linker employed, work by the NAKAMURA group demonstrated that only a very narrow NDI cyclophane which was linked by six methylene groups was suitable for the binding of a naphthalene guest in fast exchange at room temperature.[292] Elongation of the six atom linker led to complete loss of binding. Therefore, diamine linkers **235**-**238** were considered herein based on these findings to create functional hollow binding pockets. Seven atom linker **238** additionally features a base in a position to potentially deprotonate substrates within the binding pocket. However, diamine linkers of the type **236** and **238** did require multistep synthetic efforts while **235** and **237** were commercially available. Diamine **235** was used as the linker of choice since its mono-Boc protected derivative

was commercially available and the rigidity from the benzene core was expected to promote dimerization during the last step compared to a fully saturated aliphatic linker which might have introduced additional entropic barriers due to its flexibility. Mono-Boc protection should be necessary to circumvent polymerization.

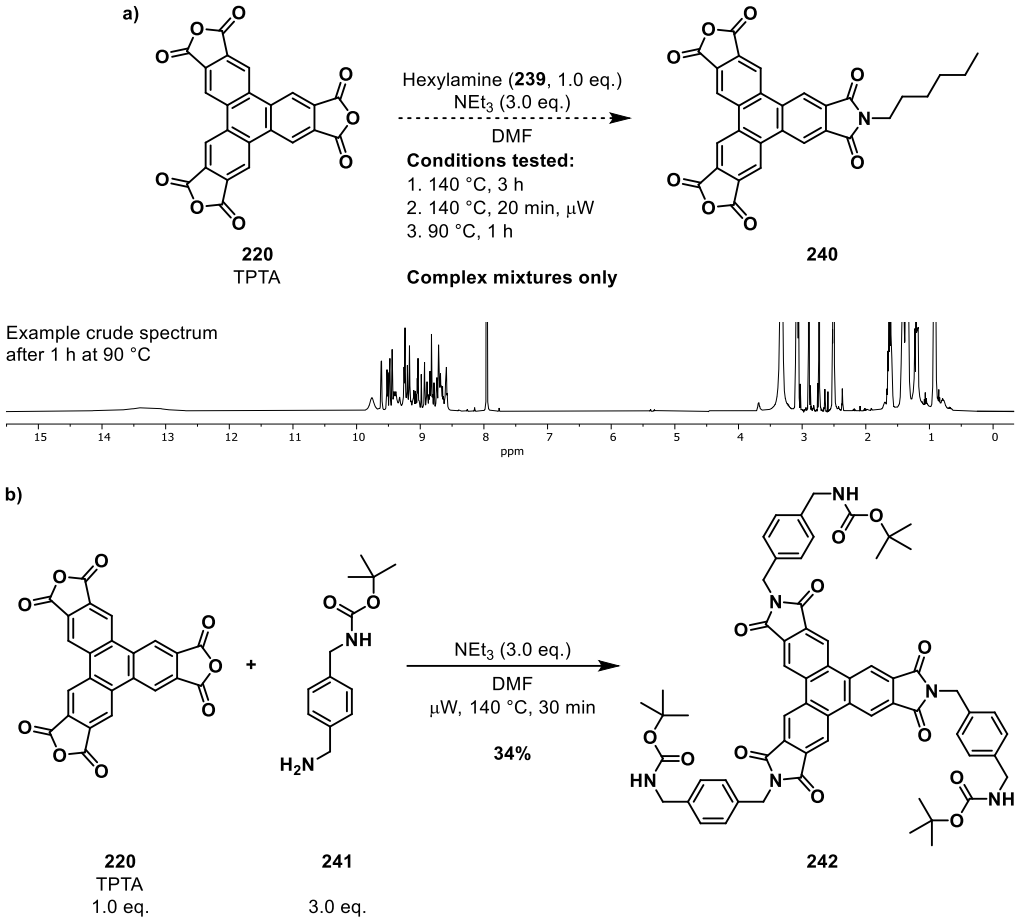

Scheme 50: a) Reaction conditions tested for the imide condensation between TPTA (**220**) and hexylamine (**239**). b) Synthesis of TPTI **242** *via* threefold imide condensation between TPTA (**220**) and mono-Boc protected diamine **241**.

Hexylamine (**239**) was explored as the solubilizing group for the pathway leading to potential tweezer compounds **234** (Scheme 49a). TPTA (**220**, 1.0 eq.) and hexylamine (**239**, 1.0 eq.) were combined in DMF. Triethylamine (1.0 eq.) was added to neutralize potential dicarboxylic acids forming in solution during the imide condensation with TPTA (**220**). A complex mixture was obtained after 3 h at 140 °C oilbath temperature. Using microwave irradiation to heat up the reaction mixture to the same temperature for 20 min led to the same result. Running the reaction at 90 °C for 1 h did not lead to a more defined product distribution either and its crude spectrum, measured in DMSO-d_6, is shown as an example. Broad resonances around the chemical shift range for carboxylic acids (12.5-14.0 ppm) were observed as well as a disproportionate amount of aromatic proton signals (8.50-10.0 ppm). It seemed like the imide groups were partially opened at high temperatures to form carboxylates and/or carboxylic acids in solution. The addition of only one equivalent of hexylamine should have led to a defined set of peaks if one single product dominated. No further experiments were conducted pursuing tweezers **234** because the same stability problems with triphenylene compounds were observed as in chapter 3.2.4.

The imide condensation between TPTA (**220**, 1.0 eq.) and mono-Boc protected diamine linker **241** (3.0 eq.) on the other hand gave a more defined signal set after 30 min at 140 °C using microwave irradiation and furnished TPTI **242** in 34% yield after column chromatographic purification where a significant amount of product was lost due to solubility issues (Scheme 50b). The desired product formed during this first test reaction and no more time was invested into the screening of this step or further workup optimizations as the material gained was sufficient for the following investigations.

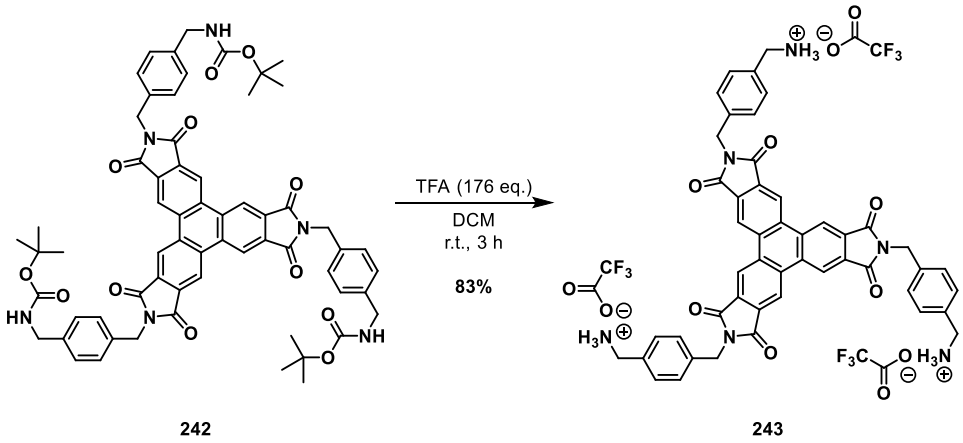

242 **243**

Scheme 51: Boc-deprotection of TPTI **242** with TFA towards TPTI **243** as the ammonium trifluoroacetate salt.

Deprotection of the Boc groups proceeded using TFA in DCM at room temperature over 3 h to generate the corresponding ammonium trifluoroacetate salt in the form of TPTI **243** in 83% yield. TFA was chosen as the acidic reagent instead of HCl because trifluoroacetate salts of organic compounds should display better solubility in organic solvents in comparison to their respective chloride salts as was previously the case for ammonium cage **XVIIa/XXVa** (see Scheme 28, Chapter 3.1.4). The MAYOR group showed that direct formation of NDI cyclophanes from the corresponding diamines and NDA (**179**) was possible in very small yields (2-3%) by refluxing the substrates in *i*-PrOH for three days.[293] They also showed that the stepwise approach over ammonium trifluoroacetate salts gave target cyclophanes in 40% yield under otherwise identical reaction conditions which is why TPTI **243** was pursued directly. With the successful preparation of TPTI **243** the synthesis of TPTI cyclophane **244** was envisioned as the next step (Scheme 52). TPTI **243** (1.0 eq.) was combined with TPTA (**220**, 1.0 eq.) in *i*-PrOH. Triethylamine (40 eq.) was added to deprotonate the ammonium groups of the substrate and the mixure was refluxed for three days under high dilution conditions (c(**243**) = 0.40 mM) to prevent polymerization and promote ring-closing reactions instead (Table 19, Entry 1). Despite these measures, the target cyclophane **244** was not obtained. Instead, a rather complex set of signals was observed suggesting the formation of different open systems. Some broad resonances did hint at oligomeric side-products as well. Another reaction was run simultanously introducing MeOH to the reaction as a co-solvent, but this did not change the outcome to the better and instead a more complex mixture was obtained (Table 19, Entry 2). MeOH is certainly a better nucleophile than *i*-PrOH and might have attacked some of the anhydrides in TPTA (**220**) or might have interfered with the reaction by attacking the imides of TPTI **243**. Next, DMF was tested as it was usually the solvent of choice for imide condensation reactions (Table 19, Entries 3-6), but it did not furnish the desired cyclophane **244** either. After 3 h at 150 °C, 96 h at 150 °C or even 30 min at 150 °C using microwave irradiation only decomposition of the material was observed.

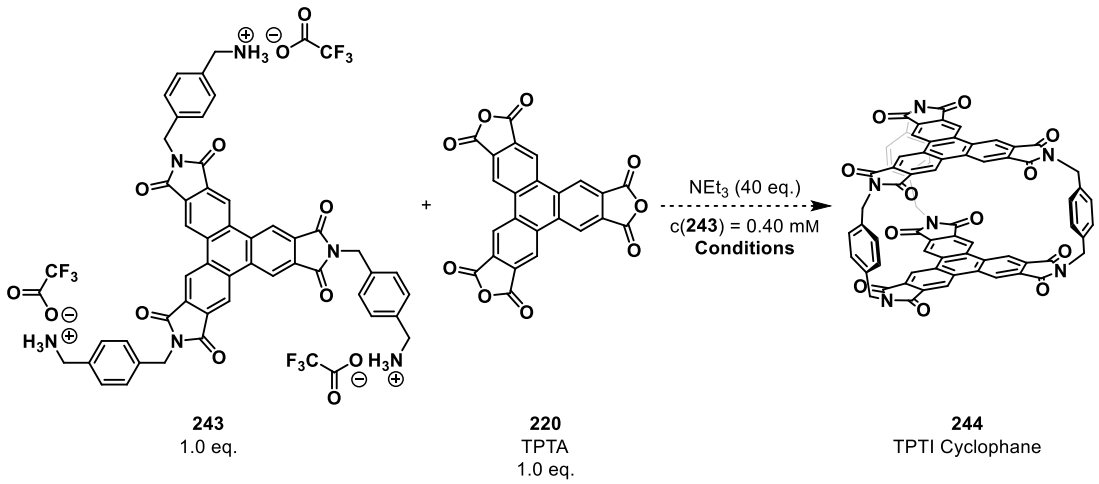

Scheme 52: General conditions used for the ring-closing reaction between TPTI **243** and TPTA (**220**).

Table 19: Detailed conditions tested for the reaction shown in scheme 52 towards cyclophane **244**.

Entry	Solvent	T [°C]	t [h]	Observation
1	*i*-PrOH	90 (reflux)	72	Oligomeric and open side-products
2	*i*-PrOH/MeOH = 8:2	90 (reflux)	72	Complex mixture
3	DMF	150	3	Decomposition
4	DMF	150	96	Decomposition
5*	DMF	150	0.5	Decomposition

*Heat source: microwave irradiation.

Since this was more of a sideproject, the reactions tested were run simultanously with the reactions shown in chapter 3.2.4 towards coordination cages and were not investigated in much more detail. Having failed in the construction of a novel coordination cage based on TPTI scaffolds that should enable anion-π interactions and meet the requirements concerning water/base stability and size, as well as novel tweezers or cyclophanes, a less ambitious path was pursued.

3.2.6 Synthesis of Iminopyridine-Based $Zn_4L_4(NTf_2)_8$ Tetrahedron Zn-XLIII

Face-capped **$Zn_4L_4(SO_4)_4$** cage **VIII** was shown to be stable in D_2O at room temperature for months and only showed decomposition above 80 °C (Scheme 53a).[202] The cage was easily prepared in three steps and is based on trialdehyde ligand **155**.[202,294,295] No guest uptake studies with this water-soluble cage have been reported so far. However, its acetonitrile-soluble derivative, featuring triflimide counter anions, has been shown to bind small anions like ReO_4^-, PF_6^- or SbF_6^- exclusively while no binding of neutral organic molecules was observed.[220] Even though the ligand does not provide a panel for anion-π interactions, anions and anionic intermediates should still experience significant stabilization through ion-ion interactions since the Zn^{II} metal ions at the vertices of the cage give it a charge of +8 in total.

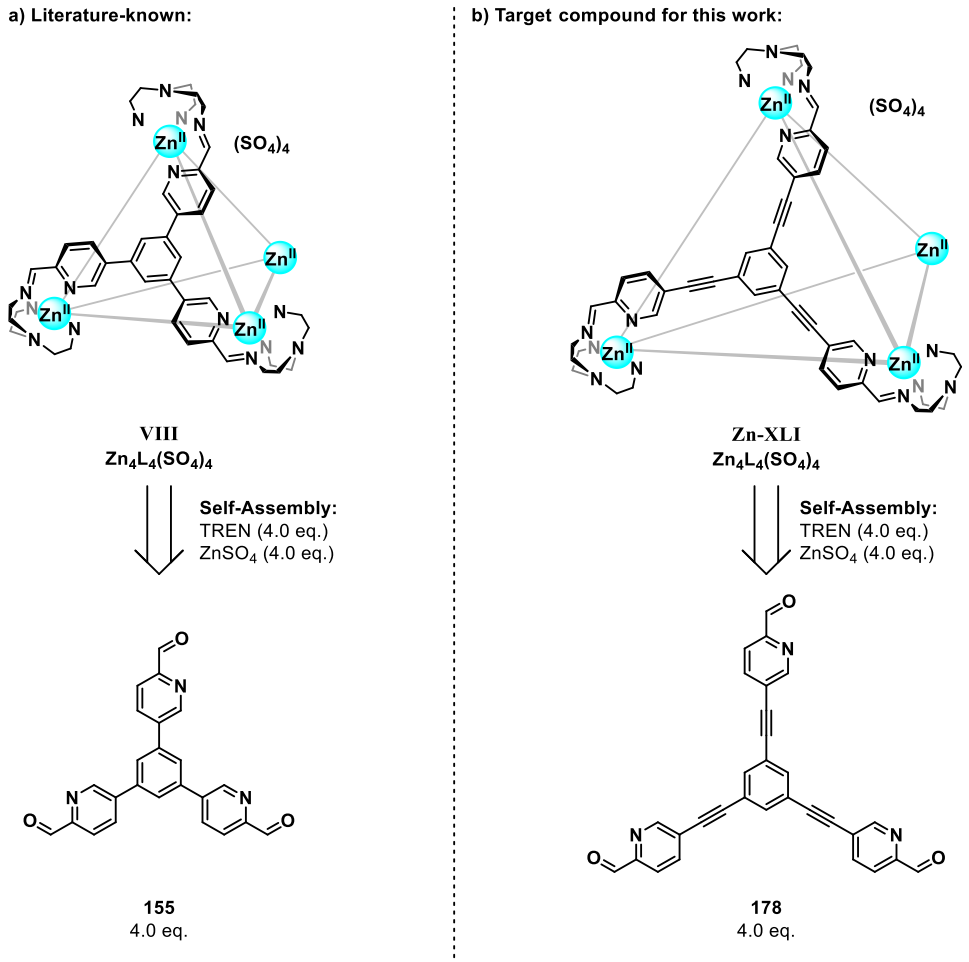

Scheme 53: a) Literature-known **$Zn_4L_4(SO_4)_4$** tetrahedron **VIII** was synthesized *via* self-assembly from ligand **155**. b) The alkyne extended derivative **$Zn_4L_4(SO_4)_4$** tetrahedron **Zn-XLI** should be accessible through ligand **178**.

This work aimed at the construction of acetylene extended **$Zn_4L_4(SO_4)_4$** tetrahedron **Zn-XLI** which should be able to bind larger organic molecules due to its bigger cavity (Scheme 53b). Like its predecessor, it should also display stability towards water and possibly even bases in aqueous solution due to the stabilizing chelating effect of the TREN caps. For this, novel trialdehyde ligand **178** had to be prepared. Its core trialkyne benzene unit was synthesized from 1,3,5-tribromobenzene (**245**) *via* SONOGASHIRA coupling with TMS-acetylene to deliver the

protected trialkyne **246** in 98% yield (Scheme 54).[296] Deprotection under basic conditions furnished trialkyne **247** in 94% yield without problems.[297]

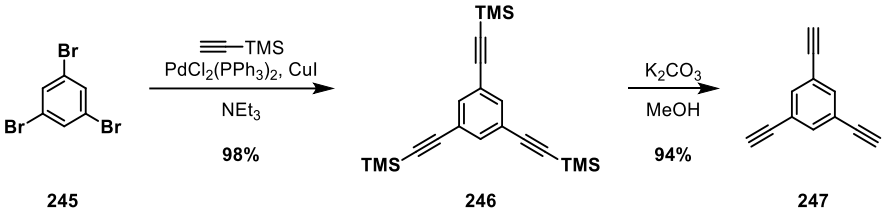

Scheme 54: Literature-known synthesis of trialkyne **247** *via* SONOGASHIRA coupling of 1,3,5-tribromobenzene (**245**) with TMS-acetylene and follow-up cleavage of the TMS groups under basic conditions in MeOH.

From here, a second literature known SONOGASHIRA coupling towards triester **249** (Scheme 55) was carried out in 70% yield[298] and either direct reduction to the target trialdehyde ligand **178** or reduction to the triol **250** (Scheme 55) followed by oxidation to the trialdehyde **178** were envisioned first. A few different reduction protocols were applied which are shown in table 20. The table gives information about at which temperature the reducing agents were added to the reaction mixture containing triester **249** and about the temperature profile applied after the addition. Treatment of triester **249** with an excess of $NaBH_4$ in refluxing EtOH for 2 h or MeOH at room temperature overnight (Table 20, Entries 1-2) led to decomposition of the material.

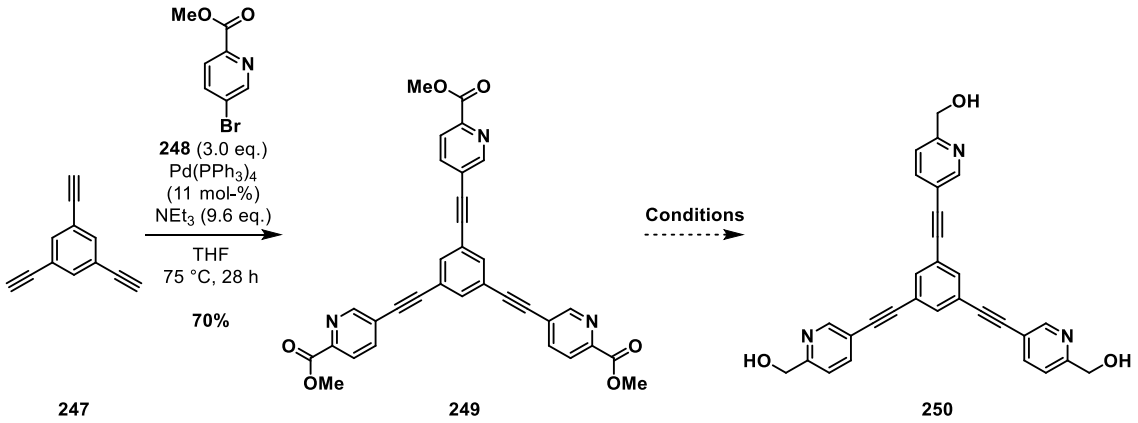

Scheme 55: Literature-known synthesis of triester **249**. The reaction conditions for the reduction towards triol **250** are listed in table 20.

Table 20: Conditions tested for the reduction of triester **249**.

Entry	Reagent (eq.)	Solvent	Addition Temperature	Temperature Profile	Observation
1	$NaBH_4$ (9.0)	EtOH	0 °C	90 °C, 2 h	Decomposition
2	$NaBH_4$ (13)	MeOH	0 °C	23 °C, 20 h	Decomposition
3	$BH_3 \cdot THF$ (12)	THF	0 °C	50 °C, 18 h	Very Low Conversion
4	$LiAlH_4$ (2.0)	THF	0 °C	0 °C, 0.5 h; 23 °C, 0.5 h	Complex Mixture
5	$LiAlH_4$ (3.5)	THF	–78 °C	0 °C, 0.5 h; 23 °C, 0.5 h	Complex Mixture
6	DIBAL-H (11)	Toluene	–78 °C	–78 °C, 2 h; 0 °C, 2 h	Aldehyde Species!*
7	DIBAL-H (14)	Toluene	–78 °C	–78 °C, 4 h	Aldehyde Species!*

*Accompanied by many side-products. Low overall crude yield.

The use of $BH_3 \bullet THF$ gave very low conversion of the starting material at 50 °C (Table 20, Entry 3) and reactions with $LiAlH_4$ (Table 20, Entries 4-5) produced complex mixtures. Using diisobutylaluminium hydride (DIBAL-H)

in toluene at −78 °C gave rise to an interesting product mixture (Table 20, Entries 6-7). An aldehyde species was observed but the crude product yield (44%) was quite low already after tedious aqueous workup and the purity was lackluster. Further purification attempts were not conducted, and no further experiments were performed, such as attempting the reduction with $NaBH_4$ at 0 °C or −78 °C, because a different, more efficient idea was tested (Scheme 56).

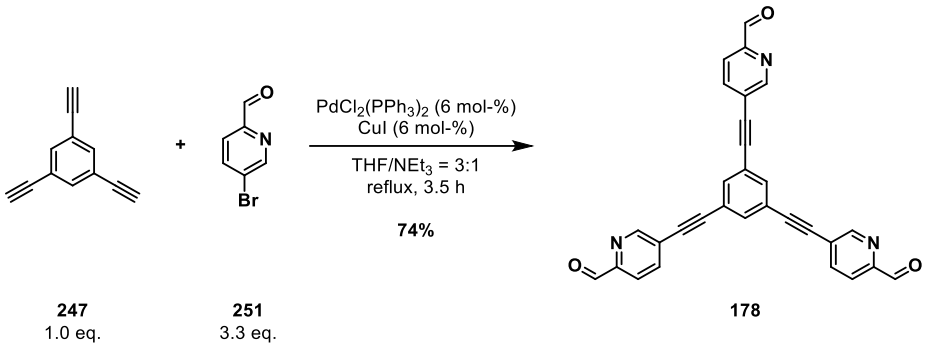

Scheme 56: Synthesis of trialdehyde **178** *via* direct SONOGASHIRA coupling between trialkyne **247** and 5-bromopicolinaldeyhde (**251**).

Trialkyne **247** (1.0 eq.) was subjected to direct SONOGASHIRA coupling with commercially available 5-bromopicolinaldehyde (**251**, 3.3 eq.) instead of its methylester derivative **248**. The reaction was not literature-known but a first attempt already showed significant product formation in the crude ^{1}H-NMR spectrum underlining the strength of this named reaction to also tolerate aldehyde groups and eliminating the need for reduction and oxidation steps. The initial reaction conditions worked quite well for this transformation with catalytic amounts of $PdCl_2(PPh_3)_2$ and copper(I) iodide in anhydrous and degassed THF/NEt_3 = 3:1. Purification of the crude product *via* column chromatography on silica gel with solvent mixtures which seemed promising on the TLC ($CHCl_3$/Toluene = 1:1 + 1% NEt_3 and $CHCl_3$ + 1% MeOH) were successful but the yields were low due to product tailing and mixed fractions being inevitable. However, the final purification procedure did not require any column: the solvent of the reaction mixture was removed, and the crude material was resuspended in acetone and heated to the boiling point. The poor solubility of the target product in refluxing acetone allowed for a simple and effective purification *via* filtration to give trialdehyde **178** in 74% yield and sufficient purity.

The self-assembly between ligand **178** (4.0 eq.), TREN (**128a**, 4.0 eq.) and metal sulfate salts (4.0 eq.) for the formation of sizable tetrahedral and face-capped cages of the water-soluble type $\mathbf{M_4L_4(SO_4)_4}$ was investigated next (Scheme 57, Table 21). Starting with the heptahydrate of $ZnSO_4$, the reactions were run using conventional heating with an oilbath at 50 °C, 70 °C and 85 °C at different concentrations of ligand **178** in MeCN/H_2O = 1:1 (Table 21, Entries 1-6). The reaction mixtures obtained were brown suspensions in all cases and the first purification step for these self-assembly reactions are filtrations over a celite pad to separate insoluble side-products from dissolved cages. In these experiments, no cage was obtained. In fact, the ^{1}H-NMR spectra showed no peaks in the aromatic region at all while some amount of TREN (**128a**) was observed. The brown solid material formed during the reaction could either be polymeric material, simple starting material or a combination of both, but it was not analysed because sulfate cages of this type have reportedly been soluble in water and should have been found in the filtrate. Next, the reactions were run at elevated temperatures (120-180 °C) using microwave irradiation for 1 h each under otherwise identical reaction conditions (Table 21, Entries 7-9 and 14-15).

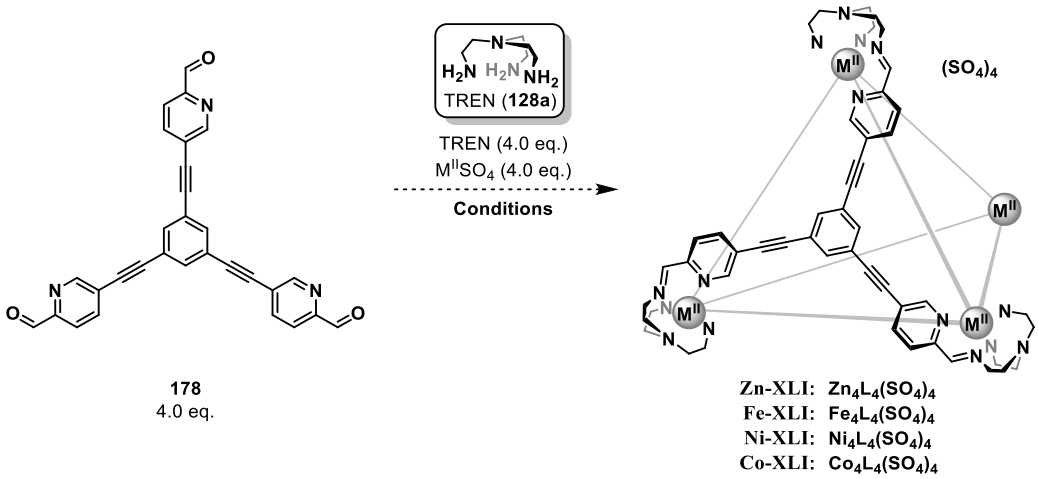

Scheme 57: General reaction scheme for table 21 towards **M$_4$L$_4$(SO$_4$)$_4$** cages from ligand **178** (**M** = **Zn**, **Fe**, **Ni**, **Co**).

Table 21: Reaction conditions tested towards **M$_4$L$_4$(SO$_4$)$_4$** cages from ligand **178** (Scheme 57, **M** = **Zn**, **Fe**, **Ni**, **Co**).

Entry	M^{II}SO$_4$ · x H$_2$O	Solvent	T [°C]	t [h]	c(178) [mM]	Observation
1	Zn^{II}SO$_4$ · 7 H$_2$O	MeCN/H$_2$O = 1:1	50	20	2.5	Insoluble Brown Solid
2	Zn^{II}SO$_4$ · 7 H$_2$O	MeCN/H$_2$O = 1:1	70	20	2.5	Insoluble Brown Solid
3	Zn^{II}SO$_4$ · 7 H$_2$O	MeCN/H$_2$O = 1:1	85	20	2.5	Insoluble Brown Solid
4	Zn^{II}SO$_4$ · 7 H$_2$O	MeCN/H$_2$O = 1:1	50	20	10	Insoluble Brown Solid
5	Zn^{II}SO$_4$ · 7 H$_2$O	MeCN/H$_2$O = 1:1	70	20	10	Insoluble Brown Solid
6	Zn^{II}SO$_4$ · 7 H$_2$O	MeCN/H$_2$O = 1:1	85	20	10	Insoluble Brown Solid
7*	Zn^{II}SO$_4$ · 7 H$_2$O	MeCN/H$_2$O = 1:1	120	1	10	Traces of Product
8*	Zn^{II}SO$_4$ · 7 H$_2$O	MeCN/H$_2$O = 1:1	130	1	10	Traces of Product
9*	Zn^{II}SO$_4$ · 7 H$_2$O	MeCN/H$_2$O = 1:1	140	1	10	Traces of Product
10*	Zn^{II}SO$_4$ · 7 H$_2$O	MeCN/H$_2$O = 3:1	140	1	10	Insoluble Brown Solid
11*	Zn^{II}SO$_4$ · 7 H$_2$O	H$_2$O	140	1	10	Insoluble Brown Solid
12**	Zn^{II}SO$_4$ · 7 H$_2$O	MeCN/H$_2$O = 1:1	140	1	10	Traces of Product
13**	Zn^{II}SO$_4$ · 7 H$_2$O	MeCN/H$_2$O = 1:1	140	24	10	Insoluble Brown Solid
14*	Zn^{II}SO$_4$ · 7 H$_2$O	MeCN/H$_2$O = 1:1	160	1	10	Insoluble Brown Solid
15*	Zn^{II}SO$_4$ · 7 H$_2$O	MeCN/H$_2$O = 1:1	180	1	10	Decomposition
16	Fe^{II}SO$_4$ · 7 H$_2$O	MeCN/H$_2$O = 1:1	60	18	10	Insoluble Brown Solid
17	Fe^{II}SO$_4$ · 7 H$_2$O	MeCN/H$_2$O = 1:1	90	18	10	Insoluble Brown Solid
18	Fe^{II}SO$_4$ · 7 H$_2$O	H$_2$O	90	18	10	Insoluble Brown Solid
19	Ni^{II}SO$_4$	MeCN/H$_2$O = 1:1	25	18	10	Insoluble Beige Solid
20	Ni^{II}SO$_4$	MeCN/H$_2$O = 1:1	60	18	10	Insoluble Beige Solid
21	Ni^{II}SO$_4$	MeCN/H$_2$O = 1:1	90	18	10	Insoluble Beige Solid
22	Co^{II}SO$_4$	MeCN/H$_2$O = 1:1	25	18	10	Decomposition
23	Co^{II}SO$_4$	MeCN/H$_2$O = 1:1	60	18	10	Decomposition
24	Co^{II}SO$_4$	MeCN/H$_2$O = 1:1	90	18	10	Decomposition

*Heat source: microwave irradiation. **Pressure tube used with an oil bath as heating source.

Traces of potential cage product were observed in the filtrate this time, but the crude yields remained very low (< 5%) as a major amount of brown solid material formed that was insoluble. At 180 °C an insoluble black solid

was observed in the reaction mixture instead and no traces of product were detected, suggesting the decomposition of the material at this temperature. Using MeCN/H_2O = 3:1 or just H_2O as the solvent of choice at 140 °C did not improve product formation (Tabel 21, Entries 10-11) and neither did the use of a pressure tube as the reaction vessel to enable investigations using an oilbath to compare the results to microwave irradiation (Table 21, Entries 12-13). Alternative metal sulfates were investigated such as $Fe^{II}SO_4$ as its heptahydrate (Table 21, Entries 16-18), $Ni^{II}SO_4$ (Table 21, Entries 19-21) and $Co^{II}SO_4$ (Table 21, Entries 22-24) at different reaction temperatures but the same issues with insoluble solids and no cage formation were observed.

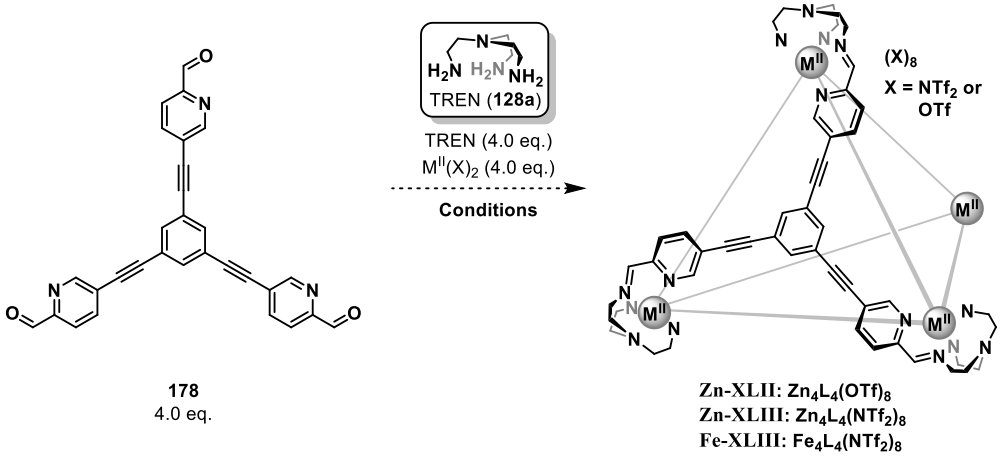

Scheme 58: General reaction scheme for table 22 towards triflimide and triflate based **M_4L_4** cages from ligand **178**.

Table 22: Reaction conditions tested towards triflimide or triflate based **M_4L_4** cages from ligand **178** (Scheme 58).

Entry	$M^{II}(X)_2$	Solvent	T [°C]	t [h]	c(178) [mM]	Observation
1	$Zn(OTf)_2$	MeCN	70	18	10	Complex Mixture
2	$Zn(OTf)_2$	MeCN/$CHCl_3$ = 1:1	70	18	10	Complex Mixture
3	$Zn(NTf_2)_2$	MeCN	70	18	10	Complex Mixture
4	**$Zn(NTf_2)_2$**	**MeCN/$CHCl_3$ = 1:1**	**70**	**18**	**10**	**Cage Zn-XLIII + Oligomers**
5	$Zn(NTf_2)_2$	MeCN/$CHCl_3$ = 1:1	70	18	3.3	Incomplete Reaction
6	$Zn(NTf_2)_2$	MeCN/$CHCl_3$ = 1:1	50	18	10	Incomplete Reaction
7*	**$Zn(NTf_2)_2$**	**MeCN/$CHCl_3$ = 1:1**	**90**	**18**	**10**	**Cage Zn-XLIII in 19% yield**
8*	**$Zn(NTf_2)_2$**	**MeCN/$CHCl_3$ = 1:1**	**110**	**18**	**10**	**Cage Zn-XLIII in 20% yield**
9*	$Zn(NTf_2)_2$	MeCN/$CHCl_3$ = 1:1	130	18	10	Cage **Zn-XLIII** + Oligomers
10	$Fe(NTf_2)_2$	MeCN/$CHCl_3$ = 1:1	60	18	10	Oligomers
11*	$Fe(NTf_2)_2$	MeCN/$CHCl_3$ = 1:1	90	18	10	Oligomers

*Pressure tube used with an oil bath as heating source.

Having failed to acquire a water-soluble sulfate cage, screening of metal precursors has been extended to $Zn(OTf)_2$ and $Zn(NTf_2)_2$ (Scheme 58, Table 22). Initial test reactions at 70 °C in either MeCN or MeCN/$CHCl_3$ = 1:1 (Table 22, Entries 1-4) mostly gave complex mixtures except for the reaction with $Zn(NTf_2)_2$ in MeCN/$CHCl_3$ = 1:1 for which all peaks corresponding to a potential **$Zn_4L_4(NTf_2)_8$** cage **Zn-XLIII** were found in the crude ^{1}H-NMR accompanied by broad resonances, hinting at oligomeric side-products (Table 22, Entry 4). The selectivity for cage formation over other minor side-products seemed a bit better at 90 °C (Table 22, Entry 7). The reaction mixture appeared as a yellow solution with just a minor amount of turbid material and the crude yield (90%) obtained from the filtrate for this reaction was quite high. The crude product was subjected to size-exclusion chromatography to

remove most of the oligomeric material, followed by recrystallization *via* slow diffusion of Et_2O into an acetonitrile solution of the cage. Cage crystals and a thin film formed, presumably consisting of residual polymeric side-products. The cage crystals were separated from the latter *via* trituration with acetonitrile as the thin film did not re-dissolve easily. **$Zn_4L_4(NTf_2)_8$** tetrahedron **Zn-XLIII** was obtained in 19% yield this way at 90 °C over 18 h. This temperature was not sufficient anymore upon scale-up, presumably due to heat transfer issues, and 110 °C was necessary for the reaction to complete (Table 22, Entry 8). The cage was obtained in 20% yield on higher scale as well. Further temperature increase to 130 °C did not seem to improve product formation (Table 22, Entry 9) and the reaction was incomplete after 18 h at 50 °C (Table 22, Entry 6) or at lower concentration (Table 22, Entry 5). Test reactions with $Fe(NTf_2)_2$ at 60 °C and 90 °C (Table 22, Entries 10-11) only showed oligomeric side-products and no further conditions were explored since **$Zn_4L_4(NTf_2)_8$** cage **Zn-XLIII** has already been obtained in good purity. The finalized reaction conditions are shown in scheme 59.

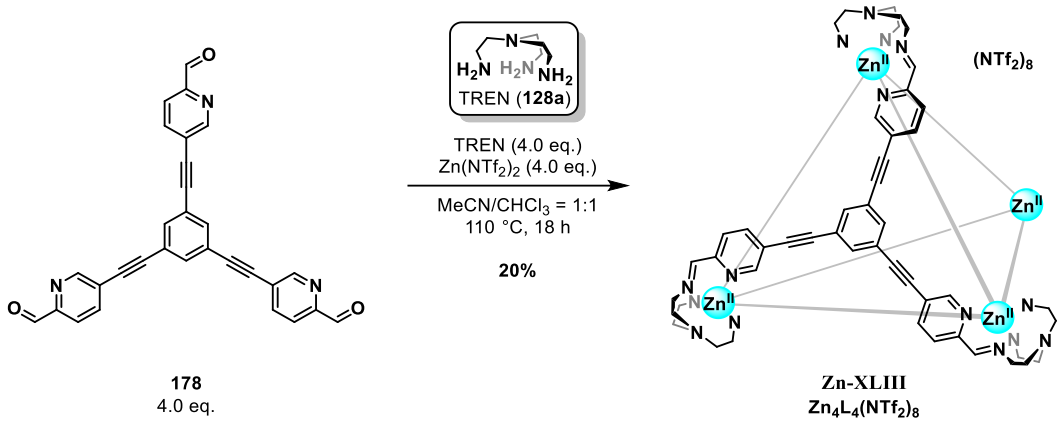

Scheme 59: Optimized reaction conditons for the self-assembly of **$Zn_4L_4(NTf_2)_8$** tetrahedron **Zn-XLIII** from ligand **178**.

The **$Zn_4L_4(NTf_2)_8$** cage **Zn-XLIII** was obtained as a single diastereomer as indicated by the single set of resonances expected for the formation of the most symmetric tetrahedron with *T* point symmetry (1:1 mixture between the enantiomers with ΛΛΛΛ- and ΔΔΔΔ-configuration for the vertices). The cage displayed good solubility in polar aprotic solvents such as acetone, $MeNO_2$ and MeCN. It did not dissolve in alkanes, alcohols, chlorinated solvents and toluene or benzene. With triflimides as counter anions it was not soluble in water compared to its predecessor **$Zn_4L_4(SO_4)_4$** cage **VIII** (Scheme 53a). A final attempt to render **$Zn_4L_4(NTf_2)_8$** cage **Zn-XLIII** soluble in water was an anion exchange reaction in which an excess of tetrabutylammonium sulfate salt (50% in H_2O) was added to **Zn-XLIII** in acetonitrile to obtain its derivative sulfate cage **Zn-XLI** (Scheme 60) *via* precipitation. This methodology was reported by NITSCHKE and coworkers and only worked for some cage compounds of this type.[202] In this case, the **Zn_4L_4** sulfate cage **Zn-XLI** seemed to form immediately but decomposed quickly over time as indicated by an increase of TREN (**128a**) peaks in the ^{1}H-NMRs in D_2O immediately after the reaction and after 18 h (Figure 37). The high binding cooperativity of the subcomponents seemed not to ensure stability in water as a water-soluble complex. This may have been caused by the poor water solubility of ligand **178**, which may have reached saturation too quickly once it formed reversibly within the imine equilibrium. As it precipitated, the ligand got gradually removed from the equilibrium, shifting it entirely to the side of the subcomponents. Similar observations have been reported before.[202]

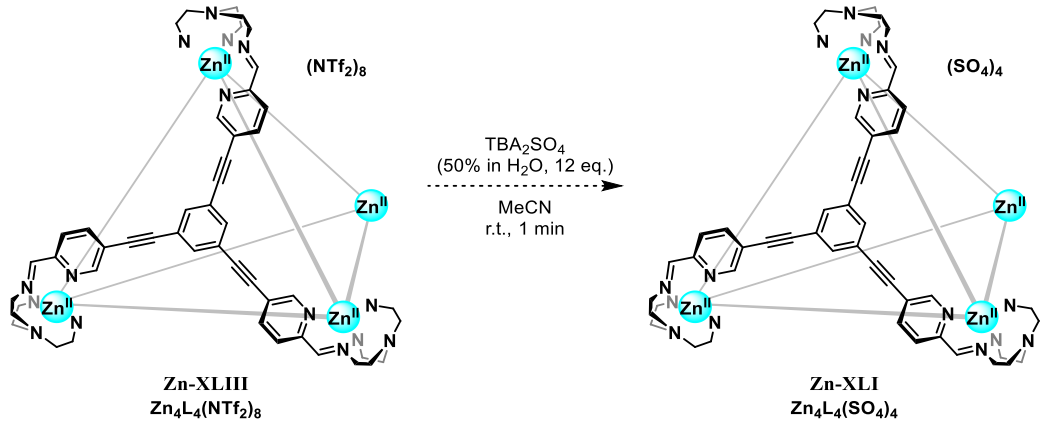

Scheme 60: Anion exchange reaction from $Zn_4L_4(NTf_2)_8$ cage **Zn-XLIII** to $Zn_4L_4(SO_4)_4$ cage **Zn-XLI**.

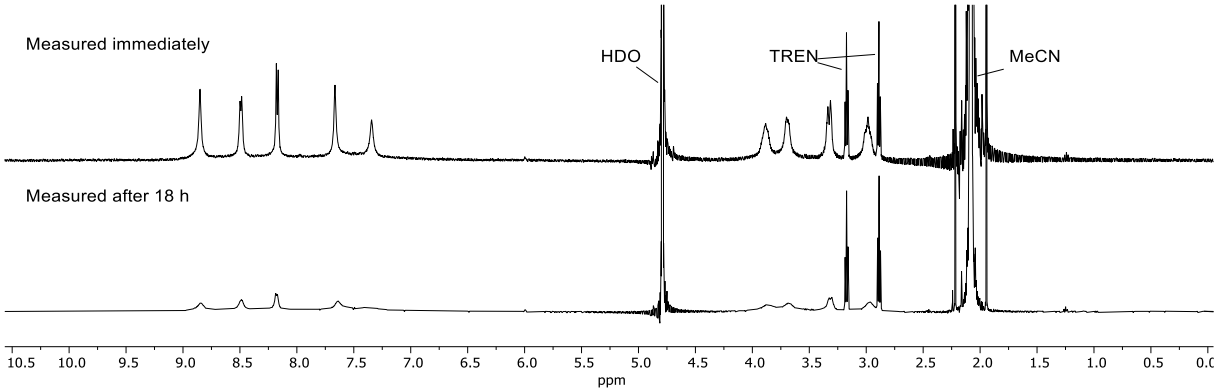

Figure 37: $Zn_4L_4(SO_4)_4$ cage **Zn-XLI** decomposes quickly in D_2O at room temperature.

3.2.7 Water and Base Stability of $Zn_4L_4(NTf_2)_8$ Cage Zn-XLIII

With **$Zn_4L_4(NTf_2)_8$** cage **Zn-XLIII** in hand, its properties were explored next. First, its stability towards water was investigated. For this, an NMR tube was charged with 500 µL of a stock solution of **Zn_4L_4** cage **Zn-XLIII** in MeCN-d_3 at a concentration of c = 1.00 mM. A ^{1}H-NMR spectrum was measured before and after each addition of distilled H_2O (c = 55.5 M). After each addition the NMR tube was shaken manually. The resulting spectra are shown in figure 38.

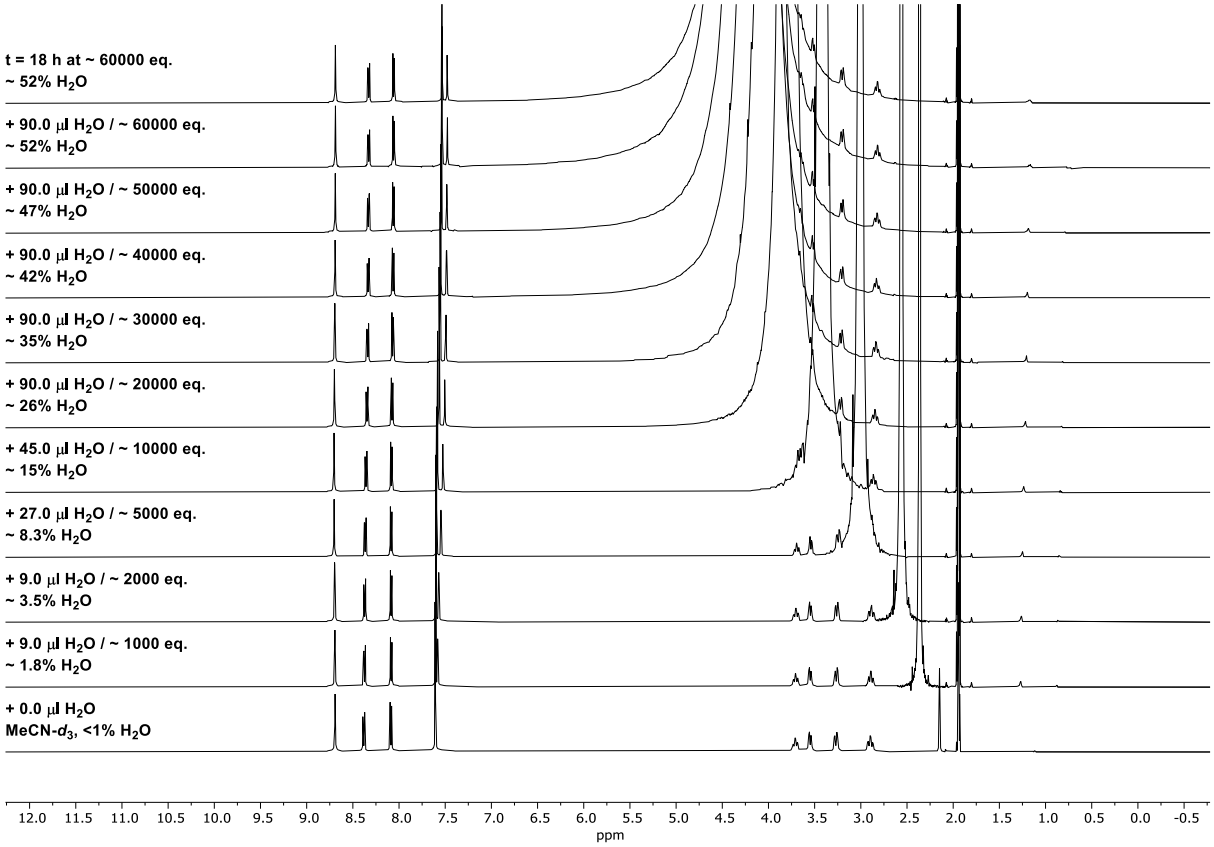

Figure 38: Titration of water to a solution of **Zn_4L_4** cage **Zn-XLIII** (c = 1.00 mM) in MeCN-d_3 at 298 K.

The spectra showed that the cage remained stable even at 52% water content after 18 h at room remperature. Further experiments revealed that the **Zn_4L_4** cage **Zn-XLIII** (c = 1.00 mM) also remained stable in MeCN-d_3/H_2O = 6:4 at elevated temperatures of up to 80 °C for 24 h (Figure 39). Face-capped **Zn_4L_4** tetrahedron **Zn-XLIII** already proved to be much more stable than edge-linked **Fe_4L_6** tetrahedron **XXIX** (see chapter 3.2.1), presumably due to the higher binding cooperativity of the subcomponents and the stabilizing chelating effect of TREN (**128a**). The stability increase was further underlined by the following experiments testing the cages resistance towards basic conditions.

Next, the effect of $KHCO_3$ as a base was explored. For this experiment, an NMR tube was charged with 500 µL of a stock solution of **Zn_4L_4** cage **Zn-XLIII** in MeCN-d_3:H_2O = 6:4 at a concentration of c = 0.125 mM. This solvent mixture was necessary to ensure solubility of the base. And again, a ^{1}H-NMR spectrum was measured before and after each addition of a $KHCO_3$ stock solution in MeCN-d_3:H_2O = 6:4 at a concentration of c = 62.5 mM corresponding to 1.0 eq./µL titrated. After each addition the NMR tube was shaken manually. The resulting spectra are shown in figure 40. The cage remained stable across the whole titration experiment ranging from 0-100 eq. of $KHCO_3$ added in total.

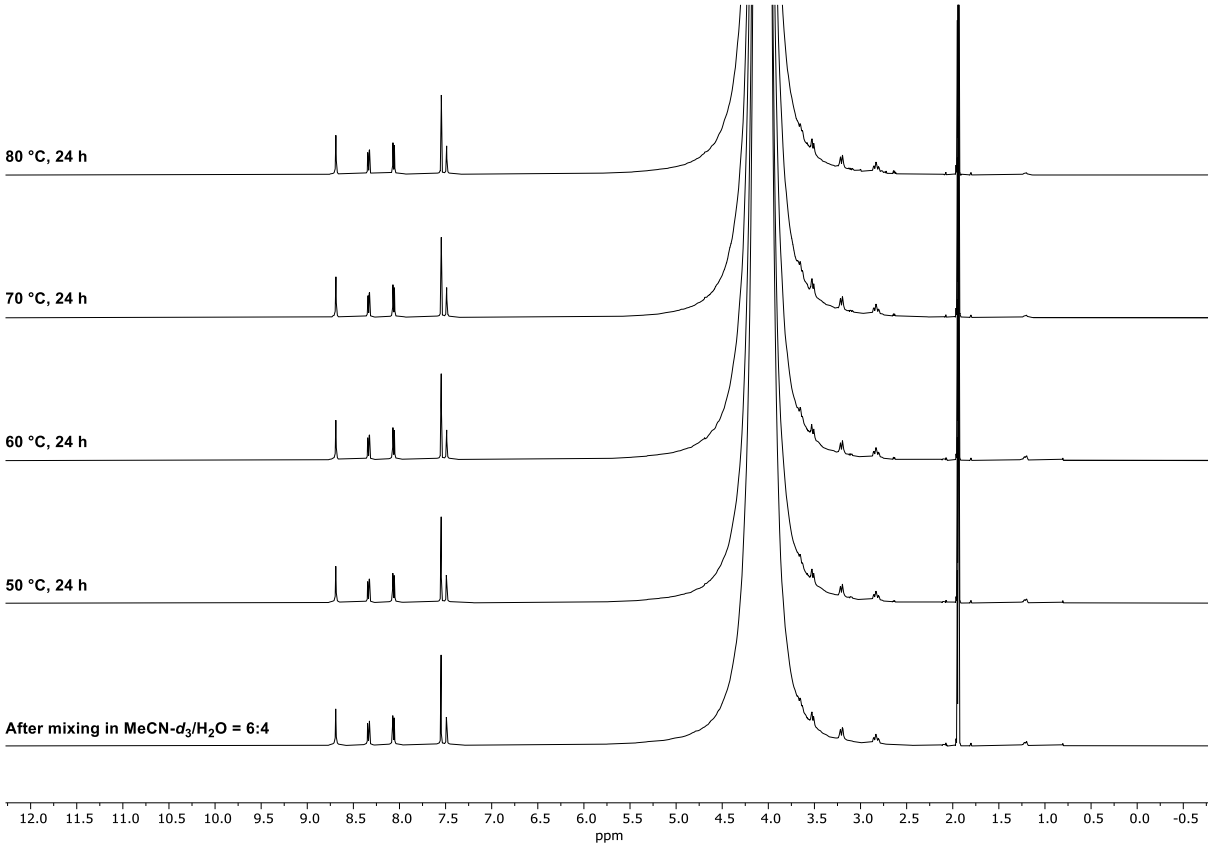

Figure 39: Water stability of **Zn_4L_4** cage **Zn-XLIII** (c = 1.00 mM) in MeCN-d_3/H_2O = 6:4 at elevated temperatures.

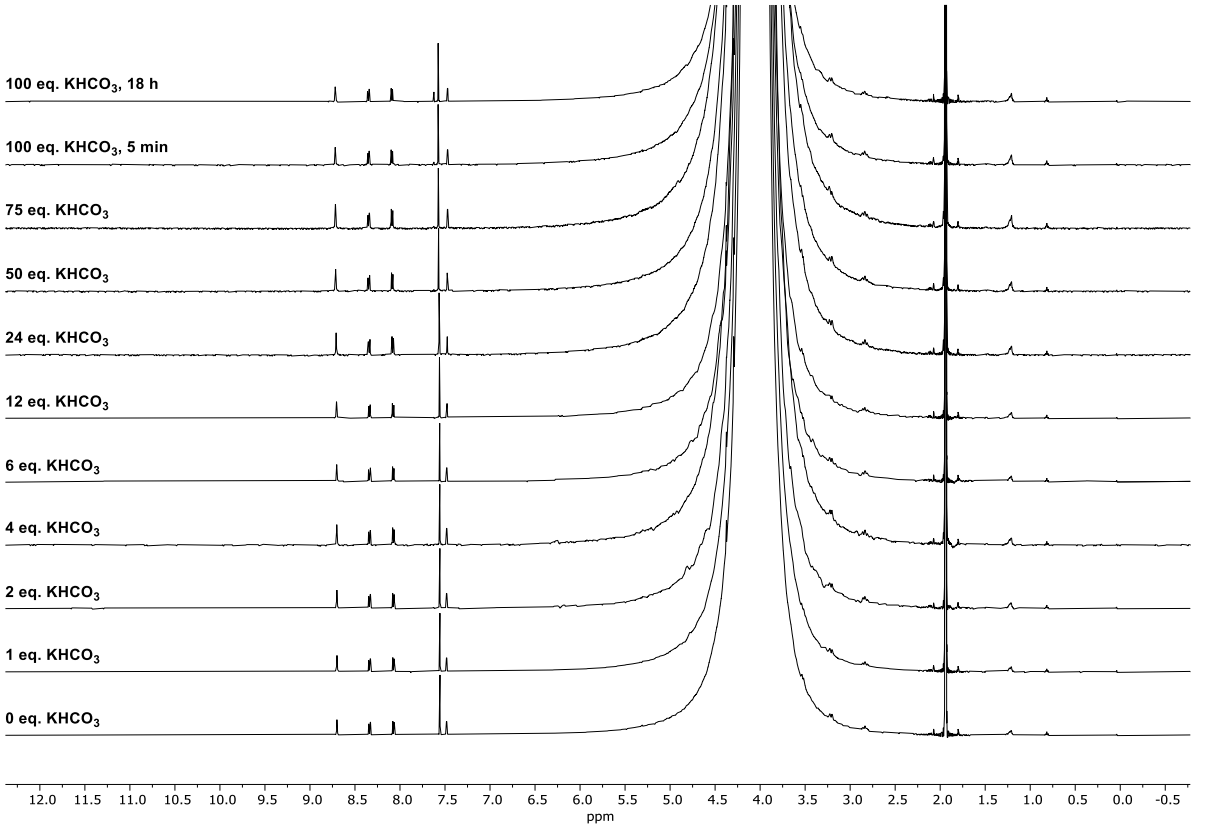

Figure 40: Titration of $KHCO_3$ to a solution of **Zn_4L_4** cage **Zn-XLIII** (c = 0.125 mM) in MeCN-d_3/H_2O = 6:4 at 298 K.

The new signal observed after 18 h with 100 eq. of $KHCO_3$ at 7.62 ppm (singlet) likely stems from 2,2,2-trideuterioacetamide. This signal was also observed in the experiment without cage under otherwise identical conditions.

Additionally, base stability investigations at elevated temperatures were conducted with cage **Zn-XLIII** to test its limitations, including 30 eq. of $KHCO_3$, NEt_3 and *i*-Pr_2NEt. For each base, the following procedure was applied:

Two NMR tubes were each charged with 300 µL of a stock solution of Zn_4L_4 cage **Zn-XLIII** at a concentration of c = 2.00 mM and 300 µL of a base stock solution at a concentration of c = 60.0 mM. The solvent used was MeCN-d_3:H_2O = 6:4. The final mixture (600 µL) was shaken manually and allowed to equilibrate, reaching a concentration of c = 1.00 mM for Zn_4L_4 cage **Zn-XLIII** and a concentration of c = 30.0 mM for the corresponding base. (1.00 eq. of cage and 30.0 eq. of base.) A ^{1}H-NMR spectrum was measured right after mixing. One NMR sample for each base was allowed to equilibrate at 50 °C for 24 h and then at 60 °C for 24 h in a heating block. For the second NMR experiment of each base, the sample was allowed to equilibrate at 70 °C for 24 h and then at 80 °C for 24 h in a heating block. A ^{1}H-NMR spectrum was measured after each equilibration time. The resulting spectra are shown below in figures 41-43. Zn_4L_4 cage **Zn-XLIII** remained stable at temperatures of up to 60 °C and started decomposing at 70 °C in every single case. Decomposition of the material was indicated by precipitation of a brown solid within the NMR tube and intensity decrease of cage related peaks in the ^{1}H-NMR spectra. The decomposition seemed to occur a bit faster at 70 °C when $KHCO_3$ was used (Figure 41) compared to NEt_3 and *i*-Pr_2NEt (Figures 42 and 43, respectively) but each of these options could potentially be used for catalytic experiments under basic conditions of anionic reactions using Zn_4L_4 cage **Zn-XLIII**.

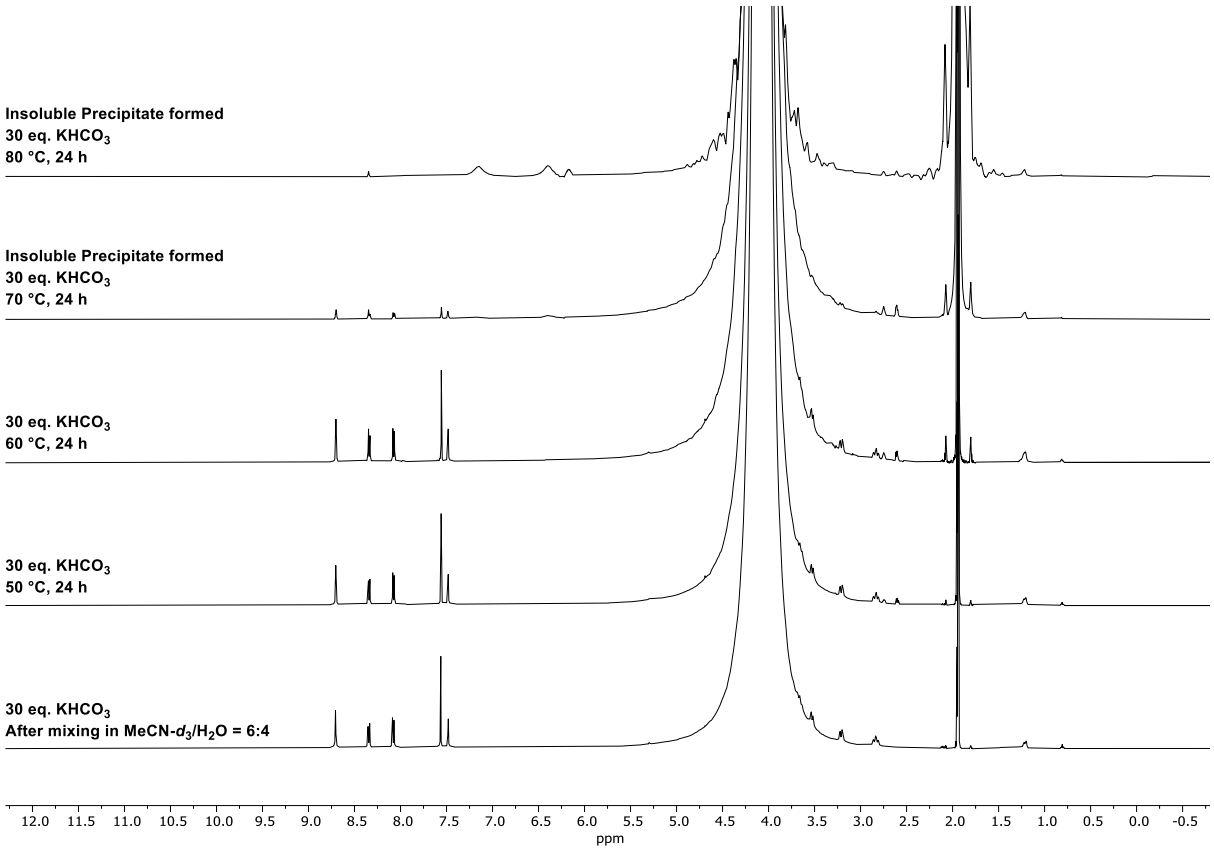

Figure 41: Stability limitations for Zn_4L_4 cage **Zn-XLIII** (c = 1.00 mM) in MeCN-d_3/H_2O = 6:4 with 30 eq. of $KHCO_3$.

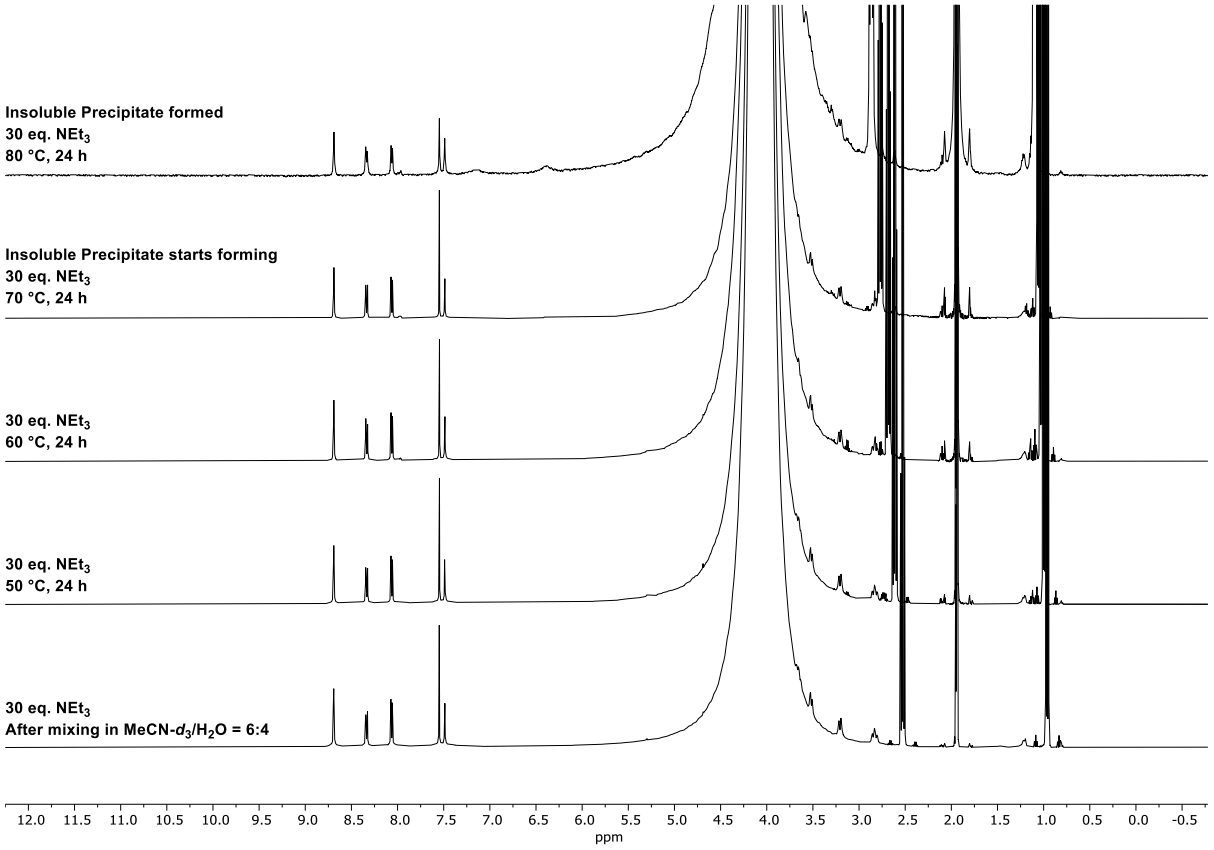

Figure 42: Stability limitations for **Zn_4L_4** cage **Zn-XLIII** (c = 1.00 mM) in MeCN-d_3/H_2O = 6:4 with 30 eq. of NEt_3.

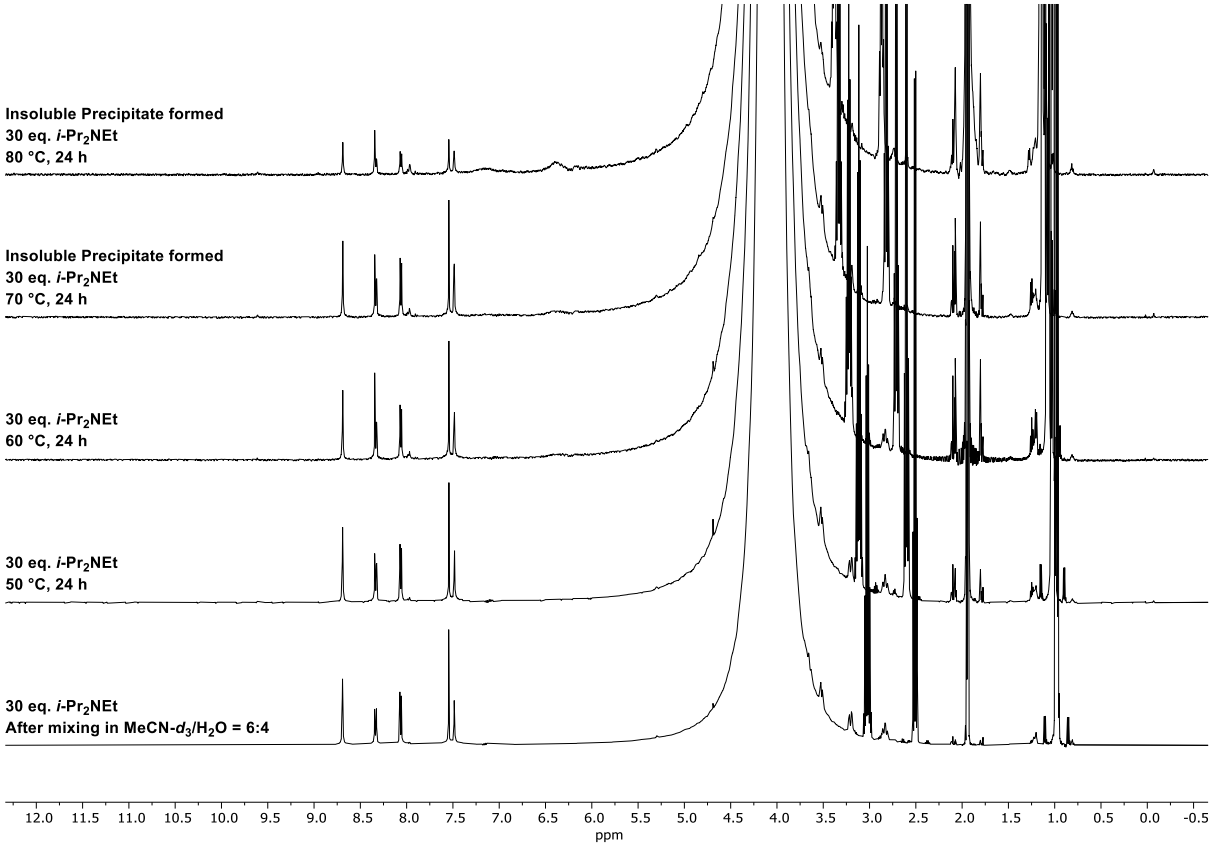

Figure 43: Stability limitations for **Zn_4L_4** cage **Zn-XLIII** (c = 1.00 mM) in MeCN-d_3/H_2O = 6:4 with 30 eq. of *i*-$PrNEt_2$.

3.2.8 Guest-Uptake Experiments with $Zn_4L_4(NTf_2)_8$ Cage Zn-XLIII

Subsequently, the binding properties of **$Zn_4L_4(NTf_2)_8$** cage **Zn-XLIII** were explored. This was especially of interest, as the original cage (**$Zn_4L_4(NTf_2)_8$** cage **XVI**, Scheme 16a, Chapter 1.3.2c) was only able to bind small anions in acetonitrile.[220] Ideally, triflimide cage **Zn-XLIII** will bind larger organic molecules for potential applications in the catalysis of anionic reactions. Guest binding studies were performed in MeCN-d_3/H_2O = 9:1 to ensure good solubility of the cage as well as of the ionic guests investigated. H_2O was used instead of D_2O because of shimming problems during the ^{1}H-NMR measurements. Due to the limited solubility of cage **Zn-XLIII**, guest uptake studies in purely aqueous solutions were not possible as it started precipitating out of acetonitrile at around 55% water content. With that clarified, a series of neutral (Scheme 61a) and anionic guests (Scheme 61b) was explored. No significant shifts of the cage or guest signals was observed for the neutral guests. However, all ionic guests displayed some interactions in the fast-binding regime on the ^{1}H chemical shift timescale. A series of titrations was performed to estimate the binding constants, which ranged from 40 to 850 M^{-1}. All experimental details can be found in the experimental section (chapter 5.3.1 and chapter 5.3.5).

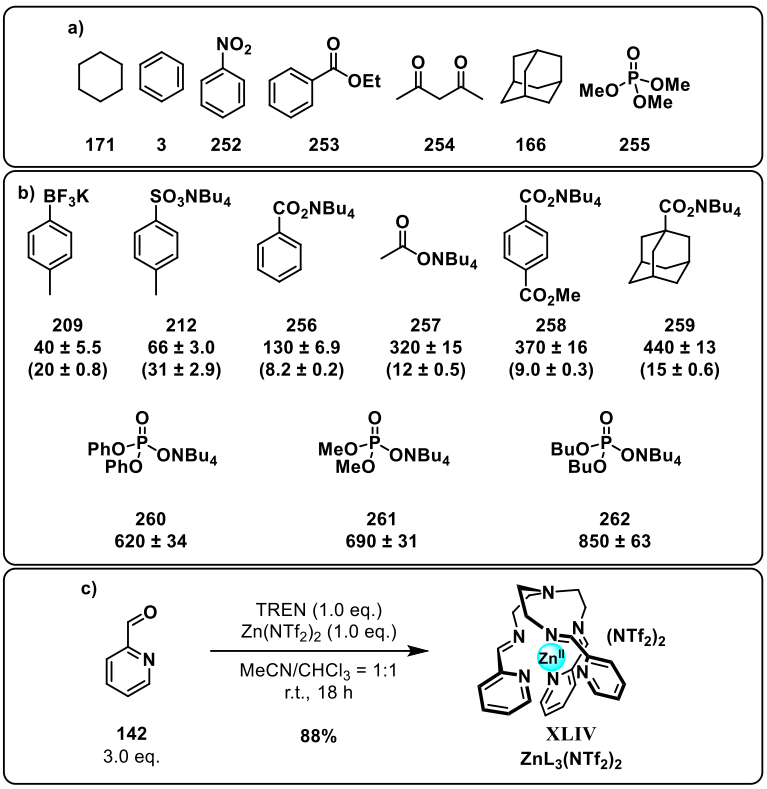

Scheme 61: Guest screening for cage **Zn-XLIII**. a) Neutral guests that showed no binding. b) Organic salts for which fast exchange was observed for the anionic component as determined by NMR spectroscopy in MeCN-d_3/H_2O = 9:1. Binding constants are shown for cage **Zn-XLIII**. For guests **209**, **212**, and **256-259** the binding constants of the **$ZnL_3(NTf_2)_2$** complex **XLIV** are shown in parentheses for comparison. c) Synthesis of the mononuclear **$ZnL_3(NTf_2)_2$** complex **XLIV**.

In order to elucidate if indeed a guest uptake into the cage was taking place, or if this binding was rather an outside interaction with the charged vertices, control titrations were performed with the simple cationic model complex **XLIV** (Scheme 61c) which was synthesized from picolinaldehyde (**142**), TREN (**128a**) and $Zn(NTf_2)_2$ in MeCN/$CHCl_3$ = 1:1 at room temperature. It represents the charged vertex of cage **Zn-XLIII**, and thus was used in four-fold higher concentration as cage **Zn-XLIII** for the guest titration experiments. In general, the binding

constants obtained with mononuclear complex **XLIV** were significantly lower than for $\mathbf{Zn_4L_4(NTf_2)_8}$ tetrahedron **Zn-XLIII** (Scheme 61b). While comparable for guests **209** and **212**, the cage showed much higher affinity for the anions of **256-259** while phosphate salts **260-262** showed even stronger binding to cage **Zn-XLIII**. Determining the binding constants of phosphate salts **260-262** with model complex **XLIV** was not possible due to solubility issues during the titrations. The best binding guests in this series turned out to be the phosphates **260-262**, potentially due to a good shape fit to the tetrahedral cage.[299,300] While the binding constants for diphenyl phosphate **260** and dimethyl phosphate **261** were similar, better binding was observed for dibutyl phosphate **262**. The more flexible butyl chains may enable a better shape fit than the phenyl and methyl groups of guests **260** and **261**.

The binding constants showcased were determined assuming a 1:1 binding model to be present in every single case using the bindfit app. More details on this are shown in chapter 5.3.2 of the experimental section. Nevertheless, molecular models for cage **Zn-XLIII** with 1-2 eq. of each anionic guest were generated using the SPARTAN (Wavefunction, Version 1.1.2, Wavefunction, Inc., MMFF molecular mechanics modeling) software. Space-wise, all guests could potentially also form higher guest:host ratios. However, due to charge repulsion this seemed unlikely. These models are shown in chapter 5.4 of the experimental part.

To determine the stoichiometry of the complexes, it was decided to systematically fit data to reasonable binding models. This was suggested by recent studies, that identified the Job plot method as unreliable in many cases.[301] Thus, as suggested, the titration results were analysed using the 1:1 and 1:2 binding models of the Bindfit app for NMR titrations (http://app.supramolecular.org/bindfit/). The comparison showed that a 1:1 binding was more reasonable in most cases, as for the 1:2 binding models, binding constants K_{11} were unrealistically high with exorbitant error values, and for the binding constants K_{12} even negative values were observed in several cases. An exception was the smallest guest **257**, acetate. In this case, indeed also a 1:2 binding mode seemed reasonable according to the fit data. The data is also depicted in chapter 5.4 together with the models calculated *via* SPARTAN.

3.2.9 Catalysis Experiments with $Zn_4L_4(NTf_2)_8$ Cage Zn-XLIII

Having finally access to a base-stable cationic cage with a sizable cavity, the catalytic potential of cage **Zn-XLIII** was explored. Four substrates and in total three different reaction types were chosen (Figure 44) with anionic transition states and intermediates under basic conditions: a) phosphate hydrolysis of trimethyl phosphate (**255**), b) ester hydrolysis of ethyl benzoate (**253**), c) decarboxylation of β-ketoacid **265** and d) ester hydrolysis of monocarboxylate mono methyl ester **258**. The reactions were run in MeCN-d_3/H_2O = 6:4 at different temperature profiles depending on the reaction rate at a substrate concentration of 20 mM in the presence of 10 mol-% of cage **Zn-XLIII** and 3 eq. of base (either $KHCO_3$, NEt_3, or *i*-Pr_2NEt). As control experiments, the respective background reactions without $\mathbf{Zn_4L_4}$ cage **Zn-XLIII** were investigated as well. Durene was used as an internal standard to follow the reaction progress *via* ^{1}H-NMR. All experimental details can be found in chapter 5.5 of the experimental section.

Interestingly, in all four reactions explored the reaction rate slowed down in the presence of cage **Zn-XLIII**. Even though two neutral substrates (**255** and **253**) were used in this study that showed no significant uptake, it was assumed that even very little uptake into cage **Zn-XLIII** may lead to rate accelerations, as subsequent anionic transition states, as well as intermediates, should be stabilized inside the positively charged cage environment. A

similar result was observed even when using the anionic substrates **265** (in its deprotonated carboxylate form) and **258**. This was surprising since catalysis within metal-organic cages under basic conditions has previously been achieved.[188,263] The reduced conversion rate with cage **Zn-XLIII** in the case of the neutral substrates **253** and **255** might be a result of the failure of guest binding, combined with a local increase in hydroxide concentration around the cage, as observed for another cationic cage.[188] However, the failure of acceleration in the cases of the anionic substrates remains unknown.

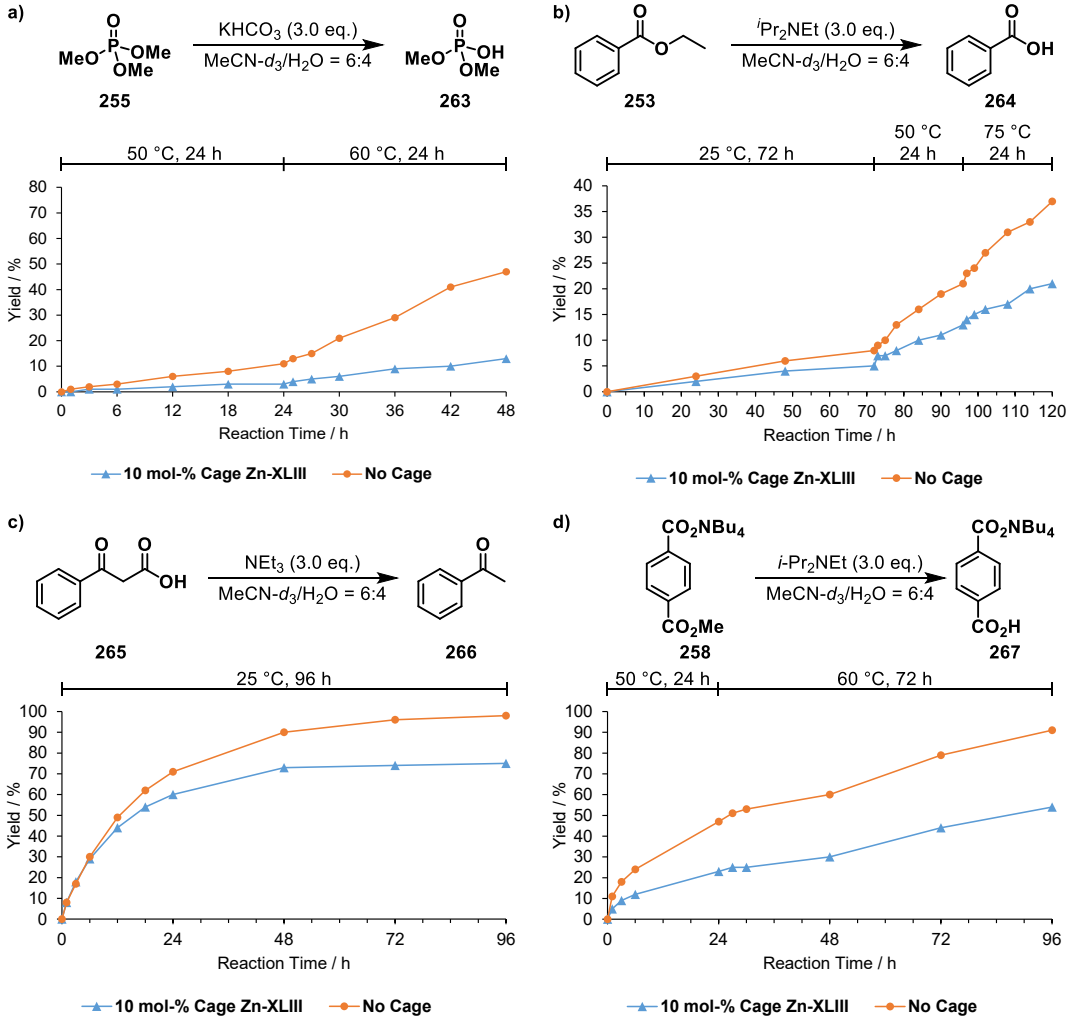

Figure 44: Catalysis experiments with cage **Zn-XLIII** utilizing neutral (a-b), and anionic substrates (c-d). Three different reaction types were investigated: a) phosphate hydrolysis, b) and d) ester hydrolysis, and c) decarboxylation of a β-ketoacid.

3.2.10 Crystallisation Experiments with $Zn_4L_4(NTf_2)_8$ Cage Zn-XLIII

Single crystals of cage **Zn-XLIII** for X-ray analysis were obtained *via* slow diffusion of either Et_2O or *i*-Pr_2O from a reservoir into an acetonitrile solution of cage **Zn-XLIII** (5 mg in 0.5 mL) at room temperature or −20 °C. However, they did not diffract the X-rays and no crystal structure could be obtained. This may have been caused by the cavity of the cage being filled with disordered solvent molecules. Therefore, the experiments were expanded to include other solvents in the reservoir such as benzene and TBME coupled with the addition of an excess (12 eq.) of a different counter anion like in LiOTf, $NaBF_4$, KBF_4 and $KSbF_6$ (Scheme 62) which could possibly also fill up the cage cavity but with no success. In most cases, precipitation of the cage material was observed over time. When crystals were obtained, they either did not diffract the X-rays as well or were of poor quality. The same results were obtained with organic salts **209**, **216**, **268**, **269**, **256**, **259** and **260-262** as potential guest molecules to fill up and establish a higher order within the cavity. While mostly MeCN could be used as the main solvent, MeCN/H_2O = 5:1 was necessary to ensure solubility of tetrabutylammonium phosphate guests **260-262**. These crystallization attempts are listed in tables 23.

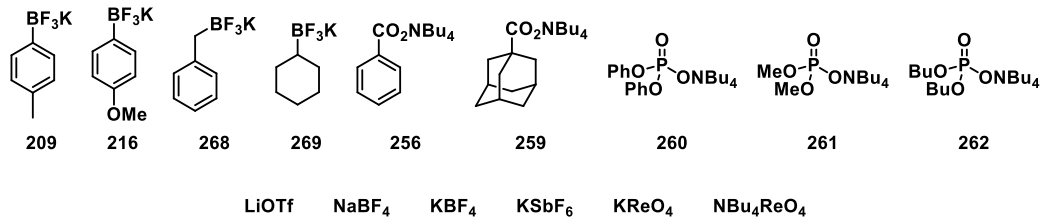

Scheme 62: Organic and inorganic salts used as an additive for the crystallization attempts of **$Zn_4L_4(NTf_2)_8$** cage **Zn-XLIII**.

Further investigations revealed that the cage material (3 mg for each experiment this time) could be dissolved in other polar aprotic solvents (0.5 mL) such as acetone, DMF, DMSO, sulfolane, nitromethane ($MeNO_2$), nitrobenzene ($PhNO_2$) and benzonitrile (PhCN) quite easily. For each of these solvents, slow diffusion of Et_2O, TBME, EtOH or MeOH from a reservoir into the cage solution was set up. The results were mostly the same and are listed in table 24. On top of that, potassium perrhenate ($KReO_4$) and tetrabutylammonium perrhenate (NBu_4ReO_4) were investigated as additives with the above-mentioned solvents for the cage and TBME and MeOH as solvents for the reservoir (Table 25).

Overall, single crystals of presumably good enough quality for X-ray analysis were obtained every now and then but none of them were able to diffract the X-rays other than at low angles. The data gathered was never sufficient to resolve a structure.

Table 23: Slow diffusion crystallization experiments for **$Zn_4L_4(NTf_2)_8$** cage **Zn-XLIII**.

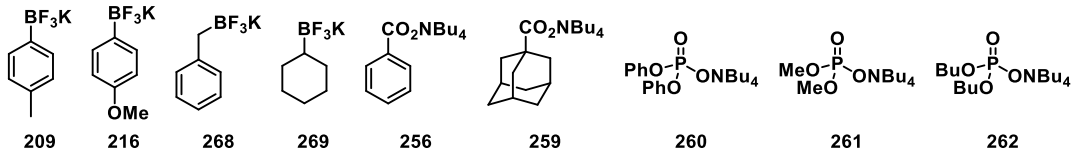

209 216 268 269 256 259 260 261 262

Entry	Zn-XLIII	Solvent (0.5 mL)	Reservoir	Guest	T [°C]	Crystals	Result
1	5 mg	MeCN	Et_2O	-	23	Yes	No Diffraction
2	5 mg	MeCN	Et_2O	-	–20	Yes	No Diffraction
3	5 mg	MeCN	*i*-Pr_2O	-	23	Yes	No Diffraction
4	5 mg	MeCN	*i*-Pr_2O	-	–20	Yes	No Diffraction
5	5 mg	MeCN	Et_2O	LiOTf (12 eq.)	23	No	Precipitation
6	5 mg	MeCN	Et_2O	LiOTf (12 eq.)	5	No	Precipitation
7	5 mg	MeCN	*i*-Pr_2O	LiOTf (12 eq.)	23	No	Precipitation
8	5 mg	MeCN	*i*-Pr_2O	LiOTf (12 eq.)	5	No	Precipitation
9	5 mg	MeCN	Benzene	LiOTf (12 eq.)	23	No	Precipitation
10	5 mg	MeCN	Benzene	LiOTf (12 eq.)	5	No	Precipitation
11	5 mg	MeCN	Et_2O	$NaBF_4$ (12 eq.)	23	No	Precipitation
12	5 mg	MeCN	Et_2O	$NaBF_4$ (12 eq.)	5	No	Precipitation
13	5 mg	MeCN	*i*-Pr_2O	$NaBF_4$ (12 eq.)	23	Yes	Low Quality Crystals
14	5 mg	MeCN	*i*-Pr_2O	$NaBF_4$ (12 eq.)	5	Yes	Low Quality Crystals
15	5 mg	MeCN	Benzene	$NaBF_4$ (12 eq.)	23	Yes	No Diffraction
16	5 mg	MeCN	Benzene	$NaBF_4$ (12 eq.)	5	Yes	Low Quality Crystals
17	5 mg	MeCN	Et_2O	KBF_4 (12 eq.)	23	Yes	No Diffraction
18	5 mg	MeCN	*i*-Pr_2O	KBF_4 (12 eq.)	23	Yes	Low Quality Crystals
19	5 mg	MeCN	Et_2O	$KSbF_6$ (12 eq.)	23	No	Precipitation
20	5 mg	MeCN	*i*-Pr_2O	$KSbF_6$ (12 eq.)	23	No	Precipitation
21	5 mg	MeCN	*i*-Pr_2O	**209** (8 eq.)	23	No	Precipitation
22	5 mg	MeCN	TBME	**209** (8 eq.)	23	Yes	No Diffraction
23	5 mg	MeCN	Et_2O	**209** (8 eq.)	23	No	Precipitation
24	5 mg	MeCN	Et_2O	**209** (8 eq.)	5	No	Precipitation
25	5 mg	MeCN	Et_2O	**209** (1 eq.)	23	Yes	No Diffraction
26	5 mg	MeCN	Et_2O	**216** (1 eq.)	23	Yes	No Diffraction
27	5 mg	MeCN	Et_2O	**268** (1 eq.)	23	Yes	No Diffraction
28	5 mg	MeCN	Et_2O	**269** (1 eq.)	23	Yes	No Diffraction
29	5 mg	MeCN	Et_2O	**256** (1 eq.)	23	Yes	No Diffraction
30	5 mg	MeCN	Et_2O	**259** (1 eq.)	23	Yes	No Diffraction
31	5 mg	MeCN/H_2O = 5:1	Et_2O	**259** (8 eq.)	23	No	Material Oiled Out
32	5 mg	MeCN/H_2O = 5:1	Et_2O	**260** (8 eq.)	23	No	Material Oiled Out
33	5 mg	MeCN/H_2O = 5:1	Et_2O	**261** (8 eq.)	23	No	Material Oiled Out
34	5 mg	MeCN/H_2O = 5:1	Et_2O	**262** (8 eq.)	23	Yes	No Diffraction

Table 24: Slow diffusion crystallization experiments for **$Zn_4L_4(NTf_2)_8$** cage **Zn-XLIII**.

Entry	Zn-XLIII	Solvent (0.5 mL)	Reservoir	Guest	T [°C]	Crystals	Result
1	3 mg	Acetone	Et_2O	-	23	No	Precipitation
2	3 mg	Acetone	TBME	-	23	No	Precipitation
3	3 mg	Acetone	EtOH	-	23	No	Precipitation
4	3 mg	Acetone	MeOH	-	23	No	Precipitation
5	3 mg	DMF	Et_2O	-	23	Yes	No Diffraction
6	3 mg	DMF	TBME	-	23	Yes	No Diffraction
7	3 mg	DMF	EtOH	-	23	No	Stayed Dissolved
8	3 mg	DMF	MeOH	-	23	No	Stayed Dissolved
9	3 mg	DMSO	Et_2O	-	23	No	Immiscible Layers
10	3 mg	DMSO	TBME	-	23	No	Immiscible Layers
11	3 mg	DMSO	EtOH	-	23	No	Stayed Dissolved
12	3 mg	DMSO	MeOH	-	23	No	Stayed Dissolved
13	3 mg	Sulfolane	Et_2O	-	23	No	Immiscible Layers
14	3 mg	Sulfolane	TBME	-	23	No	Immiscible Layers
15	3 mg	Sulfolane	EtOH	-	23	No	Stayed Dissolved
16	3 mg	Sulfolane	MeOH	-	23	No	Stayed Dissolved
17	3 mg	$MeNO_2$	Et_2O	-	23	No	Precipitation
18	3 mg	$MeNO_2$	TBME	-	23	No	Precipitation
19	3 mg	$MeNO_2$	EtOH	-	23	No	Stayed Dissolved
20	3 mg	$MeNO_2$	MeOH	-	23	No	Stayed Dissolved
21	3 mg	$PhNO_2$	Et_2O	-	23	No	Precipitation
22	3 mg	$PhNO_2$	TBME	-	23	No	Precipitation
23	3 mg	$PhNO_2$	EtOH	-	23	Yes	No Diffraction
24	3 mg	$PhNO_2$	MeOH	-	23	No	Stayed Dissolved
25	3 mg	PhCN	Et_2O	-	23	No	Precipitation
26	3 mg	PhCN	TBME	-	23	No	Precipitation
27	3 mg	PhCN	EtOH	-	23	Yes	No Diffraction
28	3 mg	PhCN	MeOH	-	23	No	Low Quality Crystals

Table 25: Slow diffusion crystallization experiments for **$Zn_4L_4(NTf_2)_8$** cage **Zn-XLIII**.

Entry	Zn-XLIII	Solvent (0.5 mL)	Reservoir	Guest	T [°C]	Crystals	Result
1	3 mg	Acetone	TBME	NBu_4ReO_4 (12 eq.)	23	No	Precipitation
2	3 mg	Acetone	MeOH	NBu_4ReO_4 (12 eq.)	23	No	Precipitation
3	3 mg	DMF	TBME	NBu_4ReO_4 (12 eq.)	23	No	Precipitation
4	3 mg	DMF	MeOH	NBu_4ReO_4 (12 eq.)	23	Yes	Low Quality Crystals
5	3 mg	DMSO	TBME	NBu_4ReO_4 (12 eq.)	23	No	Precipitation
6	3 mg	DMSO	MeOH	NBu_4ReO_4 (12 eq.)	23	No	Stayed Dissolved
7	3 mg	Sulfolane	TBME	NBu_4ReO_4 (12 eq.)	23	No	Precipitation
8	3 mg	Sulfolane	MeOH	NBu_4ReO_4 (12 eq.)	23	No	Stayed Dissolved
9	3 mg	$MeNO_2$	TBME	NBu_4ReO_4 (12 eq.)	23	No	Precipitation
10	3 mg	$MeNO_2$	MeOH	NBu_4ReO_4 (12 eq.)	23	No	Precipitation
11	3 mg	$PhNO_2$	TBME	NBu_4ReO_4 (12 eq.)	23	No	Precipitation
12	3 mg	$PhNO_2$	MeOH	NBu_4ReO_4 (12 eq.)	23	No	Precipitation
13	3 mg	PhCN	TBME	NBu_4ReO_4 (12 eq.)	23	No	Precipitation
14	3 mg	PhCN	MeOH	NBu_4ReO_4 (12 eq.)	23	No	Precipitation
15	3 mg	PhCN/MeCN = 1:1	TBME	NBu_4ReO_4 (12 eq.)	23	No	Precipitation
16	3 mg	PhCN/MeCN = 1:1	MeOH	NBu_4ReO_4 (12 eq.)	23	Yes	No Diffraction
17	3 mg	DMF	TBME	$KReO_4$ (12 eq.)	23	No	Precipitation
18	3 mg	DMF	MeOH	$KReO_4$ (12 eq.)	23	No	Precipitation
19	3 mg	DMSO	TBME	$KReO_4$ (12 eq.)	23	No	Immiscible Layers
20	3 mg	DMSO	MeOH	$KReO_4$ (12 eq.)	23	No	Stayed Dissolved
21	3 mg	Sulfolane	TBME	$KReO_4$ (12 eq.)	23	No	Immiscible Layers
22	3 mg	Sulfolane	MeOH	$KReO_4$ (12 eq.)	23	No	Stayed Dissolved

4 Summary and Outlook

In recent years, π-acidic naphthalene diimide (NDI) scaffolds were used in open, non-capsular systems as anion-π catalysts for various reactions. In this thesis, two strategies for the synthesis of positively charged, supramolecular cages with subcomponents featuring π-acidic surfaces were investigated for potential applications in the catalysis of reactions with anionic transition states.

First, NDI dialdehyde **175** was obtained *via* initial imide condensation between NDA (**179**) and literature known acetal protected amine **193** and follow-up acetal deprotection with a combined yield of 76% (Scheme 63). **Tri^{2}Di^3** ammonium cage **XVIIa** was then accessible *via* sixfold reductive amination in 70% yield over two steps, utilizing dynamic imine condensation. Anion exchange gave access to its ammonium trifluoroacetate derivative **XXVa** in 95% yield, which was able to bind a few anionic guests in fast exchange on the ^{1}H-NMR chemical shift timescale with moderate binding constants between 75 and 460 M^{-1}. The cage was considered too small for our endeavours and the binding constants not convincing enough. A few more imine species, which appeared to be highly symmetric based on ^{1}H-NMR experiments at this stage, formed with increasing TREN (**128a**) concentration during the imine-forming step, but none of them could be assigned to an interesting cage after reduction and partial purification.

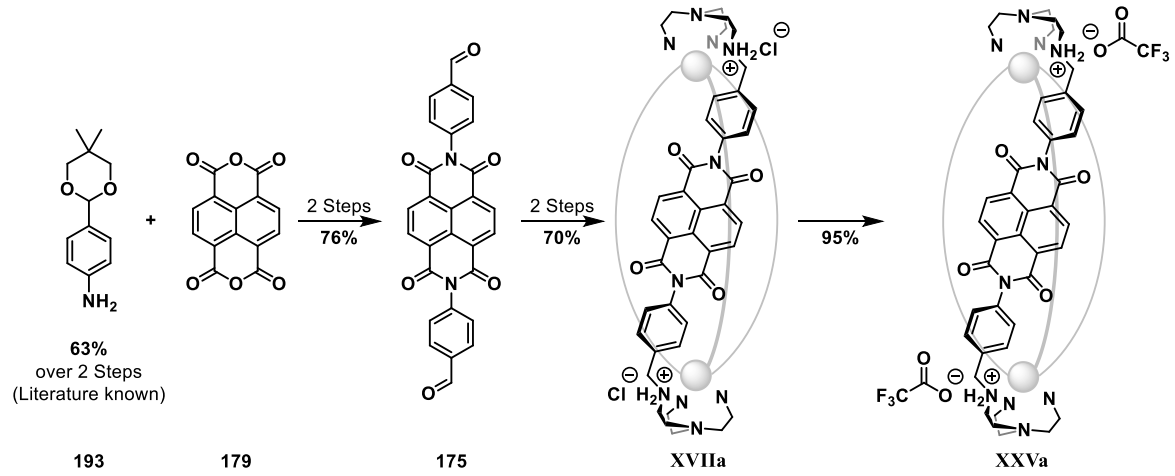

Scheme 63: Synthetic route towards ammonium cages **XVIIa** and **XXVa**.

In the second part of this thesis, novel metal-organic coordination cages were pursued. The two-step synthesis of NDI dialdehyde **176** was optimized, giving a combined yield of 42%. **$Zn_2L_3(NTf_2)_4$** helicate **XXXII** was then obtained through subcomponent self-assembly in 22% yield (Scheme 64a). Its crystal structure was elucidated, showing no cavity due to π-π stacking between the NDI ligands. However, an edge-linked tetrahedral **M_4L_6** cage was not accessible with the same subcomponents. Instead, the literature known **$Fe_4L_6(NTf_2)_8$** tetrahedron **XXIX**, accessible in two steps and 36% total yield, was provided by the LÜTZEN group from the University of Bonn but was shown herein to be unstable against water and bases (Scheme 64b).

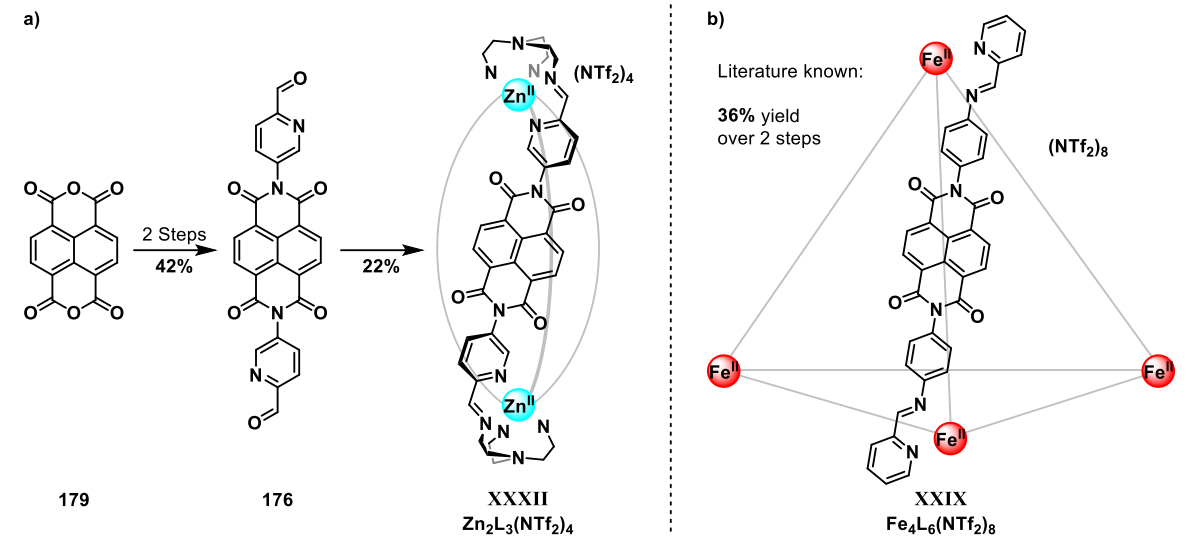

Scheme 64: a) $Zn_2L_3(NTf_2)_4$ helicate **XXXII** was synthesized over three steps *via* the subcomponent self-assembly method. b) Literature known $Fe_4L_6(NTf_2)_8$ tetrahedron **XXIX** was shown to be unstable towards water and bases at room temperature.

Next, a panelling approach was investigated to remove the possibility for helicate formation. The π-acidic triphenylene triimide (TPTI) compound **229** was synthesized *via* threefold anyhdride condensation, followed by imide condensation from literature known hexacarboxylic acid **225** with a combined yield of 47% over two steps (Scheme 65). A follow-up oxidation to the desired TPTI ligand **177** with three 2-formylpyridyl groups for subcomponent self-assembly towards coordination cages was not achieved. Moreover, the TPTI scaffold was found to be instable, and decomposed, for instance, during aqueous workups.

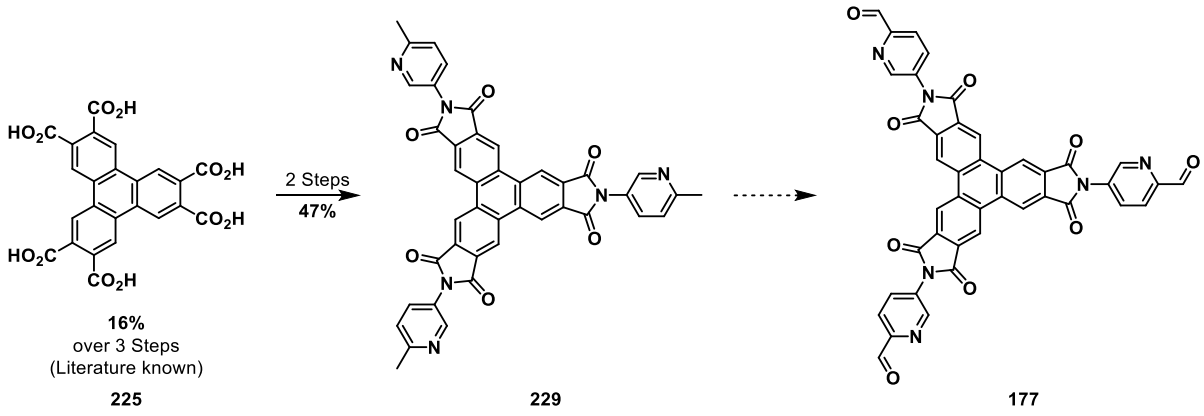

Scheme 65: Synthetic route towards TPTI compound **229**. TPTI ligand **177** was not obtained.

Therefore, trialdehyde **178**, bearing no π-acidic moiety, was synthesized instead from literature known trialkyne **247** in 74% yield (Scheme 66). Subcomponent self-assembly between tritopic ligand **178** with TREN (**128a)** and $Zn(NTf_2)_2$ gave face-capped $Zn_4L_4(NTf_2)_8$ tetrahedron **Zn-XLIII** in 20% yield. No water-soluble derivative was accessible. The cage proved to be stable against water and various bases at elevated temperatures. It was able to bind anionic guests in fast exchange on the ^{1}H-NMR chemical shift timescale with binding constants between 40 and 850 M^{-1} in MeCN-d_3/H_2O = 9:1. Neutral guests were not bound by cage **Zn-XLIII**. To elucidate if indeed a guest uptake into the cage was taking place, or if this binding was rather an outside interaction with the charged vertices, control titrations were performed with the simple mononuclear $ZnL_3(NTf_2)_2$ complex **XLIV**, which was synthesized in one step and 88% yield (Scheme 66). In general, the binding constants obtained with mononuclear

complex **XLIV** were significantly lower than for $\mathbf{Zn_4L_4(NTf_2)_8}$ tetrahedron **Zn-XLIII**. Moreover, cage **Zn-XLIII** was shown to remain stable against water and various bases at elevated temperatures.

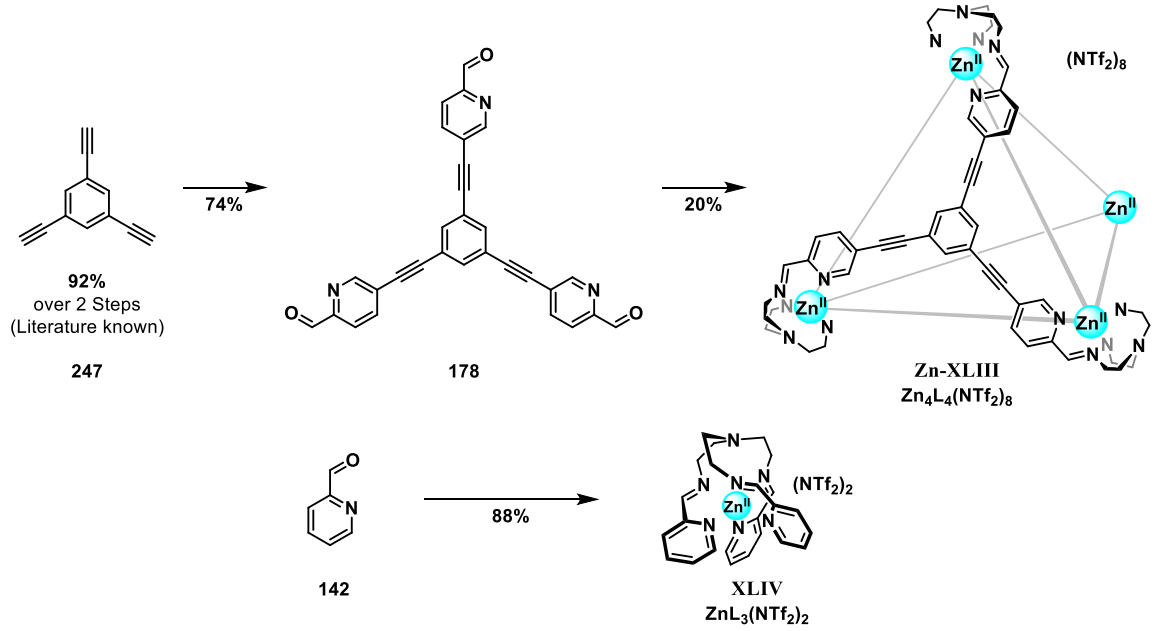

Scheme 66: Top: $\mathbf{Zn_4L_4(NTf_2)_8}$ tetrahedron **Zn-XLIII** was synthesized in four steps *via* the subcomponent self-assembly method. Bottom: $\mathbf{ZnL_3(NTf_2)_2}$ complex **XLIV** was synthesized in one step from picolinalehyde (**142**).

Despite its net positive charge of +8, $\mathbf{Zn_4L_4(NTf_2)_8}$ tetrahedron **Zn-XLIII** was not able to accelerate reactions with anionic transition states. Deceleration occurred instead in every single case investigated. Even though two neutral substrates were used in this study that showed no significant uptake, it was assumed that even very little uptake into cage **Zn-XLIII** may lead to rate accelerations. The reduced conversion with cage **Zn-XLIII** in the case of the neutral substrates might be a result of the failure of guest binding, combined with a local increase in hydroxide concentration around the cage. However, the failure of acceleration in the cases of the anionic substrates remained unknown.

This thesis demonstrated that the catalysis of reactions with anionic transition states within supramolecular cages remains a challenge. The desired tetrahedral cage topology is not guaranteed to form with ditopic ligands. Besides that, this work showed with extensive screening that only a specific combination of subcomponents can lead to cage formation. The generally low solubility of the ligands employed herein may have been the reason for this observation. As such, equipping the subcomponents used with solubilizing groups could make it easier to access cage structures with the desired solubility properties but their effect on the π-acidity of ligands with π-acidic surfaces should also be considered. However, functionalized ligands most likely require more laborious synthetic effort.

5 Experimental Section

5.1 General Information

Experimental: All reactions were carried out under an atmosphere of dry argon as inert gas using standard SCHLENK techniques and the glassware was heated out under high vacuum (10^{-2} mbar) using a heat gun at 500-600 °C unless stated otherwise. Reactions carried out at elevated temperatures were heated using oil baths. Microwave experiments were conducted using an ANTON PAAR Monowave 400 microwave synthesis reactor.

Thin-Layer Chromatography (TLC): Analytical thin-layer chromatography (TLC) was performed on MERCK silica gel 60 F254 glass-baked plates, which were analysed under UV light (λ = 254 nm, [UV]).

Flash Column Chromatography: Column chromatographic separations were performed as flash chromatography with Merck silica gel 60 (230-240 mesh ASTM, pore size 40-63 μm).

Size-Exclusion Column Chromatography:

(1) For organic solvents: Size-Exclusion column chromatographic separations were performed with Bio-Beads S-X1 support resins from BIO-RAD (1% cross-linkage, 40-80 μm bead size, 600-14000 MW exclusion range) using gravity flow. The beads were swollen overnight in DCM/MeCN = 7:3 and washed extensively *via* filtration before use with the same solvent system to remove baseline impurities.

(2) For aqueous solvent systems: Size-Exclusion column chromatographic separations were performed with Sephadex G10/G25/G50/G75 beads from CYTIVA using compressed air. Fractionation ranges are given as follows: <700 Da for Sephadex G10; 100-5000 Da for Sephadex G25; 500-10000 Da for Sephadex G50; 1000-50000 Da for Sephadex G75. The beads were swollen over 24 h in H_2O (+0.1% formic acid) and washed extensively before use with the same solvent system to remove baseline impurities.

NMR-Spectroscopy: ^{1}H-NMR spectra were recorded at 298 K at 400 MHz, 500 MHz, 600 MHz or 700 MHz using a BRUKER Ascend 400 spectrometer, a BRUKER UltraShield 500 spectrometer, a BRUKER Avance III NMR spectrometer equipped with a cryogenic QCI-F probe or a BRUKER Avance 700 spectrometer, respectively. ^{13}C-NMR spectra were recorded at 298 K at 126 MHz, 151 MHz or 176 MHz using a BRUKER UltraShield 500 spectrometer, a BRUKER Avance III NMR spectrometer equipped with a cryogenic QCI-F probe or a BRUKER Avance 700 spectrometer, respectively. ^{31}P-NMR spectra were recorded at 202 MHz on a BRUKER UltraShield 500 spectrometer. ^{19}F-NMR spectra were recorded at 471 MHz on a BRUKER UltraShield 500 spectrometer. Chemical shifts of ^{1}H-NMR and ^{13}C-NMR spectra are given in ppm by using residual solvent signals as references ($CDCl_3$: 7.26 ppm and 77.16 ppm, respectively; DCM-d_2: 5.32 ppm and 53.84 ppm, respectively; DMSO-d_6: 2.50 ppm and 39.52 ppm, respectively; MeOD-d_4: 3.31 ppm and 49.00 ppm, respectively; MeCN-d_3: 1.94 ppm and 1.32 ppm, respectively; Acetone-d_6: 2.05 ppm and 206.26 ppm, respectively; D_2O: 4.79 ppm; 1% *t*-BuOH is added as a reference (70.36 ppm) for ^{13}C-NMRs in D_2O); chemical shifts of ^{31}P-NMR spectra are given in ppm, referenced to 85% H_3PO_4 (0.00 ppm) using a coaxial insert; chemical shifts of ^{19}F-NMR spectra are given in ppm, referenced to either $CFCl_3$ (0.00 ppm) or C_6F_6 (−164.9 ppm). Coupling constants (*J*) are reported in Hertz (Hz). Standard abbreviations indicating multiplicity were used as follows: s (singlet), d (doublet), t (triplet), q (quartet), m (multiplet), m_c (centered multiplet), br. (broad).

DOSY-NMR experiments were performed on a Bruker Avance III HD four-channel NMR spectrometer operating at 600.13 MHz proton frequency. The instrument was equipped with a cryogenic 5 mm four-channel QCI probe (H/C/N/F) with self-shielded z-gradient. The experiments were performed at 298 K and the temperature was calibrated using a methanol standard showing accuracy within ± 0.2 K. For the PFGSE (pulsed field gradient spin echo) diffusion experiment, the sample was placed in a 3 mm outer diameter tube and the 3 mm tube was then inserted in a standard 5 mm round bottom tube. This setup allowed reproducible measurements inside a cryogenic probe. The PFGSE experiments were performed using a bipolar gradient pulse sequence.[302] The sigmoidal intensity decrease was fitted with a two-parameter fit (I_0 and diffusion coefficient D) with the DOSY routine implemented in topspin 3.6.1 [Bruker Biospin GmbH]. A representative observed intensity decrease of **Zn$_4$L$_4$** cage **Zn-XLIII** in MeCN-d_3 is depicted below in figure 45.

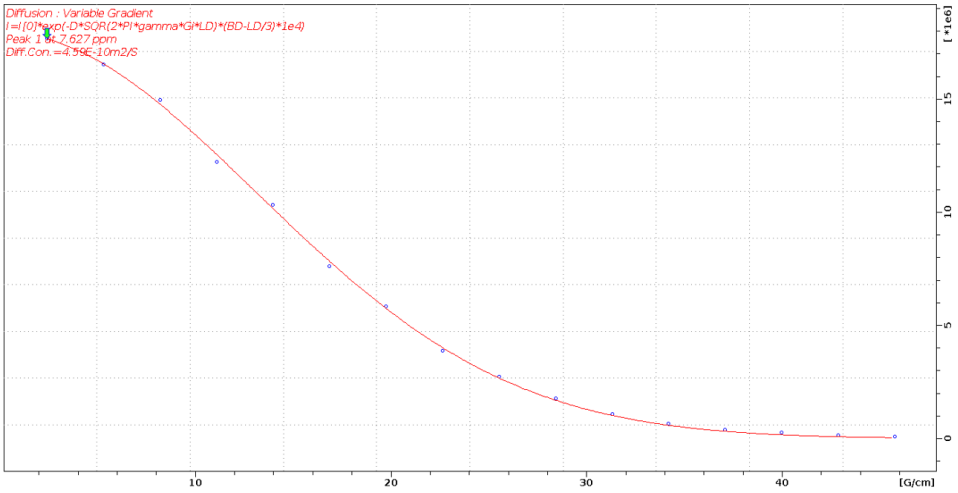

Figure 45: Observed intensity decrease of **Zn$_4$L$_4$** cage **Zn-XLIII** in MeCN-d_3.

IR-Spectroscopy: Infrared spectra were recorded on a BRUKER ALPHA spectrometer (attenuated total reflection, ATR). Only selected absorbances ($\tilde{\nu}_{max}$) are reported. Standard abbreviations indicating signal intensity were used as follows: vs (very strong), s (strong), m (medium), w (weak) and b (broad).

ESI-HRMS: High resolution mass spectra were obtained using the electrospray ionization - time of flight (ESI-TOF) technique on a BRUKER maXis 4G mass spectrometer.

EI-MS: Electron ionization mass spectra were obtained using a MAT 95XL mass spectrometer.

Melting Point: Melting Points were recorded on a BÜCHI Melting Point M-565 apparatus using open capillary tubes.

Solvents: Anhydrous $CHCl_3$ was purchased from Sigma-Aldrich. All other anhydrous solvents were purchased from ACROS ORGANICS and were used without prior purification. Solvents for extractions, chromatography, filtrations and non-anhydrous reactions were purchased from VWR as HPLC grade solvents and were used without prior purification. NMR Solvents were purchased from CAMBRIDGE ISOTOPE LABORATORIES and were used without prior purification.

Sources of Chemicals: All reagents used were purchased from commercial distributors (ACROS, ALFA AESAR, FLUOROCHEM, SIGMA-ALDRICH, TCI, VWR) and were used without prior purification.

5.2 Synthetic Procedures and Analytical Data

5.2.1 Synthesis of Tri[2]Di[3] Ammonium Cages XVIIa and XXVa

5,5-Dimethyl-2-(4-nitrophenyl)-1,3-dioxane (192)

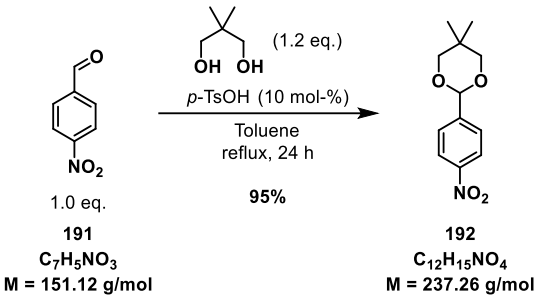

The title compound (**192**) was synthesized as previously described.[279] The spectroscopic data match those reported in literature.[303]

^{1}H-NMR (500 MHz, $CDCl_3$): δ [ppm] = 8.22 (m_c, 2H), 7.68 (m_c, 2H), 5.46 (s, 1H), 3.79 (d, *J* = 11.2 Hz, 2H), 3.67 (d, *J* = 11.2 Hz, 2H), 1.27 (s, 3H), 0.82 (s, 3H).

^{13}C-NMR (126 MHz, $CDCl_3$): δ [ppm] = 148.3, 145.1, 127.4, 123.6, 100.1, 77.8, 30.4, 23.1, 21.9.

4-(5,5-Dimethyl-1,3-dioxan-2-yl)aniline (193)

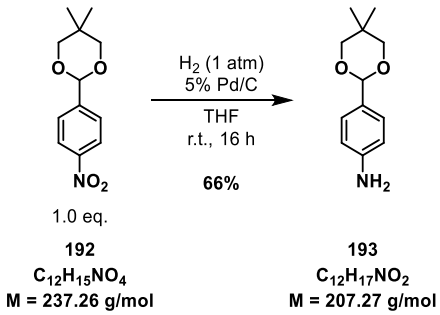

The title compound (**193**) was synthesized as previously described and the spectroscopic data match those reported in literature.[279]

^{1}H-NMR (500 MHz, $CDCl_3$): δ [ppm] = 7.29 (m_c, 2H), 6.67 (m_c, 2H), 5.29 (s, 1H), 3.74 (d, *J* = 11.2 Hz, 2H), 3.69 (br. s, 2H), 3.62 (d, *J* = 11.1 Hz, 2H), 1.29 (s, 3H), 0.78 (s, 3H).

2,7-Bis(4-(5,5-dimethyl-1,3-dioxan-2-yl)phenyl)benzo[*lmn*][3,8]phenanthroline-1,3,6,8(2*H*,7*H*)-tetraone (196)

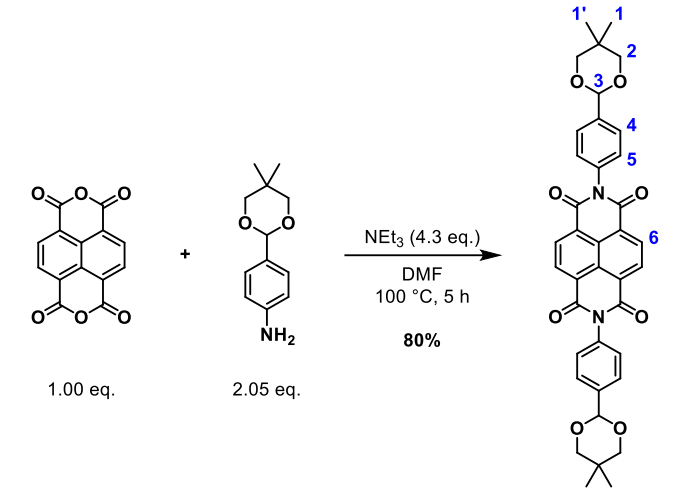

A dried 50 mL flask was charged with a stir bar and NDA (**179**, 85%, 5.49 g, 17.4 mmol, 1.00 eq.). Dry DMF (200 mL) and dry NEt_3 (10.4 mL, 7.57 g, 74.8 mmol, 4.30 eq.) were added and the mixture was stirred for 15 min at room temperature. Then, 4-(5,5-Dimethyl-1,3-dioxan-2-yl)aniline (**193**, 7.39 g, 35.7 mmol, 2.05 eq.) was added to the dark brown solution and the mixture was heated to 100 °C for 5 h. The reaction mixture was allowed to cool down to room temperature and was stored at 4 °C over night. The formed crystals were filtered off and washed with Acetone (4 x 30 mL). NDI-Compound **196** (9.04 g, 14.0 mmol, 80%) was obtained as a yellow solid.

M.p.: Decomposition observed at 370 °C onwards.

IR (ATR): $\tilde{\nu}$ [cm^{-1}] = 3074 (w), 2962 (m), 2861 (m), 1715 (m), 1672 (vs), 1580 (m), 1472 (m), 1446 (m), 1389 (m), 1331 (s), 1245 (s), 1211 (m), 1186 (s), 1178 (s), 1096 (vs), 1039 (m), 1014 (s), 992 (s), 975 (s), 933 (m), 881 (m), 849 (m), 830 (s), 789 (m), 767 (s), 750 (s), 713 (m), 629 (m), 558 (m), 434 (m).

^{1}H-NMR (500 MHz, $CDCl_3$): δ [ppm] = 8.83 (s, 4H, 6-H), 7.73 (m_c, 4H, 5-H), 7.35 (m_c, 4H, 4-H), 5.50 (s, 2H, 3-H), 3.82 (d, *J* = 11.1 Hz, 4H), 3.70 (d, *J* = 11.1 Hz, 4H), 1.32 (s, 6H), 0.83 (s, 6H).

^{13}C-NMR (126 MHz, $CDCl_3$): δ [ppm] = 163.0, 139.7, 135.0, 131.6, 128.5, 127.6, 127.3, 127.2, 101.1, 77.8, 30.4, 23.2, 22.1.

HR-MS (pos. ESI): calculated for $C_{38}H_{35}N_2O_8$ $[M+H]^+$: 647.2388, found: 647.2400

calculated for $C_{38}H_{34}N_2O_8Na$ $[M+Na]^+$: 669.2207, found: 669.2220

4,4'-(1,3,6,8-Tetraoxo-1,3,6,8-tetrahydrobenzo[*lmn*][3,8]phenanthroline-2,7- diyl)dibenz aldehyde (175)

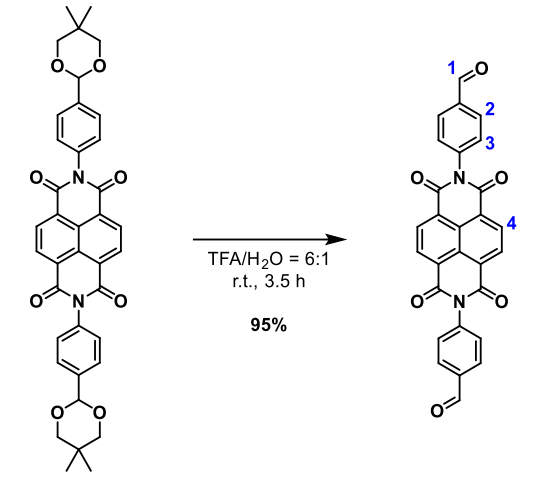

196
$C_{38}H_{34}N_2O_8$
M = 646.70 g/mol

175
$C_{28}H_{14}N_2O_6$
M = 474.43 g/mol

A 500 mL flask was charged with a stir bar, NDI compound **196** (4.87 g, 7.53 mmol, 1.00 eq.) and H_2O (20 mL). TFA (120 mL) was added, and the reaction mixture was stirred at room temperature for 3.5 h. The white suspension was added dropwise to a stirring aqueous solution of K_2CO_3 (6.4 M, 20 mL) under cooling with an ice-bath. Then, aqueous K_2CO_3 (6.4 M, 150 mL) was added slowly under stirring in an ice-bath until pH = 8-9 was reached and gas formation (CO_2) ceased. The yellow precipitate was filtered and washed with excess H_2O (4 x 80 mL) and Et_2O (4 x 50 mL). The solid residue was dried under high vacuum at 50 °C over night. The title compound (**175**, 3.38 g, 7.12 mmol, 95%) was obtained as a yellow powder.

Note: Only carefully apply vacuum since the product is a very fine powder which disperses quickly.

M.p.: No melting or visual decomposition observed up until maximum temperature (400 °C).

IR (ATR): $\tilde{\nu}$ [cm^{-1}] = 3374 (w), 3110 (w), 3085 (w), 3044 (w), 2834 (w), 2733 (w), 1712 (s), 1678 (vs), 1604 (m), 1575 (m), 1508 (w), 1446 (m), 1419 (w), 1332 (s), 1305 (m), 1244 (s), 1207 (s), 1187 (s), 1169 (m), 1116 (m), 1015 (w), 982 (w), 880 (w), 821 (s), 788 (s), 763 (s), 741 (s), 705 (w), 657 (w), 629 (w), 577 (w), 515 (s), 435 (w), 421 (m), 405 (s).

^{1}H-NMR (500 MHz, DMSO-d_6): δ [ppm] = 10.13 (s, 2H, 1-H), 8.75 (s, 4H, 4-H), 8.12 (m_c, 4H, 3-H), 7.74 (m_c, 4H, 2-H).

^{13}C-NMR (151 MHz, DMSO-d_6): δ [ppm] = 192.7, 162.9, 141.1, 136.1, 130.5, 130.2, 127.1, 126.8.

HR-MS (pos. ESI): calculated for $(C_{28}H_{14}N_2O_6)_4Na_2$ $[4M+2Na]^{2+}$: 971.6612, found: 971.6641

Tri^{2}Di^3 Imine Cage XXIIIa

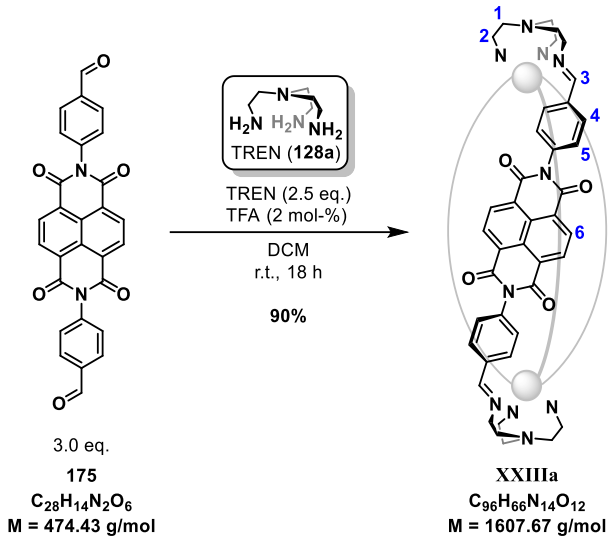

A dried 250 mL flask was charged with a stir bar, dialdehyde **175** (100 mg, 0.211 mmol, 3.00 eq.) and DCM (57 mL). Trifluoroacetic acid (1.41 mM in DCM, 0.1 mL, 1.41 µmol, 2 mol-%) and tris(2-aminoethyl)amine (**128a**, 26.4 µL, 25.8 mg, 0.176 mmol, 2.50 eq.) were added and the reaction mixture was stirred at room temperature for 18 h. *n*-Pentane (57 mL) was added and the mixture was cooled at –20 °C for 3 h. The precipitate was filtered off and the brown solid was washed with DCM (5 x 3 mL) and dried under high vacuum. Imine cage **XXIIIa** (101 mg, 0.0628 mmol, 90%) was obtained as a brown powder and was used in the next step without further purification.

M.p.: Decomposition observed at 120 °C onwards.

IR (ATR): $\tilde{\nu}$ [cm^{-1}] = 3082 (w), 3052 (w), 2848 (w), 2778 (w), 1712 (s), 1668 (vs), 1606 (w), 1579 (s), 1509 (m), 1447 (m), 1344 (vs), 1246 (vs), 1210 (m), 1192 (s), 1136 (m), 1118 (m), 1104 (m), 1082 (w), 1060 (w), 1020 (w), 979 (m), 903 (w), 882 (w), 833 (s), 794 (w), 765 (vs), 748 (w), 736 (s), 707 (m), 578 (w), 526 (m), 500 (w), 432 (m), 407 (m).

^{1}H-NMR (500 MHz, DMSO-*d*$_6$): δ [ppm] = 8.50 (s, 6H, 3-H), 7.87 (br. s, 12H, 6-H), 7.43 (m$_c$, 12H, 5-H), 7.28 (m$_c$, 12H, 4-H), 3.95-3.81 (m, 12H, 2-H), 2.88-2.74 (m, 12H, 1-H).

^{13}C-NMR: No useful data obtained due to solubility issues and stability issues at increased temperatures.

HR-MS (pos. ESI): calculated for $C_{96}H_{68}N_{14}O_{12}$ $[M+2H]^{2+}$: 804.7580, found: 804.7591

Tri[2]Di[3] Ammonium Chloride Cage XVIIa

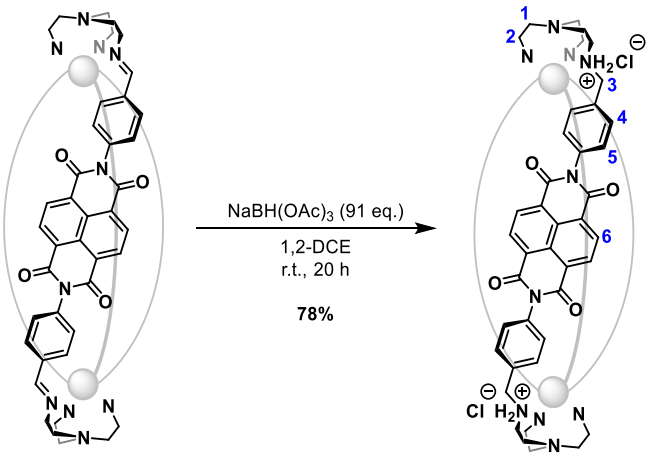

XXIIIa
$C_{96}H_{66}N_{14}O_{12}$
M = 1607.67 g/mol

XVIIa
$C_{96}H_{84}Cl_6N_{14}O_{12}$
M = 1838.51 g/mol

A 250 mL flask was charged with a stir bar, imine cage **XXIIIa** (1.00 g, 0.622 mmol, 1.00 eq.) and 1,2-DCE (100 mL). Sodium triacetoxyborohydride (3.00 g, 14.2 mmol, 22.8 eq.) was added and the mixture was stirred at room temperature for 1 h. Sodium triacetoxyborohydride (9.00 g, 42.5 mmol, 68.3 eq). was then added in 3 equal portions. The suspension was stirred for 1 h at room temperature between each addition and finally stirred for another 16 h. The dark green reaction mixture was quenched with 4.0 M HCl in Dioxane (30 mL). The purple suspension was stirred for 15 min and then allowed to rest at –20 °C for 30 min. The suspension was filtered off and the purple solid was washed with THF (2 x 50 mL). The yellow solid material was mortared to a fine powder and again placed onto a filtering paper. It was then washed with aqueous 1 M HCl (4 x 25 mL). The solid residue was collected and dried under reduced pressure. The TREN-derived hexaammonium chloride cage **XVIIa** (891 mg, 0.485 mmol, 78%) was obtained as a yellow-brownish solid.

M.p.: Decomposition observed at 190 °C onwards.

IR (ATR): $\tilde{\nu}$ [cm^{-1}] = 3841 (b), 3255 (m), 2162 (b), 1738 (s), 1700 (s), 1638 (s), 1546 (s), 1508 (m), 1391 (s), 1291 (s), 1237 (vs), 1190 (w), 1064 (m), 1033 (m), 993 (m), 905 (s), 873 (s), 854 (s), 820 (s), 779 (m), 759 (s), 737 (s), 715 (m), 658 (m), 565 (m), 484 (m), 417 (m).

^{1}H-NMR (500 MHz, D_2O): δ [ppm] = 8.30 (s, 12H, 6-H), 7.69 (m_c, 12H, 5-H), 7.39 (m_c, 12H, 4-H), 4.46 (s, 12H, 3-H), 3.45-3.28 (m, 12H), 3.03-2.90 (m, 12H).

^{1}H-NMR (500 MHz, DMSO-*d*$_6$): δ [ppm] = 9.25 (br. s, 12H, NH_2), 8.37 (s, 12H, 6-H), 7.92 (m_c, 12H, 5-H), 7.48 (m_c, 12H, 4-H), 4.39 (br. s, 12H, 3-H), 3.53 (br. s, 12H), 3.02 (br. s, 12H).

^{13}C-NMR: No useful data obtained due to solubility issues. A spectrum was obtained in the next step.

HR-MS (pos. ESI): calculated for $C_{96}H_{80}N_{14}O_{12}$ $[M–6Cl–4H]^{2+}$: 810.8050, found: 810.8066

Tri[2]Di[3] Ammonium Trifluoroacetate Cage XXVa

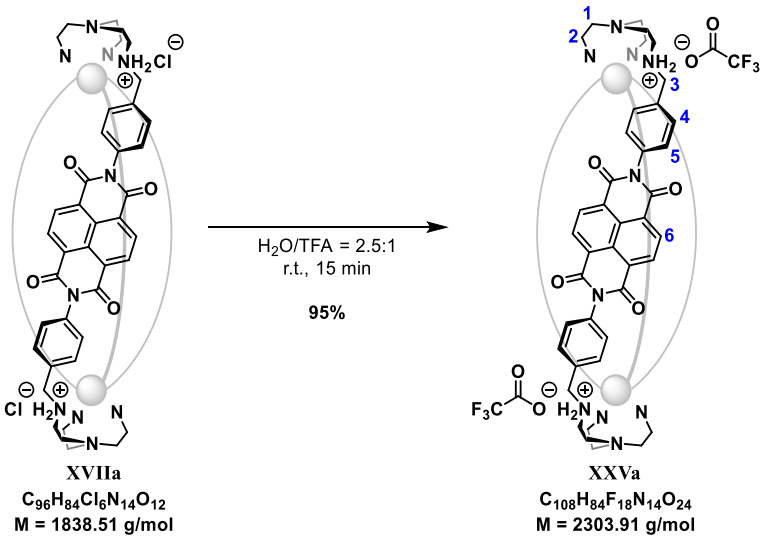

XVIIa
$C_{96}H_{84}Cl_6N_{14}O_{12}$
M = 1838.51 g/mol

XXVa
$C_{108}H_{84}F_{18}N_{14}O_{24}$
M = 2303.91 g/mol

A 250 mL flask was charged with a stir bar, ammonium chloride cage **XVIIa** (891 mg, 0.485 mmol, 1.00 eq.) and H_2O (85 mL). Trifluoroacetic acid (34 mL) was added slowly, and the mixture was stirred at room temperature for 15 min. The white suspension was centrifuged. The supernatant was decanted, and the white solid residue was dried under reduced pressure. The TREN-derived hexaammonium trifluoroacetate cage **XXVa** (1.06 g, 0.460 mmol, 95%) was obtained as an off-white solid.

M.p.: Decomposition observed at 230 °C onwards.

IR (ATR): $\tilde{\nu}$ [cm^{-1}] = 3671 (m), 3094 (b), 2842 (w), 1777 (m), 1715 (m), 1671 (s),1584 (m), 1519 (w), 1467 (w), 1416 (w), 1352 (m), 1253 (m), 1131 (vs), 1024 (w), 1010 (w), 986 (m), 928 (w), 905 (w), 862 (m), 836 (m), 797 (s), 769 (s), 751 (m), 720 (s), 705 (s), 634 (w), 613 (w), 598 (w), 584 (w), 568 (w), 519 (w), 433 (m), 422 (w), 412 (w).

^{1}H-NMR (500 MHz, MeCN-d_3): δ [ppm] = 8.77 (br. s, 12H, NH_2), 7.95 (s, 12H, 6-H), 7.81 (d, J = 8.1 Hz, 12H, 5-H), 7.42 (d, J = 8.2 Hz, 12H, 4-H), 4.51-4.39 (m, 12H, 3-H), 3.49 (br. s, 12H), 2.94 (br. s, 12H).

^{13}C-NMR (126 MHz, MeCN-d_3): δ [ppm] = 163.5, 137.2, 133.5, 132.5, 131.1, 130.3, 128.2, 127.9, 52.6, 50.4, 45.8.

^{19}F-NMR (471 MHz, MeCN-d_3, $CFCl_3$ as int. Std.): δ [ppm] = –74.7.

HR-MS (pos. ESI):

calculated for $C_{96}H_{80}N_{14}O_{12}$ $[M–6TFA–4H]^{2+}$: 810.8050, found: 810.8050

calculated for $C_{96}H_{81}N_{14}O_{12}$ $[M–6TFA–3H]^{3+}$: 540.8725, found: 540.8732

5.2.2 Synthesis of Tri[2]Di[3] Imine Cage XXIIIc

2,2',2''-((2,4,6-Triethylbenzene-1,3,5-triyl)tris(methylene))tris(isoindoline-1,3-dione) (200)

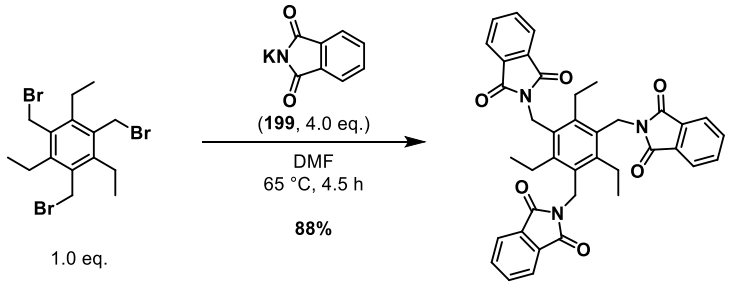

The title compound (**200**) was synthesized according to a modified procedure that was previously described for the tributyl derivative.[281]

A dried 50 mL flask was charged with a stir bar, tribromide **198** (1.00 g, 2.27 mmol, 1.00 eq.), potassium phthalimide (**199**, 1.68 g, 9.08 mmol, 4.00 eq.) and dry DMF (20 mL). The mixture was ultrasonicated and then stirred vigorously at 65 °C oilbath temperature for 4.5 h. The reaction mixture was cooled to room temperature and slowly poured into sat. aq. $NaHCO_3$ (50 mL). $CHCl_3$ (100 mL) was added, and the phases were separated. The aq. phase was extracted with $CHCl_3$ (2 x 100 mL). The combined org. phases were washed with brine (80 mL) and dried over Na_2SO_4. The solvent was removed under reduced pressure to give a colourless oily solid. DCM (30 mL) was added, and the solvent was removed under reduced pressure. This was repeated once more to remove residual DMF. The crude product was purified by column chromatography (SiO_2, Toluene/EtOAc = 8:1). The white solid was again dissolved in $CHCl_3$ (150 mL). The org. phase was washed with aq. NaOH (0.5 M, 2 x 40 mL) and dried over Na_2SO_4. The solvent was removed under reduced pressure. The title compound (**200**, 1.27 g, 1.99 mmol, 88%) was obtained as a white solid.

The spectroscopic data match those reported in literature.[304]

^{1}H-NMR (500 MHz, $CDCl_3$): δ [ppm] = 7.83-7.77 (m, 6H), 7.71-7.65 (m, 6H), 4.94 (s, 6H), 3.10 (q, *J* = 7.6 Hz, 6H), 0.96 (t, *J* = 7.5 Hz, 9H).

^{13}C-NMR (126 MHz, $CDCl_3$): δ [ppm] = 168.4, 145.7, 134.0, 132.2, 129.6, 123.4, 37.6, 23.5, 15.9.

(2,4,6-Triethylbenzene-1,3,5-triyl)trimethanamine (128c)

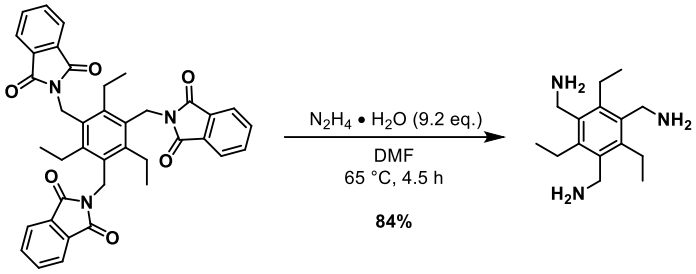

1.0 eq.
200
$C_{39}H_{33}N_3O_6$
M = 639.71 g/mol

128c
$C_{15}H_{27}N_3$
M = 249.40 g/mol

The title compound (**128c**) was synthesized according to the procedure that was previously described for the tributyl derivative.[281]

A dried 25 mL flask was charged with a stir bar, trisphthalimide **200** (291 mg, 0.455 mmol, 1.00 eq.) and dry EtOH (8.7 mL). Hydrazine monohydrate (0.20 mL, 210 mg, 4.2 mmol, 9.2 eq.) was added and the reaction mixture was refluxed (90 °C oilbath temperature) for 30 min. The mixture was cooled to room temperature and aq. HCl (6 M, 3 mL) was added. The mixture was refluxed (90 °C oilbath temperature) for 30 min and again cooled to room temperature. The reaction mixture was poured into aq. NaOH (1 M, 50 mL). $CHCl_3$ (50 mL) was added, and the phases were separated. The aq. phase was extracted with $CHCl_3$ (2 x 50 mL). The combined org. phases were washed with brine (40 mL) and dried over Na_2SO_4. The solvent was removed under reduced pressure. The title compound (**128c**, 94.8 mg, 0.380 mmol, 84%) was obtained as a white solid.

The spectroscopic data match those reported in literature.[304]

^{1}H-NMR (500 MHz, $CDCl_3$): δ [ppm] = 3.87 (s, 6H), 2.82 (q, *J* = 7.5 Hz, 6H), 1.23 (t, *J* = 7.5 Hz, 6H).

^{13}C-NMR (126 MHz, $CDCl_3$): δ [ppm] = 140.5, 137.5, 39.8, 22.7, 16.9.

Tri^{2}Di^3 Imine Cage XXIIIc

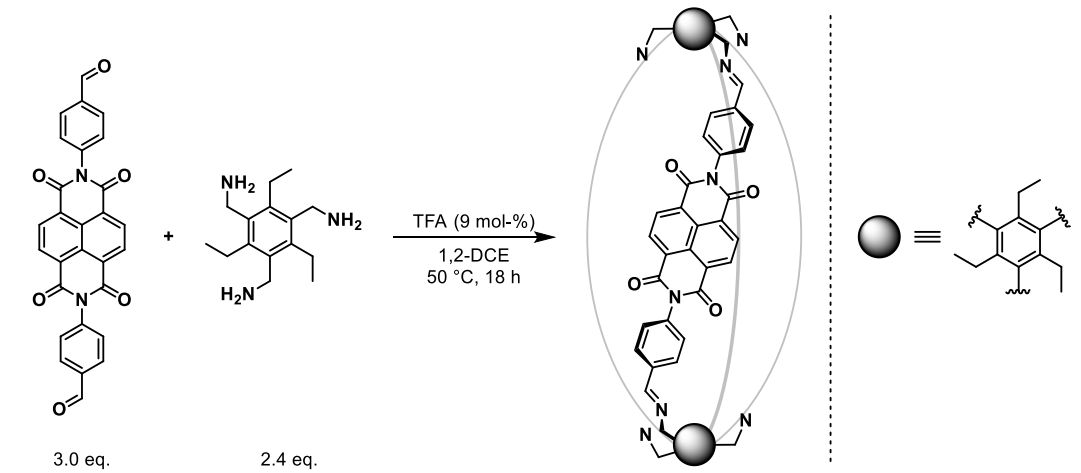

The title compound **XXIIIc** has not been isolated and evidence for its possible formation has only been gathered during a screening process:

A 25 mL flask was charged with a stir bar, dialdehyde **175** (15.0 mg, 0.0316 mmol, 3.00 eq.), triamine **128c** (6.28 mg, 0.0252 mmol, 2.40 eq.) and 1,2-DCE (16.5 mL). A stock solution of trifluoroacetic acid (1.88 mM, 0.5 mL, 9 mol-%) was added and 0.8 mL of the mixture was transferred into a 1 mL Vial, equipped with a stirrer. The reaction mixture was placed into a heating block and stirred at 50 °C for 18 h. A clear colourless solution formed, and a sample of 0.3 mL was taken to remove the solvent under a gentle stream of nitrogen gas. The solid residue was diluted with DMSO-d_6 and subjected to ^{1}H-NMR spectroscopy. The rest of the reaction mixture was diluted with *n*-pentane (1 mL). The precipitate was centrifuged, and the solid residue was used to make a stock solution for HR-MS analysis in MeCN with the following analytical data as the only evidence for the formation of the title product **XXIIIc**:

^{1}H-NMR (500 MHz, DMSO-d_6): δ [ppm] = 7.84 (s, 12H, NDI-H), 7.68 (s, 6H, Imine-H), 7.38 (m_c, 12H), 7.32 (m_c, 12H), 5.10 (s, 12H, N-CH_2), 2.76 (q, J = 7.5 Hz, 12H, CH_2-CH$_3$), 1.13 (t, J = 7.2 Hz, 18H, CH$_2$-CH_3).

HR-MS (pos. ESI):

calculated for $C_{114}H_{86}N_{12}O_{12}$	$[M+2H]^{2+}$:	907.8254,	found: 907.8260
calculated for $C_{114}H_{85}N_{12}O_{12}$	$[M+H]^{+}$:	1814.6438,	found: 1814.6428

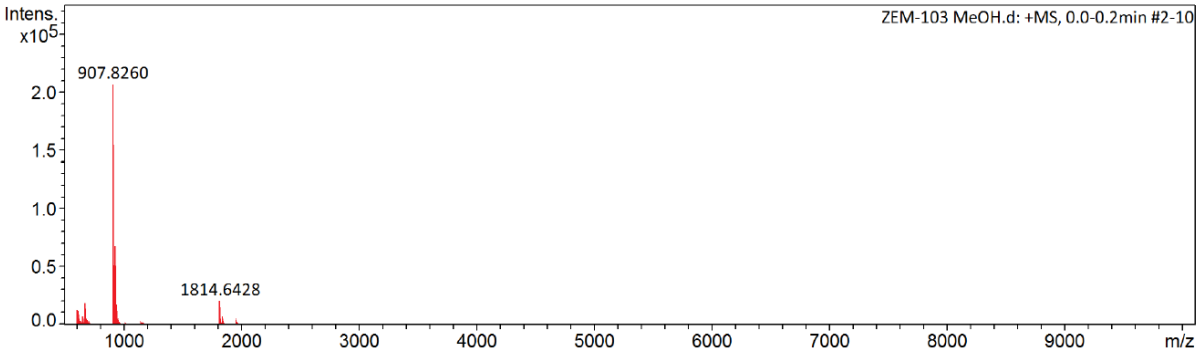

Figure 46: Full HR-MS report of the reaction towards **XXIIIc**.

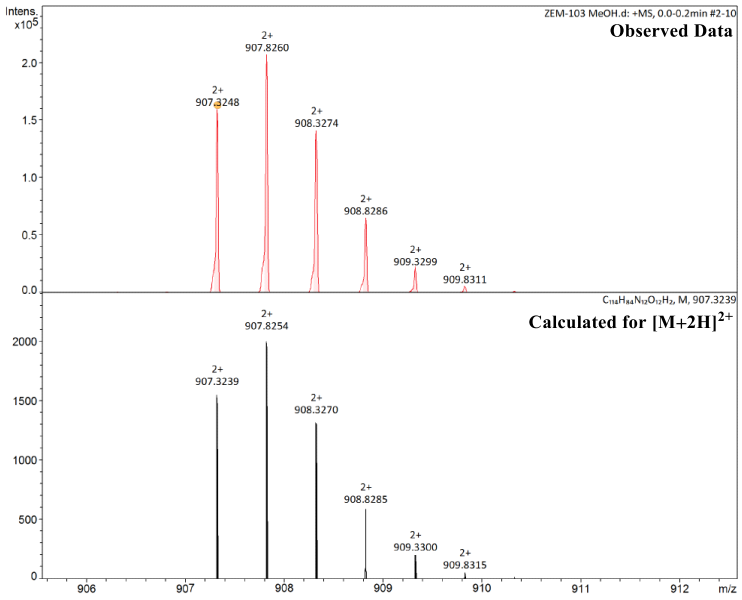

Figure 47: Observed and calculated HR-MS data for the $[M+2H]^{2+}$ species of **XXIIIc**.

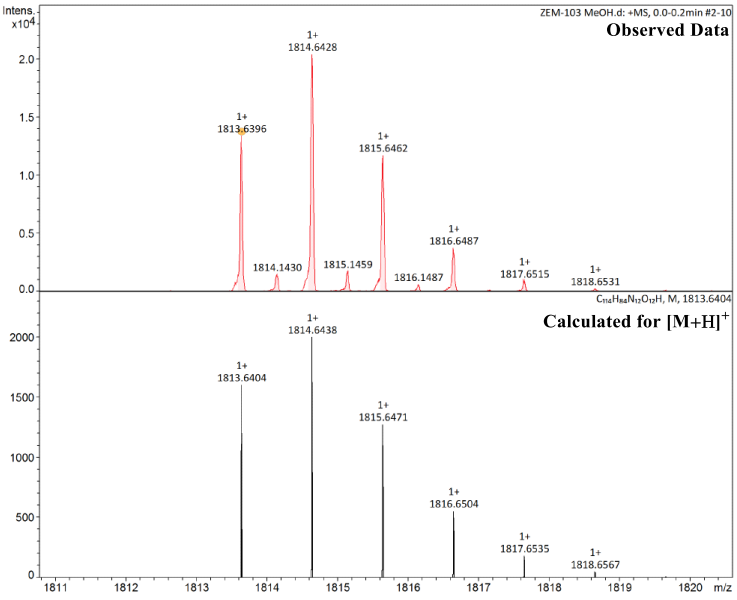

Figure 48: Observed and calculated HR-MS data for the $[M+H]^{+}$ species of **XXIIIc**.

5.2.3 Synthesis of $Fe_4L_6(NTf_2)_8$ Tetrahedron XXIX

2,7-Bis(4-aminophenyl)benzo[*lmn*][3,8]phenanthroline-1,3,6,8(2*H*,7*H*)-tetraone (215)

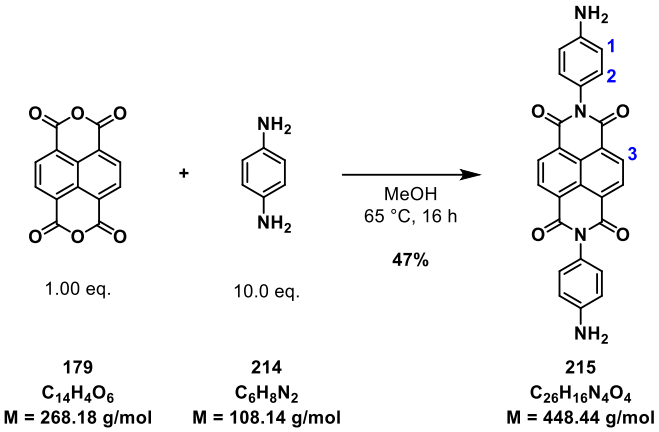

The title compound (**215**) was synthesized as previously described in literature.[286]

A dried 100 mL two-neck flask was charged with a stir bar, 1,4-diaminobenzene (**214**, 811 mg, 7.50 mmol, 10.0 eq.) and NDA (**179**, 0.201 g, 0.750 mmol, 1.00 eq.). Dry MeOH (34 mL) was added, and the reaction mixture was stirred at 65 °C for 16 h. The mixture was allowed to cool down to room temperature and the resulting suspension was filtered off. The solid material was washed with excess MeOH and dried under high vacuum. The brown solid was suspended in $CHCl_3$, stirred and filtered off again. The solid material was dissolved in hot DMF. After hot filtration, the filtrate was allowed to cool down to room temperature. The solvent of the resulting filtrate was removed under reduced pressure and the residue was dried under high vacuum. The title compound (**215**, 157 mg, 0.350 mmol, 47%) was obtained as a brown solid.

^{1}H-NMR (500 MHz, DMSO-*d*$_6$): δ [ppm] = 8.69 (s, 4H, 3-H), 7.01 (d, $^3J_{ortho}$ = 8.6 Hz, 4H, 2-H), 6.66 (d, $^3J_{ortho}$ = 8.6 Hz, 4H, 1-H), 5.30 (br. s, 4H, N*H*$_2$).

^{13}C-NMR (126 MHz, DMSO-*d*$_6$): δ [ppm] = 163.2, 148.8, 130.4, 129.1, 127.0, 126.6, 123.3, 113.7.

MS (EI): 448.1 {$C_{26}H_{14}N_4O_4$ $[M]^{+\bullet}$}

The analytical data are in accordance with those reported in the literature.[286]

$Fe_4L_6(NTf_2)_8$ Tetrahedron XXIX

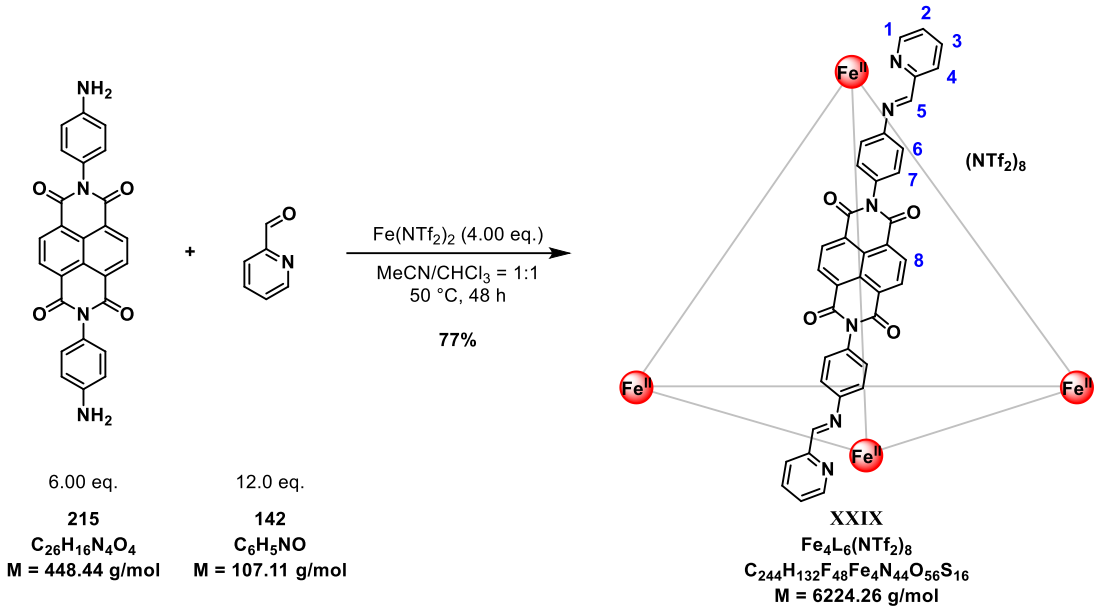

6.00 eq. **215** $C_{26}H_{16}N_4O_4$ **M = 448.44 g/mol**

12.0 eq. **142** C_6H_5NO **M = 107.11 g/mol**

XXIX $Fe_4L_6(NTf_2)_8$ $C_{244}H_{132}F_{48}Fe_4N_{44}O_{56}S_{16}$ **M = 6224.26 g/mol**

The title compound (**XXIX**) was synthesized as previously described and the spectroscopic data match those reported in literature.[98]

A dried 100 mL Schlenk tube was charged with a stir bar, NDI diamine (**215**, 100 mg, 0.223 mmol, 6.00 eq.) and iron(II) triflimide (91.8 mg, 0.149 mmol, 4.00 eq.). Picolinaldehyde (**142**, 42.4 µL, 47.7 mg, 0.446 mmol, 12.0 eq.) and dry MeCN (10 mL) were added to the mixture. The reaction mixture was stirred at 50 °C for 48 h. The resulting purple solution was allowed to cool down to room temperature, filtered through cotton and poured into methyl *tert*-butyl ether. The resulting purple solid material was collected by filtration. **$Fe_4L_6(NTf_2)_8$** cage **XXIX** (178 mg, 0.0286 mmol, 77%) was obtained as a fine purple powder.

^{1}H-NMR (700 MHz, MeCN-d_3): δ [ppm] = 9.14-8.94 (m, 12H, 5-H), 8.83-8.47 (m, 36H, 1-H, 8-H), 8.47-8.35 (m, 12H, 2-H), 7.84-7.71 (m, 12H, 3-H), 7.63-7.24 (m, 36H, 4-H, 7-H), 6.12-5.21 (m, 24H, 6-H).

^{13}C-NMR (176 MHz, MeCN-d_3): δ [ppm] = 176.8, 176.4, 176.2, 164.6, 164.4, 164.4, 164.3, 164.3, 164.0, 159.2, 159.1, 159.1, 157.0, 156.9, 151.5, 151.4, 151.0, 140.9, 140.8, 140.8, 137.0, 136.7, 136.7, 132.7, 132.5, 132.4, 132.2, 131.8, 131.8, 131.6, 131.0, 130.9, 130.8, 130.3, 128.4, 128.4, 128.4, 128.3, 128.3, 128.3, 128.2, 128.1, 124.8, 123.5, 123.4, 123.3, 123.1, 120.9 (q, J = 322.8 Hz, CF$_3$).

The ^{1}H- and ^{13}C-NMR data are in accordance with those reported in the literature.[98]

^{19}F-NMR (471 MHz, MeCN-d_3, C_6F_6 as int. Std.): δ [ppm] = –80.6.

DOSY-NMR (600 MHz, MeCN-d_3, 298 K): Diffusion coefficient D = 3.78 • 10^{-6} cm^{2}s^{-1}

HR-MS (pos. ESI):

calculated for $C_{228}H_{132}Fe_4N_{36}O_{24}$	$[M-8NTf_2]^{8+}$:	497.8455,	found: 497.8461
calculated for $C_{230}H_{132}F_6Fe_4N_{37}O_{28}S_2$	$[M-7NTf_2]^{7+}$:	608.9545,	found: 608.9550
calculated for $C_{232}H_{132}F_{12}Fe_4N_{38}O_{32}S_4$	$[M-6NTf_2]^{6+}$:	757.0999,	found: 757.0999
calculated for $C_{234}H_{132}F_{18}Fe_4N_{39}O_{36}S_6$	$[M-5NTf_2]^{5+}$:	964.5034,	found: 964.5045
calculated for $C_{236}H_{132}F_{24}Fe_4N_{40}O_{40}S_8$	$[M-4NTf_2]^{4+}$:	1275.6087,	found: 1275.6123

The HR-MS data are in accordance with those reported in the literature.[98]

5.2.4 Synthesis of $Zn_2L_3(NTf_2)_4$ Helicate XXXII

2,7-Bis(6-methylpyridin-3-yl)benzo[*lmn*][3,8]phenanthroline-1,3,6,8 (2*H*,7*H*)-tetraone (219)

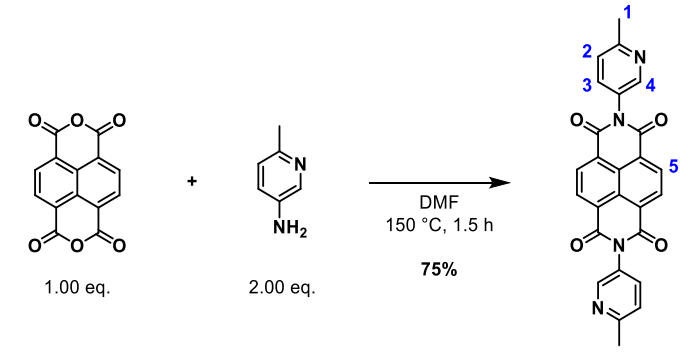

179
$C_{14}H_4O_6$
M = 268.18 g/mol

218
$C_6H_8N_2$
M = 108.14 g/mol

219
$C_{26}H_{16}N_4O_4$
M = 448.44 g/mol

A dried 250 mL flask was charged with a stir bar, 6-methylpyridine-3-amine (**218**, 1.61 g, 14.9 mmol, 2.00 eq.) and NDA (**179**, 85%, 2.35 g, 7.45 mmol, 1.00 eq.). Dry DMF (100 mL) was added, and the reaction mixture was stirred at 150 °C oilbath temperature for 1.5 h. The mixture was allowed to slowly cool down to room temperature and was then further cooled with an ice bath for 1 h. The crystals were filtered off, washed with excess acetone and dried under high vacuum. The title compound (**219**, 2.50 g, 5.57 mmol, 75%) was obtained in the form of a beige fuzzy solid.

M.p.: No melting or visual decomposition observed up until maximum temperature (400 °C).

IR (ATR): $\tilde{\nu}$ [cm^{-1}] = 3370 (w), 3084 (w), 3036 (w), 3015 (w), 2919 (w), 1708 (s), 1667 (vs), 1599 (m), 1579 (s), 1488 (s), 1445 (s), 1385 (m), 1347 (vs), 1293 (m), 1245 (vs), 1209 (s), 1191 (vs), 1129 (s), 1119 (s), 1027 (s), 975 (s), 879 (m), 862 (s), 845 (m), 834 (m), 777 (s), 761 (vs), 742 (vs), 642 (m), 573 (s), 520 (s), 429 (s), 415 (vs).

^{1}H-NMR (500 MHz, DMSO-*d*$_6$): δ [ppm] = 8.74 (s, 4H, 5-H), 8.53 (d, $^4J_{meta}$ = 2.5 Hz, 2H, 4-H), 7.81 (dd, $^3J_{ortho}$ = 8.1 Hz, $^4J_{meta}$ = 2.5 Hz, 2H, 3-H), 7.48 (d, $^3J_{ortho}$ = 8.1 Hz, 2H, 2-H), 2.59 (s, 6H, 1-H).

^{13}C-NMR (151 MHz, DMSO-*d*$_6$): δ [ppm] = 163.1, 158.1, 148.8, 137.0, 130.6, 129.8, 127.0, 126.7, 123.4, 23.9.

HR-MS (pos. ESI): calculated for $C_{26}H_{16}N_4O_4H$ $[M+H]^+$: 449.1244, found: 449.1244

5,5'-(1,3,6,8-Tetraoxo-1,3,6,8-tetrahydrobenzo[*lmn*][3,8]phenanthroline-2,7-diyl)di picolinaldehyde (176)

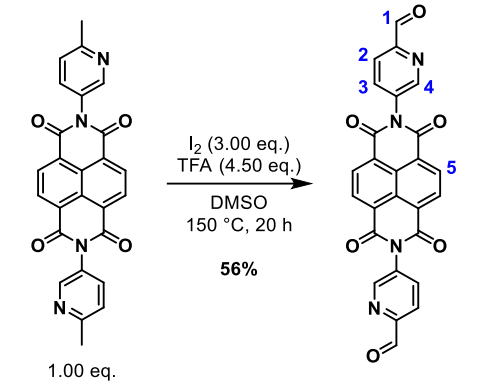

A dried 500 mL two-neck flask was charged with a stir bar, naphthalene diimide **219** (2.35 g, 5.25 mmol, 1.00 eq.) and dry DMSO (200 mL). Iodine (4.00 g, 15.8 mmol, 3.00 eq.) was added to the suspension. The mixture was stirred for 10 min at room temperature. Then, TFA (1.75 mL, 2.69 g, 23.6 mmol, 4.50 eq.) was added dropwise at room temperature and the reaction mixture was stirred at 150 °C for 20 h. The mixture was allowed to cool down to room temperature and then poured into ice-cold H_2O (400 mL). The suspension was filtered off and the solid material was successively washed with aq. Na_2SO_3 (3.6%, 4 x 70 mL), sat. aq. $NaHCO_3$ (1 x 50 mL), distilled H_2O (1 x 50 mL) and acetone (4 x 50 mL). The beige solid was dissolved in refluxing DMSO (150 mL). After hot filtration, the orange filtrate was allowed to cool down to room temperature. Ice-cold H_2O (150 mL) was added, and the precipitate was filtered off. The solid material was washed thoroughly with excess THF and acetone and then dried under high vacuum. The title compound (**176**, 1.40 g, 2.94 mmol, 56%) was obtained as a beige solid and used without further purification.

Note: Dry DMSO for the reaction was purged with dry argon gas for 30 min before use and an oven-dried reflux condenser was used and attached to the reaction flask under argon counterflow.

M.p.: Decomposition observed at 380 °C onwards.

IR (ATR): $\tilde{\nu}$ [cm^{-1}] = 3381 (w), 3075 (w), 3026 (w), 2853 (w), 1714 (s), 1704 (s), 1672 (vs), 1576 (s), 1474 (w), 1444 (m), 1346 (vs), 1247 (vs), 1195 (vs), 1145 (m), 1121 (m), 1022 (m), 984 (m), 901 (m), 861 (m), 821 (s), 786 (s), 770 (vs), 752 (s), 620 (m), 580 (m), 521 (w), 432 (m), 406 (s).

^{1}H-NMR (500 MHz, DMSO-d_6): δ [ppm] = 10.09 (s, 2H, 1-H), 8.96 (d, $^4J_{meta}$ = 2.2 Hz, 2H, 4-H), 8.79 (s, 4H, 5-H), 8.24 (dd, $^3J_{ortho}$ = 8.2 Hz, $^4J_{meta}$ = 2.2 Hz, 2H, 3-H), 8.19 (d, $^3J_{ortho}$ = 8.2 Hz, 2H, 2-H).

^{13}C-NMR (151 MHz, DMSO-d_6): δ [ppm] = 192.9, 162.9, 151.9, 150.6, 138.7, 136.1, 130.6, 127.0, 126.8, 122.1.

HR-MS (pos. ESI): calculated for $(C_{26}H_{12}N_4O_6)_2Na$ $[2M+Na]^+$: 975.1420, found: 975.1406

$Zn_2L_3(NTf_2)_4$ Helicate XXXII

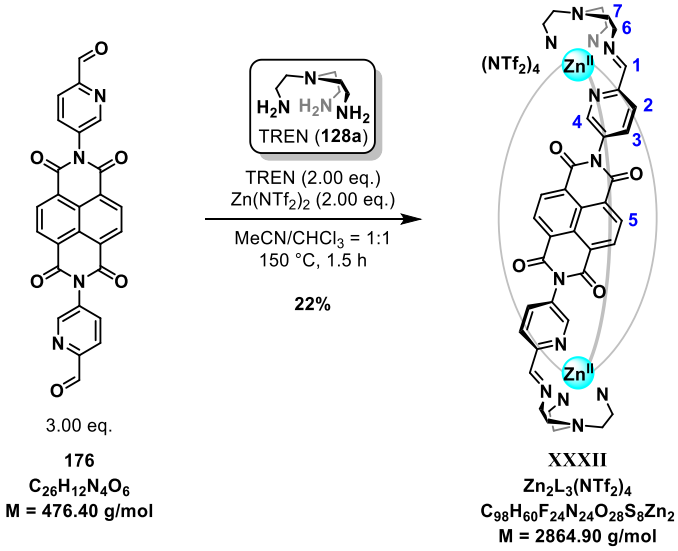

A dried 120 mL pressure tube was charged with a stir bar, NDI dialdehyde **176** (167 mg, 0.351 mmol, 3.00 eq.) and zinc(II) triflimide (146 mg, 0.233 mmol, 2.00 eq.). Dry MeCN (20 mL), dry $CHCl_3$ (20 mL) and tris(2-aminoethyl)amine (**128a**, 35.0 µL, 34.2 mg, 0.234 mmol, 2.00 eq.) were added and the mixture was ultrasonicated to form a homogenous suspension. The reaction mixture was heated to 150 °C while stirring vigorously for 1.5 h. The mixture was then cooled to room temperature and filtered over a celite pad. The solvent was removed under reduced pressure and the residue re-dissolved in just enough MeCN. The dark solution was diluted with excess Et_2O, and the suspension was centrifuged. The supernatant was decanted, and the black residue (310 mg divided into 100-105 mg aliquots) was subjected to size-exclusion chromatography with 1% cross-linked Bio-Beads SX-1 Support Resin (DCM/MeCN = 7:3, Column Dimensions: Diameter d = 4.5 cm, Height h = 34 cm, Gravity Flow). Residual side-products and polymers were removed by crystallization *via* slow diffusion of Et_2O into an MeCN solution of the product mixture. The supernatant was removed, and the crystals were dissolved in MeCN. Et_2O was added and the suspension was centrifuged. The supernatant was decanted, and the residue dried under high vacuum. **$Zn_2L_3(NTf_2)_4$** helicate **XXXII** (75.0 mg, 0.0262 mmol, 22%) was obtained as a microcrystalline yellow solid.

Note: Dry MeCN and dry $CHCl_3$ for the reaction were purged with dry argon gas for 30 min before use. During crystallization, a polymer precipitate forms alongside the product crystals which does not readily dissolve back when adding MeCN to re-dissolve the crystals.

M.p.: Decomposition observed at 330 °C onwards.

IR (ATR): $\tilde{\nu}$ [cm^{-1}] = 3629 (w), 3552 (w), 3084 (w), 2945 (w), 2865 (w), 1722 (m), 1674 (s), 1578 (m), 1492 (w), 1449 (m), 1324 (vs), 1174 (vs), 1128 (vs), 1048 (vs), 983 (s), 939 (m), 875 (s), 846 (s), 788 (m), 764 (vs), 732 (s), 649 (m), 599 (s), 569 (vs), 545 (m), 507 (vs), 474 (m), 428 (s), 407 (s).

^{1}H-NMR (500 MHz, MeCN-d_3): δ [ppm] = 8.85 (d, J = 1.0 Hz, 6H, 1-H), 8.44 (dd, $^3J_{ortho}$ = 8.2 Hz, $^4J_{meta}$ = 2.3 Hz, 6H, 3-H), 8.23 (dd, $^3J_{ortho}$ = 8.2 Hz, 6H, 2-H), 8.11 (d, $^4J_{meta}$ = 2.2 Hz, 6H, 4-H), 7.91 (br. s, 12H, 5-H), 4.08-3.97 (m, 6H, 6-H), 3.74 (dd, J = 11.5 Hz, J = 3.4 Hz, 6H, 6-H), 3.35 (dd, J = 13.7 Hz, J = 3.5 Hz, 6H, 7-H), 3.08 (ddd, J = 13.6 Hz, J = 13.6 Hz, J = 3.7 Hz, 6H, 7-H).

^{13}C-NMR (126 MHz, MeCN-d_3): δ [ppm] = 165.0, 162.7, 150.0, 147.2, 142.2, 135.7, 132.0, 129.6, 127.0, 126.9, 120.9 (q, J = 320.8 Hz, CF_3), 58.3, 55.1.

^{19}F-NMR (471 MHz, MeCN-d_3, $CFCl_3$ as int. Std.): δ [ppm] = –78.9.

DOSY-NMR (600 MHz, MeCN-d_3, 298 K): Diffusion coefficient $D = 6.40 \cdot 10^{-6}$ cm²s^{-1}

HR-MS (pos. ESI):

calculated for $C_{90}H_{60}N_{20}O_{12}Zn_2$ $[M–4NTf_2]^{4+}$: 435.5807, found: 435.5826

calculated for $C_{92}H_{60}F_6N_{21}O_{16}S_2Zn_2$ $[M–3NTf_2]^{3+}$: 675.0811, found: 675.0828

calculated for $C_{94}H_{60}F_{12}N_{22}O_{20}S_4Zn_2$ $[M–2NTf_2]^{2+}$: 1152.0801, found: 1152.0820

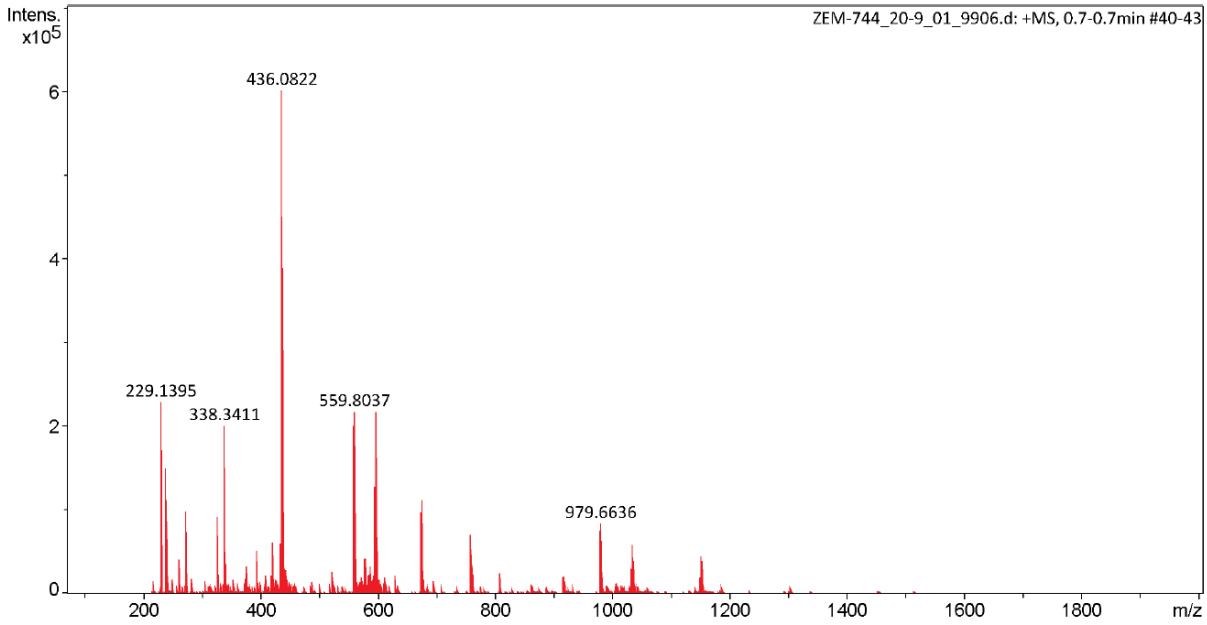

Figure 49: Full HR-MS report of **$Zn_2L_3(NTf_2)_4$** helicate **XXXII**.

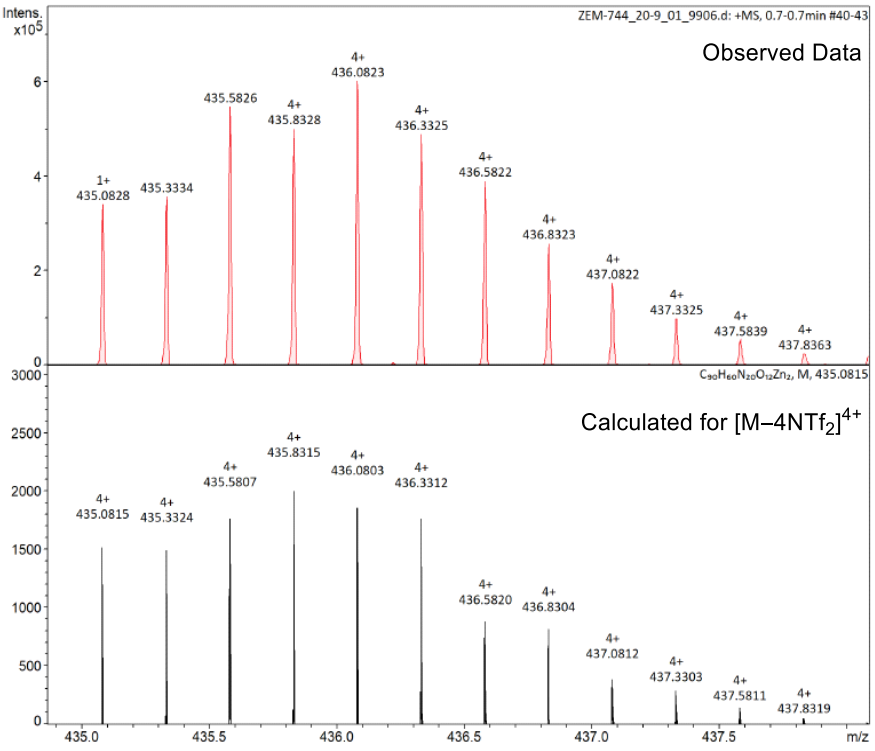

Figure 50: Observed and calculated HR-MS data for the $[M–4NTf_2]^{4+}$ species of **$Zn_2L_3(NTf_2)_4$** helicate **XXXII**.

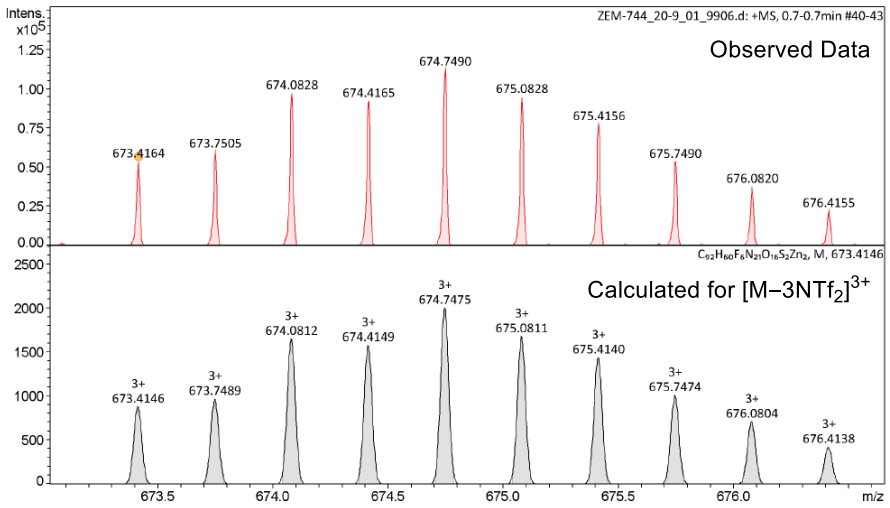

Figure 51: Observed and calculated HR-MS data for the $[M–3NTf_2]^{3+}$ species of **$Zn_2L_3(NTf_2)_4$** helicate **XXXII**.

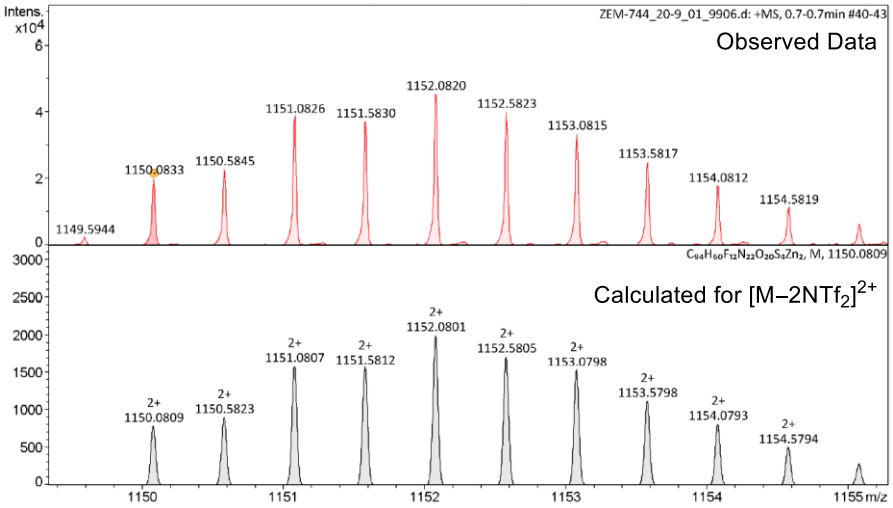

Figure 52: Observed and calculated HR-MS data for the $[M–2NTf_2]^{2+}$ species of **$Zn_2L_3(NTf_2)_4$** helicate **XXXII**.

5.2.5 Synthesis of $Zn_4L_4(NTf_2)_8$ Tetrahedron Zn-XLIII

1,3,5-Tris((trimethylsilyl)ethynyl)benzene (246)

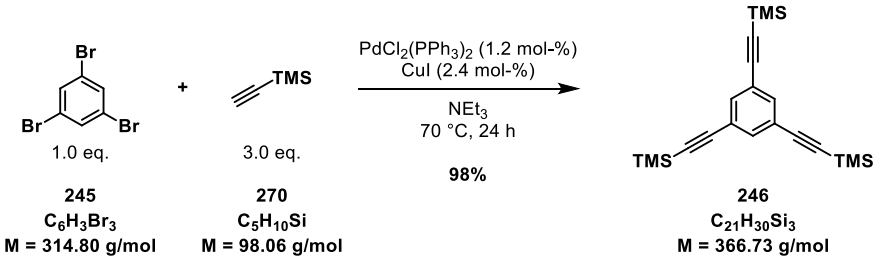

1,3,5-Tris((trimethylsilyl)ethynyl)benzene (**246**) was synthesized as previously described and the spectroscopic data match those reported in literature.[296]

^{1}H-NMR (500 MHz, $CDCl_3$): δ [ppm] = 7.49 (s, 3H), 0.23 (s, 27H).

^{13}C-NMR (151 MHz, $CDCl_3$): δ [ppm] = 135.1, 123.8, 103.3, 95.7, 0.0.

1,3,5-Triethynylbenzene (247)

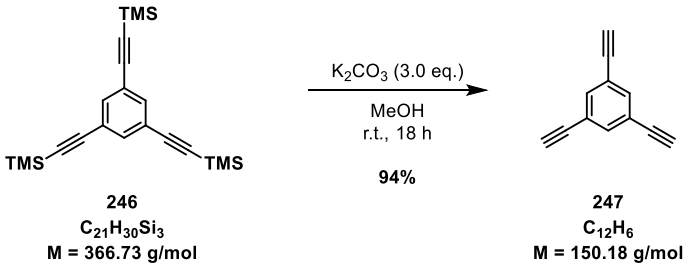

1,3,5-Triethynylbenzene (**247**) was synthesized as previously described and the spectroscopic data match those reported in literature.[297]

^{1}H-NMR (500 MHz, $CDCl_3$): δ [ppm] = 7.57 (s, 3H), 3.10 (s, 3H).

^{13}C-NMR (151 MHz, $CDCl_3$): δ [ppm] = 135.8, 123.0, 81.7, 78.8.

5,5',5''-(Benzene-1,3,5-triyltris(ethyne-2,1-diyl))tripicolinaldehyde (178)

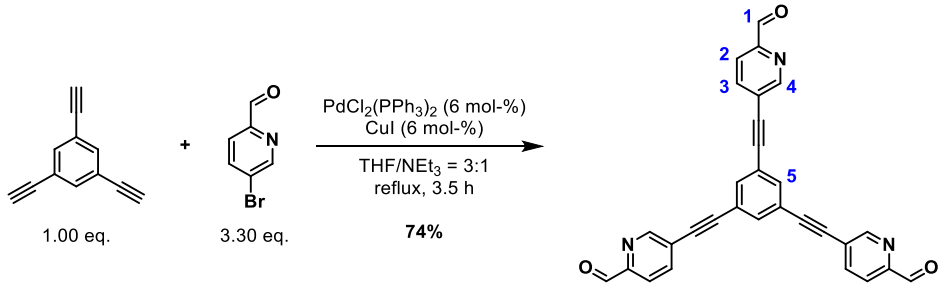

A dried 100 mL round-bottom flask was charged with 1,3,5-triethynylbenzene (**247**, 751 mg, 5.00 mmol, 1.00 eq.), 5-bromopyridine-2-carbaldeyhde (**251**, 3.07 g, 16.5 mmol, 3.30 eq.), $PdCl_2(PPh_3)_2$ (212 mg, 0.302 mmol, 6.04 mol-%) and copper(I)-iodide (60.4 mg, 0.317 mmol, 6.34 mol-%). Dry THF (45 mL) and dry NEt_3 (15 mL) were added, and the reaction mixture was refluxed at 85 °C oil bath temperature for 3.5 h. The solvent was removed under reduced pressure and the crude product was suspended in acetone. The suspension was ultrasonicated, heated to reflux and subjected to hot filtration. The filtering cake was washed with excess hot acetone and a beige solid was collected. This hot filtration procedure was repeated once again with the beige solid residue. The title product (**178**, 1.78 g, 3.82 mmol, 76%) was obtained as a beige powder and used without further purification.

Note: Dry THF and dry NEt_3 for the reaction were purged with dry argon gas for 30 min before use and an oven-dried reflux condenser was used and attached to the reaction flask under argon counterflow.

M.p.: Decomposition observed at 200 °C onwards.

IR (ATR): $\tilde{\nu}$ [cm^{-1}] = 3051 (m), 2822 (m), 2709 (w), 2207 (m), 1706 (vs), 1576 (s), 1553 (m), 1477 (w), 1416 (w), 1364 (m), 1289 (m), 1267 (w), 1206 (s), 1116 (m), 1019 (m), 928 (w), 878 (m), 842 (s), 726 (vs), 677 (m), 644 (m), 610 (m), 587 (m), 524 (w), 408 (s).

^{1}H-NMR (500 MHz, DCM-d_2): δ [ppm] = 10.07 (d, $^5J_{1,3}$ = 0.8 Hz, 3H, 1-H), 8.94 (dd, $^4J_{meta}$ = 2.0 Hz, $^5J_{para}$ = 0.8 Hz, 3H, 4-H), 8.03 (ddd, $^3J_{ortho}$ = 8.1 Hz, $^4J_{meta}$ = 2.0 Hz, $^5J_{3,1}$ = 0.8 Hz, 3H, 3-H), 7.96 (dd, $^3J_{ortho}$ = 8.1 Hz, $^5J_{para}$ = 0.9 Hz, 3H, 2-H), 7.83 (s, 3H, 5-H).

^{13}C-NMR (151 MHz, DCM-d_2): δ [ppm] = 192.92, 152.97, 151.84, 139.98, 135.62, 124.29, 123.80, 121.24, 93.08, 87.57.

HR-MS (pos. ESI): calculated for $C_{30}H_{16}N_3O_3$ $[M+H]^+$: 466.1186, found: 466.1188

Note: The ^{1}H-NMR coupling pattern was assigned with the ^5J coupling between protons 1 and 3 in mind. This long-range spin-spin coupling constant in pyridine-2-aldehydes has been extensively studied by WOOD *et al.* in 1974 in various solvents[305] and could sometimes be observed for this compound and sometimes not in the ^{1}H-NMR spectra.

$Zn_4L_4(NTf_2)_8$ Tetrahedron Zn-XLIII

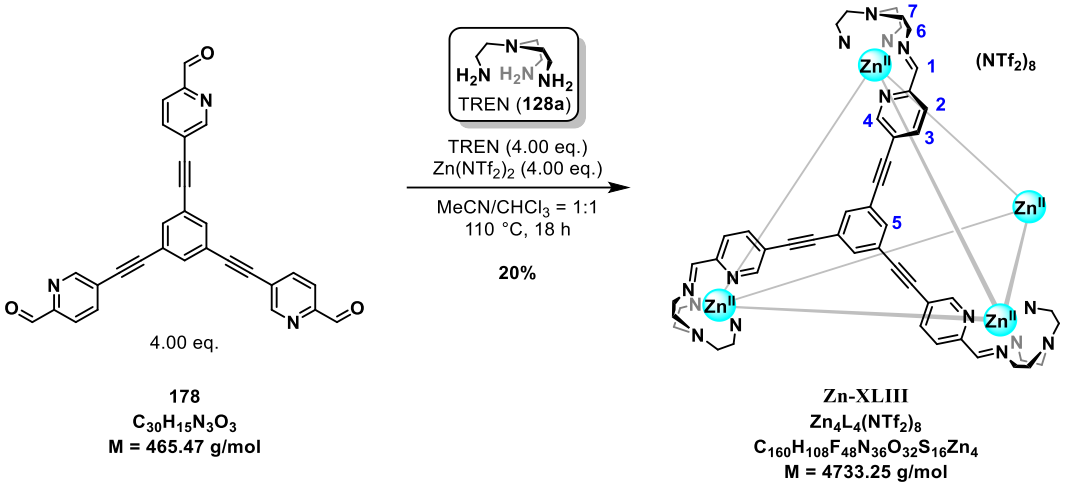

178
$C_{30}H_{15}N_3O_3$
M = 465.47 g/mol

Zn-XLIII
$Zn_4L_4(NTf_2)_8$
$C_{160}H_{108}F_{48}N_{36}O_{32}S_{16}Zn_4$
M = 4733.25 g/mol

A dried 350 mL pressure tube was charged with a stir bar, trialdehyde **178** (354 mg, 0.761 mmol, 4.00 eq.) and zinc(II) triflimide (476 mg, 0.761 mmol, 4.00 eq.). Dry MeCN (38 mL), dry $CHCl_3$ (38 mL) and tris(2-aminoethyl)amine (**128a**, 114 µL, 111 mg, 0.759 mmol, 3.99 eq.) were added and the mixture was ultrasonicated. The reaction mixture was heated to 110 °C while stirring vigorously for 18 h. The mixture was then cooled to room temperature and filtered over a celite pad. The solvent was removed under reduced pressure and the residue re-dissolved in just enough MeCN. The dark solution was diluted with excess Et_2O, and the suspension was centrifuged. The supernatant was decanted, and the black residue (781 mg divided into 80-105 mg aliquots) was subjected to size-exclusion chromatography with 1% cross-linked Bio-Beads SX-1 Support Resin (DCM/MeCN = 7:3, Column Dimensions: Diameter d = 4.5 cm, Height h = 34 cm, Gravity Flow). Residual side-products and polymers were removed by crystallization *via* slow diffusion of Et_2O into an MeCN solution of the product mixture. The supernatant was removed, and the crystals were dissolved in MeCN. Et_2O was added and the suspension was centrifuged. The supernatant was decanted, and the residue dried under high vacuum. **$Zn_4L_4(NTf_2)_8$** tetrahedron **Zn-XLIII** (180 mg, 0.0380 mmol, 20%) was obtained as a microcrystalline amber solid.

Note: Dry MeCN and dry $CHCl_3$ for the reaction were purged with dry argon gas for 30 min before use. During crystallization, a polymer precipitate forms alongside the product crystals which does not readily dissolve back when adding MeCN to re-dissolve the crystals.

M.p.: Decomposition observed at 250 °C onwards.

IR (ATR): $\tilde{\nu}$ [cm^{-1}] = 3071 (w), 2931 (w), 2863 (w), 2211 (w), 1656 (m), 1592 (m), 1558 (m), 1462 (w), 1450 (w), 1419 (w), 1345 (s), 1174 (vs), 1128 (vs), 1048 (vs), 965 (m), 936 (m), 878 (m), 849 (m), 787 (m), 759 (m), 738 (m), 652 (m), 598 (s), 569 (s), 506 (s), 464 (m), 415 (m).

^{1}H-NMR (500 MHz, MeCN-d_3): δ [ppm] = 8.69 (s, 12H, 1-H), 8.38 (dd, $^3J_{ortho}$ = 8.1 Hz, $^4J_{meta}$ = 2.0 Hz, 12H, 3-H), 8.09 (d, $^3J_{ortho}$ = 8.1 Hz, 12H, 2-H), 7.61 (s, 12H, 5-H), 7.60 (d, $^4J_{meta}$ = 2.0 Hz, 12H, 4-H), 3.77-3.63 (m, 12H, 6-H), 3.55 (dd, *J* = 11.3 Hz, *J* = 3.2 Hz, 12H, 6-H), 3.27 (dd, *J* = 13.7 Hz, *J* = 3.3 Hz, 12H, 7-H), 2.90 (ddd, *J* = 13.7 Hz, *J* = 13.7 Hz, *J* = 3.5 Hz, 12H, 7-H).

^{13}C-NMR (151 MHz, MeCN-d_3): δ [ppm] = 164.1, 151.7, 146.7, 144.9, 136.2, 129.5, 125.8, 124.0, 120.9 (q, *J* = 321.0 Hz, *C*F_3), 94.7, 87.6, 57.6, 55.9.

^{19}F-NMR (471 MHz, MeCN-d_3, $CFCl_3$ as int. Std.): δ [ppm] = –78.8.

DOSY-NMR (600 MHz, MeCN-d_3, 298 K): Diffusion coefficient D = 4.59 • 10^{-6} cm^2s^{-1}

HR-MS (pos. ESI):

calculated for $C_{144}H_{108}N_{28}Zn_4$ $[M–8NTf_2]^{8+}$: 311.4551, found: 311.4563

calculated for $C_{146}H_{108}F_6N_{29}O_4S_2Zn_4$ $[M–7NTf_2]^{7+}$: 396.3650, found: 396.3666

calculated for $C_{148}H_{108}F_{12}N_{30}O_8S_4Zn_4$ $[M–6NTf_2]^{6+}$: 509.0787, found: 509.0805

calculated for $C_{150}H_{108}F_{18}N_{31}O_{12}S_6Zn_4$ $[M–5NTf_2]^{5+}$: 666.4787, found: 666.4798

calculated for $C_{152}H_{108}F_{24}N_{32}O_{16}S_8Zn_4$ $[M–4NTf_2]^{4+}$: 903.0778, found: 903.0790

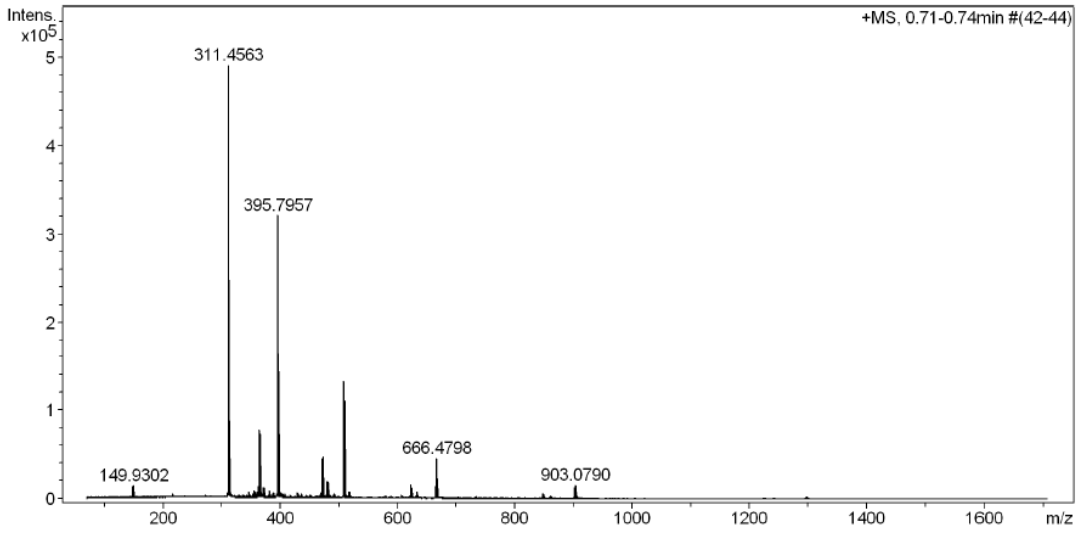

Figure 53: Full HR-MS report of **$Zn_4L_4(NTf_2)_8$** tetrahedron **Zn-XLIII**.

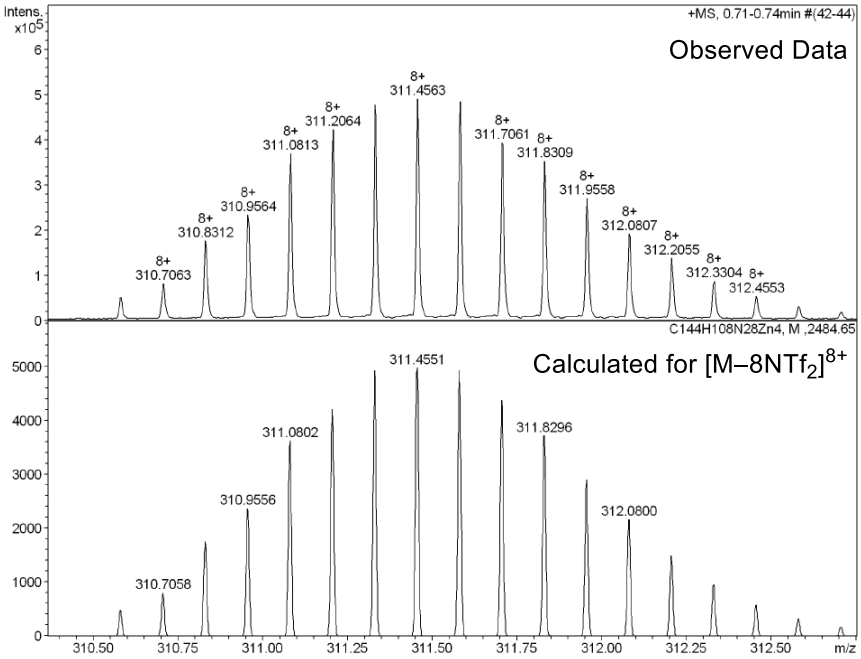

Figure 54: Observed and calculated HR-MS data for the $[M–8NTf_2]^{8+}$ species of **$Zn_4L_4(NTf_2)_8$** tetrahedron **Zn-XLIII**.

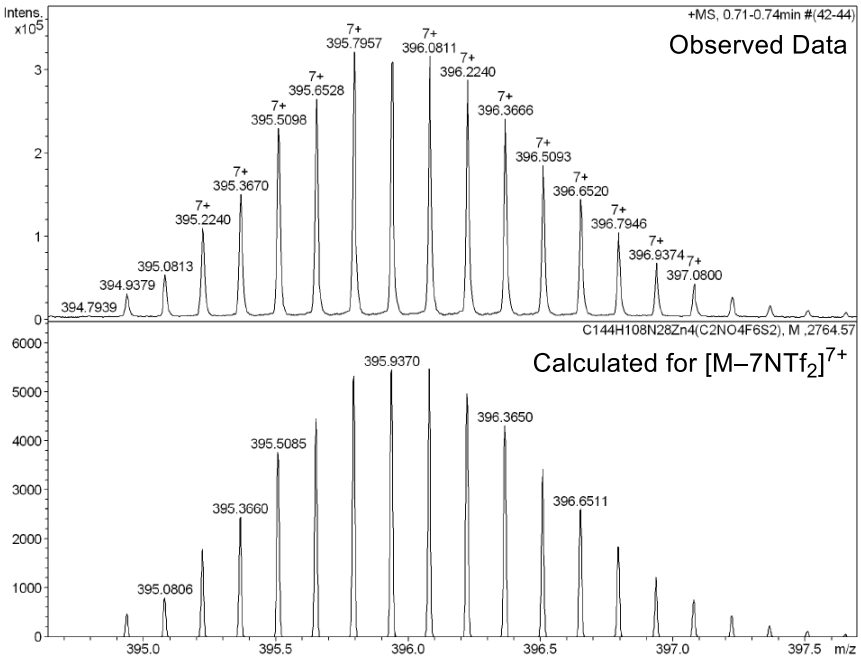

Figure 55: Observed and calculated HR-MS data for the $[M–7NTf_2]^{7+}$ species of **$Zn_4L_4(NTf_2)_8$** tetrahedron **Zn-XLIII**.

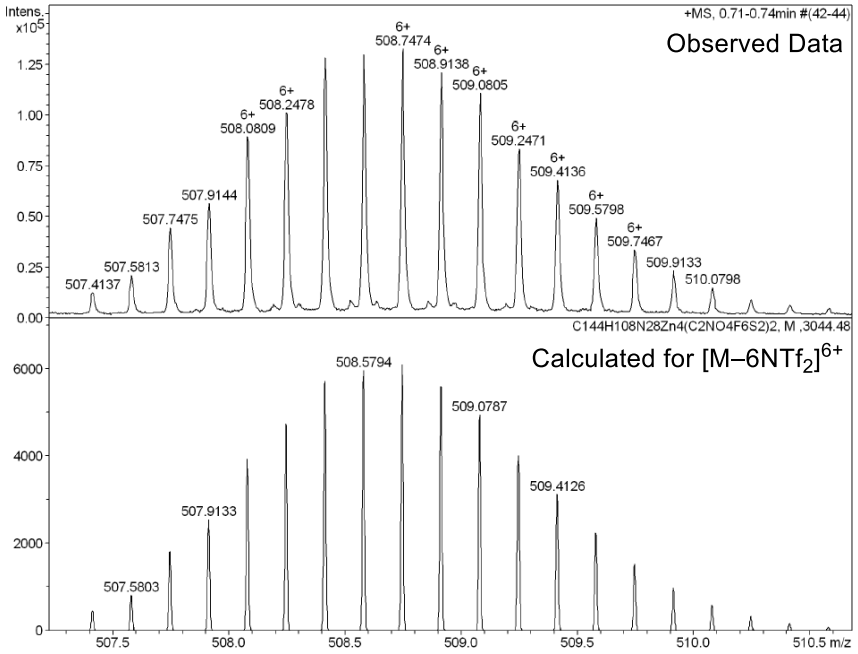

Figure 56: Observed and calculated HR-MS data for the $[M–6NTf_2]^{6+}$ species of **$Zn_4L_4(NTf_2)_8$** tetrahedron **Zn-XLIII**.

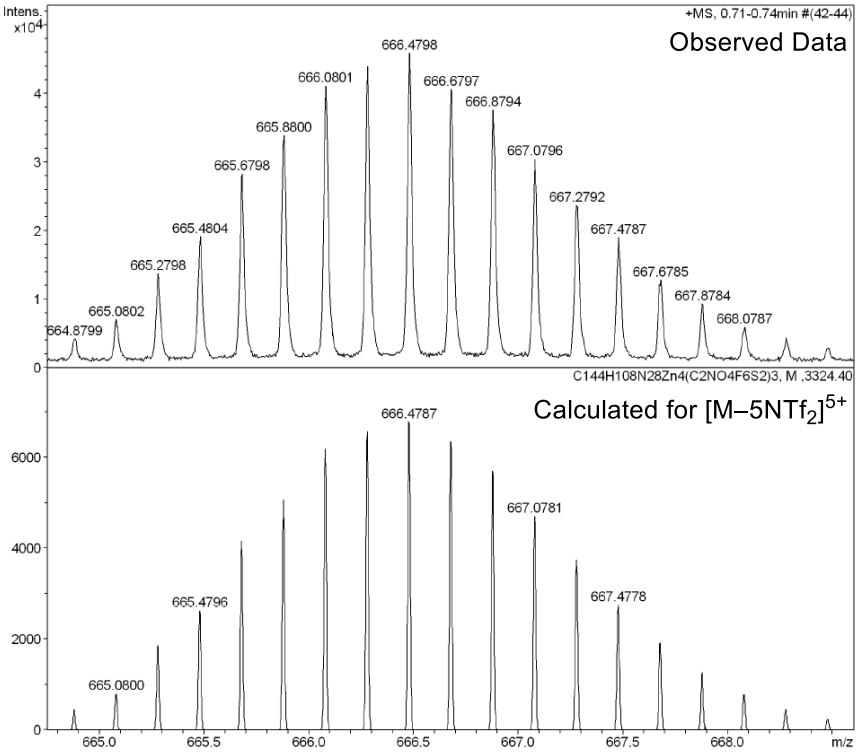

Figure 57: Observed and calculated HR-MS data for the $[M–5NTf_2]^{5+}$ species of **$Zn_4L_4(NTf_2)_8$** tetrahedron **Zn-XLIII**.

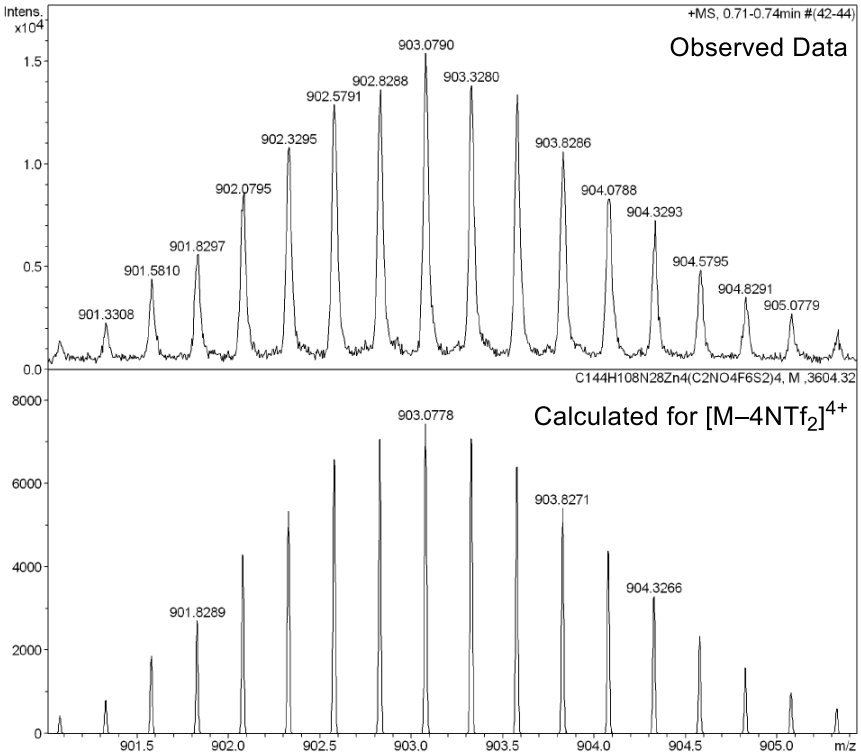

Figure 58: Observed and calculated HR-MS data for the $[M–4NTf_2]^{4+}$ species of **$Zn_4L_4(NTf_2)_8$** tetrahedron **Zn-XLIII**.

5.2.6 Synthesis of Mononuclear $ZnL_3(NTf_2)_2$ Complex XLIV

Mononuclear $ZnL_3(NTf_2)_2$ Complex XLIV

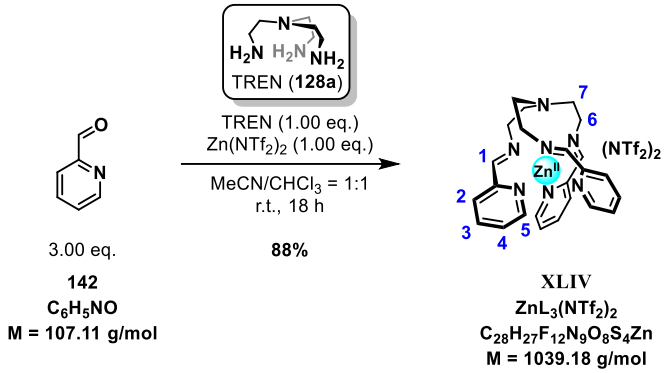

A dried 25 mL two-neck flask was charged with a stir bar, picolinaldehyde **142** (38.2 µL, 42.8 mg, 0.400 mmol, 3.00 eq.) and zinc(II) triflimide (83.4 mg, 0.133 mmol, 1.00 eq.). Dry MeCN (10 mL), dry $CHCl_3$ (10 mL) and tris(2-aminoethyl)amine (**128a**, 20.0 µL, 19.5 mg, 0.133 mmol, 1.00 eq.) were added to give a yellow solution. The reaction mixture was stirred at room temperature for 18 h. The solvent was removed under reduced pressure. The solid residue was triturated with ice-cold $CHCl_3$. The yellow supernatant was removed. This was repeated once more to give the title product (**XLIV**, 122 mg, 0.117 mmol, 88%) as a white solid.

M.p.: Decomposition observed at 180 °C onwards.

IR (ATR): $\tilde{\nu}$ [cm^{-1}] = 3073 (w), 2946 (w), 2867 (w), 2826 (w), 1661 (m), 1599 (m), 1447 (m), 1347 (s), 1330 (s), 1309 (m), 1226 (m), 1179 (vs), 1134 (vs), 1108 (m), 1047 (vs), 1013 (s), 979 (m), 931 (m), 892 (m), 872 (m), 776 (s), 739 (s), 637 (m), 610 (vs), 568 (vs), 504 (vs), 457 (m), 416 (s).

^{1}H-NMR (500 MHz, MeCN-d_3): δ [ppm] = 8.62 (d, J = 1.7 Hz, 3H, 1-H), 8.22 (ddd, J = 7.7 Hz, J = 7.7 Hz, J = 1.7 Hz, 3H, 3-H), 7.97 (ddd, J = 7.7 Hz, J = 1.0 Hz, J = 1.0 Hz, 3H, 2-H), 7.59 (ddd, J = 7.8 Hz, J = 5.0 Hz, J = 1.2 Hz, 3H, 4-H), 7.30 (m, 3H, 5-H), 3.69 (m, 3H, 6-H), 3.51 (dd, J = 11.7 Hz, J = 3.6 Hz, 3H, 6-H), 3.22 (dd, J = 13.9 Hz, J = 3.9 Hz, 3H, 7-H), 2.86 (ddd, J = 13.6 Hz, J = 13.6 Hz, J = 3.8 Hz, 3H, 7-H).

^{13}C-NMR (151 MHz, MeCN-d_3): δ [ppm] = 164.0, 149.4, 147.8, 142.4, 130.4, 129.5, 120.9 (q, J = 320.0 Hz, CF_3), 57.2, 55.5.

^{19}F-NMR (471 MHz, MeCN-d_3, $CFCl_3$ as int. Std.): δ [ppm] = −78.9.

DOSY-NMR (600 MHz, MeCN-d_3, 298 K): Diffusion coefficient D = 1.27 • 10^{-5} cm^2s^{-1}

HR-MS (pos. ESI):

calculated for $C_{26}H_{27}F_6N_8O_4S_2Zn$	$[M–NTf_2]^+$:	757.0787,	found: 757.0793
calculated for $C_{28}H_{27}F_{12}N_9O_8S_4ZnNa$	$[M+Na]^+$:	1059.9857,	found: 1059.9880

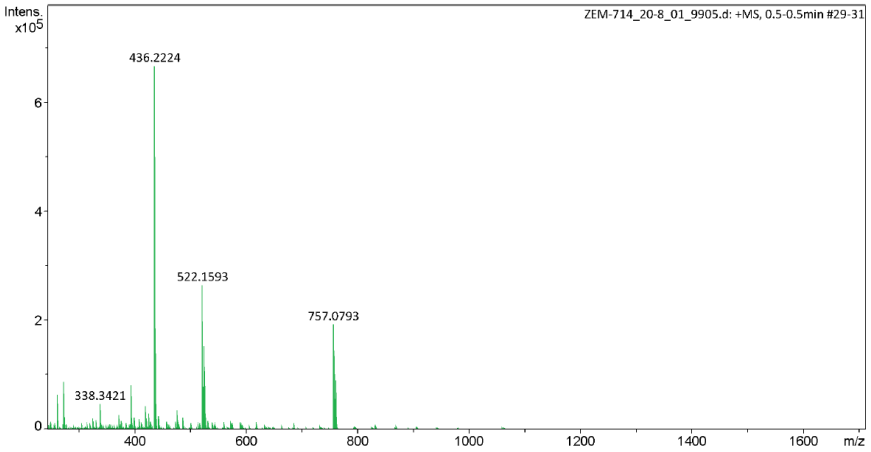

Figure 59: Full HR-MS report of **$ZnL_3(NTf_2)_2$** complex **XLIV**.

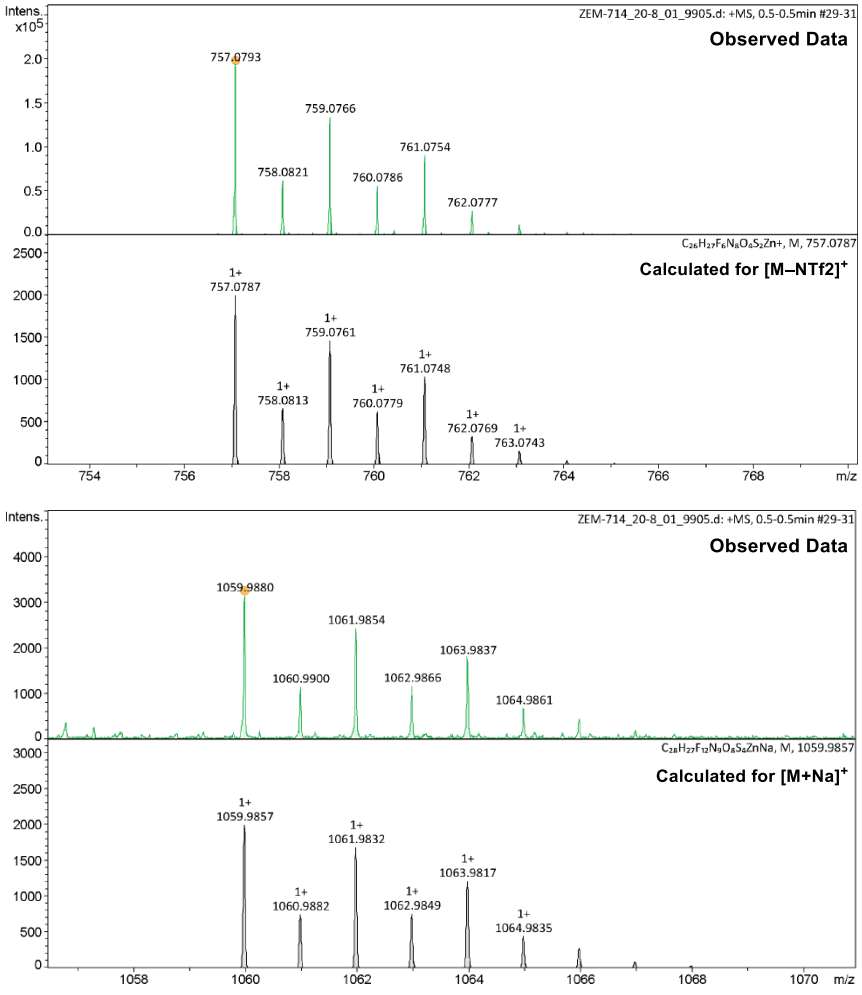

Figure 60: Observed and calculated HR-MS data for the $[M–NTf_2]^+$ and $[M+Na]^+$ species of **$ZnL_3(NTf_2)_2$** complex **XLIV**.

5.2.7 Synthetic Pathway towards the TPTI Scaffold

Hexaethyl 1,4,5,8,9,12-hexahydrotriphenylene-2,3,6,7,10,11-hexacarboxylate (223)

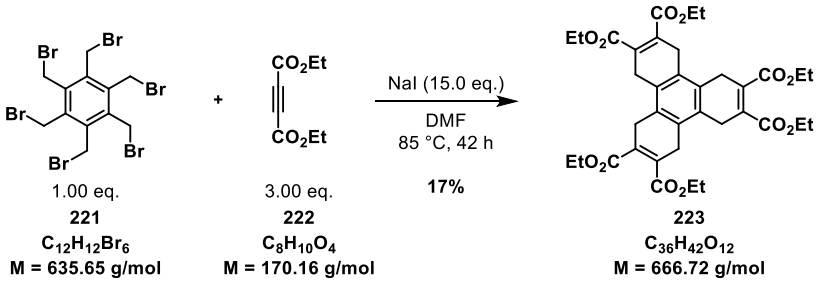

1.00 eq.
221
$C_{12}H_{12}Br_6$
M = 635.65 g/mol

3.00 eq.
222
$C_8H_{10}O_4$
M = 170.16 g/mol

223
$C_{36}H_{42}O_{12}$
M = 666.72 g/mol

The title compound (**223**) was synthesized as previously described and the spectroscopic data match those reported in literature.[306]

^{1}H-NMR (500 MHz, $CDCl_3$): δ [ppm] = 4.30 (q, *J* = 7.2 Hz, 12H), 3.57 (s, 12H), 1.35 (t, *J* = 7.2 Hz, 18H).

^{13}C-NMR (126 MHz, $CDCl_3$): δ [ppm] = 167.9, 131.8, 127.5, 61.6, 29.4, 14.2.

Hexaethyl triphenylene-2,3,6,7,10,11-hexacarboxylate (224)

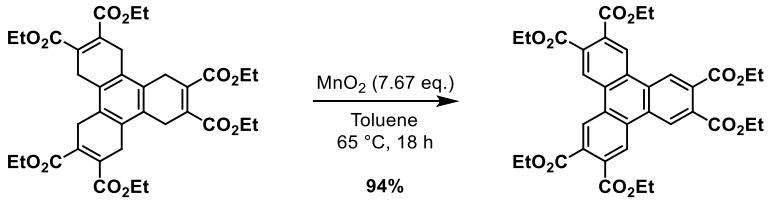

1.00 eq.
223
$C_{36}H_{42}O_{12}$
M = 666.72 g/mol

224
$C_{36}H_{36}O_{12}$
M = 660.67 g/mol

The title compound (**224**) was synthesized as previously described and the spectroscopic data match those reported in literature.[306]

^{1}H-NMR (400 MHz, $CDCl_3$): δ [ppm] = 9.04 (s, 6H), 4.51 (q, *J* = 7.2 Hz, 12H), 1.47 (t, *J* = 7.2 Hz, 18H).

^{13}C-NMR (126 MHz, $CDCl_3$): δ [ppm] = 167.3, 132.0, 131.0, 125.5, 62.4, 14.3.

Triphenylene-2,3,6,7,10,11-hexacarboxylic acid (225)

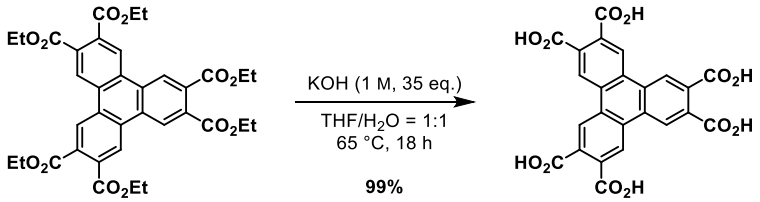

1.00 eq.
224
$C_{36}H_{36}O_{12}$
M = 660.67 g/mol

225
$C_{24}H_{12}O_{12}$
M = 492.35 g/mol

The title compound (**225**) was synthesized as previously described and the spectroscopic data match those reported in literature.[307]

^{1}H-NMR (500 MHz, DMSO-d_6): δ [ppm] = 13.48 (br. s, 6H), 9.15 (s, 6H).

^{13}C-NMR (126 MHz, DMSO-d_6): δ [ppm] = 168.2, 132.8, 130.0, 125.0.

Triphenyleno[2,3-*c*:6,7-*c*':10,11-*c*'']trifuran-1,3,6,8,11,13-hexaone (220)

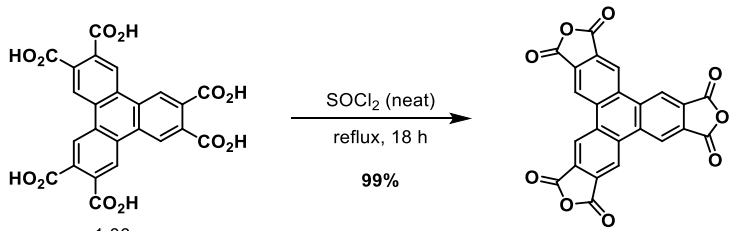

1.00 eq.
225
$C_{24}H_{12}O_{12}$
M = 492.35 g/mol

220
$C_{24}H_6O_9$
M = 438.30 g/mol

A dried 50 mL two-neck flask was charged with a stir bar, hexacarboxylic acid **225** (279 mg, 0.567 mmol, 1.00 eq.) and thionyl chloride (28 mL). The reaction mixture was stirred under reflux at 90 °C oil bath temperature for 18 h. The solvent was removed under reduced pressure. The solid residue was washed with DCM and acetone *via* centrifugation and dried under high vacuum overnight. The title product (**220**, 247 mg, 0.564 mmol, 99%) was obtained as an off-white solid and used without further purification.

M.p.: Decomposition observed at 300 °C onwards.

IR (ATR): $\tilde{\nu}$ [cm^{-1}] = 3141 (w), 3986 (w), 3051 (w), 2925 (w), 2857 (w), 1870 (w), 1846 (s), 1770 (s), 1341 (m), 1297 (m), 1251 (s), 1181 (m), 1120 (m), 966 (m), 919 (m), 891 (vs), 758 (m), 725 (vs), 638 (m), 620 (m), 557 (m), 452 (m), 437 (m), 411 (m).

^{1}H-NMR (600 MHz, MeCN-*d*$_3$:HCl-saturated $CDCl_3$ = 1:1): δ [ppm] = 9.62 (s, 6H).

^{13}C-NMR (151 MHz, MeCN-*d*$_3$:HCl-saturated $CDCl_3$ = 1:1): δ [ppm] = 162.7, 136.2, 131.4, 124.4.

HR-MS (pos. ESI): calculated for $C_{24}H_7O_9$ $[M+H]^+$: 439.0085, found: 439.0076

Note: HCl-saturated $CDCl_3$ was prepared by bubbling HCl gas through a flask filled with $CDCl_3$. To sodium chloride (12 g) in a 50 mL flask was added concentrated H_2SO_4 (15 mL) *via* a dropping funnel. The formed HCl gas was then bubbled through $CDCl_3$ for 30-40 min until complete consumption of the concentrated H_2SO_4. The HCl-saturated $CDCl_3$ was then transferred to vials (4 mL) and stored in a refrigerator. The experimental setup for this method has been described previously.[308]

2,7,12-Tris(6-methylpyridin-3-yl)-1*H*-benzo[1,2-*f*:3,4-*f*':5,6-*f*'']triisoindole-1,3,6,8,11,13(2*H*,7*H*,12*H*)-hexaone (229)

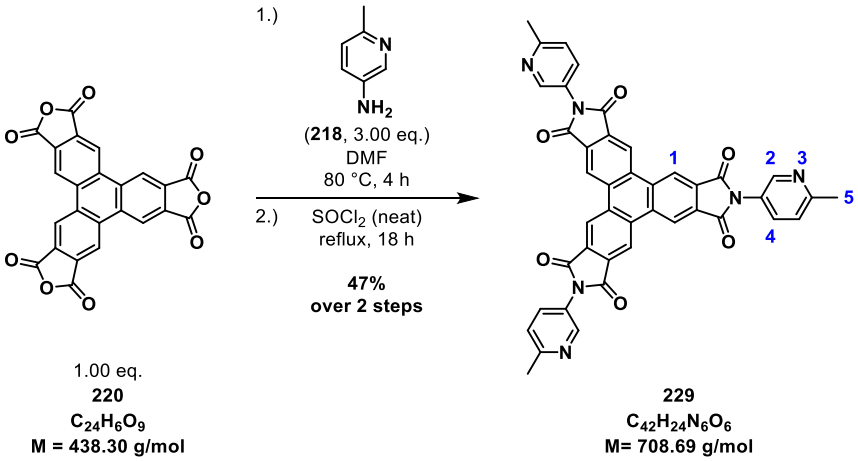

A dried 10 mL flask was charged with a stir bar, trianhydride **220** (75.0 mg, 0.171 mmol, 1.00 eq.), 5-amino-2-methylpyridine (**218**, 55.5 mg, 0.513 mmol, 3.00 eq.) and dry DMF (7 mL). The reaction mixture was stirred vigorously at 80 °C oil bath temperature for 4 h. The mixture was allowed to cool down to room temperature and diluted with acetone (30 mL), followed by centrifugation. The supernatant was decanted, and this washing step was repeated 3 times. The residue was dried to receive a crude brown solid (119 mg) which was placed into a dried 25 mL two-neck flask equipped with a stirrer. Thionyl chloride (16 mL) was added, and the mixture was stirred under reflux at 90 °C oil bath temperature for 18 h. The solvent was removed under reduced pressure. The solid residue was suspended in acetone. The mixture was centrifuged, and the supernatant decanted. This washing step was repeated once more. The residue was dried under high vacuum overnight. The title product (**229**, 57.0 mg, 0.0804 mmol, 47%) was obtained as an off-white solid and not subjected to further purification.

M.p.: Decomposition observed at 295 °C onwards.

IR (ATR): $\tilde{\nu}$ [cm^{-1}] = 3412 (b), 3049 (w), 2403 (b), 2046 (w), 2027 (w), 2013 (w), 1781 (m), 1715 (vs), 1638 (w), 1613 (m), 1556 (m), 1490 (w), 1466 (w), 1437 (w), 1379 (vs), 1292 (w), 1234 (s), 1182 (w), 1145 (w), 1118 (m), 1087 (m), 1022 (w), 998 (w), 900 (w), 868 (m), 800 (m), 776 (m), 733 (s), 702 (w), 641 (m), 619 (m), 596 (s), 524 (m), 469 (m), 448 (w), 409 (m).

^{1}H-NMR (500 MHz, MeOH-*d*$_4$): δ [ppm] = 9.76 (s, 6H, 1-H), 9.18 (d, $^{4}J_{meta}$ = 2.2 Hz, 3H, 4-H), 8.90 (dd, $^{3}J_{ortho}$ = 8.7 Hz, $^{4}J_{meta}$ = 2.3 Hz, 3H, 2-H), 8.17 (d, $^{3}J_{ortho}$ = 8.7 Hz, 3H, 3-H), 2.92 (s, 9H, 5-H).

^{13}C-NMR (151 MHz, MeOH-*d*$_4$): δ [ppm] = 166.5, 154.5, 143.9, 139.2, 136.4, 132.4, 131.6, 129.7, 123.0, 19.7.

HR-MS (pos. ESI): calculated for $C_{42}H_{25}N_6O_6$ $[M+H]^+$: 709.1830, found: 709.1821

5.2.8 Synthesis of Guests and Starting Materials

Tetrabutylammonium (1*S*)-(+)-10-camphorsulfonate (210)

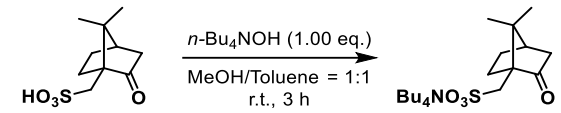

1.00 eq.
271
$C_{10}H_{16}O_4S$
M = 232.29 g/mol

210
$C_{26}H_{51}NO_4S$
M = 473.76 g/mol

A dried 25 mL round-bottom flask was charged with a stir bar and camphor-10-sulfonic acid (**271**, 232 mg, 1.00 mmol, 1.00 eq.). Tetrabutylammonium hydroxide solution (0.1 N in MeOH/Toluene = 1:1, 10.0 mL, 1.00 mmol, 1.00 eq.) was added and the reaction mixture was stirred at room temperature for 3 h. The solvent was removed under reduced pressure and the residue was dried under high vacuum over night. The title compound (**210**, 471 mg, 0.994 mmol, 99%) was obtained as a white solid and used without further purification.

The spectroscopic data match those reported in literature.[309]

^{1}H-NMR (500 MHz, MeCN-*d*$_3$): δ [ppm] = 3.08 (m_c, 8H, N-CH_2), 2.99 (d, *J* = 14.7 Hz, 1H), 2.81-2.73 (m, 1H), 2.51 (d, *J* = 14.7 Hz, 1H), 2.26 (dt, *J* = 18.2 Hz, *J* = 4.1 Hz, 1H), 1.99-1.96 (m, 2H), 1.81 (d, *J* = 18.0 Hz, 1H), 1.60 (m_c, 8H, N-CH_2-CH_2), 1.45 (ddd, *J* = 14.2 Hz, *J* = 9.6 Hz, *J* = 4.6 Hz, 1H), 1.39-1.31 (m, 8H, N-CH_2-CH_2-CH_2), 1.39-1.31 (m, 1H, overlapping), 1.10 (s, 3H), 0.97 (t, *J* = 7.4 Hz, 12H, N-CH_2-CH_2-CH_2-CH_3), 0.80 (s, 3H).

Tetrabutylammonium (*R*)-(−)-binaphthyl-2,2'-diyl phosphate (213)

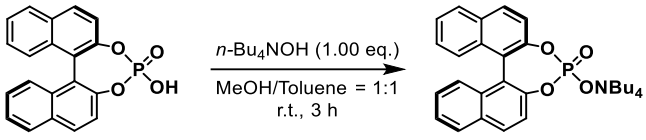

1.00 eq.
272
$C_{20}H_{13}O_4P$
M = 348.29 g/mol

213
$C_{36}H_{48}NO_4P$
M = 589.76 g/mol

A dried 25 mL round-bottom flask was charged with a stir bar and (*R*)-(−)-binaphthyl-2,2'-diyl hydrogenphosphate (**272**, 348 mg, 1.00 mmol, 1.00 eq.). Tetrabutylammonium hydroxide solution (0.1 N in MeOH/Toluene = 1:1, 10.0 mL, 1.00 mmol, 1.00 eq.) was added and the reaction mixture was stirred at room temperature for 3 h. The solvent was removed under reduced pressure and the residue was dried under high vacuum over night. The title compound (**213**, 584 mg, 0.990 mmol, 99%) was obtained as a white solid and used without further purification.

The spectroscopic data match those reported in literature.[310]

^{1}H-NMR (500 MHz, DMSO-*d*$_6$): δ [ppm] = 8.04-7.99 (m, 4H), 7.41 (m, 2H), 7.37 (d, *J* = 8.8 Hz, 2H), 7.32-7.26 (m, 2H), 7.21 (d, *J* = 8.6 Hz, 2H), 3.18-3.12 (m, 8H, N-CH_2), 1.60-1.52 (m, 8H, N-CH_2-CH_2), 1.35-1.25 (m, 8H, N-CH_2-CH_2-CH_2), 0.93 (t, *J* = 7.4 Hz, 12H, N-CH_2-CH_2-CH_2-CH_3).

$Fe(NTf_2)_2$, Iron(II) bis((trifluoromethyl)sulfonyl)amide (274)

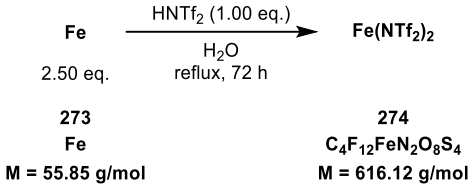

The title compound (**274**) was synthesized as previously described and the spectroscopic data match those reported in literature.[311]

^{19}F-NMR (471 MHz, MeCN-d_3, C_6F_6 as int. Std): δ [ppm] = –80.62.

Elemental Analysis:

Found: C, 6.84; H, 1.81; N, 4.49 %.

Calculated for $C_4F_{12}FeN_2O_8S_4$ • 5 H_2O: C, 6.80; H, 1.43; N, 3.97 %.

Note: The product is a deliquescent white powder and needs to be manipulated within a glove box.

$Cd(NTf_2)_2$, Cadmium(II) bis((trifluoromethyl)sulfonyl)amide (276)

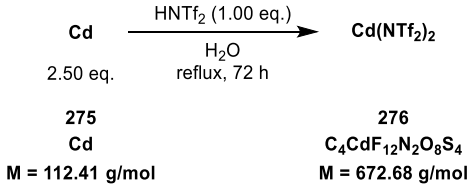

The title compound (**276**) was synthesized as previously described and the spectroscopic data match those reported in literature.[276]

^{19}F-NMR (471 MHz, MeCN-d_3, C_6F_6 as int. Std): δ [ppm] = –80.62.

Elemental Analysis:

Found: C, 6.33; H, 1.71; N, 4.37 %.

Calculated for $C_4CdF_{12}N_2O_8S_4$ • 6 H_2O: C, 6.15; H, 1.55; N, 3.59 %.

Note: The product is a deliquescent white powder and needs to be manipulated within a glove box.

Tetrabutylammonium monomethylterephthalate (258)

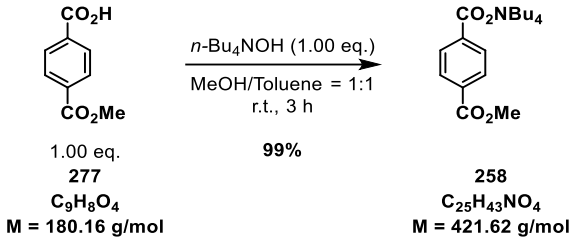

1.00 eq.
277
$C_9H_8O_4$
M = 180.16 g/mol

99%

258
$C_{25}H_{43}NO_4$
M = 421.62 g/mol

A dried 25 mL round-bottom flask was charged with a stir bar and 4-(methoxycarbonyl)benzoic acid (**277**, 180 mg, 1.00 mmol, 1.00 eq.). Tetrabutylammonium hydroxide solution (0.1 N in MeOH/toluene = 1:1, 10.0 mL, 1.00 mmol, 1.00 eq.) was added and the reaction mixture was stirred at room temperature for 3 h. The solvent was removed under reduced pressure and the residue was dried under high vacuum overnight. The title compound (**258**, 418 mg, 0.993 mmol, 99%) was obtained as a white solid and used without further purification. The spectroscopic data match those reported in literature.[312]

M.p.: ϑ_m = 150-154 °C

IR (ATR): $\tilde{\nu}$ [cm^{-1}] = 3157 (b), 2984 (m), 2957 (m), 2933 (w), 2873 (m), 1693 (s), 1607 (s), 1558 (m), 1497 (m), 1481 (m), 1459 (m), 1434 (w), 1382 (w), 1356 (s), 1281 (vs), 1223 (w), 1175 (w), 1147 (w), 1126 (w), 1110 (m), 1085 (w), 1056 (w), 1030 (w), 1017 (w), 964 (w), 875 (w), 840 (w), 806 (m), 779 (w), 739 (vs), 699 (w), 588 (w), 571 (w), 528 (w), 495 (w).

^{1}H-NMR (500 MHz, D_2O): δ [ppm] = 8.06 (m_c, 2H), 7.93 (m_c, 2H), 3.95 (s, 3H, O-C*H*$_3$), 3.17 (m_c, 8H, N-C*H*$_2$), 1.68-1.56 (m, 8H, N-CH$_2$-C*H*$_2$), 1.41-1.30 (m, 8H, N-CH$_2$-CH$_2$-C*H*$_2$), 0.94 (t, *J* = 7.3 Hz, 12H, N-CH$_2$-CH$_2$-CH$_2$-C*H*$_3$).

^{1}H-NMR (500 MHz, 1% *t*-BuOH, D_2O): δ [ppm] = 8.06 (m_c, 2H), 7.93 (m_c, 2H), 3.95 (s, 3H, O-C*H*$_3$), 3.17 (m_c, 8H, N-C*H*$_2$), 1.68-1.57 (m, 8H, N-CH$_2$-C*H*$_2$), 1.40-1.30 (m, 8H, N-CH$_2$-CH$_2$-C*H*$_2$), 0.94 (t, *J* = 7.3 Hz, 12H, N-CH$_2$-CH$_2$-CH$_2$-C*H*$_3$).

^{13}C-NMR (126 MHz, 1% *t*-BuOH, D_2O): δ [ppm] = 175.1, 169.6, 141.7, 132.0, 130.0, 129.4, 58.7, 53.4, 23.7, 19.8, 13.4.

HR-MS (neg. ESI): calculated for $C_9H_7O_4$ [M–NBu_4]$^-$: 179.0350, found: 179.0350

Tetrabutylammonium adamantane-1-carboxylate (259)

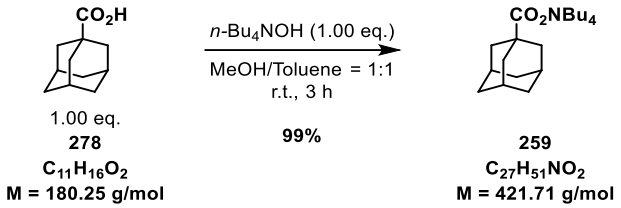

1.00 eq.
278
$C_{11}H_{16}O_2$
M = 180.25 g/mol

259
$C_{27}H_{51}NO_2$
M = 421.71 g/mol

A dried 25 mL round-bottom flask was charged with a stir bar and 1-adamantanecarboxylic acid (**278**, 360 mg, 2.00 mmol, 1.00 eq.). Tetrabutylammonium hydroxide solution (0.1 N in MeOH/toluene = 1:1, 20.0 mL, 2.00 mmol, 1.00 eq.) was added and the reaction mixture was stirred at room temperature for 3 h. The solvent was removed under reduced pressure and the residue was dried under high vacuum overnight. The title compound (**259**, 838 mg, 1.99 mmol, 99%) was obtained as a white solid and used without further purification.

The title compound (**259**) was synthesized following a slightly modified literature procedure and the spectroscopic data for the ^{1}H-NMR match those reported in literature.[313]

^{1}H-NMR (500 MHz, 1% *t*-BuOH, D_2O): δ [ppm] = 3.25-3.14 (m_c, 8H), 1.97 (br. s, 3H), 1.80 (d, J = 2.7 Hz, 6H), 1.75-1.59 (m, 14H), 1.41-1.32 (m, 8H), 0.95 (t, J = 7.3 Hz, 12H).

^{13}C-NMR (126 MHz, 1% *t*-BuOH, D_2O): δ [ppm] = 188.9, 58.8, 42.8, 40.1, 36.9, 28.7, 23.8, 19.8, 13.4.

Tetrabutylammonium diphenyl phosphate (260)

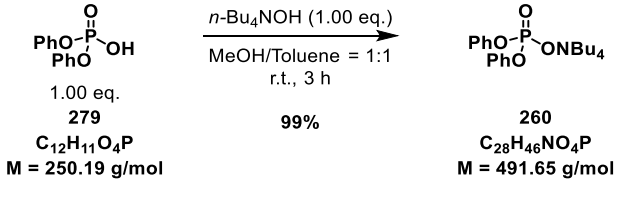

1.00 eq.
279
$C_{12}H_{11}O_4P$
M = 250.19 g/mol

260
$C_{28}H_{46}NO_4P$
M = 491.65 g/mol

A dried 25 mL round-bottom flask was charged with a stir bar and diphenyl hydrogen phosphate (**279**, 250 mg, 1.00 mmol, 1.00 eq.). Tetrabutylammonium hydroxide solution (0.1 N in MeOH/toluene = 1:1, 10.0 mL, 1.00 mmol, 1.00 eq.) was added and the reaction mixture was stirred at room temperature for 3 h. The solvent was removed under reduced pressure and the residue was dried under high vacuum overnight. The title compound (**260**, 488 mg, 0.993 mmol, 99%) was obtained as a white solid and used without further purification.

M.p.: ϑ_m = 64-68 °C

IR (ATR): $\tilde{\nu}$ [cm^{-1}] = 3059 (w), 3007 (w), 2959 (m), 2938 (m), 2874 (m), 1598 (m), 1588 (m), 1490 (s), 1460 (m), 1385 (w), 1292 (s), 1247 (m), 1215 (s), 1151 (w), 1095 (vs), 1067 (m), 1027 (w), 1002 (w), 913 (m), 886 (s), 873 (vs), 843 (w), 783 (s), 757 (s), 726 (s), 692 (s), 617 (m), 573 (m), 525 (vs), 504 (s), 472 (s).

^{1}H-NMR (500 MHz, 1% *t*-BuOH, D_2O): δ [ppm] = 7.44-7.37 (m, 4H), 7.26-7.19 (m, 6H), 3.20-3.10 (m_c, 8H, N-C*H*$_2$), 1.67-1.56 (m, 8H, N-CH$_2$-C*H*$_2$), 1.40-1.30 (m, 8H, N-CH$_2$-CH$_2$-C*H*$_2$), 0.94 (t, *J* = 7.4 Hz, 12H, N-CH$_2$-CH$_2$-CH$_2$-C*H*$_3$).

^{13}C-NMR (126 MHz, 1% *t*-BuOH, D_2O): δ [ppm] = 152.3, 130.5, 125.1, 120.9, 58.7, 23.7, 19.8, 13.5.

^{31}P{^{1}H}-NMR (202 MHz, D_2O, 85% H_3PO_4 as external Std.): δ [ppm] = –8.18.

HR-MS (neg. ESI): calculated for $C_{12}H_{10}O_4P$ $[M–NBu_4]^-$: 249.0322, found: 249.0321

Tetrabutylammonium dimethyl phosphate (261)

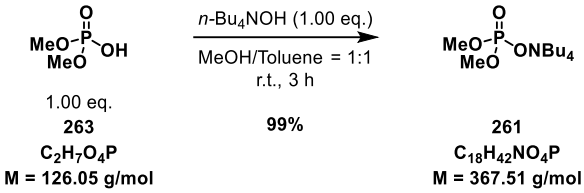

A dried 25 mL round-bottom flask was charged with a stir bar and dimethyl hydrogen phosphate (**263**, 95.2 µl, 126 mg, 1.00 mmol, 1.00 eq.). Tetrabutylammonium hydroxide solution (0.1 N in MeOH/toluene = 1:1, 10.0 mL, 1.00 mmol, 1.00 eq.) was added and the reaction mixture was stirred at room temperature for 3 h. The solvent was removed under reduced pressure and the residue was dried under high vacuum overnight. The title compound (**261**, 363 mg, 0.988 mmol, 99%) was obtained as a white solid and used without further purification.

M.p.: ϑ_m = 64-67 °C

IR (ATR): $\tilde{\nu}$ [cm^{-1}] = 2959 (m), 2935 (m), 2874 (m), 2831 (w), 1492 (m), 1465 (m), 1379 (w), 1252 (s), 1241 (s), 1183 (w), 1095 (m), 1054 (vs), 884 (m), 762 (s), 741 (s), 724 (s), 542 (m), 519 (m), 464 (s).

^{1}H-NMR (500 MHz, 1% *t*-BuOH, D_2O): δ [ppm] = 3.58 (d, *J* = 10.7 Hz, 6H, O-C*H*$_3$), 3.24-3.15 (m_c, 8H, N-C*H*$_2$), 1.71-1.59 (m, 8H, N-CH$_2$-C*H*$_2$), 1.42-1.31 (m, 8H, N-CH$_2$-CH$_2$-C*H*$_2$), 0.95 (t, *J* = 7.4 Hz, 12H, N-CH$_2$-CH$_2$-CH$_2$-C*H*$_3$).

^{13}C-NMR (126 MHz, 1% *t*-BuOH, D_2O): δ [ppm] = 58.8, 53.4, 23.8, 19.8, 13.5.

^{31}P{^{1}H}-NMR (202 MHz, D_2O, 85% H_3PO_4 as external Std.): δ [ppm] = 3.75.

HR-MS (neg. ESI): calculated for $C_2H_6O_4P$ $[M–NBu_4]^-$: 125.0009, found: 125.0011

Tetrabutylammonium dibutyl phosphate (262)

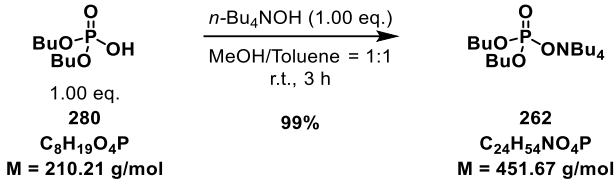

A dried 25 mL round-bottom flask was charged with a stir bar and dibutyl hydrogen phosphate (**280**, 198 µl, 210 mg, 1.00 mmol, 1.00 eq.). Tetrabutylammonium hydroxide solution (0.1 N in MeOH/toluene = 1:1, 10.0 mL, 1.00 mmol, 1.00 eq.) was added and the reaction mixture was stirred at room temperature for 3 h. The solvent was removed under reduced pressure and the residue was dried under high vacuum overnight. The title compound (**262**, 449 mg, 0.994 mmol, 99%) was obtained as a white waxy solid and used without further purification.

M.p.: ϑ_m = 27-30 °C

IR (ATR): $\tilde{\nu}$ [cm^{-1}] = 2958 (m), 2932 (m), 2873 (m), 1465 (m), 1379 (w), 1256 (s), 1067 (vs), 1030 (s), 972 (m), 881 (m), 789 (m), 735 (m), 550 (m), 540 (m), 504 (m), 468 (m), 427 (w).

^{1}H-NMR (500 MHz, 1% *t*-BuOH, D_2O): δ [ppm] = 3.87 (dt, *J* = 6.6 Hz, *J* = 6.6 Hz, 4H, O-C*H*$_2$), 3.24-3.15 (m$_c$, 8H, N-C*H*$_2$), 1.70-1.56 (m, 12H, O-CH$_2$-C*H*$_2$ and N-CH$_2$-C*H*$_2$), 1.43-1.31 (m, 12H, O-CH$_2$-CH$_2$-C*H*$_2$ and N-CH$_2$-CH$_2$-C*H*$_2$), 0.95 (t, *J* = 7.3 Hz, 12H, N-CH$_2$-CH$_2$-CH$_2$-C*H*$_3$), 0.92 (t, *J* = 7.4 Hz, 6H, O-CH$_2$-CH$_2$-CH$_2$-C*H*$_3$).

^{13}C-NMR (126 MHz, 1% *t*-BuOH, D_2O): δ [ppm] = 66.6, 58.8, 32.6, 23.8, 19.8, 19.0, 13.7, 13.5.

^{31}P{^{1}H}-NMR (202 MHz, D_2O, 85% H_3PO_4 as external Std.): δ [ppm] = 1.72.

HR-MS (neg. ESI): calculated for $C_8H_{18}O_4P$ [M–NBu_4]$^-$: 209.0948, found: 209.0952

3-Oxo-3-phenylpropanoic acid (265)

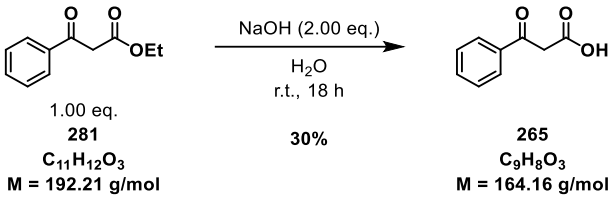

A 25 mL round-bottom flask was charged with a stir bar and ethyl 3-oxo-3-phenylpropanoate (**281**, 1.92 g, 10.0 mmol, 1.00 eq.). Aq. NaOH (2.0 M, 10.0 mL, 20.0 mmol, 2.00 eq.) was added and the reaction mixture was stirred at room temperature for 18 h. Et_2O (10 mL) was added, and the phases were separated. The aq. phase was extracted with Et_2O (2 x 10 mL) and then cooled with an ice-bath. The aq. phase was acidified with aq. HCl (3 M) to pH = 1. The white precipitate was filtered off, washed with ice-cold H_2O and dried under high vacuum. The crude product (820 mg) was further purified by quick recrystallization from DCM. The crystals were filtered off, washed with ice-cold DCM and dried under high vacuum. The title compound (**265**, 485 mg, 2.95 mmol, 30%) was obtained in the form of colourless crystals. The spectroscopic data match those reported in literature.[314]

Note: Recrystallization needs to be performed quickly due to decarboxylation of the product under reflux in DCM. The hot mixture was then first cooled to r.t., then in an ice-bath and then at –20 °C.

M.p.: Decomposition observed at 114 °C onwards. (Decarboxylation)

^{1}H-NMR (500 MHz, Acetone-*d*$_6$): δ [ppm] = Keto Form: 11.13 (br. s, 1H), 8.06-8.01 (m, 2H), 7.69-7.64 (m, 1H), 7.58-7.52 (m, 2H, keto form / m, 1H, enol form), 4.09 (s, 2H); Enol Form: 13.31 (s, 1H), 7.90-7.86 (m, 2H), 7.58-7.52 (m, 2H, keto form / m, 1H, enol form), 7.52-7.47 (m, 2H), 5.84 (s, 1H).

^{13}C-NMR (151 MHz, Acetone-*d*$_6$): δ [ppm] = 193.9, 175.7, 173.3, 169.2, 137.3, 134.4, 134.3, 132.4, 129.6, 129.6, 129.4, 126.9, 87.3, 46.0.

HR-MS (neg. ESI): calculated for $C_9H_8O_3Na$ $[M+Na]^+$: 187.0366, found: 187.0366

Ethyl benzoate (253)

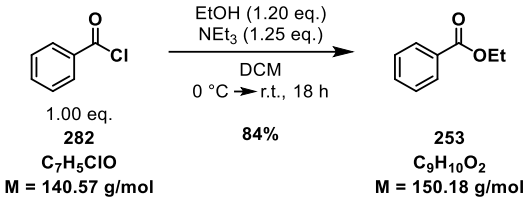

1.00 eq.
282
C_7H_5ClO
M = 140.57 g/mol

84%

253
$C_9H_{10}O_2$
M = 150.18 g/mol

The title compound (**253**) was synthesized according to a general procedure as previously described.[315] The spectroscopic data match those reported in literature.[316]

^{1}H-NMR (500 MHz, $CDCl_3$): δ [ppm] = 8.08-8.01 (m, 2H), 7.57-7.52 (m, 1H), 7.46-7.40 (m, 2H), 4.38 (q, ^3J = 7.2 Hz, 2H, O-CH_2-CH$_3$), 1.39 (t, ^3J = 7.2 Hz, 3H, O-CH$_2$-CH_3).

^{13}C-NMR (126 MHz, $CDCl_3$): δ [ppm] = 166.7, 132.9, 130.6, 129.6, 128.4, 61.0, 14.4.

5.2.9 Other Synthetic Routes and Procedures Explored

2,7-Di-*p*-tolylbenzo[*lmn*][3,8]phenanthroline-1,3,6,8(2*H*,7*H*)-tetraone (181)

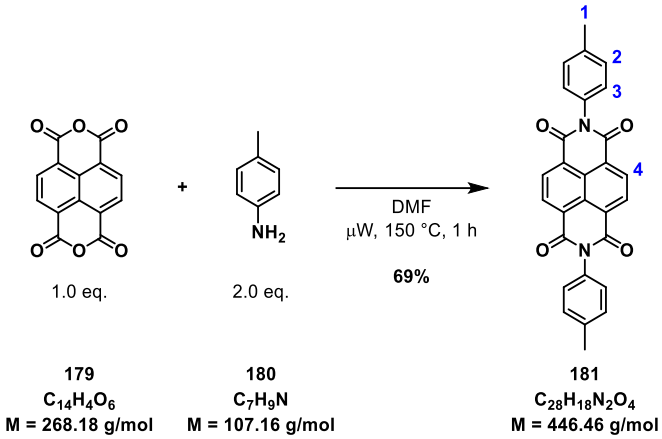

A dried 20 mL microwave vial was charged with a stir bar, NDA (**179**, 85%, 470 mg, 1.49 mmol, 1.00 eq.) and *p*-toluidine (**180**, 319 mg, 2.98 mmol, 2.00 eq.). Dry DMF (20 mL) was added, and the mixture was ultrasonicated. The homogenous suspension was heated to 150 °C over 4 min and then stirred at 150 °C for 1 h using microwave irradiation. The reaction mixture was allowed to cool down to room temperature. The solvent was filtered off and the solid residue was washed with acetone (4 x 5 mL) and then dried under high vacuum. The title compound (**181**, 456 mg, 1.02 mmol, 69%) was obtained in the form of fine yellow needles.

The spectroscopic data match those reported in literature.[317]

M.p.: No melting or visual decomposition observed up until maximum temperature (400 °C).

IR (ATR): $\tilde{\nu}$ [cm^{-1}] = 3372 (w), 3052 (w), 1708 (m), 1663 (s), 1579 (m), 1512 (m), 1443 (m), 1344 (s), 1243 (s), 1188 (s), 1136 (m), 1118 (m), 1106 (m), 978 (m), 879 (m), 858 (m), 819 (s), 770 (m), 760 (s), 738 (vs), 698 (m), 580 (m), 556 (m), 514 (s), 430 (m), 412 (s).

^{1}H-NMR (500 MHz, DMSO-d_6): δ [ppm] = 8.71 (s, 4H, 4-H), 7.38-7.30 (m, 8H, 2-H, 3-H), 2.42 (s, 6H, 1-H).

^{13}C-NMR (151 MHz, DMSO-d_6): δ [ppm] = 163.0, 137.9, 133.0, 130.5, 129.5, 128.7, 127.0, 126.7, 20.9.

HR-MS (pos. ESI):	calculated for $C_{28}H_{19}N_2O_4$	$[M+H]^+$:	447.1339, found: 447.1337
	calculated for $(C_{28}H_{18}N_2O_4)_2Na$	$[2M+Na]^+$:	915.2425, found: 915.2430

A_2B Type Ammonium Chloride Species 204a

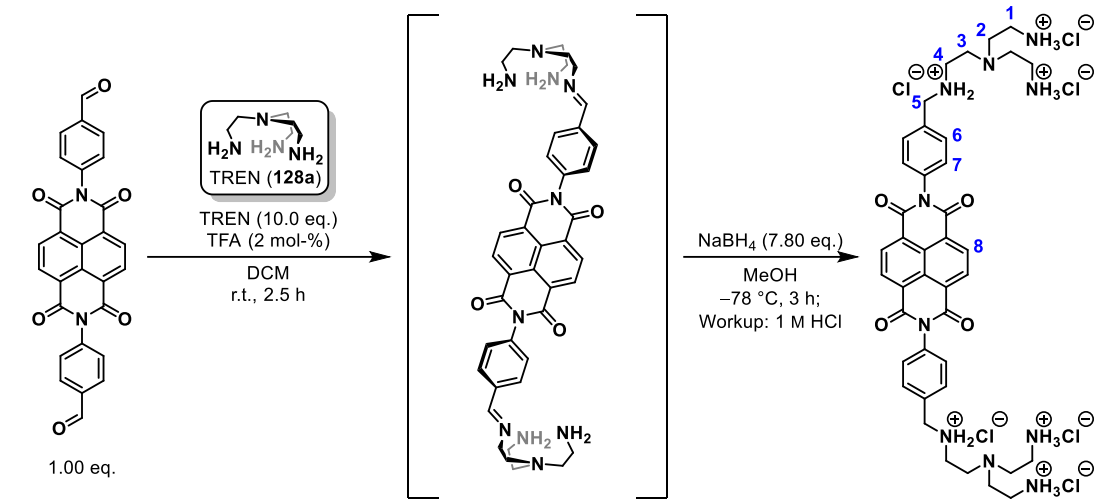

175
$C_{28}H_{14}N_2O_6$
M = 474.43 g/mol

202a
$C_{40}H_{46}N_{10}O_4$
M = 730.87 g/mol

204a
$C_{40}H_{56}Cl_6N_{10}O_4$
M = 953.65 g/mol

A dried 250 mL flask was charged with a stir bar, dialdehyde **175** (212 mg, 0.446 mmol, 1.00 eq.) and TFA in dry DCM (120 mL, 0.025 mM, 3.0 µmol, 2.0 mol-%). Tris(2-aminoethyl)amine (**128a**, 668 µL, 652 mg, 4.46 mmol, 10.0 eq.) was added and the mixture was stirred at room temperature for 2.5 h. The resulting yellow solution was added slowly over 10 min to a solution of $NaBH_4$ (43.8 mg, 1.16 mmol, 2.60 eq.) in MeOH (120 mL) at −78 °C. The mixture was stirred at −78 °C for 3 h. Aqueous HCl (30 mL, 1 M) was added, and the solvent was removed under reduced pressure. MeOH (50 mL) was added, and the solvent was removed under reduced pressure. This was repeated once and the solid residue was dried under high vacuum and the solid residue (376 mg divided into 20 mg aliquots) was subjected to size-exclusion chromatography with Sephadex G-10 Fine Resin (H_2O + 0.1% formic acid, column dimensions: diameter d = 3 cm, height h = 36.5 cm, using compressed air). Some fractions still contained a low to medium amount of tris(2-aminoethyl)amine hydrochloride and they were once again subjected to the same column chromatography conditions. This way tris(2-aminoethyl)amine hydrochloride was effectively removed. However, the title compound (**204a**) could only be obtained as a mixture with other undefined side-products.

M.p.: Decomposition observed at 130 °C onwards.

IR (ATR): $\tilde{\nu}$ [cm^{-1}] = 3379 (b), 2964 (b), 1758 (w), 1713 (m), 1667 (vs), 1582 (m), 1515 (m), 1448 (m), 1351 (s), 1250 (s), 1197 (s), 1138 (vs), 1048 (m), 1009 (m), 983 (s), 883 (w), 861 (w), 833 (m), 813 (m), 785 (m), 767 (s), 746 (m), 721 (m), 705 (m), 650 (m), 605 (m), 580 (m), 539 (m), 517 (m), 498 (m), 472 (m), 430 (m), 413 (m).

^{1}H-NMR (500 MHz, D_2O): δ [ppm] = 8.82 (s, 4H, 8-H), 7.79 (m_c, 4H, 7-H), 7.57 (m_c, 4H, 6-H), 4.46 (s, 4H, 5-H), 3.34 (t, *J* = 6.8 Hz, 4H, 4-H), 3.16 (t, *J* = 6.8 Hz, 8H, 1-H), 2.99 (t, *J* = 6.8 Hz, 4H, 3-H), 2.92 (t, *J* = 6.8 Hz, 8H, 2-H).

^{13}C-NMR (126 MHz, D_2O): δ [ppm] = 165.1, 135.7, 132.0, 131.7, 131.5, 129.3, 127.0, 126.9, 50.8, 49.8, 48.7, 43.8, 36.4.

HR-MS (pos. ESI): calculated for $C_{40}H_{52}N_{10}O_4$ $[M–6Cl–4H]^{2+}$: 368.2081, found: 368.2079

4-(((Triisopropylsilyl)oxy)methyl)aniline (190)

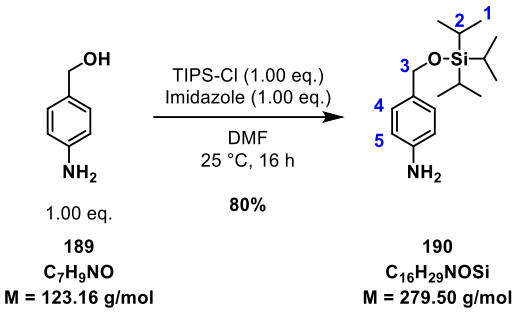

1.00 eq.

189
C_7H_9NO
M = 123.16 g/mol

190
$C_{16}H_{29}NOSi$
M = 279.50 g/mol

The title compound (**190**) was synthesized as previously described and the spectroscopic data match those reported in literature.[318]

^{1}H-NMR (500 MHz, $CDCl_3$): δ [ppm] = 7.14 (m_c, 2H), 6.67 (m_c, 2H), 4.72 (s, 2H, 3-H), 3.65 (br. s, 2H, N*H*$_2$), 1.22-1.11 (m, 3H, 2-H), 1.11-1.05 (m, 18H, 1-H).

2,7-Bis(4-(((triisopropylsilyl)oxy)methyl)phenyl)benzo[*lmn*][3,8]phenanthroline-1,3,6,8(2*H*,7*H*)-tetraone (194)

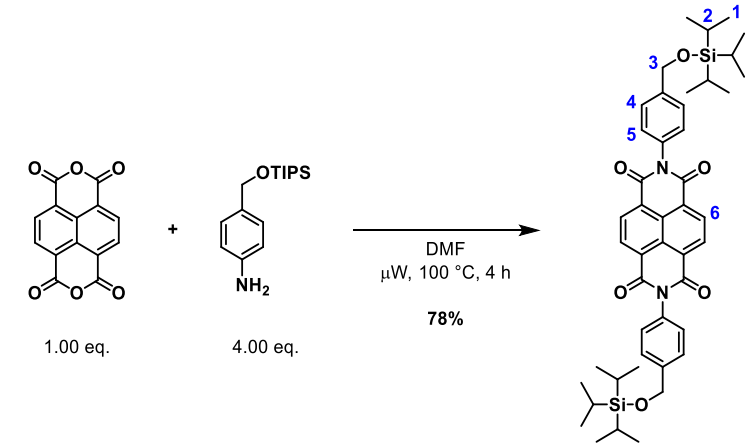

1.00 eq. 4.00 eq.

179
$C_{14}H_4O_6$
M = 268.18 g/mol

190
$C_{16}H_{29}NOSi$
M = 279.50 g/mol

194
$C_{46}H_{58}N_2O_6Si_2$
M = 791.15 g/mol

A dried 6 mL microwave vial was charged with a stir bar, NDA (**179**, 85%, 28.2 mg, 0.0895 mmol, 1.00 eq.) and amine **190** (100 mg, 0.358 mmol, 4.00 eq.). Dry DMF (2.4 mL) was added, and the mixture was ultrasonicated. The orange solution was heated to 100 °C over 4 min and then stirred at 100 °C for 4 h using microwave irradiation. The reaction mixture was allowed to cool down to room temperature. The solvent was removed under reduced pressure. The residue was diluted with DCM (10 mL) and the solvent was removed under reduced pressure. This was repeated twice to remove residual DMF. The crude mixture was purified *via* column chromatography (SiO_2, DCM/Pentane = 8:2, R_f = 0.13). The title compound (**194**, 55.0 mg, 0.0695 mmol, 78%) was obtained as an off-white solid.

M.p.: ϑ_m = 310-314 °C

IR (ATR): $\tilde{\nu}$ [cm^{-1}] = 3050 (w), 2942 (s), 2890 (m), 2864 (s), 1712 (s), 1672 (vs), 1581 (m), 1510 (m), 1461 (m), 1446 (m), 1344 (vs), 1245 (vs), 1192 (s), 1111 (s), 1093 (s), 1069 (m), 1017 (m), 981 (m), 879 (s), 860 (m), 823 (m), 799 (m), 766 (s), 740 (s), 681 (s), 660 (m), 643 (m), 603 (m), 579 (m), 515 (m), 431 (m), 415 (m).

^{1}H-NMR (500 MHz, CDCl$_3$): δ [ppm] = 8.85 (s, 4H, 6-H), 7.58 (m$_c$, 4H, 5-H), 7.31 (m$_c$, 4H, 4-H), 4.96 (s, 4H, 3-H), 1.28-1.18 (m, 6H, 2-H), 1.16-1.10 (m, 36H, 1-H).

^{13}C-NMR (126 MHz, CDCl$_3$): δ [ppm] = 163.2, 143.1, 133.1, 131.6, 128.3, 127.4, 127.2, 126.9, 64.7, 18.2, 12.2.

HR-MS (pos. ESI): calculated for $C_{46}H_{58}N_2O_6Si_2Na$ [M+Na]$^+$: 813.3726, found: 813.3718

Trimethyl 5,5',5''-(benzene-1,3,5-triyltris(ethyne-2,1-diyl))tripicolinate (249)

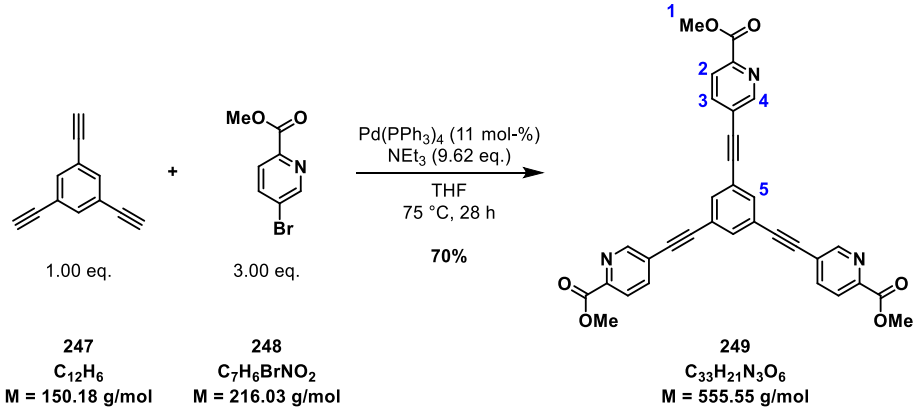

The title compound (**249**) was synthesized as previously described and the spectroscopic data match those reported in literature.[298]

^{1}H-NMR (500 MHz, CDCl$_3$): δ [ppm] = 8.87 (dd, $^4J_{meta}$ = 2.0 Hz, $^5J_{para}$ = 0.8 Hz, 3H, 4-H), 8.16 (dd, $^3J_{ortho}$ = 8.1 Hz, $^5J_{para}$ = 0.8 Hz, 3H, 2-H), 7.96 (dd, $^3J_{ortho}$ = 8.1 Hz, $^4J_{meta}$ = 2.1 Hz, 3H, 3-H), 7.78 (s, 3H, 5-H), 4.03 (s, 12H, 1-H).

^{13}C-NMR (126 MHz, CDCl$_3$): δ [ppm] = 165.2, 152.3, 146.8, 139.6, 135.3, 124.7, 123.5, 123.3, 93.2, 87.3, 53.3.

2-((6-Methylpyridin-3-yl)carbamoyl)benzoic acid (227)

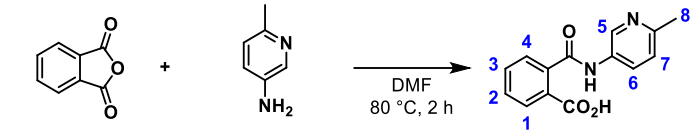

1.00 eq. | 1.00 eq. | **55%**

226 $C_8H_4O_3$ M = 148.12 g/mol | **218** $C_6H_8N_2$ M = 108.14 g/mol | **227** $C_{14}H_{12}N_2O_3$ M = 256.26 g/mol

A dried 100 mL flask was charged with a stir bar, phthalic anhydride (**226**, 200 mg, 1.35 mmol, 1.00 eq.) and amine **218** (146 mg, 1.35 mmol, 1.00 eq.). Dry DMF (38 mL) was added, and the solution was stirred at 80 °C oil bath temperature for 2 h. The mixture was allowed to cool down to room temperature. The solvent was removed under reduced pressure and the solid residue was recrystallized from DMF. The title compound (**227**, 189 mg, 0.738 mmol, 55%) was obtained as a white solid.

M.p.: ϑ_m = 245-249 °C

IR (ATR): $\tilde{\nu}$ [cm^{-1}] = 3709 (b), 3286 (m), 3254 (m), 3193 (m), 3130 (m), 3101 (m), 3066 (m), 2924 (w), 2868 (w), 1764 (m), 1739 (m), 1693 (m), 1675 (s), 1617 (m), 1595 (m), 1550 (s), 1496 (m), 1485 (m), 1433 (w), 1375 (m), 1314 (s), 1298 (s), 1222 (m), 1144 (s), 1052 (s), 994 (w), 917 (s), 890 (s), 870 (s), 853 (s), 816 (s), 799 (s), 777 (s), 755 (s), 715 (s), 686 (vs), 634 (s), 571 (m), 534 (s), 512 (m), 484 (s), 423 (m), 409 (m).

^{1}H-NMR (500 MHz, DMSO-d_6): δ [ppm] = 13.10 (br. s, 1H, CO_2H), 10.44 (s, 1H, N*H*), 8.69 (d, 1H, 5-H), 7.99 (dd, $^3J_{ortho}$ = 8.3 Hz, $^4J_{meta}$ = 2.3 Hz, 1H, 6-H), 7.92-7.86 (m, 1H), 7.69-7.63 (m, 1H), 7.62-7.53 (m, 2H), 7.23 (d, $^3J_{ortho}$ = 8.3 Hz, 1H, 7-H), 2.43 (s, 3H, 8-H).

^{13}C-NMR (126 MHz, DMSO-d_6): δ [ppm] = 167.7, 167.4, 152.4, 140.4, 138.5, 133.7, 131.8, 129.9, 129.6, 129.6, 127.8, 127.1, 122.7, 23.4.

HR-MS (pos. ESI): calculated for $C_{14}H_{13}N_2O_3$ $[M+H]^+$: 257.0921, found: 257.0924

2-(6-Methylpyridin-3-yl)isoindoline-1,3-dione (228)

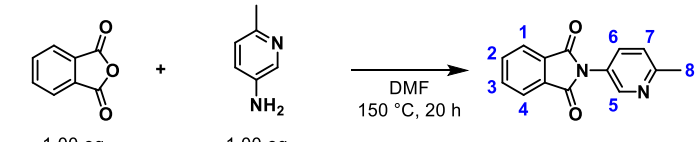

1.00 eq. | 1.00 eq. | **61%**

226 $C_8H_4O_3$ M = 148.12 g/mol | **218** $C_6H_8N_2$ M = 108.14 g/mol | **228** $C_{14}H_{10}N_2O_2$ M = 238.25 g/mol

A dried 100 mL flask was charged with a stir bar, phthalic anhydride (**226**, 200 mg, 1.35 mmol, 1.00 eq.) and amine **218** (146 mg, 1.35 mmol, 1.00 eq.). Dry DMF (38 mL) was added, and the solution was stirred at 150 °C oil bath temperature for 20 h. The mixture was allowed to cool down to room temperature. The solvent was removed under reduced pressure and the solid residue was recrystallized from EtOH. The title compound (**228**, 195 mg, 0.818 mmol, 61%) was obtained in the form of fine beige needles.

M.p.: ϑ_m = 230-234 °C

IR (ATR): $\tilde{\nu}$ [cm^{-1}] = 3096 (w), 3062 (w), 3026 (w), 2859 (b), 1771 (m), 1746 (m), 1719 (s), 1698 (m), 1599 (m), 1534 (m), 1493 (s), 1464 (m), 1431 (w), 1377 (s), 1291 (m), 1220 (m), 1134 (m), 1100 (m), 1078 (m), 1031 (m), 918 (m), 881 (m), 860 (w), 824 (m), 790 (m), 755 (w), 715 (vs), 691 (m), 640 (m), 598 (m), 571 (w), 548 (w), 529 (m), 510 (m), 410 (m).

^{1}H-NMR (500 MHz, CDCl$_3$): δ [ppm] = 8.63 (d, $^4J_{meta}$ = 2.5 Hz, 1H, 5-H), 7.99-7.92 (m, 2H, 1-H, 4-H), 7.84-7.77 (m, 2H, 2-H, 3-H), 7.70 (dd, $^3J_{ortho}$ = 8.2 Hz, $^4J_{meta}$ = 2.5 Hz, 1H, 6-H), 7.31 (d, $^3J_{ortho}$ = 8.2 Hz, 1H, 7-H), 2.63 (s, 3H, 8-H).

^{13}C-NMR (126 MHz, CDCl$_3$): δ [ppm] = 167.1, 158.1, 146.7, 134.8, 134.2, 131.8, 126.3, 124.1, 123.5, 24.3.

HR-MS (pos. ESI): calculated for $C_{14}H_{11}N_2O_2$ $[M+H]^+$: 239.0815, found: 239.0819

2-(6-Methylpyridin-3-yl)isoindoline-1,3-dione (228)

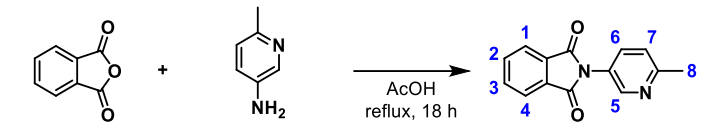

1.00 eq. **226** $C_8H_4O_3$ M = 148.12 g/mol

1.00 eq. **218** $C_6H_8N_2$ M = 108.14 g/mol

228 $C_{14}H_{10}N_2O_2$ M = 238.25 g/mol

A dried 25 mL flask was charged with a stir bar, phthalic anhydride (**226**, 200 mg, 1.35 mmol, 1.00 eq.) and amine **218** (146 mg, 1.35 mmol, 1.00 eq.). Glacial acetic acid (20 mL) was added, and the solution was stirred under reflux at 140 °C oil bath temperature for 18 h. The mixture was allowed to cool down to room temperature. The solvent was removed under reduced pressure and the solid residue was recrystallized from EtOH. The title compound (**228**, 203 mg, 0.851 mmol, 63%) was obtained in the form of long and robust beige needles.

M.p.: ϑ_m = 234-238 °C

IR (ATR): $\tilde{\nu}$ [cm^{-1}] = 3678 (b), 3096 (w), 3061 (w), 3039 (w), 3026 (w), 1771 (m), 1746 (m), 1718 (vs), 1700 (s), 1600 (m), 1535 (w), 1494 (s), 1464 (m), 1431 (w), 1378 (vs), 1292 (m), 1220 (w), 1178 (w), 1135 (w), 1100 (m), 1079 (m), 1032 (m), 963 (w), 918 (w), 881 (m), 861 (w), 824 (s), 790 (s), 755 (w), 715 (vs), 691 (s), 640 (m), 598 (w), 570 (w), 548 (w), 529 (m), 510 (m), 461 (w), 437 (w), 410 (m).

^{1}H-NMR (500 MHz, CDCl$_3$): δ [ppm] = 8.63 (d, $^4J_{meta}$ = 2.5 Hz, 1H, 5-H), 7.99-7.92 (m, 2H, 1-H, 4-H), 7.84-7.77 (m, 2H, 2-H, 3-H), 7.70 (dd, $^3J_{ortho}$ = 8.2 Hz, $^4J_{meta}$ = 2.5 Hz, 1H, 6-H), 7.31 (d, $^3J_{ortho}$ = 8.2 Hz, 1H, 7-H), 2.63 (s, 3H, 8-H).

^{13}C-NMR (126 MHz, CDCl$_3$): δ [ppm] = 167.1, 158.1, 146.7, 134.8, 134.2, 131.8, 126.3, 124.1, 123.5, 24.3.

HR-MS (pos. ESI): calculated for $C_{14}H_{11}N_2O_2$ $[M+H]^+$: 239.0815, found: 239.0817

Tri-*tert*-butyl ((((1,3,6,8,11,13-hexaoxo-6,8,11,13-tetrahydro-1*H*-benzo[1,2-*f*:3,4-*f*':5,6-*f*'']triisoindole-2,7,12(3*H*)-triyl)tris(methylene))tris(benzene-4,1-diyl))tris(methylene)) tricarbamate (242)

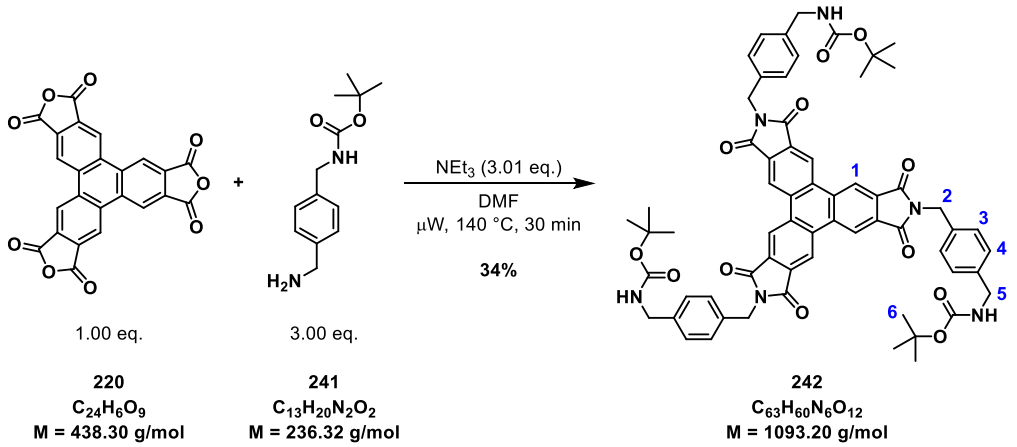

A dried 6 mL microwave vial was charged with a stir bar, trianhydride (**220**, 74.5 mg, 0.170 mmol, 1.00 eq.) and amine **241** (121 mg, 0.512 mmol, 3.01 eq.). Dry DMF (2.0 mL) and dry NEt_3 (70.7 µL, 51.6 mg, 0.510 mmol, 3.00 eq.) were added. The yellow solution was heated to 140 °C over 4 min and then stirred at 140 °C for 30 min using microwave irradiation. The reaction mixture was allowed to cool down to room temperature. The solvent was removed under reduced pressure and the solid residue was diluted with acetone (2 mL). The suspension was centrifuged, and the supernatant was decanted. This was repeated twice. The beige solid residue was dried under reduced pressure and purified by column chromatography (SiO_2, $CHCl_3$/EtOAc = 9:1 → 1:1, R_f = 0.05 in $CHCl_3$/EtOAc = 9:1). The title compound (**242**, 63.1 mg, 0.0577 mmol, 34%) was obtained as a white solid.

M.p.: No melting or visual decomposition observed up until maximum temperature (400 °C).

IR (ATR): $\tilde{\nu}$ [cm^{-1}] = 3364 (m), 3008 (w), 2981 (w), 2936 (w), 2874 (w), 1771 (m), 1703 (vs), 1689 (vs), 1612 (w), 1525 (m), 1514 (m), 1441 (w), 1427 (w), 1381 (vs), 1333 (m), 1274 (m), 1251 (m), 1213 (w), 1167 (s), 1130 (m), 1082 (w), 1052 (w), 1021 (w), 964 (m), 919 (w), 900 (w), 871 (w), 841 (w), 792 (w), 779 (w), 756 (m), 742 (m), 730 (m), 622 (s), 577 (w), 504 (w), 477 (m), 432 (w), 411 (w).

^{1}H-NMR (500 MHz, $CDCl_3$): δ [ppm] = 9.24 (s, 6H, 1-H), 7.48 (m_c, 6H, 3-H), 7.27 (m_c, 6H, 4-H), 4.96 (s, 6H, 2-H), 4.87-4.71 (m, 3H, N*H*), 4.28 (d, J = 5.4 Hz, 6H, 5-H), 1.43 (s, 27H, 6-H).

^{13}C-NMR (126 MHz, $CDCl_3$): δ [ppm] = 177.8, 167.0, 139.1, 135.2, 134.4, 131.8, 129.3, 128.0, 120.3, 79.8, 44.5, 42.1, 28.5.

HR-MS (pos. ESI): calculated for $C_{63}H_{60}N_6O_{12}Na$ $[M+Na]^+$: 1115.4161, found: 1115.4152

(((1,3,6,8,11,13-Hexaoxo-6,8,11,13-tetrahydro-1*H*-benzo[1,2-*f*:3,4-*f*':5,6-*f*'']triisoindole-2,7,12(3*H*)-triyl)tris(methylene))tris(benzene-4,1-diyl))trimethan aminium 2,2,2-trifluoro acetate (243)

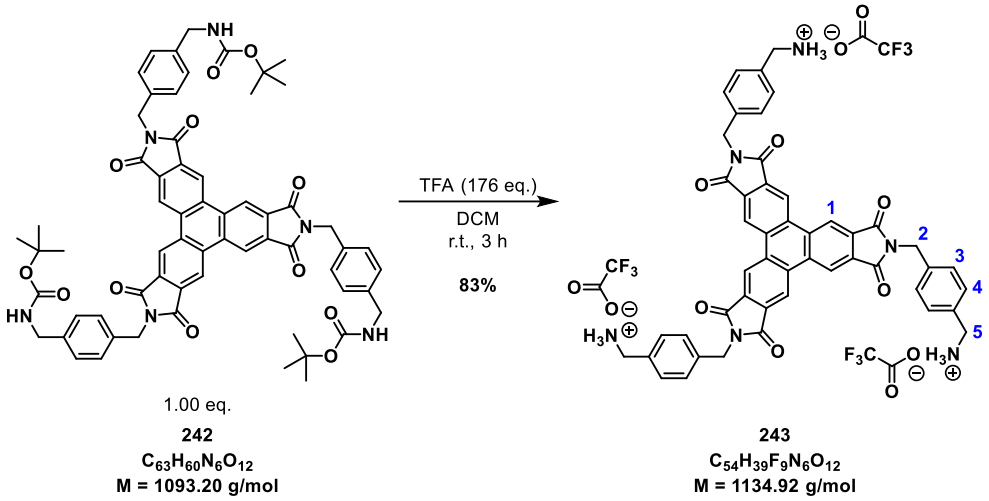

A 4 mL vial was charged with a stir bar and TPTI **242** (30.0 mg, 0.0274 mmol, 1.00 eq.). DCM (2.0 mL) was added, and the white suspension was ultrasonicated. TFA (372 µL, 551 mg, 0.483 mmol, 176 eq.) was added and the yellow suspension was stirred at room temperature for 3 h. The solvent was removed under reduced pressure. The solid residue was diluted with acetone (2 mL) and the suspension was centrifuged. The supernatant was decanted, and this washing procedure was repeated once with DCM (2 mL). The solid residue was dried under reduced pressure. The title compound (**243**, 25.9 mg, 0.0228 mmol, 83%) was obtained as an off-white solid.

M.p.: Decomposition observed at 200 °C onwards.

IR (ATR): $\tilde{\nu}$ [cm^{-1}] = 3437 (w), 2932 (b), 1771 (m), 1708 (s), 1671 (s), 1519 (m), 1428 (m), 1382 (vs), 1343 (s), 1198 (s), 1179 (s), 1126 (vs), 1079 (m), 1022 (w), 963 (m), 900 (m), 835 (m), 798 (m), 756 (m), 721 (s), 642 (w), 621 (s), 596 (w), 551 (m), 513 (m), 461 (m), 440 (m), 409 (m).

^{1}H-NMR (600 MHz, MeOD-*d*$_4$): δ [ppm] = 8.93 (s, 6H, 1-H), 7.58 (m$_c$, 6H, 3-H), 7.47 (m$_c$, 6H, 4-H), 4.95 (s, 6H, 2-H), 4.08 (s, 6H, 5-H).

^{13}C-NMR (151 MHz, MeOD-*d*$_4$): δ [ppm] = 168.2, 163.0 (q, ^{2}J = 34.3 Hz, *C*(=O)CF$_3$), 138.9, 135.0, 134.2, 132.4, 130.5, 130.3, 121.2, 118.2 (q, ^{1}J = 292.3 Hz, *C*F$_3$), 43.9, 42.6.

^{19}F-NMR (471 MHz, MeOD-*d*$_4$, C$_6$F$_6$ as int. Std.): δ [ppm] = –76.48.

HR-MS (pos. ESI):

calculated for $C_{48}H_{37}N_6O_6$ [M–3TFA–2H]$^+$: 793.2769, found: 793.2770

calculated for $C_{49}H_{41}N_6O_7$ [M–3TFA–2H+MeOH]$^+$: 825.3031, found: 825.3026

5.3 NMR Titration Experiments towards Guest-Uptake

5.3.1 Titration Procedures

Titration Procedures with Ammonium Trifluoroacetate Cage XXVa as Host

NMR titrations were performed measuring ^{1}H-NMR spectra at 400 MHz or 500 MHz using a BRUKER Ascend 400 spectrometer or a BRUKER UltraShield 500 spectrometer at 298 K, respectively. GILSON Microman Micropipettes (1-10 µL and 1-100 µL) were used for the addition of stock solutions during the titrations. The following solvents were used for the corresponding guests: MeCN-d_3 for **209**-**211**; D_2O for **212** and DMSO-d_6 for **213**.

The titrations with host **XXVa** were initially only meant for qualitative analysis to see if binding occurred or not. These initial titration experiments have also been the first ones conducted in this study. Therefore, guest solubility properties and other factors have been explored for the first time leading to slightly different titration procedures fo every guest during the process.

(1) For guest **209**:

498 µL of a stock solution of **XXVa** (Host, H) in MeCN-d_3 at a concentration of [H] = 0.410 mM was added to an NMR tube. A ^{1}H-NMR spectrum was measured before and after each addition of guest (G) at set equivalents using a guest stock solution in MeCN-d_3 at a concentration of [G] = 51.0 mM corresponding to 0.25 eq./µL. (Titration range: 0-10 eq.) Upon each addition, the mixture was manually stirred and allowed to equilibrate for 5 min before acquiring a spectrum.

(2) For guest **210**:

498 µL of a stock solution of **XXVa** (Host, H) in MeCN-d_3 at a concentration of [H] = 0.445 mM was added to an NMR tube. A ^{1}H-NMR spectrum was measured before and after each addition of guest (G) at set equivalents using a guest stock solution in MeCN-d_3 at a concentration of [G] = 111 mM corresponding to 0.5 eq./µL. (Titration range: 0-10 eq.) Upon each addition, the mixture was manually stirred and allowed to equilibrate for 5 min before acquiring a spectrum.

(3) For guest **211**:

498 µL of a stock solution of **XXVa** (Host, H) in MeCN-d_3 at a concentration of [H] = 0.471 mM was added to an NMR tube. A ^{1}H-NMR spectrum was measured before and after each addition of guest (G) at set equivalents using a guest stock solution in MeCN-d_3 at a concentration of [G] = 118 mM corresponding to 0.5 eq./µL. (Titration range: 0-10 eq.) Upon each addition, the mixture was manually stirred and allowed to equilibrate for 5 min before acquiring a spectrum.

(4) For guest **212**:

498 µL of a stock solution of **XXVa** (Host, H) in MeCN-d_3 at a concentration of [H] = 0.497 mM was added to an NMR tube. A ^{1}H-NMR spectrum was measured before and after each addition of guest (G) at set equivalents using a guest stock solution in MeCN-d_3 at a concentration of [G] = 123 mM corresponding to 0.500 eq./µL. (Titration

range: 0-10.0 eq.) Upon each addition, the mixture was manually stirred and allowed to equilibrate for 5 min before acquiring a spectrum.

(5) For guest **213**:

498 µL of a stock solution of **XXVa** (Host, H) in MeCN-d_3 at a concentration of [H] = 0.445 mM was added to an NMR tube. A ^{1}H-NMR spectrum was measured before and after each addition of guest (G) at set equivalents using a guest stock solution in MeCN-d_3 at a concentration of [G] = 111 mM corresponding to 0.500 eq./µL. (Titration range: 0-10.0 eq.) Upon each addition, the mixture was manually stirred and allowed to equilibrate for 5 min before acquiring a spectrum.

Fast exchange on the NMR timescale was observed for the formation of host-guest complexes in all cases except compound **211** for which the fit failed due to insufficient data. Changes in chemical shift were observed and plotted using nonlinear regression *via* the bindfit app (THORDARSON *et al*., http://app.supramolecular.org/bindfit/)[301,319] for signals that could be observed over the entire course of the titration experiment. The resulting fits were used to calculate K_a in addition to an error margin for 95% confidence of fit and the root mean square (RMS) for the entire signal set.

Titration Procedures with Fe_4L_6 Tetrahedron XXIX as Host

NMR titrations were performed measuring ^{1}H-NMR spectra at 500 MHz using a BRUKER UltraShield 500 spectrometer at 298 K. GILSON Microman Micropipettes (1-10 µL and 1-100 µL) were used for the addition of stock solutions during the titrations. MeCN-d_3 was used as solvent for all stock solutions. $CHCl_3$ and *tert*-butylmethylether (TBME) were present in the host material in residual amounts, explaining the extra peaks.

(1) For guest **211**:

500 µL of a stock solution of **XXIX** (Host, H) in MeCN-d_3 at a concentration of [H] = 0.357 mM was added to an NMR tube. A ^{1}H-NMR spectrum was measured before and after each addition of guest (G) at set equivalents using a guest stock solution in MeCN-d_3 at a concentration of [G] = 89.2 mM corresponding to 0.50 eq./µL. (Titration range: 0-10 eq.) Upon each addition, the mixture was manually stirred and allowed to equilibrate for 5 min before acquiring a spectrum.

(2) For guest **209**, **210**, **212**, **213**, and **216**:

To a solution of **Fe_4L_6** cage **XXIX** (Host, H) in MeCN-d_3 was added a stock solution of guest (G) with the same host concentration [H] as the host solution so that samples with 500 µL of a solution with constant host concentration of [H] = 0.100 mM and with varying guest concentrations [G] were obtained.

Fast exchange on the NMR timescale was only observed for the formation of host-guest complexes with anionic guest **211**. Changes in chemical shift were observed and plotted using nonlinear regression *via* the bindfit app (THORDARSON *et al*., http://app.supramolecular.org/bindfit/)[301,319] for signals that could be observed over the entire course of the titration experiment. The resulting fits were used to calculate K_a in addition to an error margin for 95% confidence of fit and the root mean square (RMS) for the entire signal set. Partial disassembly of the cage was observed for anionic guests **209**, **210**, **212**, **213**, and **216**. No binding was observed for neutral guest **217**.

Titration Procedures with Zn_4L_4 Cage Zn-XLIII and ZnL_3 Complex XLIV as Hosts

NMR titrations were performed measuring ^{1}H-NMR spectra at 500 MHz using a BRUKER UltraShield 500 spectrometer at 298 K. GILSON Microman Micropipettes (1-10 µL and 1-100 µL) were used for the addition of guest stock solutions during the titrations. MeCN-d_3/H_2O = 9:1 was used as a solvent mixture for all stock solutions. Using D_2O instead of H_2O led to shimming problems and, therefore, was substituted.

(1) Due to the low accessibility (tedious workup) of **$Zn_4L_4(NTf_2)_8$** cage **Zn-XLIII** titration experiments for guests **209**, **212**, and **256-262** were performed according to the following procedure to save material:

500 µL of a stock solution of **$Zn_4L_4(NTf_2)_8$** cage **Zn-XLIII** (Host, H) in MeCN-d_3/H_2O = 9:1 at a concentration of [H] = 0.125 mM was added to an NMR tube. A ^{1}H-NMR spectrum was measured before and after each addition of guest (G) at set equivalents using guest stock solutions in MeCN-d_3/H_2O = 9:1 at concentrations of 6.25 mM, 62.5 mM and 625 mM corresponding to 0.10 eq./µL, 1.0 eq./µL and 10 eq./µL, respectively, to reduce dilution of the host concentration during the titration. (Titration range: 0-300 eq.) Upon each addition, the mixture was manually stirred and allowed to equilibrate for 5 min before acquiring a spectrum.

(2) For the same guests **209**, **212**, and **256-262**, titrations with mononuclear **$ZnL_3(NTf_2)_2$** complex **XLIV** were performed similarly as described above, but with a four times higher concentration of the complex to simulate the 4 equivalents of Zn^{II} metal ions present in **$Zn_4L_4(NTf_2)_8$** cage **Zn-XLIII** for better comparison of the binding constants:

500 µL of a stock solution of mononuclear **$ZnL_3(NTf_2)_2$** complex **XLIV** (Host, H) in MeCN-d_3/H_2O = 9:1 at a concentration of [H] = 0.500 mM was added to an NMR tube. A ^{1}H-NMR spectrum was measured before and after each addition of guest (G) at set equivalents using guest stock solutions in MeCN-d_3/H_2O = 9:1 at concentrations of 6.25 mM, 62.5 mM and 625 mM to reduce dilution of the host concentration during the titration. (Titration range: 0-1250 eq. or 0-312.5 eq. when divided by 4 equivalents of Zn^{II} metal ions.) Upon each addition, the mixture was manually stirred and allowed to equilibrate for 5 min before acquiring a spectrum.

(3) Initially, for phosphate guests **260-262**, titrations with **$Zn_4L_4(NTf_2)_8$** cage **Zn-XLIII** were performed using a more accurate method at the expense of more cage material in total as follows:

To a solution of **$Zn_4L_4(NTf_2)_8$** cage **Zn-XLIII** (Host, H) in MeCN-d_3/H_2O = 9:1 was added a stock solution of guest (G) with the same host concentration [H] as the host solution so that samples with 500 µL of a solution with constant host concentration of [H] = 0.100 mM and with varying guest concentrations [G] were obtained.

Fast exchange on the NMR timescale was observed for the formation of host-guest complexes in all cases except the neutral compounds **171**, **3**, **252**, **253**, **254**, **166**, and **255** for which no binding was observed. Changes in chemical shift were observed and plotted using nonlinear regression *via* the bindfit app (THORDARSON *et al.*, http://app.supramolecular.org/bindfit/) for signals that could be observed over the entire course of the titration experiment.[319,301] The resulting fits were used to calculate K_a in addition to an error margin for 95% confidence of fit and the root mean square (RMS) for the entire signal set.

5.3.2 Bindfit Links

Bindfit Links with Ammonium Trifluoroacetate Cage XXVa as Host

Guest **209**: http://app.supramolecular.org/bindfit/view/5376da06-5cf3-408d-8d8b-450b7e090020

Guest **210**: http://app.supramolecular.org/bindfit/view/8a881bce-c303-435f-9ada-ca528a777576

Guest **212**: http://app.supramolecular.org/bindfit/view/e22d144c-c4d1-469f-99fc-50e1a87ad445

Guest **213**: http://app.supramolecular.org/bindfit/view/99fdba4e-0e27-462c-8c06-74f4a07c102b

Bindfit Links with $Fe_4L_6(NTf_2)_8$ Cage XXIX as Host

Guest **211**: http://app.supramolecular.org/bindfit/view/9e61f18e-abb4-40b9-9390-8733dbd045b9

Bindfit Links with $Zn_4L_4(NTf_2)_8$ Cage Zn-XLIII as Host

Guest **209**: http://app.supramolecular.org/bindfit/view/3a8daf41-ee97-49ef-ad3f-f81dee13e1b9

Guest **212**: http://app.supramolecular.org/bindfit/view/9c6f3daf-3f9a-43d1-975b-9f7f9fb129c2

Guest **256**: http://app.supramolecular.org/bindfit/view/ff633152-79a7-486e-9465-fe79d6b513d6

Guest **257**: http://app.supramolecular.org/bindfit/view/06faccdd-14aa-4d11-9969-fe6d7a432050

Guest **258**: http://app.supramolecular.org/bindfit/view/fb7e47eb-26ce-4dc6-a78c-7eb9ebff4bcd

Guest **259**: http://app.supramolecular.org/bindfit/view/0a177a28-6d7d-4345-a9ac-7d30f4837a5d

Guest **260**: http://app.supramolecular.org/bindfit/view/b3c35e0f-3771-4557-97f3-559815fb9c26

Guest **261**: http://app.supramolecular.org/bindfit/view/6151f9e4-5053-4016-a8d1-0cceebc1909d

Guest **262**: http://app.supramolecular.org/bindfit/view/61699461-60eb-4e7b-b461-6517bdf6db16

Bindfit Links with $ZnL_3(NTf_2)_2$ Complex XLIV as Host

Guest **209**: http://app.supramolecular.org/bindfit/view/714d12da-7b0a-4b84-829e-56ed4d02ff31

Guest **212**: http://app.supramolecular.org/bindfit/view/c201f420-0422-49ae-80ac-e9cd083304eb

Guest **256**: http://app.supramolecular.org/bindfit/view/af3583a3-adee-457f-be0e-01c706f134dd

Guest **257**: http://app.supramolecular.org/bindfit/view/36dffe9d-45f8-4a9c-8dbb-52f4aef817bf

Guest **258**: http://app.supramolecular.org/bindfit/view/df65f2d8-e7d1-47d5-abc5-10489d5670a0

Guest **259**: http://app.supramolecular.org/bindfit/view/ad2f9fd0-2e1f-4e50-a789-67d4b0b2c8a3

5.3.3 Guest Titration Data with Ammonium Trifluoroacetate Cage XXVa

Guest Titrations that showed Binding (Fast Exchange)

Titration of potassium *p*-tolyltrifluoroborate (209@XXVa)

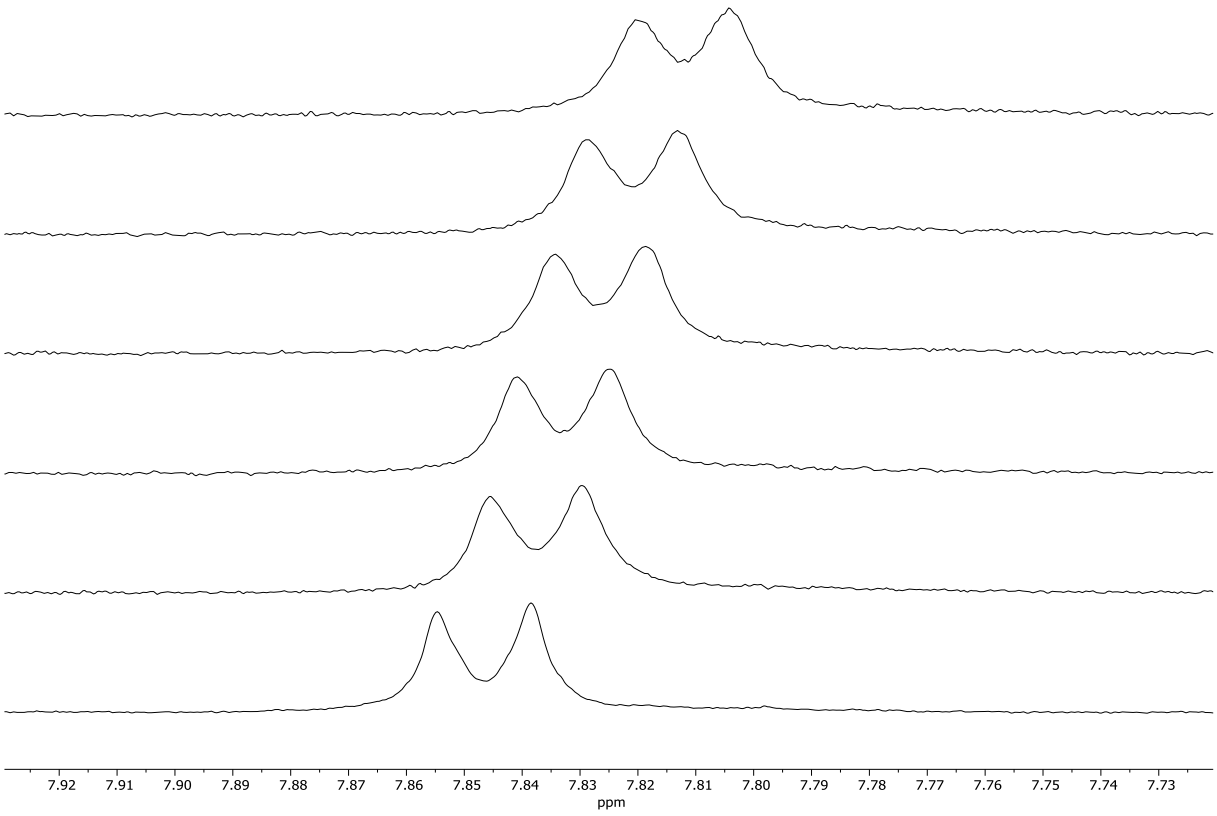

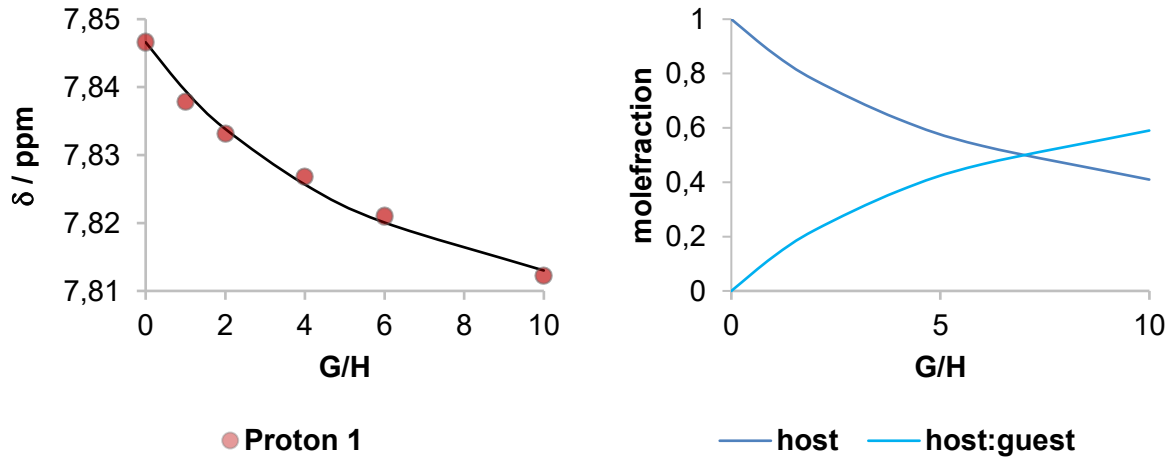

Titrated at $[H]_0$ = 0.410 mM. K_a = 400 ± 64 M^{-1}. RMS = 1.0088 • 10^{-3}.

Titration of tetrabutylammonium (1*S*)-(+)-10-camphorsulfonate (210@XXVa)

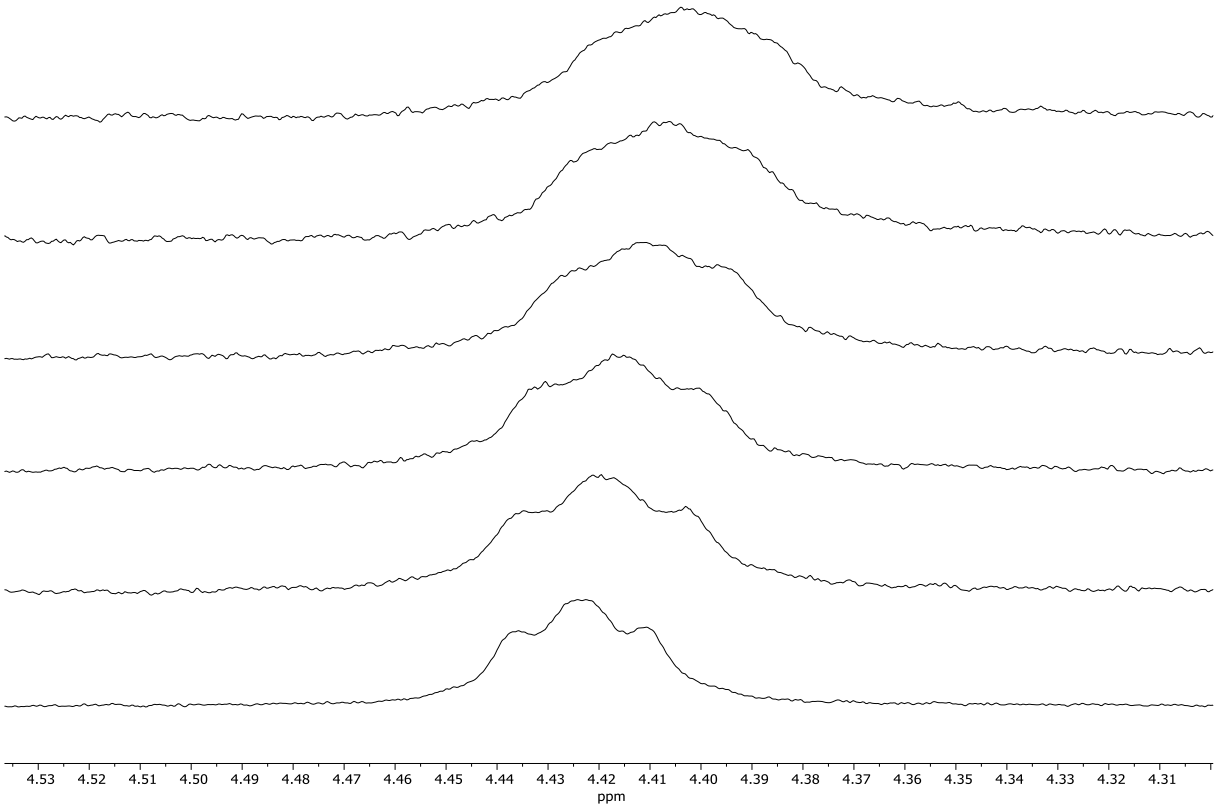

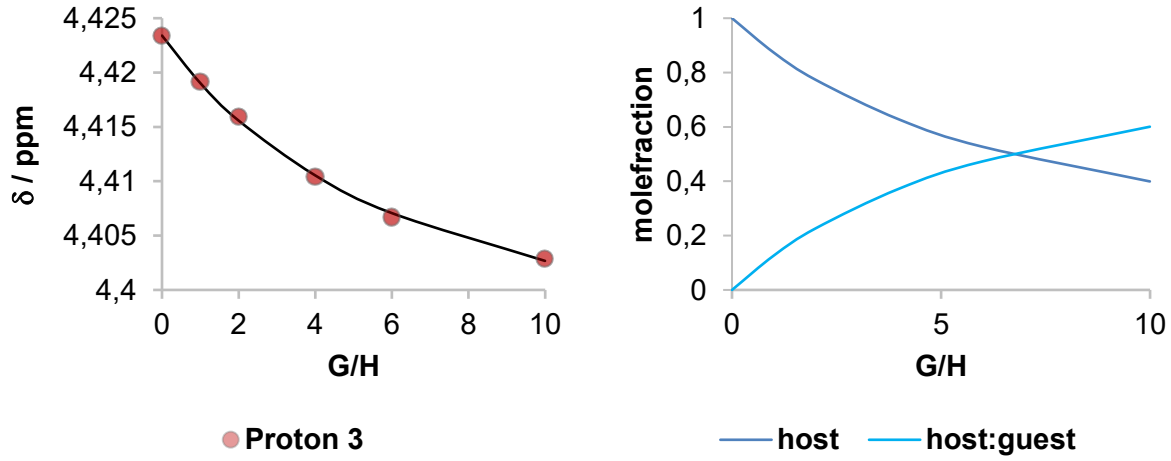

Titrated at $[H]_0$ = 0.445 mM. K_a = 370 ± 23 M^{-1}. RMS = 2.3641 • 10^{-4}.

Titration of tetrabutylammonium *p*-toluenesulfonate (212@XXVa)

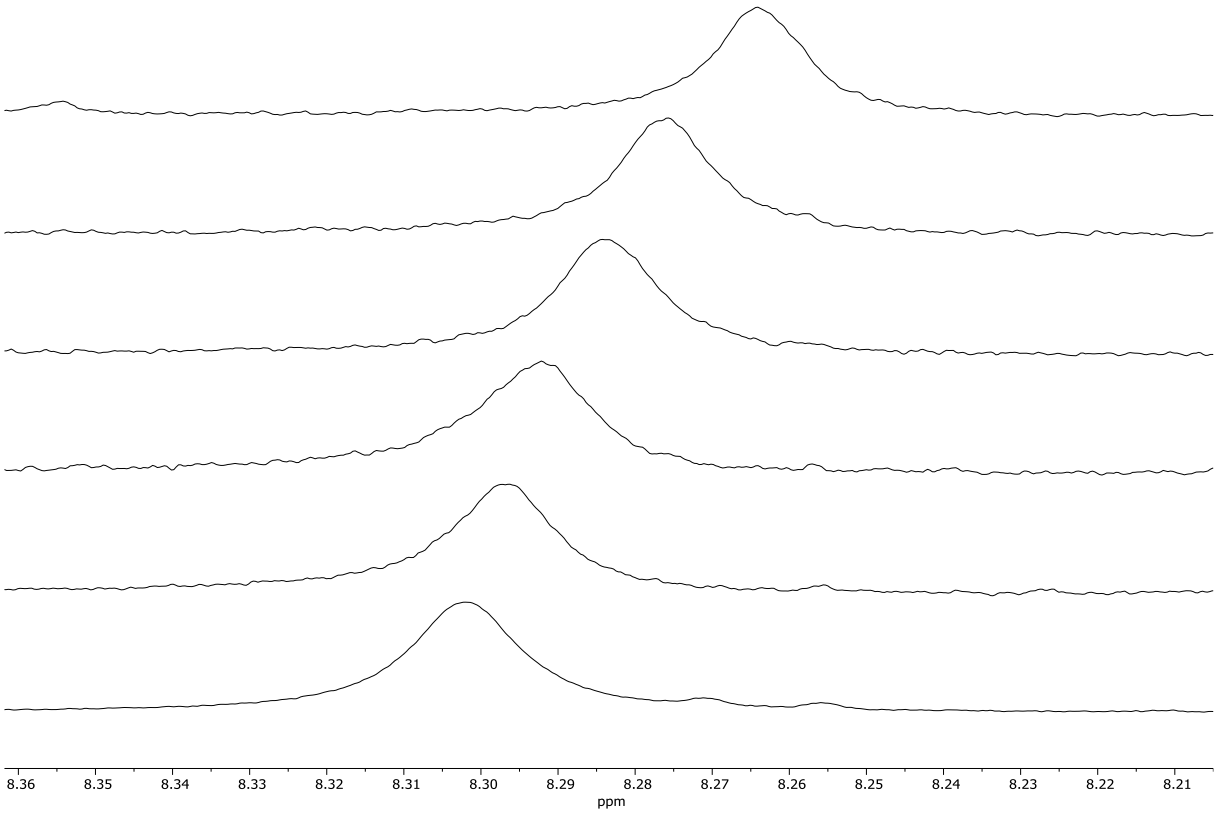

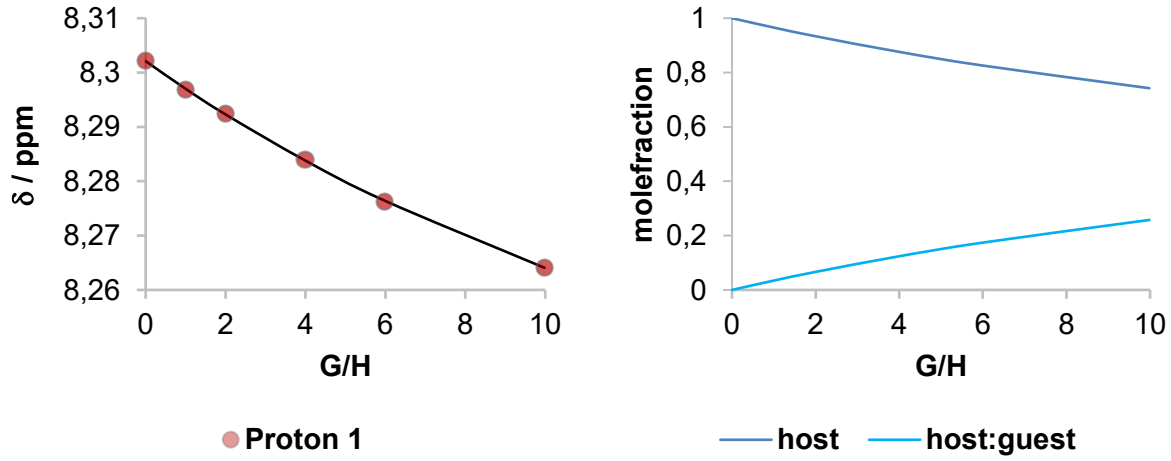

Titrated at $[H]_0$ = 0.497 mM. K_a = 75 ± 1 M^{-1}. RMS = 8.3240 • 10^{-5}.

Titration of tetrabutylammonium *R*-(+)-binaphthylphosphate (213@XXVa)

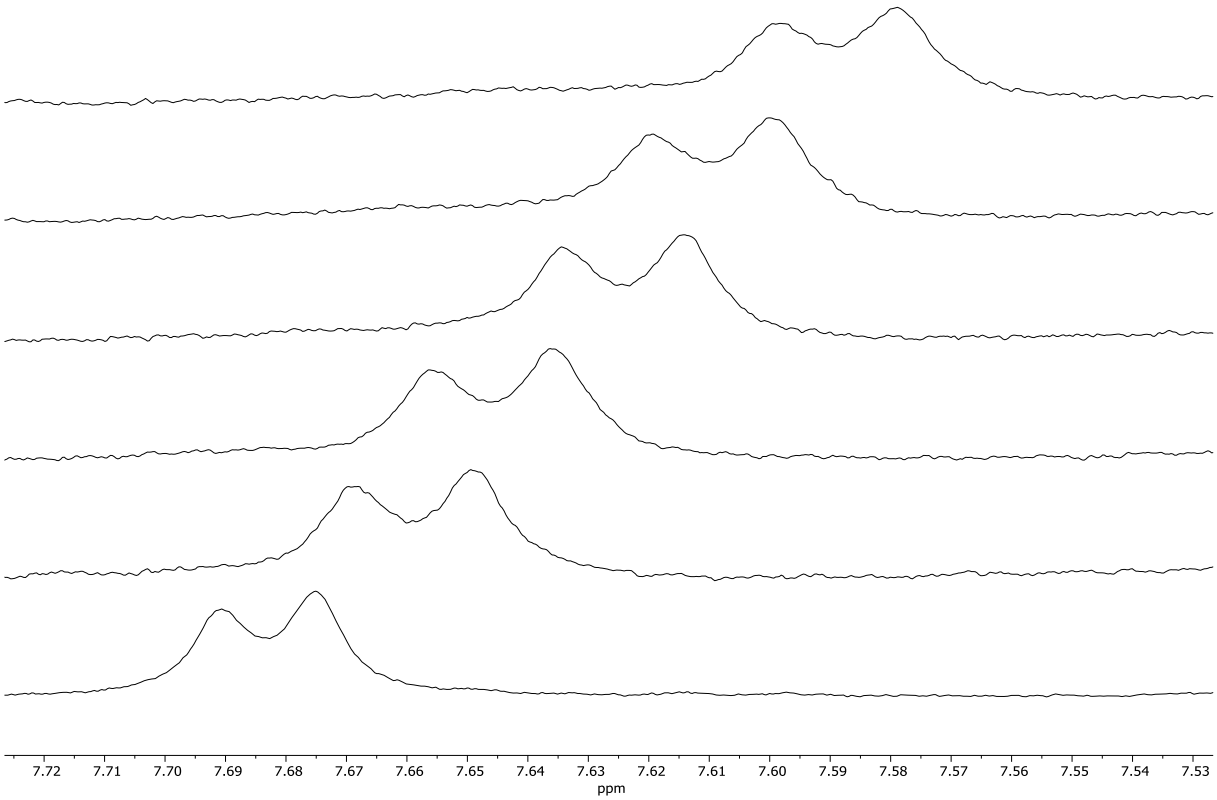

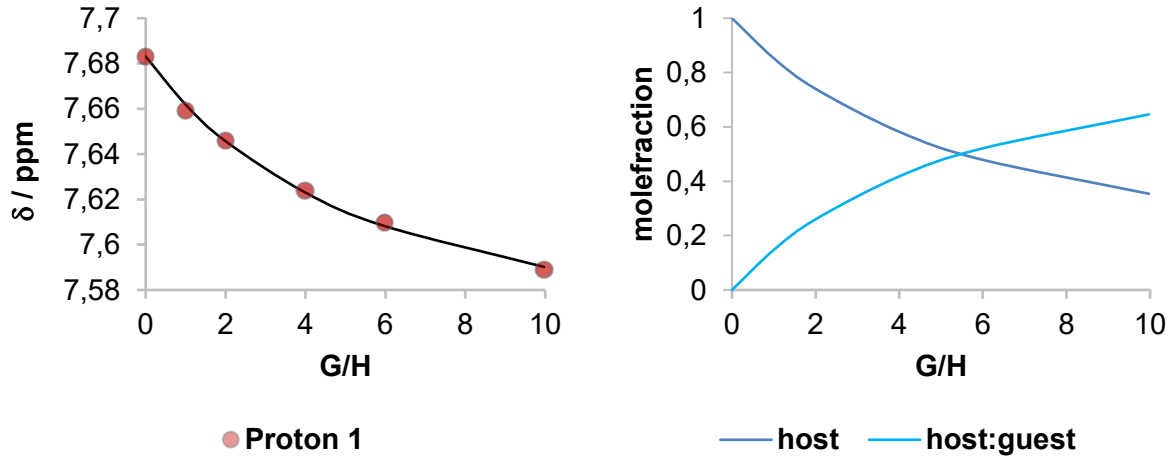

Titrated at $[H]_0$ = 0.445 mM. K_a = 460 ± 40 M^{-1}. RMS = 1.4434 • 10^{-3}.

Guest Titrations for which insufficient Data was obtained

Titration of tetrabutylammonium tetraphenylborate (211@XXVa)

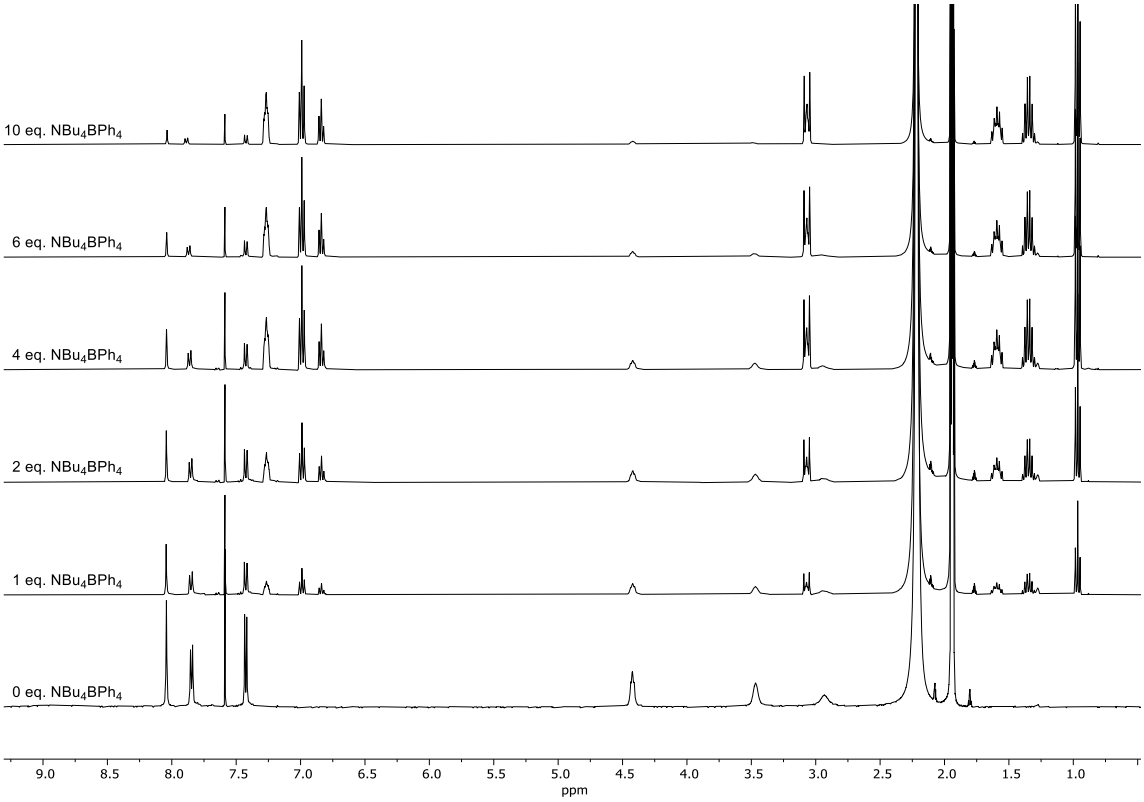

5.3.4 Guest Titration Data with $Fe_4L_6(NTf_2)_8$ Cage XXIX

Guest Titrations that showed Binding (Fast Exchange)

Titration of tetrabutylammonium tetraphenylborate (211@XXIX)

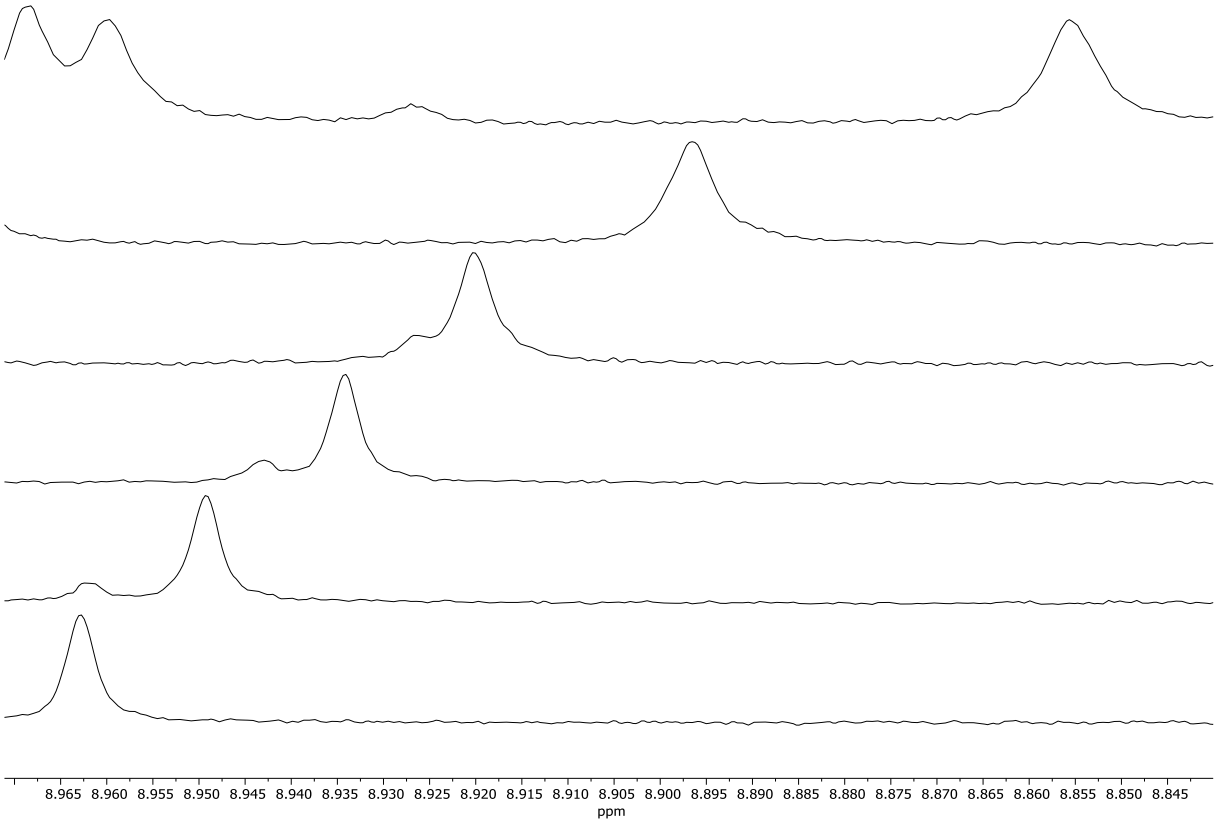

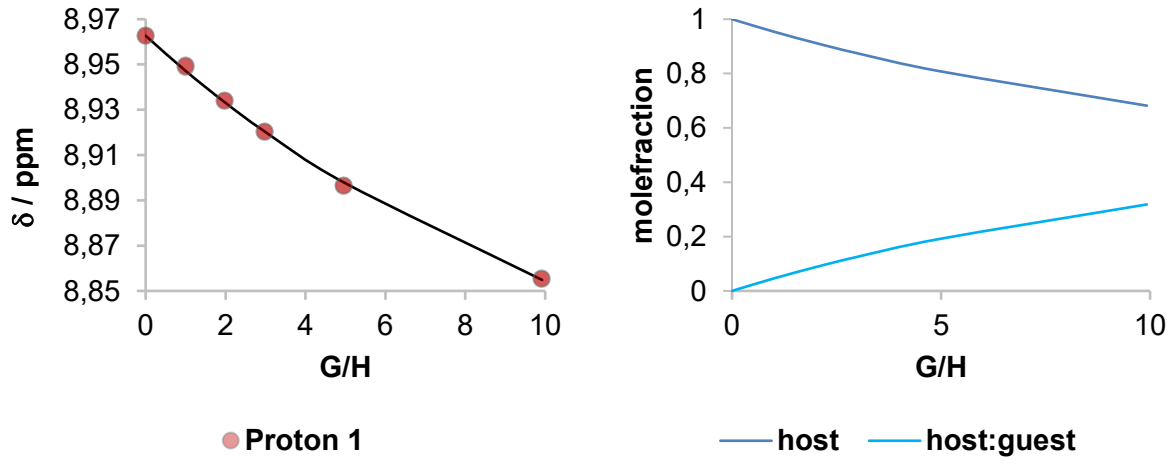

Titrated at $[H]_0$ = 0.357 mM. K_a = 140 ± 5.9 M^{-1}. RMS = 1.0517 • 10^{-3}.

Titration of Guests which induced (partial) Disassembly of $Fe_4L_6(NTf_2)_8$ Cage XXIX

Titration of potassium *p*-tolyltrifluoroborate (209@XXIX)

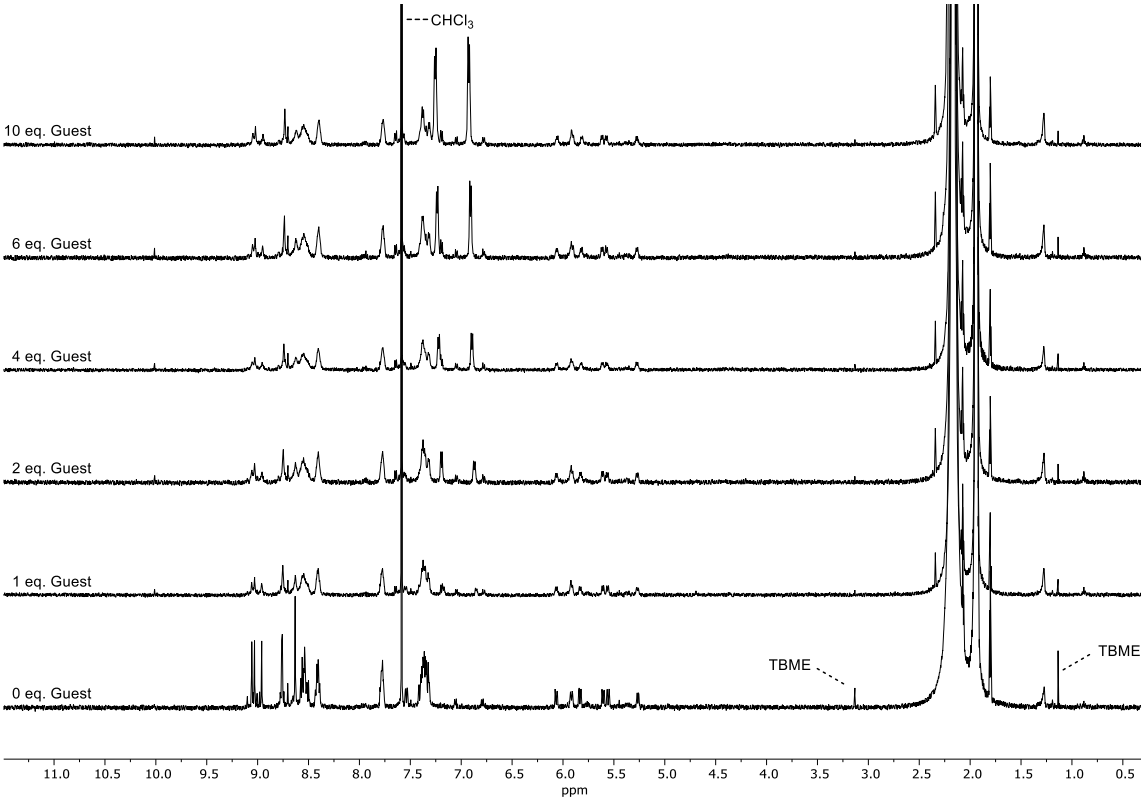

Titration of tetrabutylammonium (1*S*)-(+)-10-camphorsulfonate (210@XXIX)

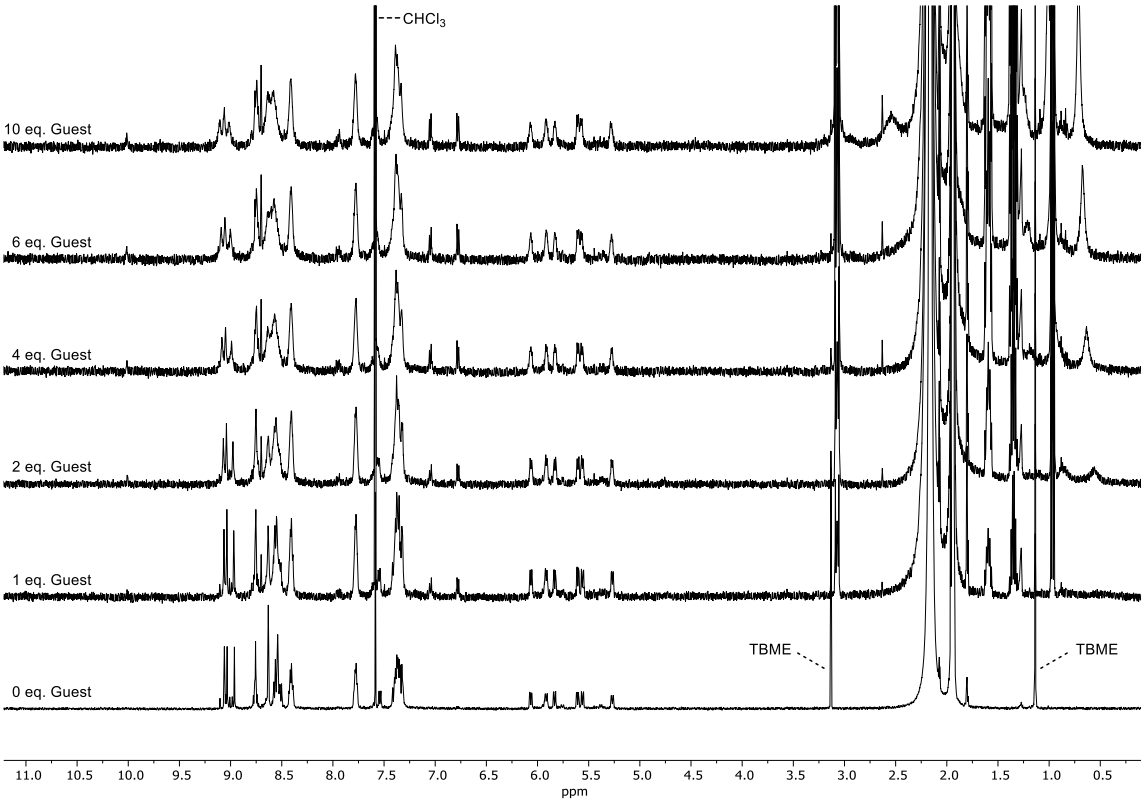

Titration of tetrabutylammonium *p*-tolylsulfonate (212@XXIX)

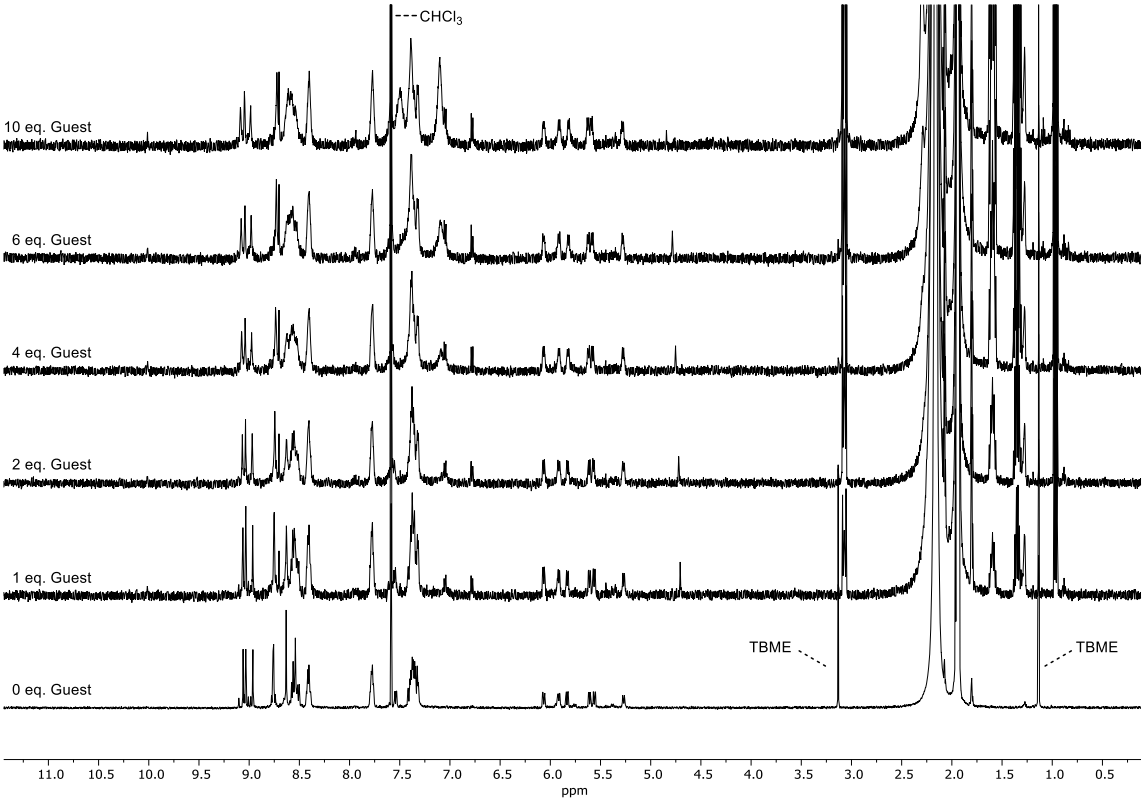

Titration of tetrabutylammonium *R*-(+)-binaphthylphosphate (213@XXIX)

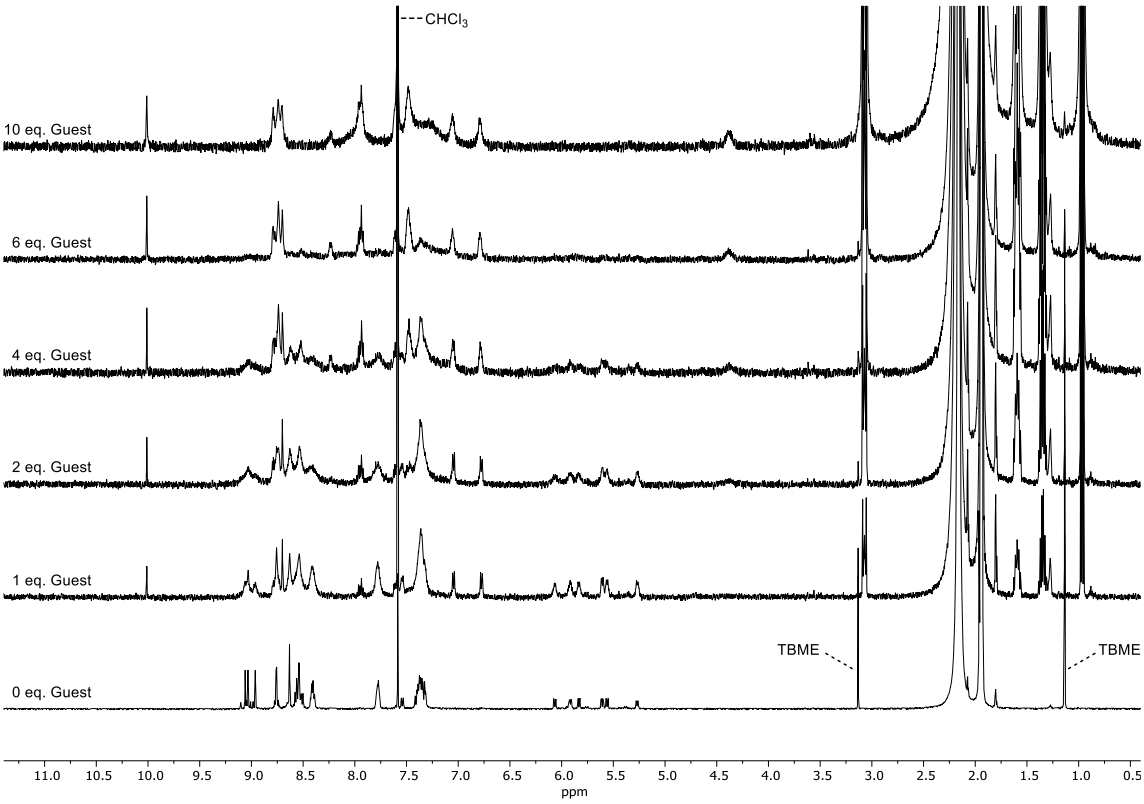

Titration of potassium *p*-methoxyphenyltrifluoroborate (216@XXIX)

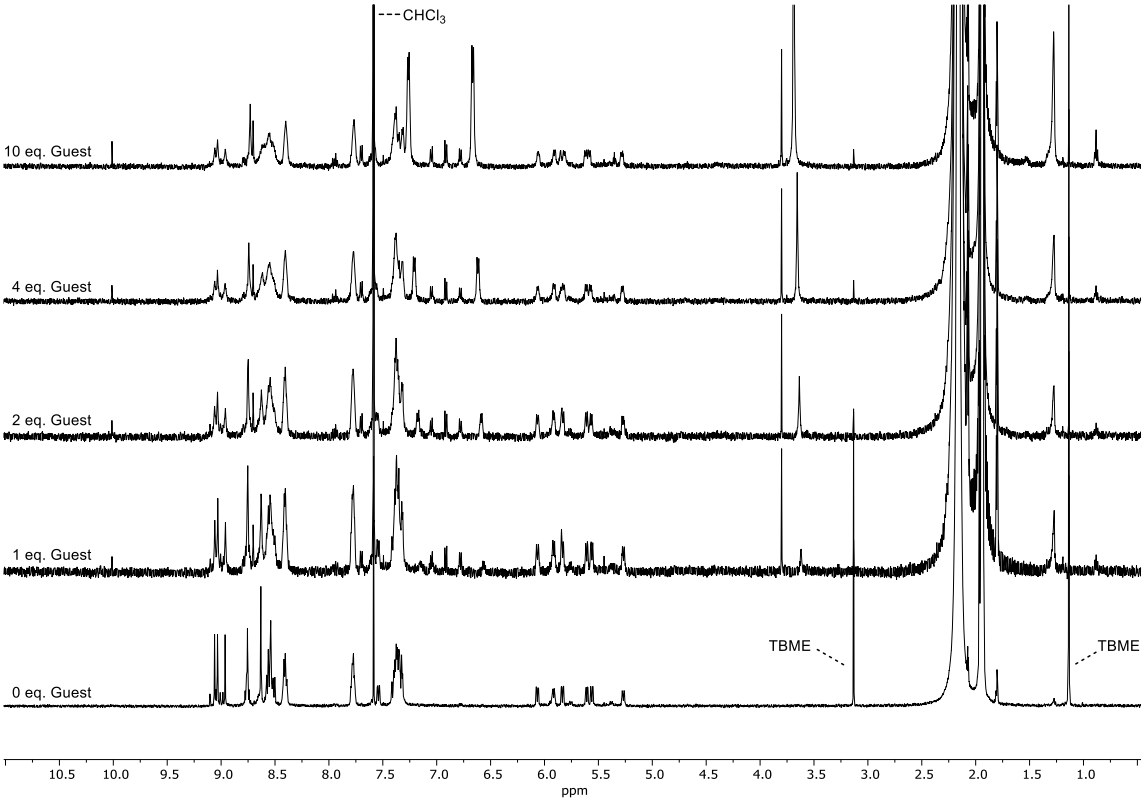

Titration of Neutral Guests showing no Binding with $Fe_4L_6(NTf_2)_8$ Cage XXIX as Host

Titration of allylphenylether (217@XXIX)

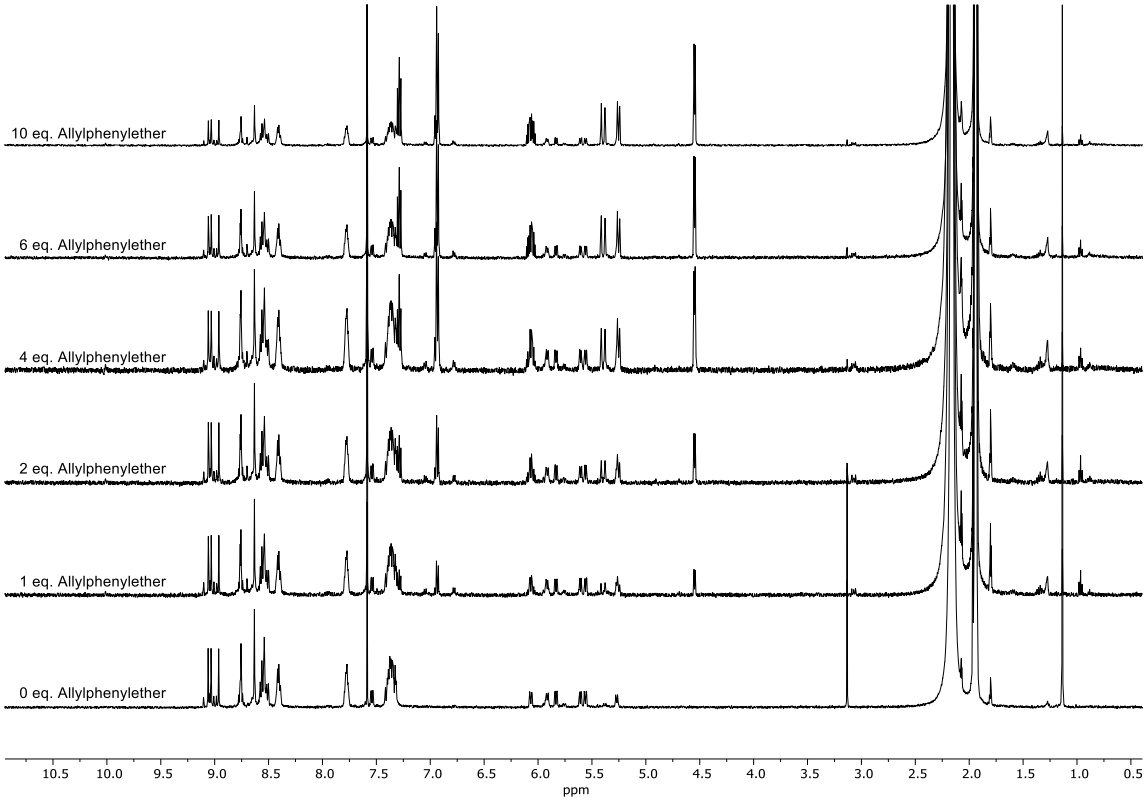

5.3.5 Guest Titration Data with $Zn_4L_4(NTf_2)_8$ Cage Zn-XLIII

Guest Titrations that showed Binding (Fast Exchange)

Titration of potassium *p*-tolyltrifluoroborate (209@Zn-XLIII)

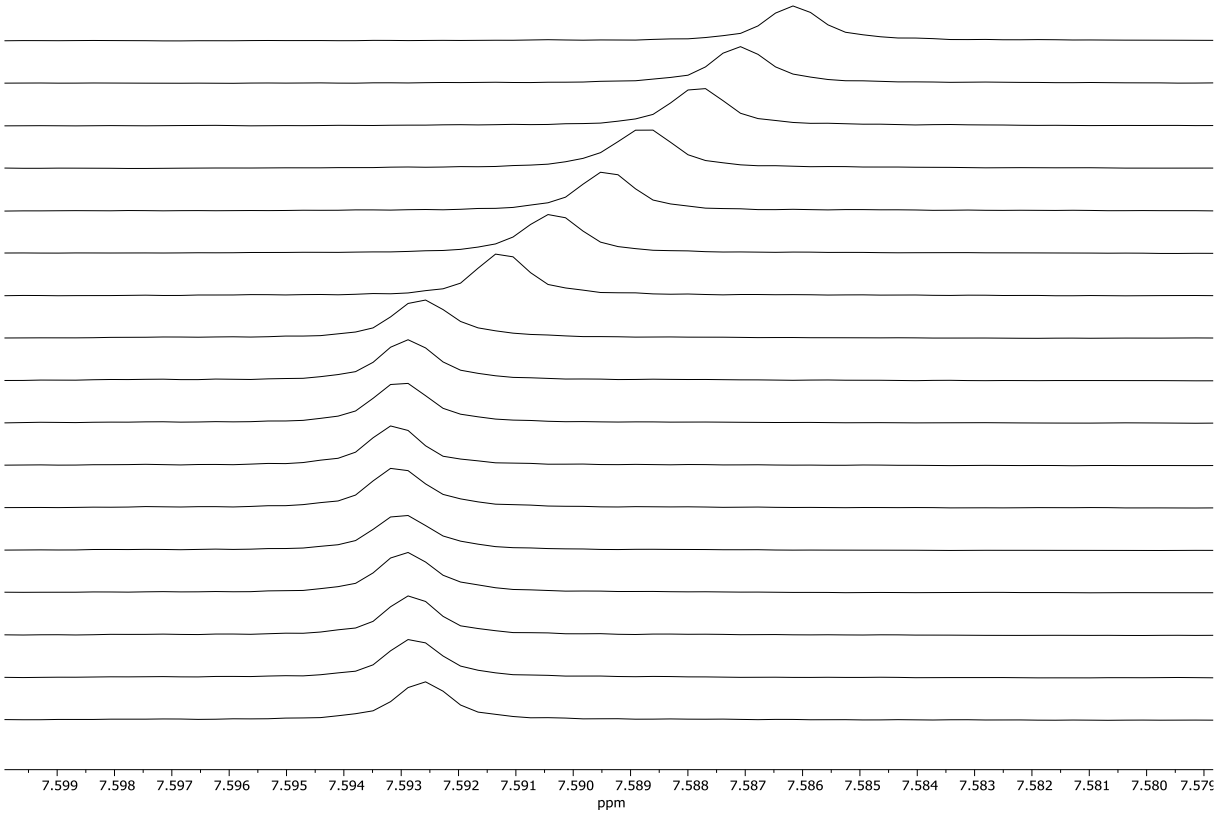

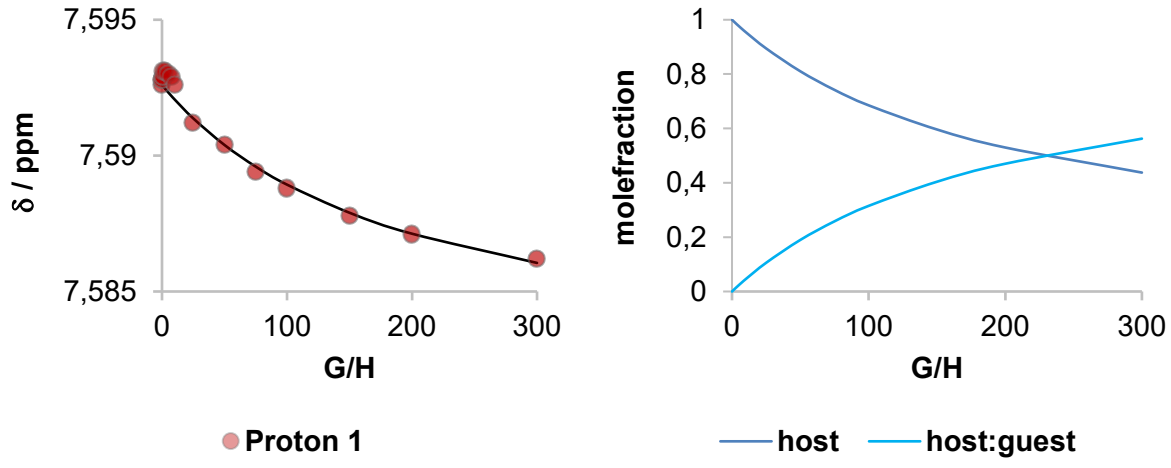

Titrated at $[H]_0$ = 0.125 mM. K_a = 40 ± 5.5 M^{-1}. RMS = 3.7350 • 10^{-4}.

Titration of tetrabutylammonium *p*-toluenesulfonate (212@Zn-XLIII)

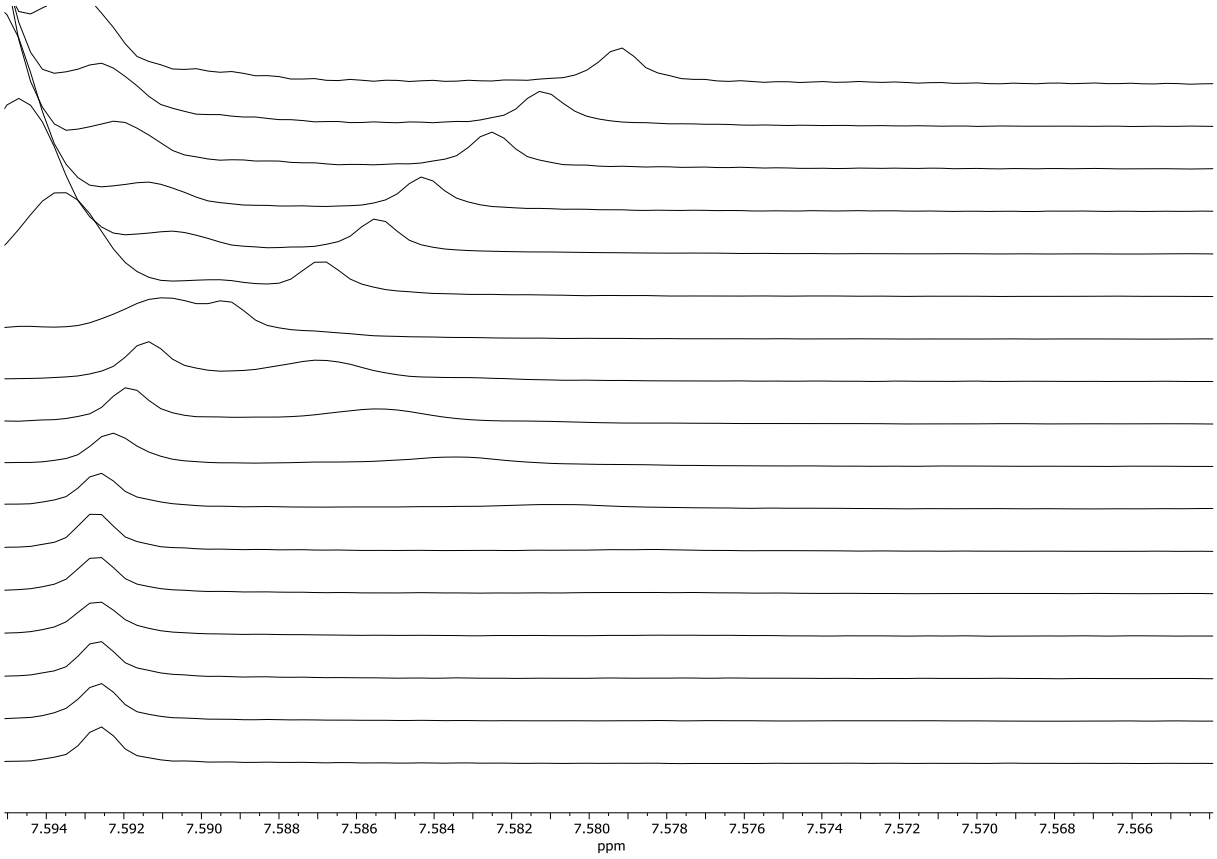

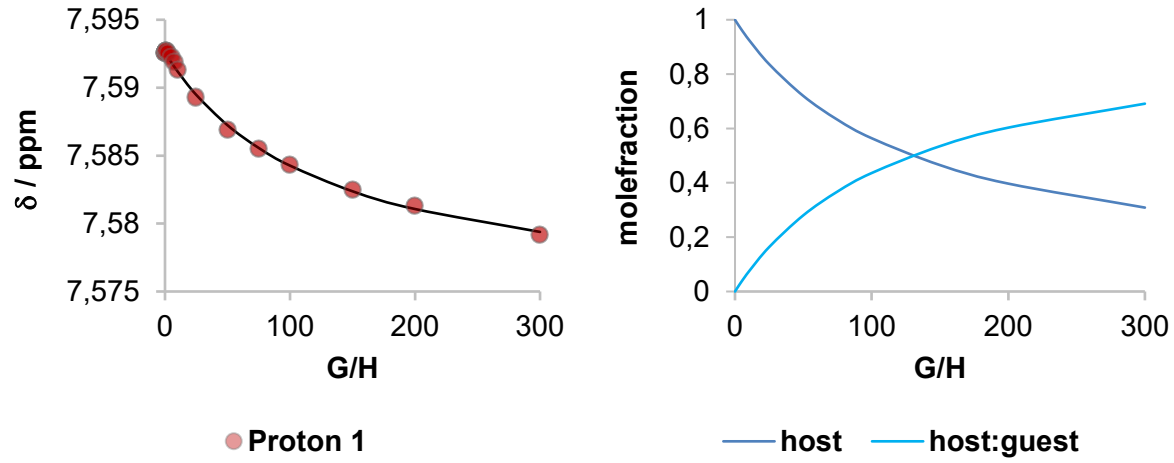

Titrated at $[H]_0$ = 0.125 mM. K_a = 66 ± 3.1 M^{-1}. RMS = 2.2469 • 10^{-4}.

Titration of tetrabutylammonium benzoate (256@Zn-XLIII)

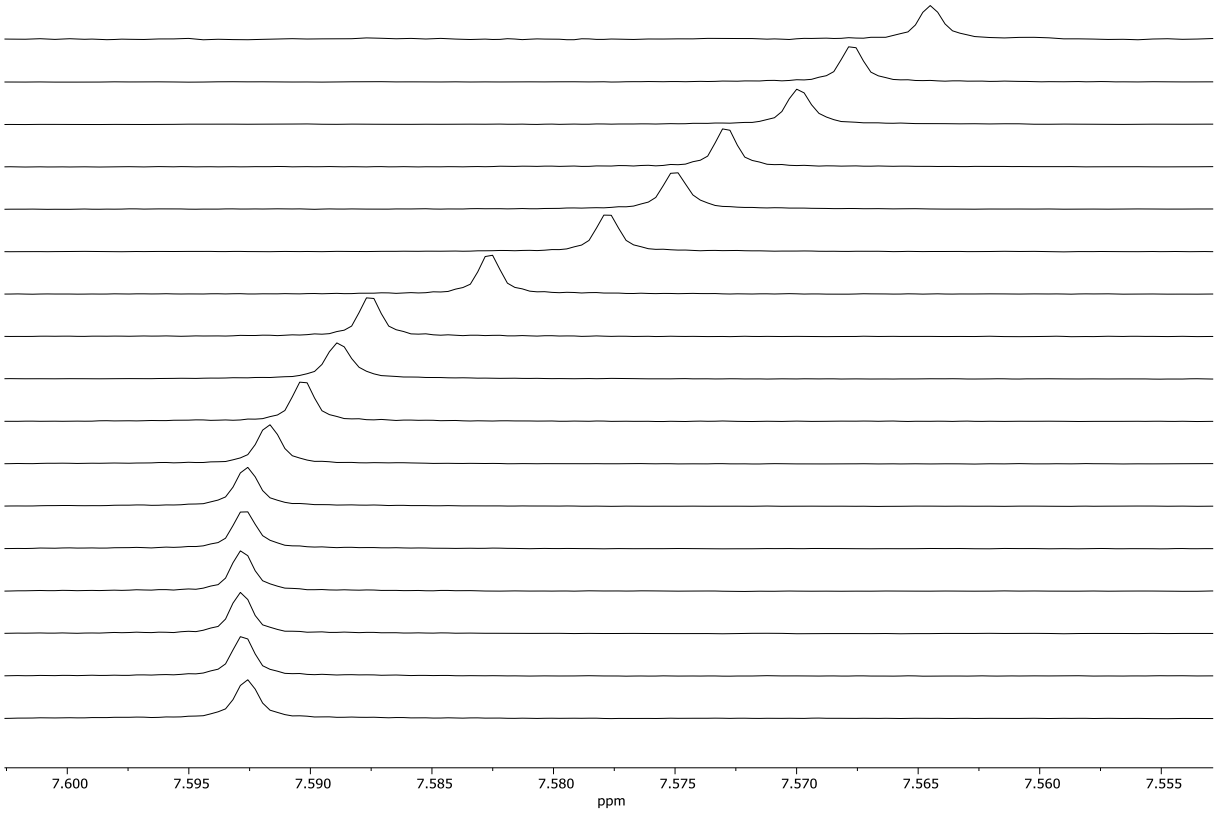

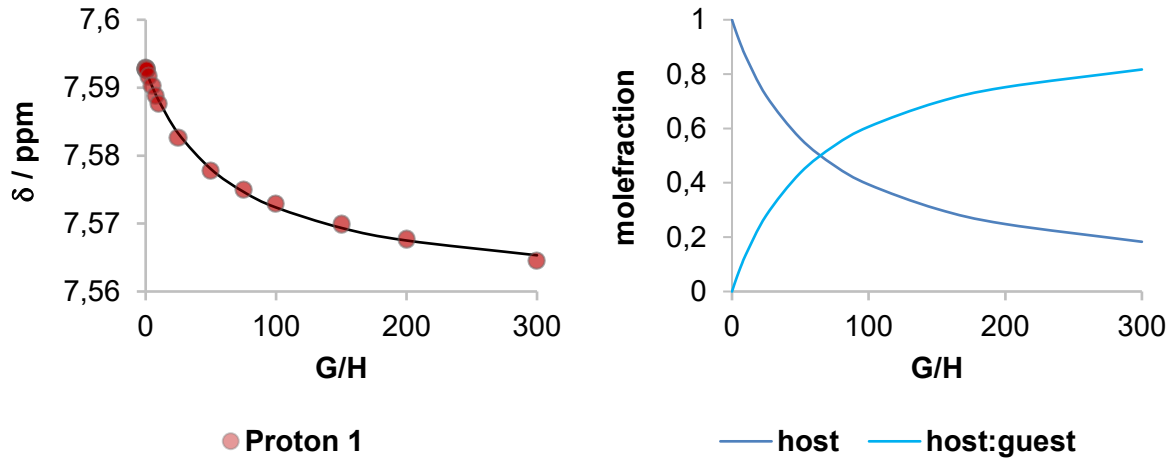

Titrated at $[H]_0$ = 0.125 mM. K_a = 130 ± 6.9 M^{-1}. RMS = 4.4497 • 10^{-4}.

Titration of tetrabutylammonium acetate (257@Zn-XLIII)

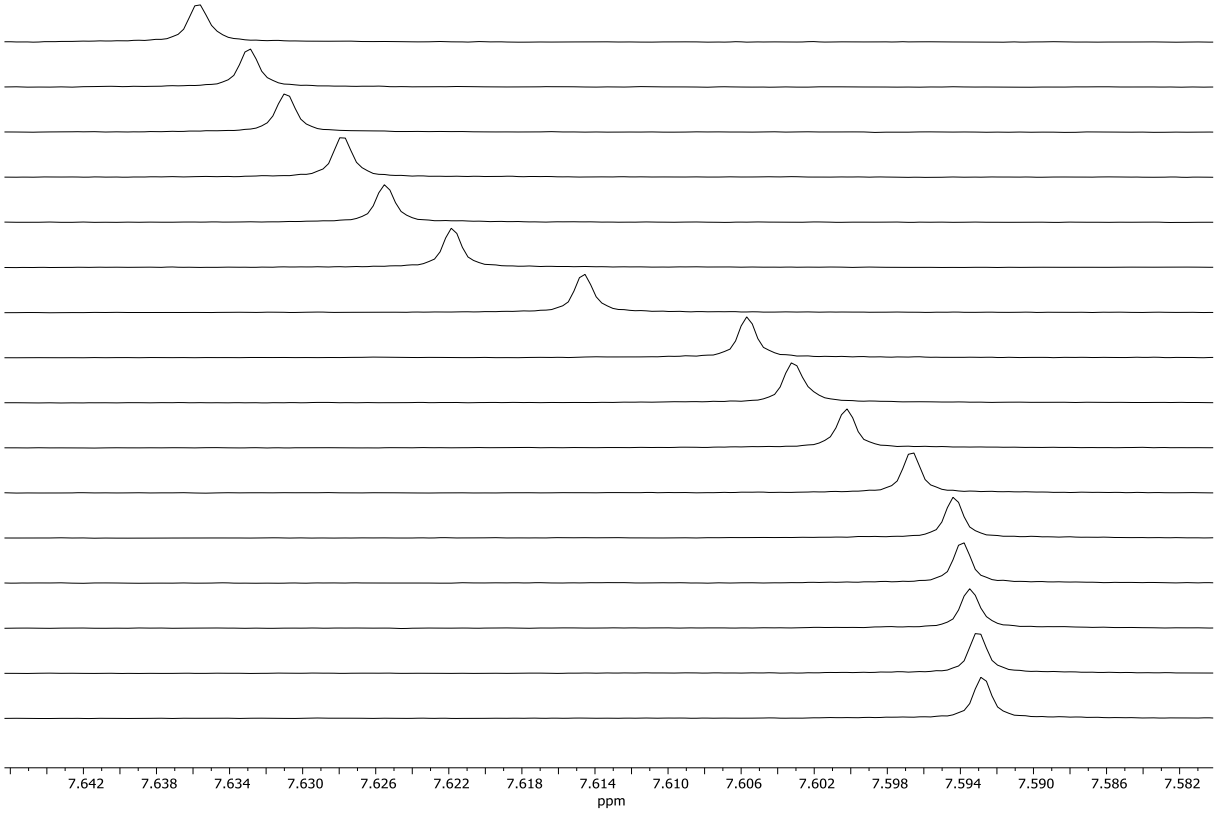

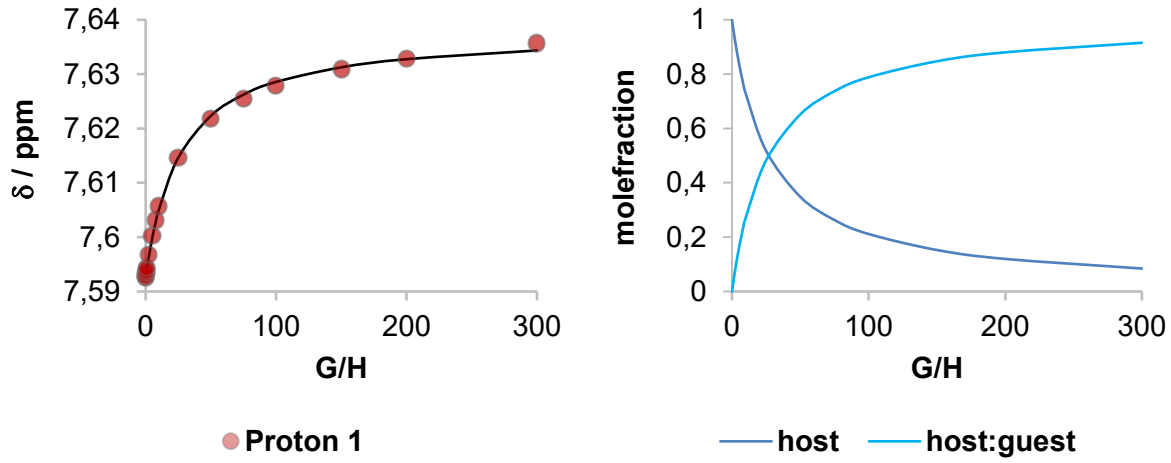

Titrated at $[H]_0$ = 0.125 mM. K_a = 320 ± 15 M^{-1}. RMS = 5.1317 • 10^{-4}.

Titration of tetrabutylammonium monomethylterephthalate (258@Zn-XLIII)

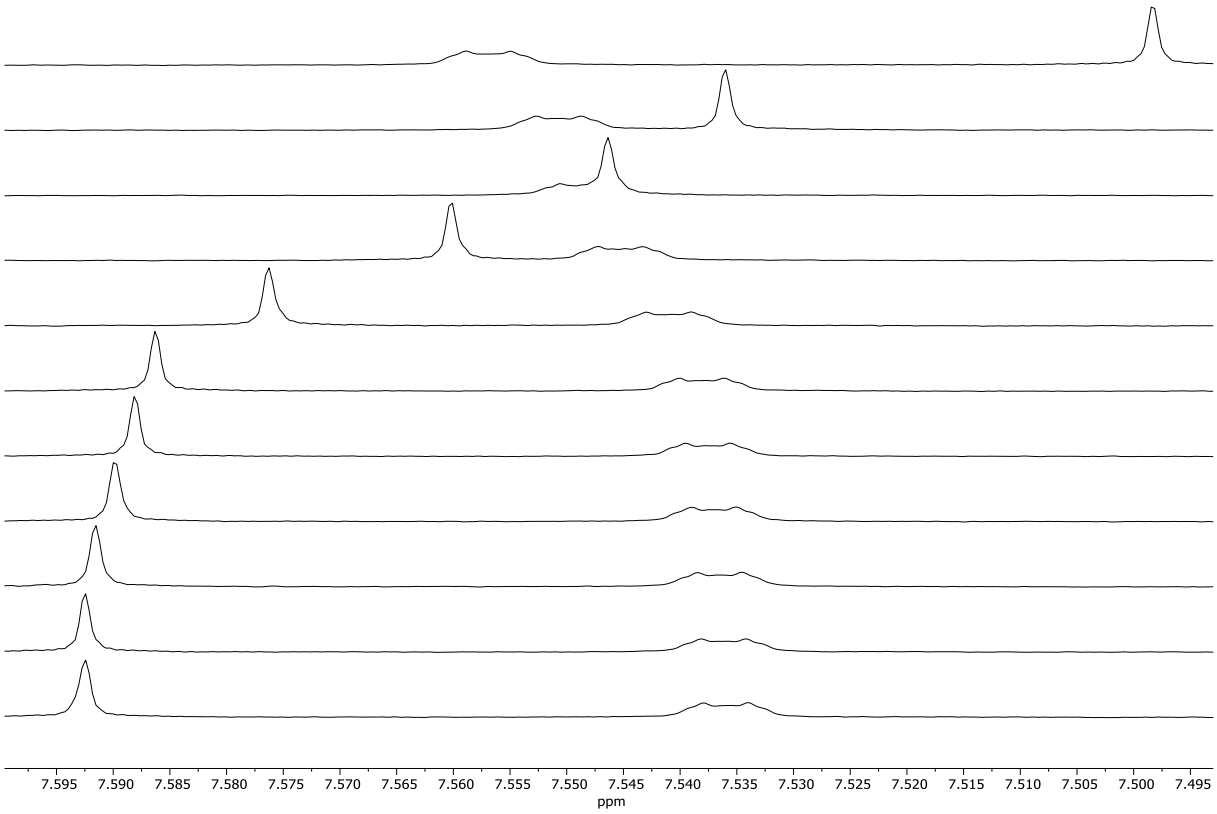

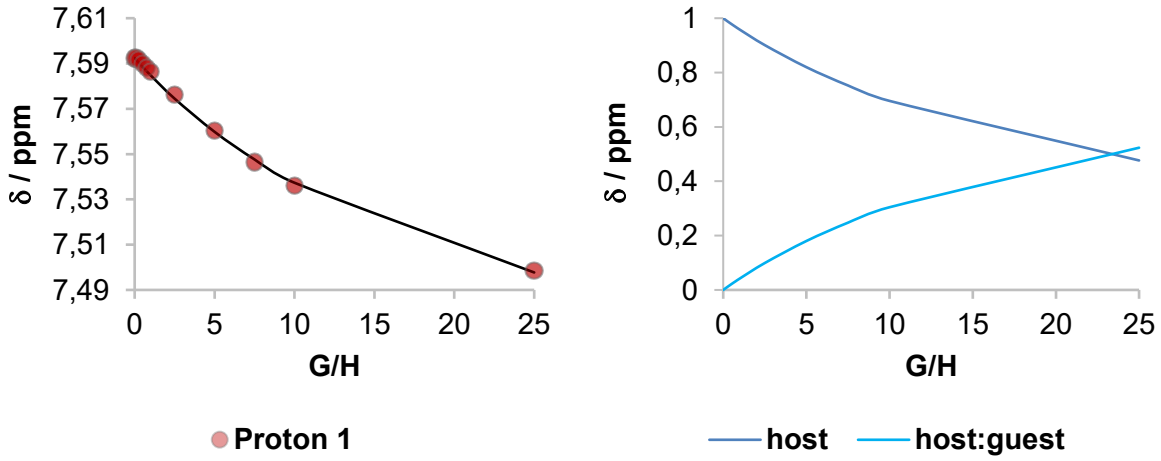

Titrated at $[H]_0$ = 0.125 mM. K_a = 370 ± 16 M^{-1}. RMS = 1.1781 • 10^{-3}.

Titration of tetrabutylammonium adamantane-1-carboxylate (259@Zn-XLIII)

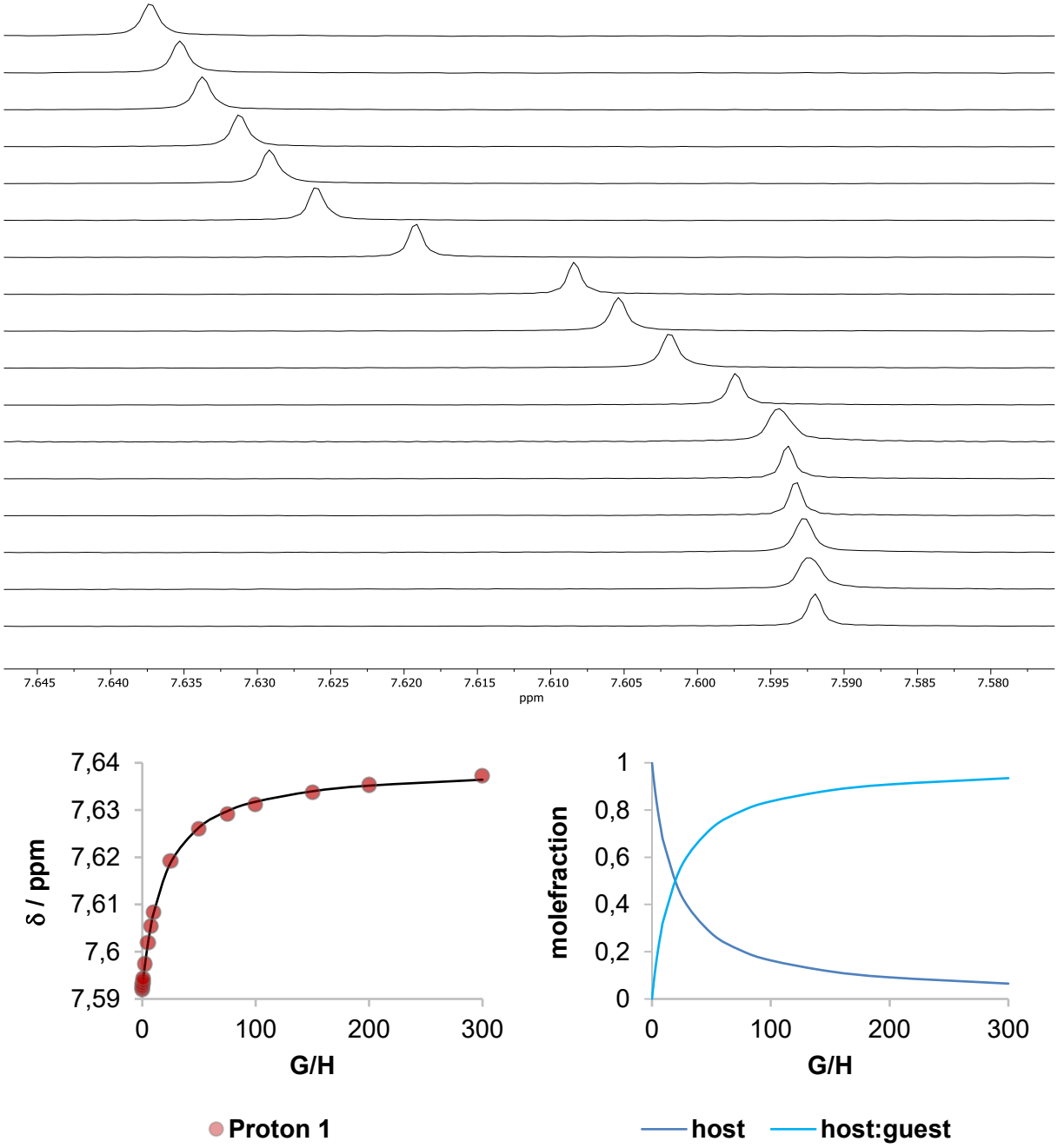

Titrated at $[H]_0$ = 0.125 mM. K_a = 440 ± 13 M^{-1}. RMS = 3.2266 • 10^{-4}.

Titration of tetrabutylammonium diphenyl phosphate (260@Zn-XLIII)

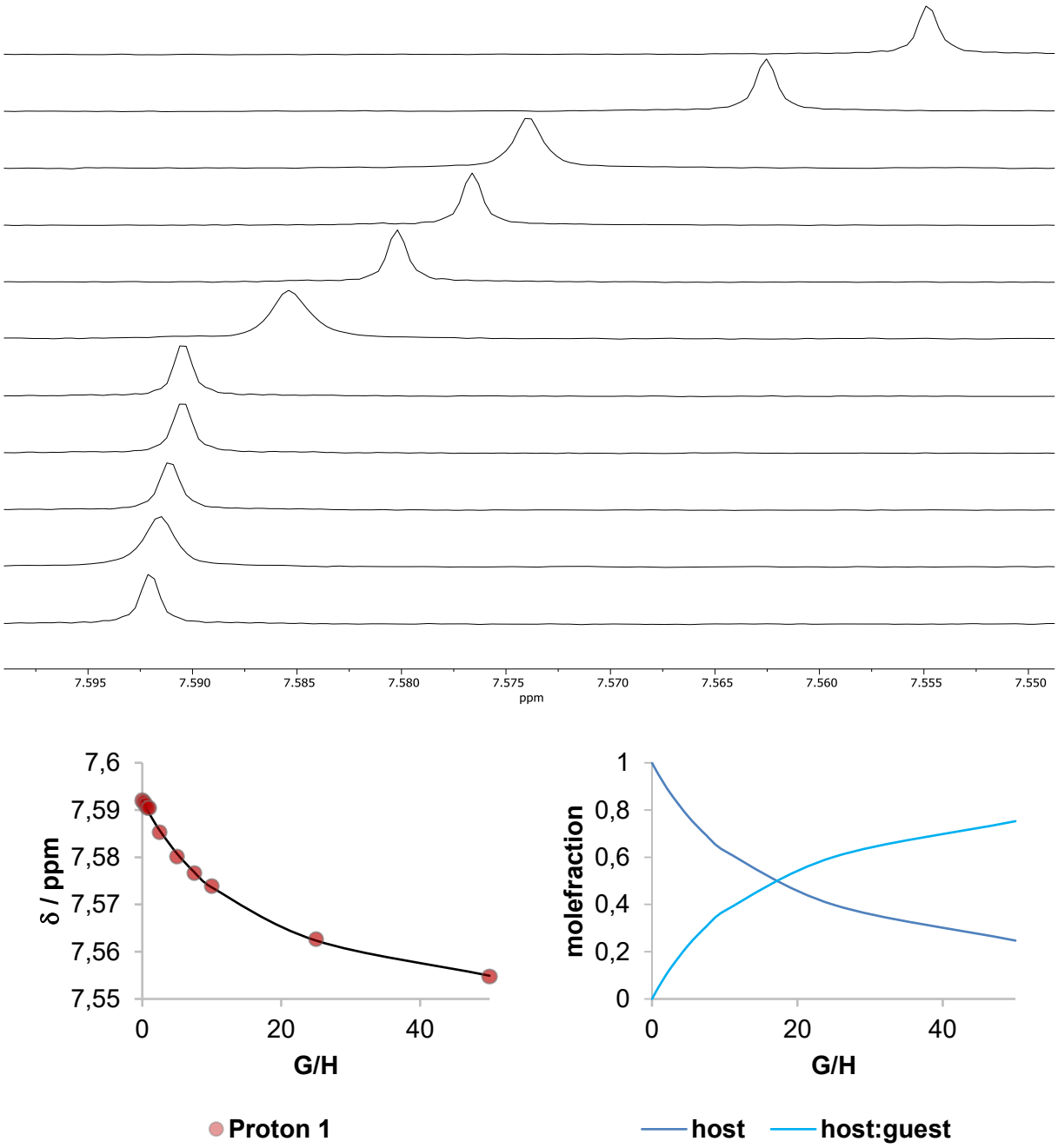

Titrated at [H] = 0.100 mM. K_a = 620 ± 34 M^{-1}. RMS = 4.8649 • 10^{-4}.

Titration of tetrabutylammonium dimethyl phosphate (261@Zn-XLIII)

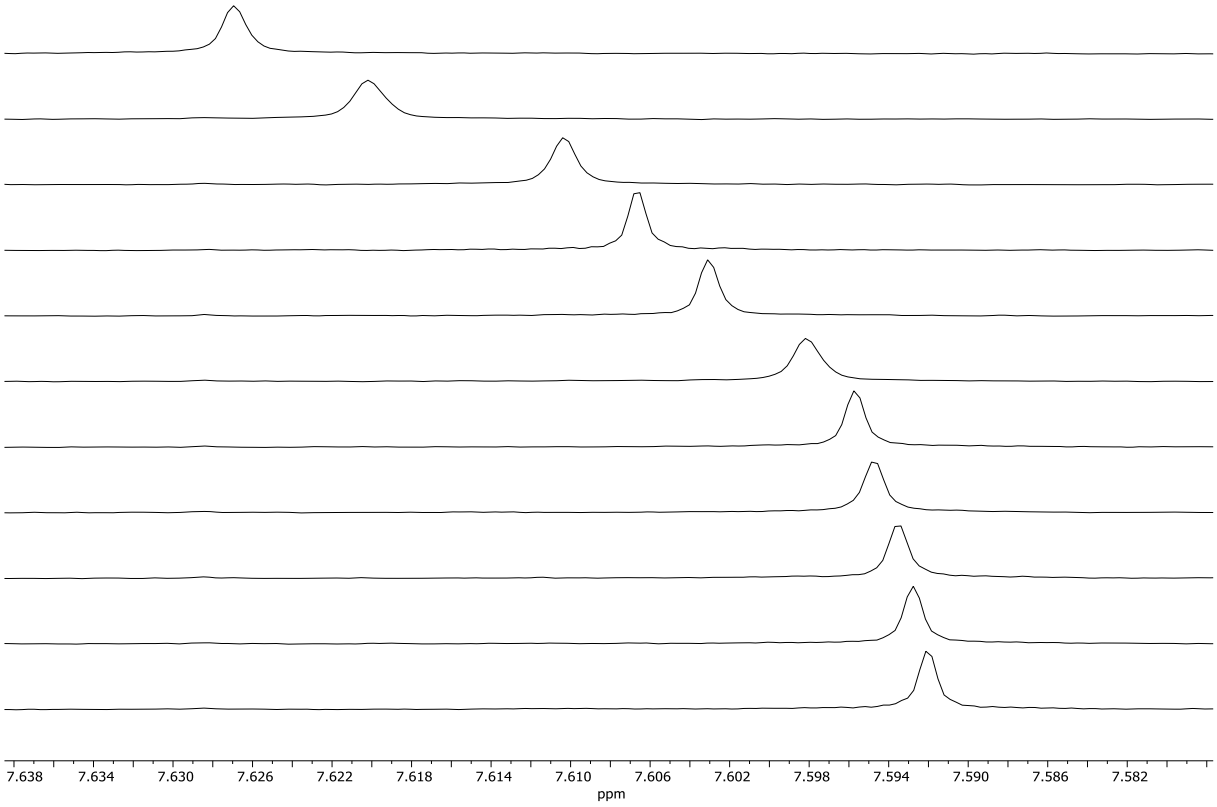

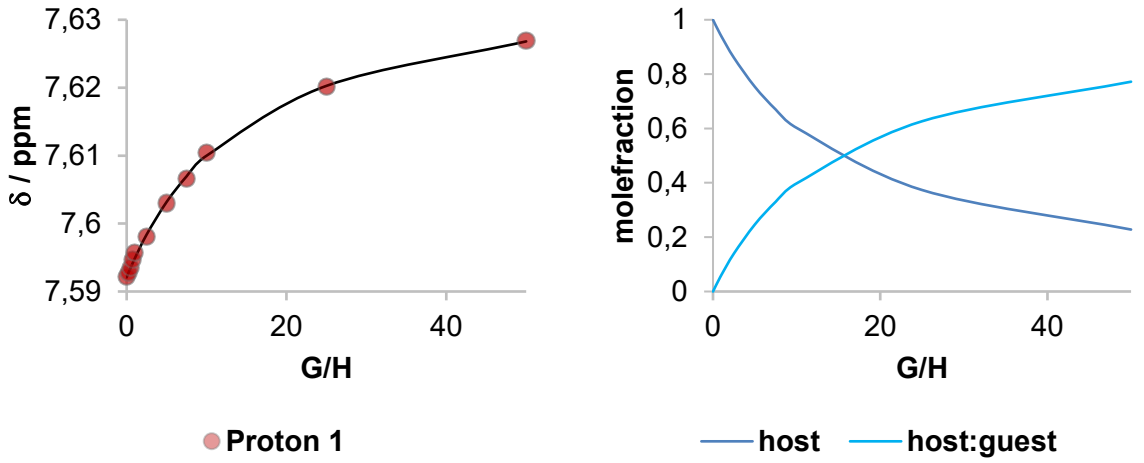

Titrated at [H] = 0.100 mM. K_a = 690 ± 31 M^{-1}. RMS = 3.6607 • 10^{-4}.

Titration of tetrabutylammonium dibutyl phosphate (262@Zn-XLIII)

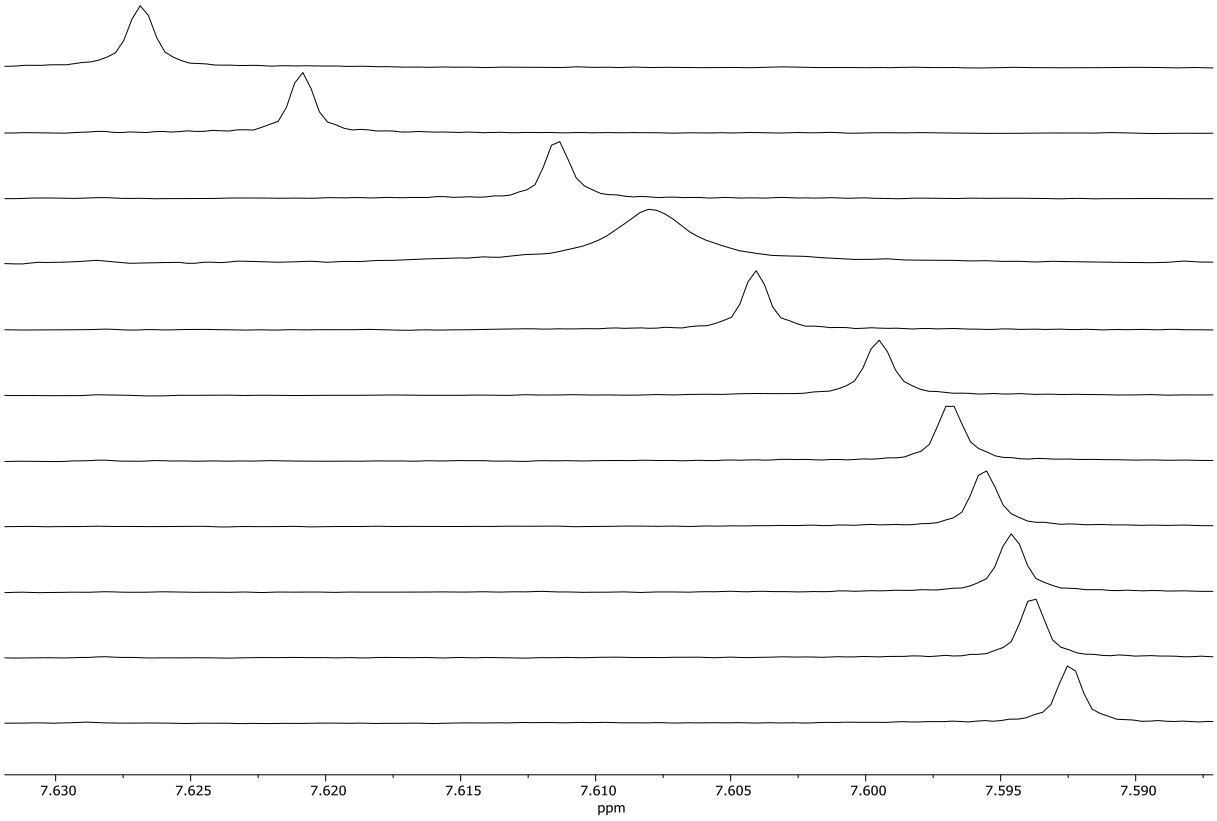

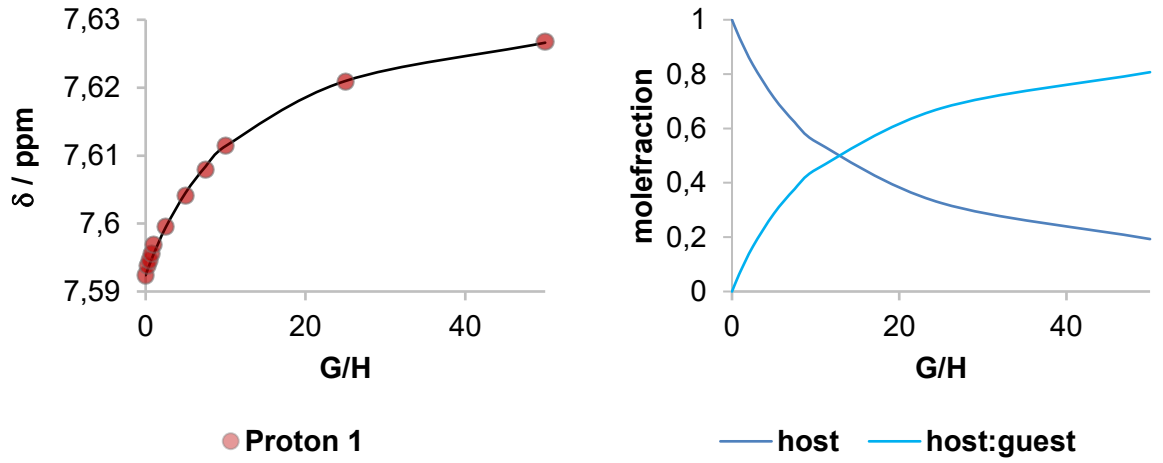

Titrated at [H] = 0.100 mM. K_a = 850 ± 63 M^{-1}. RMS = 5.8387 • 10^{-4}.

Titration of Neutral Guests showing no Binding with Zn_4L_4 Cage Zn-XLIII as Host

Titration of cyclohexane (171@Zn-XLIII)

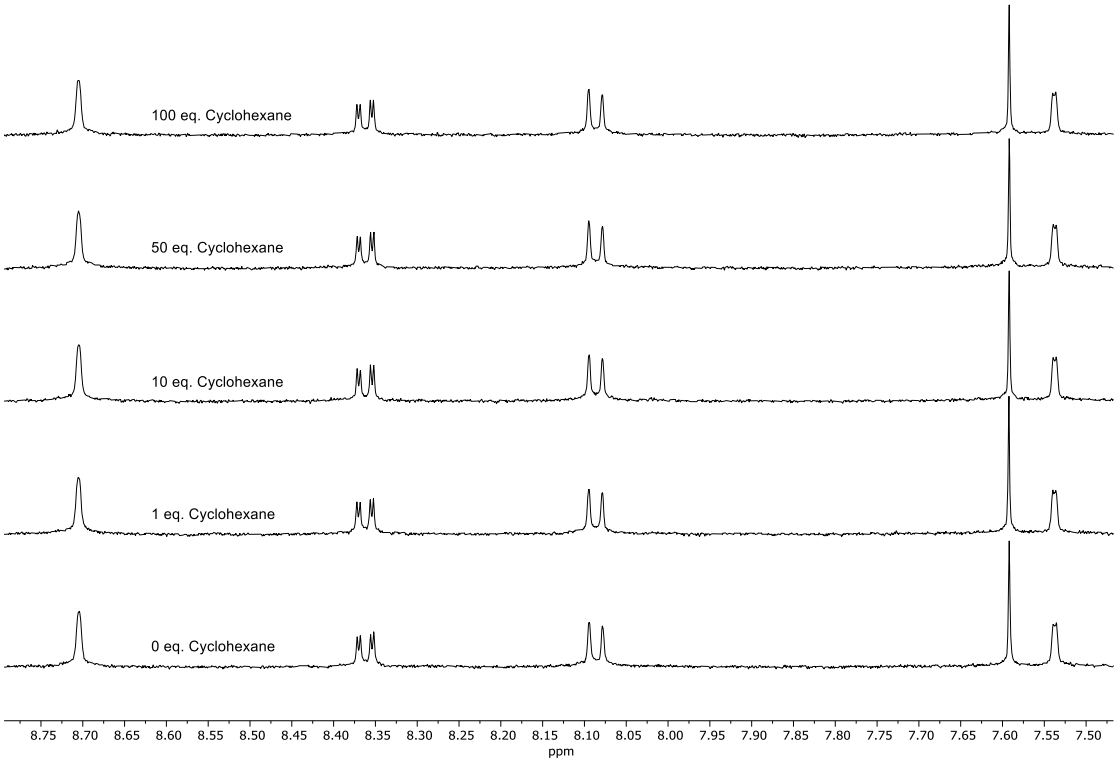

Titration of benzene (3@Zn-XLIII)

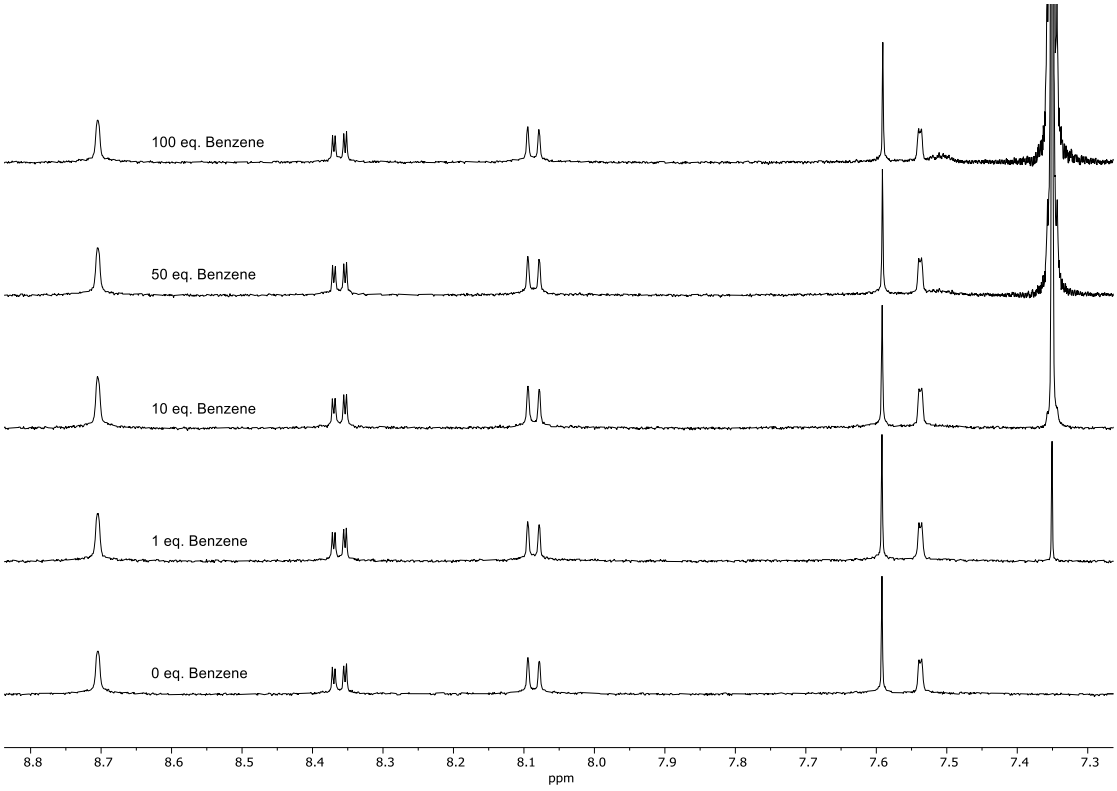

Titration of nitrobenzene (252@Zn-XLIII)

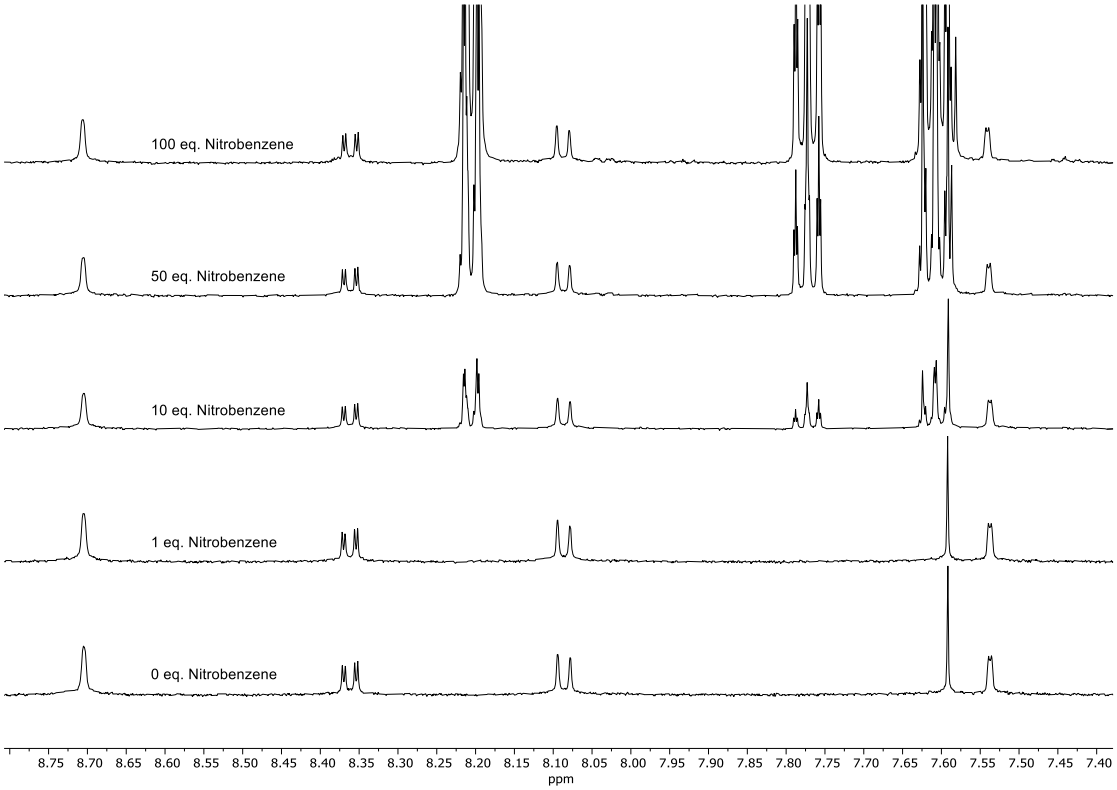

Titration of ethyl benzoate (253@Zn-XLIII)

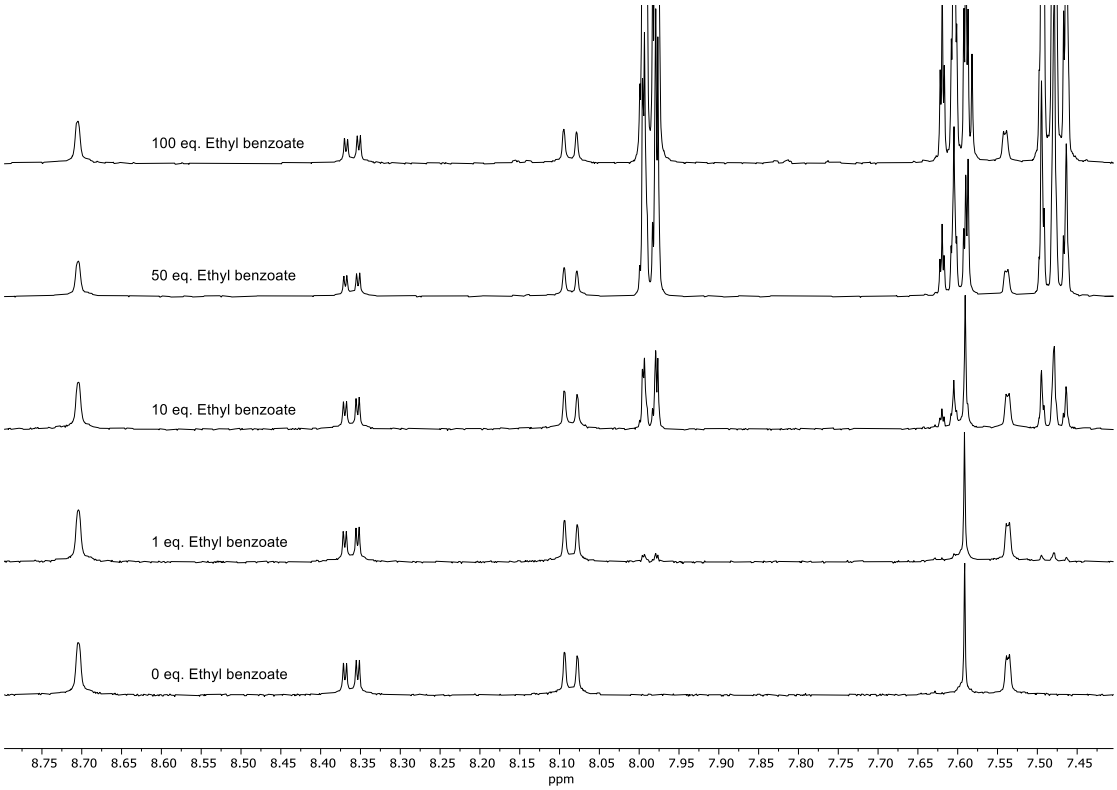

Titration of acetylacetone (254@Zn-XLIII)

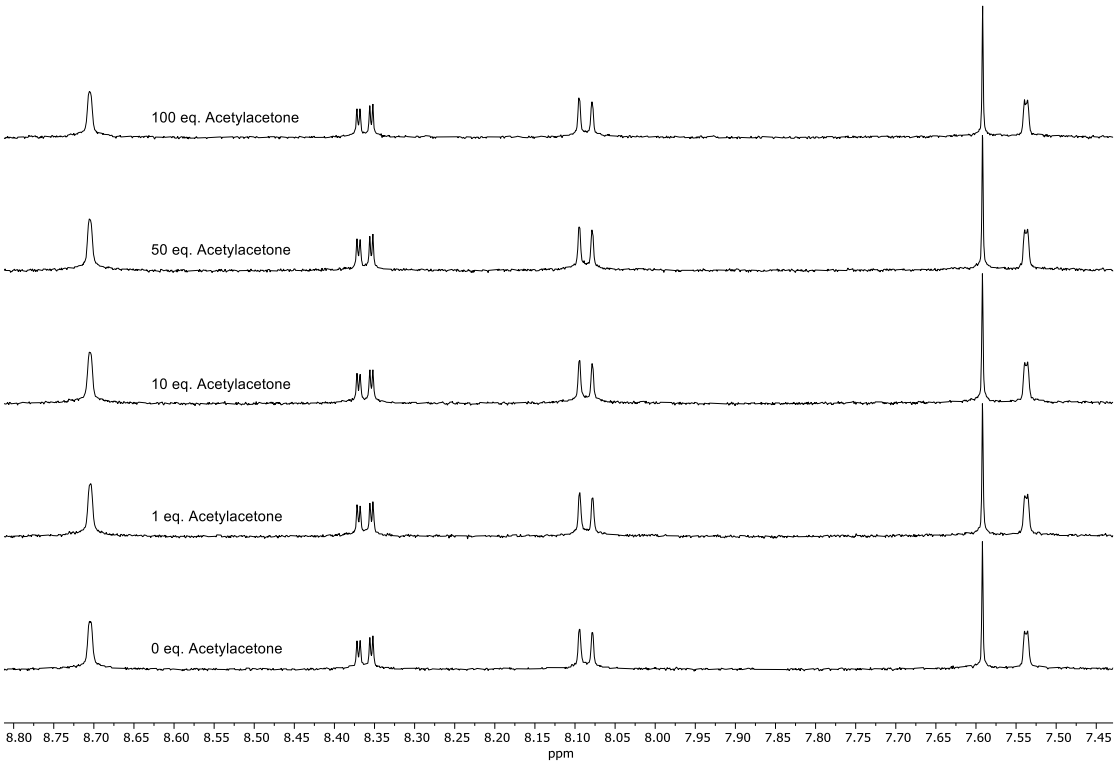

Titration of adamantane (166@Zn-XLIII)

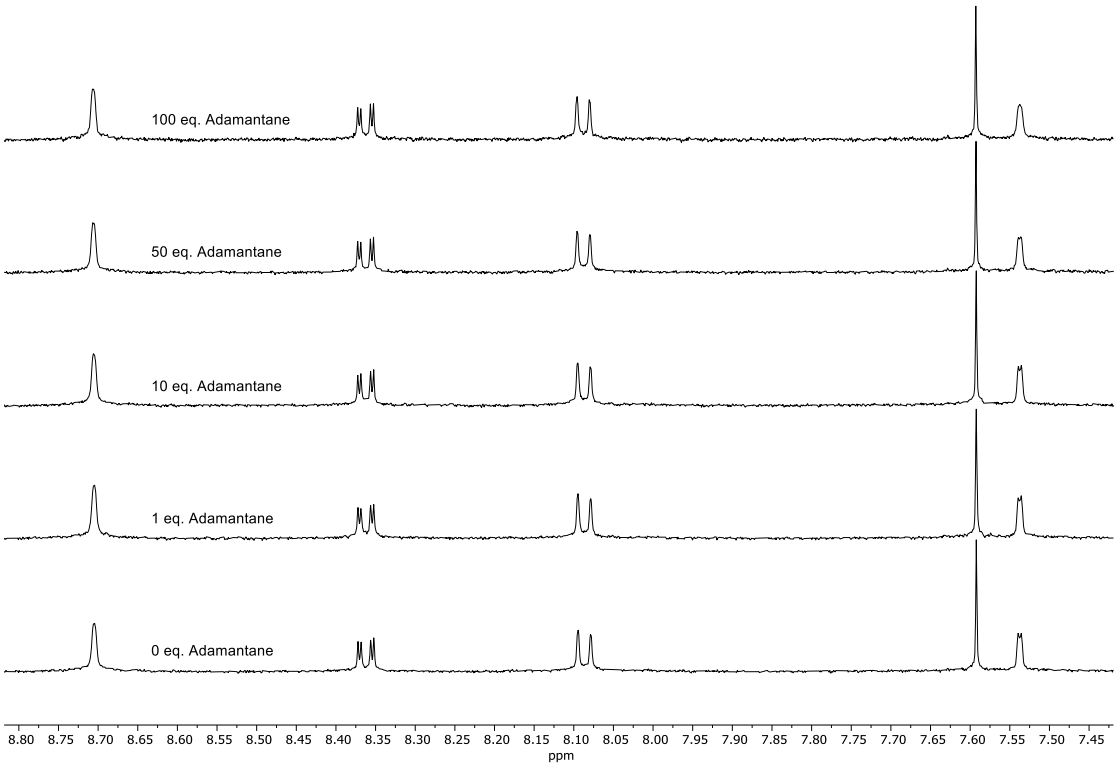

Titration of trimethyl phosphate (255@Zn-XLIII)

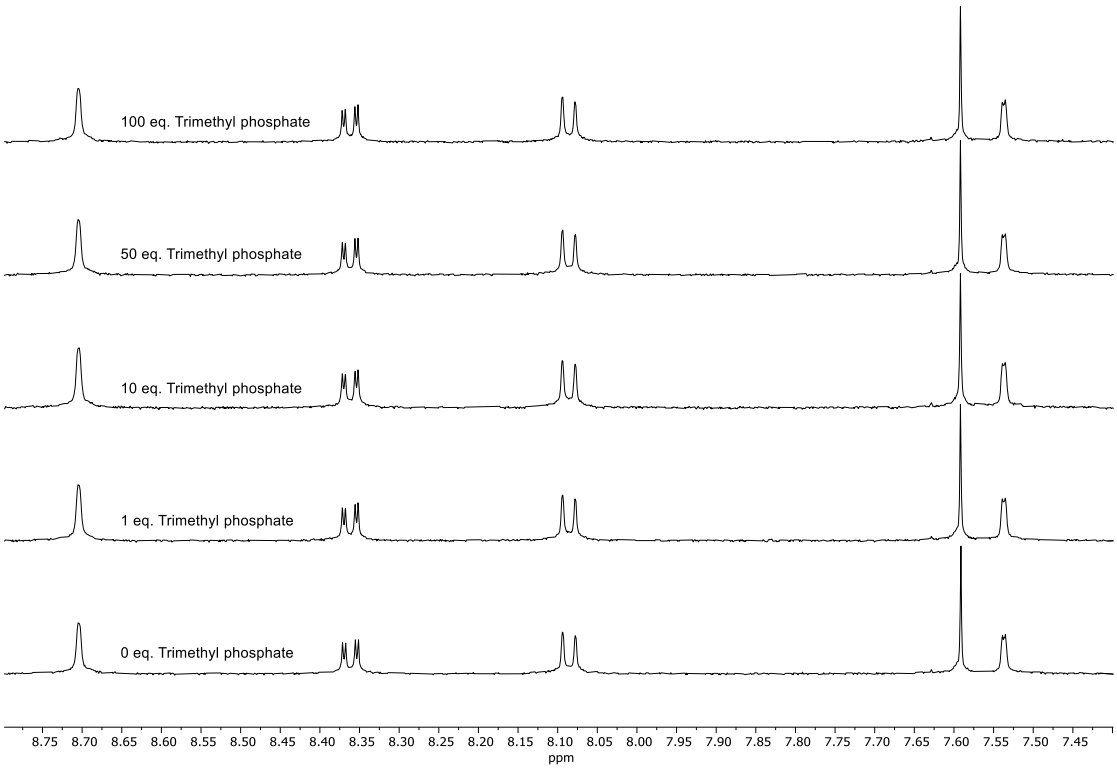

5.3.6 Guest Titration Data with $ZnL_3(NTf_2)_2$ Complex XLIV

Guest Titrations that showed Binding (Fast Exchange)

Titration of potassium *p*-tolyltrifluoroborate (209@XLIV)

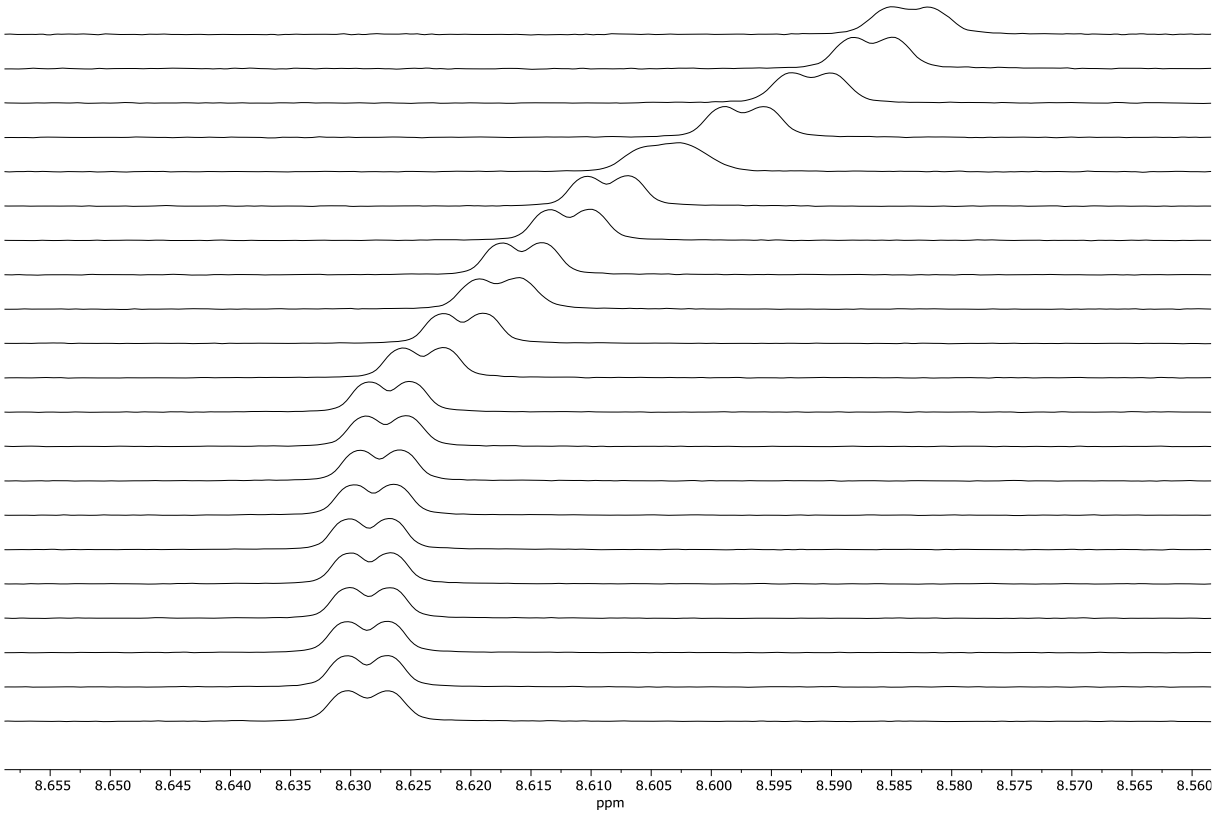

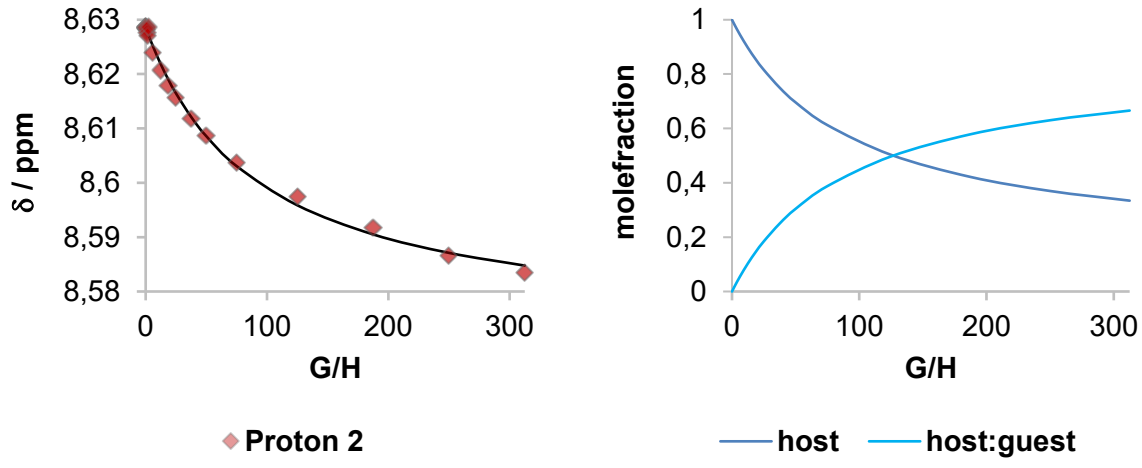

Titrated at $[H]_0$ = 0.500 mM. K_a = 20 ± 0.8 M^{-1}. RMS = 7.7960 • 10^{-4}.

Titration of tetrabutylammonium *p*-toluenesulfonate (212@XLIV)

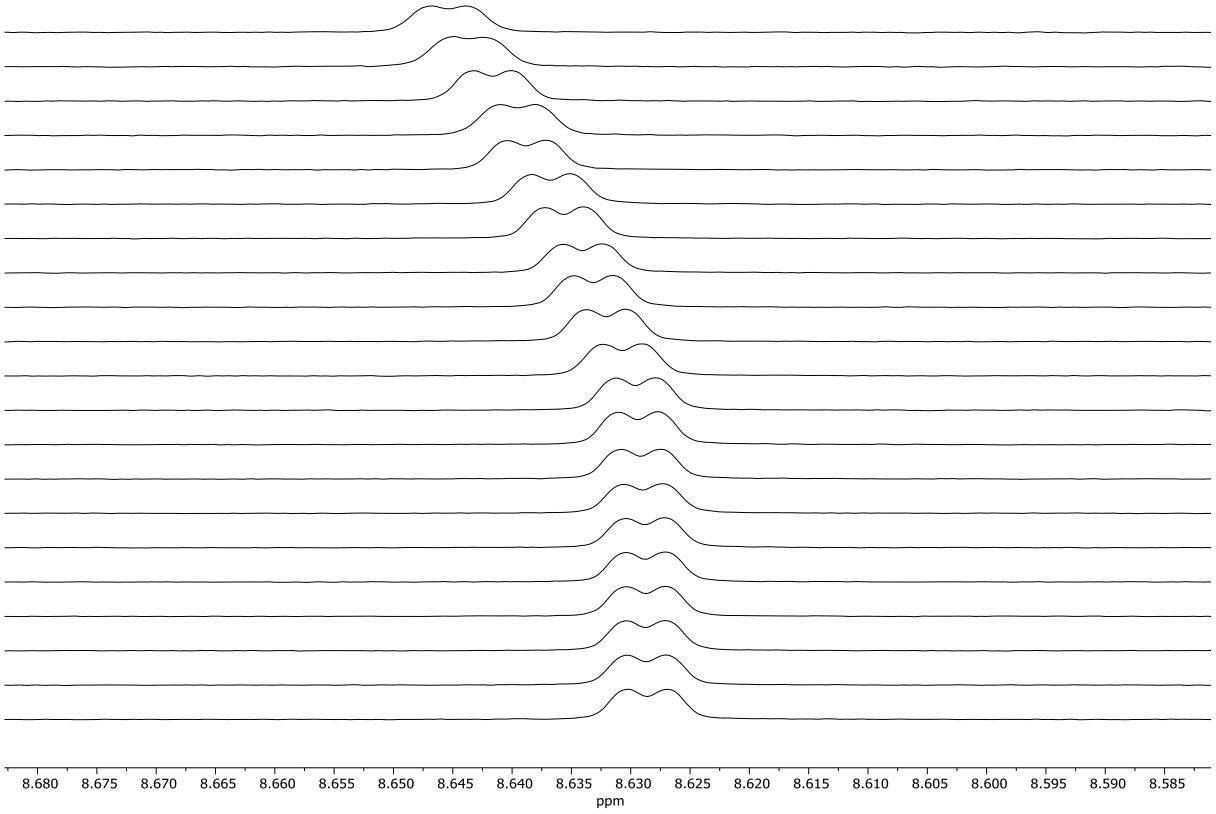

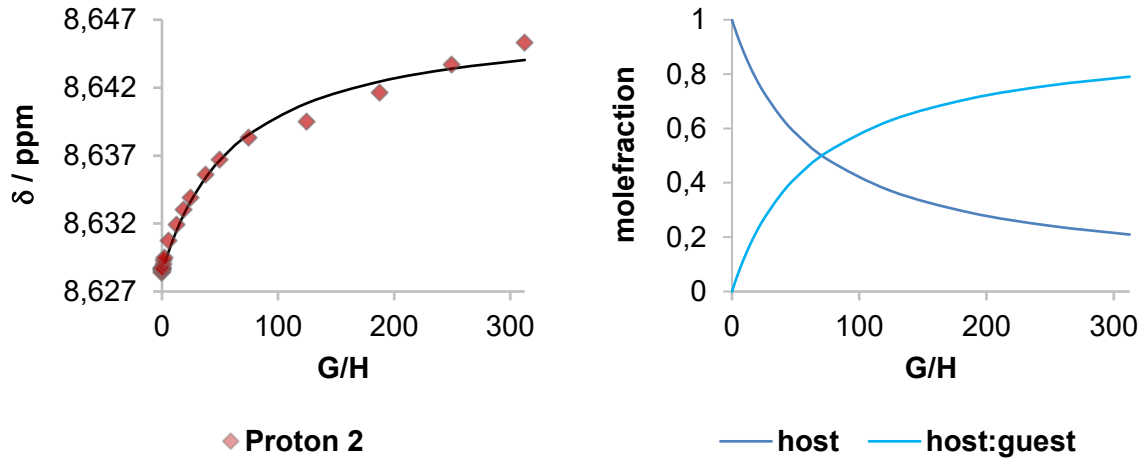

Titrated at $[H]_0$ = 0.500 mM. K_a = 31 ± 2.9 M^{-1}. RMS = 5.2051 • 10^{-4}.

Titration of tetrabutylammonium benzoate (256@XLIV)

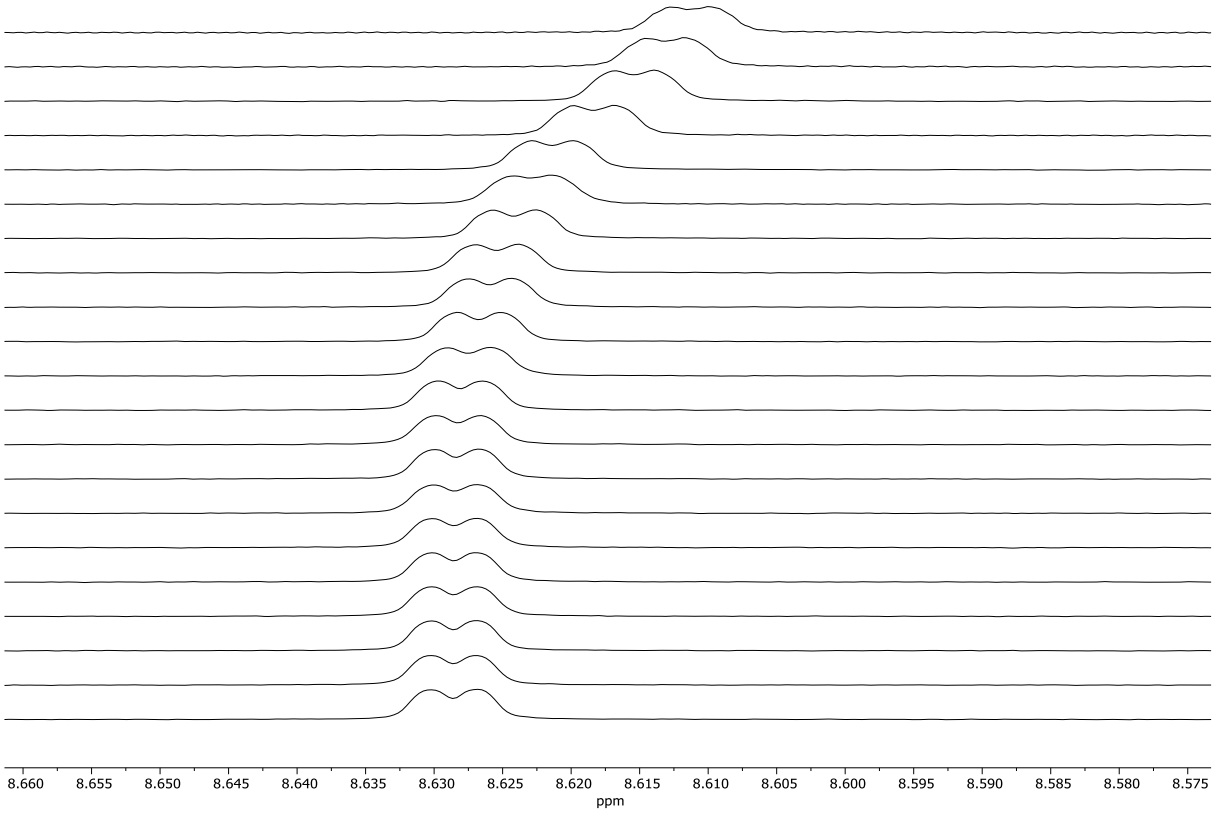

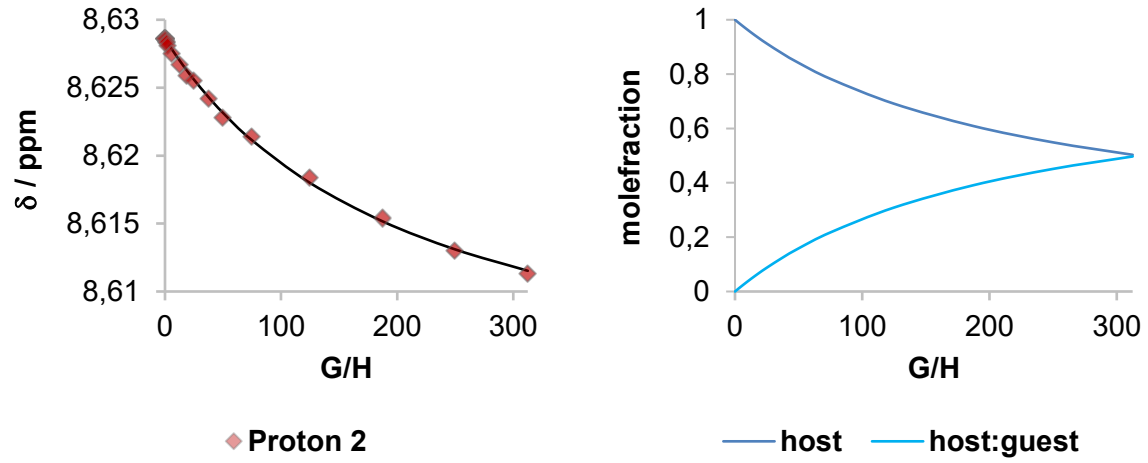

Titrated at $[H]_0$ = 0.500 mM. K_a = 8.2 ± 0.2 M^{-1}. RMS = 2.0208 • 10^{-4}.

Titration of tetrabutylammonium acetate (257@XLIV)

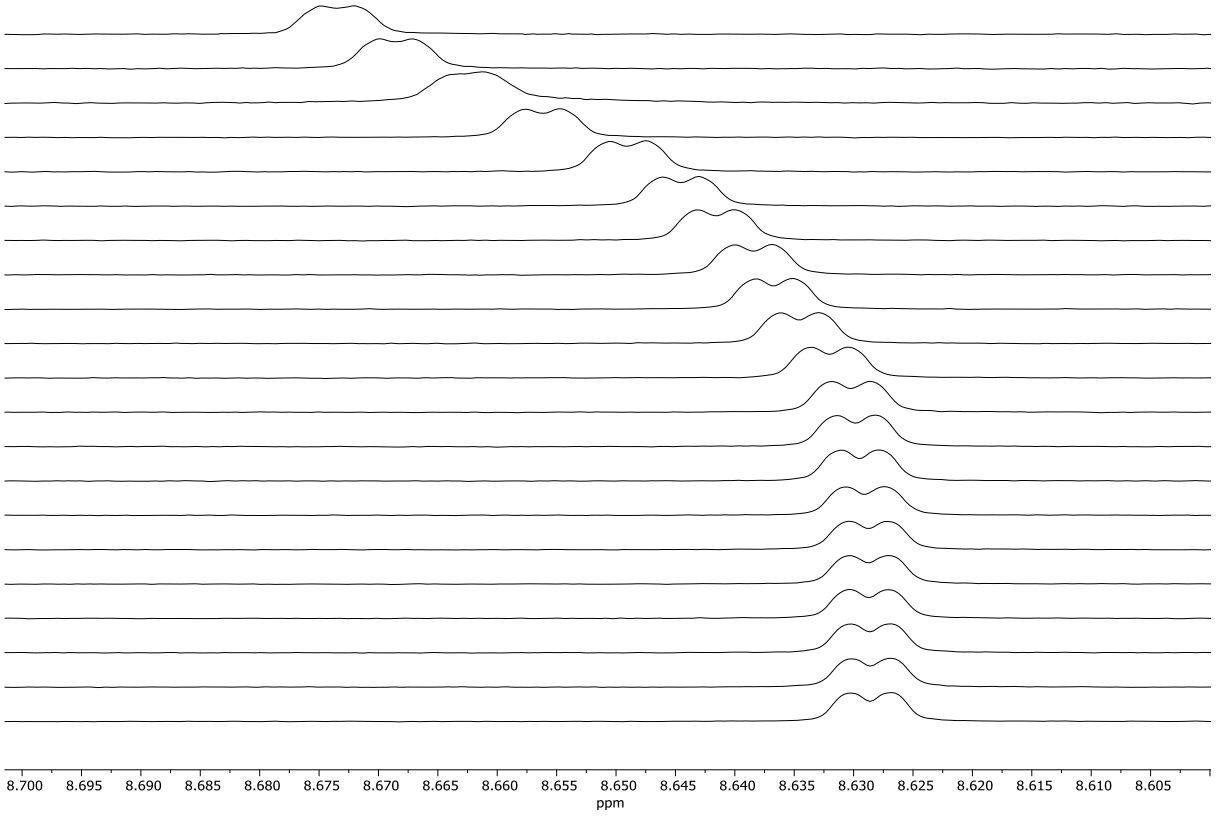

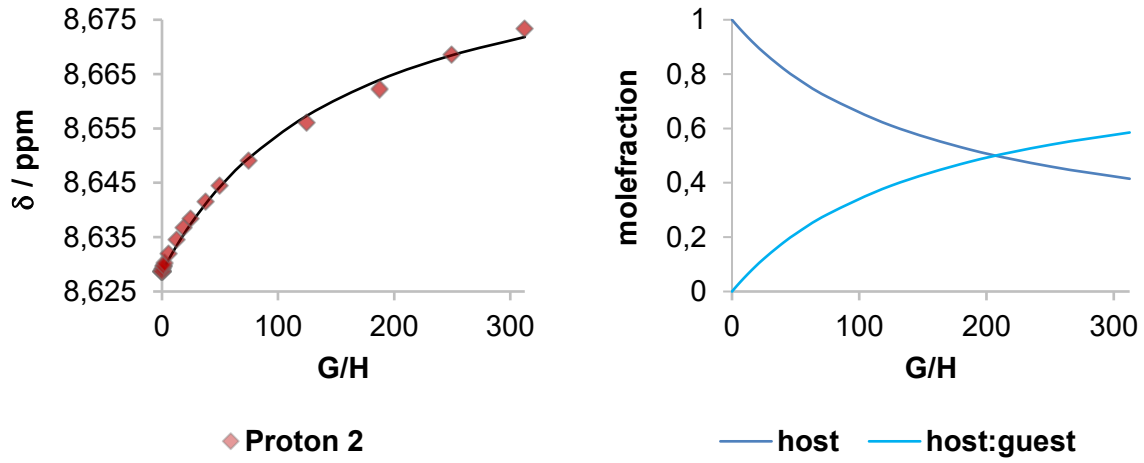

Titrated at $[H]_0$ = 0.500 mM. K_a = 12 ± 0.5 M^{-1}. RMS = 7.7848 • 10^{-4}.

Titration of tetrabutylammonium monomethylterephthalate (258@XLIV)

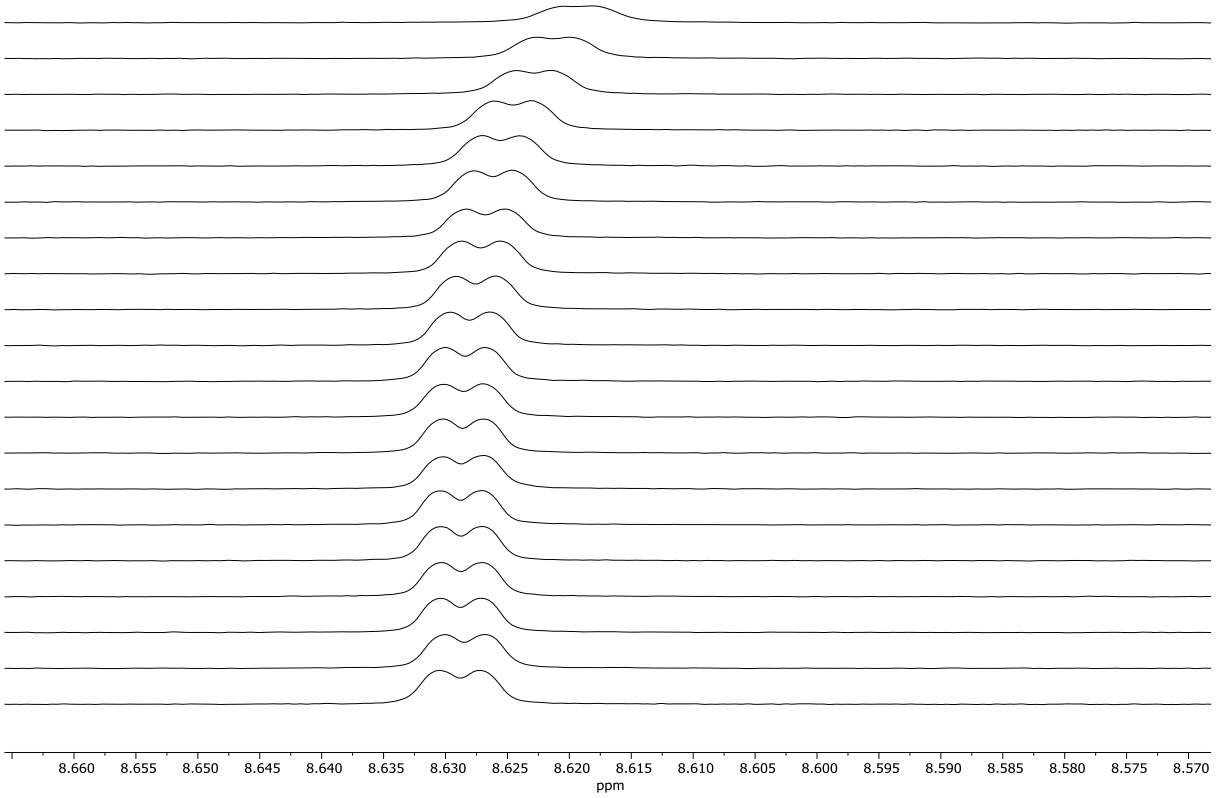

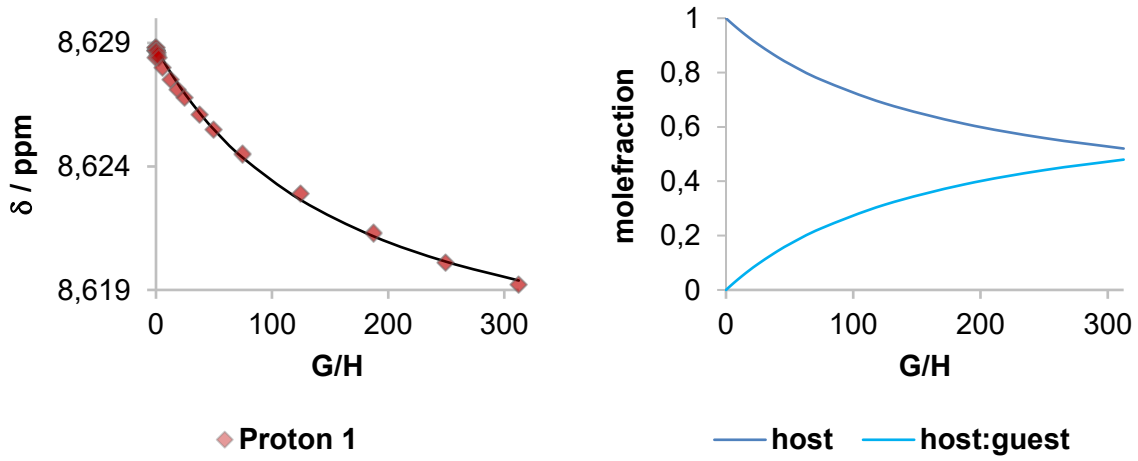

Titrated at $[H]_0$ = 0.500 mM. K_a = 9.0 ± 0.3 M^{-1}. RMS = 1.7616 • 10^{-4}.

Titration of tetrabutylammonium adamantane-1-carboxylate (259@XLIV)

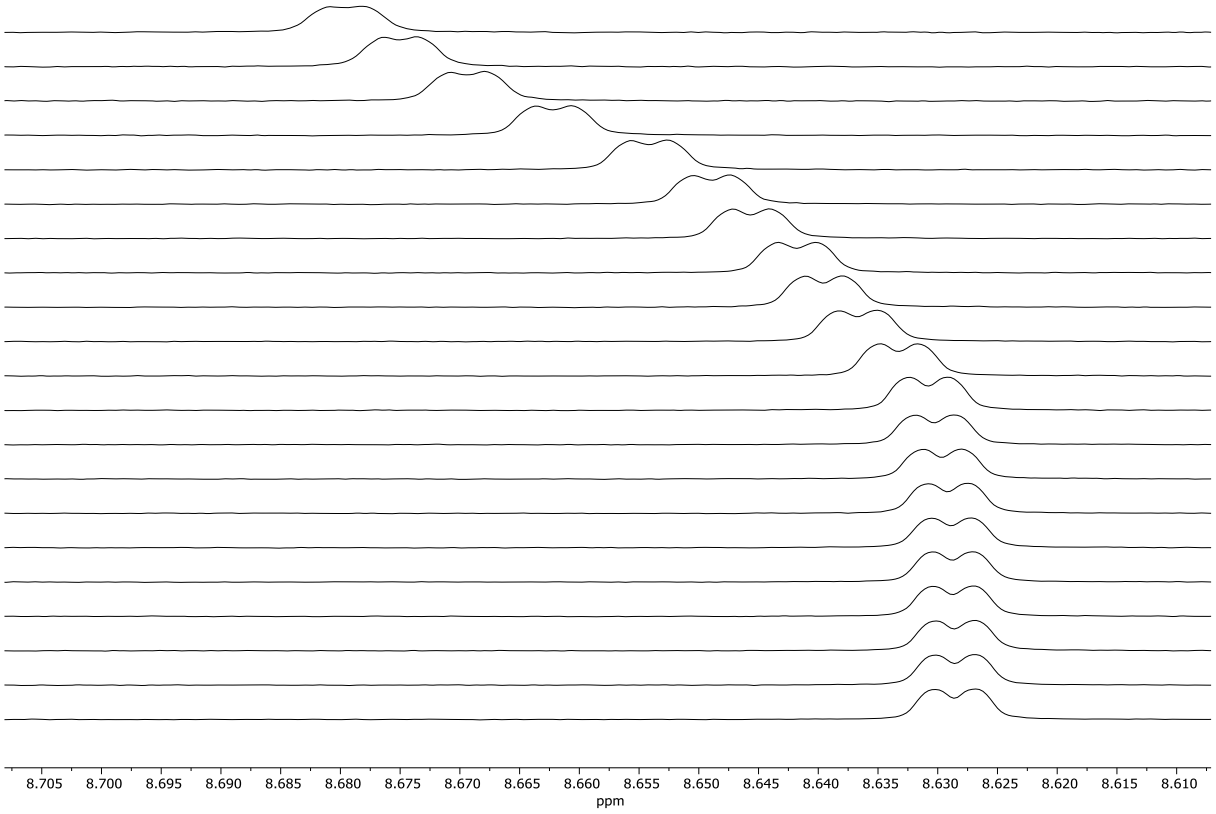

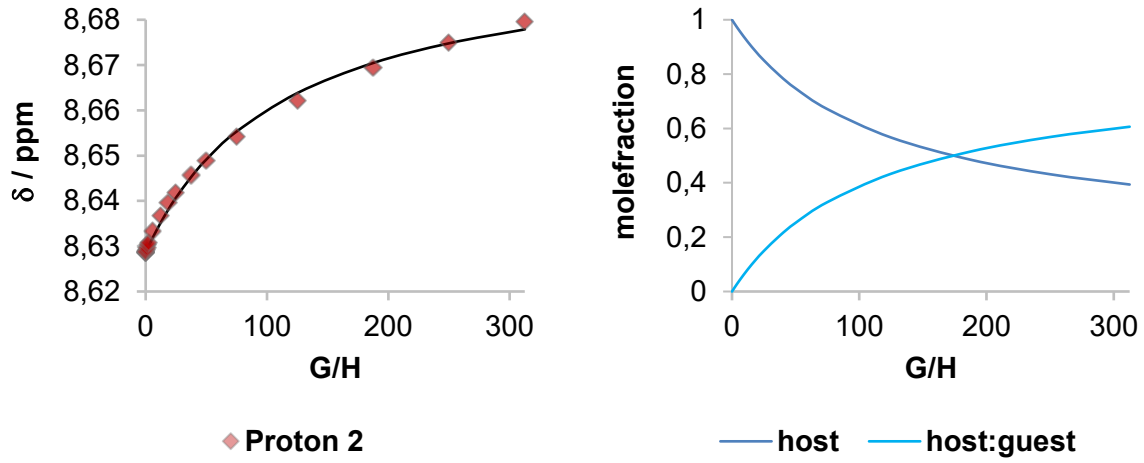

Titrated at $[H]_0$ = 0.500 mM. K_a = 15 ± 0.6 M^{-1}. RMS = 8.8001 • 10^{-4}.

5.4 SPARTAN Models and Data Fit Quality for 1:1 or 1:2 Host:Guest Binding with $Zn_4L_4(NTf_2)_8$ Cage Zn-XLIII

Molecular models for **$Zn_4L_4(NTf_2)_8$** cage **Zn-XLIII** with 1-2 eq. of each anionic guest **(209**, **212**, and **256-262)** were generated using the SPARTAN (Wavefunction, Version 1.1.2, Wavefunction, Inc., MMFF molecular mechanics modeling) software. Space-wise, all guests could potentially also form higher guest:host ratios. However, due to charge repulsion this seemed unlikely to us.

To determine the stoichiometry of the complexes, it was decided to systematically fit data to reasonable binding models. This was suggested by recent studies, that identified the JOB plot method as unreliable in many cases.[301] Thus, as suggested, we analysed our titration results using the 1:1 and 1:2 binding models via the Bindfit model for NMR titrations (http://app.supramolecular.org/bindfit/). The comparison clearly speaks for a 1:1 binding in most cases, as for the 1:2 binding models, binding constants K_{11} were unrealistically high with exorbitant error values, and for the binding constants K_{12} even negative values were observed in several cases. An exception was the smallest guest **257**, acetate. In this case, indeed also a 1:2 binding mode seems reasonable according to the fitted data.

Model for $Zn_4L_4(NTf_2)_8$ cage Zn-XLIII

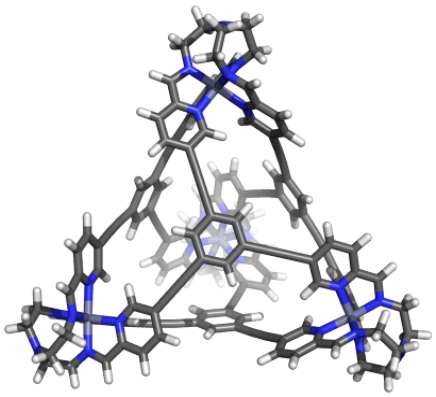

Models/Data Fit Quality for potassium *p*-tolyltrifluoroborate (209@Zn-XLIII)

1:1 Zn-XLIII/209

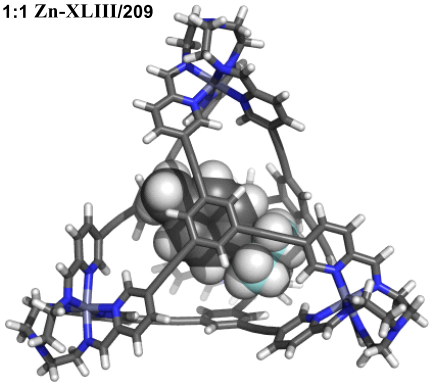

1:2 Zn-XLIII/209

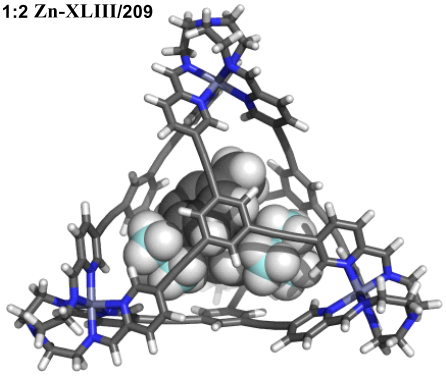

1:1 Binding Model Zn-XLIII/209

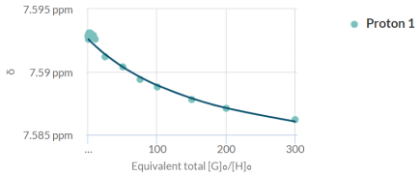

Parameter (bounds)	Optimised	Error	Initial
K (0 → ∞)	39.63 M^{-1}	± 13.7799 %	40.00 M^{-1}

1:2 Binding Model Zn-XLIII/209

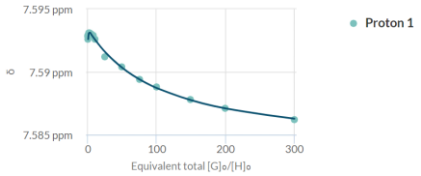

Parameter (bounds)	Optimised	Error	Initial
K_{11} (0 → ∞)	55555.81 M^{-1}	± 195.5012 %	1000.00 M^{-1}
K_{12} (0 → ∞)	75.42 M^{-1}	± 4.8905 %	100.00 M^{-1}

Models for tetrabutylammonium *p*-toluenesulfonate (212@Zn-XLIII)

1:1 Zn-XLIII/212

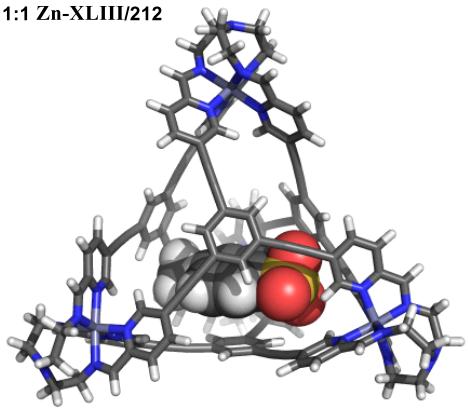

1:2 Zn-XLIII/212

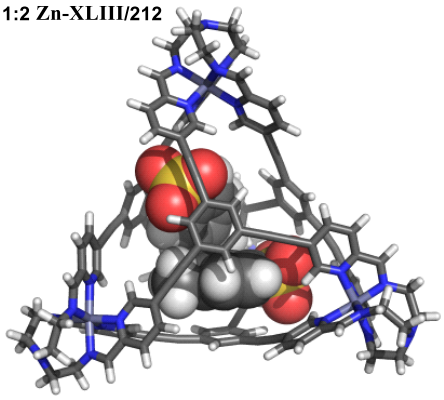

1:1 Binding Model Zn-XLIII/212

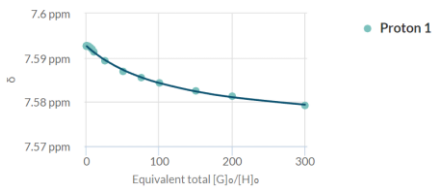

Parameter (bounds)	Optimised	Error	Initial
K (0 → ∞)	65.57 M^{-1}	± 4.6912 %	66.00 M^{-1}

1:2 Binding Model Zn-XLIII/212

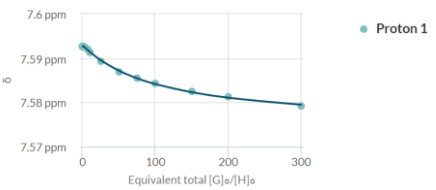

Parameter (bounds)	Optimised	Error	Initial
K_{11} (0 → ∞)	163858.05 M^{-1}	± 1102.5973 %	1000.00 M^{-1}
K_{12} (0 → ∞)	75.35 M^{-1}	± 3.6200 %	100.00 M^{-1}

Models for tetrabutylammonium benzoate (256@Zn-XLIII)

1:1 Zn-XLIII/256

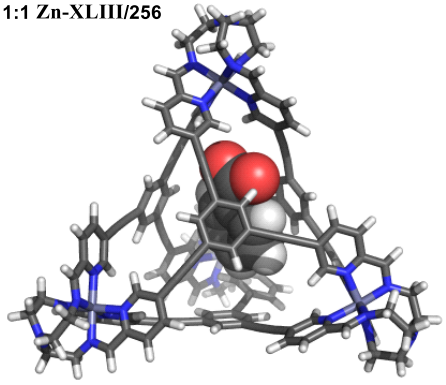

1:2 Zn-XLIII/256

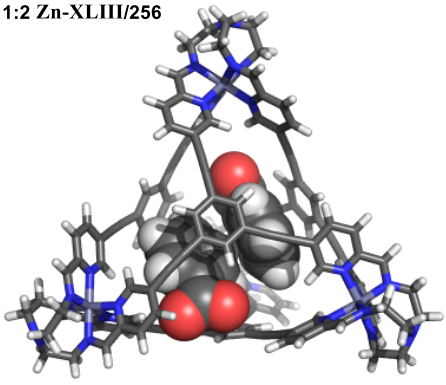

1:1 Binding Model Zn-XLIII/256

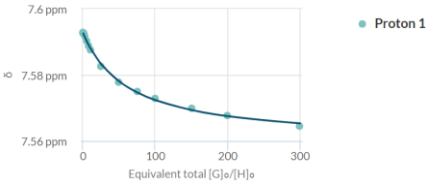

Parameter (bounds)	Optimised	Error	Initial
K (0 → ∞)	130.87 M⁻¹	± 5.3103 %	100.00 M⁻¹

1:2 Binding Model Zn-XLIII/256

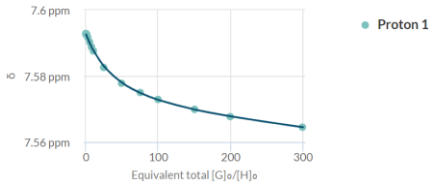

Parameter (bounds)	Optimised	Error	Initial
K_{11} (0 → ∞)	156.73 M⁻¹	± 4.0833 %	1000.00 M⁻¹
K_{12} (0 → ∞)	-13.15 M⁻¹	± -25.7139 %	100.00 M⁻¹

Models for tetrabutylammonium acetate (257@Zn-XLIII)

1:1 Zn-XLIII/257

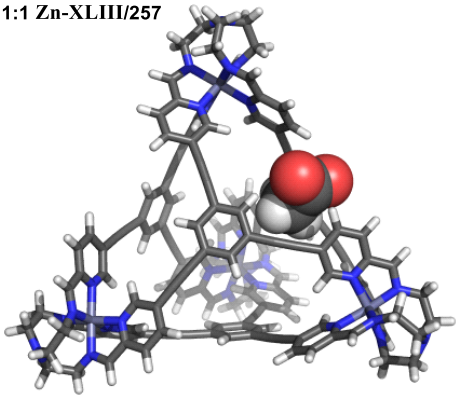

1:2 Zn-XLIII/257

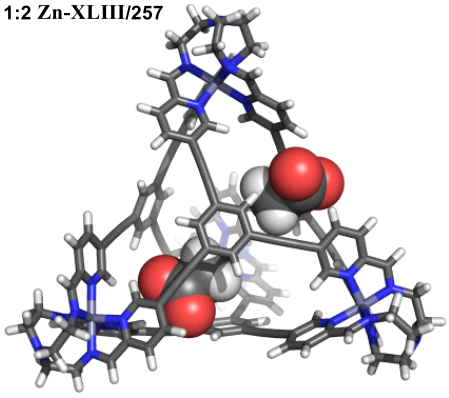

1:1 Binding Model Zn-XLIII/257

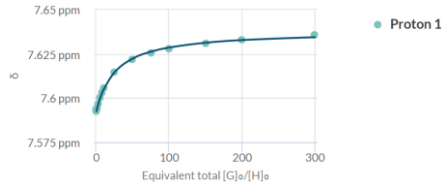

Parameter (bounds)	Optimised	Error	Initial
K (0 → ∞)	317.31 M⁻¹	± 4.8162 %	100.00 M⁻¹

1:2 Binding Model Zn-XLIII/257

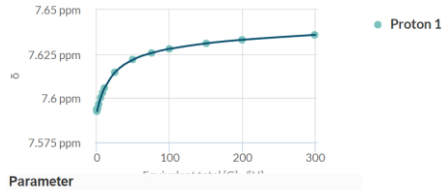

Parameter (bounds)	Optimised	Error	Initial
K_{11} (0 → ∞)	412.02 M⁻¹	± 1.0586 %	1000.00 M⁻¹
K_{12} (0 → ∞)	9.78 M⁻¹	± 2.8106 %	100.00 M⁻¹

Models for tetrabutylammonium monomethylterephthalate (258@Zn-XLIII)

1:1 Zn-XLIII/258

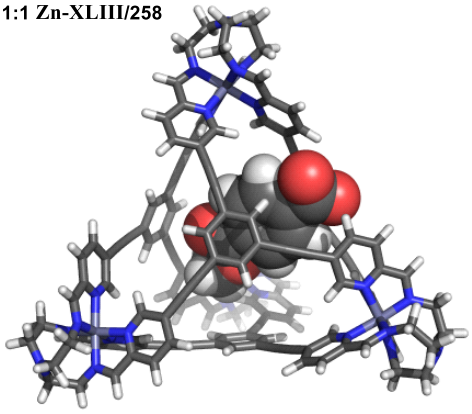

1:2 Zn-XLIII/258

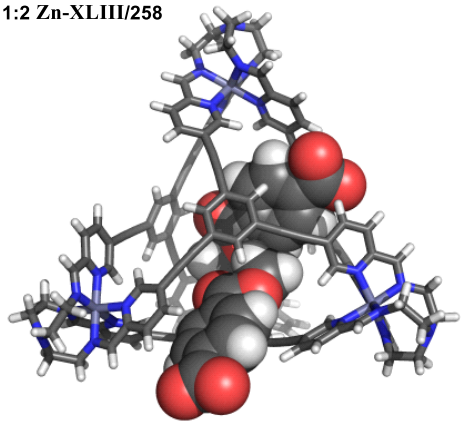

1:1 Binding Model Zn-XLIII/258

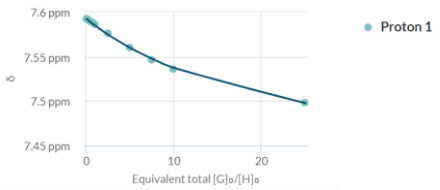

Parameter (bounds)	Optimised	Error	Initial
K (0 → ∞)	374.72 M^{-1}	± 4.2180 %	100.00 M^{-1}

1:2 Binding Model Zn-XLIII/258

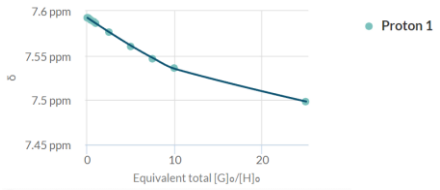

Parameter (bounds)	Optimised	Error	Initial
K_{11} (0 → ∞)	-0.13 M^{-1}	± -3.0397 %	1000.00 M^{-1}
K_{12} (0 → ∞)	-677251.44 M^{-1}	± -7.8076 %	100.00 M^{-1}

Models for tetrabutylammonium adamantane-1-carboxylate (259@Zn-XLIII)

1:1 Zn-XLIII/259

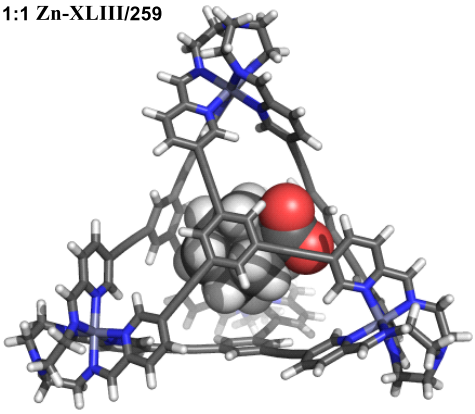

1:2 Zn-XLIII/259

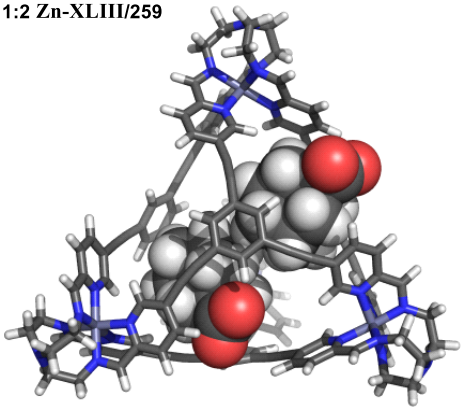

1:1 Binding Model Zn-XLIII/259

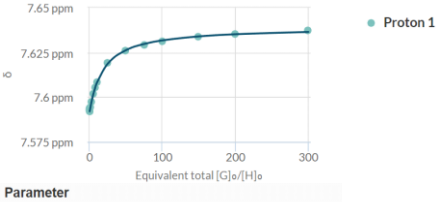

Parameter (bounds)	Optimised	Error	Initial
K (0 → ∞)	444.03 M^{-1}	± 2.9596 %	440.00 M^{-1}

1:2 Binding Model Zn-XLIII/259

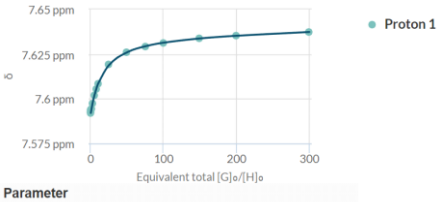

Parameter (bounds)	Optimised	Error	Initial
K_{11} (0 → ∞)	467.12 M^{-1}	± 1.2791 %	1000.00 M^{-1}
K_{12} (0 → ∞)	-11.27 M^{-1}	± -15.5746 %	100.00 M^{-1}

Data fit quality for tetrabutylammonium diphenyl phosphate (260@Zn-XLIII)

1:1 Zn-XLIII/260

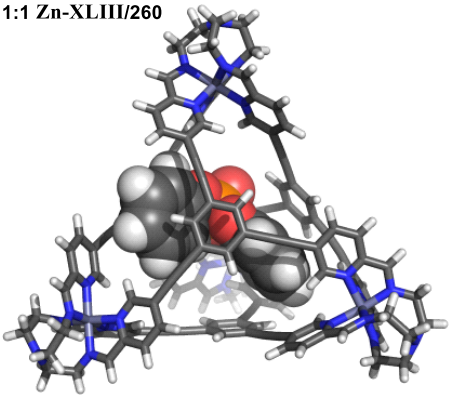

1:2 Zn-XLIII/260

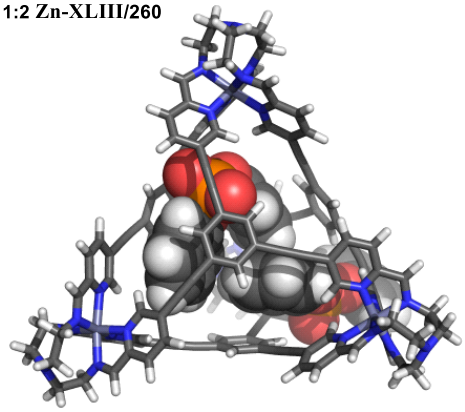

1:1 Binding Model Zn-XLIII/260

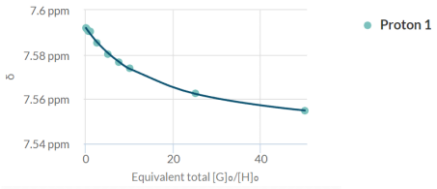

Parameter (bounds)	Optimised	Error	Initial
K (0 → ∞)	618.27 M^{-1}	± 5.4554 %	600.00 M^{-1}

1:2 Binding Model Zn-XLIII/260

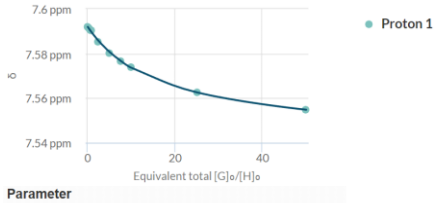

Parameter (bounds)	Optimised	Error	Initial
K_{11} (0 → ∞)	478.17 M^{-1}	± 4.4679 %	600.00 M^{-1}
K_{12} (0 → ∞)	-206.30 M^{-1}	± -4.4679 %	100.00 M^{-1}

Data fit quality for tetrabutylammonium dimethyl phosphate (261@Zn-XLIII)

1:1 Zn-XLIII/261

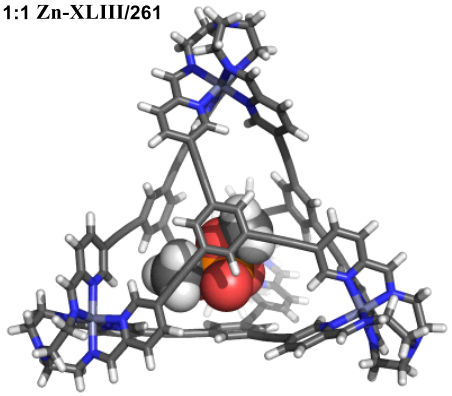

1:2 Zn-XLIII/261

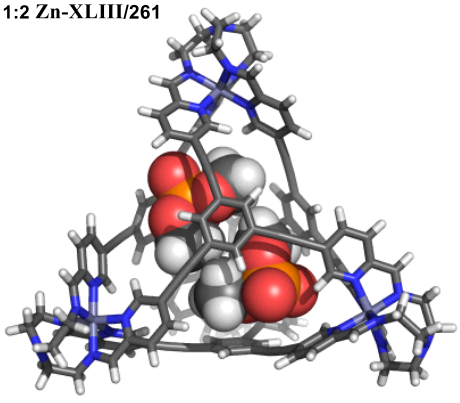

1:1 Binding Model Zn-XLIII/261

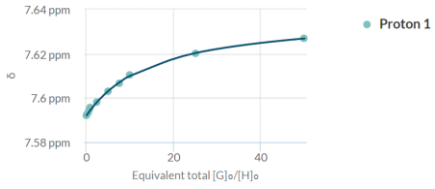

Parameter (bounds)	Optimised	Error	Initial
K (0 → ∞)	687.97 M^{-1}	± 4.4471 %	600.00 M^{-1}

1:2 Binding Model Zn-XLIII/261

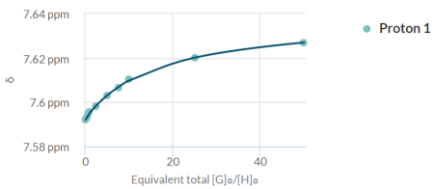

Parameter (bounds)	Optimised	Error	Initial
K_{11} (0 → ∞)	2253817674331100.00 M^{-1}	± 107367513.0541 %	1000.00 M^{-1}
K_{12} (0 → ∞)	596.31 M^{-1}	± 4.9418 %	100.00 M^{-1}

Data fit quality for tetrabutylammonium dibutyl phosphate (262@Zn-XLIII)

1:1 Zn-XLIII/262

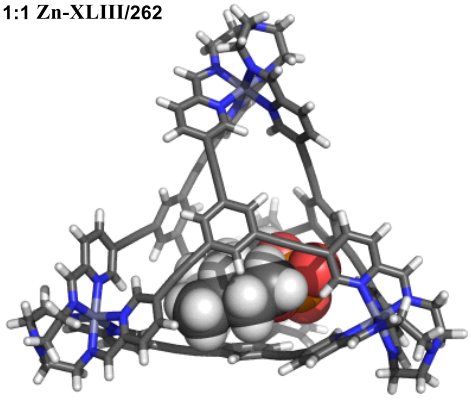

1:2 Zn-XLIII/262

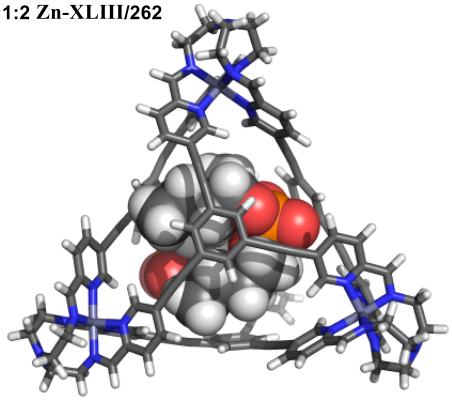

1:1 Binding Model Zn-XLIII/262

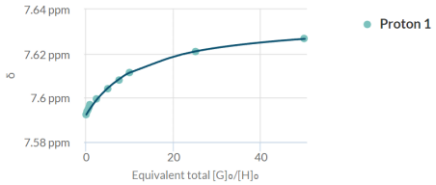

Parameter (bounds)	Optimised	Error	Initial
K (0 → ∞)	850.61 M^{-1}	± 7.3866 %	800.00 M^{-1}

1:2 Binding Model Zn-XLIII/262

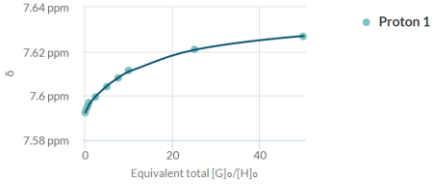

Parameter (bounds)	Optimised	Error	Initial
K_{11} (0 → ∞)	882855.38 M^{-1}	± 659.2214 %	850.00 M^{-1}
K_{12} (0 → ∞)	638.95 M^{-1}	± 5.3951 %	100.00 M^{-1}

5.5 Catalysis Experiments

Catalysis experiments were run within NMR tubes using heating blocks when elevated temperatures were needed to heat up the reaction mixture. NMR experiments were performed measuring ^{1}H-NMR spectra at 500 MHz using a BRUKER UltraShield 500 spectrometer at 298 K. MeCN-d_3/H_2O = 6:4 was used as a solvent mixture for all stock solutions. Using D_2O instead of H_2O led to shimming problems and, therefore, was substituted.

Catalysis experiments were performed according to the following procedure:

An NMR tube was charged with 200 µL of each of the following stock solutions in MeCN-d_3/H_2O = 6:4:

a) with the corresponding base for each experiment (either $KHCO_3$, NEt_3 or *i*-Pr_2NEt) at a concentration of c(Base) = 180 mM and durene as an internal standard at a concentration of c(Durene) = 15.0 mM,

b) with **$Zn_4L_4(NTf_2)_8$** cage **Zn-XLIII** (Host, H) at a concentration of c(H) = 6.00 mM and

c) with the corresponding substrate (S) for each experiment at a concentration of c(S) = 60.0 mM ending up with a total volume of 600 µL of a reaction mixture containing 1.00 eq. of the corresponding substrate, 3.00 eq. of the corresponding base, 0.25 eq. of durene as an internal standard and 0.10 eq. = 10 mol-% of **$Zn_4L_4(NTf_2)_8$** cage **Zn-XLIII**.

For the corresponding background reactions, 200 µL of the used solvent mixture (MeCN-d_3/H_2O = 6:4) was added instead of the stock solution of **$Zn_4L_4(NTf_2)_8$** cage **Zn-XLIII**.

Product NMR yields were calculated by comparing the relative integrals between the new product signals (either aromatic or aliphatic) and the corresponding signals from durene (either aromatic or aliphatic), whichever signal was more practical to use (due to no overlaps with other signals for example).

The mole fraction of guest G that is bound by the host H under the concentrations used for catalysis can be determined as follows. Under the assumption that 1:1 host:guest binding is taking place we can write the basic reaction equation

$$\mathrm{H} + \mathrm{G} \rightleftharpoons \mathrm{HG} \tag{1}$$

and formulate the equilibriums association constant K_a:

$$K_a = \frac{[\mathrm{HG}]}{[\mathrm{H}][\mathrm{G}]} \tag{2}$$

with [H], [G] and [HG] being the concentration of the host H, guest G and host-guest complex HG at any given time, respectively. [H] and [G] can be substituted by the following terms:

$$[\mathrm{H}] = [\mathrm{H}]_0 - [\mathrm{HG}] \tag{3}$$

$$[\mathrm{G}] = [\mathrm{G}]_0 - [\mathrm{HG}] \tag{4}$$

$[H]_0$ and $[G]_0$ describe the initial (total) concentration of the host H or guest G, respectively. With this, the following quadratic equation can be derived:

$$[\mathrm{HG}] = \frac{1}{2}\left\{\left([\mathrm{H}]_0 + [\mathrm{G}]_0 + \frac{1}{K_a}\right) - \sqrt{\left([\mathrm{H}]_0 + [\mathrm{G}]_0 + \frac{1}{K_a}\right)^2 - 4[\mathrm{H}]_0[\mathrm{G}]_0}\right\} \tag{5}$$

From here, we can determine the theoretical concentration of the host-guest complex [HG] at a given total concentration for the host $[H]_0$ and guest $[G]_0$ after the association constant K_a for a specific guest has been determined in a separate experiment.

Subsequently, the mole fraction of bound substrate X_{HG} can be determined *via* the equation:

$$X_{\mathrm{HG}} = \frac{[\mathrm{HG}]}{[\mathrm{H}]_0} \cdot 100\% \tag{6}$$

During the catalysis experiments described in this chapter the following initial concentrations were used for **$Zn_4L_4(NTf_2)_8$** cage **Zn-XLIII** as the host H and for the corresponding guests G as substrates:

$$[\mathrm{H}]_0 = 0.002\ \mathrm{mol} \cdot \mathrm{L}^{-1};\ [\mathrm{G}]_0 = 0.02\ \mathrm{mol} \cdot \mathrm{L}^{-1}$$

For example, the mole fractions of bound guest at these concentrations for guests **258** and **256** with binding constants of $K_{a,\mathbf{258}} = 370\ \mathrm{L} \cdot \mathrm{mol}^{-1}$ and $K_{a,\mathbf{256}} = 130\ \mathrm{L} \cdot \mathrm{mol}^{-1}$ were calculated to be $X_{\mathbf{258}} = 87\%$ and $X_{\mathbf{256}} = 71\%$.

5.6 NMR Spectra of New and Key Compounds

2,7-Di-*p*-tolylbenzo[*lmn*][3,8]phenanthroline-1,3,6,8(2*H*,7*H*)-tetraone (181)

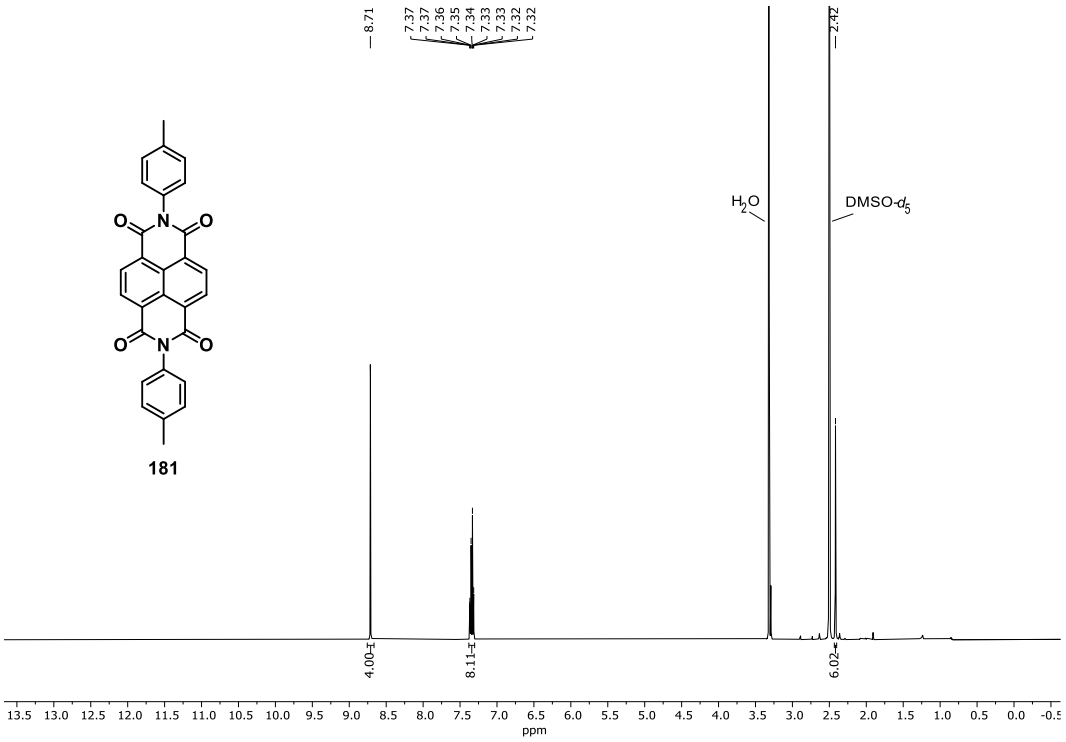

Figure 61: ^{1}H-NMR (500 MHz) spectrum of NDI compound **181** in DMSO-d_6 at 298 K.

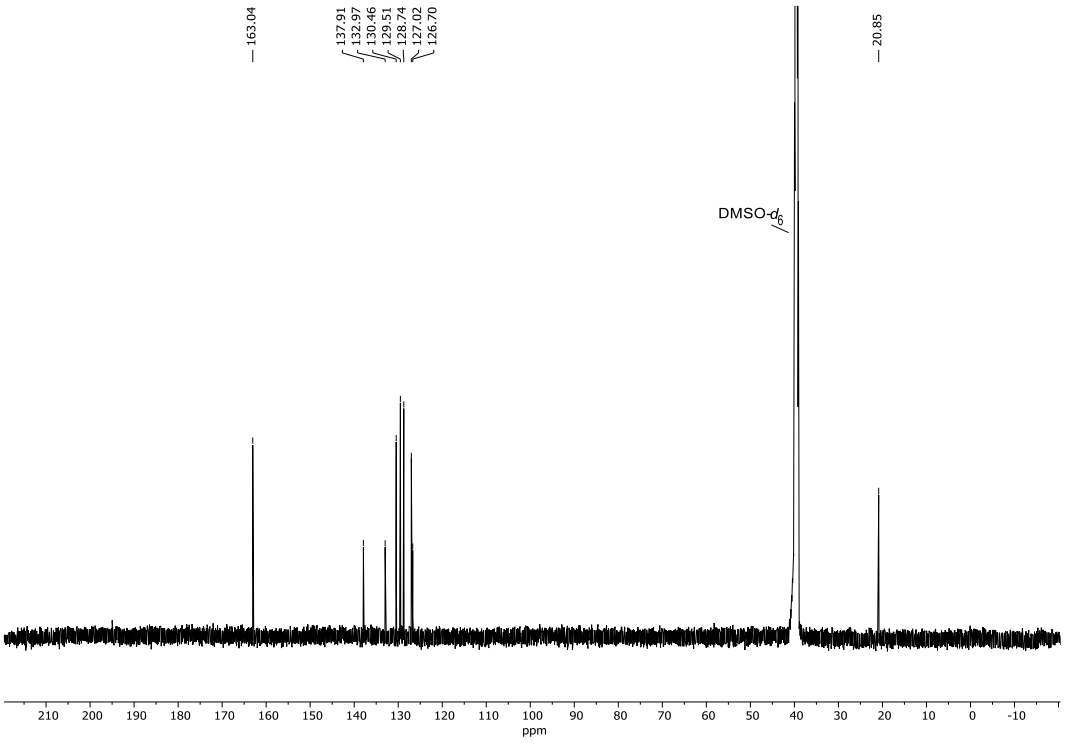

Figure 62: ^{13}C-NMR (151 MHz) spectrum of NDI compound **181** in DMSO-d_6 at 298 K.

2,7-Bis(4-(((triisopropylsilyl)oxy)methyl)phenyl)benzo[*lmn*][3,8]phenanthroline-1,3,6,8 (2*H*,7*H*)-tetraone (194)

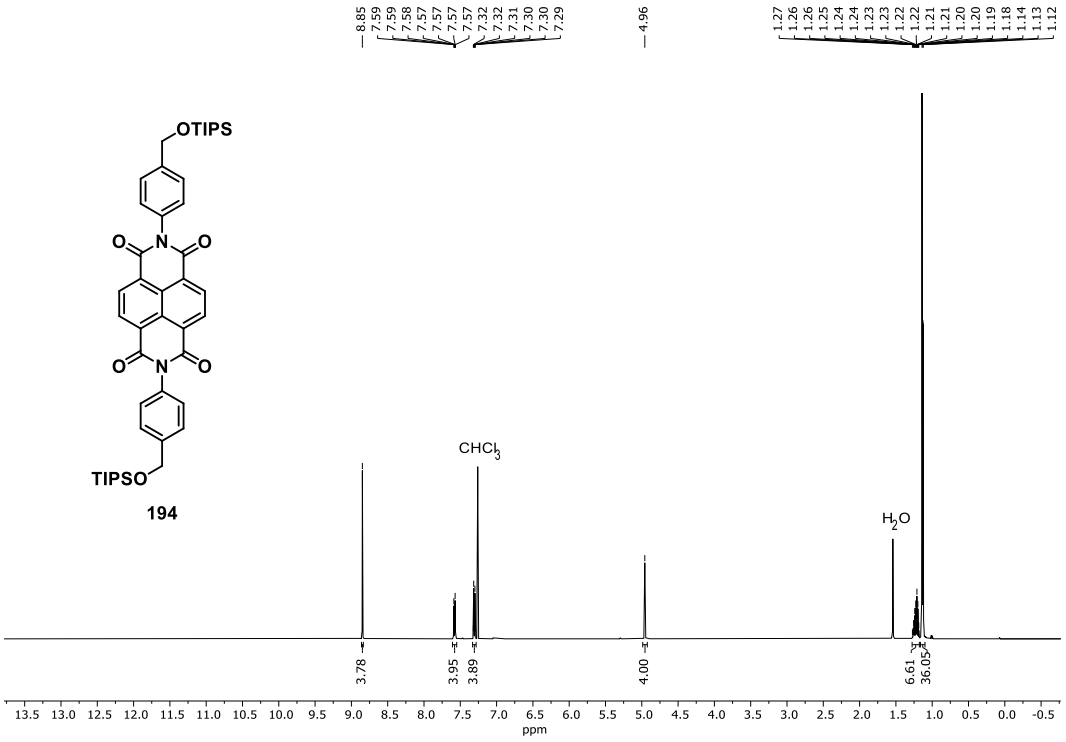

Figure 63: ^{1}H-NMR (500 MHz) spectrum of NDI compound **194** in $CDCl_3$ at 298 K.

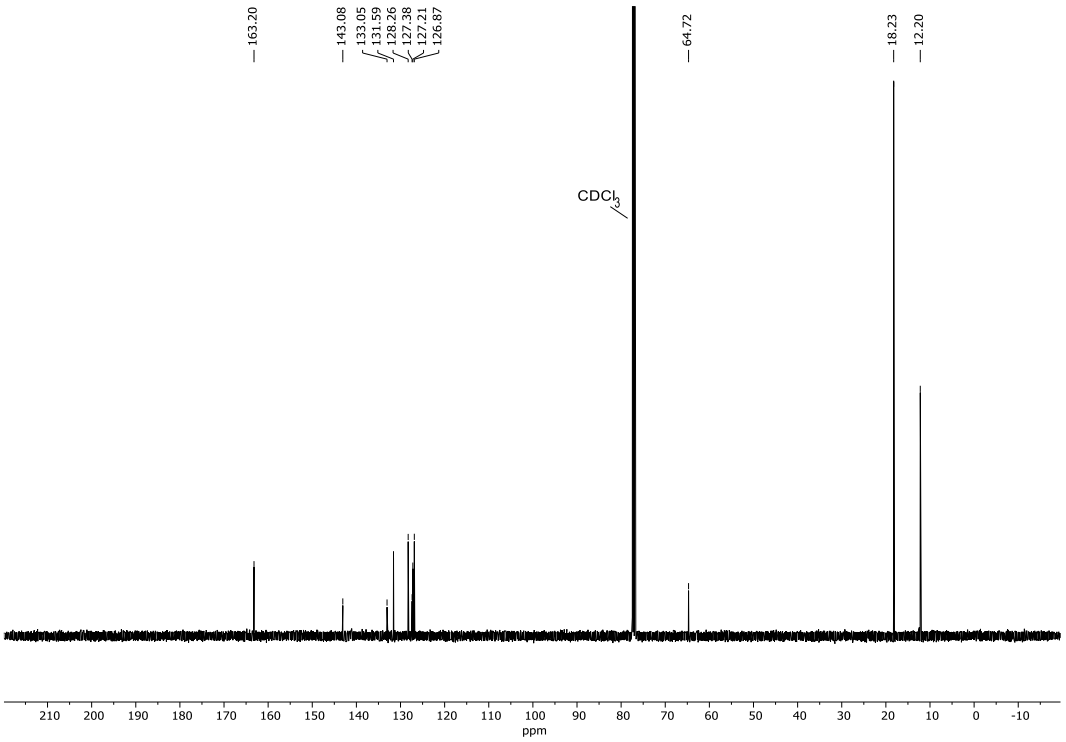

Figure 64: ^{13}C-NMR (126 MHz) spectrum of NDI compound **194** in $CDCl_3$ at 298 K.

2,7-Bis(4-(5,5-dimethyl-1,3-dioxan-2-yl)phenyl)benzo[*lmn*][3,8]phenanthroline-1,3,6,8 (2*H*,7*H*)-tetraone (196)

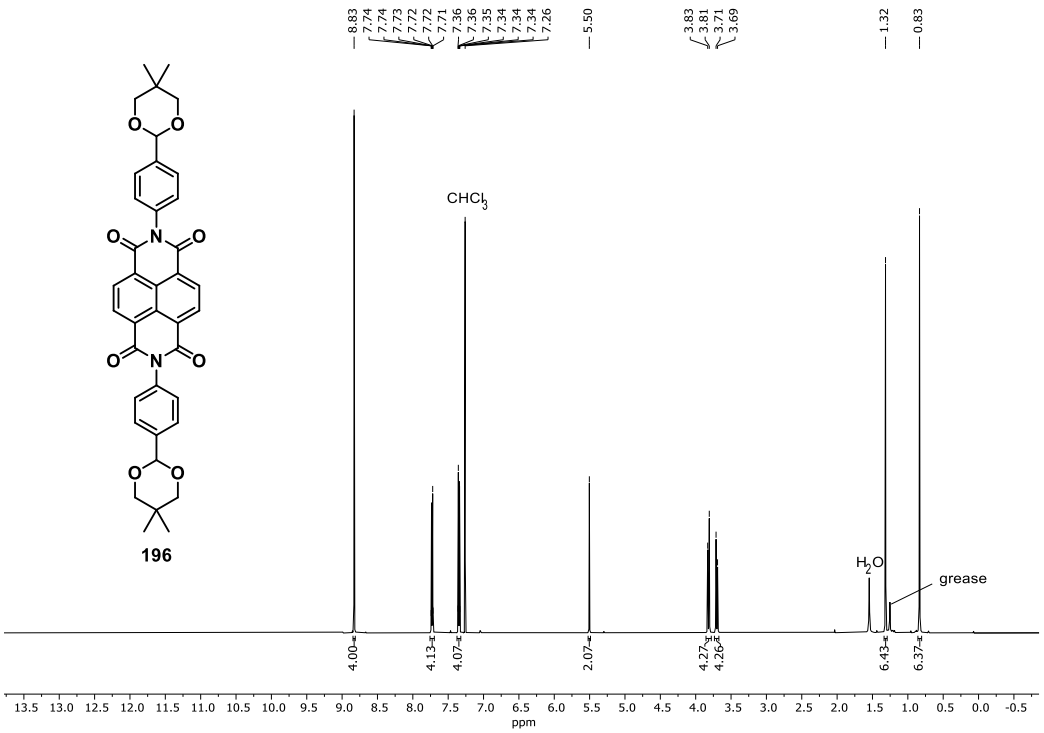

Figure 65: ^{1}H-NMR (500 MHz) spectrum of NDI compound **196** in $CDCl_3$ at 298 K.

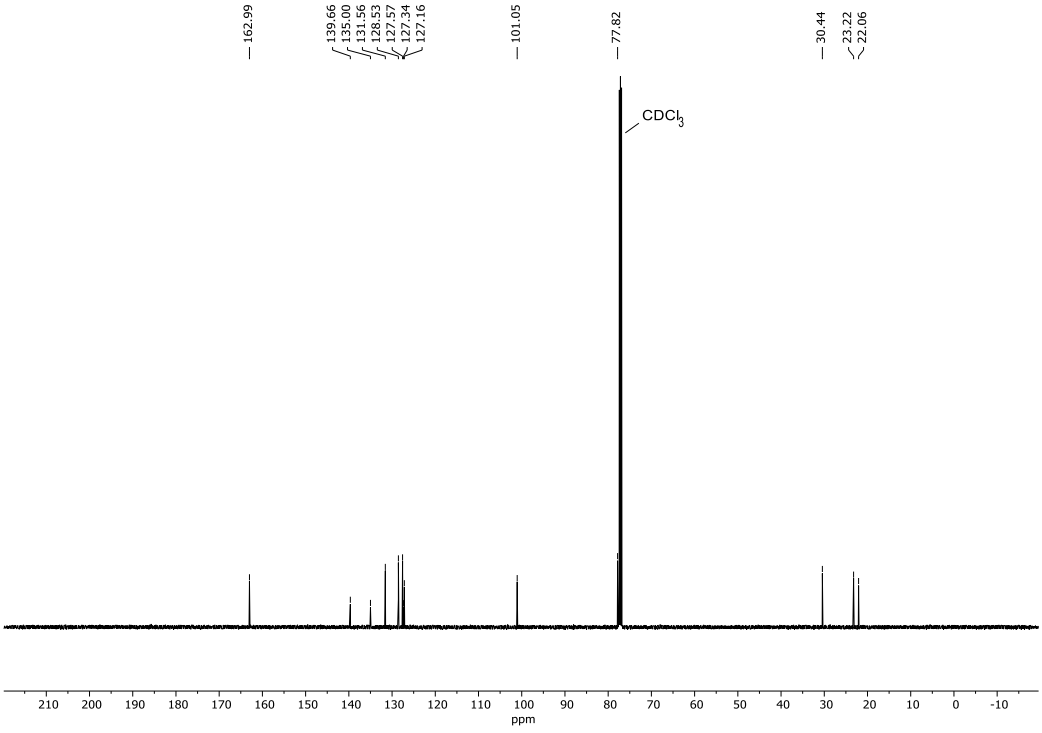

Figure 66: ^{13}C-NMR (126 MHz) spectrum of NDI compound **196** in $CDCl_3$ at 298 K.

4,4'-(1,3,6,8-Tetraoxo-1,3,6,8-tetrahydrobenzo[*lmn*][3,8]phenanthroline-2,7-diyl)dibenz aldehyde (175)

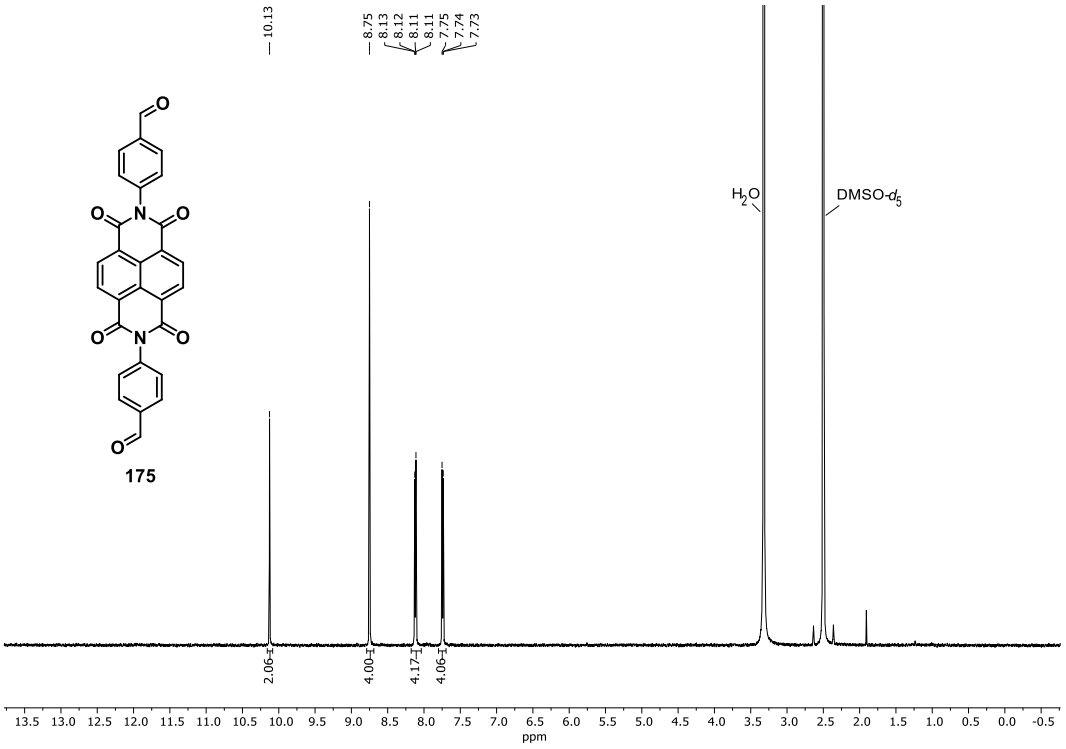

Figure 67: ^{1}H-NMR (500 MHz) spectrum of NDI compound **175** in DMSO-d_6 at 298 K.

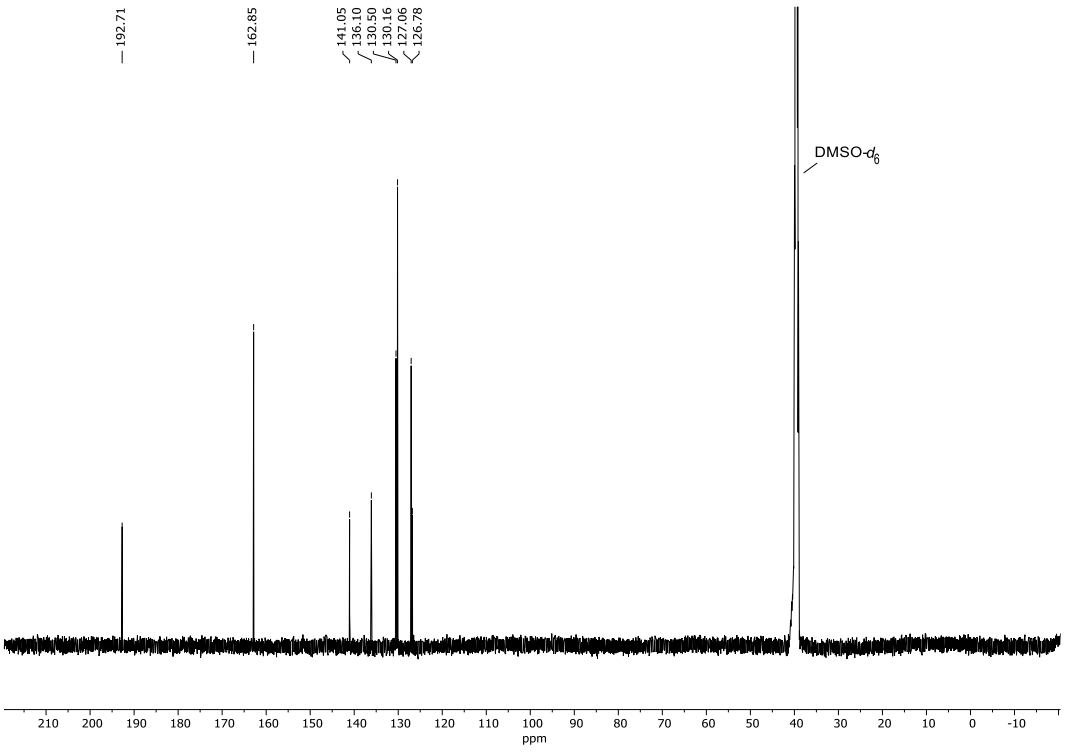

Figure 68: ^{13}C-NMR (151 MHz) spectrum of NDI compound **175** in DMSO-d_6 at 298 K.

Imine Cage XXIIIa

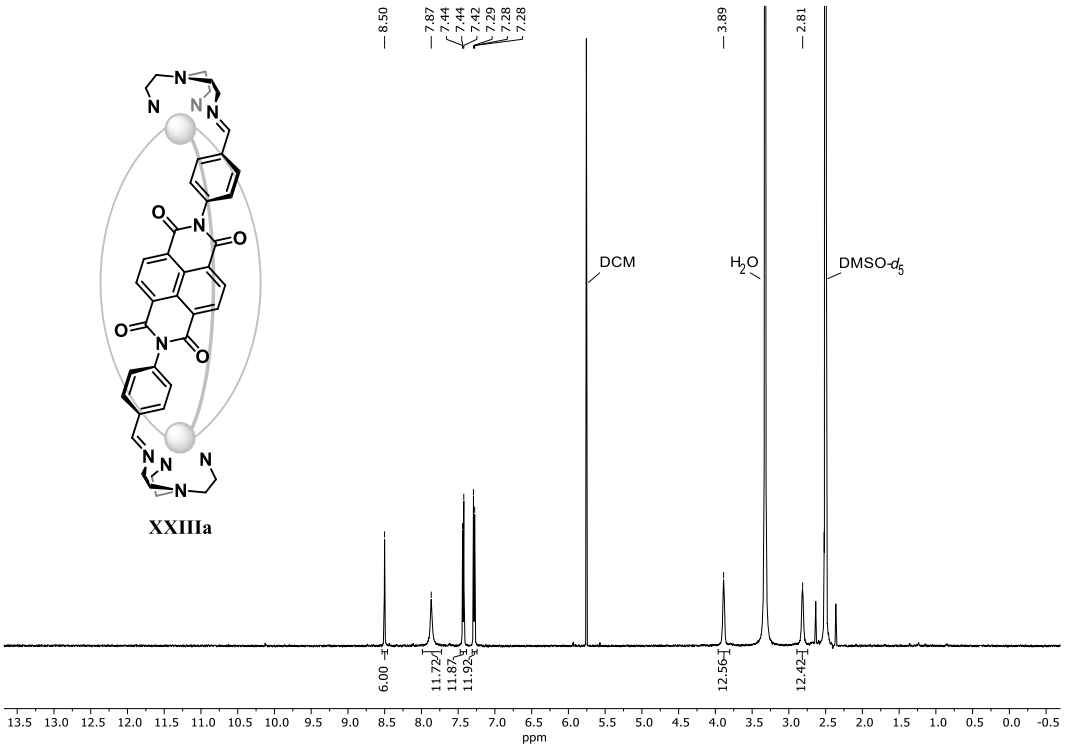

Figure 69: ^{1}H-NMR (500 MHz) spectrum of imine cage **XXIIIa** in DMSO-d_6 at 298 K.

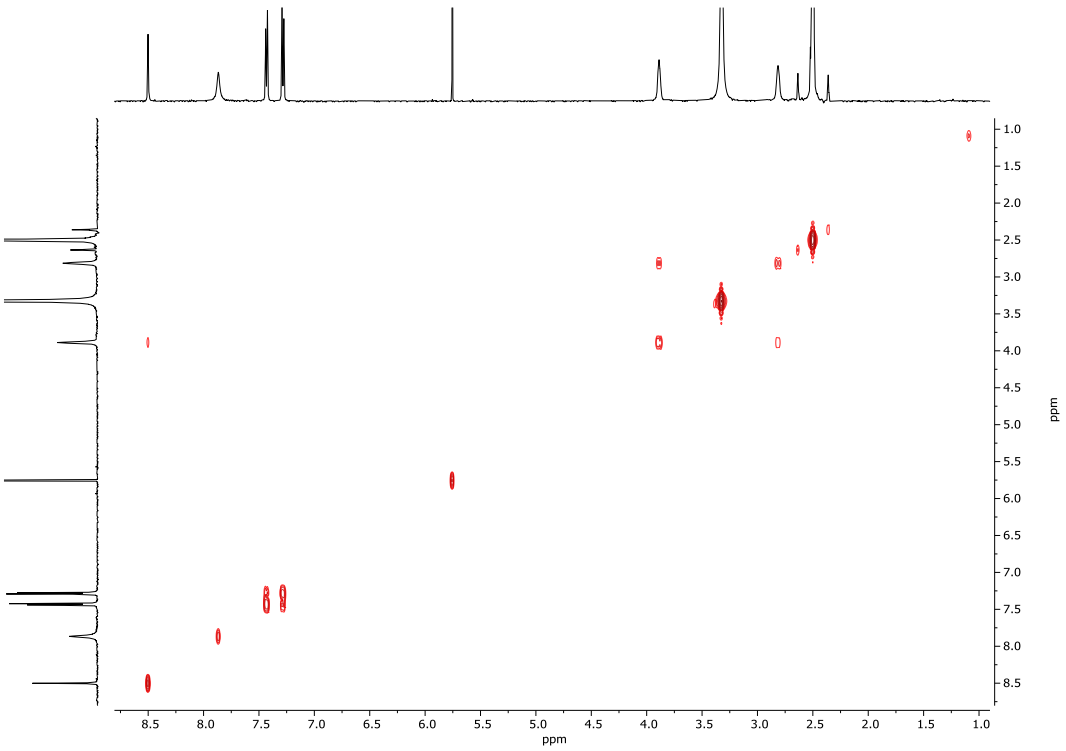

Figure 70: COSY spectrum of imine cage **XXIIIa** in DMSO-d_6 at 298 K.

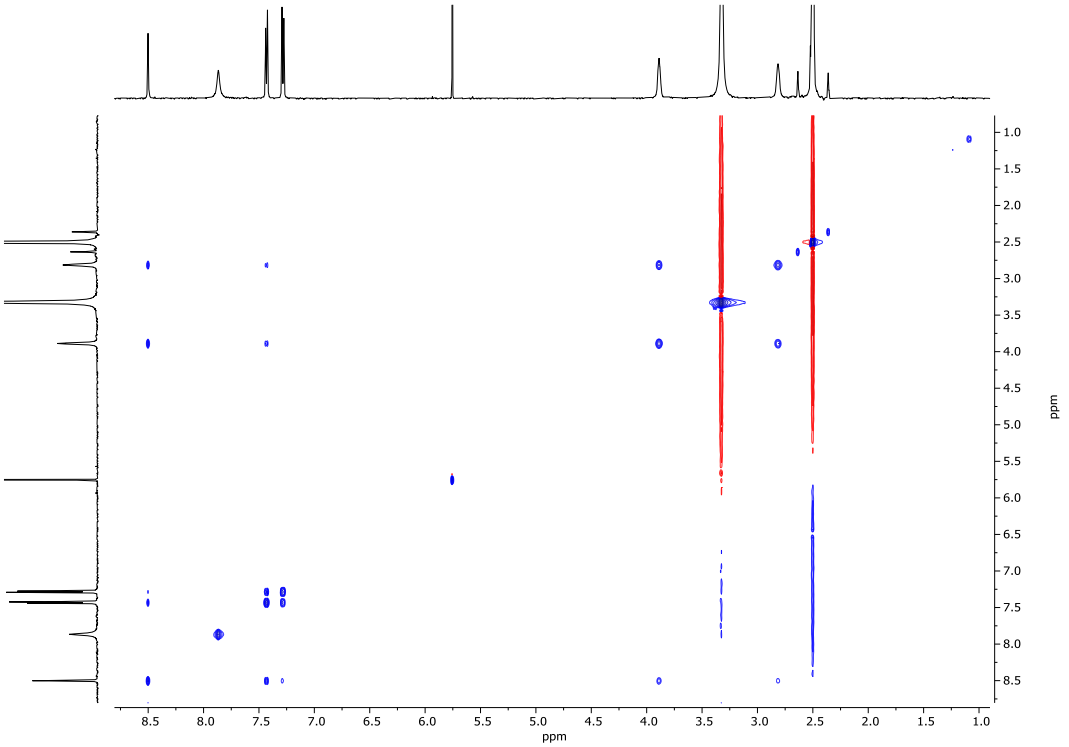

Figure 71: NOESY spectrum of imine cage **XXIIIa** in DMSO-d_6 at 298 K.

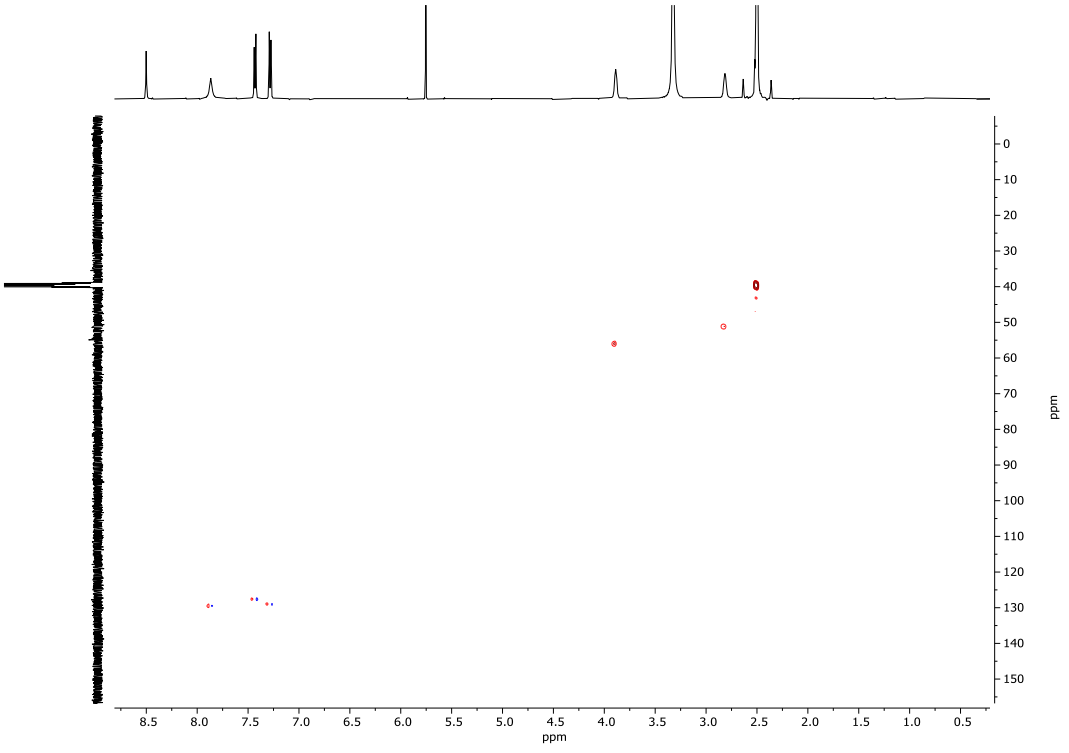

Figure 72: HMQC spectrum of imine cage **XXIIIa** in DMSO-d_6 at 298 K.

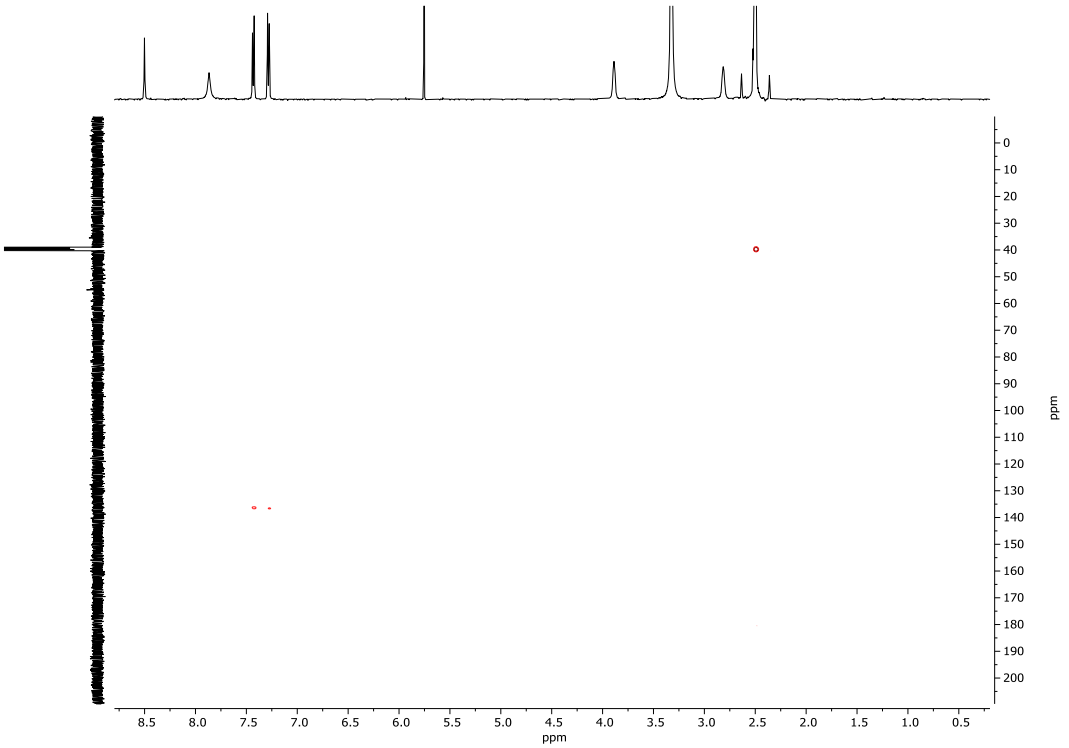

Figure 73: HMBC spectrum of imine cage **XXIIIa** in DMSO-d_6 at 298 K.

Ammonium Chloride Cage XVIIa

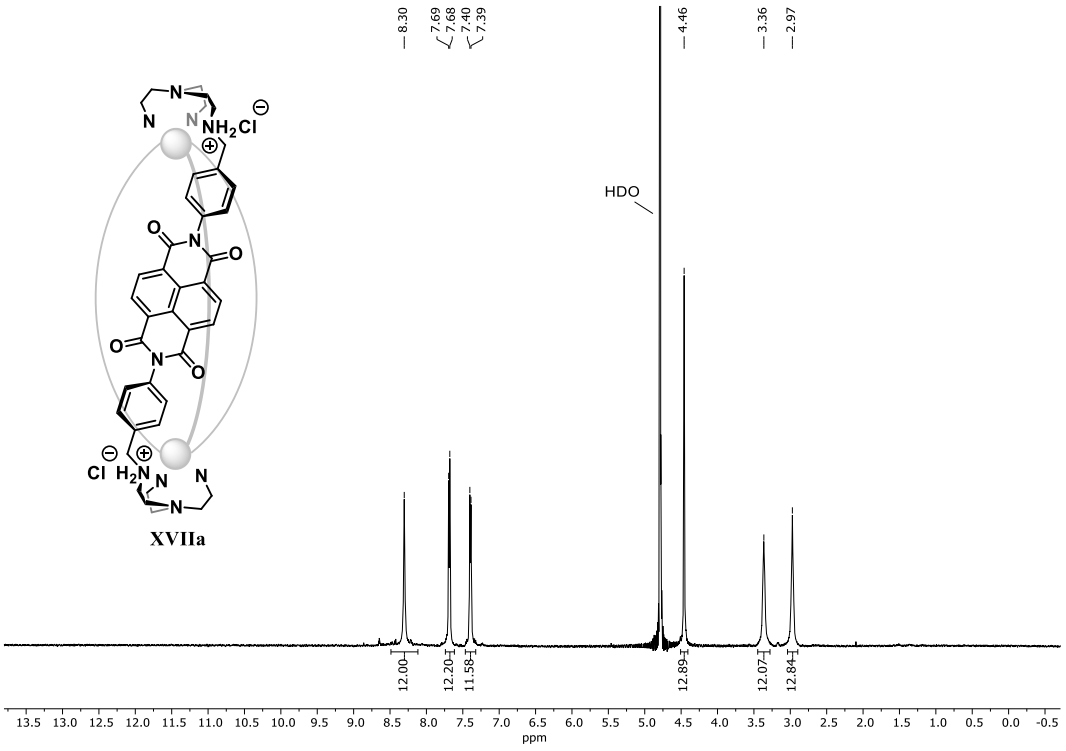

Figure 74: ^{1}H-NMR (500 MHz) spectrum of ammonium chloride cage **XVIIa** in D_2O at 298 K.

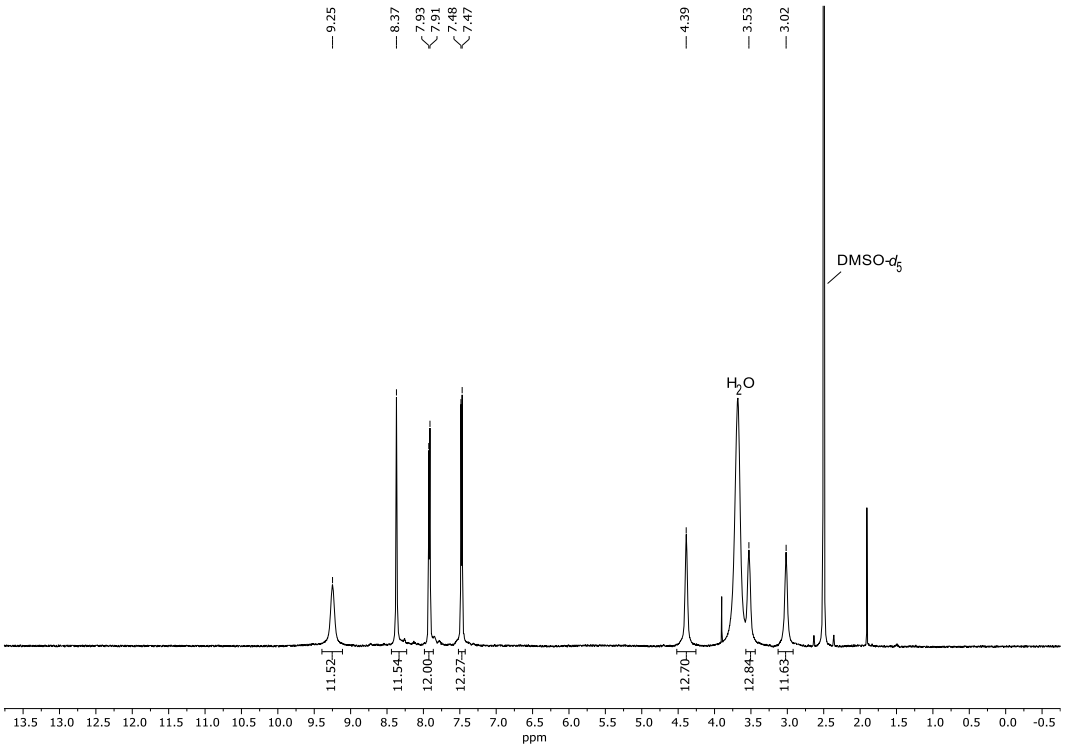

Figure 75: [1]H-NMR (500 MHz) spectrum of ammonium chloride cage **XVIIa** in DMSO-d_6 at 298 K.

Ammonium Trifluoroacetate Cage XXVa

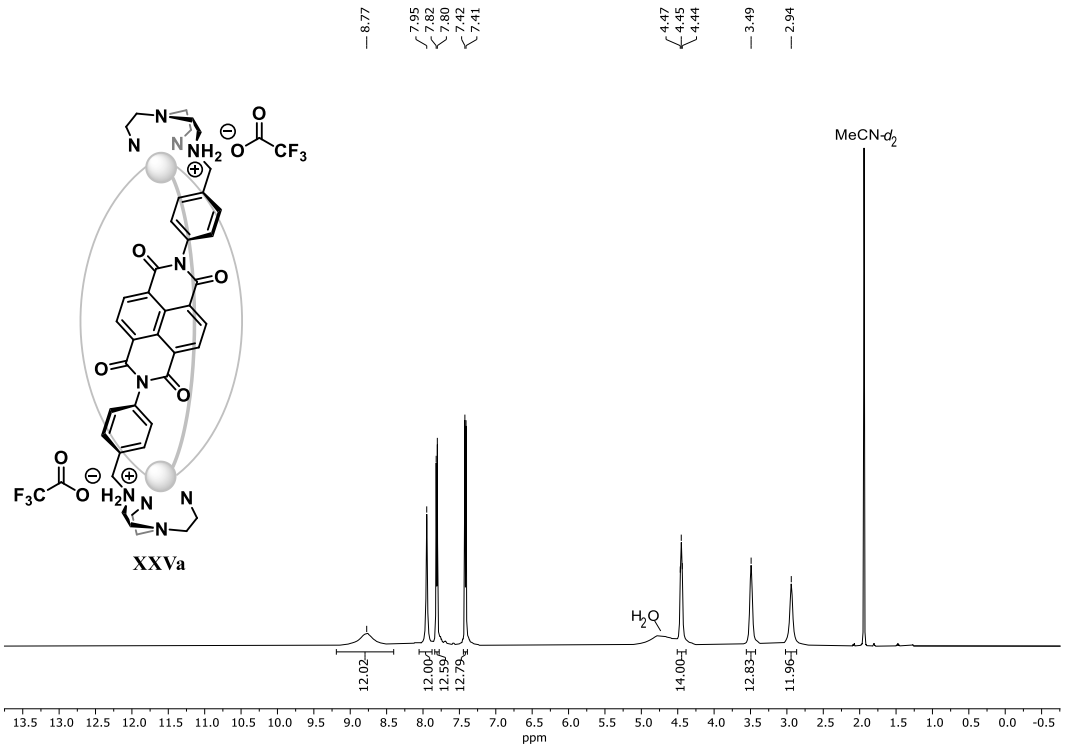

XXVa

Figure 76: [1]H-NMR (500 MHz) spectrum of ammonium trifluoroacetate cage **XXVa** in MeCN-d_3 at 298 K.

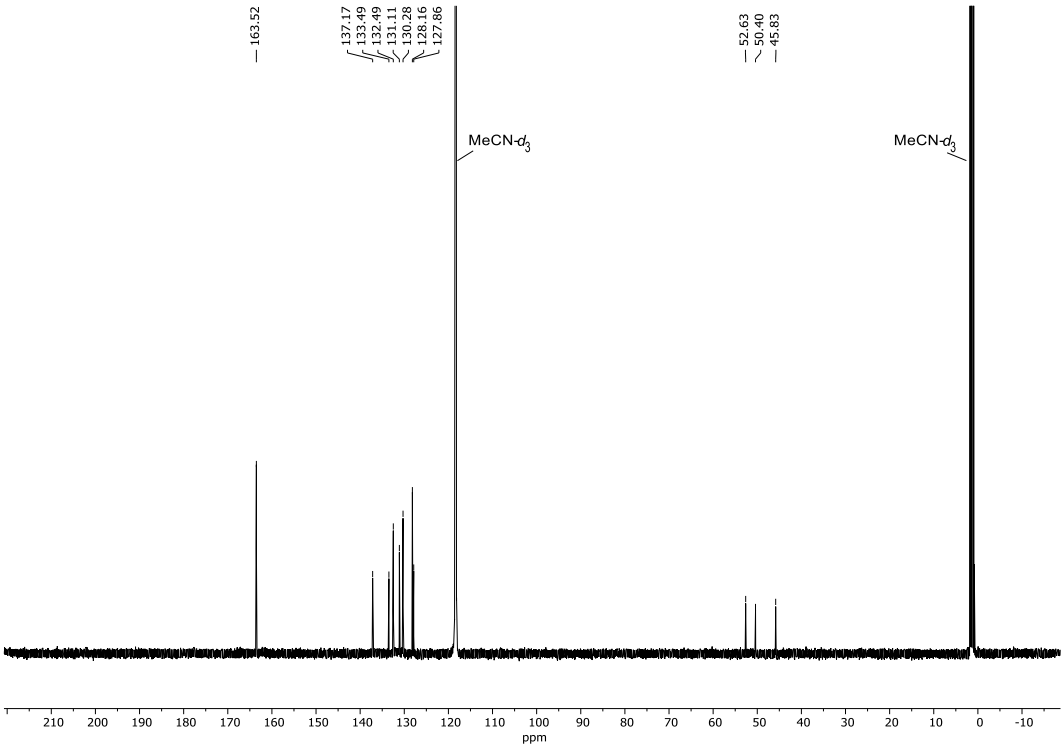

Figure 77: ^{13}C-NMR (126 MHz) spectrum of ammonium trifluoroacetate cage **XXVa** in MeCN-d_3 at 298 K.

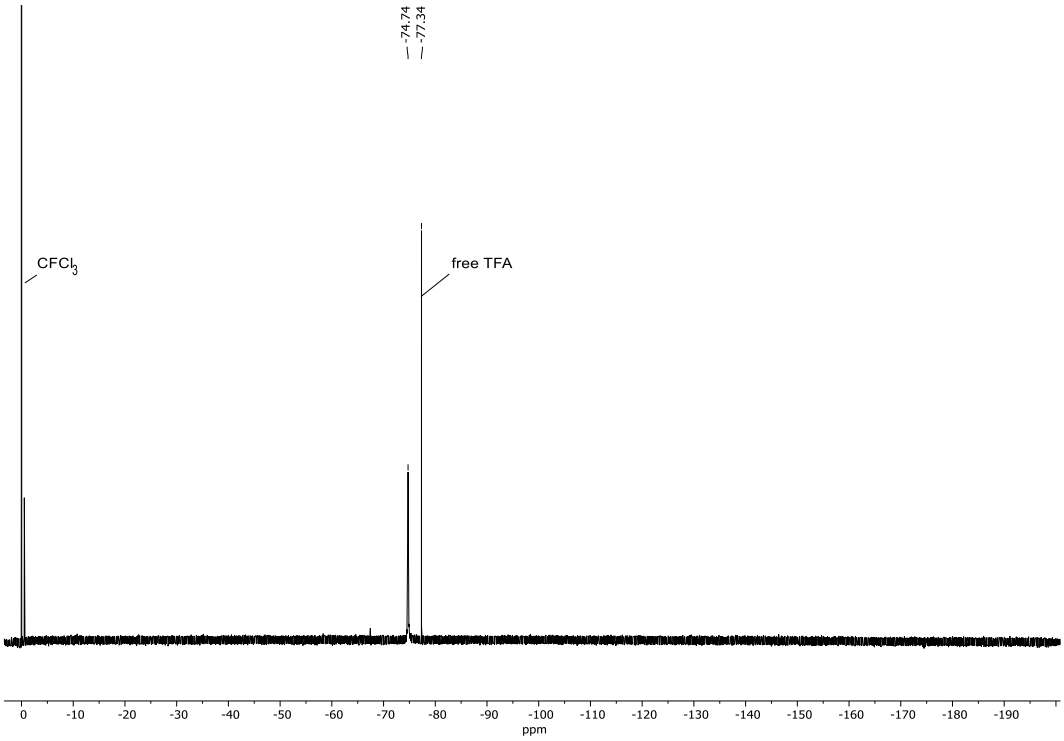

Figure 78: ^{19}F-NMR (471 MHz) spectrum of ammonium trifluoroacetate cage **XXVa** in MeCN-d_3 at 298 K with $CFCl_3$ as int. Std.

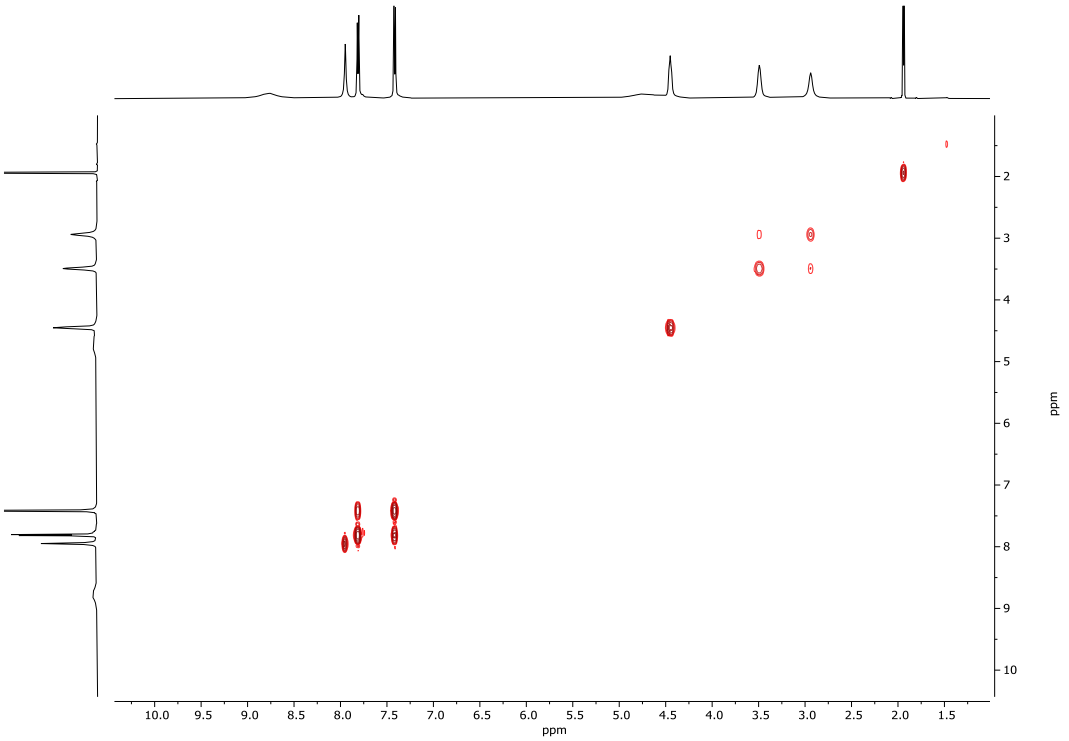

Figure 79: COSY spectrum of ammonium trifluoroacetate cage **XXVa** in MeCN-d_3 at 298 K.

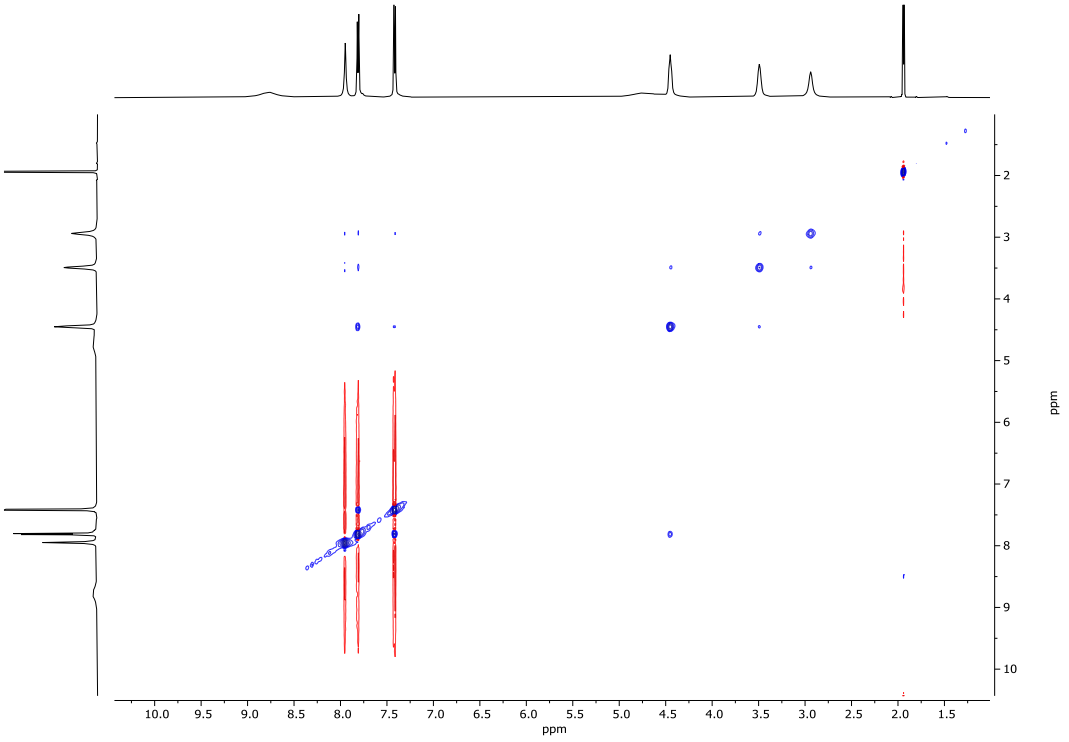

Figure 80: NOESY spectrum of ammonium trifluoroacetate cage **XXVa** in MeCN-d_3 at 298 K.

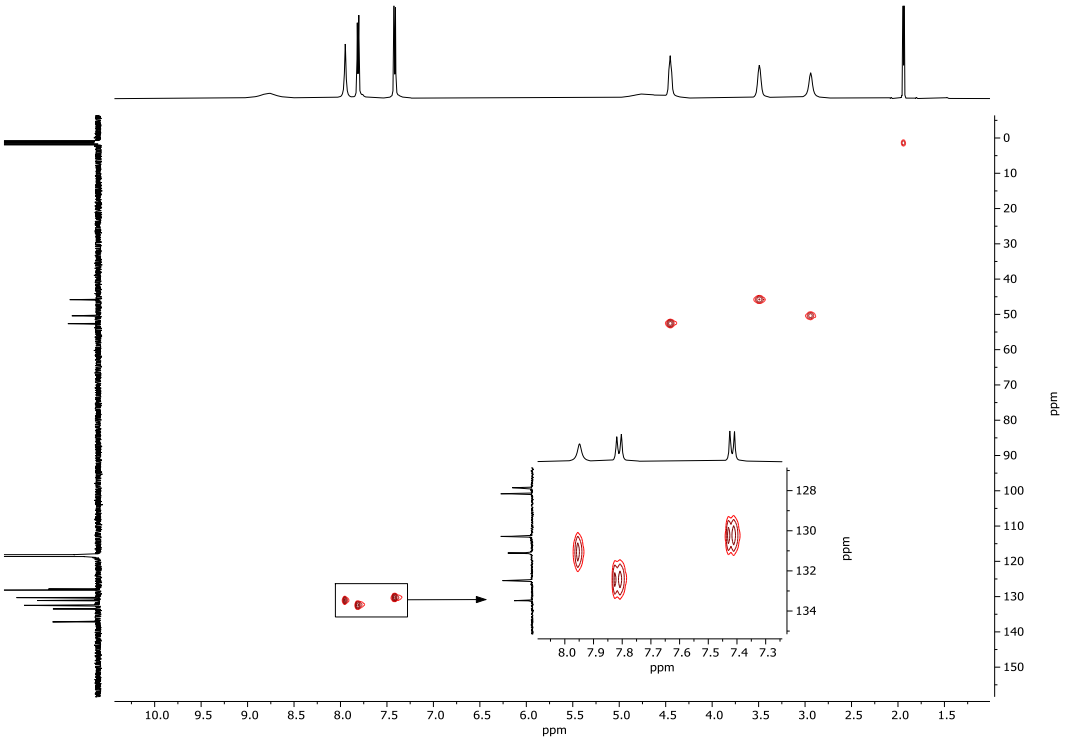

Figure 81: HMQC spectrum of ammonium trifluoroacetate cage **XXVa** in MeCN-d_3 at 298 K.

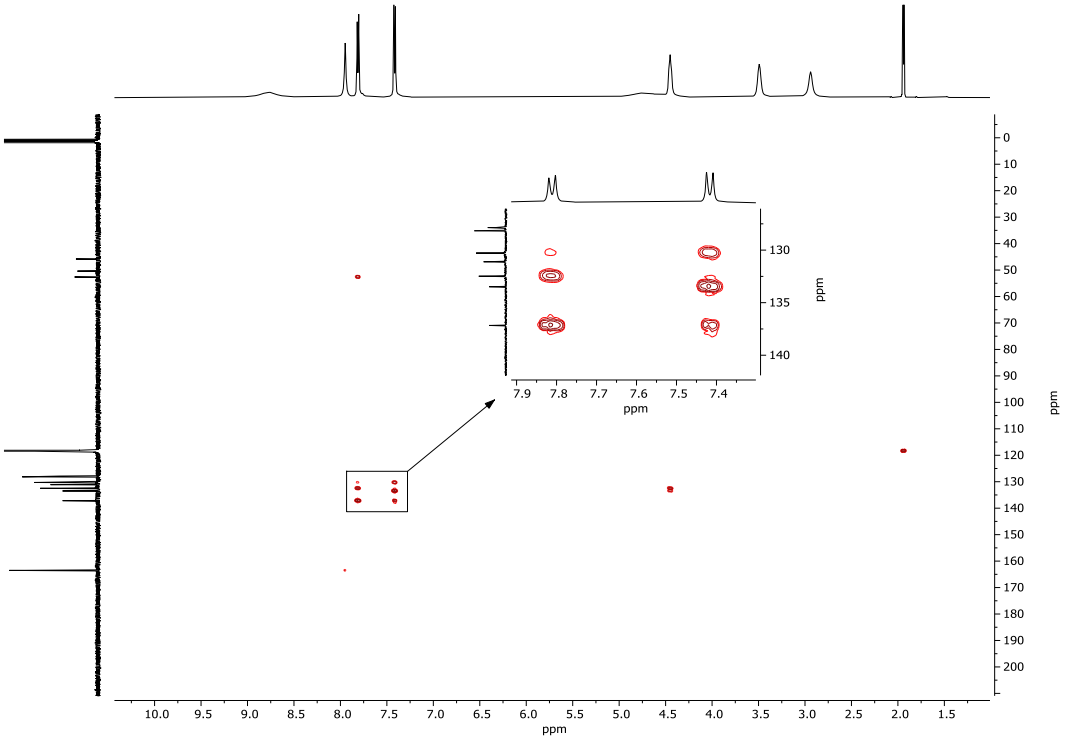

Figure 82: HMBC spectrum of ammonium trifluoroacetate cage **XXVa** in MeCN-d_3 at 298 K.

Ammonium chloride species 204a of the type A_2B (with impurities)

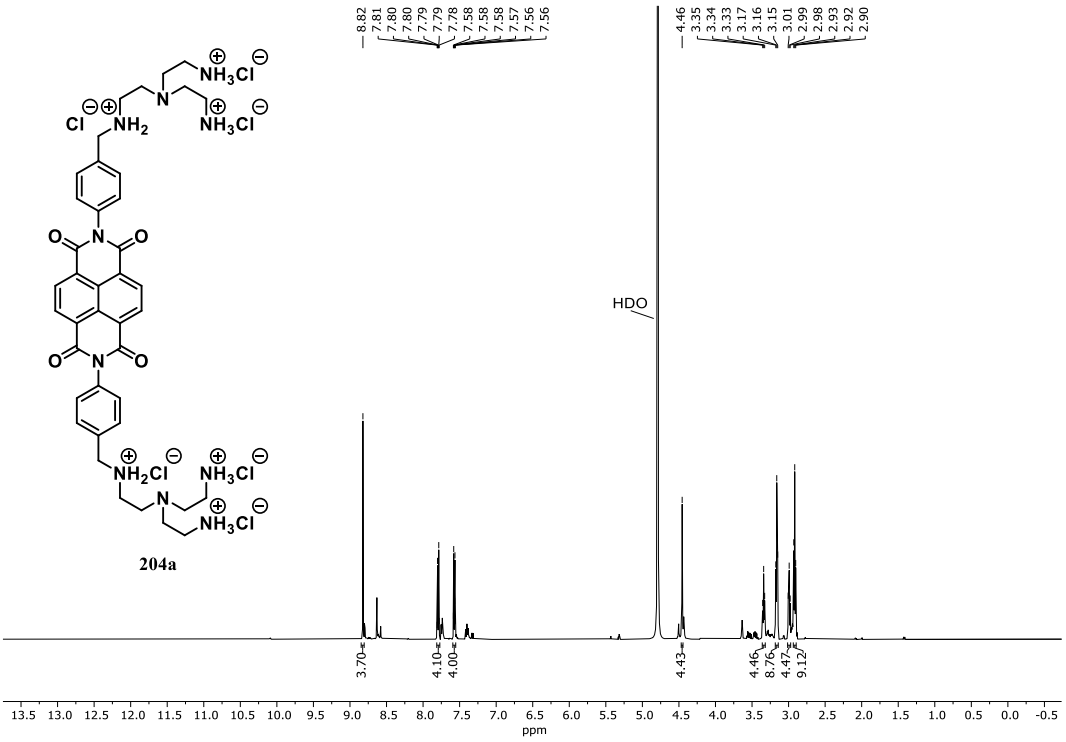

Figure 83: ^{1}H-NMR (500 MHz) spectrum of ammonium chloride species **204a** in D_2O at 298 K.

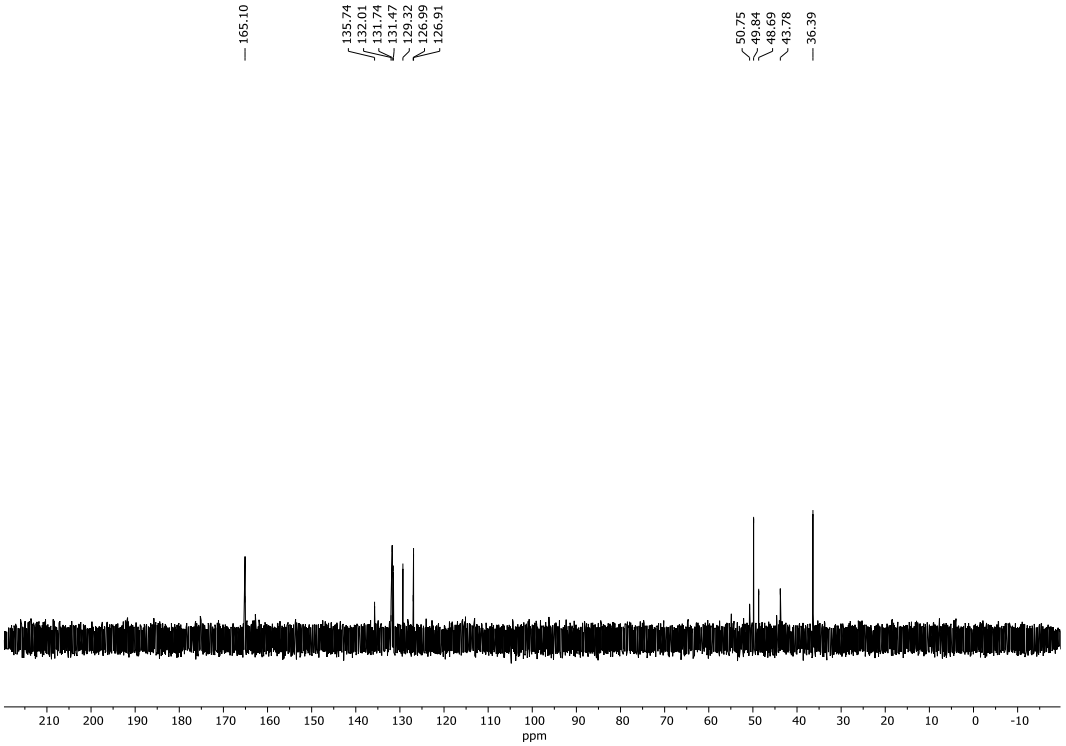

Figure 84: ^{13}C-NMR (126 MHz) spectrum of ammonium chloride species **204a** in D_2O at 298 K.

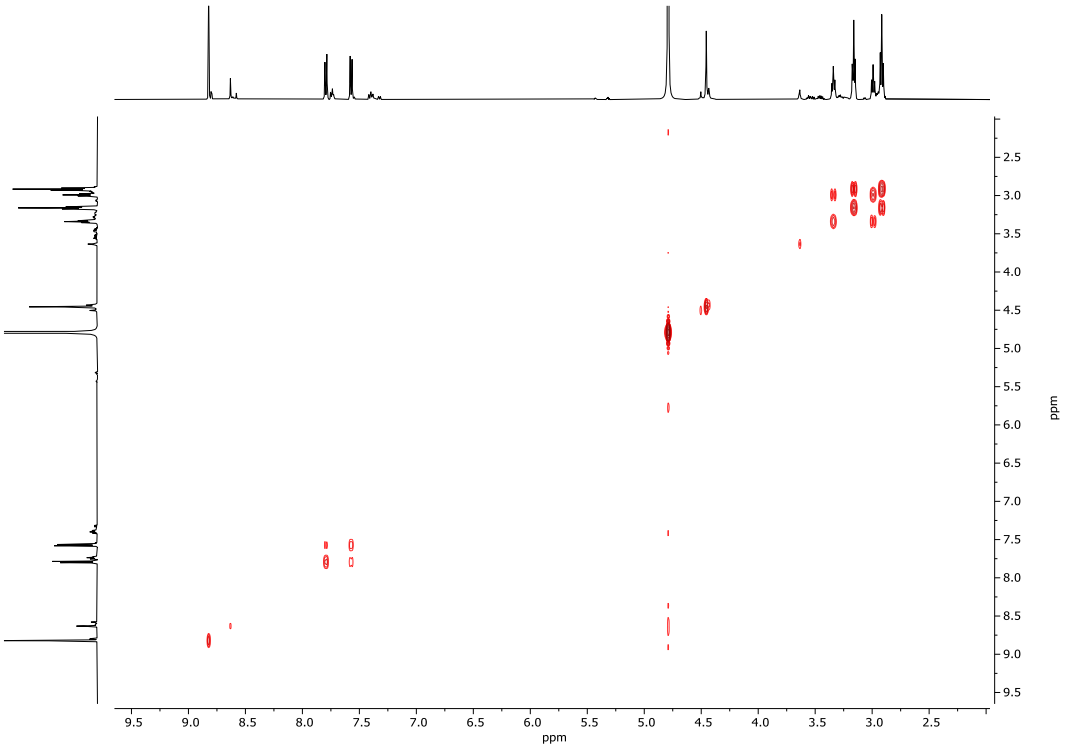

Figure 85: COSY spectrum of ammonium chloride species **204a** in D_2O at 298 K.

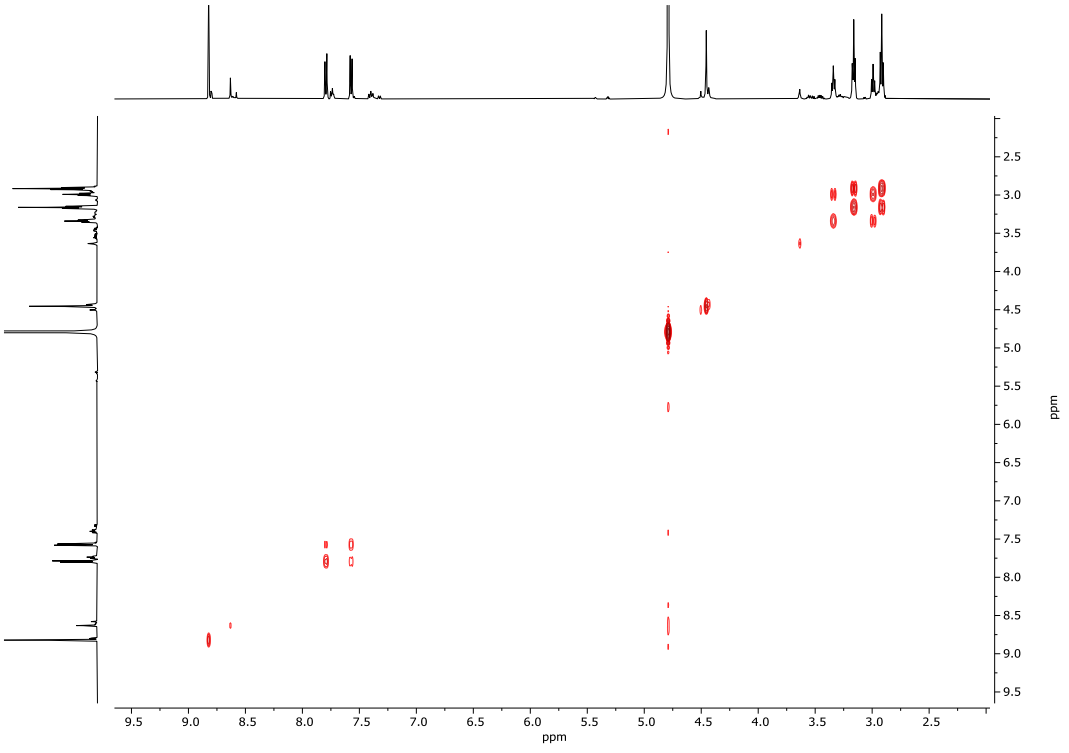

Figure 86: NOESY spectrum of ammonium chloride species **204a** in D_2O at 298 K.

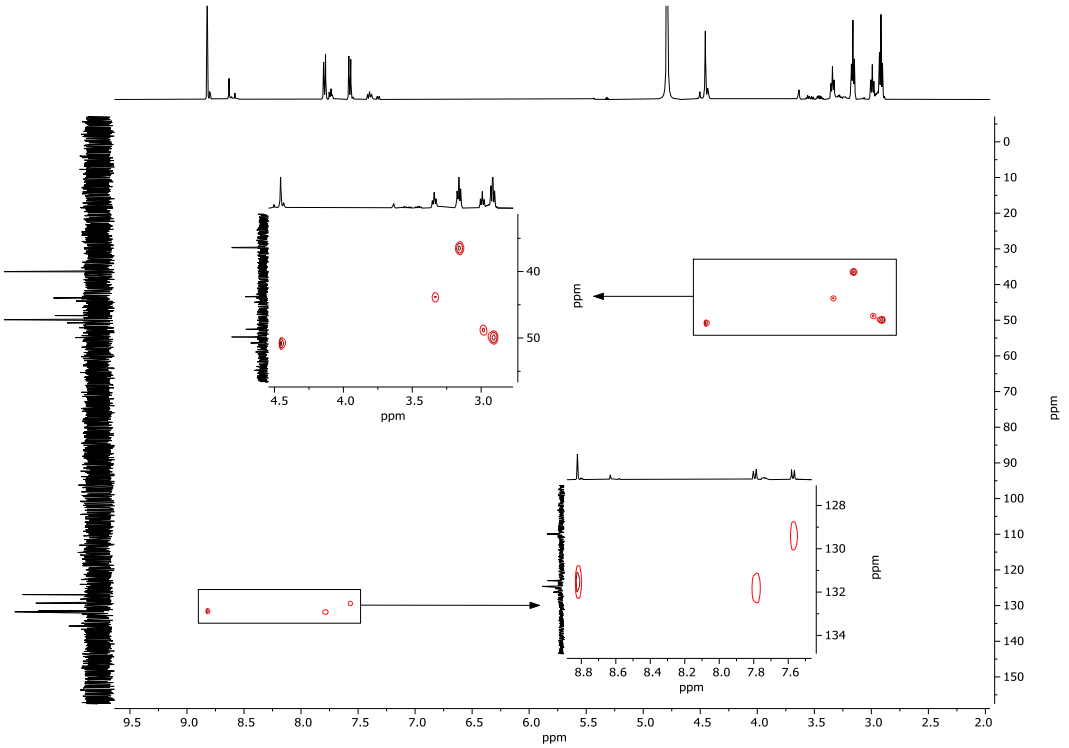

Figure 87: HMQC spectrum of ammonium chloride species **204a** in D_2O at 298 K.

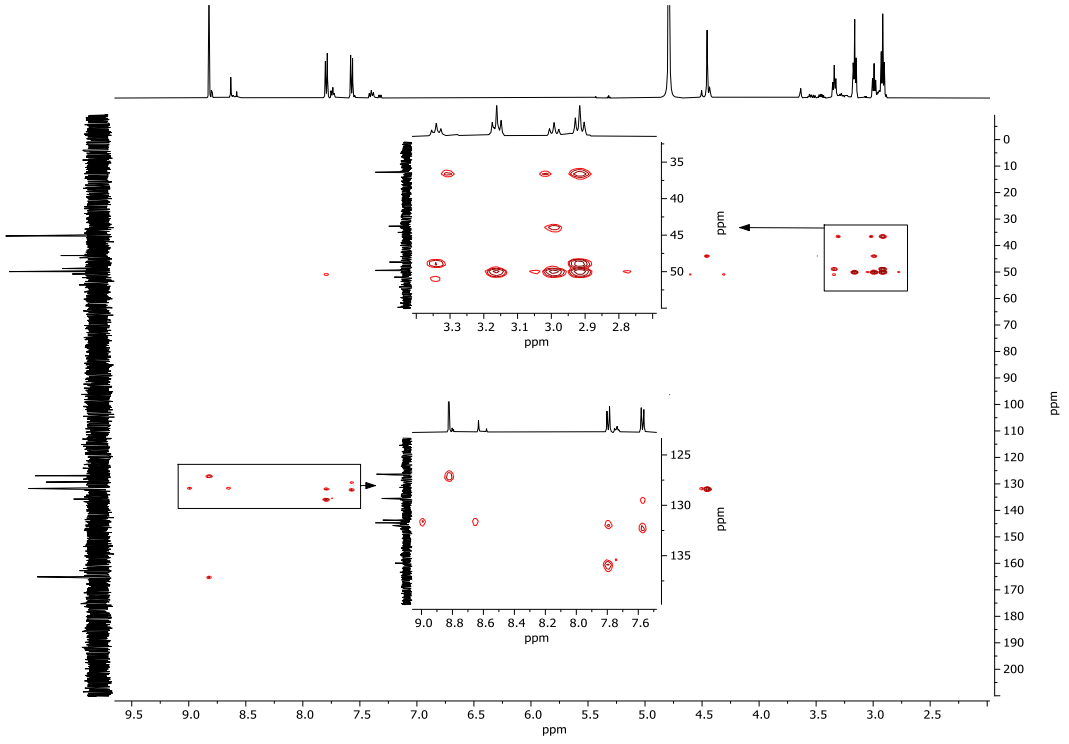

Figure 88: HMBC spectrum of ammonium chloride species **204a** in D_2O at 298 K.

Imine Cage XXIIIc (Derived from Triamine 128c and Dialdehyde 175)

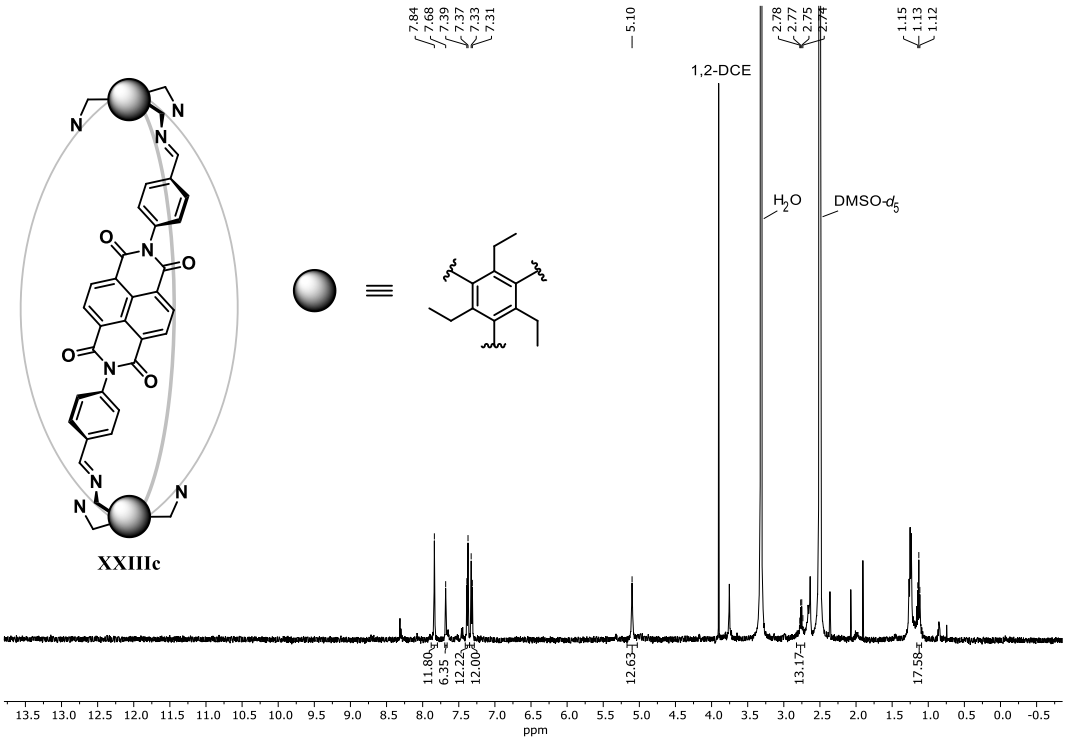

Figure 89: ^{1}H-NMR (500 MHz) spectrum of the reaction mixture for imine cage **XXIIIc** in DMSO-d_6 at 298 K.

2,7-Bis(6-methylpyridin-3-yl)benzo[*lmn*][3,8]phenanthroline-1,3,6,8(2*H*,7*H*)-tetraone (219)

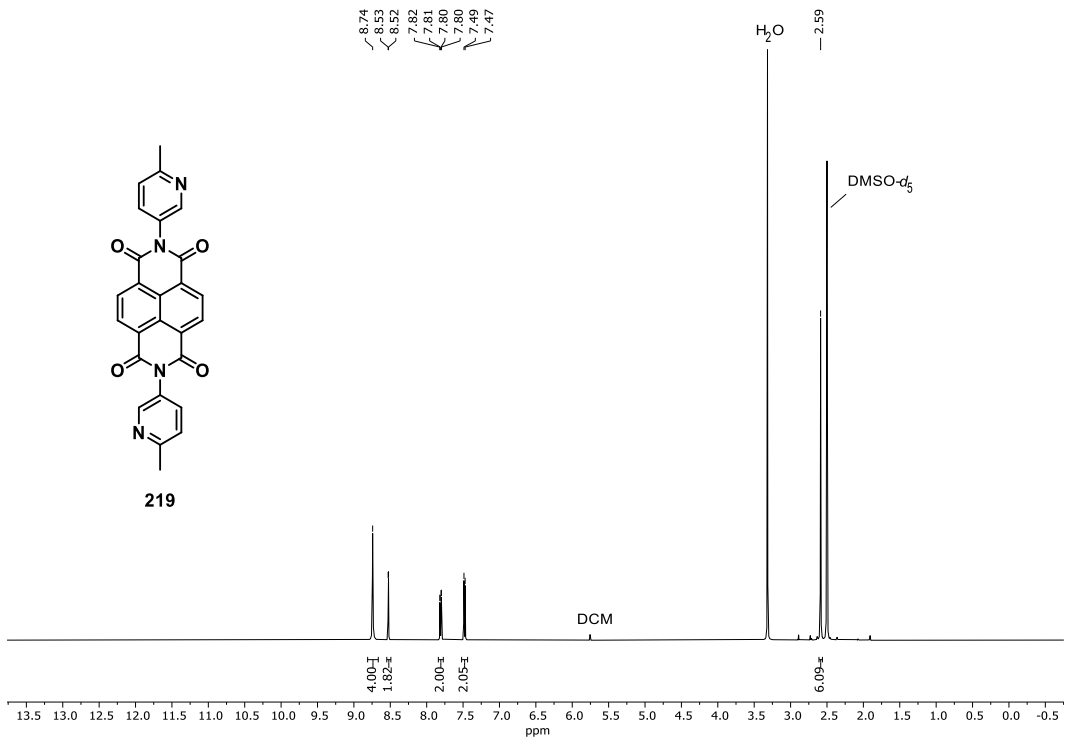

Figure 90: ^{1}H-NMR (500 MHz) spectrum of NDI compound **219** in DMSO-d_6 at 298 K.

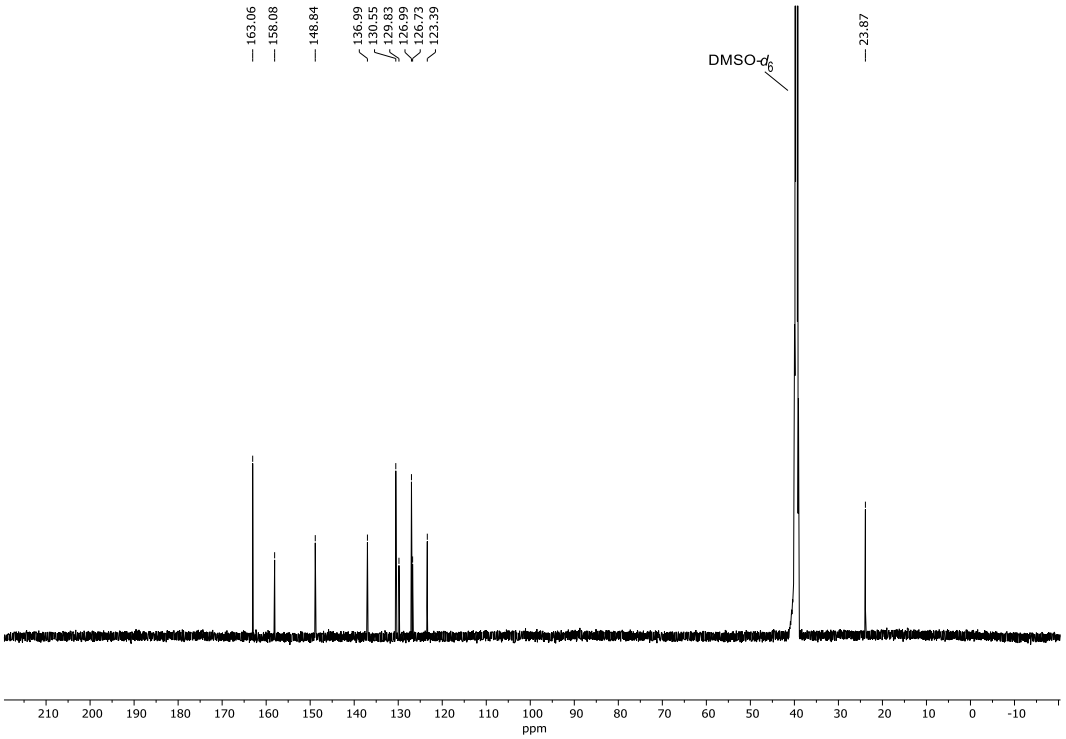

Figure 91: ^{13}C-NMR (151 MHz) spectrum of NDI compound **219** in DMSO-d_6 at 298 K.

5,5'-(1,3,6,8-Tetraoxo-1,3,6,8-tetrahydrobenzo[*lmn*][3,8]phenanthroline-2,7-diyl)dipicolinaldehyde (176)

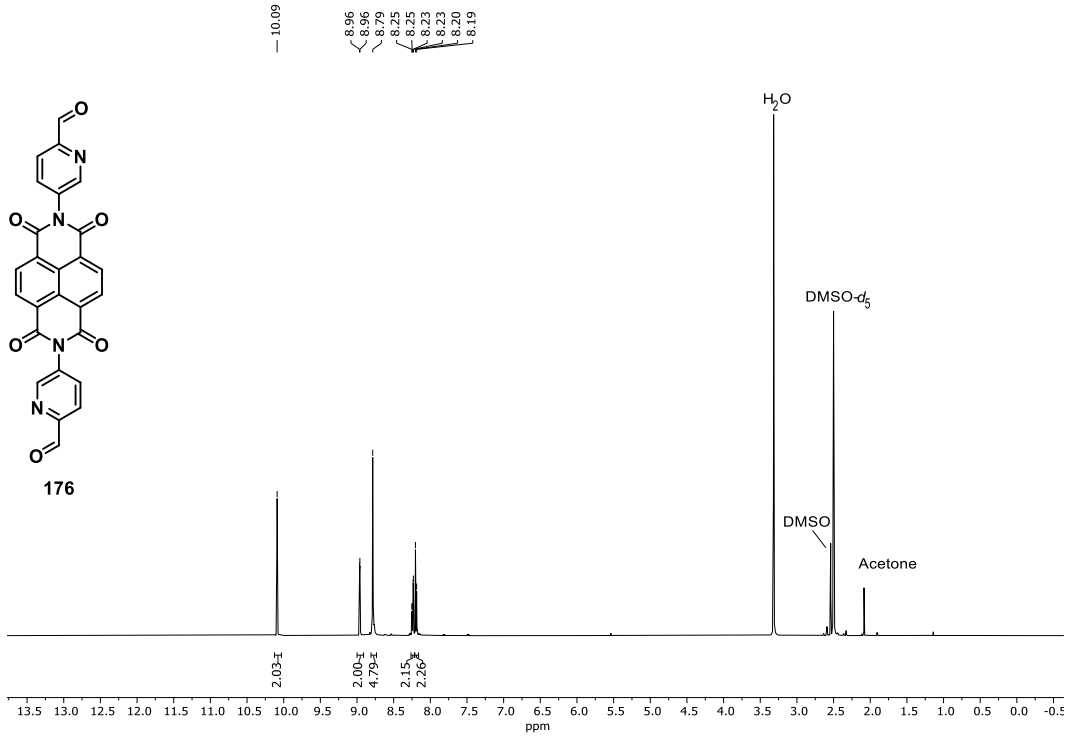

176

Figure 92: ^{1}H-NMR (500 MHz) spectrum of dialdehyde **176** in DMSO-d_6 at 298 K.

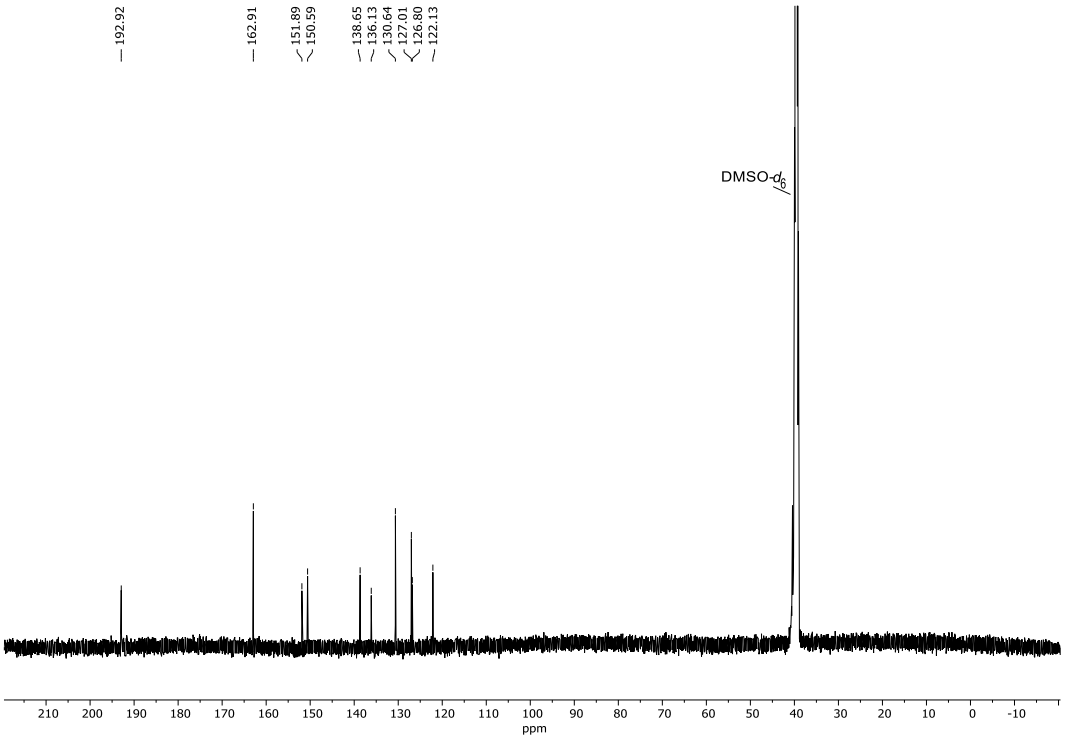

Figure 93: ^{13}C-NMR (151 MHz) spectrum of dialdehyde **176** in DMSO-d_6 at 298 K.

$Zn_2L_3(NTf_2)_4$ Helicate XXXII

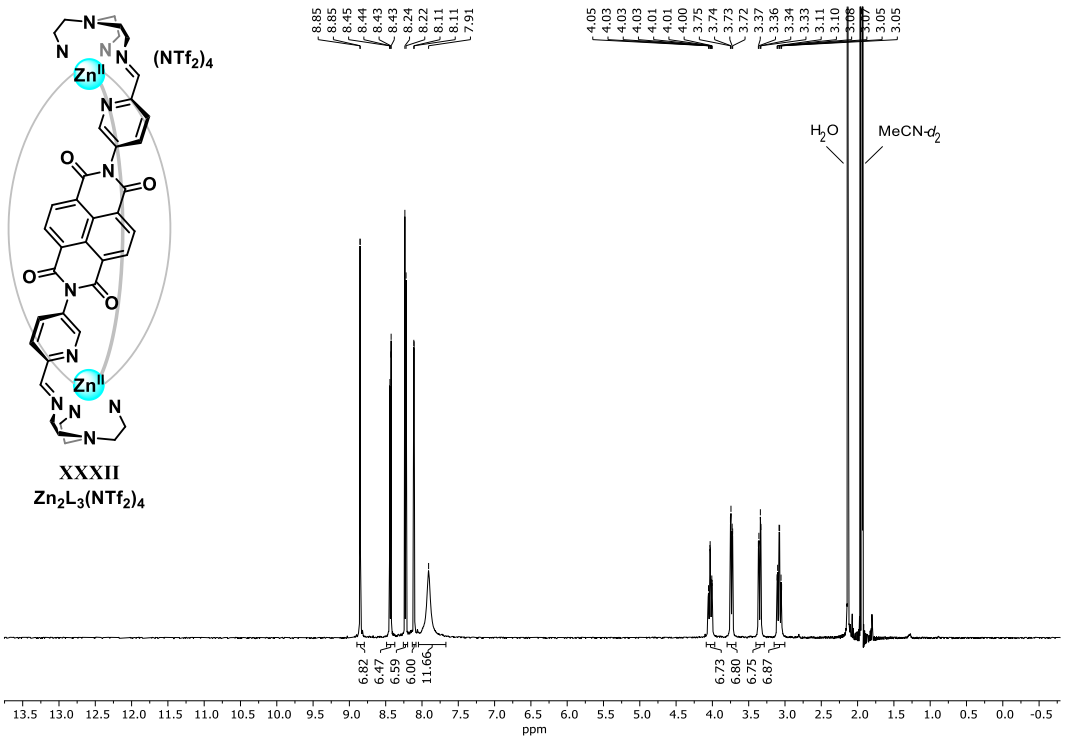

Figure 94: ^{1}H-NMR (500 MHz) spectrum of **$Zn_2L_3(NTf_2)_4$** helicate **XXXII** in MeCN-d_3 at 298 K.

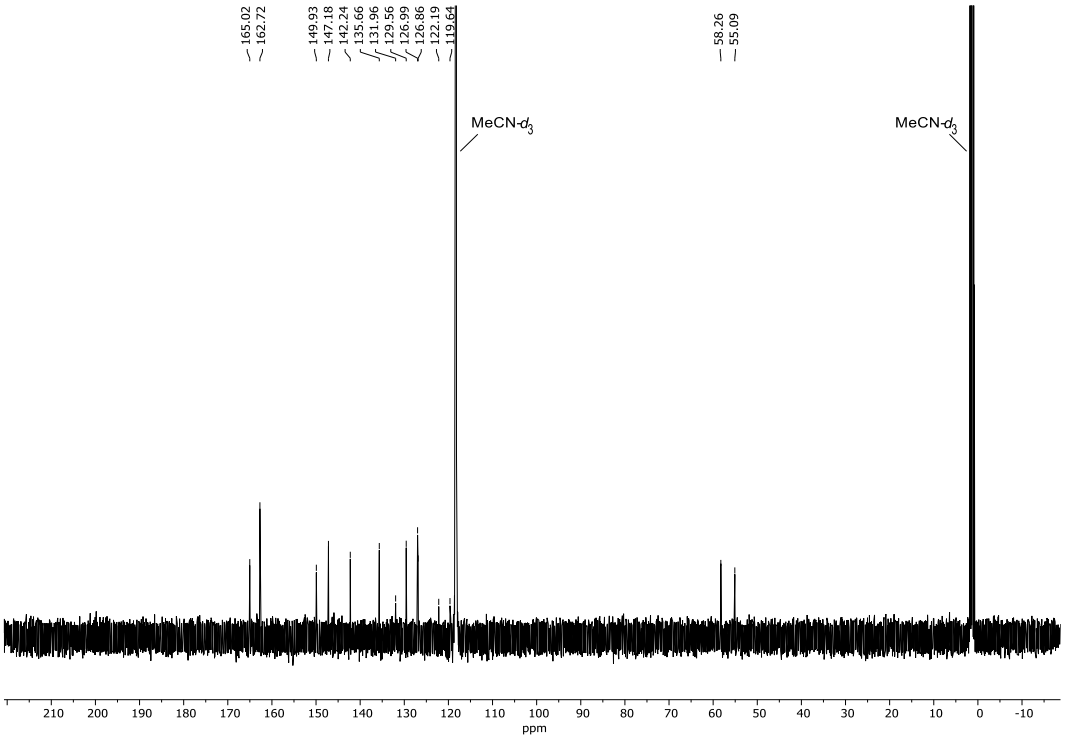

Figure 95: ^{13}C-NMR (126 MHz) spectrum of **$Zn_2L_3(NTf_2)_4$** helicate **XXXII** in MeCN-d_3 at 298 K.

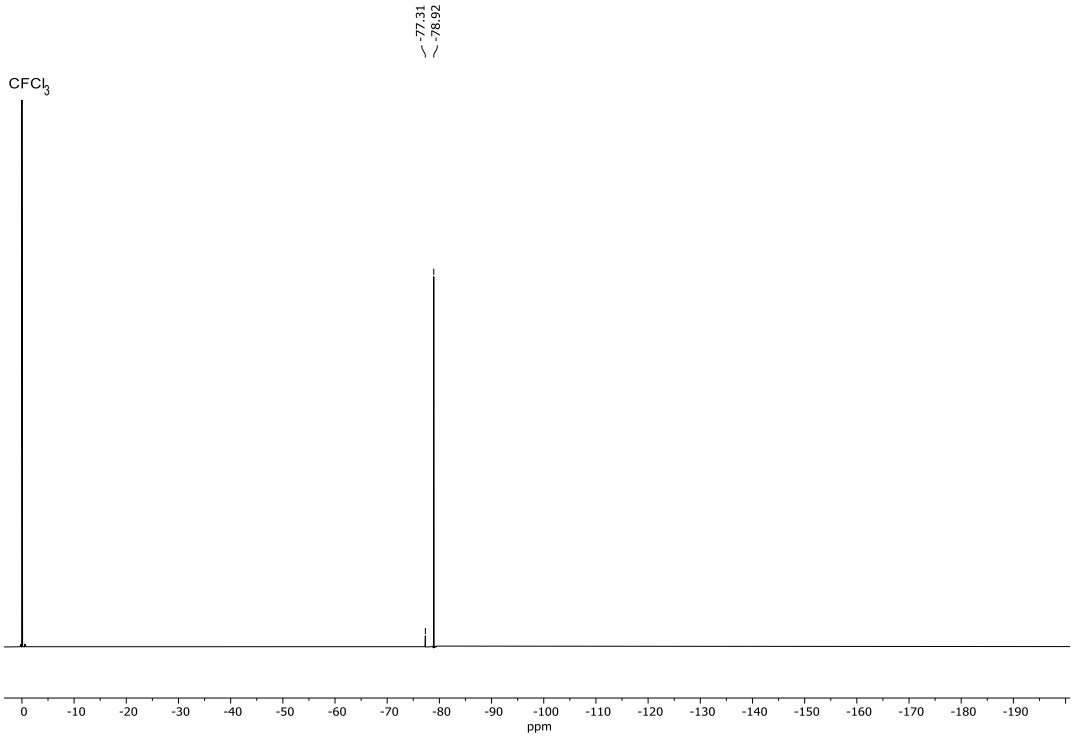

Figure 96: ^{19}F-NMR (471 MHz) spectrum of **$Zn_2L_3(NTf_2)_4$** helicate **XXXII** in MeCN-d_3 at 298 K with $CFCl_3$ as int. Std.

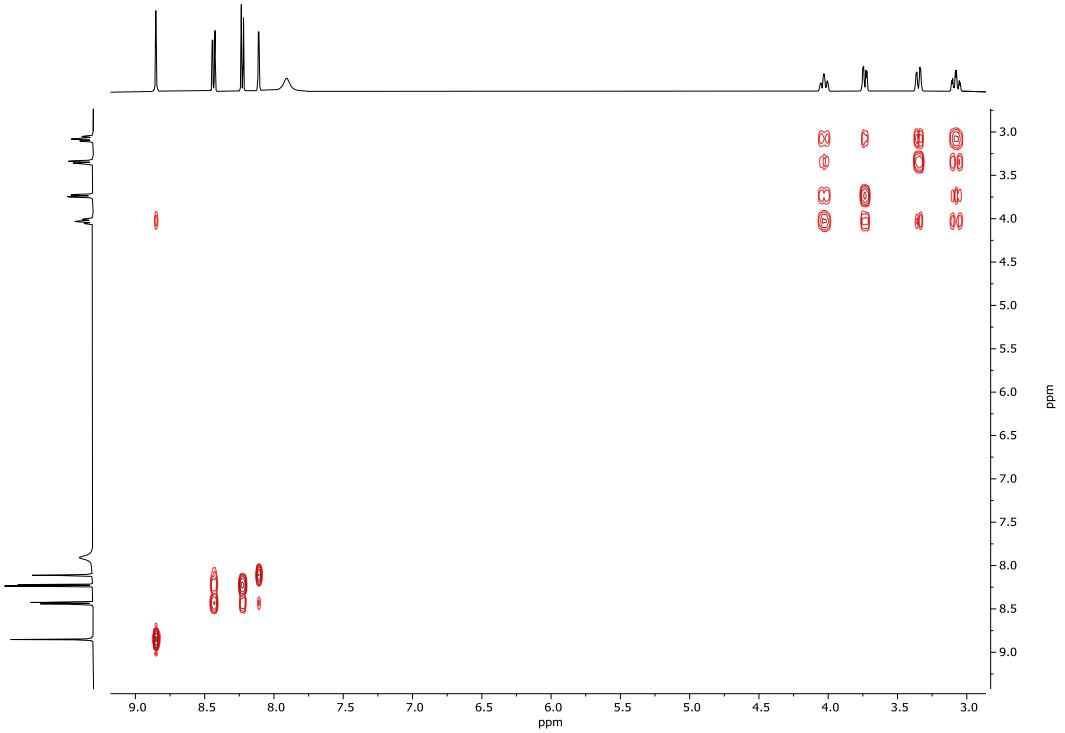

Figure 97: COSY spectrum of **$Zn_2L_3(NTf_2)_4$** helicate **XXXII** in MeCN-d_3 at 298 K.

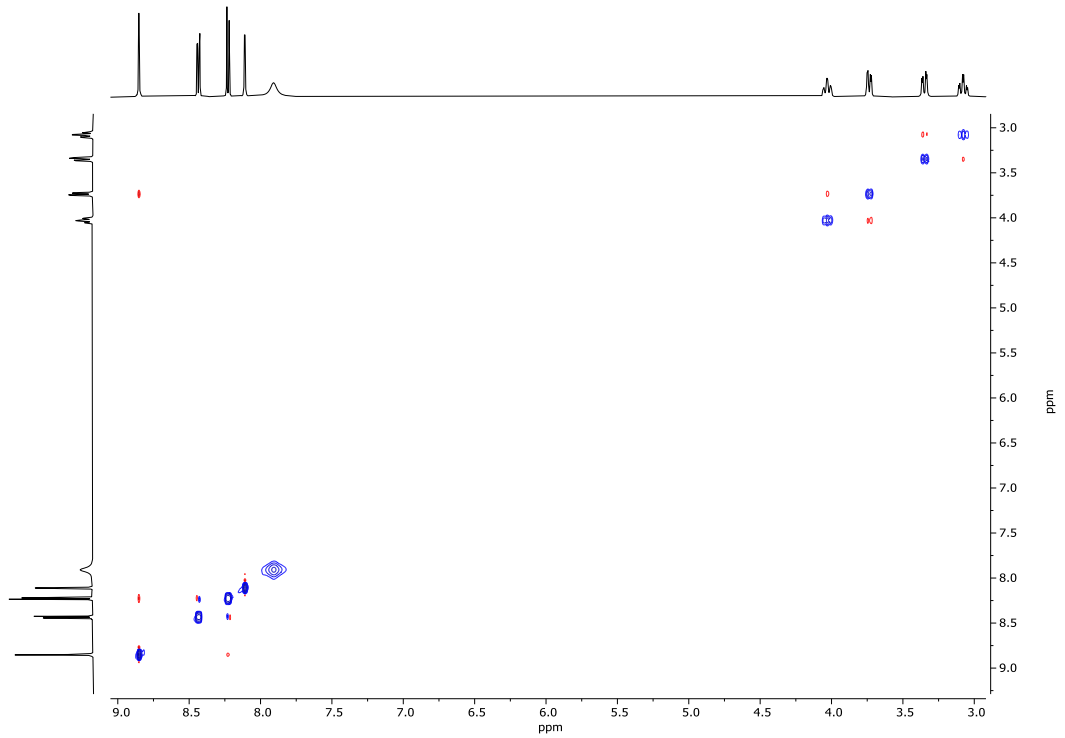

Figure 98: NOESY spectrum of **$Zn_2L_3(NTf_2)_4$** helicate **XXXII** in MeCN-d_3 at 298 K.

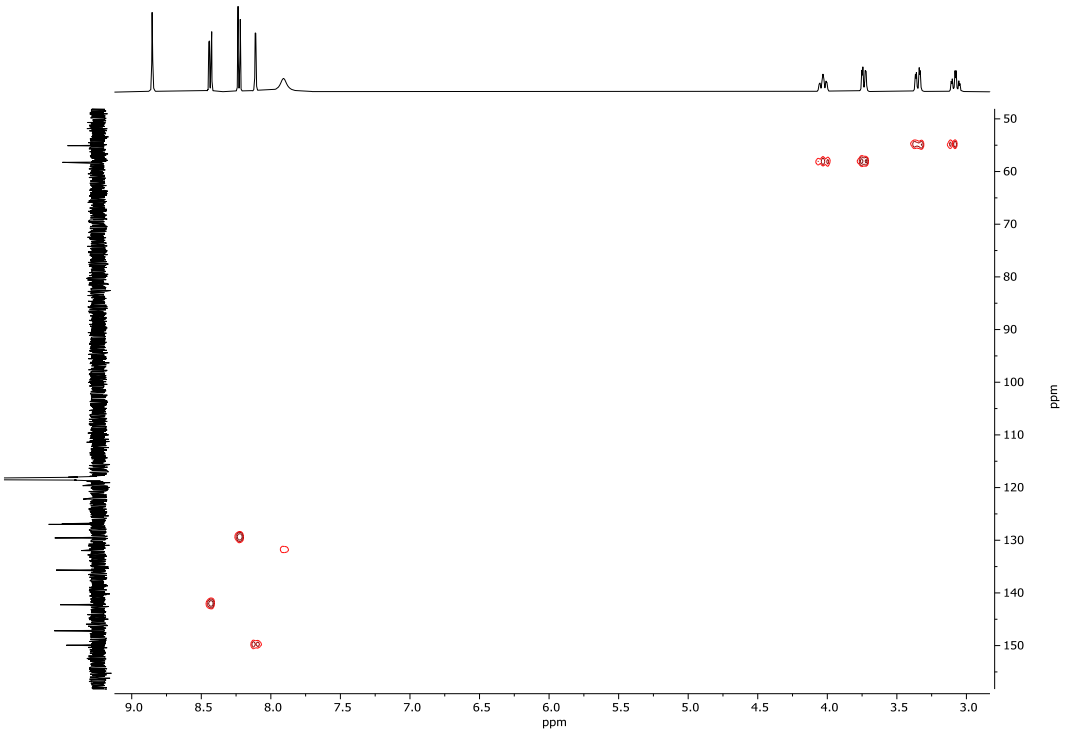

Figure 99: HMQC spectrum of **$Zn_2L_3(NTf_2)_4$** helicate **XXXII** in MeCN-d_3 at 298 K.

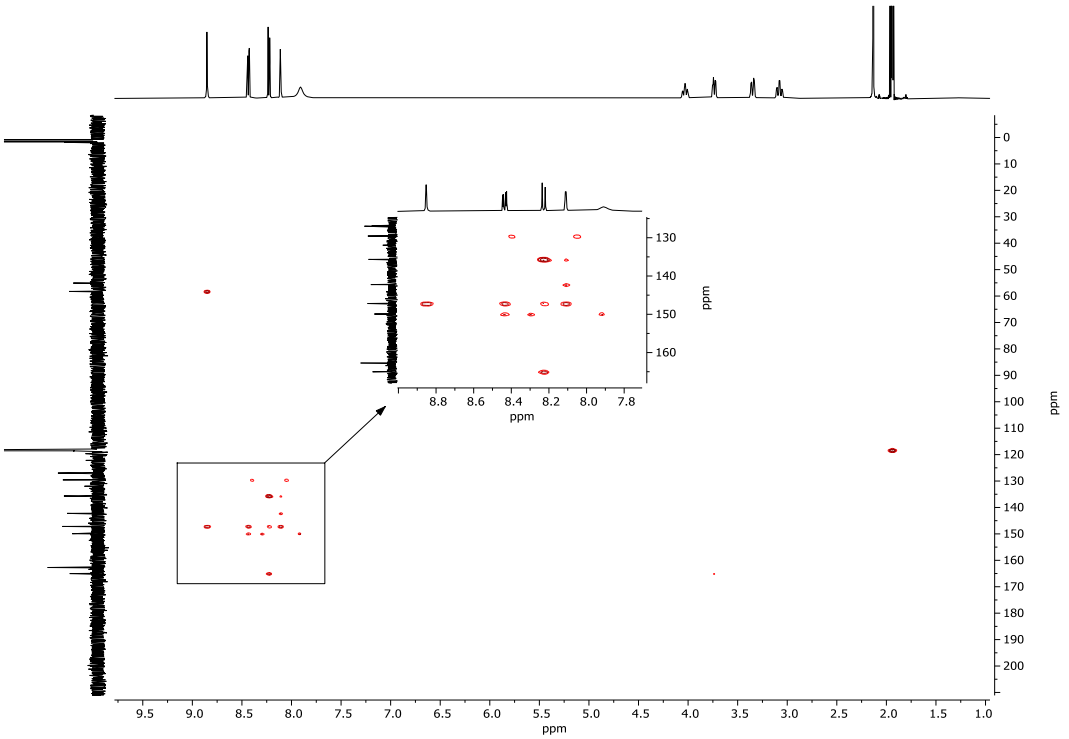

Figure 100: HMBC spectrum of **$Zn_2L_3(NTf_2)_4$** helicate **XXXII** in MeCN-d_3 at 298 K.

2-((6-Methylpyridin-3-yl)carbamoyl)benzoic acid (227)

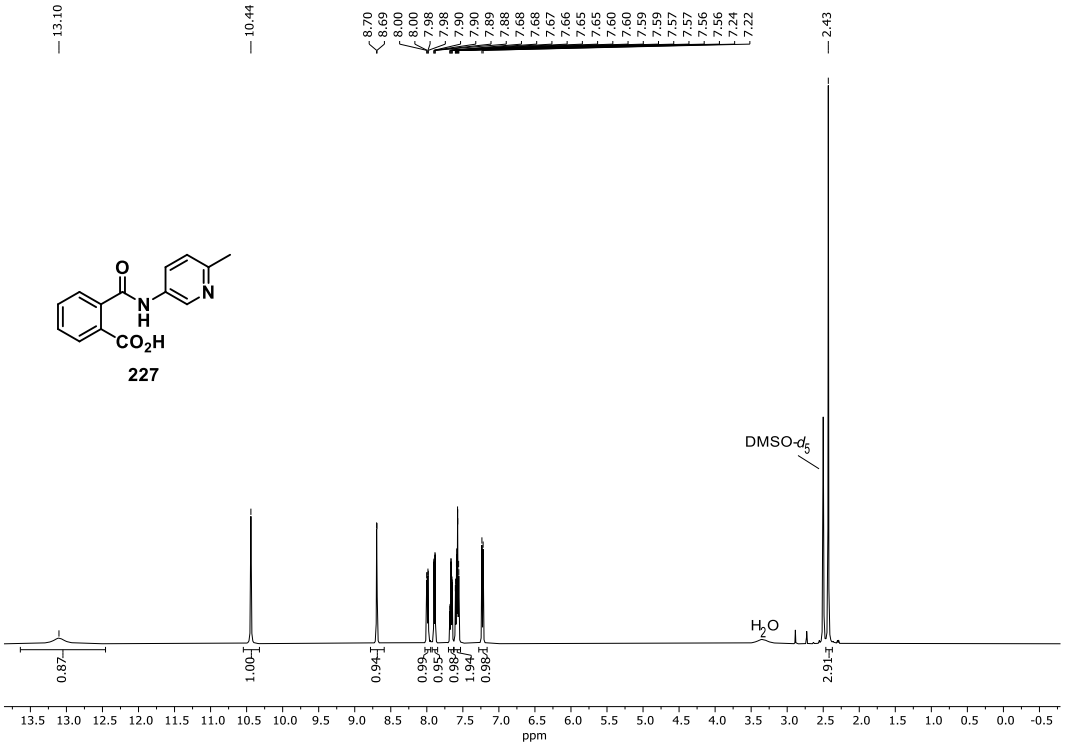

Figure 101: ^{1}H-NMR (500 MHz) spectrum of amide **227** in DMSO-d_6 at 298 K.

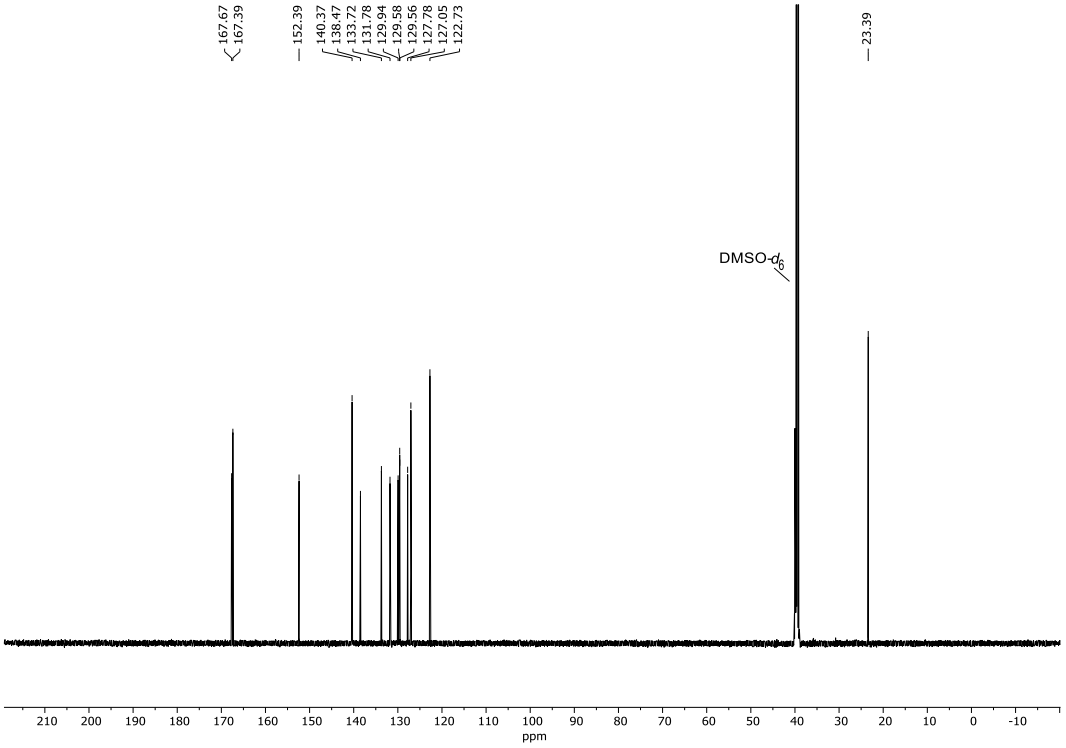

Figure 102: ^{13}C-NMR (126 MHz) spectrum of amide **227** in DMSO-d_6 at 298 K.

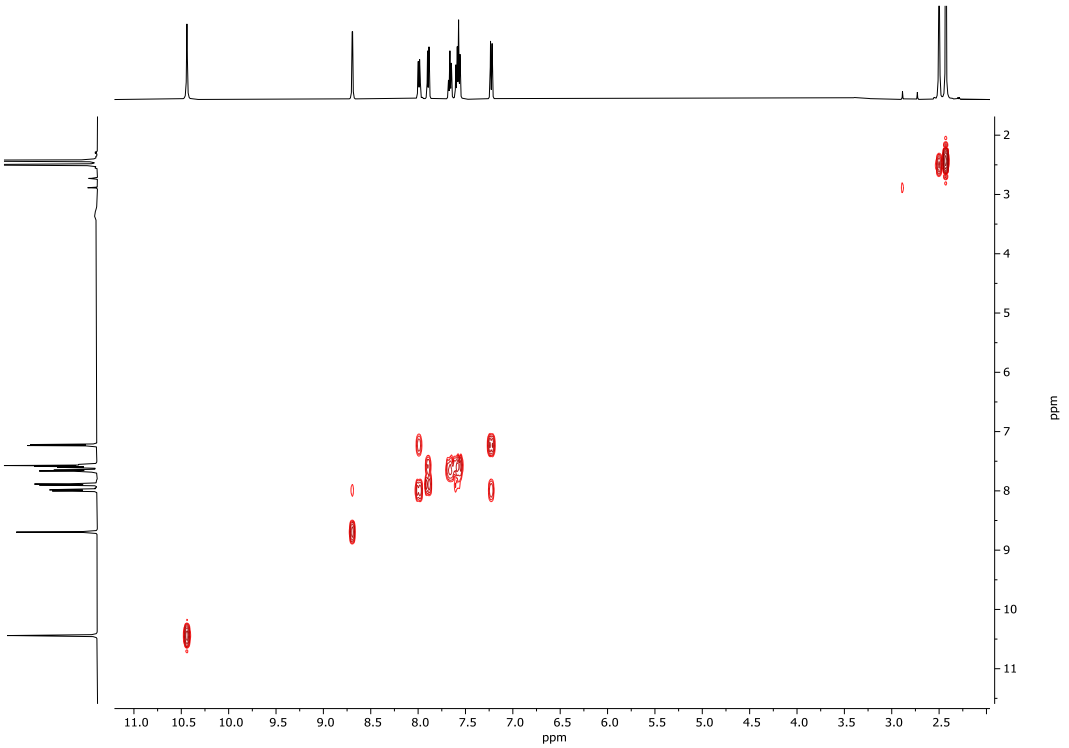

Figure 103: COSY spectrum of amide **227** in DMSO-d_6 at 298 K.

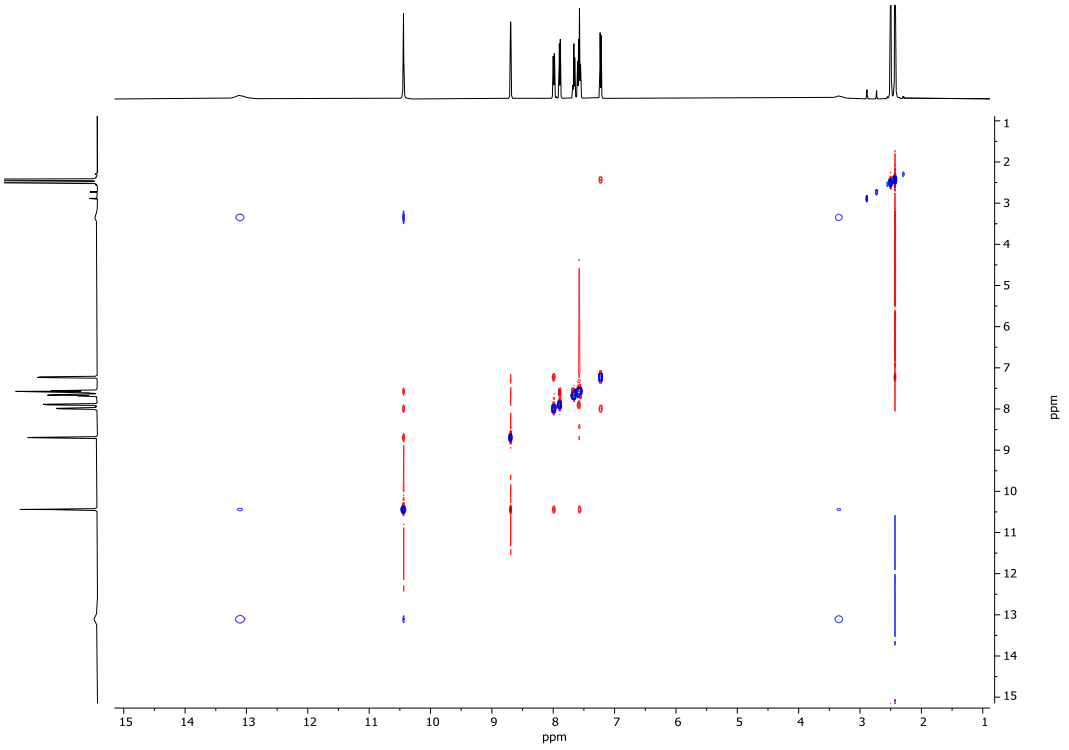

Figure 104: NOESY spectrum of amide **227** in DMSO-d_6 at 298 K.

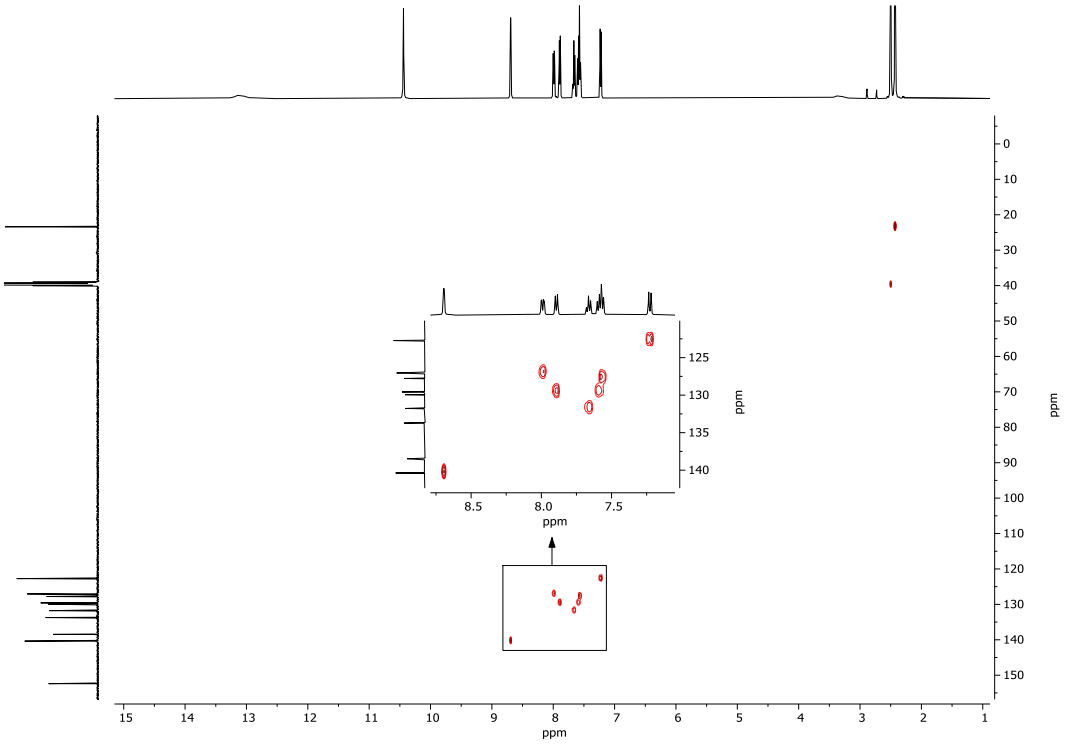

Figure 105: HMQC spectrum of amide **227** in DMSO-d_6 at 298 K.

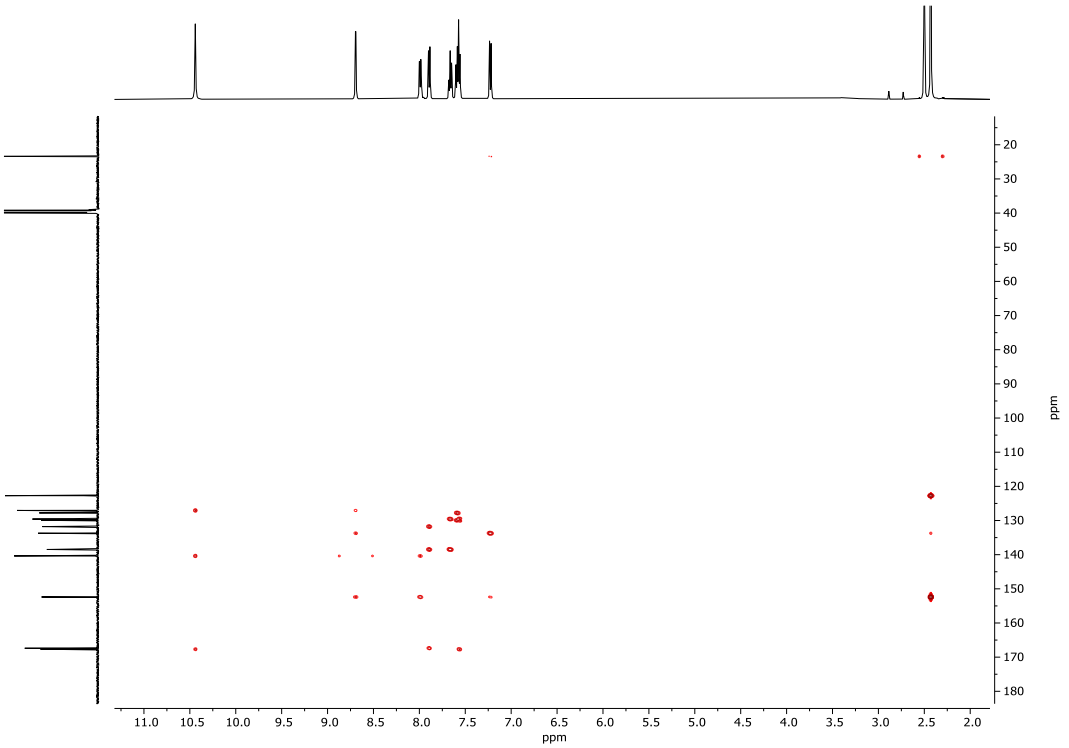

Figure 106: HMBC spectrum of amide **227** in DMSO-d_6 at 298 K.

2-(6-Methylpyridin-3-yl)isoindoline-1,3-dione (228)

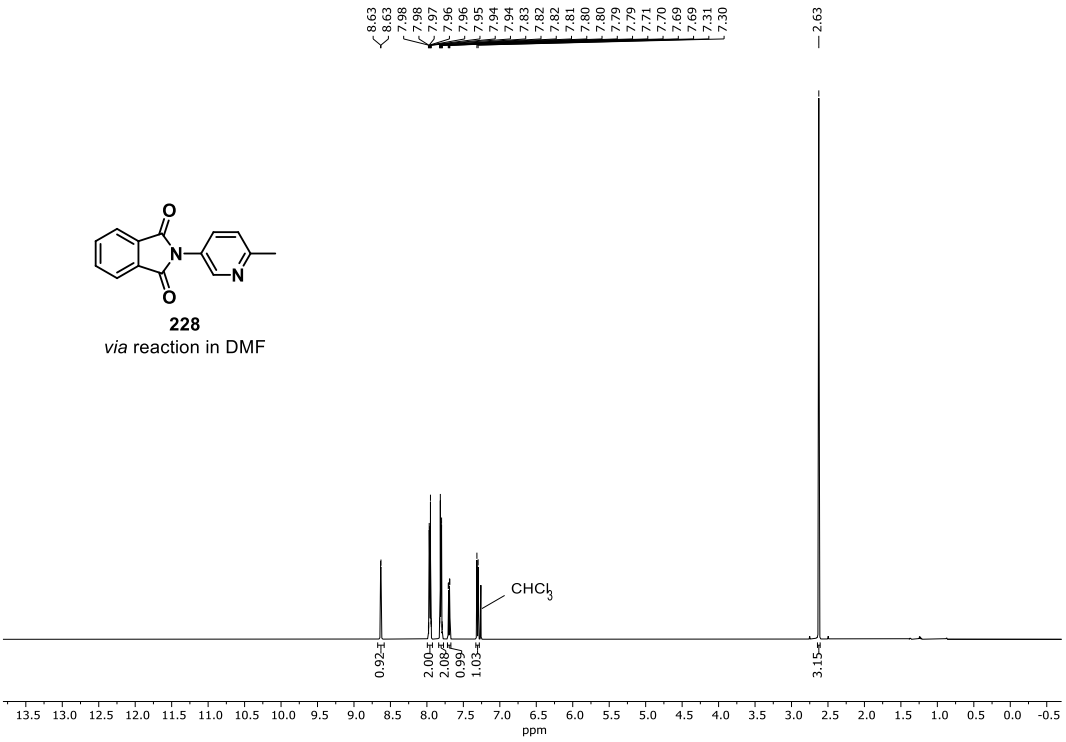

Figure 107: ^{1}H-NMR (500 MHz) spectrum of imide **228** in $CDCl_3$ at 298 K.

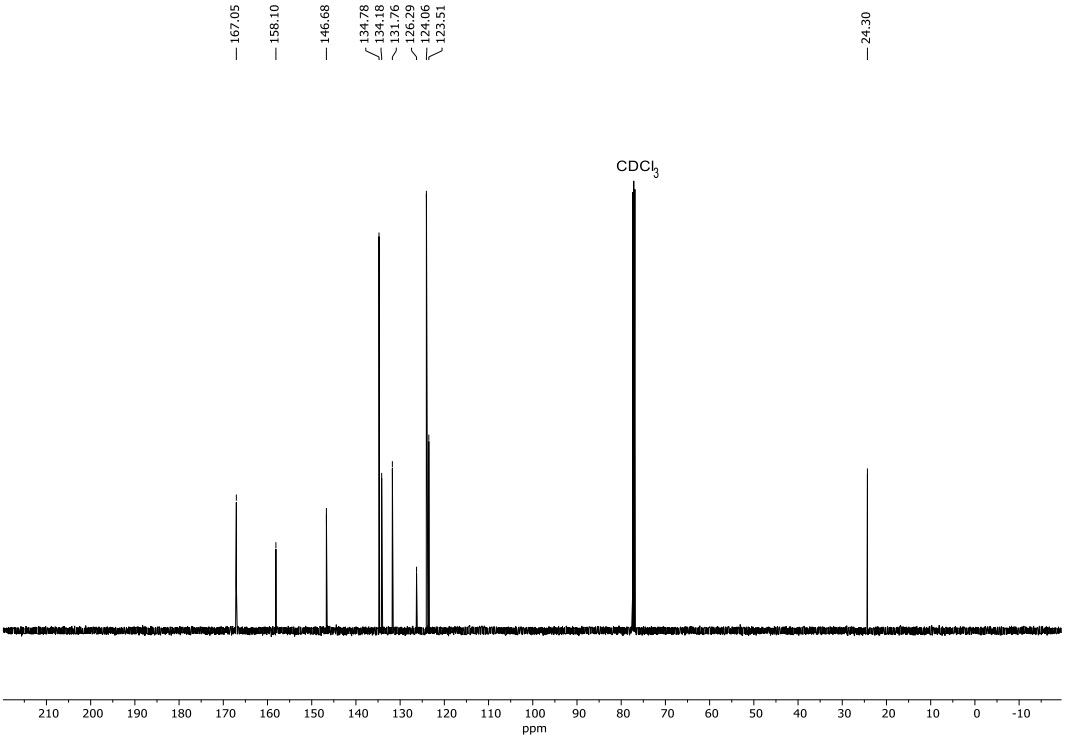

Figure 108: ^{13}C-NMR (126 MHz) spectrum of imide **228** in $CDCl_3$ at 298 K.

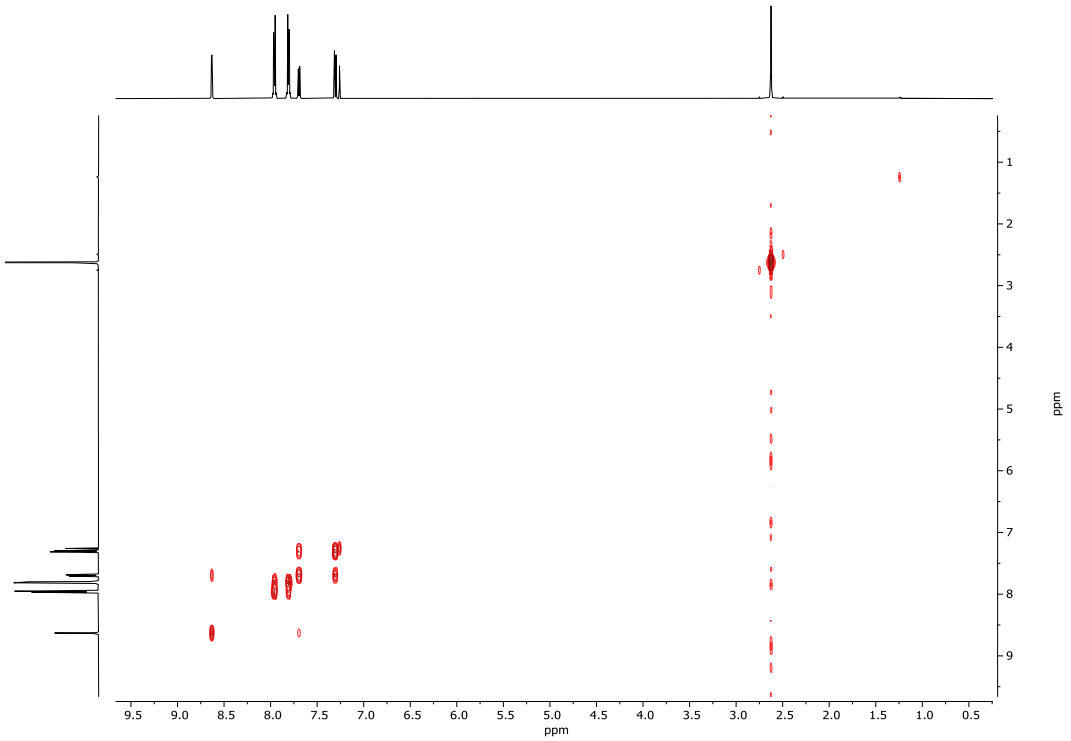

Figure 109: COSY spectrum of imide **228** in $CDCl_3$ at 298 K.

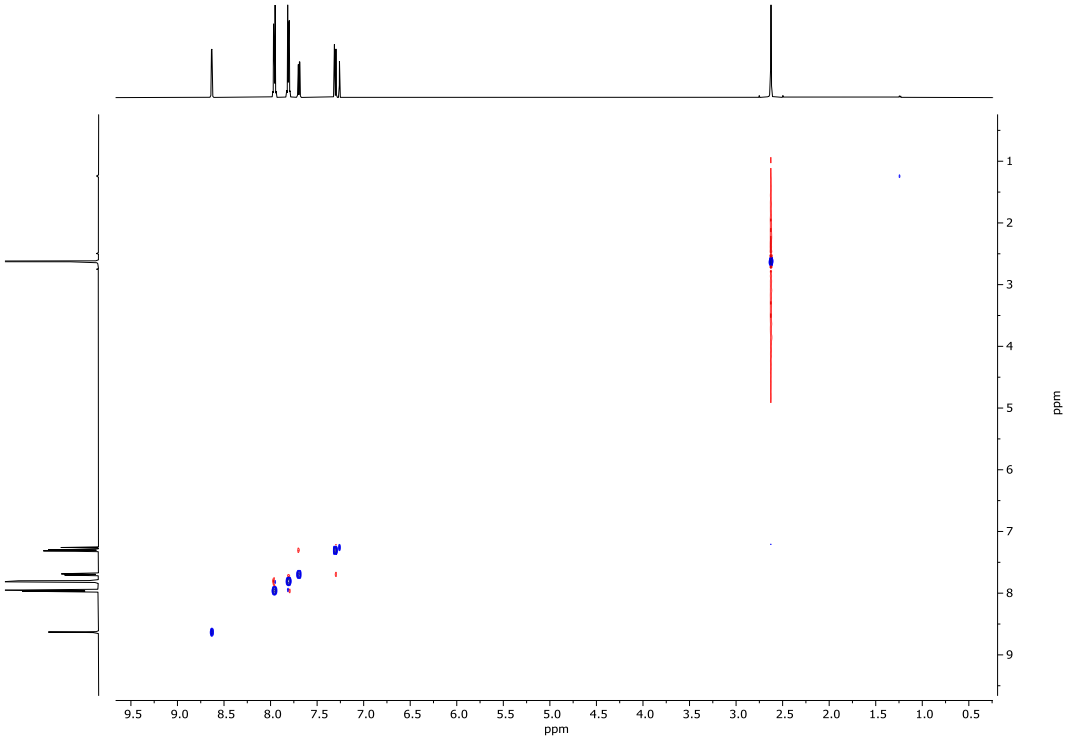

Figure 110: NOESY spectrum of imide **228** in $CDCl_3$ at 298 K.

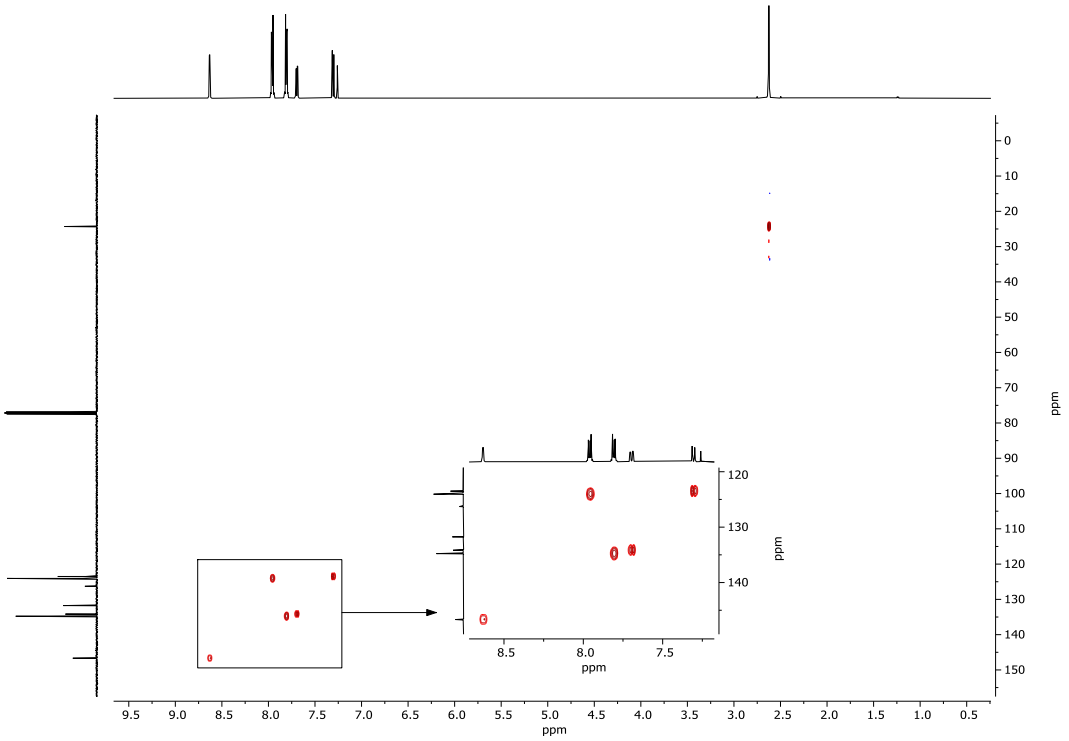

Figure 111: HMQC spectrum of imide **228** in $CDCl_3$ at 298 K.

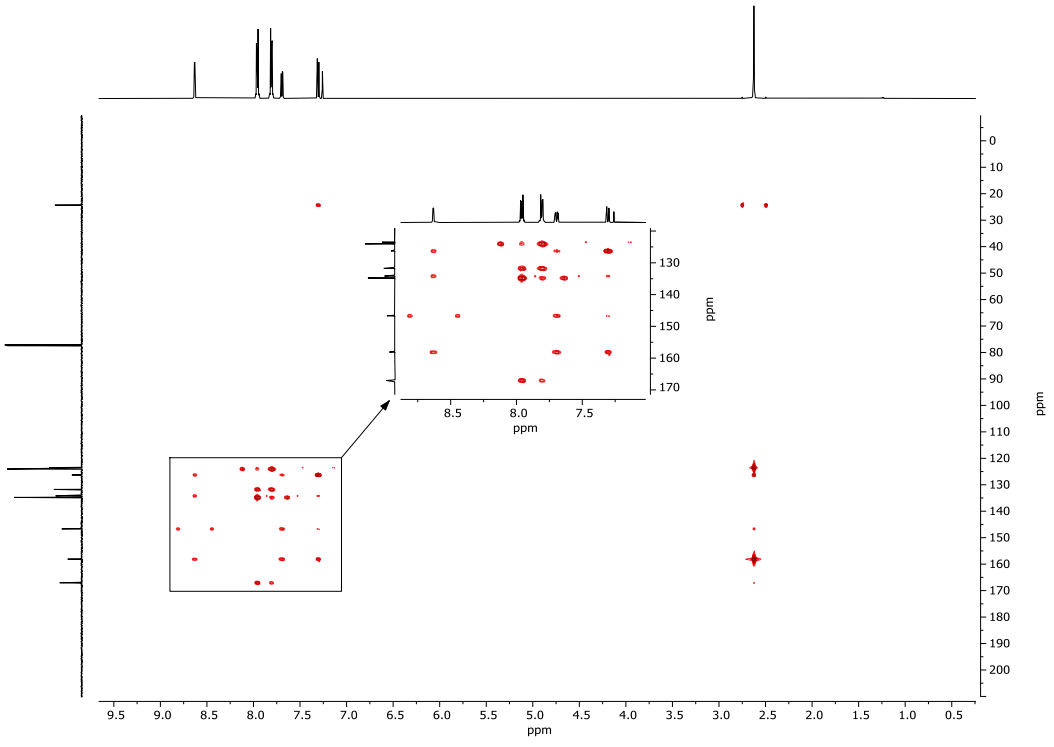

Figure 112: HMBC spectrum of imide **228** in $CDCl_3$ at 298 K.

2-(6-Methylpyridin-3-yl)isoindoline-1,3-dione (228)

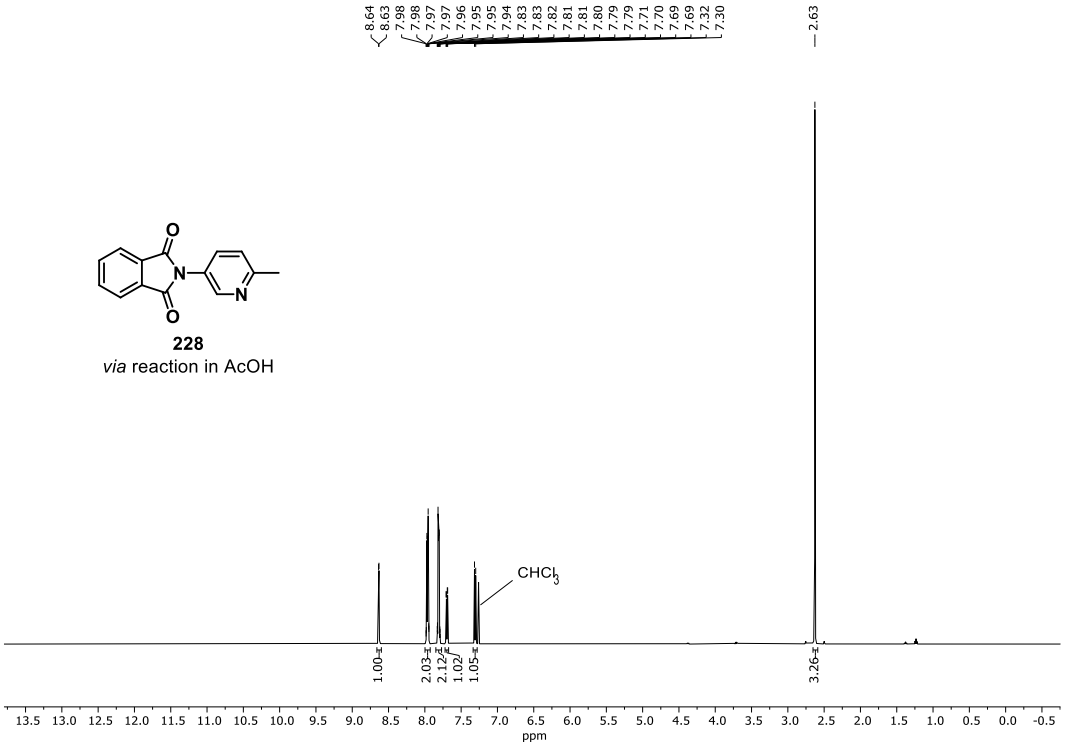

Figure 113: ^{1}H-NMR (500 MHz) spectrum of imide **228** in $CDCl_3$ at 298 K.

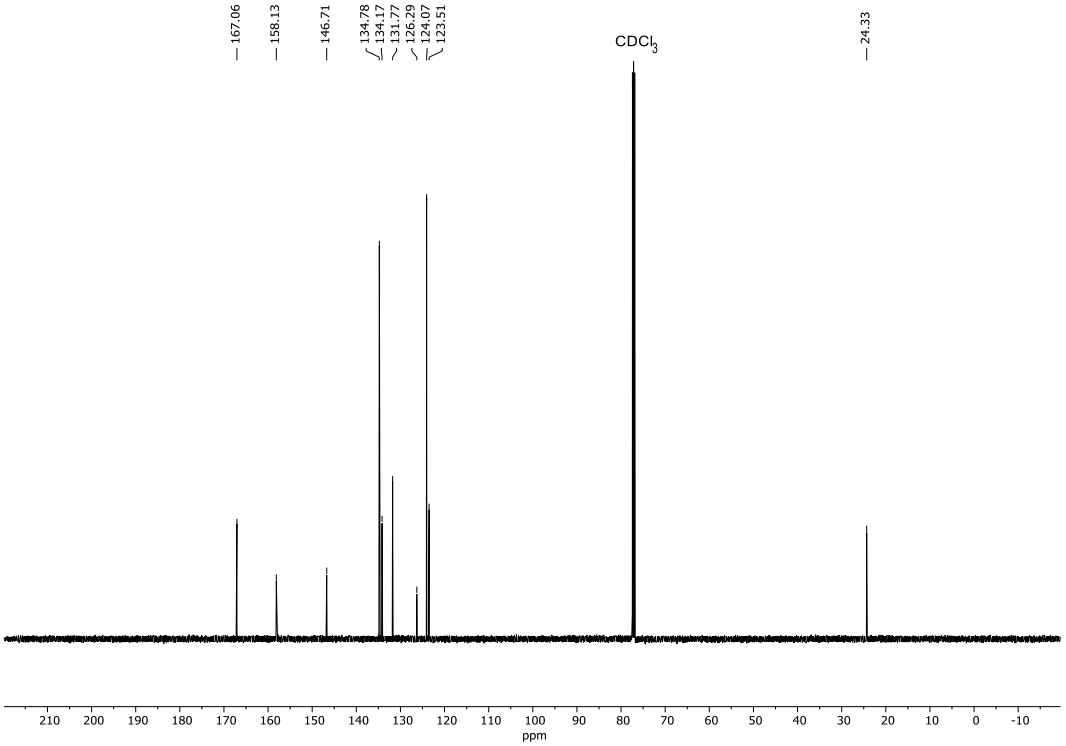

Figure 114: ^{13}C-NMR (126 MHz) spectrum of imide **228** in $CDCl_3$ at 298 K.

Tri-*tert*-butyl ((((1,3,6,8,11,13-hexaoxo-6,8,11,13-tetrahydro-1*H*-benzo[1,2-*f*:3,4-*f*':5,6-*f*'']triisoindole-2,7,12(3*H*)-triyl)tris(methylene))tris(benzene-4,1-diyl))tris(methylene))tricarbamate (242)

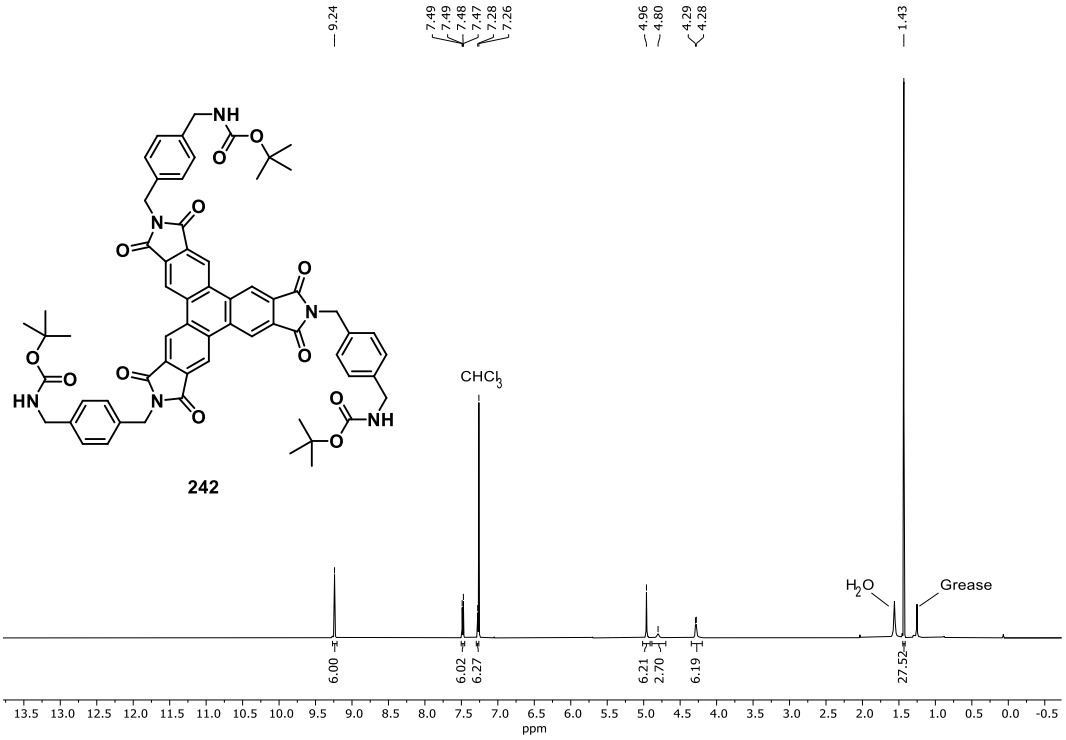

Figure 115: ^{1}H-NMR (500 MHz) spectrum of TPTI **242** in $CDCl_3$ at 298 K.

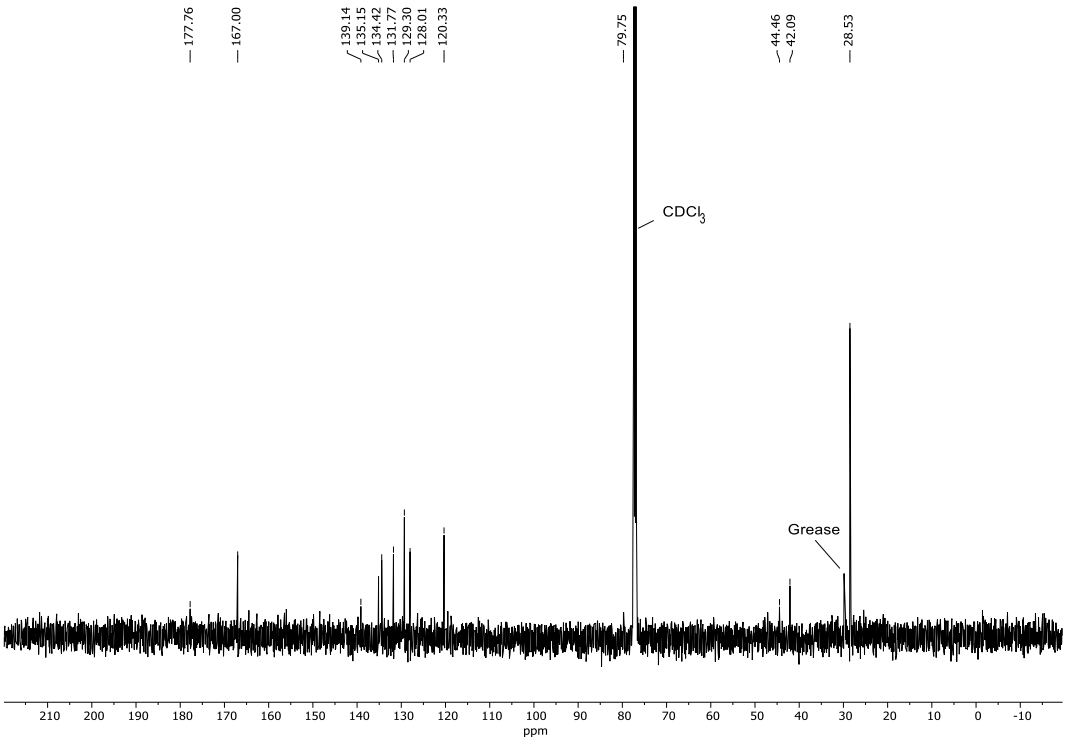

Figure 116: ^{13}C-NMR (126 MHz) spectrum of TPTI **242** in $CDCl_3$ at 298 K.

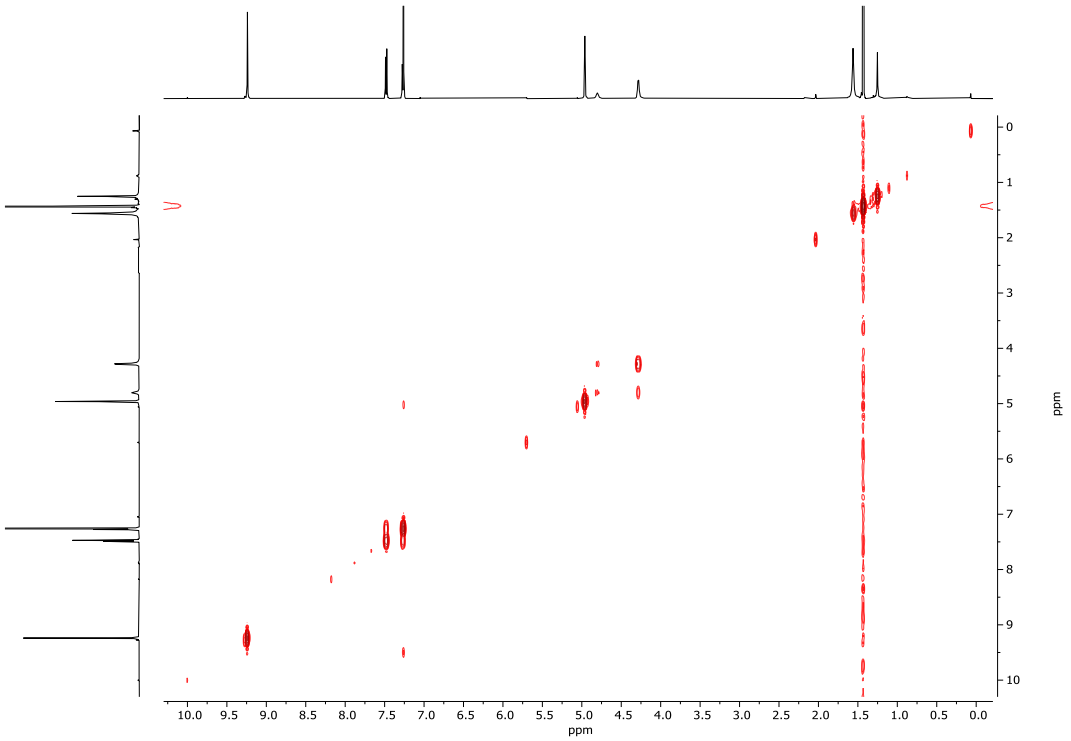

Figure 117: COSY spectrum of TPTI **242** in $CDCl_3$ at 298 K.

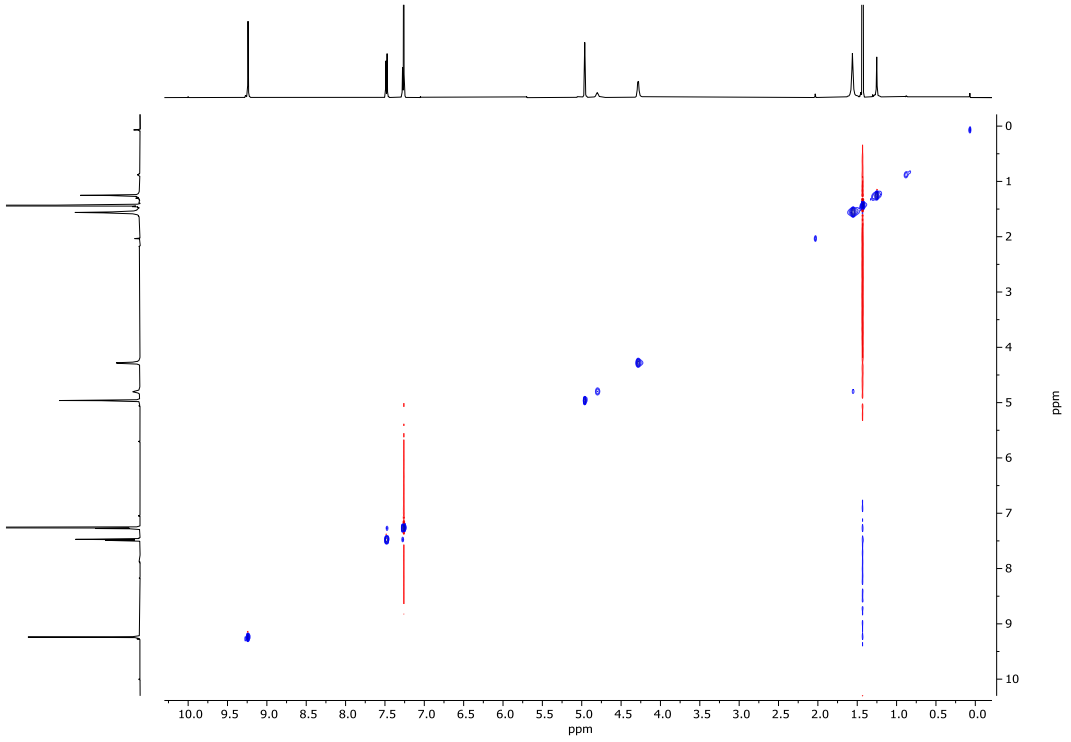

Figure 118: NOESY spectrum of TPTI **242** in $CDCl_3$ at 298 K.

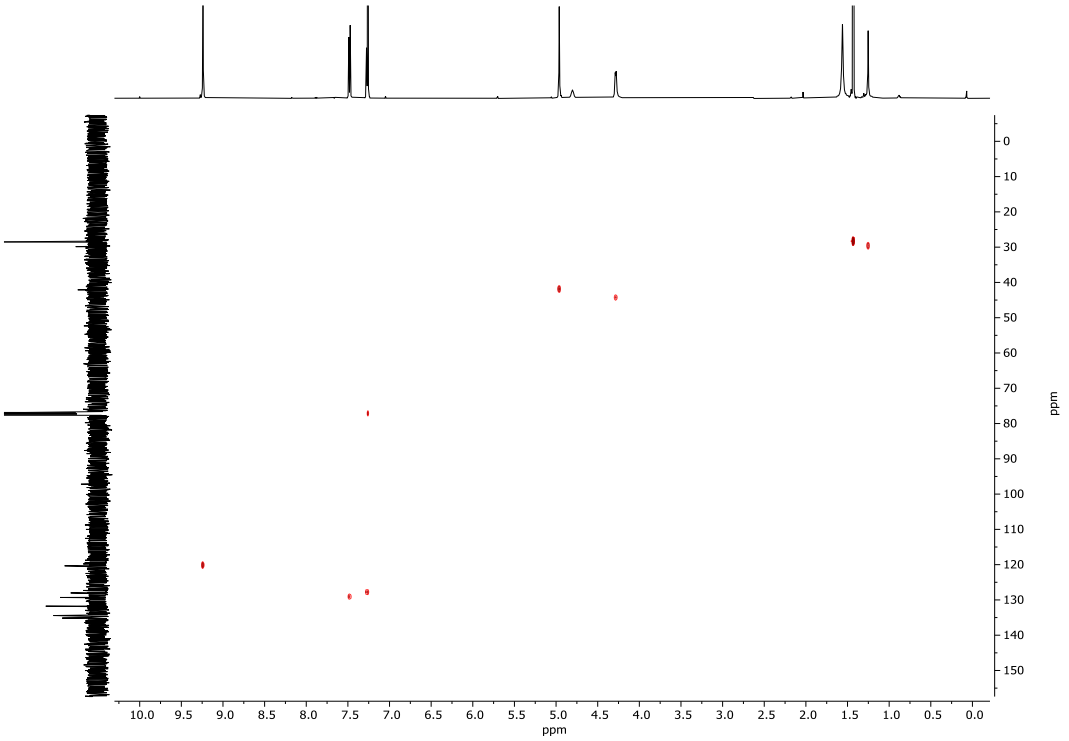

Figure 119: HMQC spectrum of TPTI **242** in $CDCl_3$ at 298 K.

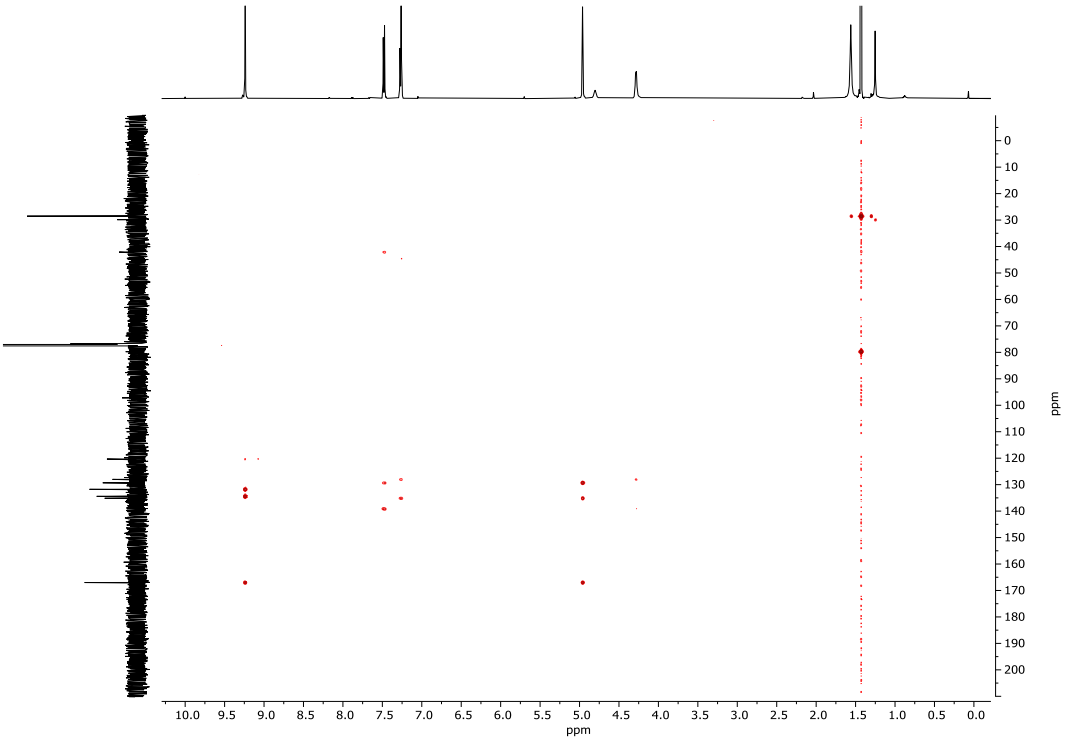

Figure 120: HMBC spectrum of TPTI **242** in $CDCl_3$ at 298 K.

(((1,3,6,8,11,13-Hexaoxo-6,8,11,13-tetrahydro-1*H*-benzo[1,2-*f*:3,4-*f*': 5,6-*f*'']triisoindole-2,7,12(3*H*)-triyl)tris(methylene))tris(benzene-4,1-diyl))trimethan aminium 2,2,2-trifluoro acetate (TPTI 243)

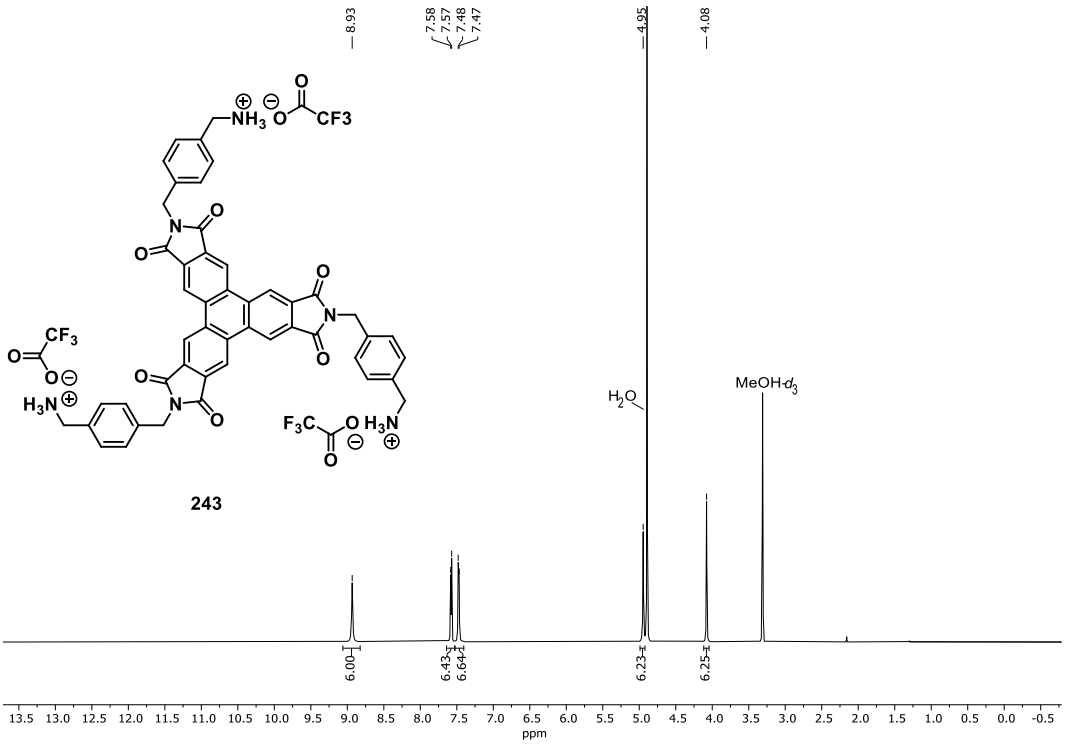

Figure 121: [1]H-NMR (600 MHz) spectrum of TPTI **243** in MeOD-d_4 at 298 K.

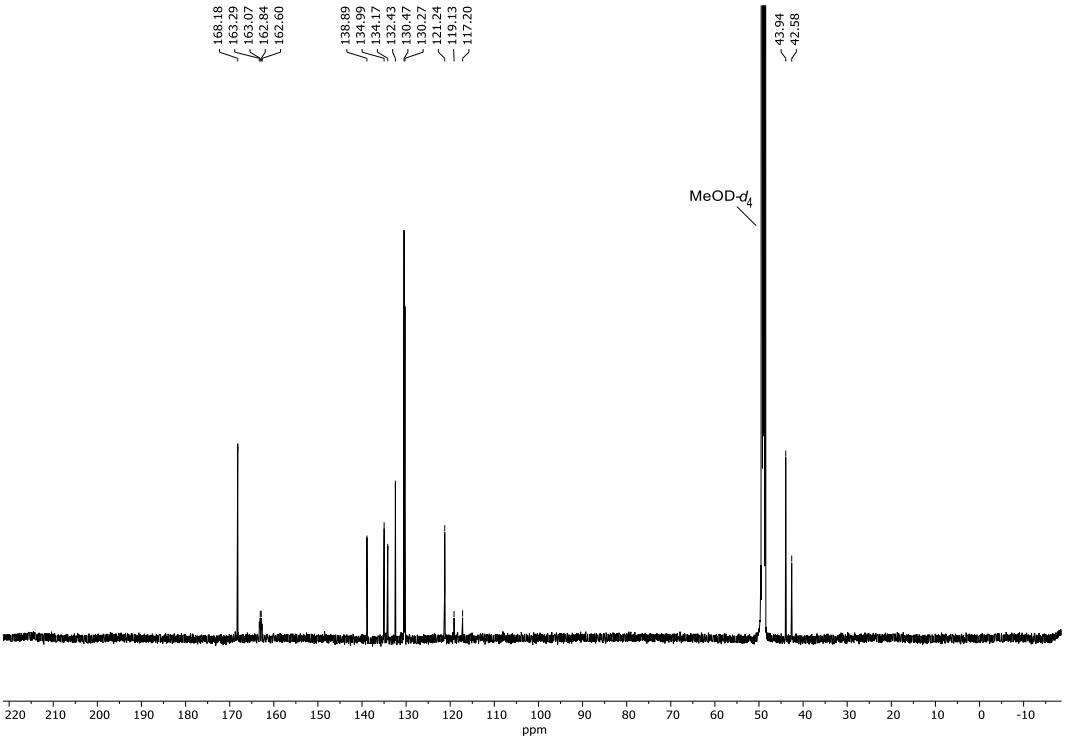

Figure 122: [13]C-NMR (151 MHz) spectrum of TPTI **243** in MeOD-d_4 at 298 K.

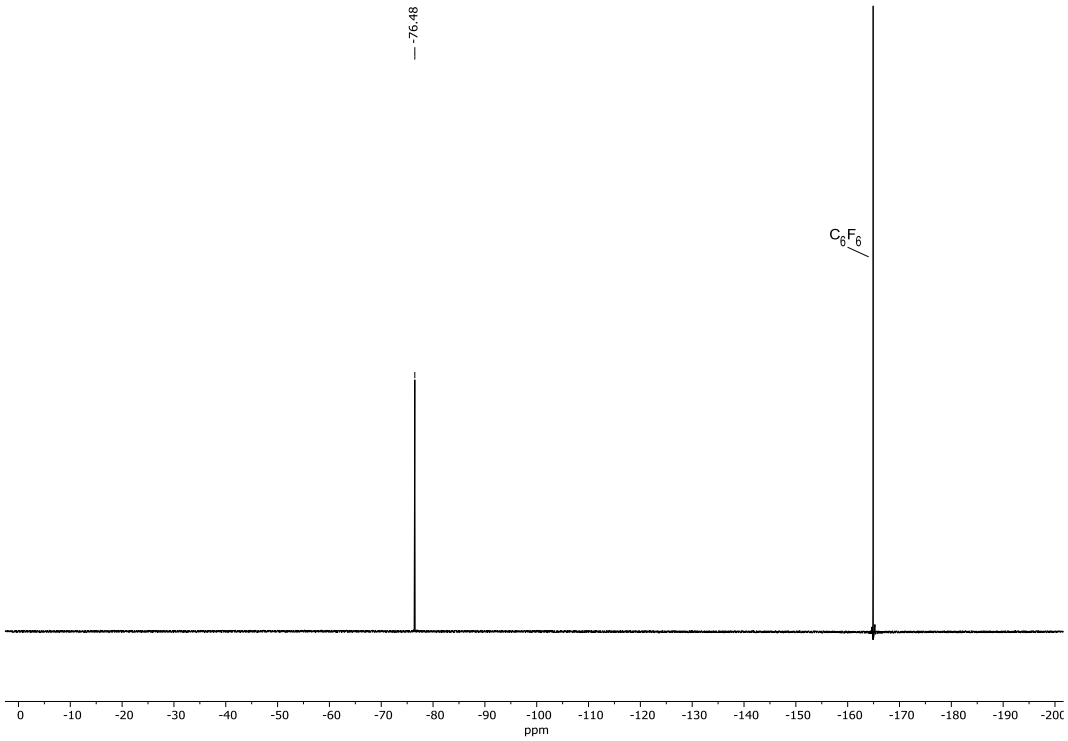

Figure 123: ^{19}F-NMR (471 MHz) spectrum of TPTI **243** in MeOD-d_4 with C_6F_6 as internal Standard at 298 K.

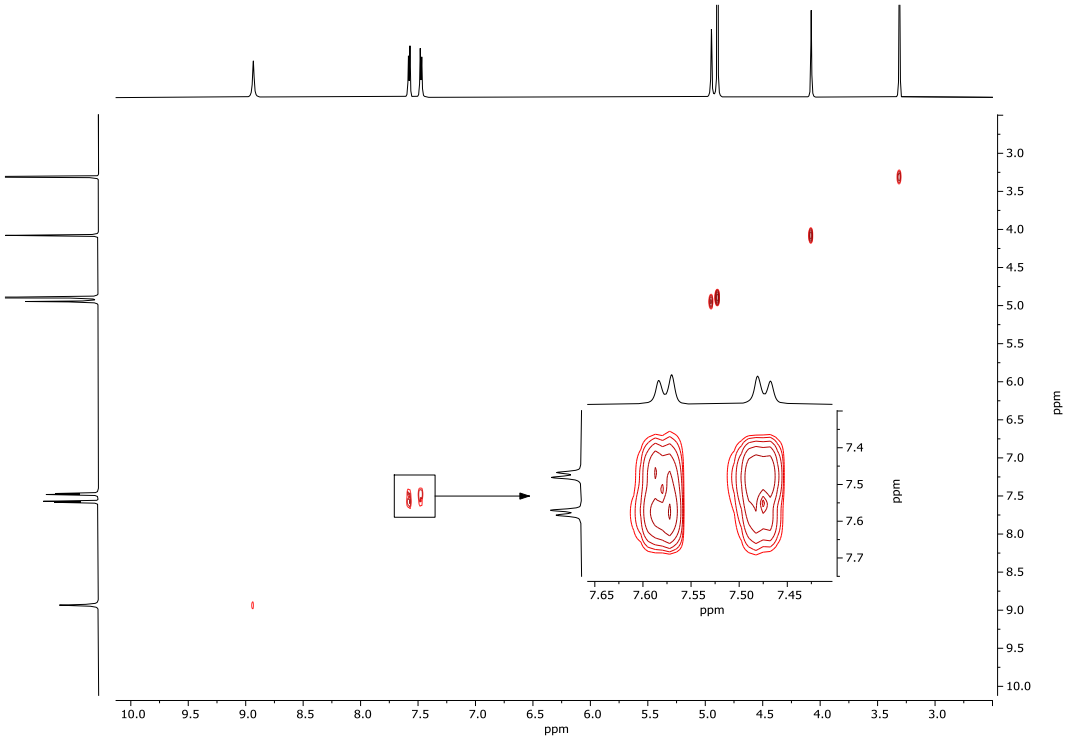

Figure 124: COSY spectrum of TPTI **243** in MeOD-d_4 at 298 K.

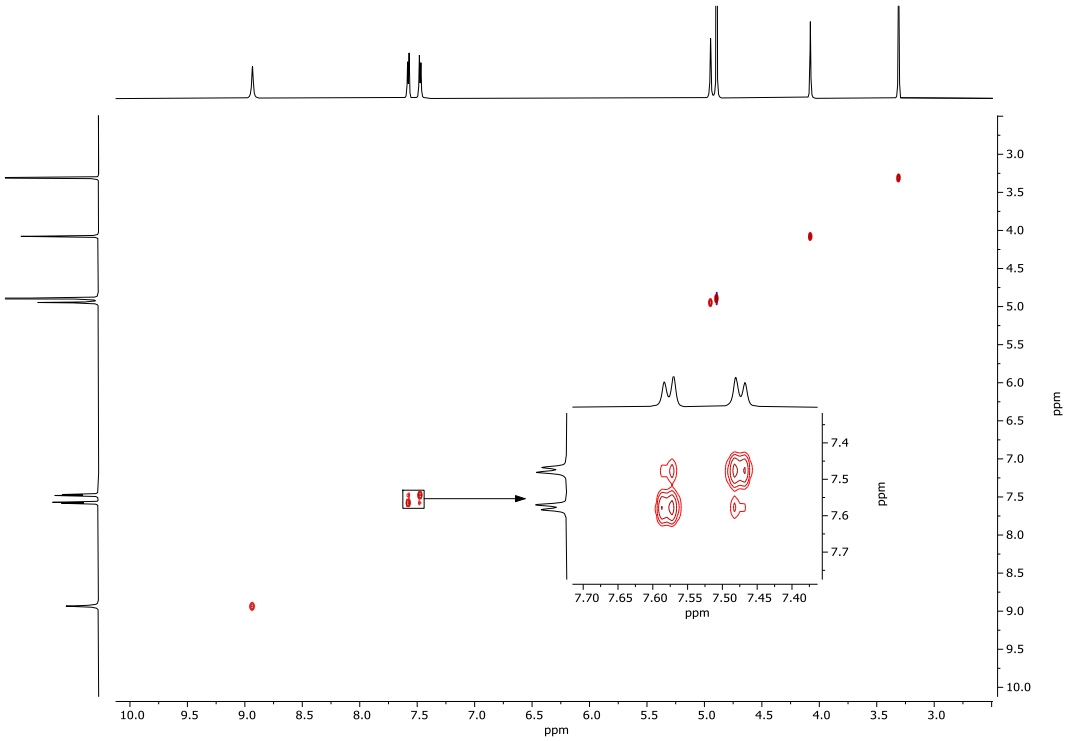

Figure 125: NOESY spectrum of TPTI **243** in MeOD-d_4 at 298 K.

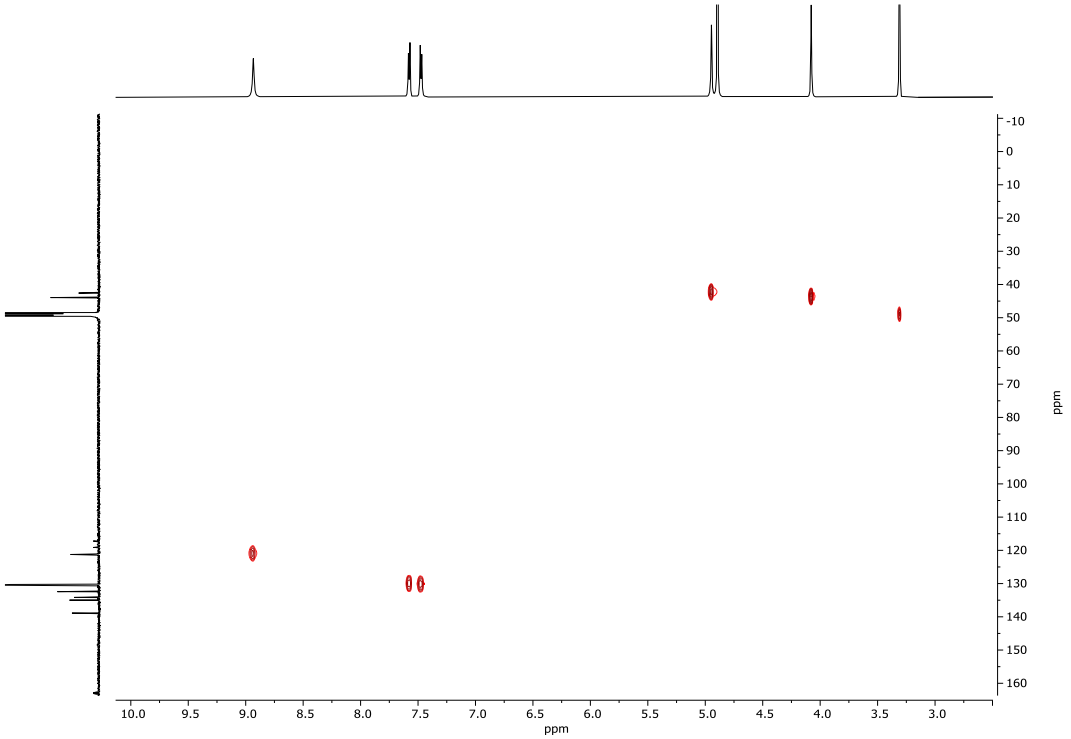

Figure 126: HMQC spectrum of TPTI **243** in MeOD-d_4 at 298 K.

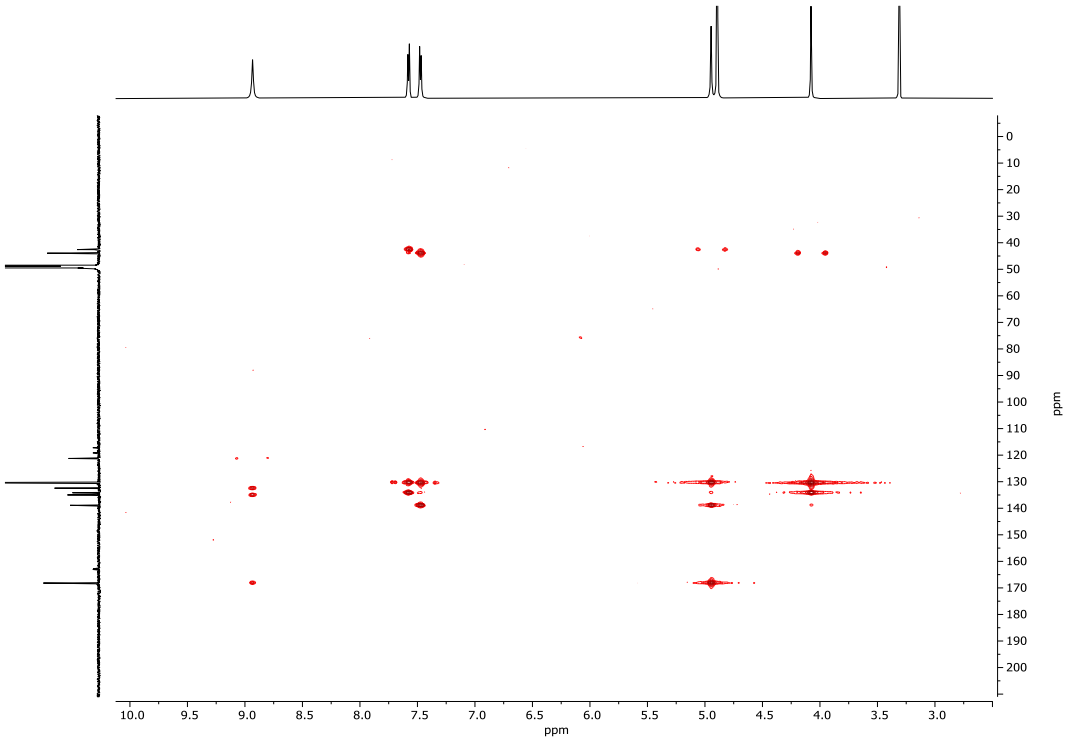

Figure 127: HMBC spectrum of TPTI **243** in MeOD-d_4 at 298 K.

5,5',5''-(Benzene-1,3,5-triyltris(ethyne-2,1-diyl))tripicolinaldehyde (178)

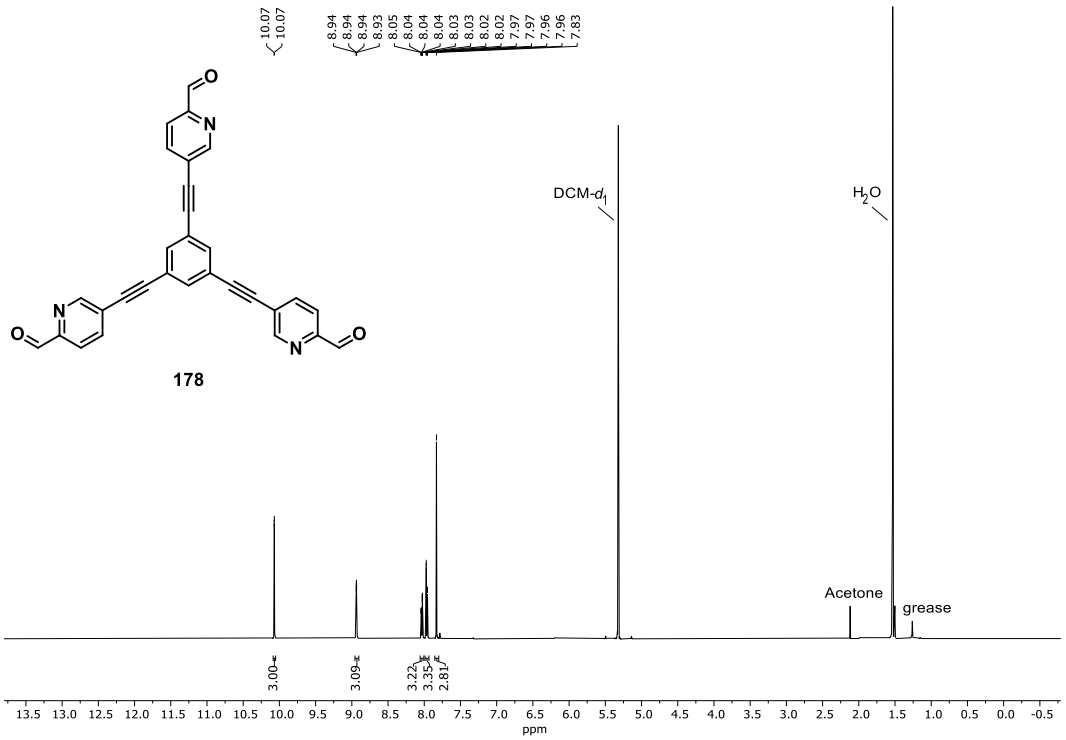

Figure 128: [1]H-NMR (500 MHz) spectrum of trialdehlyde **178** in DCM-d_2 at 298 K.

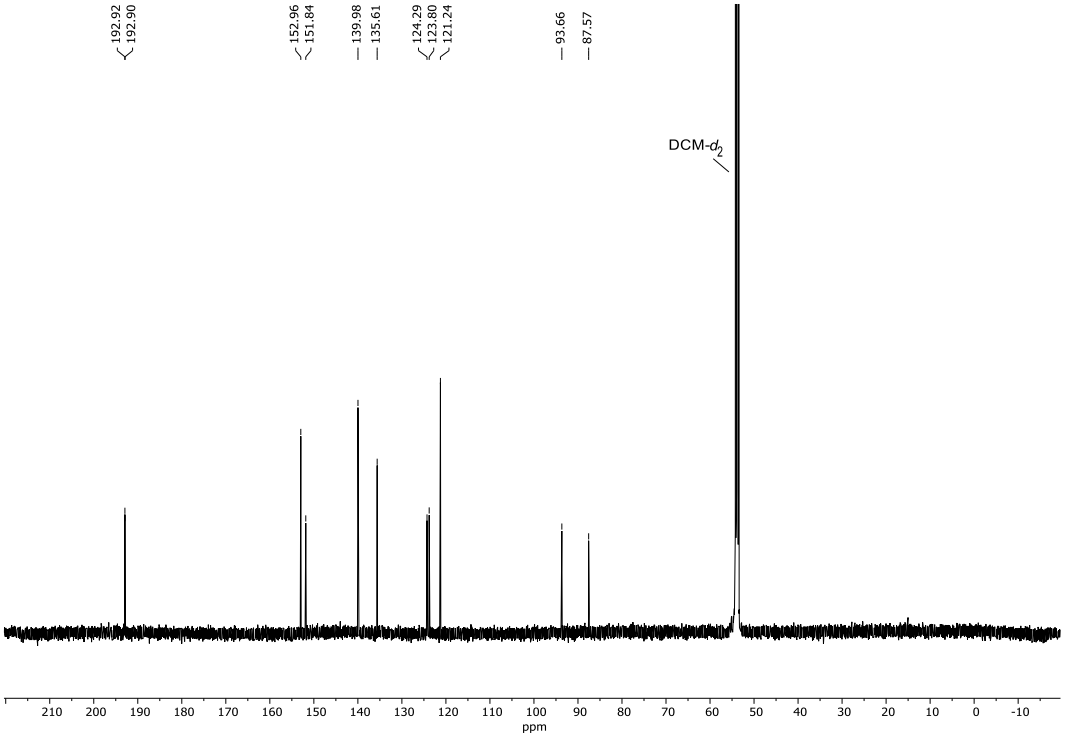

Figure 129: [13]C-NMR (151 MHz) spectrum of trialdehyde **178** in DCM-d_2 at 298 K.

$Zn_4L_4(NTf_2)_8$ Tetrahedron Zn-XLIII

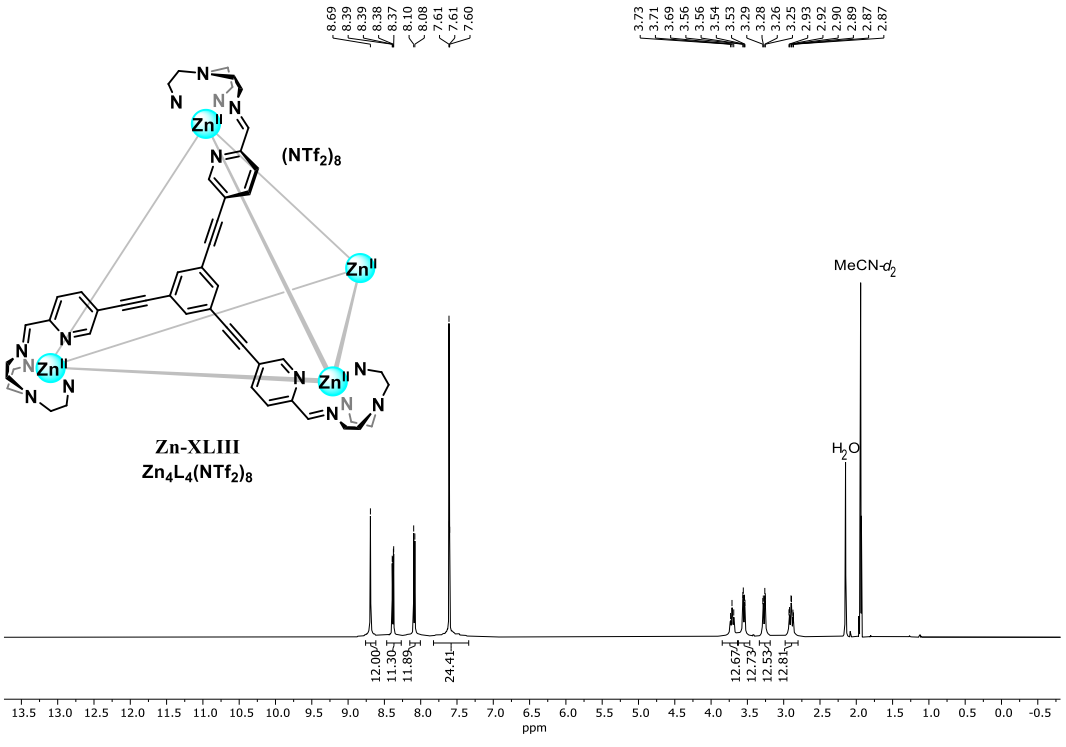

Figure 130: ^{1}H-NMR (500 MHz) spectrum of **$Zn_4L_4(NTf_2)_8$** tetrahedron **Zn-XLIII** in MeCN-d_3 at 298 K.

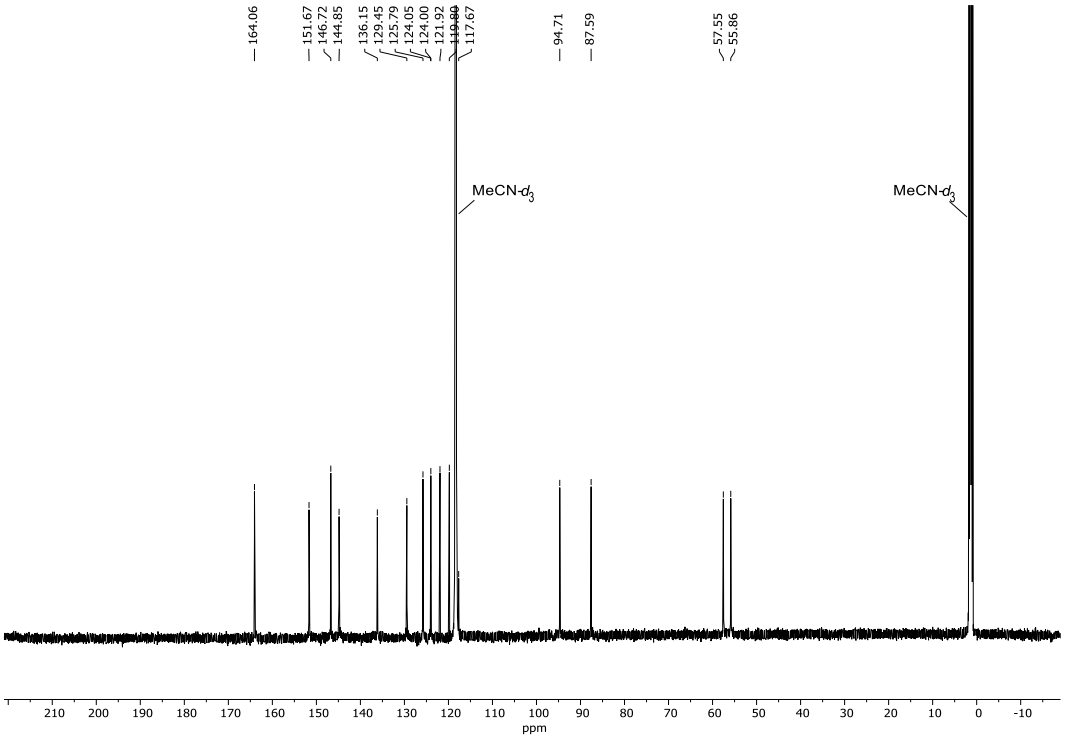

Figure 131: ^{13}C-NMR (151 MHz) spectrum of **$Zn_4L_4(NTf_2)_8$** tetrahedron **Zn-XLIII** in MeCN-d_3 at 298 K.

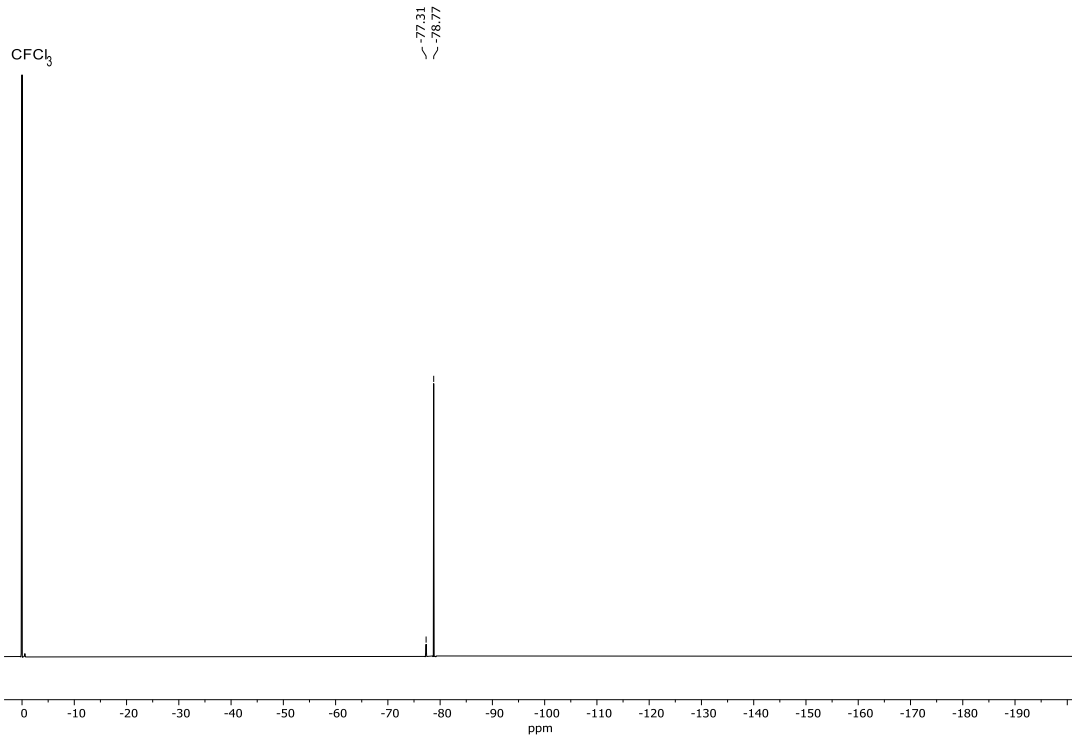

Figure 132: ^{19}F-NMR (471 MHz) spectrum of **$Zn_4L_4(NTf_2)_8$** tetrahedron **Zn-XLIII** in MeCN-d_3 at 298 K with $CFCl_3$ as int. Std.

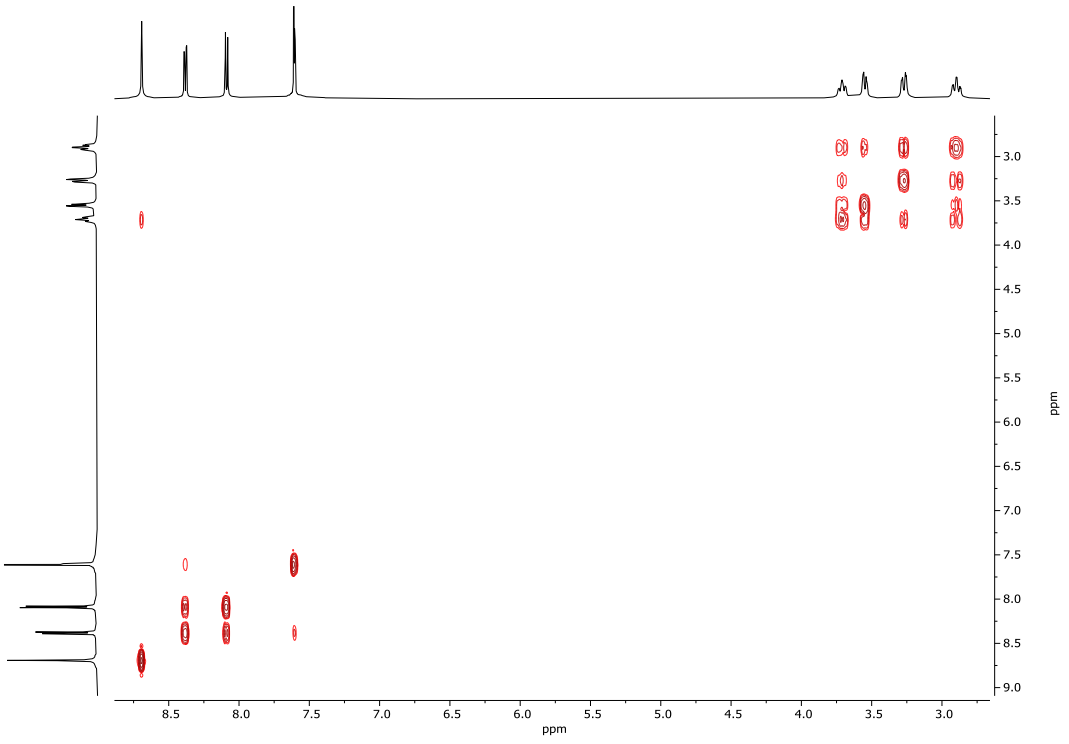

Figure 133: COSY spectrum of **$Zn_4L_4(NTf_2)_8$** tetrahedron **Zn-XLIII** in MeCN-d_3 at 298 K.

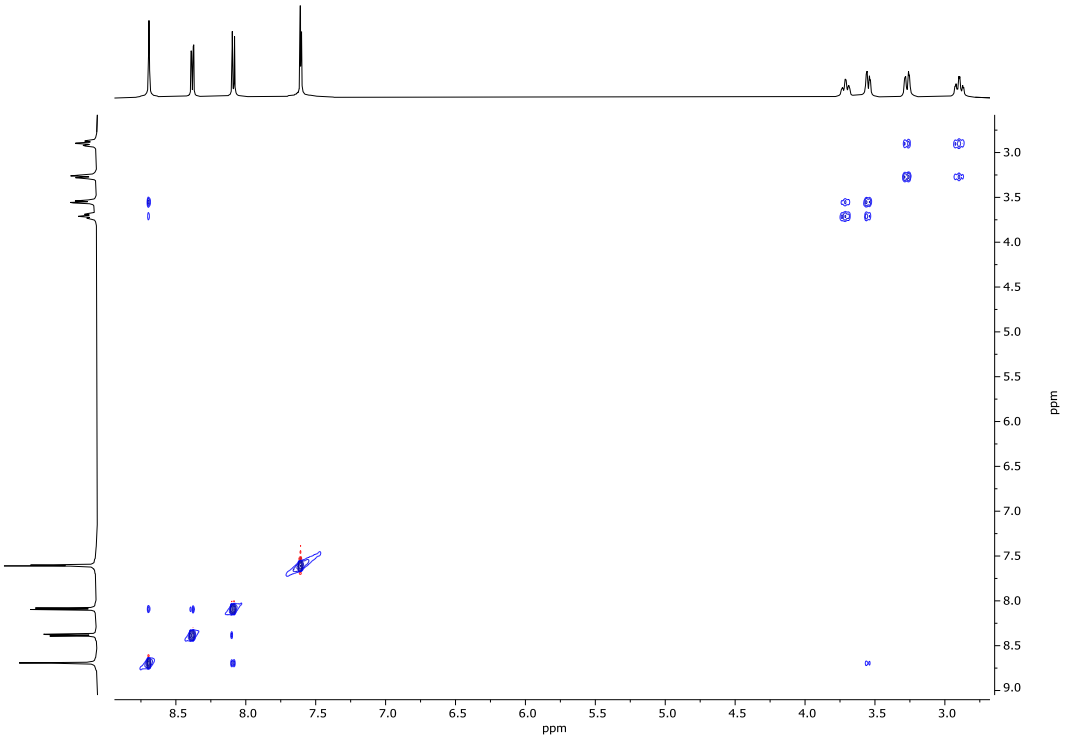

Figure 134: NOESY spectrum of **$Zn_4L_4(NTf_2)_8$** tetrahedron **Zn-XLIII** in MeCN-d_3 at 298 K.

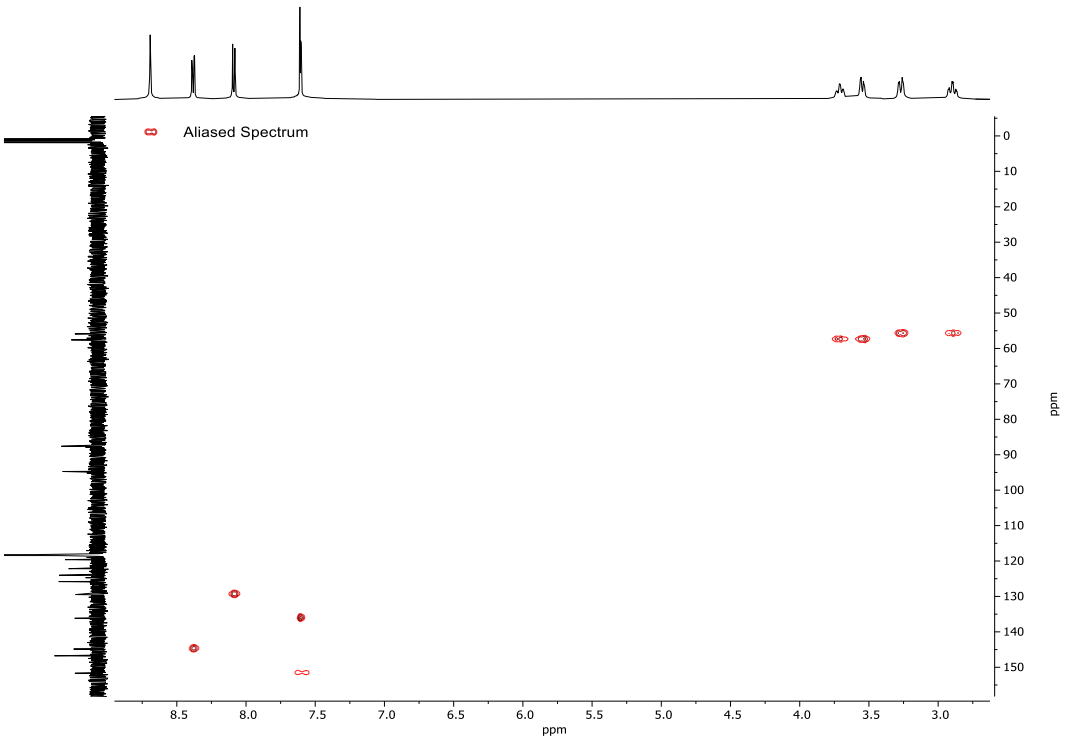

Figure 135: HMQC spectrum of **$Zn_4L_4(NTf_2)_8$** tetrahedron **Zn-XLIII** in MeCN-d_3 at 298 K.

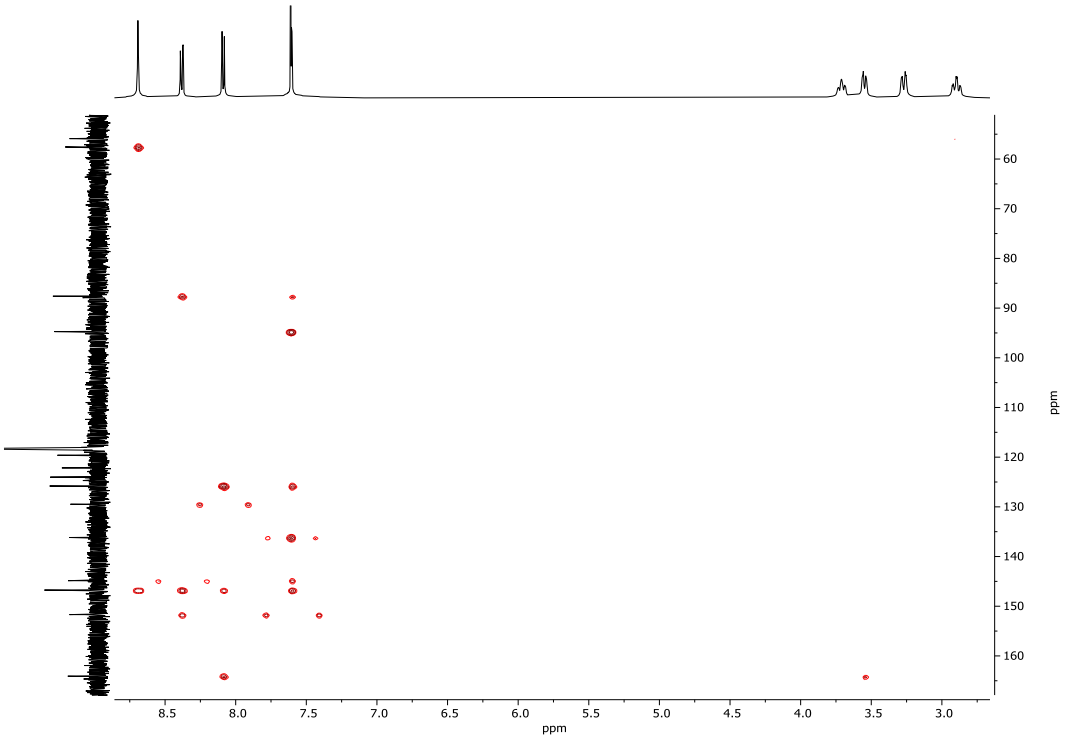

Figure 136: HMBC spectrum of **$Zn_4L_4(NTf_2)_8$** tetrahedron **Zn-XLIII** in MeCN-d_3 at 298 K.

$ZnL_3(NTf_2)_2$ Complex XLIV

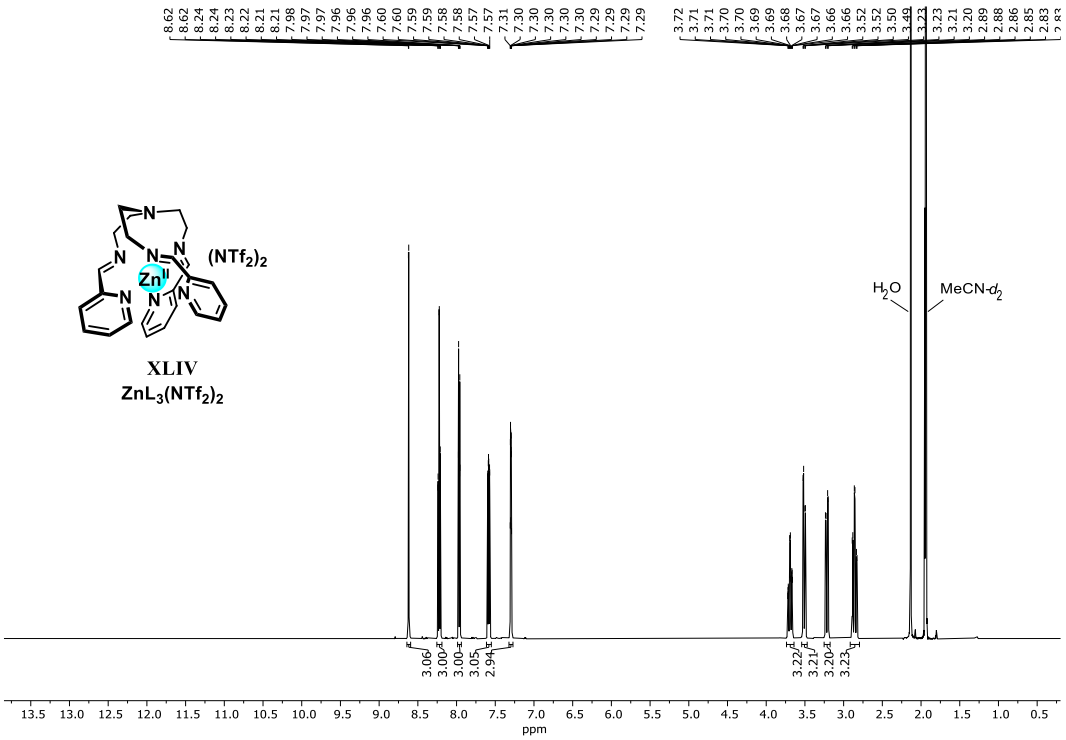

Figure 137: ^{1}H-NMR (500 MHz) spectrum of **$ZnL_3(NTf_2)_2$** complex **XLIV** in MeCN-d_3 at 298 K.

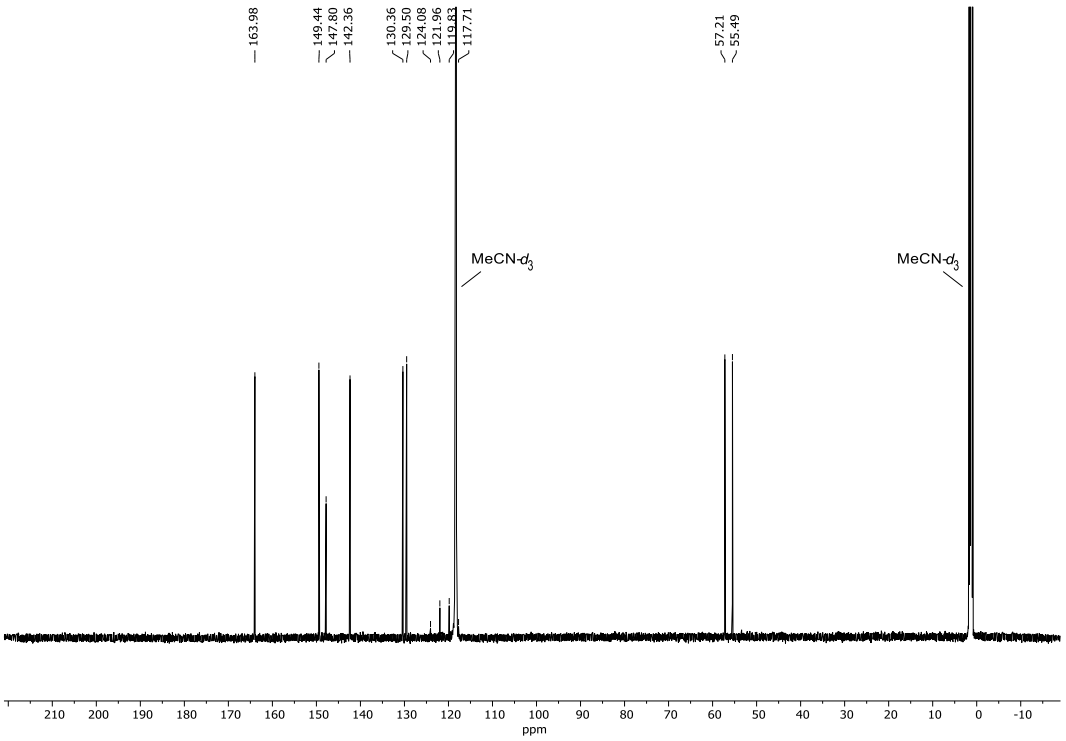

Figure 138: ^{13}C-NMR (151 MHz) spectrum of **$ZnL_3(NTf_2)_2$** complex **XLIV** in MeCN-d_3 at 298 K.

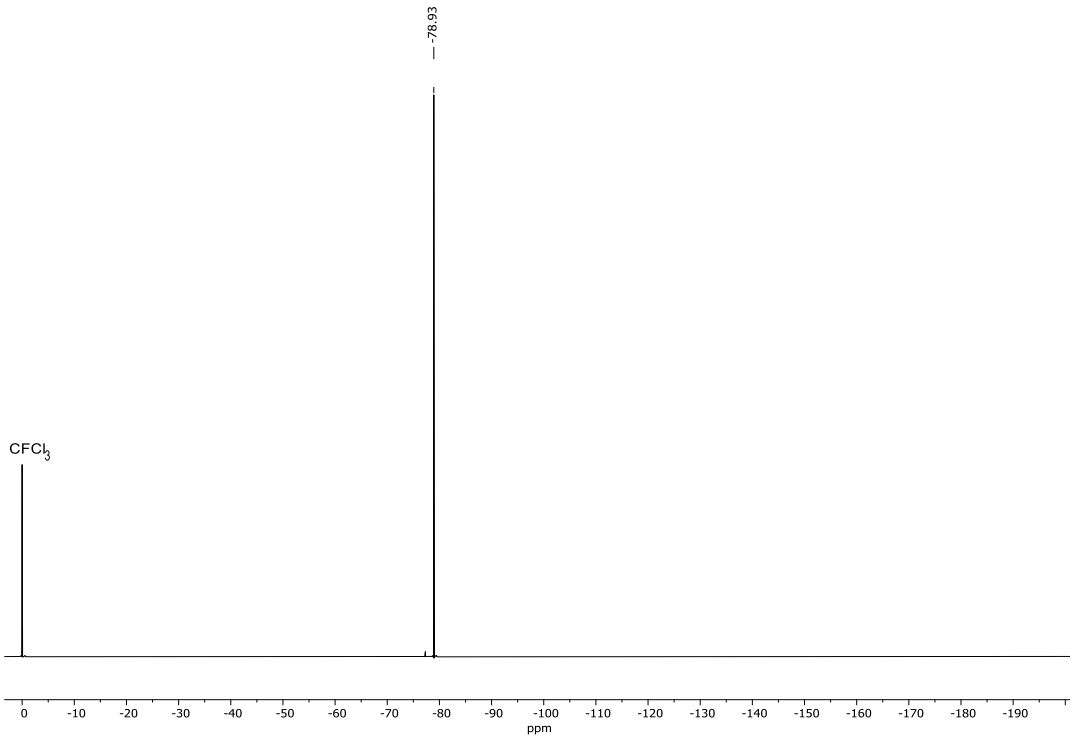

Figure 139: ^{19}F-NMR (471 MHz) spectrum of **ZnL$_3$(NTf$_2$)$_2$** complex **XLIV** in MeCN-d_3 at 298 K with $CFCl_3$ as int. Std.

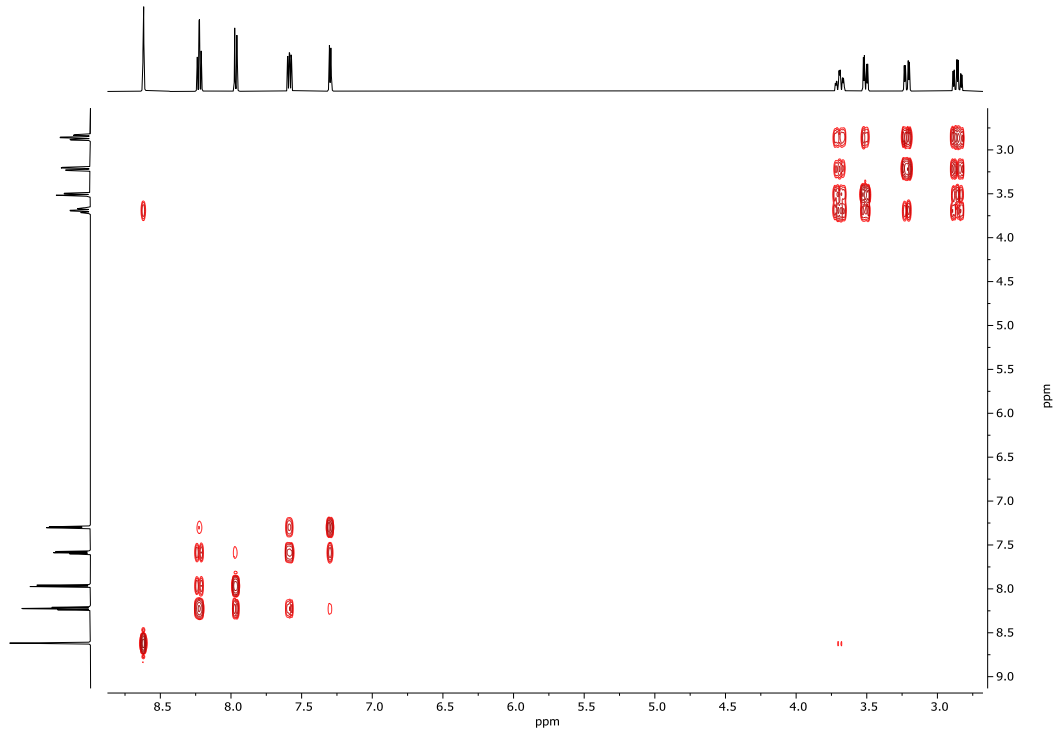

Figure 140: COSY spectrum of **ZnL$_3$(NTf$_2$)$_2$** complex **XLIV** in MeCN-d_3 at 298 K.

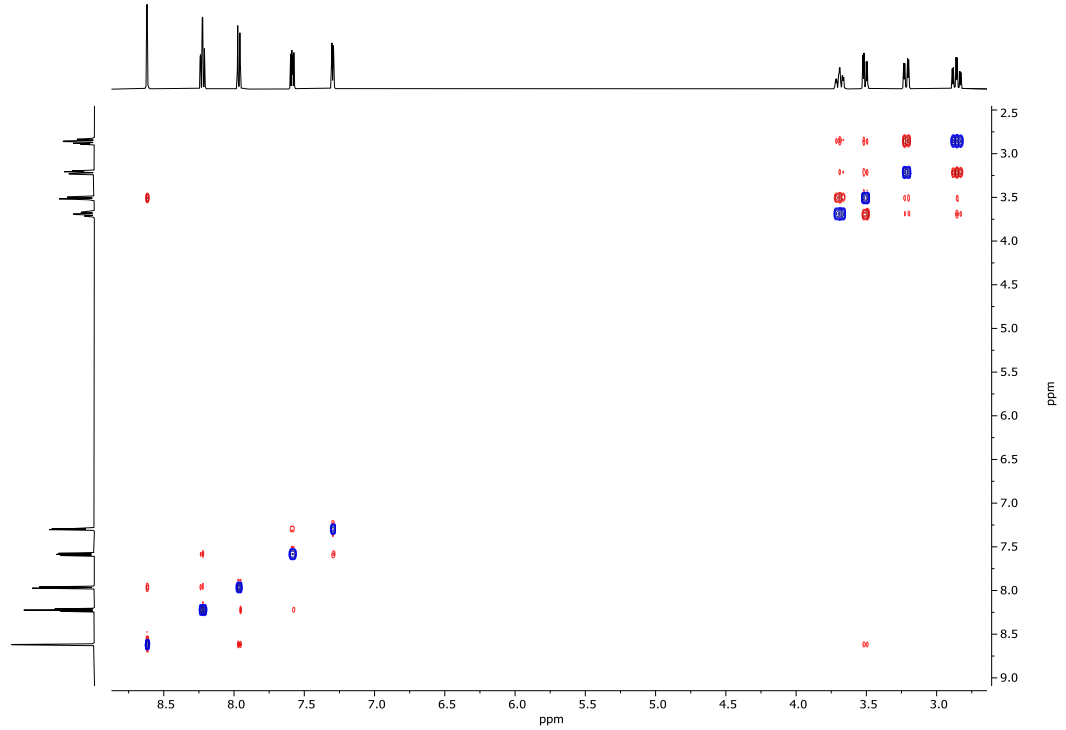

Figure 141: NOESY spectrum of **ZnL$_3$(NTf$_2$)$_2$** complex **XLIV** in MeCN-d_3 at 298 K.

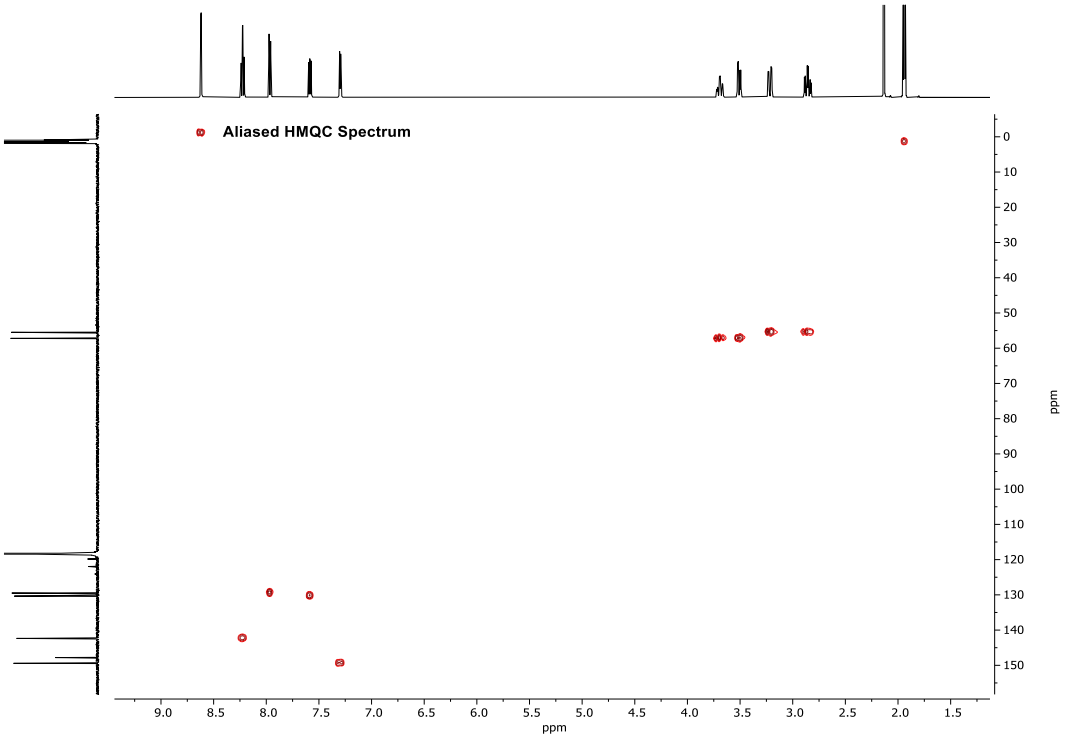

Figure 142: HMQC spectrum of **ZnL$_3$(NTf$_2$)$_2$** complex **XLIV** in MeCN-d_3 at 298 K.

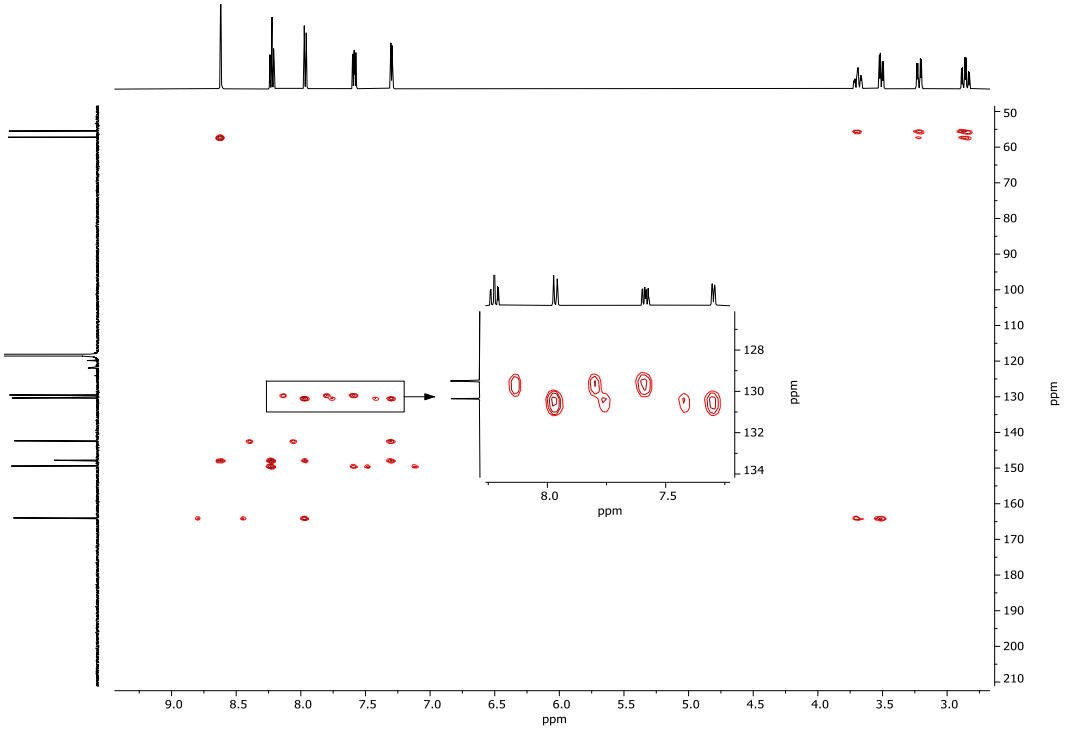

Figure 143: HMBC spectrum of **$ZnL_3(NTf_2)_2$** complex **XLIV** in MeCN-d_3 at 298 K.

Triphenyleno[2,3-*c*:6,7-*c*':10,11-*c*'']trifuran-1,3,6,8,11,13-hexaone (220)

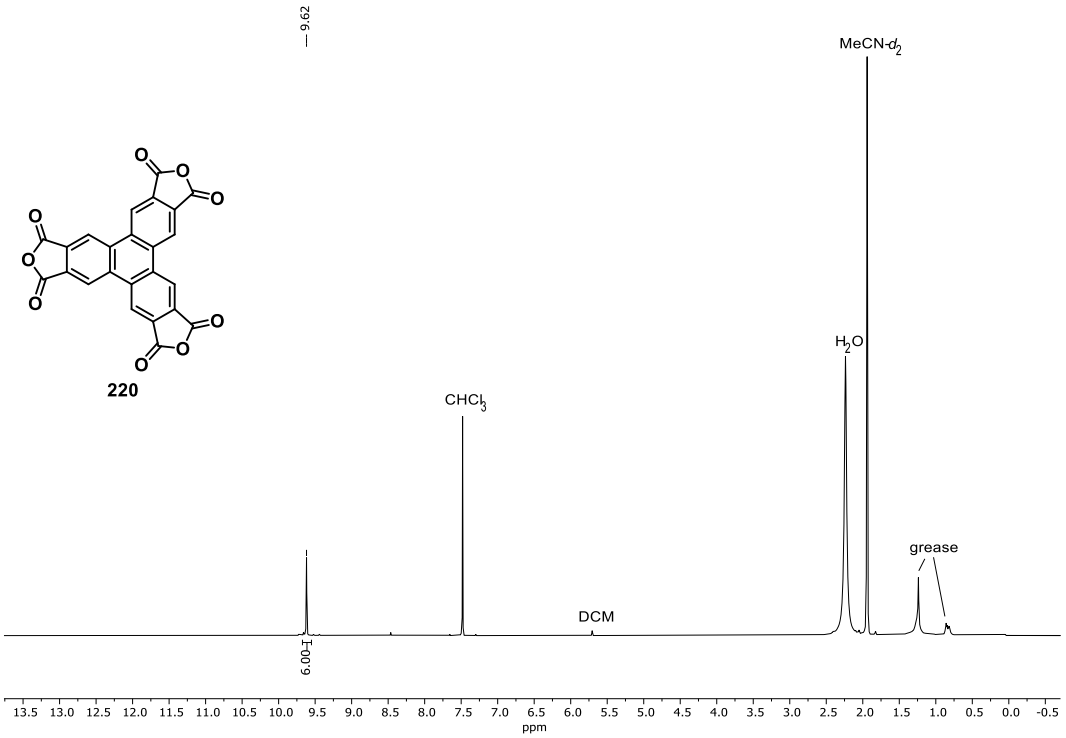

Figure 144: ^{1}H-NMR (600 MHz) spectrum of trianhydride **220** in MeCN-d_3:HCl-saturated $CDCl_3$ = 1:1 at 298 K.

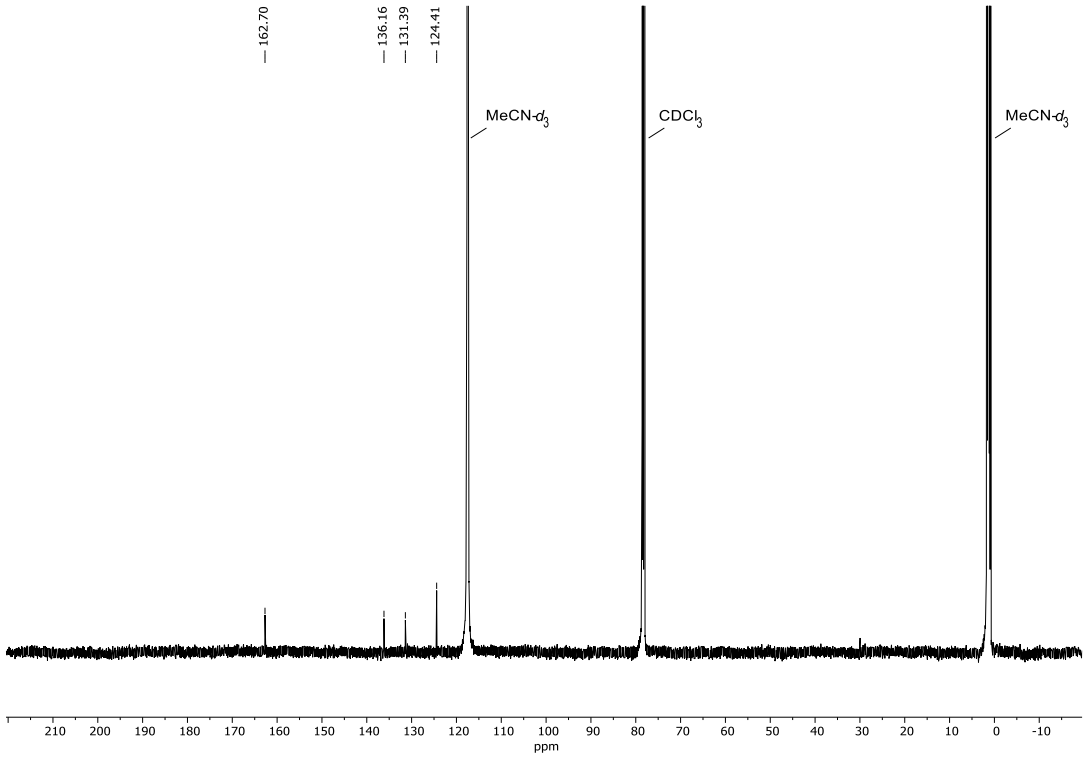

Figure 145: ^{13}C-NMR (151 MHz) spectrum of trianhydride **220** in MeCN-d_3:HCl-saturated $CDCl_3$ = 1:1 at 298 K.

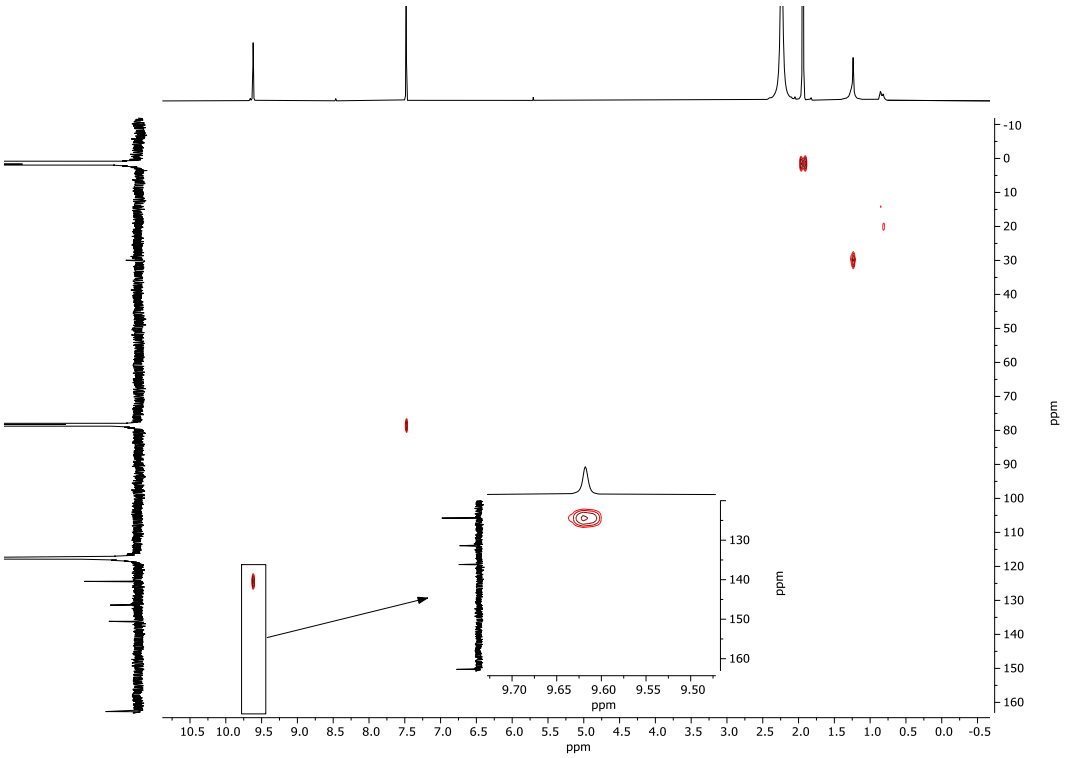

Figure 146: HMQC spectrum of trianhydride **220** in MeCN-d_3:HCl-saturated $CDCl_3$ = 1:1 at 298 K.

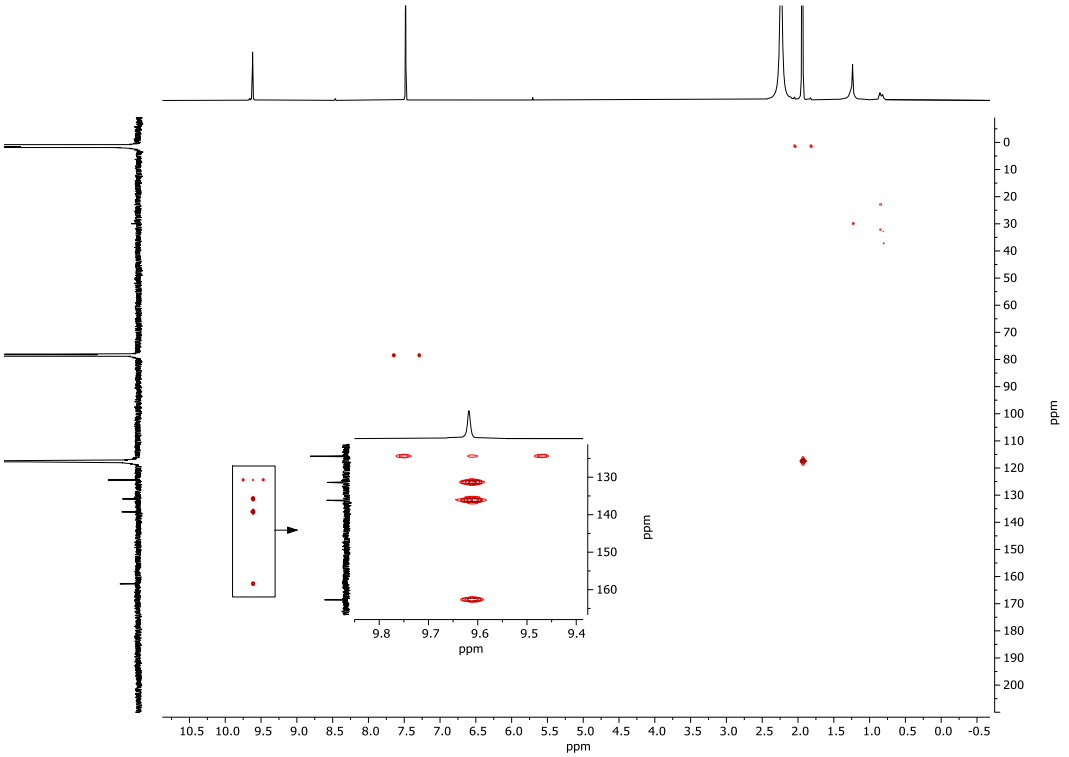

Figure 147: HMBC spectrum of trianhydride **220** in MeCN-d_3:HCl-saturated $CDCl_3$ = 1:1 at 298 K.

2,7,12-Tris(6-methylpyridin-3-yl)-1*H*-benzo[1,2-*f*:3,4-*f*':5,6-*f*'']triisoindole-1,3,6,8,11,13(2*H*,7*H*,12*H*)-hexaone (229)

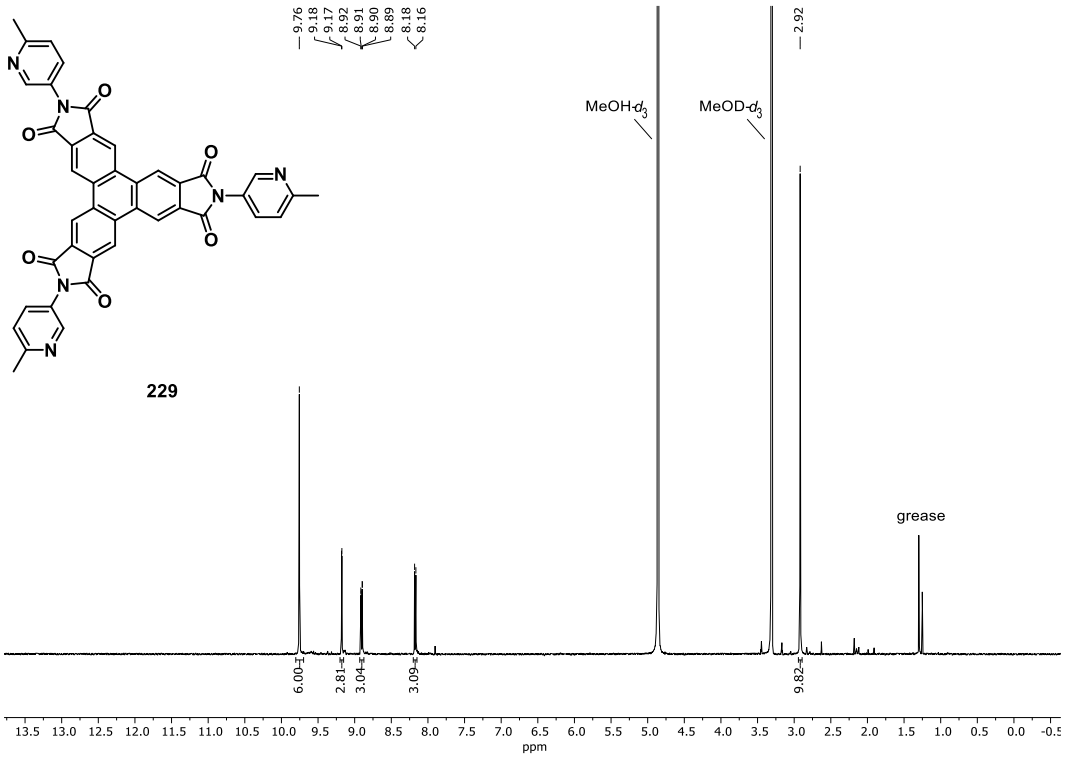

Figure 148: ^{1}H-NMR (500 MHz) spectrum of TPTI **229** in MeOD-d_4 at 298 K.

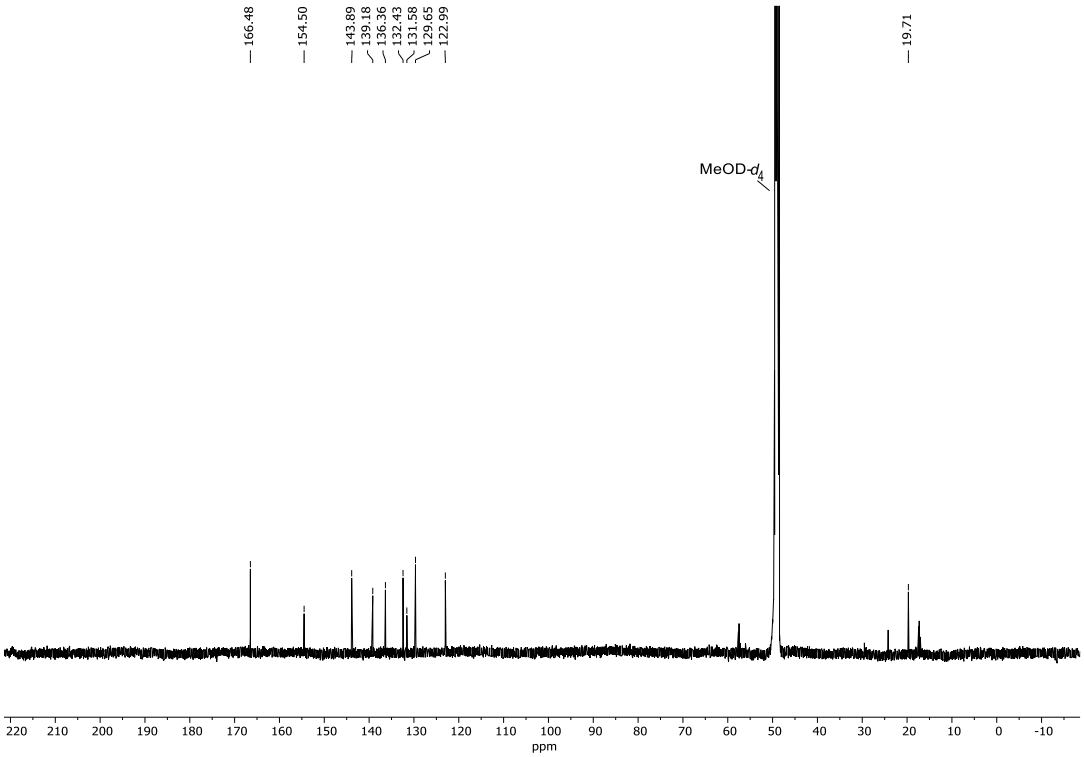

Figure 149: ^{13}C-NMR (151 MHz) spectrum of TPTI **229** in MeOD-d_4 at 298 K.

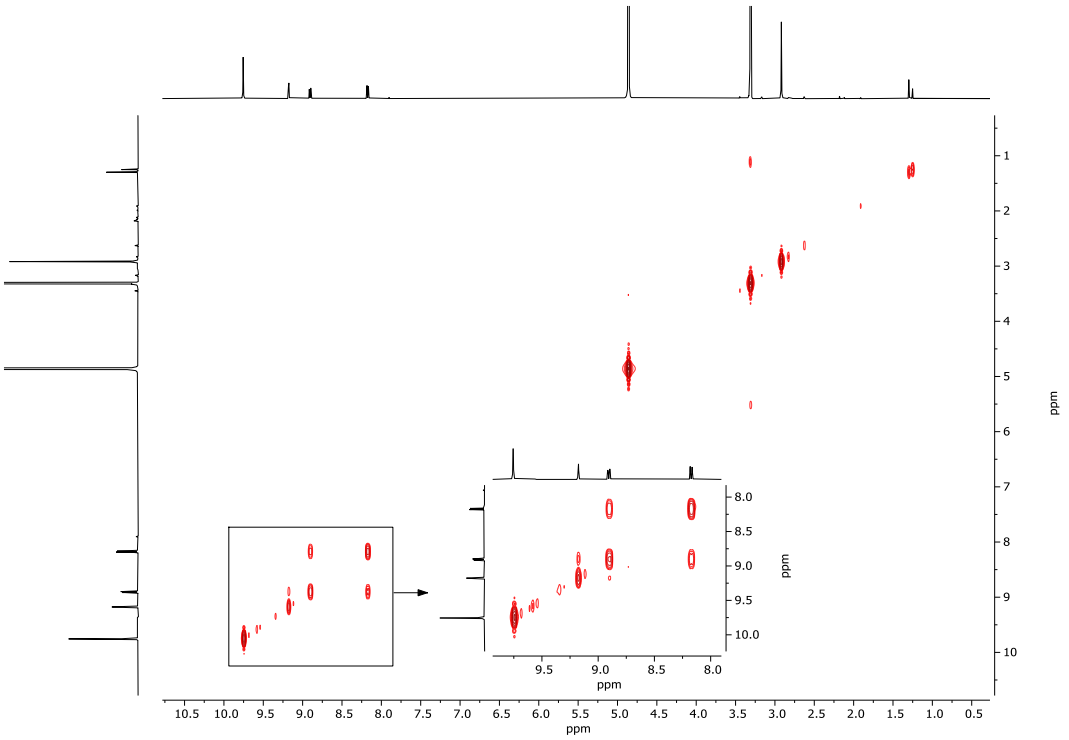

Figure 150: COSY spectrum of TPTI **229** in MeOD-d_4 at 298 K.

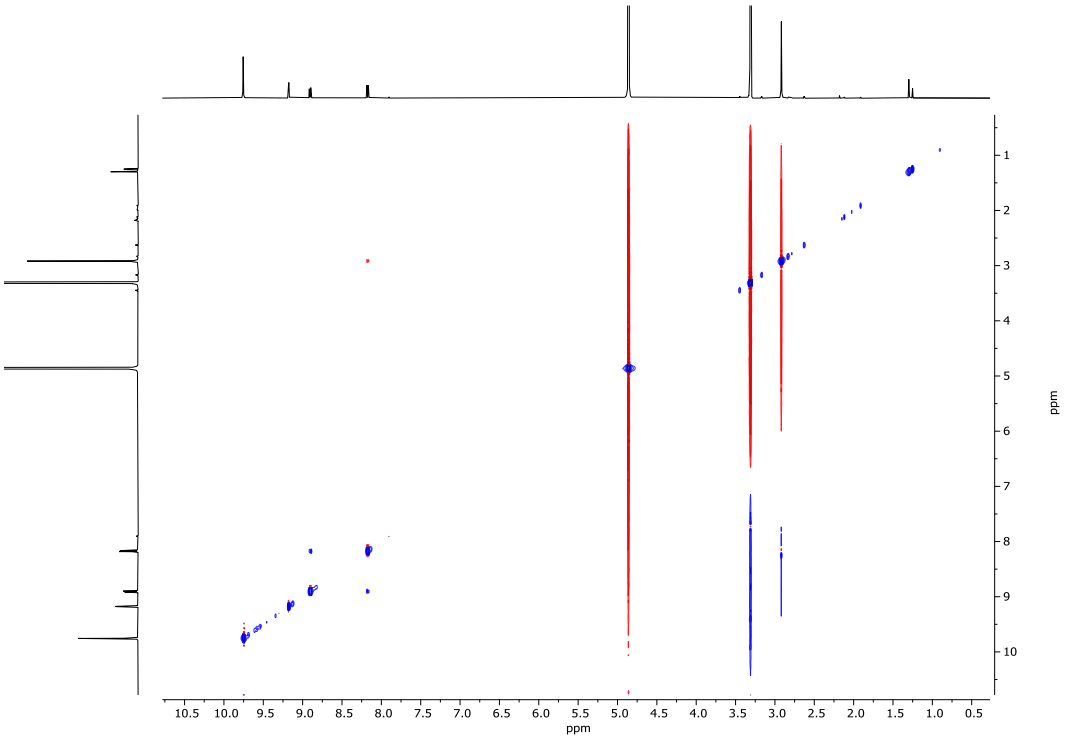

Figure 151: NOESY spectrum of TPTI **229** in MeOD-d_4 at 298 K.

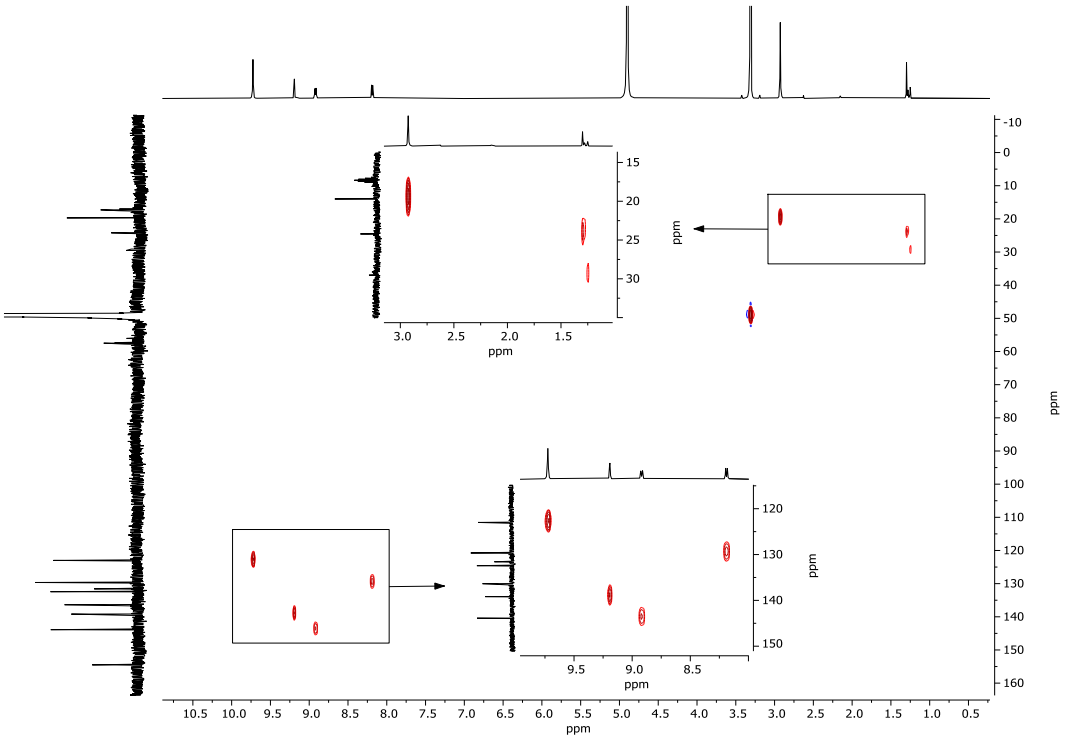

Figure 152: HMQC spectrum of TPTI **229** in MeOD-d_4 at 298 K.

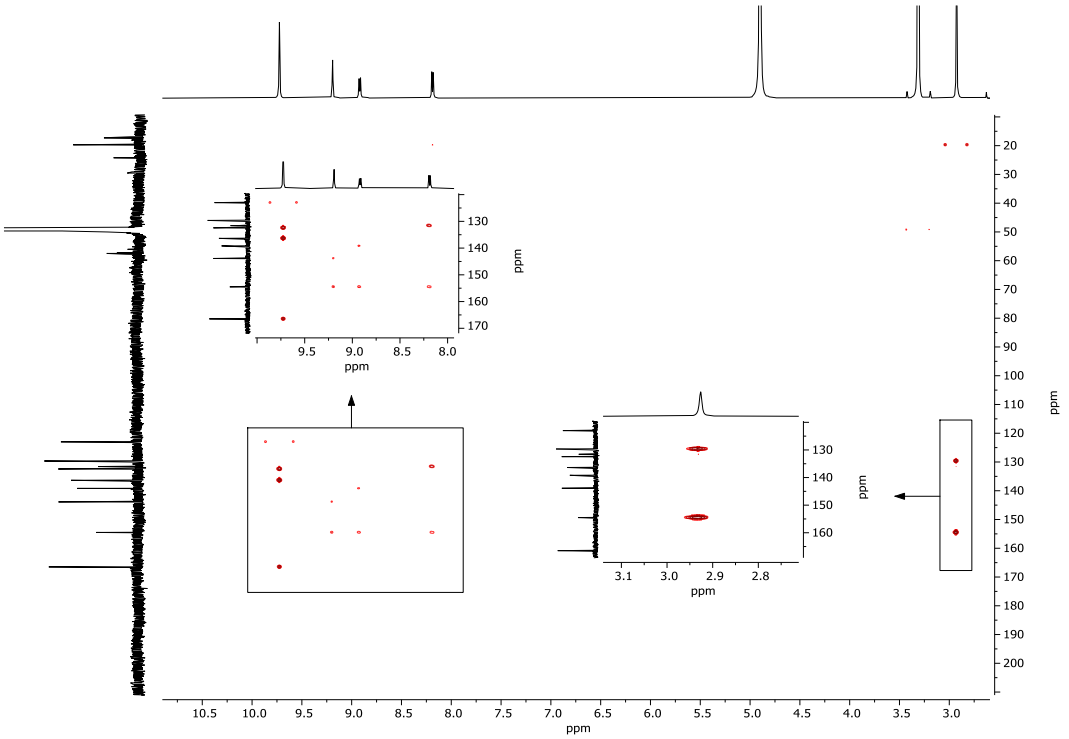

Figure 153: HMBC spectrum of TPTI **229** in MeOD-d_4 at 298 K.

Tetrabutylammonium monomethylterephthalate (258)

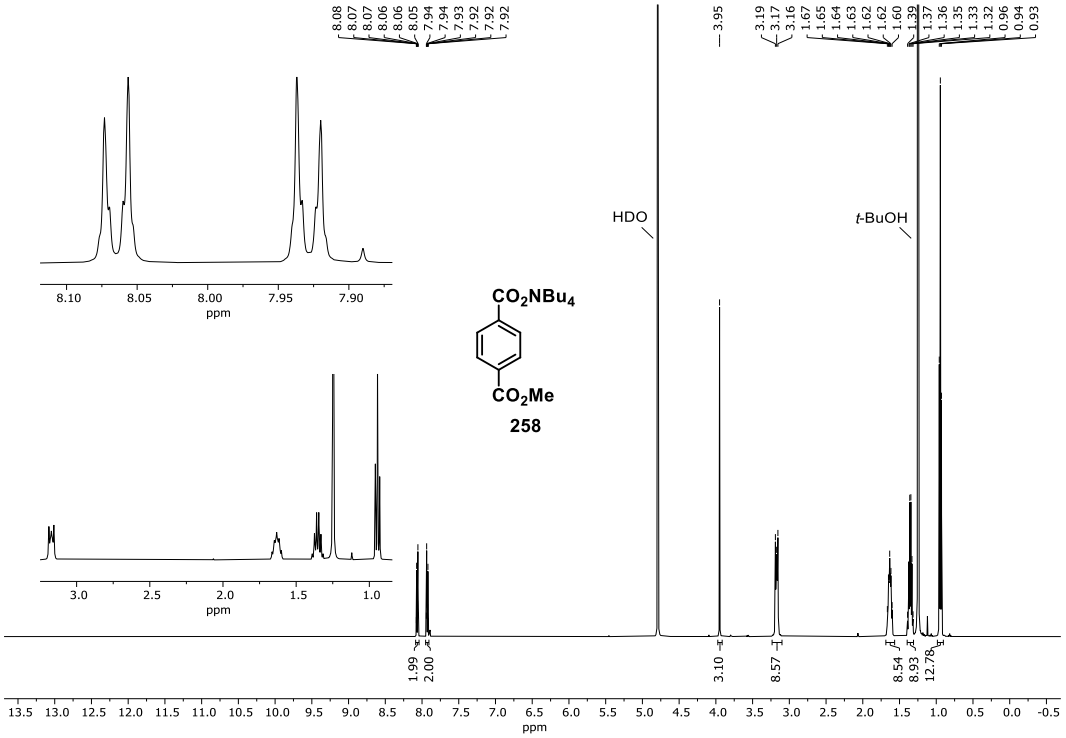

Figure 154: ^{1}H-NMR (500 MHz) spectrum of monomethylterephthalate salt **258** in D_2O with 1% *t*-BuOH at 298 K.

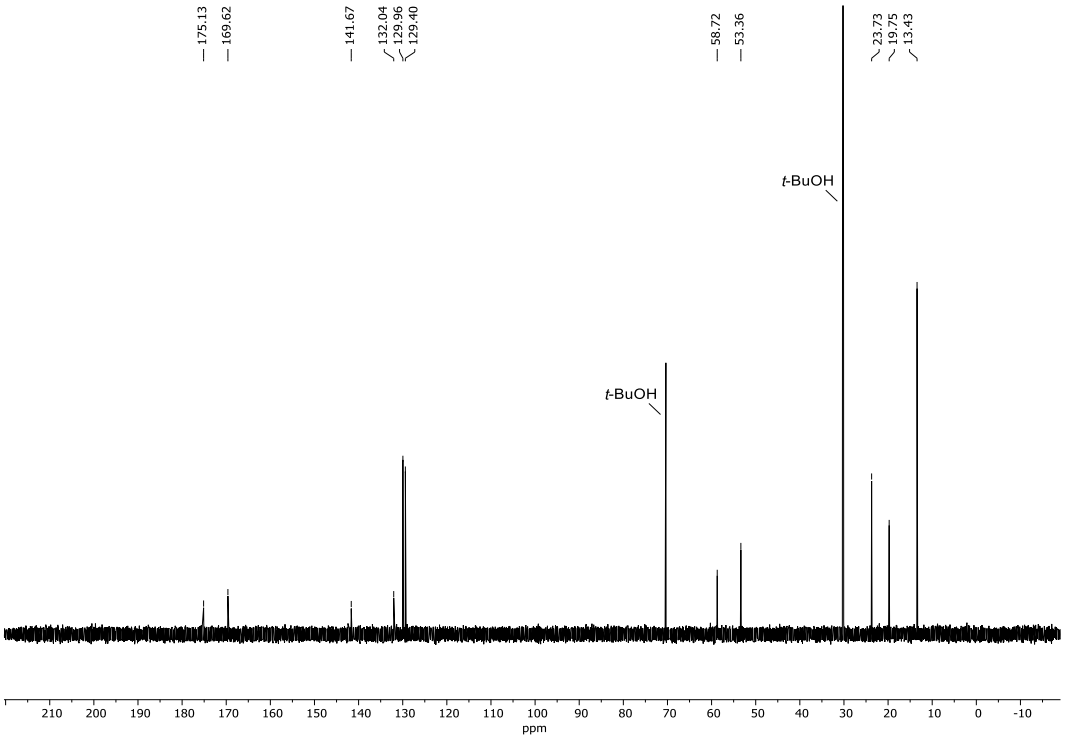

Figure 155: ^{13}C-NMR (126 MHz) spectrum of monomethylterephthalate salt **258** in D_2O with 1% *t*-BuOH at 298 K.

Tetrabutylammonium adamantane-1-carboxylate (259)

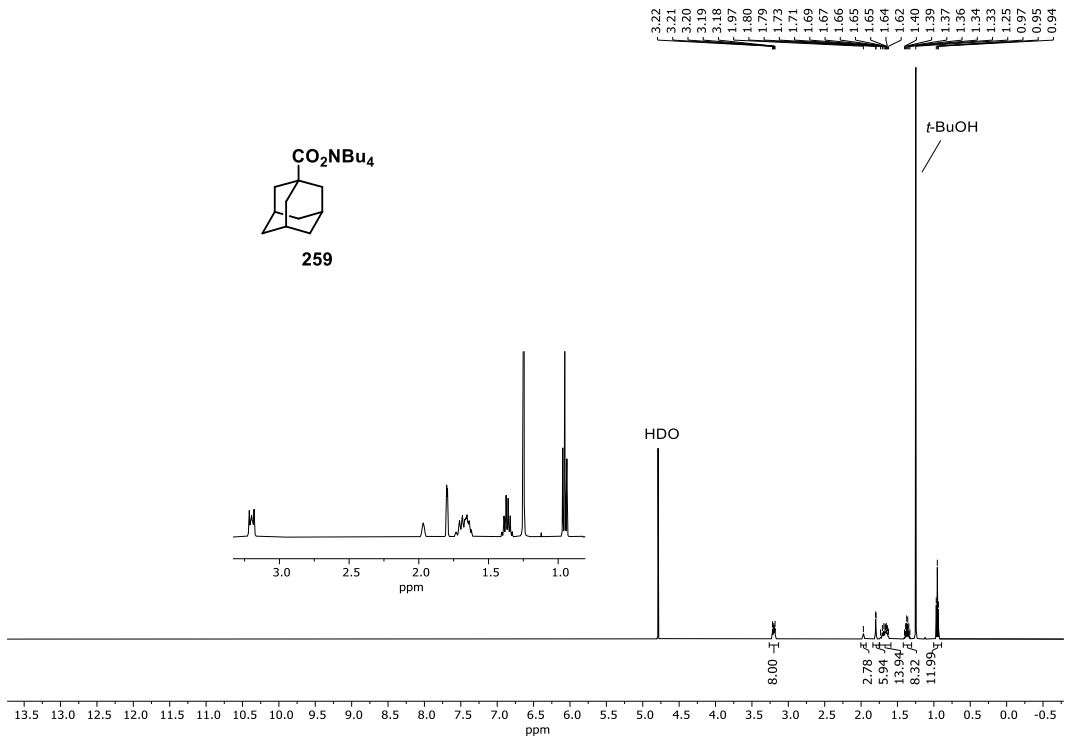

Figure 156: ^{1}H-NMR (500 MHz) spectrum of adamantane carboxylate salt **259** in D_2O with 1% *t*-BuOH at 298 K.

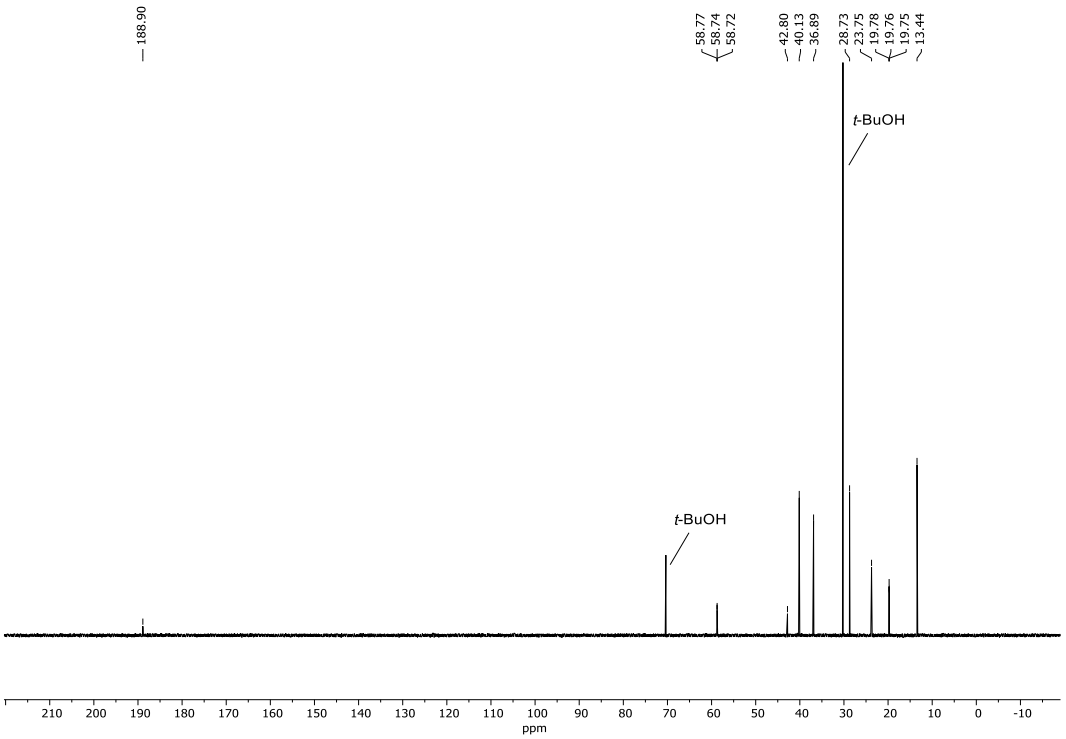

Figure 157: ^{13}C-NMR (126 MHz) spectrum of adamantane carboxylate salt **259** in D_2O with 1% *t*-BuOH at 298 K.

Tetrabutylammonium diphenyl phosphate (260)

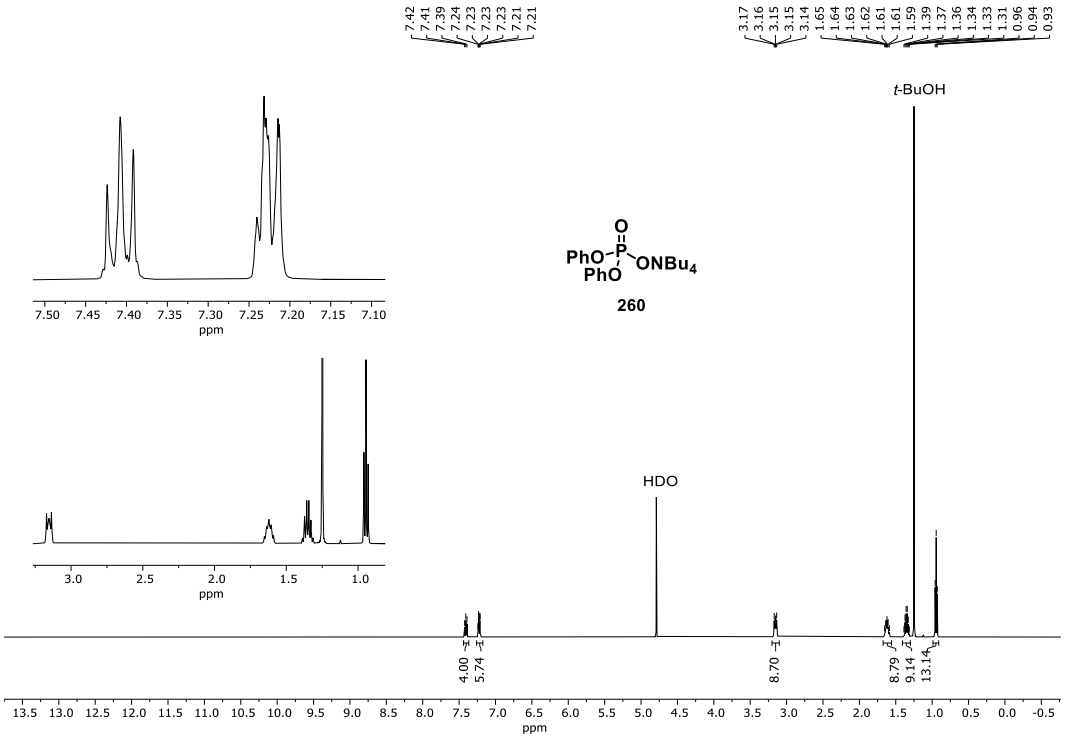

Figure 158: ^{1}H-NMR (500 MHz) spectrum of diphenyl phosphate salt **260** in D_2O with 1% *t*-BuOH at 298 K.

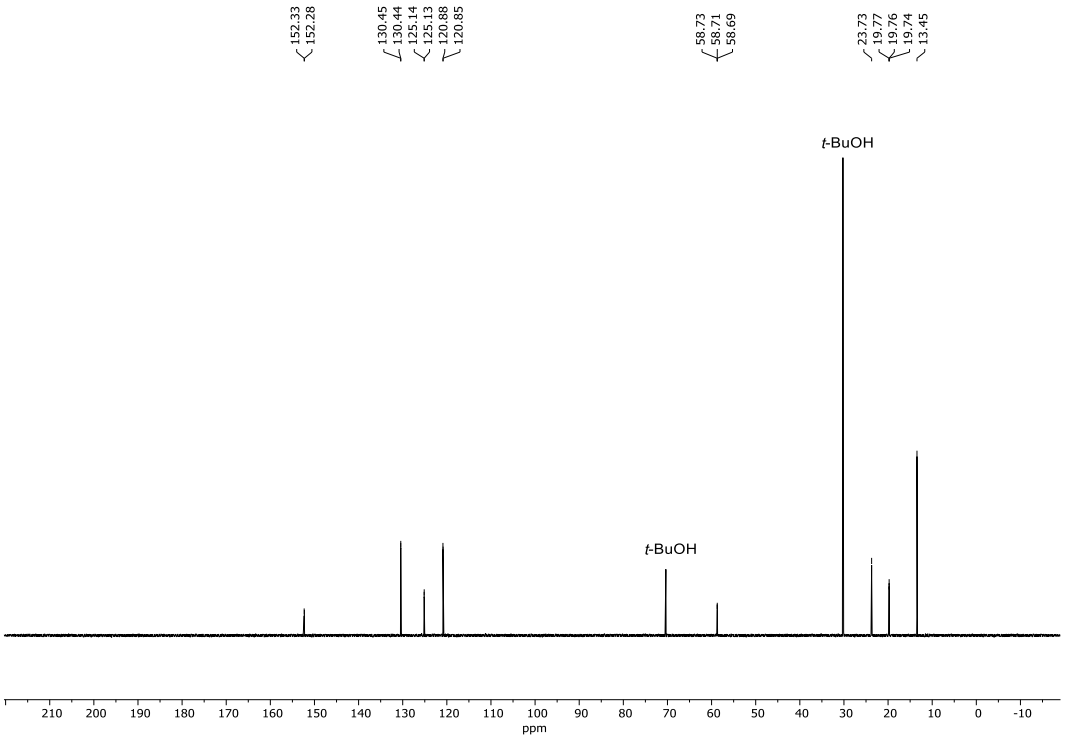

Figure 159: ^{13}C-NMR (126 MHz) spectrum of diphenyl phosphate salt **260** in D_2O with 1% *t*-BuOH at 298 K.

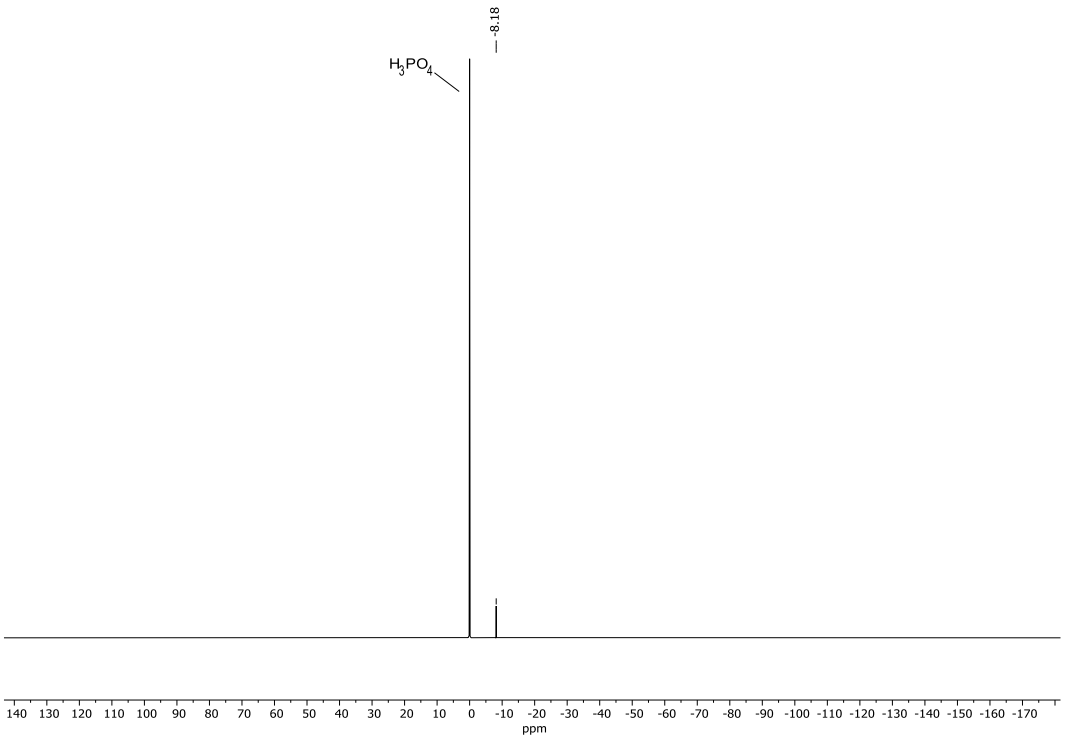

Figure 160: ^{31}P-NMR (202 MHz) spectrum of diphenyl phosphate salt **260** in D_2O with 85% H_3PO_4 as ext. Std. at 298 K.

Tetrabutylammonium dimethyl phosphate (261)

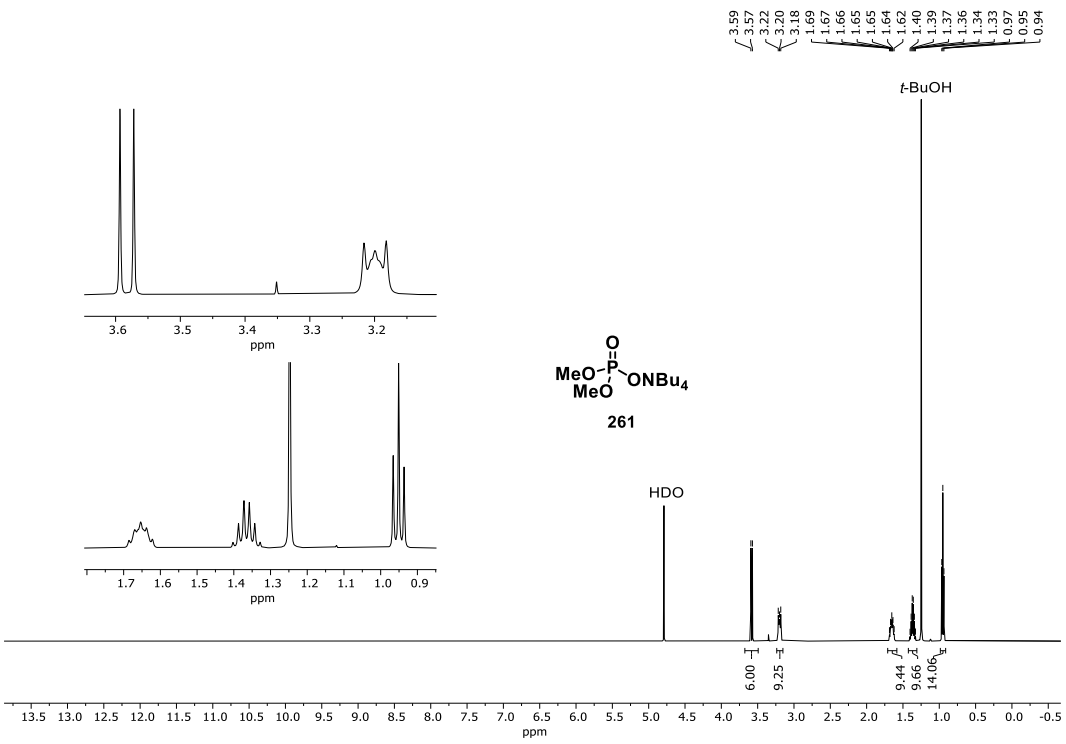

Figure 161: ^{1}H-NMR (500 MHz) spectrum of dimethyl phosphate salt **261** in D_2O with 1% *t*-BuOH at 298 K.

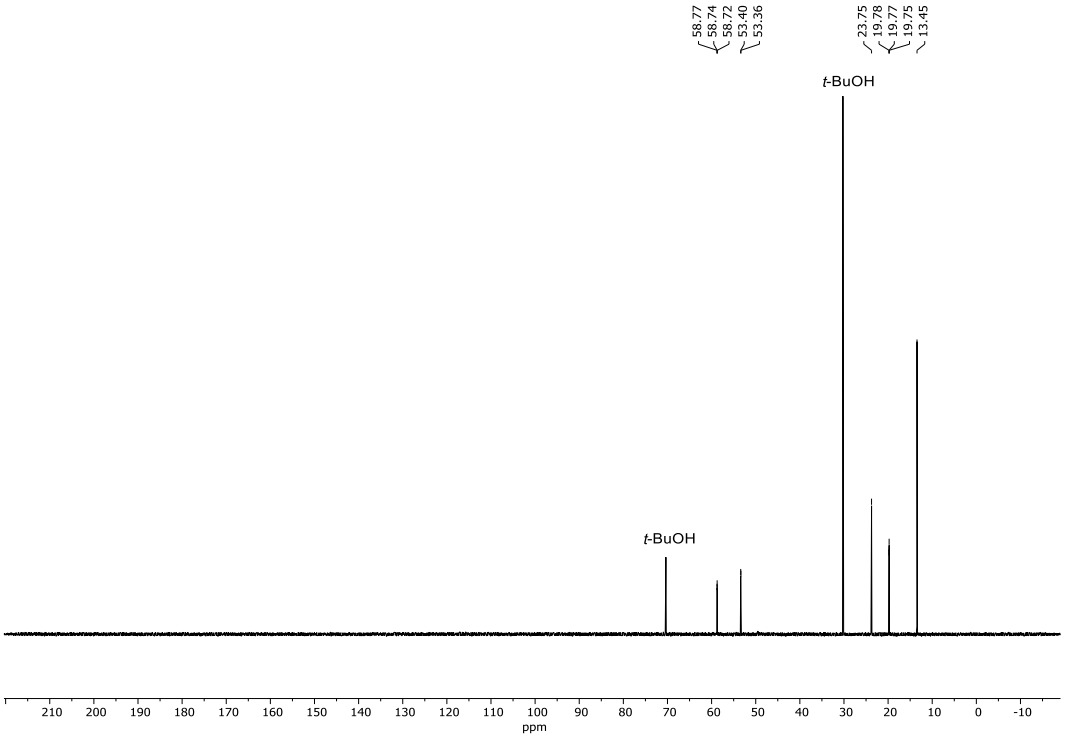

Figure 162: ^{13}C-NMR (126 MHz) spectrum of dimethyl phosphate salt **261** in D_2O with 1% *t*-BuOH at 298 K.

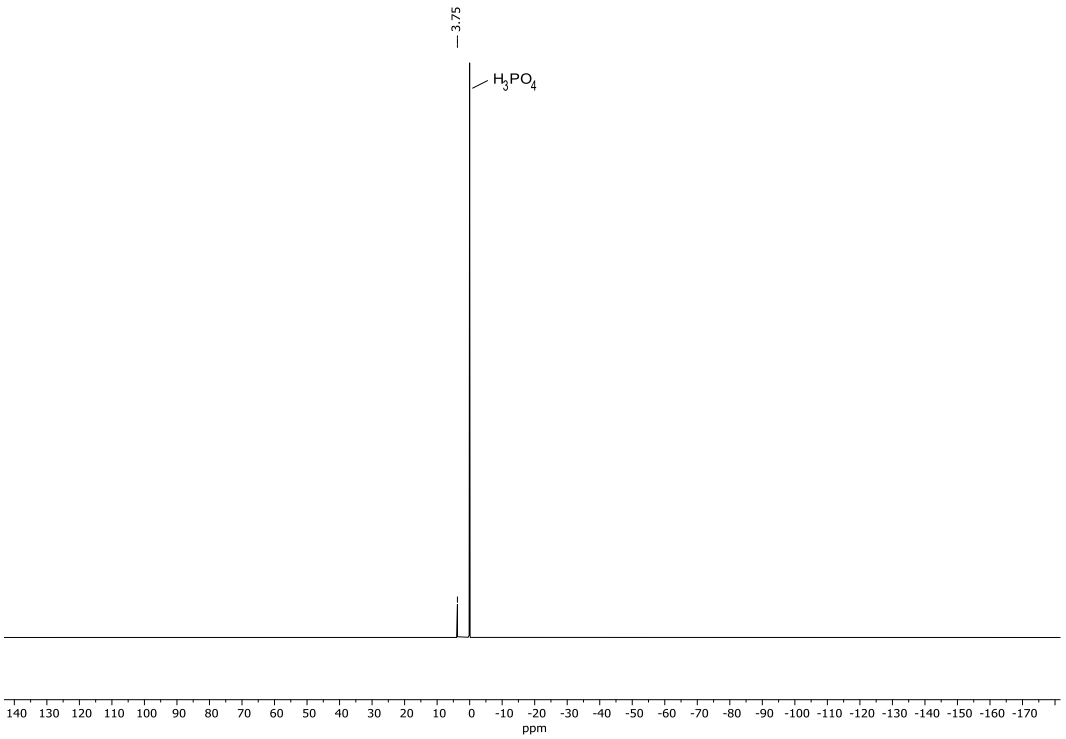

Figure 163: ^{31}P-NMR (202 MHz) spectrum of dimethyl phosphate salt **261** in D_2O with 85% H_3PO_4 as ext. Std. at 298 K.

Tetrabutylammonium dibutyl phosphate (262)

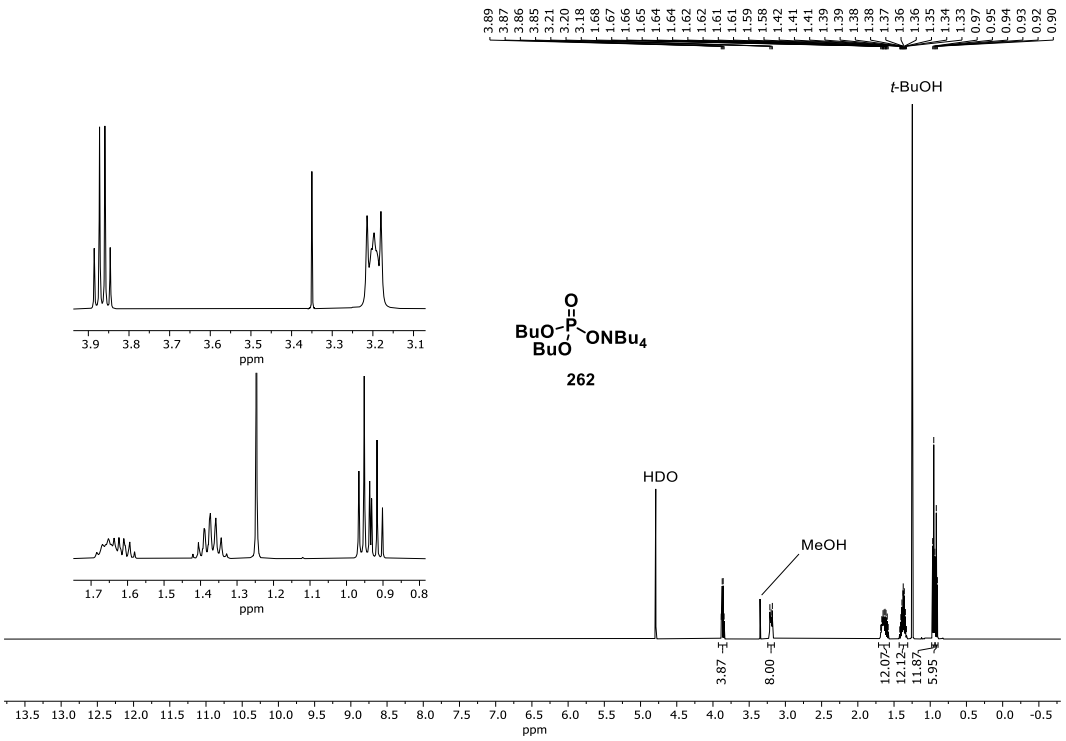

Figure 164: ^{1}H-NMR (500 MHz) spectrum of dibutyl phosphate salt **262** in D_2O with 1% *t*-BuOH at 298 K.

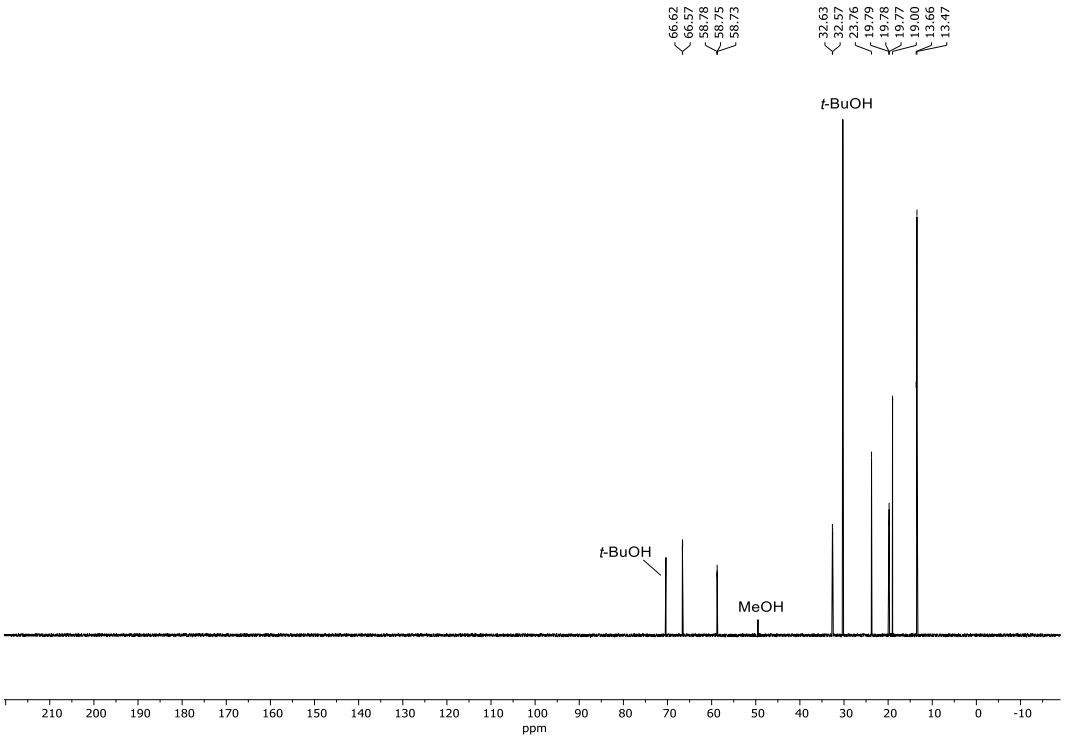

Figure 165: ^{13}C-NMR (126 MHz) spectrum of dibutyl phosphate salt **262** in D_2O with 1% *t*-BuOH at 298 K.

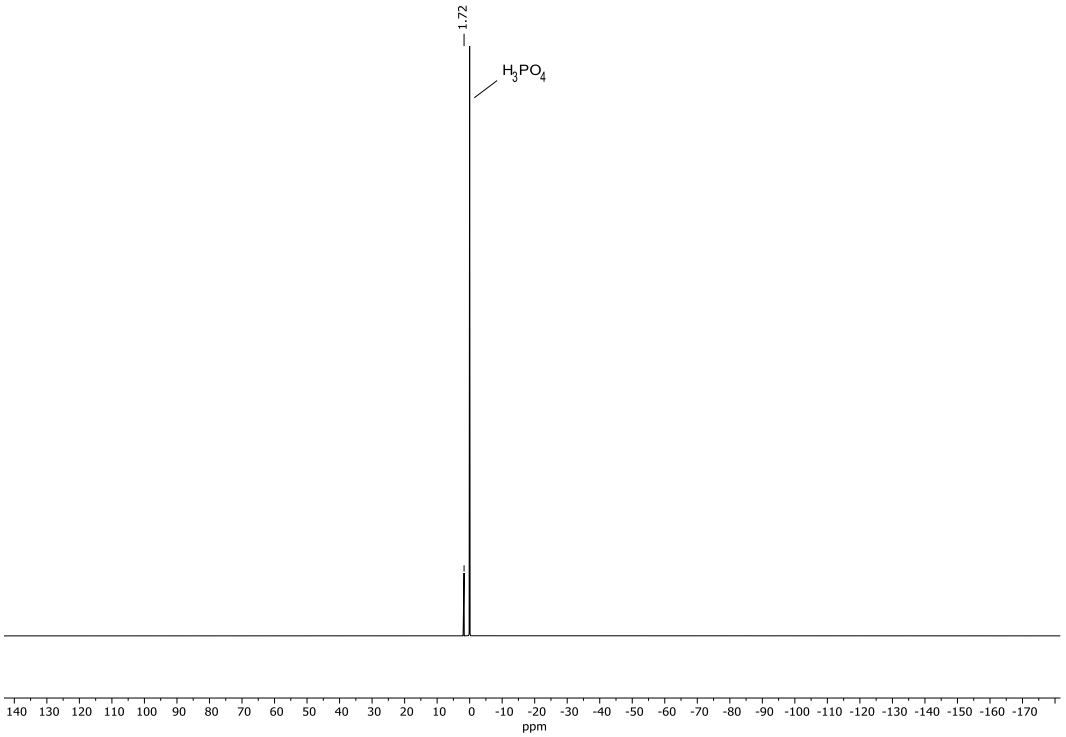

Figure 166: ^{31}P-NMR (202 MHz) spectrum of dibutyl phosphate salt **262** in D_2O with 85% H_3PO_4 as ext. Std. at 298 K.

3-Oxo-3-phenylpropanoic acid (Keto and Enol Form 265 and 265')

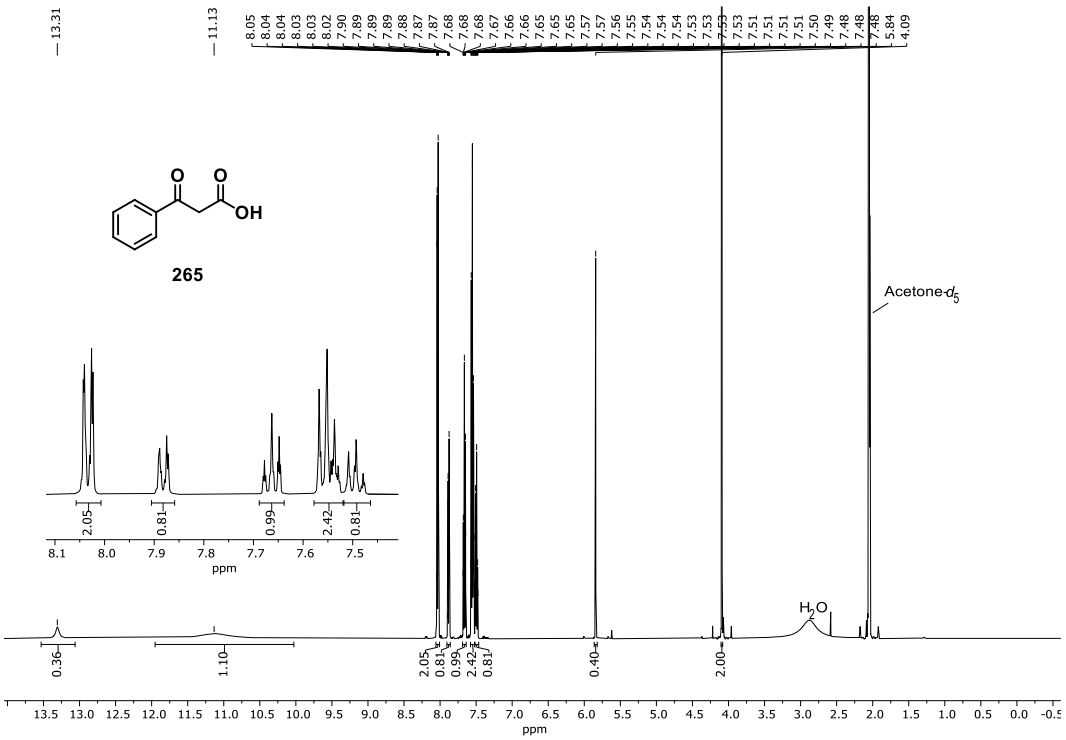

Figure 167: ^{1}H-NMR (500 MHz) spectrum of β-ketoacid **265** (keto form) in acetone-d_6 at 298 K.

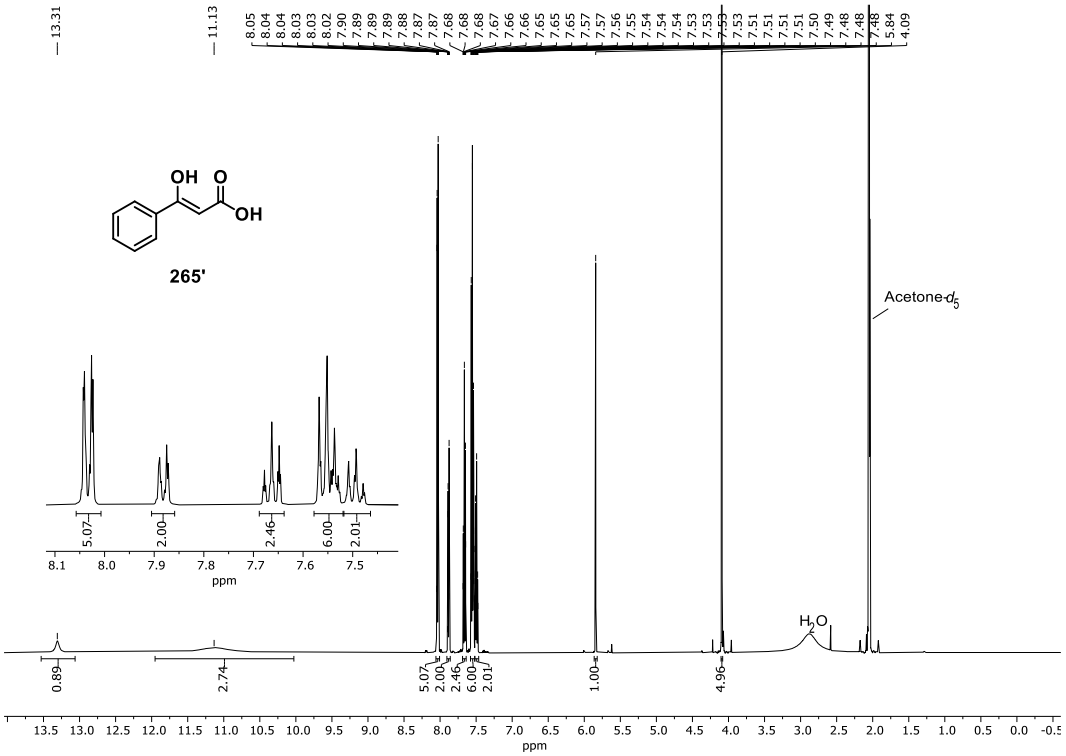

Figure 168: ^{1}H-NMR (500 MHz) spectrum of β-ketoacid **265'** (enol form) in acetone-d_6 at 298 K.

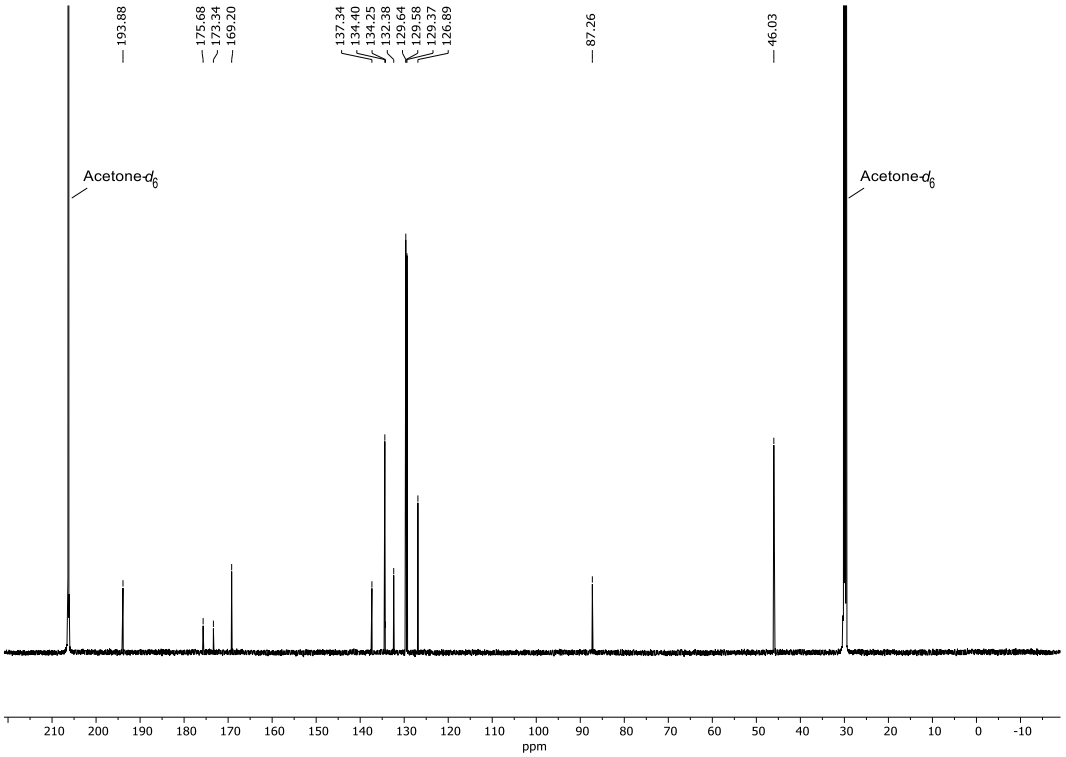

Figure 169: ^{13}C-NMR (151 MHz) spectrum of β-ketoacid **265/265'** (keto and enol form) in acetone-d_6 at 298 K.

6 Index of Abbreviations

χ	mole fraction
1,2-DCE	1,2-dichloroethane
Å	Ångström, 10^{-10} m
a. u.	arbitrary unit
AcOH	acetic acid
AIBN	azobisisobutyronitrile
α_{II}	molecular polerizability
aq.	aqueous
ATR	attenuated total reflection
B	Buckingham
b	broad
β	beta
br.	broad
BSSE	basis set superposition error
Bu	butyl
C	coulomb
c	concentration
ca.	circa
CD	circular dichroism
CDC	constitutional dynamic chemistry
$CDCl_3$	Deuterated chloroform
$CFCl_3$	trichlorfluormethane
$CHCl_3$	chloroform
CO_2	carbon dioxide
COSY	correlation spectroscopy
CSD	crystal structure database
CuI	copper(I) iodide
D	diffusion coefficient
δ	chemical shift
D_2O	deuterated water
Da	Dalton
DCC	dynamic combinatorial chemistry
DCL	dynamic combinatorial library
DCM	dichloromethane
DCM-d_2	deuterated dichloromethane
DCvC	dynamic covalent chemistry
ΔG	GIBBS free energy
Di	ditopic
DIBAL-H	diisobutylaluminium hydride
DMF	dimethylformamide
DMSO	dimethyl sulfoxide
DMSO-d_6	deuterated dimethyl sulfoxide
DOSY	diffusion ordered spectroscopy
dr	diastereomeric ratio
ee	enantiomeric excess
EI	electron ionization
eq.	equivalent(s)
ESI	electrospray ionization
Et	ethyl
et al.	*et alii* (and others)
Et_2O	diethyl ether
EtOAc	ethyl acetate
EtOH	ethanol
ext.	external
fac	facial
G	guest
η	yield
η	hapticity
H	host
H_2	hydrogen
H_2O	water
H_2SO_4	sulfuric acid

H_3PO_4	phosphoric acid	$MeNO_2$	nitromethane
HCl	hydrogen chloride	MeOD-d_4	deuterated methanol
HFIP	hexafluoroisopropanol	MeOH	methanol
HG	host-guest complex	*mer*	meridional
HMBC	heteronuclear multiple bond correlation	MHT	malonate half thioester
HMQC	heteronuclear multiple quantum coherence	MHz	megahertz
HOMO	highest occupied molecular orbital	min	minute(s)
HPLC	high-pressure liquid chromatography	mL	milliliter(s)
HR-MS	high-resolution mass spectrometry	µL	microliter(s)
Hz	hertz	mM	millimolar
I_0	unattenuated signal intensity	µm	micrometer(s)
I_2	iodine	mmol	millimole
IBX	2-iodobenzoic acid	MnO_2	manganese dioxide
int.	internal	MS	mass spectrometry
i-Pr_2NEt	*N*,*N*-diisoproplyethylamine	MW	molecular weight
i-Pr_2O	diisopropyl ether	µW	microwave
IR	infrared	Na	sodium
J	coupling constant	Na_2SO_3	sodium carbonate
K_2CO_3	potassium carbonate	Na_2SO_4	sodium sulfate
K_a	association constant / binding constant	$NaBH(OAc)_3$	sodium triacetoxyborohydride
kcal	kilocalories	$NaBH_4$	sodium borohydride
k_{cat}	catalysed reaction rate	$NaHCO_3$	sodium bicarbonate
$KHCO_3$	potassium bicarbonate	NaOH	sodium hydroxide
kJ	kilojoule	NBS	*N*-bromosuccinimide
K_M	MICHAELIS-MENTEN constant	*n*-Bu_4NOH	tetrabutylammonium hydroxide
k_{non}	noncatalysed reaction rate	NDA	naphthalene-1,4,5,8-tetracarboxylic acid
KOH	potassium hydroxide	NDI	naphthalene diimide
LUMO	lowest unoccupied molecular orbital	neg.	negative
M	molar	NEt_3	triethylamine
m	medium	nm	nanometer(s)
m	meta	NMR	nuclear magnetic resonance
M.p.	melting point	NOESY	nuclear overhauser enhancement spectroscopy
MAHT	malonic acid half thioester	*o*	ortho
mbar	millibar	*p*	para
m_c	centered multiplet	Pd/C	palladium on charcoal
Me	methyl	PDI	perylene diimide
MeCN	acetonitrile	PF_6^-	hexafluorophosphate
MeCN-d_3	deuterated acetonitrile	PFGSE	pulsed field gradient spin echo

Ph	phenyl
pD	potential of deuterium
pH	potential of hydrogen
PhCN	benzonitrile
$PhNO_2$	nitrobenzene
POC	porous organic cage
pos.	positive
PPh_3	triphenylphosphine
ppm	parts per million
p-TsOH	*para*-toluenesulfonic acid
Q_{zz}	quadrupole moment
r.t.	room temperature
R_e	equilibrium distance
ReO_4^-	perrhenate
R_f	retention factor
RMS	root mean square
s	singlet
s	strong
S	substrate
sat.	saturated
SbF_6^-	hexafluoroantimonate
SiO_2	silica gel
$SOCl_2$	thionyl chloride
Std.	standard
t	triplet
TAZ	*s*-triazine
TBA	tetrabutylammonium
TBAF	tetrabutylammonium fluoride
TBME	*tert*.-butyl methyl ether
t-BuOH	*tert*.-butanol
tert.	tertiary
Tet	tetratopic
Tf	triflate
TFA	trifluoroacetic acid
TFE	trifluoroethanol
TFZ	trifluoro-*s*-triazine
THF	tetrahydrofuran
THP	tetrahydropyran
TIPS	trisopropyl
TLC	thin layer chromatography
TOF	time of flight
TPTI	triphenylene triimide
TREN	tris(2-aminoethyl)amine
Tri	tritopic
TRPN	tris(3-aminopropyl)amine
TS	transition state
TTA	triphenylene trianhydride
UV	ultraviolet
vs	very strong
τ	lifetime
$\tau_{1/2}$	half-life
ϑ_m	melting point

7 References

[1] Fischer, E. Einfluss Der Configuration Auf Die Wirkung Der Enzyme. *Ber. Dtsch. Chem. Ges.* **1894**, *27* (3), 2985–2993.

[2] Koshland Jr., D. E. Application of a Theory of Enzyme Specificity to Protein Synthesis. *Proc. Natl. Acad. Sci.* **1958**, *44* (2), 98–104.

[3] Koshland Jr., D. E. The Key-Lock Theory and the Induced Fit Theory. *Angew. Chem. Int. Ed.* **1995**, *33* (23–24), 2375–2378.

[4] Huang, F.; Anslyn, E. V. Introduction: Supramolecular Chemistry. *Chem. Rev.* **2015**, *115* (15), 6999–7000.

[5] Burley, S. K.; Petsko, G. A. Aromatic-Aromatic Interaction: A Mechanism of Protein Structure Stabilization. *Science* **1985**, *229* (4708), 23–28.

[6] Rutledge, L. R.; Campbell-Verduyn, L. S.; Wetmore, S. D. Characterization of the Stacking Interactions between DNA or RNA Nucleobases and the Aromatic Amino Acids. *Chem. Phys. Lett.* **2007**, *444* (1), 167–175.

[7] Li, S.; Cooper, V. R.; Thonhauser, T.; Lundqvist, B. I.; Langreth, D. C. Stacking Interactions and DNA Intercalation. *J. Phys. Chem. B* **2009**, *113* (32), 11166–11172.

[8] Fagnani, D. E.; Sotuyo, A.; Castellano, R. K. 1.06 - π–π Interactions. In *Comprehensive Supramolecular Chemistry II*; Atwood, J. L., Ed.; Elsevier: Oxford, 2017; pp 121–148.

[9] Zhuang, W.-R.; Wang, Y.; Cui, P.-F.; Xing, L.; Lee, J.; Kim, D.; Jiang, H.-L.; Oh, Y.-K. Applications of π–π Stacking Interactions in the Design of Drug-Delivery Systems. *J. Controlled Release* **2019**, *294*, 311–326.

[10] Ma, J. C.; Dougherty, D. A. The Cation-π Interaction. *Chem. Rev.* **1997**, *97* (5), 1303–1324.

[11] Mahadevi, A. S.; Sastry, G. N. Cation–π Interaction: Its Role and Relevance in Chemistry, Biology, and Material Science. *Chem. Rev.* **2013**, *113* (3), 2100–2138.

[12] Kumar, N.; Gaur, A. S.; Sastry, G. N. A Perspective on the Nature of Cation–π Interactions. *J. Chem. Sci.* **2021**, *133* (4), 97.

[13] Tsuzuki, S.; Yoshida, M.; Uchimaru, T.; Mikami, M. The Origin of the Cation/π Interaction: The Significant Importance of the Induction in Li^+ and Na^+ Complexes. *J. Phys. Chem. A* **2001**, *105* (4), 769–773.

[14] Kennedy, C. R.; Lin, S.; Jacobsen, E. N. The Cation–π Interaction in Small-Molecule Catalysis. *Angew. Chem. Int. Ed.* **2016**, *55* (41), 12596–12624.

[15] Yamada, S. Cation–π Interactions in Organic Synthesis. *Chem. Rev.* **2018**, *118* (23), 11353–11432.

[16] Knowles, R. R.; Lin, S.; Jacobsen, E. N. Enantioselective Thiourea-Catalyzed Cationic Polycyclizations. *J. Am. Chem. Soc.* **2010**, *132* (14), 5030–5032.

[17] Faraldos, J. A.; Antonczak, A. K.; González, V.; Fullerton, R.; Tippmann, E. M.; Allemann, R. K. Probing Eudesmane Cation–π Interactions in Catalysis by Aristolochene Synthase with Non-Canonical Amino Acids. *J. Am. Chem. Soc.* **2011**, *133* (35), 13906–13909.

[18] Holland, M. C.; Paul, S.; Schweizer, W. B.; Bergander, K.; Mück-Lichtenfeld, C.; Lakhdar, S.; Mayr, H.; Gilmour, R. Noncovalent Interactions in Organocatalysis: Modulating Conformational Diversity and Reactivity in the MacMillan Catalyst. *Angew. Chem. Int. Ed.* **2013**, *52* (31), 7967–7971.

[19] Zhao, C.; Toste, F. D.; Raymond, K. N.; Bergman, R. G. Nucleophilic Substitution Catalyzed by a Supramolecular Cavity Proceeds with Retention of Absolute Stereochemistry. *J. Am. Chem. Soc.* **2014**, *136* (41), 14409–14412.

[20] Zhang, Q.; Tiefenbacher, K. Terpene Cyclization Catalysed inside a Self-Assembled Cavity. *Nat. Chem.* **2015**, *7* (3), 197–202.

[21] Hiraoka, K.; Mizuse, S.; Yamabe, S. A Determination of the Stabilities and Structures of $F^-(C_6H_6)$ and $F^-(C_6F_6)$ Clusters. *J. Chem. Phys.* **1987**, *86* (7), 4102–4105.

[22] Hiraoka, K.; Mizuse, S.; Yamabe, S. High-Symmetric Structure of the Gas-Phase Cluster Ions $X\cdots C_6F_6$ (X = Cl, Br, and I). *J. Phys. Chem.* **1987**, *91* (20), 5294–5297.

[23] Meisenheimer, J. Ueber Reactionen Aromatischer Nitrokörper. *Justus Liebigs Ann. Chem.* **1902**, *323* (2), 205–246.

[24] Schneider, H.-J. Mechanisms of Molecular Recognition: Investigations of Organic Host-Guest Complexes. *Angew. Chem. Int. Ed. Engl.* **1991**, *30* (11), 1417–1436.

[25] Schneider, H.-J.; Werner, F.; Blatter, T. Attractive Interactions between Negative Charges and Polarizable Aryl Parts of Host-Guest Systems. *J. Phys. Org. Chem.* **1993**, *6* (10), 590–594.

[26] Alkorta, I.; Rozas, I.; Elguero, J. An Attractive Interaction between the π-Cloud of C_6F_6 and Electron-Donor Atoms. *J. Org. Chem.* **1997**, *62* (14), 4687–4691.

[27] Danten, Y.; Tassaing, T.; Besnard, M. On the Nature of the Water-Hexafluorobenzene Interaction. *J. Phys. Chem. A* **1999**, *103* (18), 3530–3534.

[28] Gallivan, J. P.; Dougherty, D. A. Can Lone Pairs Bind to a π System? The Water···Hexafluorobenzene Interaction. *Org. Lett.* **1999**, *1* (1), 103–106.

[29] Mascal, M.; Armstrong, A.; Bartberger, M. D. Anion-Aromatic Bonding: A Case for Anion Recognition by π-Acidic Rings. *J. Am. Chem. Soc.* **2002**, *124* (22), 6274–6276.

[30] Alkorta, I.; Rozas, I.; Elguero, J. Interaction of Anions with Perfluoro Aromatic Compounds. *J. Am. Chem. Soc.* **2002**, *124* (29), 8593–8598.

[31] Quiñonero, D.; Garau, C.; Rotger, C.; Frontera, A.; Ballester, P.; Costa, A.; Deyà, P. M. Anion–π Interactions: Do They Exist? *Angew. Chem. Int. Ed.* **2002**, *41* (18), 3389–3392.

[32] Zhao, Y.; Domoto, Y.; Orentas, E.; Beuchat, C.; Emery, D.; Mareda, J.; Sakai, N.; Matile, S. Catalysis with Anion–π Interactions. *Angew. Chem. Int. Ed.* **2013**, *52* (38), 9940–9943.

[33] Zhao, Y.; Cotelle, Y.; Liu, L.; López-Andarias, J.; Bornhof, A.-B.; Akamatsu, M.; Sakai, N.; Matile, S. The Emergence of Anion–π Catalysis. *Acc. Chem. Res.* **2018**, *51* (9), 2255–2263.

[34] Garau, C.; Frontera, A.; Quiñonero, D.; Ballester, P.; Costa, A.; Deyà, P. M. A Topological Analysis of the Electron Density in Anion–π Interactions. *ChemPhysChem* **2003**, *4* (12), 1344–1348.

[35] Kim, D.; Tarakeshwar, P.; Kim, K. S. Theoretical Investigations of Anion−π Interactions: The Role of Anions and the Nature of π Systems. *J. Phys. Chem. A* **2004**, *108* (7), 1250–1258.

[36] Kim, D.; Lee, E. C.; Kim, K. S.; Tarakeshwar, P. Cation–π–Anion Interaction: A Theoretical Investigation of the Role of Induction Energies. *J. Phys. Chem. A* **2007**, *111* (32), 7980–7986.

[37] Kim, D. Y.; Singh, N. J.; Lee, J. W.; Kim, K. S. Solvent-Driven Structural Changes in Anion–π Complexes. *J. Chem. Theory Comput.* **2008**, *4* (7), 1162–1169.

[38] Kim, D. Y.; Singh, N. J.; Kim, K. S. Cyameluric Acid as Anion–π Type Receptor for ClO_4^- and NO_3^-: π-Stacked and Edge-to-Face Structures. *J. Chem. Theory Comput.* **2008**, *4* (8), 1401–1407.

[39] Battaglia, M. R.; Buckingham, A. D.; Williams, J. H. The Electric Quadrupole Moments of Benzene and Hexafluorobenzene. *Chem. Phys. Lett.* **1981**, *78* (3), 421–423.

[40] Schottel, B. L.; Chifotides, H. T.; Dunbar, K. R. Anion–π Interactions. *Chem. Soc. Rev.* **2008**, *37* (1), 68–83.

[41] Mareda, J.; Matile, S. Anion–π Slides for Transmembrane Transport. *Chem. - Eur. J.* **2009**, *15* (1), 28–37.

[42] Hernández-Trujillo, J.; Vela, A. Molecular Quadrupole Moments for the Series of Fluoro- and Chlorobenzenes. *J. Phys. Chem.* **1996**, *100* (16), 6524–6530.

[43] Garau, C.; Quiñonero, D.; Frontera, A.; Ballester, P.; Costa, A.; Deyà, P. M. Dual Binding Mode of *s*-Triazine to Anions and Cations. *Org. Lett.* **2003**, *5* (13), 2227–2229.

[44] Frontera, A.; Saczewski, F.; Gdaniec, M.; Dziemidowicz-Borys, E.; Kurland, A.; Deyà, P. M.; Quiñonero, D.; Garau, C. Anion–π Interactions in Cyanuric Acids: A Combined Crystallographic and Computational Study. *Chem. - Eur. J.* **2005**, *11* (22), 6560–6567.

[45] Frontera, A.; Gamez, P.; Mascal, M.; Mooibroek, T. J.; Reedijk, J. Putting Anion–π Interactions Into Perspective. *Angew. Chem. Int. Ed.* **2011**, *50* (41), 9564–9583.

[46] Garau, C.; Quiñonero, D.; Frontera, A.; Ballester, P.; Costa, A.; Deyà, P. M. Approximate Additivity of Anion–π Interactions: An Ab Initio Study on Anion–π, Anion–π_2 and Anion–π_3 Complexes. *J. Phys. Chem. A* **2005**, *109* (41), 9341–9345.

[47] Berryman, O. B.; Bryantsev, V. S.; Stay, D. P.; Johnson, D. W.; Hay, B. P. Structural Criteria for the Design of Anion Receptors: The Interaction of Halides with Electron-Deficient Arenes. *J. Am. Chem. Soc.* **2007**, *129* (1), 48–58.

[48] Albrecht, M.; Wessel, C.; de Groot, M.; Rissanen, K.; Lüchow, A. Structural Versatility of Anion–π Interactions in Halide Salts with Pentafluorophenyl Substituted Cations. *J. Am. Chem. Soc.* **2008**, *130* (14), 4600–4601.

[49] Estarellas, C.; Bauzá, A.; Frontera, A.; Quiñonero, D.; Deyà, P. M. On the Directionality of Anion–π Interactions. *Phys. Chem. Chem. Phys.* **2011**, *13* (13), 5696–5702.

[50] Hay, B. P.; Custelcean, R. Anion–π Interactions in Crystal Structures: Commonplace or Extraordinary? *Cryst. Growth Des.* **2009**, *9* (6), 2539–2545.

[51] Mascal, M.; Yakovlev, I.; Nikitin, E. B.; Fettinger, J. C. Fluoride-Selective Host Based on Anion–π Interactions, Ion Pairing, and Hydrogen Bonding: Synthesis and Fluoride-Ion Sandwich Complex. *Angew. Chem. Int. Ed.* **2007**, *46* (46), 8782–8784.

[52] Dawson, R. E.; Hennig, A.; Weimann, D. P.; Emery, D.; Ravikumar, V.; Montenegro, J.; Takeuchi, T.; Gabutti, S.; Mayor, M.; Mareda, J.; Schalley, C. A.; Matile, S. Experimental Evidence for the Functional Relevance of Anion–π Interactions. *Nat. Chem.* **2010**, *2* (7), 533–538.

[53] Chifotides, H. T.; Schottel, B. L.; Dunbar, K. R. The π-Accepting Arene HAT$(CN)_6$ as a Halide Receptor through Charge Transfer: Multisite Anion Interactions and Self-Assembly in Solution and the Solid State. *Angew. Chem. Int. Ed.* **2010**, *49* (40), 7202–7207.

[54] Berryman, O. B.; Hof, F.; Hynes, M. J.; Johnson, D. W. Anion–π Interaction Augments Halide Binding in Solution. *Chem. Commun.* **2006**, No. 5, 506–508.

[55] Gorteau, V.; Bollot, G.; Mareda, J.; Matile, S. Rigid-Rod Anion–π Slides for Multiion Hopping across Lipid Bilayers. *Org. Biomol. Chem.* **2007**, *5* (18), 3000–3012.

[56] Gil-Ramírez, G.; Escudero-Adán, E. C.; Benet-Buchholz, J.; Ballester, P. Quantitative Evaluation of Anion–π Interactions in Solution. *Angew. Chem. Int. Ed.* **2008**, *47* (22), 4114–4118.

[57] Wang, D.-X.; Zheng, Q.-Y.; Wang, Q.-Q.; Wang, M.-X. Halide Recognition by Tetraoxacalix[2]arene[2]triazine Receptors: Concurrent Noncovalent Halide–π and Lone-Pair–π Interactions in Host–Halide–Water Ternary Complexes. *Angew. Chem. Int. Ed.* **2008**, *47* (39), 7485–7488.

[58] Berryman, O. B.; Sather, A. C.; Hay, B. P.; Meisner, J. S.; Johnson, D. W. Solution Phase Measurement of Both Weak σ and C−H···X⁻ Hydrogen Bonding Interactions in Synthetic Anion Receptors. *J. Am. Chem. Soc.* **2008**, *130* (33), 10895–10897.

[59] de Hoog, P.; Gamez, P.; Mutikainen, I.; Turpeinen, U.; Reedijk, J. An Aromatic Anion Receptor: Anion–π Interactions Do Exist. *Angew. Chem. Int. Ed.* **2004**, *43* (43), 5815–5817.

[60] Demeshko, S.; Dechert, S.; Meyer, F. Anion−π Interactions in a Carousel Copper(II)−Triazine Complex. *J. Am. Chem. Soc.* **2004**, *126* (14), 4508–4509.

[61] Schottel, B. L.; Chifotides, H. T.; Shatruk, M.; Chouai, A.; Pérez, L. M.; Bacsa, J.; Dunbar, K. R. Anion−π Interactions as Controlling Elements in Self-Assembly Reactions of Ag(I) Complexes with π-Acidic Aromatic Rings. *J. Am. Chem. Soc.* **2006**, *128* (17), 5895–5912.

[62] Zhou, X.-P.; Zhang, X.; Lin, S.-H.; Li, D. Anion−π-Interaction-Directed Self-Assembly of Ag(I) Coordination Networks. *Cryst. Growth Des.* **2007**, *7* (3), 485–487.

[63] Black, C. A.; Hanton, L. R.; Spicer, M. D. A Coordination Polymer Strategy for Anion Encapsulation: Anion–π Interactions in (4,4) Nets Formed from Ag(I) Salts and a Flexible Pyrimidine Ligand. *Chem. Commun.* **2007**, (30), 3171–3173.

[64] Kennan, A. J.; Whitlock, H. W. Host-Catalyzed Isoxazole Ring Opening: A Rationally Designed Artificial Enzyme. *J. Am. Chem. Soc.* **1996**, *118* (12), 3027–3028.

[65] Hollfelder, F.; Kirby, A. J.; Tawfik, D. S. On the Magnitude and Specificity of Medium Effects in Enzyme-like Catalysts for Proton Transfer. *J. Org. Chem.* **2001**, *66* (17), 5866–5874.

[66] Hu, Y.; Houk, K. N.; Kikuchi, K.; Hotta, K.; Hilvert, D. Nonspecific Medium Effects versus Specific Group Positioning in the Antibody and Albumin Catalysis of the Base-Promoted Ring-Opening Reactions of Benzisoxazoles. *J. Am. Chem. Soc.* **2004**, *126* (26), 8197–8205.

[67] Röthlisberger, D.; Khersonsky, O.; Wollacott, A. M.; Jiang, L.; DeChancie, J.; Betker, J.; Gallaher, J. L.; Althoff, E. A.; Zanghellini, A.; Dym, O.; Albeck, S.; Houk, K. N.; Tawfik, D. S.; Baker, D. Kemp Elimination Catalysts by Computational Enzyme Design. *Nature* **2008**, *453* (7192), 190–195.

[68] Zhao, Y.; Benz, S.; Sakai, N.; Matile, S. Selective Acceleration of Disfavored Enolate Addition Reactions by Anion–π Interactions. *Chem. Sci.* **2015**, *6* (11), 6219–6223.

[69] Cotelle, Y.; Benz, S.; Avestro, A.-J.; Ward, T. R.; Sakai, N.; Matile, S. Anion–π Catalysis of Enolate Chemistry: Rigidified Leonard Turns as a General Motif to Run Reactions on Aromatic Surfaces. *Angew. Chem. Int. Ed.* **2016**, *55* (13), 4275–4279.

[70] Leonard, N. J. Trimethylene Bridges as Synthetic Spacers for the Detection of Intramolecular Interactions. *Acc. Chem. Res.* **1979**, *12* (12), 423–429.

[71] Zhao, Y.; Cotelle, Y.; Avestro, A.-J.; Sakai, N.; Matile, S. Asymmetric Anion–π Catalysis: Enamine Addition to Nitroolefins on π-Acidic Surfaces. *J. Am. Chem. Soc.* **2015**, *137* (36), 11582–11585.

[72] Akamatsu, M.; Matile, S. Expanded Chiral Surfaces for Asymmetric Anion–π Catalysis. *Synlett* **2016**, *27* (7), 1041–1046.

[73] Hayashi, Y.; Gotoh, H.; Hayashi, T.; Shoji, M. Diphenylprolinol Silyl Ethers as Efficient Organocatalysts for the Asymmetric Michael Reaction of Aldehydes and Nitroalkenes. *Angew. Chem. Int. Ed.* **2005**, *44* (27), 4212–4215.

[74] Marigo, M.; Wabnitz, T. C.; Fielenbach, D.; Jørgensen, K. A. Enantioselective Organocatalyzed α Sulfenylation of Aldehydes. *Angew. Chem. Int. Ed.* **2005**, *44* (5), 794–797.

[75] Seebach, D.; Sun, X.; Sparr, C.; Ebert, M.-O.; Schweizer, W. B.; Beck, A. K. 1,2-Oxazine N-Oxides as Catalyst Resting States in Michael Additions of Aldehydes to Nitro Olefins Organocatalyzed by α,α-Diphenylprolinol Trimethylsilyl Ether. *Helv. Chim. Acta* **2012**, *95* (7), 1064–1078.

[76] Jensen, K. L.; Dickmeiss, G.; Jiang, H.; Albrecht, Ł.; Jørgensen, K. A. The Diarylprolinol Silyl Ether System: A General Organocatalyst. *Acc. Chem. Res.* **2012**, *45* (2), 248–264.

[77] Wiesner, M.; Revell, J. D.; Wennemers, H. Tripeptides as Efficient Asymmetric Catalysts for 1,4-Addition Reactions of Aldehydes to Nitroolefins - A Rational Approach. *Angew. Chem. Int. Ed.* **2008**, *47* (10), 1871–1874.

[78] Duschmalé, J.; Wahl, J.; Wiesner, M.; Wennemers, H. Effects of Internal and External Carboxylic Acids on the Reaction Pathway of Organocatalytic 1,4-Addition Reactions between Aldehydes and Nitroolefins. *Chem. Sci.* **2013**, *4* (3), 1312–1318.

[79] Wang, C.; Miros, F. N.; Mareda, J.; Sakai, N.; Matile, S. Asymmetric Anion–π Catalysis on Perylenediimides. *Angew. Chem. Int. Ed.* **2016**, *55* (46), 14422–14426.

[80] Zhang, X.; Hao, X.; Liu, L.; Pham, A.-T.; López-Andarias, J.; Frontera, A.; Sakai, N.; Matile, S. Primary Anion−π Catalysis and Autocatalysis. *J. Am. Chem. Soc.* **2018**, *140* (51), 17867–17871.

[81] Baldwin, J. E. Rules for Ring Closure. *J. Chem. Soc., Chem. Commun.* **1976**, (18), 734–736.

[82] Paraja, M.; Matile, S. Primary Anion–π Catalysis of Epoxide-Opening Ether Cyclization into Rings of Different Sizes: Access to New Reactivity. *Angew. Chem. Int. Ed.* **2020**, *59* (15), 6273–6277.

[83] Paraja, M.; Hao, X.; Matile, S. Polyether Natural Product Inspired Cascade Cyclizations: Autocatalysis on π-Acidic Aromatic Surfaces. *Angew. Chem. Int. Ed.* **2020**, *59* (35), 15093–15097.

[84] Liu, L.; Cotelle, Y.; Avestro, A.-J.; Sakai, N.; Matile, S. Asymmetric Anion−π Catalysis of Iminium/Nitroaldol Cascades To Form Cyclohexane Rings with Five Stereogenic Centers Directly on π-Acidic Surfaces. *J. Am. Chem. Soc.* **2016**, *138* (25), 7876–7879.

[85] Liu, L.; Cotelle, Y.; Bornhof, A.-B.; Besnard, C.; Sakai, N.; Matile, S. Anion–π Catalysis of Diels-Alder Reactions. *Angew. Chem. Int. Ed.* **2017**, *56* (42), 13066–13069.

[86] Wang, C.; Matile, S. Anion−π Catalysts with Axial Chirality. *Chem. - Eur. J.* **2017**, *23* (49), 11955–11960.

[87] Liu, L.; Cotelle, Y.; Klehr, J.; Sakai, N.; Ward, T. R.; Matile, S. Anion–π Catalysis: Bicyclic Products with Four Contiguous Stereogenic Centers from Otherwise Elusive Diastereospecific Domino Reactions on π-Acidic Surfaces. *Chem. Sci.* **2017**, *8* (5), 3770–3774.

[88] Akamatsu, M.; Sakai, N.; Matile, S. Electric-Field-Assisted Anion−π Catalysis. *J. Am. Chem. Soc.* **2017**, *139* (19), 6558–6561.

[89] López-Andarias, J.; Frontera, A.; Matile, S. Anion−π Catalysis on Fullerenes. *J. Am. Chem. Soc.* **2017**, *139* (38), 13296–13299.

[90] Liu, L.; Matile, S. Anion–π Transaminase Mimics. *Supramol. Chem.* **2017**, *29* (10), 702–706.

[91] López-Andarias, J.; Bauzá, A.; Sakai, N.; Frontera, A.; Matile, S. Remote Control of Anion–π Catalysis on Fullerene-Centered Catalytic Triads. *Angew. Chem. Int. Ed.* **2018**, *57* (34), 10883–10887.

[92] Zhang, X.; Liu, L.; López-Andarias, J.; Wang, C.; Sakai, N.; Matile, S. Anion–π Catalysis: Focus on Nonadjacent Stereocenters. *Helv. Chim. Acta* **2018**, *101* (2), e1700288.

[93] Bornhof, A.-B.; Bauzá, A.; Aster, A.; Pupier, M.; Frontera, A.; Vauthey, E.; Sakai, N.; Matile, S. Synergistic Anion–$(\pi)_n$–π Catalysis on π-Stacked Foldamers. *J. Am. Chem. Soc.* **2018**, *140* (14), 4884–4892.

[94] Bornhof, A.-B.; Vázquez-Nakagawa, M.; Rodríguez-Pérez, L.; Herranz, M. Á.; Sakai, N.; Martín, N.; Matile, S.; López-Andarias, J. Anion–π Catalysis on Carbon Nanotubes. *Angew. Chem. Int. Ed.* **2019**, *58* (45), 16097–16100.

[95] Pham, A.-T.; Matile, S. Peptide Stapling with Anion–π Catalysts. *Chem. - Asian J.* **2020**, *15* (10), 1562–1566.

[96] López, M. Á. G.; Tan, M.-L.; Frontera, A.; Matile, S. The Origin of Anion−π Autocatalysis. *JACS Au* **2023**. https://doi.org/10.1021/jacsau.2c00656.

[97] Black, S. P.; Stefankiewicz, A. R.; Smulders, M. M. J.; Sattler, D.; Schalley, C. A.; Nitschke, J. R.; Sanders, J. K. M. Generation of a Dynamic System of Three-Dimensional Tetrahedral Polycatenanes. *Angew. Chem. Int. Ed.* **2013**, *52* (22), 5749–5752.

[98] Ronson, T. K.; Roberts, D. A.; Black, S. P.; Nitschke, J. R. Stacking Interactions Drive Selective Self-Assembly and Self-Sorting of Pyrene-Based $M^{II}_4L_6$ Architectures. *J. Am. Chem. Soc.* **2015**, *137* (45), 14502–14512.

[99] Black, S. P.; Wood, D. M.; Schwarz, F. B.; Ronson, T. K.; Holstein, J. J.; Stefankiewicz, A. R.; Schalley, C. A.; Sanders, J. K. M.; Nitschke, J. R. Catenation and Encapsulation Induce Distinct Reconstitutions within a Dynamic Library of Mixed-Ligand Zn_4L_6 Cages. *Chem. Sci.* **2016**, *7* (4), 2614–2620.

[100] Lu, Z.; Lavendomme, R.; Burghaus, O.; Nitschke, J. R. A Zn_4L_6 Capsule with Enhanced Catalytic C−C Bond Formation Activity upon C_{60} Binding. *Angew. Chem. Int. Ed.* **2019**, *58* (27), 9073–9077.

[101] Lu, Z.; Ronson, T. K.; Nitschke, J. R. Reversible Reduction Drives Anion Ejection and C_{60} Binding within an $Fe^{II}_4L_6$ Cage. *Chem. Sci.* **2020**, *11* (4), 1097–1101.

[102] Pedersen, C. J. Cyclic Polyethers and Their Complexes with Metal Salts. *J. Am. Chem. Soc.* **1967**, *89* (10), 2495–2496.

[103] Pedersen, C. J. Cyclic Polyethers and Their Complexes with Metal Salts. *J. Am. Chem. Soc.* **1967**, *89* (26), 7017–7036.

[104] Rodrigue, A.; Bovenkamp, J. W.; Lacroix, B. V.; Bannard, R. A. B.; Buchanan, G. W. Complexes of 18-Crown-6 Macrocyclic Ethers Obtained from Ethereal Solvents. Complexes of Potassium and Sodium Salts with Host:Guest Ratios of 1:2 and 1:3. *Can. J. Chem.* **1986**, *64* (4), 808–815.

[105] Atwood, J. L.; Bott, S. G.; Means, C. M.; Coleman, A. W.; Zhang, H.; May, M. T. Synthesis of Salts of the Hydrogen Dichloride Anion in Aromatic Solvents. 2. Syntheses and Crystal Structures of [K·18-Crown-6][Cl–H–Cl], $[Mg·18\text{-Crown-6}][Cl–H–Cl]_2$, $[H_3O·18\text{-Crown-6}][Cl–H–Cl]$, and the Related $[H_3O·18\text{-Crown-6}][Br–H–Br]$. *Inorg. Chem.* **1990**, *29* (3), 467–470.

[106] Sam, D. J.; Simmons, H. E. Crown Ether Chemistry. Substitution Reactions of Potassium Halide and Potassium Hydroxide Complexes of Dicyclohexyl-18-Crown-6. *J. Am. Chem. Soc.* **1974**, *96* (7), 2252–2253.

[107] Raßhofer, W.; Oepen, G.; Vögtle, F. Crown Ether Assisted Chemical Reactions, II. Crown Ether Complexes of Potassium Phthalimide, Sodium Saccharinate and Sodium Acetylacetonate: New Reagents Containing Activated Anions. *Isr. J. Chem.* **1979**, *18* (3–4), 249–252.

[108] Dietrich, B.; Lehn, J. M.; Sauvage, J. P. Diaza-polyoxa-macrocycles et macrobicycles. *Tetrahedron Lett.* **1969**, *10* (34), 2885–2888.

[109] Dietrich, B.; Lehn, J. M.; Sauvage, J. P. Les Cryptates. *Tetrahedron Lett.* **1969**, *10* (34), 2889–2892.

[110] Cox, B. G.; Schneider, H.; Stroka, J. Kinetics of Alkali Metal Complex Formation with Cryptands in Methanol. *J. Am. Chem. Soc.* **1978**, *100* (15), 4746–4749.

[111] Artz, S. P.; Cram, D. J. Host-Guest Complexation. 28. Hemispherands with Four Self-Organizing Units. *J. Am. Chem. Soc.* **1984**, *106* (7), 2160–2171.

[112] Metz, B.; Moras, D.; Weiss, R. Polyoxamacrobicyclic Diamines. Structure of 4,7,13,16,21,24-Hexaoxa-1,10-diazabicyclo[8.8.8]hexacosane and of Its Bisborohydride, $C_{18}H_{36}N_2O_6·2BH_3$. *J. Chem. Soc., Perkin Trans. 2* **1976**, (4), 423–429.

[113] Maverick, E.; Seiler, P.; Schweizer, W. B.; Dunitz, J. D. 1,4,7,10,13,16-Hexaoxacyclooctadecane: Crystal Structure at 100 K. *Acta Crystallogr., Sect. B: Struct. Sci., Cryst. Eng. Mater.* **1980**, *36* (3), 615–620.

[114] Alberto, R.; Ortner, K.; Wheatley, N.; Schibli, R.; Schubiger, A. P. Synthesis and Properties of Boranocarbonate: A Convenient in Situ CO Source for the Aqueous Preparation of $[^{99m}Tc(OH_2)_3(CO)_3]^+$. *J. Am. Chem. Soc.* **2001**, *123* (13), 3135–3136.

[115] Kotlyar, S. A.; Zubatyuk, R. I.; Shishkin, O. V.; Chuprin, G. N.; Kiriyak, A. V.; Kamalov, G. L. (18-Crown-6)Potassium Chlorochromate. *Acta Crystallogr., Sect. E: Crystallogr. Commun.* **2005**, *61* (2), m293–m295.

[116] Cram, D. J.; Lein, G. M. Host-Guest Complexation. 36. Spherand and Lithium and Sodium Ion Complexation Rates and Equilibria. *J. Am. Chem. Soc.* **1985**, *107* (12), 3657–3668.

[117] Jin, Y.; Yu, C.; Denman, R. J.; Zhang, W. Recent Advances in Dynamic Covalent Chemistry. *Chem. Soc. Rev.* **2013**, *42* (16), 6634–6654.

[118] Lehn, J.-M. From Supramolecular Chemistry towards Constitutional Dynamic Chemistry and Adaptive Chemistry. *Chem. Soc. Rev.* **2007**, *36* (2), 151–160.

[119] Corbett, P. T.; Leclaire, J.; Vial, L.; West, K. R.; Wietor, J.-L.; Sanders, J. K. M.; Otto, S. Dynamic Combinatorial Chemistry. *Chem. Rev.* **2006**, *106* (9), 3652–3711.

[120] Aida, T.; Meijer, E. W.; Stupp, S. I. Functional Supramolecular Polymers. *Science* **2012**, *335* (6070), 813–817.

[121] Mastalerz, M. Shape-Persistent Organic Cage Compounds by Dynamic Covalent Bond Formation. *Angew. Chem. Int. Ed.* **2010**, *49* (30), 5042–5053.

[122] Heppekausen, J.; Stade, R.; Goddard, R.; Fürstner, A. Practical New Silyloxy-Based Alkyne Metathesis Catalysts with Optimized Activity and Selectivity Profiles. *J. Am. Chem. Soc.* **2010**, *132* (32), 11045–11057.

[123] Jyothish, K.; Zhang, W. Towards Highly Active and Robust Alkyne Metathesis Catalysts: Recent Developments in Catalyst Design. *Angew. Chem. Int. Ed.* **2011**, *50* (37), 8478–8480.

[124] Gross, D. E.; Moore, J. S. Arylene-Ethynylene Macrocycles via Depolymerization-Macrocyclization. *Macromolecules* **2011**, *44* (10), 3685–3687.

[125] Zhang, C.; Wang, Q.; Long, H.; Zhang, W. A Highly C_{70} Selective Shape-Persistent Rectangular Prism Constructed through One-Step Alkyne Metathesis. *J. Am. Chem. Soc.* **2011**, *133* (51), 20995–21001.

[126] Zhang, C.; Long, H.; Zhang, W. A C_{84} Selective Porphyrin Macrocycle with an Adaptable Cavity Constructed through Alkyne Metathesis. *Chem. Commun.* **2012**, *48* (49), 6172–6174.

[127] Sisco, S. W.; Moore, J. S. Directional Cyclooligomers via Alkyne Metathesis. *J. Am. Chem. Soc.* **2012**, *134* (22), 9114–9117.

[128] Cacciapaglia, R.; Di Stefano, S.; Mandolini, L. Metathesis Reaction of Formaldehyde Acetals: An Easy Entry into the Dynamic Covalent Chemistry of Cyclophane Formation. *J. Am. Chem. Soc.* **2005**, *127* (39), 13666–13671.

[129] Berrocal, J. A.; Cacciapaglia, R.; Di Stefano, S. A Well-Behaved Dynamic Library of Cyclophane Formaldehyde Acetals Incorporating Diphenylmethane Units. *Org. Biomol. Chem.* **2011**, *9* (23), 8190–8194.

[130] Li, J.; Carnall, J. M. A.; Stuart, M. C. A.; Otto, S. Hydrogel Formation upon Photoinduced Covalent Capture of Macrocycle Stacks from Dynamic Combinatorial Libraries. *Angew. Chem. Int. Ed.* **2011**, *50* (36), 8384–8386.

[131] Ponnuswamy, N.; Cougnon, F. B. L.; Clough, J. M.; Pantoş, G. D.; Sanders, J. K. M. Discovery of an Organic Trefoil Knot. *Science* **2012**, *338* (6108), 783–785.

[132] Nishiyabu, R.; Kubo, Y.; James, T. D.; Fossey, J. S. Boronic Acid Building Blocks: Tools for Self Assembly. *Chem. Commun.* **2011**, *47* (4), 1124–1150.

[133] Schiff, H. Mittheilungen Aus Dem Universitätslaboratorium in Pisa: Eine Neue Reihe Organischer Basen. *Justus Liebigs Ann. Chem.* **1864**, *131* (1), 118–119.

[134] Jencks, W. P. Studies on the Mechanism of Oxime and Semicarbazone Formation[1]. *J. Am. Chem. Soc.* **1959**, *81* (2), 475–481.

[135] Jencks, W. P. Mechanism and Catalysis of Simple Carbonyl Group Reactions. In *Progress in Physical Organic Chemistry*; John Wiley & Sons, Ltd, 1964; pp 63–128.

[136] Martin, R. B. Reactions of Carbonyl Compounds with Amines and Derivatives. *J. Phys. Chem.* **1964**, *68* (6), 1369–1377.

[137] Jencks, W. P. Enforced General Acid-Base Catalysis of Complex Reactions and Its Limitations. *Acc. Chem. Res.* **1976**, *9* (12), 425–432.

[138] Mäkelä, M. J.; Korpela, T. K. Chemical Models of Enzymic Transimination. *Chem. Soc. Rev.* **1983**, *12* (3), 309–329.

[139] Ciaccia, M.; Di Stefano, S. Mechanisms of Imine Exchange Reactions in Organic Solvents. *Org. Biomol. Chem.* **2014**, *13* (3), 646–654.

[140] Belowich, M. E.; Stoddart, J. F. Dynamic Imine Chemistry. *Chem. Soc. Rev.* **2012**, *41* (6), 2003–2024.

[141] Quan, M. L. C.; Cram, D. J. Constrictive Binding of Large Guests by a Hemicarcerand Containing Four Portals. *J. Am. Chem. Soc.* **1991**, *113* (7), 2754–2755.

[142] Rue, N. M.; Sun, J.; Warmuth, R. Polyimine Container Molecules and Nanocapsules. *Isr. J. Chem.* **2011**, *51* (7), 743–768.

[143] Greenaway, R. L.; Santolini, V.; Bennison, M. J.; Alston, B. M.; Pugh, C. J.; Little, M. A.; Miklitz, M.; Eden-Rump, E. G. B.; Clowes, R.; Shakil, A.; Cuthbertson, H. J.; Armstrong, H.; Briggs, M. E.; Jelfs, K. E.; Cooper, A. I. High-Throughput Discovery of Organic Cages and Catenanes Using Computational Screening Fused with Robotic Synthesis. *Nat. Commun.* **2018**, *9* (1), 2849.

[144] Acharyya, K.; Mukherjee, P. S. Organic Imine Cages: Molecular Marriage and Applications. *Angew. Chem. Int. Ed.* **2019**, *58* (26), 8640–8653.

[145] Kołodziejski, M.; Stefankiewicz, A. R.; Lehn, J.-M. Dynamic Polyimine Macrobicyclic Cryptands – Self-Sorting with Component Selection. *Chem. Sci.* **2019**, *10* (6), 1836–1843.

[146] Gayen, K. S.; Das, T.; Chatterjee, N. Recent Advances in Tris-Primary Amine Based Organic Imine Cages and Related Amine Macrocycles. *Eur. J. Org. Chem.* **2021**, *2021* (6), 861–876.

[147] Chen, Y.; Lei, Y.; Tong, L.; Li, H. Stabilization of Dynamic Covalent Architectures by Multivalence. *Chem. - Eur. J.* **2022**, *28* (1), e202102910.

[148] Montà-González, G.; Sancenón, F.; Martínez-Máñez, R.; Martí-Centelles, V. Purely Covalent Molecular Cages and Containers for Guest Encapsulation. *Chem. Rev.* **2022**, *122* (16), 13636–13708.

[149] Self-Processes – Programmed Supramolecular Systems. In *Supramolecular Chemistry*; John Wiley & Sons, Ltd, 1995; pp 139–197. https://doi.org/10.1002/3527607439.ch9.

[150] Santolini, V.; Miklitz, M.; Berardo, E.; Jelfs, K. E. Topological Landscapes of Porous Organic Cages. *Nanoscale* **2017**, *9* (16), 5280–5298.

[151] Tranchemontagne, D. J.; Ni, Z.; O'Keeffe, M.; Yaghi, O. M. Reticular Chemistry of Metal-Organic Polyhedra. *Angew. Chem. Int. Ed.* **2008**, *47* (28), 5136–5147.

[152] Luo, X.-M.; Li, Y.-K.; Dong, X.-Y.; Zang, S.-Q. Platonic and Archimedean Solids in Discrete Metal-Containing Clusters. *Chem. Soc. Rev.* **2023**, *52* (1), 383–444.

[153] Jazwinski, J.; Lehn, J.-M.; Lilienbaum, D.; Ziessel, R.; Guilhem, J.; Pascard, C. Polyaza Macrobicyclic Cryptands: Synthesis, Crystal Structures of a Cyclophane Type Macrobicyclic Cryptand and of Its Dinuclear Copper(I) Cryptate, and Anion Binding Features. *J. Chem. Soc., Chem. Commun.* **1987**, (22), 1691–1694.

[154] MacDowell, D.; Nelson, J. Facile Synthesis of a New Family of Cage Molecules. *Tetrahedron Lett.* **1988**, *29* (3), 385–386.

[155] McDowell, D.; Nelson, J.; McKee, V. A Furan-Derived Schiff-Base Crypt and Incorporating the *trans*,*trans* Dicarbimine Link. *Polyhedron* **1989**, *8* (8), 1143–1145.

[156] Kocian, O.; Mortimer, R. J.; Beer, P. D. Novel Polytopic Macrocyclic Receptor Molecules Containing Multiple Bipyridyl and Dibenzo-18-Crown-6 Units. *Tetrahedron Lett.* **1990**, *31* (35), 5069–5072.

[157] de Mendoza, J.; Mesa, E.; Rodríguez-Ubis, J.-C.; Vázquez, P.; Vögtle, F.; Windscheif, P.-M.; Rissanen, K.; Lehn, J.-M.; Lilienbaum, D.; Ziessel, R. A New Macrobicyclic Tris-Bipyridine Ligand and Its Cu and Ag Complexes. *Angew. Chem. Int. Ed.* **1991**, *30* (10), 1331–1333.

[158] Lehn, J.-M.; Vigneron, J.-P.; Bkouche-Waksman, I.; Guilhem, J.; Pascard, C. Caro-Cryptands: Tris-Carotenoid Macrobicyclic Ligands – Synthesis, Crystal Structure, and Dinuclear Copper(I) Complexes. *Helv. Chim. Acta* **1992**, *75* (4), 1069–1077.

[159] Marrs, D. J.; McKee, V.; Nelson, J.; Lu, Q.; Harding, C. J. Pyridinophane Cryptand Hosts with Dicopper(I) or Dicopper(II) Preferences. *Inorg. Chim. Acta* **1993**, *211* (2), 195–202.

[160] Lu, Q.; Latour, J.-M.; Harding, C. J.; Martin, N.; Marrs, D. J.; McKee, V.; Nelson, J. Dicopper Cryptates with 1,1 and 1,3 Bridging Ligands: Spectroscopic, Magnetic and Electrochemical Properties. *J. Chem. Soc., Dalton Trans.* **1994**, (9), 1471–1478.

[161] Abidi, R.; Arnaud-Neu, F.; Drew, M. G. B.; Lahély, S.; Marrs, D.; Nelson, J.; Schwing-Weill, M.-J. Hexa Schiff-Base Cryptands: Solution Thermodynamic and X-Ray Crystallographic Studies of Main Group, Transition and Heavy Metal Ion Complexes. *J. Chem. Soc., Perkin Trans. 2* **1996**, (12), 2747–2755.

[162] McKee, V.; Nelson, J.; Town, R. M. Caged Oxoanions. *Chem. Soc. Rev.* **2003**, *32* (5), 309–325.

[163] Zhang, J.-H.; Xie, S.-M.; Chen, L.; Wang, B.-J.; He, P.-G.; Yuan, L.-M. Homochiral Porous Organic Cage with High Selectivity for the Separation of Racemates in Gas Chromatography. *Anal. Chem.* **2015**, *87* (15), 7817–7824.

[164] Brutschy, M.; Schneider, M. W.; Mastalerz, M.; Waldvogel, S. R. Direct Gravimetric Sensing of GBL by a Molecular Recognition Process in Organic Cage Compounds. *Chem. Commun.* **2013**, *49* (75), 8398–8400.

[165] Acharyya, K.; Mukherjee, P. S. A Fluorescent Organic Cage for Picric Acid Detection. *Chem. Commun.* **2014**, *50* (99), 15788–15791.

[166] Giri, N.; Del Pópolo, M. G.; Melaugh, G.; Greenaway, R. L.; Rätzke, K.; Koschine, T.; Pison, L.; Gomes, M. F. C.; Cooper, A. I.; James, S. L. Liquids with Permanent Porosity. *Nature* **2015**, *527* (7577), 216–220.

[167] Tozawa, T.; Jones, J. T. A.; Swamy, S. I.; Jiang, S.; Adams, D. J.; Shakespeare, S.; Clowes, R.; Bradshaw, D.; Hasell, T.; Chong, S. Y.; Tang, C.; Thompson, S.; Parker, J.; Trewin, A.; Bacsa, J.; Slawin, A. M. Z.; Steiner, A.; Cooper, A. I. Porous Organic Cages. *Nat. Mater.* **2009**, *8* (12), 973–978.

[168] Jones, J. T. A.; Hasell, T.; Wu, X.; Bacsa, J.; Jelfs, K. E.; Schmidtmann, M.; Chong, S. Y.; Adams, D. J.; Trewin, A.; Schiffman, F.; Cora, F.; Slater, B.; Steiner, A.; Day, G. M.; Cooper, A. I. Modular and Predictable Assembly of Porous Organic Molecular Crystals. *Nature* **2011**, *474* (7351), 367–371.

[169] Bojdys, M. J.; Briggs, M. E.; Jones, J. T. A.; Adams, D. J.; Chong, S. Y.; Schmidtmann, M.; Cooper, A. I. Supramolecular Engineering of Intrinsic and Extrinsic Porosity in Covalent Organic Cages. *J. Am. Chem. Soc.* **2011**, *133* (41), 16566–16571.

[170] Hasell, T.; Culshaw, J. L.; Chong, S. Y.; Schmidtmann, M.; Little, M. A.; Jelfs, K. E.; Pyzer-Knapp, E. O.; Shepherd, H.; Adams, D. J.; Day, G. M.; Cooper, A. I. Controlling the Crystallization of Porous Organic Cages: Molecular Analogs of Isoreticular Frameworks Using Shape-Specific Directing Solvents. *J. Am. Chem. Soc.* **2014**, *136* (4), 1438–1448.

[171] Slater, A. G.; Little, M. A.; Pulido, A.; Chong, S. Y.; Holden, D.; Chen, L.; Morgan, C.; Wu, X.; Cheng, G.; Clowes, R.; Briggs, M. E.; Hasell, T.; Jelfs, K. E.; Day, G. M.; Cooper, A. I. Reticular Synthesis of Porous Molecular 1D Nanotubes and 3D Networks. *Nat. Chem.* **2017**, *9* (1), 17–25.

[172] Ballester, P. Anion Binding in Covalent and Self-Assembled Molecular Capsules. *Chem. Soc. Rev.* **2010**, *39* (10), 3810–3830.

[173] Alibrandi, G.; Amendola, V.; Bergamaschi, G.; Fabbrizzi, L.; Licchelli, M. Bistren Cryptands and Cryptates: Versatile Receptors for Anion Inclusion and Recognition in Water. *Org. Biomol. Chem.* **2015**, *13* (12), 3510–3524.

[174] Heyer, D.; Lehn, J.-M. Anion Coordination Chemistry - Synthesis and Anion Binding Features of Cyclophane Type Macrobicyclic Anion Receptor Molecules. *Tetrahedron Lett.* **1986**, *27* (48), 5869–5872.

[175] Fujita, T.; Lehn, J.-M. Synthesis of Dome-Shaped Cyclophane Type Macrotricyclic Anion Receptor Molecules. *Tetrahedron Lett.* **1988**, *29* (14), 1709–1712.

[176] Menif, R.; Reibenspies, J.; Martell, A. E. Synthesis, Protonation Constants, and Copper(II) and Cobalt(II) Binding Constants of a New Octaaza Macrobicyclic Cryptand: $(MX)_3(TREN)_2$. Hydroxide and Carbonate Binding of the Dicopper(II) Cryptate and Crystal Structures of the Cryptand and of the Carbonato-Bridged Dinuclear Copper(II) Cryptate. *Inorg. Chem.* **1991**, *30* (18), 3446–3454.

[177] Farrell, D.; Gloe, K.; Gloe, K.; Goretzki, G.; McKee, V.; Nelson, J.; Nieuwenhuyzen, M.; Pál, I.; Stephan, H.; Town, R. M.; Wichmann, K. Towards Promising Oxoanion Extractants: Azacages and Open-Chain Counterparts. *Dalton Trans.* **2003**, (10), 1961–1968.

[178] Maubert, B. M.; Nelson, J.; McKee, V.; Town, R. M.; Pál, I. Selectivity for Dinegative versus Mononegative Oxoanionic Guests within a Cryptand Host. *J. Chem. Soc., Dalton Trans.* **2001**, (9), 1395–1397.

[179] Mason, S.; Clifford, T.; Seib, L.; Kuczera, K.; Bowman-James, K. Unusual Encapsulation of Two Nitrates in a Single Bicyclic Cage. *J. Am. Chem. Soc.* **1998**, *120* (34), 8899–8900.

[180] Clifford, T.; Danby, A.; Llinares, J. M.; Mason, S.; Alcock, N. W.; Powell, D.; Aguilar, J. A.; García-España, E.; Bowman-James, K. Anion Binding with Two Polyammonium Macrocycles of Different Dimensionality. *Inorg. Chem.* **2001**, *40* (18), 4710–4720.

[181] Nelson, J.; Nieuwenhuyzen, M.; Pál, I.; Town, R. M. Dual-Mode Recognition of Oxalate by Protonated Azacryptate Hosts; Conformational Response of the Guest Maximizes π-Stacking Interactions. *Chem. Commun.* **2002**, (19), 2266–2267.

[182] Lehn, J.-M.; Méric, R.; Vigneron, J.-P.; Bkouche-Waksman, I.; Pascard, C. Molecular Recognition of Anionic Substrates. Binding of Carboxylates by a Macrobicyclic Coreceptor and Crystal Structure of Its Supramolecular Cryptate with the Terephthalate Dianion. *J. Chem. Soc., Chem. Commun.* **1991**, (2), 62–64.

[183] Mateus, P.; Delgado, R.; André, V.; Duarte, M. T. Dicarboxylate Recognition Properties of a Dinuclear Copper(II) Cryptate. *Inorg. Chem.* **2015**, *54* (1), 229–240.

[184] Benchimol, E.; Nguyen, B.-N. T.; Ronson, T. K.; Nitschke, J. R. Transformation Networks of Metal-Organic Cages Controlled by Chemical Stimuli. *Chem. Soc. Rev.* **2022**, *51* (12), 5101–5135.

[185] Cook, T. R.; Stang, P. J. Recent Developments in the Preparation and Chemistry of Metallacycles and Metallacages via Coordination. *Chem. Rev.* **2015**, *115* (15), 7001–7045.

[186] Chakrabarty, R.; Mukherjee, P. S.; Stang, P. J. Supramolecular Coordination: Self-Assembly of Finite Two- and Three-Dimensional Ensembles. *Chem. Rev.* **2011**, *111* (11), 6810–6918.

[187] Cook, T. R.; Zheng, Y.-R.; Stang, P. J. Metal-Organic Frameworks and Self-Assembled Supramolecular Coordination Complexes: Comparing and Contrasting the Design, Synthesis, and Functionality of Metal-Organic Materials. *Chem. Rev.* **2013**, *113* (1), 734–777.

[188] Cullen, W.; Misuraca, M. C.; Hunter, C. A.; Williams, N. H.; Ward, M. D. Highly Efficient Catalysis of the Kemp Elimination in the Cavity of a Cubic Coordination Cage. *Nat. Chem.* **2016**, *8* (3), 231–236.

[189] Leung, D. H.; Bergman, R. G.; Raymond, K. N. Highly Selective Supramolecular Catalyzed Allylic Alcohol Isomerization. *J. Am. Chem. Soc.* **2007**, *129* (10), 2746–2747.

[190] Clegg, J. K.; Cremers, J.; Hogben, A. J.; Breiner, B.; Smulders, M. M. J.; Thoburn, J. D.; Nitschke, J. R. A Stimuli Responsive System of Self-Assembled Anion-Binding $Fe_4L_6^{8+}$ Cages. *Chem. Sci.* **2012**, *4* (1), 68–76.

[191] Howson, S. E.; Allan, L. E. N.; Chmel, N. P.; Clarkson, G. J.; Gorkum, R. van; Scott, P. Self-Assembling Optically Pure $Fe(A–B)_3$ Chelates. *Chem. Commun.* **2009**, (13), 1727–1729.

[192] Dragna, J. M.; Pescitelli, G.; Tran, L.; Lynch, V. M.; Anslyn, E. V.; Di Bari, L. In Situ Assembly of Octahedral Fe(II) Complexes for the Enantiomeric Excess Determination of Chiral Amines Using Circular Dichroism Spectroscopy. *J. Am. Chem. Soc.* **2012**, *134* (9), 4398–4407.

[193] Albrecht, M.; Kotila, S. Formation of a "Meso-Helicate" by Self-Assembly of Three Bis(Catecholate) Ligands and Two Titanium(IV) Ions. *Angew. Chem. Int. Ed.* **1995**, *34* (19), 2134–2137.

[194] Xu, J.; Parac, T. N.; Raymond, K. N. *meso* Myths: What Drives Assembly of Helical versus *meso*-$[M_2L_3]$ Clusters? *Angew. Chem. Int. Ed.* **1999**, *38* (19), 2878–2882.

[195] Zhang, Z.; Dolphin, D. A Triple-Stranded Helicate and Mesocate from the Same Metal and Ligand. *Chem. Commun.* **2009**, (45), 6931–6933.

[196] Cui, F.; Li, S.; Jia, C.; Mathieson, J. S.; Cronin, L.; Yang, X.-J.; Wu, B. Anion-Dependent Formation of Helicates versus Mesocates of Triple-Stranded M_2L_3 ($M = Fe^{2+}$, Cu^{2+}) Complexes. *Inorg. Chem.* **2012**, *51* (1), 179–187.

[197] Cullen, W.; Hunter, C. A.; Ward, M. D. An Interconverting Family of Coordination Cages and a *meso*-Helicate; Effects of Temperature, Concentration, and Solvent on the Product Distribution of a Self-Assembly Process. *Inorg. Chem.* **2015**, *54* (6), 2626–2637.

[198] Chen, X.; Mevissen, C.; Huda, S.; Göb, C.; Oppel, I. M.; Albrecht, M. Cation-Controlled Formation and Interconversion of the *fac*/*fac* and *mer*/*mer* Stereoisomers of a Triple-Stranded Helicate. *Angew. Chem. Int. Ed.* **2019**, *58* (37), 12879–12882.

[199] Paul, R. L.; Argent, S. P.; Jeffery, J. C.; Harding, L. P.; Lynam, J. M.; Ward, M. D. Structures and Anion-Binding Properties of M_4L_6 Tetrahedral Cage Complexes with Large Central Cavities. *Dalton Trans.* **2004**, (21), 3453–3458.

[200] Ward, M. D.; Hunter, C. A.; Williams, N. H. Coordination Cages Based on Bis(Pyrazolylpyridine) Ligands: Structures, Dynamic Behavior, Guest Binding, and Catalysis. *Acc. Chem. Res.* **2018**, *51* (9), 2073–2082.

[201] Bilbeisi, R. A.; Clegg, J. K.; Elgrishi, N.; de Hatten, X.; Devillard, M.; Breiner, B.; Mal, P.; Nitschke, J. R. Subcomponent Self-Assembly and Guest-Binding Properties of Face-Capped $Fe_4L_4^{8+}$ Capsules. *J. Am. Chem. Soc.* **2012**, *134* (11), 5110–5119.

[202] Percástegui, E. G.; Mosquera, J.; Ronson, T. K.; Plajer, A. J.; Kieffer, M.; Nitschke, J. R. Waterproof Architectures through Subcomponent Self-Assembly. *Chem. Sci.* **2019**, *10* (7), 2006–2018.

[203] Percástegui, E. G.; Ronson, T. K.; Nitschke, J. R. Design and Applications of Water-Soluble Coordination Cages. *Chem. Rev.* **2020**, *120* (24), 13480–13544.

[204] Bolliger, J. L.; Belenguer, A. M.; Nitschke, J. R. Enantiopure Water-Soluble $[Fe_4L_6]$ Cages: Host–Guest Chemistry and Catalytic Activity. *Angew. Chem. Int. Ed.* **2013**, *52* (31), 7958–7962.

[205] Meng, W.; Clegg, J. K.; Thoburn, J. D.; Nitschke, J. R. Controlling the Transmission of Stereochemical Information through Space in Terphenyl-Edged Fe_4L_6 Cages. *J. Am. Chem. Soc.* **2011**, *133* (34), 13652–13660.

[206] Chandler, D. Hydrophobicity: Two Faces of Water. *Nature* **2002**, *417* (6888), 491–491.

[207] Pratt, L. R.; Pohorille, A. Hydrophobic Effects and Modeling of Biophysical Aqueous Solution Interfaces. *Chem. Rev.* **2002**, *102* (8), 2671–2692.

[208] Chandler, D. Interfaces and the Driving Force of Hydrophobic Assembly. *Nature* **2005**, *437* (7059), 640–647.

[209] Granick, S.; Bae, S. C. A Curious Antipathy for Water. *Science* **2008**, *322* (5907), 1477–1478.

[210] Biedermann, F.; Nau, W. M.; Schneider, H.-J. The Hydrophobic Effect Revisited-Studies with Supramolecular Complexes Imply High-Energy Water as a Noncovalent Driving Force. *Angew. Chem. Int. Ed.* **2014**, *53* (42), 11158–11171.

[211] Bistri, O.; Reinaud, O. Supramolecular Control of Transition Metal Complexes in Water by a Hydrophobic Cavity: A Bio-Inspired Strategy. *Org. Biomol. Chem.* **2015**, *13* (10), 2849–2865.

[212] Percástegui, E. G.; Mosquera, J.; Nitschke, J. R. Anion Exchange Renders Hydrophobic Capsules and Cargoes Water-Soluble. *Angew. Chem. Int. Ed.* **2017**, *56* (31), 9136–9140.

[213] Irving, H.; Williams, R. J. P. 637. The Stability of Transition-Metal Complexes. *J. Chem. Soc. Resumed* **1953**, (0), 3192–3210.

[214] Feltham, H. L. C.; Barltrop, A. S.; Brooker, S. Spin Crossover in Iron(II) Complexes of 3,4,5-Tri-Substituted-1,2,4-Triazole (Rdpt), 3,5-Di-Substituted-1,2,4-Triazolate (Dpt^-), and Related Ligands. *Coord. Chem. Rev.* **2017**, *344*, 26–53.

[215] Hunter, C. A.; Anderson, H. L. What Is Cooperativity? *Angew. Chem. Int. Ed.* **2009**, *48* (41), 7488–7499.

[216] von Krbek, L. K. S.; Schalley, C. A.; Thordarson, P. Assessing Cooperativity in Supramolecular Systems. *Chem. Soc. Rev.* **2017**, *46* (9), 2622–2637.

[217] Calvin, M.; Wilson, K. W. Stability of Chelate Compounds. *J. Am. Chem. Soc.* **1945**, *67* (11), 2003–2007.

[218] Adamson, A. W. A Proposed Approach to the Chelate Effect[1]. *J. Am. Chem. Soc.* **1954**, *76* (6), 1578–1579.

[219] Martell, A. E.; Hancock, R. D.; Motekaitis, R. J. Factors Affecting Stabilities of Chelate, Macrocyclic and Macrobicyclic Complexes in Solution. *Coord. Chem. Rev.* **1994**, *133*, 39–65.

[220] Castilla, A. M.; Ronson, T. K.; Nitschke, J. R. Sequence-Dependent Guest Release Triggered by Orthogonal Chemical Signals. *J. Am. Chem. Soc.* **2016**, *138* (7), 2342–2351.

[221] Pluth, M. D.; Raymond, K. N. Reversible Guest Exchange Mechanisms in Supramolecular Host-Guest Assemblies. *Chem. Soc. Rev.* **2007**, *36* (2), 161–171.

[222] Löffler, S.; Lübben, J.; Krause, L.; Stalke, D.; Dittrich, B.; Clever, G. H. Triggered Exchange of Anionic for Neutral Guests inside a Cationic Coordination Cage. *J. Am. Chem. Soc.* **2015**, *137* (3), 1060–1063.

[223] Garci, A.; Mbakidi, J.-P.; Chaleix, V.; Sol, V.; Orhan, E.; Therrien, B. Tunable Arene Ruthenium Metallaprisms to Transport, Shield, and Release Porphin in Cancer Cells. *Organometallics* **2015**, *34* (16), 4138–4146.

[224] Grommet, A. B.; Nitschke, J. R. Directed Phase Transfer of an $Fe^{II}_4L_4$ Cage and Encapsulated Cargo. *J. Am. Chem. Soc.* **2017**, *139* (6), 2176–2179.

[225] Zhang, D.; Ronson, T. K.; Mosquera, J.; Martinez, A.; Nitschke, J. R. Selective Anion Extraction and Recovery Using a $Fe^{II}_4L_4$ Cage. *Angew. Chem. Int. Ed.* **2018**, *57* (14), 3717–3721.

[226] Grancha, T.; Carné-Sánchez, A.; Hernández-López, L.; Albalad, J.; Imaz, I.; Juanhuix, J.; Maspoch, D. Phase Transfer of Rhodium(II)-Based Metal-Organic Polyhedra Bearing Coordinatively Bound Cargo Enables Molecular Separation. *J. Am. Chem. Soc.* **2019**, *141* (45), 18349–18355.

[227] Nguyen, B.-N. T.; Grommet, A. B.; Tron, A.; Georges, M. C. A.; Nitschke, J. R. Heat Engine Drives Transport of an $Fe^{II}_4L_4$ Cage and Cargo. *Adv. Mater.* **2020**, *32* (19), 1907241.

[228] Antonio, A. M.; Korman, K. J.; Yap, G. P. A.; Bloch, E. D. Porous Metal-Organic Alloys Based on Soluble Coordination Cages. *Chem. Sci.* **2020**, *11* (46), 12540–12546.

[229] Zhang, D.; Ronson, T. K.; Zou, Y.-Q.; Nitschke, J. R. Metal-Organic Cages for Molecular Separations. *Nat. Rev. Chem.* **2021**, *5* (3), 168–182.

[230] Nguyen, B.-N. T.; Thoburn, J. D.; Grommet, A. B.; Howe, D. J.; Ronson, T. K.; Ryan, H. P.; Bolliger, J. L.; Nitschke, J. R. Coordination Cages Selectively Transport Molecular Cargoes Across Liquid Membranes. *J. Am. Chem. Soc.* **2021**, *143* (31), 12175–12180.

[231] Wang, J.; He, C.; Wu, P.; Wang, J.; Duan, C. An Amide-Containing Metal-Organic Tetrahedron Responding to a Spin-Trapping Reaction in a Fluorescent Enhancement Manner for Biological Imaging of NO in Living Cells. *J. Am. Chem. Soc.* **2011**, *133* (32), 12402–12405.

[232] Jiao, Y.; Wang, J.; Wu, P.; Zhao, L.; He, C.; Zhang, J.; Duan, C. Cerium-Based M_4L_4 Tetrahedra as Molecular Flasks for Selective Reaction Prompting and Luminescent Reaction Tracing. *Chem. - Eur. J.* **2014**, *20* (8), 2224–2231.

[233] Zhang, M.; Saha, M. L.; Wang, M.; Zhou, Z.; Song, B.; Lu, C.; Yan, X.; Li, X.; Huang, F.; Yin, S.; Stang, P. J. Multicomponent Platinum(II) Cages with Tunable Emission and Amino Acid Sensing. *J. Am. Chem. Soc.* **2017**, *139* (14), 5067–5074.

[234] Li, X.-Z.; Zhou, L.-P.; Yan, L.-L.; Yuan, D.-Q.; Lin, C.-S.; Sun, Q.-F. Evolution of Luminescent Supramolecular Lanthanide $M_{2n}L_{3n}$ Complexes from Helicates and Tetrahedra to Cubes. *J. Am. Chem. Soc.* **2017**, *139* (24), 8237–8244.

[235] Liu, C.-L.; Zhang, R.-L.; Lin, C.-S.; Zhou, L.-P.; Cai, L.-X.; Kong, J.-T.; Yang, S.-Q.; Han, K.-L.; Sun, Q.-F. Intraligand Charge Transfer Sensitization on Self-Assembled Europium Tetrahedral Cage Leads to Dual-Selective Luminescent Sensing toward Anion and Cation. *J. Am. Chem. Soc.* **2017**, *139* (36), 12474–12479.

[236] Sun, Y.; Chen, C.; Liu, J.; Stang, P. J. Recent Developments in the Construction and Applications of Platinum-Based Metallacycles and Metallacages via Coordination. *Chem. Soc. Rev.* **2020**, *49* (12), 3889–3919.

[237] Ziegler, M.; Brumaghim, J. L.; Raymond, K. N. Stabilization of a Reactive Cationic Species by Supramolecular Encapsulation. *Angew. Chem. Int. Ed.* **2000**, *39* (22), 4119–4121.

[238] Yoshizawa, M.; Kusukawa, T.; Fujita, M.; Yamaguchi, K. Ship-in-a-Bottle Synthesis of Otherwise Labile Cyclic Trimers of Siloxanes in a Self-Assembled Coordination Cage. *J. Am. Chem. Soc.* **2000**, *122* (26), 6311–6312.

[239] Fiedler, D.; Bergman, R. G.; Raymond, K. N. Stabilization of Reactive Organometallic Intermediates Inside a Self-Assembled Nanoscale Host. *Angew. Chem. Int. Ed.* **2006**, *45* (5), 745–748.

[240] Dong, V. M.; Fiedler, D.; Carl, B.; Bergman, R. G.; Raymond, K. N. Molecular Recognition and Stabilization of Iminium Ions in Water. *J. Am. Chem. Soc.* **2006**, *128* (45), 14464–14465.

[241] Mal, P.; Breiner, B.; Rissanen, K.; Nitschke, J. R. White Phosphorus Is Air-Stable Within a Self-Assembled Tetrahedral Capsule. *Science* **2009**, *324* (5935), 1697–1699.

[242] Galan, A.; Ballester, P. Stabilization of Reactive Species by Supramolecular Encapsulation. *Chem. Soc. Rev.* **2016**, *45* (6), 1720–1737.

[243] Yoshizawa, M.; Klosterman, J. K.; Fujita, M. Functional Molecular Flasks: New Properties and Reactions within Discrete, Self-Assembled Hosts. *Angew. Chem. Int. Ed.* **2009**, *48* (19), 3418–3438.

[244] Wiester, M. J.; Ulmann, P. A.; Mirkin, C. A. Enzyme Mimics Based Upon Supramolecular Coordination Chemistry. *Angew. Chem. Int. Ed.* **2011**, *50* (1), 114–137.

[245] Raynal, M.; Ballester, P.; Vidal-Ferran, A.; van Leeuwen, P. W. N. M. Supramolecular Catalysis. Part 2: Artificial Enzyme Mimics. *Chem. Soc. Rev.* **2014**, *43* (5), 1734–1787.

[246] Zarra, S.; Wood, D. M.; Roberts, D. A.; Nitschke, J. R. Molecular Containers in Complex Chemical Systems. *Chem. Soc. Rev.* **2015**, *44* (2), 419–432.

[247] Brown, C. J.; Toste, F. D.; Bergman, R. G.; Raymond, K. N. Supramolecular Catalysis in Metal–Ligand Cluster Hosts. *Chem. Rev.* **2015**, *115* (9), 3012–3035.

[248] Jongkind, L. J.; Caumes, X.; Hartendorp, A. P. T.; Reek, J. N. H. Ligand Template Strategies for Catalyst Encapsulation. *Acc. Chem. Res.* **2018**, *51* (9), 2115–2128.

[249] Mouarrawis, V.; Plessius, R.; van der Vlugt, J. I.; Reek, J. N. H. Confinement Effects in Catalysis Using Well-Defined Materials and Cages. *Front. Chem.* **2018**, *6*, 623.

[250] Fang, Y.; Powell, J. A.; Li, E.; Wang, Q.; Perry, Z.; Kirchon, A.; Yang, X.; Xiao, Z.; Zhu, C.; Zhang, L.; Huang, F.; Zhou, H.-C. Catalytic Reactions within the Cavity of Coordination Cages. *Chem. Soc. Rev.* **2019**, *48* (17), 4707–4730.

[251] Li, X.; Wu, J.; He, C.; Meng, Q.; Duan, C. Asymmetric Catalysis within the Chiral Confined Space of Metal-Organic Architectures. *Small* **2019**, *15* (32), 1804770.

[252] Tan, C.; Chu, D.; Tang, X.; Liu, Y.; Xuan, W.; Cui, Y. Supramolecular Coordination Cages for Asymmetric Catalysis. *Chem. - Eur. J.* **2019**, *25* (3), 662–672.

[253] Grommet, A. B.; Feller, M.; Klajn, R. Chemical Reactivity under Nanoconfinement. *Nat. Nanotechnol.* **2020**, *15* (4), 256–271.

[254] Wang, K.; Jordan, J. H.; Hu, X.; Wang, L. Supramolecular Strategies for Controlling Reactivity within Confined Nanospaces. *Angew. Chem. Int. Ed.* **2020**, *59* (33), 13712–13721.

[255] Hooley, R. J. No, Not That Way, the Other Way: Creating Active Sites in Self-Assembled Host Molecules. *Synlett* **2020**, *31* (15), 1448–1463.

[256] Morimoto, M.; Bierschenk, S. M.; Xia, K. T.; Bergman, R. G.; Raymond, K. N.; Toste, F. D. Advances in Supramolecular Host-Mediated Reactivity. *Nat. Catal.* **2020**, *3* (12), 969–984.

[257] Gaeta, C.; La Manna, P.; De Rosa, M.; Soriente, A.; Talotta, C.; Neri, P. Supramolecular Catalysis with Self-Assembled Capsules and Cages: What Happens in Confined Spaces. *ChemCatChem* **2021**, *13* (7), 1638–1658.

[258] Takezawa, H.; Fujita, M. Molecular Confinement Effects by Self-Assembled Coordination Cages. *Bull. Chem. Soc. Jpn.* **2021**, *94* (10), 2351–2369.

[259] Saha, R.; Mondal, B.; Mukherjee, P. S. Molecular Cavity for Catalysis and Formation of Metal Nanoparticles for Use in Catalysis. *Chem. Rev.* **2022**, *122* (14), 12244–12307.

[260] Solea, A. B.; Sudittapong, B.; Taylor, C. G. P.; Ward, M. D. Inside or Outside the Box? Effect of Substrate Location on Coordination-Cage Based Catalysis. *Dalton Trans.* **2022**, *51* (30), 11277–11285.

[261] Cullen, W.; Metherell, A. J.; Wragg, A. B.; Taylor, C. G. P.; Williams, N. H.; Ward, M. D. Catalysis in a Cationic Coordination Cage Using a Cavity-Bound Guest and Surface-Bound Anions: Inhibition, Activation, and Autocatalysis. *J. Am. Chem. Soc.* **2018**, *140* (8), 2821–2828.

[262] Li, K.; Wu, K.; Lu, Y.; Guo, J.; Hu, P.; Su, C. Creating Dynamic Nanospaces in Solution by Cationic Cages as Multirole Catalytic Platform for Unconventional C(sp)−H Activation Beyond Enzyme Mimics. *Angew. Chem. Int. Ed.* **2022**, *61* (5), e202114070.

[263] Ludden, M. D.; Taylor, C. G. P.; Tipping, M. B.; Train, J. S.; Williams, N. H.; Dorrat, J. C.; Tuck, K. L.; Ward, M. D. Interaction of Anions with the Surface of a Coordination Cage in Aqueous Solution Probed by Their Effect on a Cage-Catalysed Kemp Elimination. *Chem. Sci.* **2021**, *12* (44), 14781–14791.

[264] Murase, T.; Nishijima, Y.; Fujita, M. Cage-Catalyzed Knoevenagel Condensation under Neutral Conditions in Water. *J. Am. Chem. Soc.* **2012**, *134* (1), 162–164.

[265] Taylor, C. G. P.; Metherell, A. J.; Argent, S. P.; Ashour, F. M.; Williams, N. H.; Ward, M. D. Coordination-Cage-Catalysed Hydrolysis of Organophosphates: Cavity- or Surface-Based? *Chem. - Eur. J.* **2020**, *26* (14), 3065–3073.

[266] Wang, J.; Young, T. A.; Duarte, F.; Lusby, P. J. Synergistic Noncovalent Catalysis Facilitates Base-Free Michael Addition. *J. Am. Chem. Soc.* **2020**, *142* (41), 17743–17750.

[267] Whitehead, M.; Turega, S.; Stephenson, A.; Hunter, C. A.; Ward, M. D. Quantification of Solvent Effects on Molecular Recognition in Polyhedral Coordination Cage Hosts. *Chem. Sci.* **2013**, *4* (7), 2744–2751.

[268] Turega, S.; Cullen, W.; Whitehead, M.; Hunter, C. A.; Ward, M. D. Mapping the Internal Recognition Surface of an Octanuclear Coordination Cage Using Guest Libraries. *J. Am. Chem. Soc.* **2014**, *136* (23), 8475–8483.

[269] Cullen, W.; Turega, S.; Hunter, C. A.; Ward, M. D. Virtual Screening for High Affinity Guests for Synthetic Supramolecular Receptors. *Chem. Sci.* **2015**, *6* (5), 2790–2794.

[270] Cullen, W.; Turega, S.; Hunter, C. A.; Ward, M. D. pH-Dependent Binding of Guests in the Cavity of a Polyhedral Coordination Cage: Reversible Uptake and Release of Drug Molecules. *Chem. Sci.* **2014**, *6* (1), 625–631.

[271] Cullen, W.; Thomas, K. A.; Hunter, C. A.; Ward, M. D. pH-Controlled Selection between One of Three Guests from a Mixture Using a Coordination Cage Host. *Chem. Sci.* **2015**, *6* (7), 4025–4028.

[272] Tidmarsh, I. S.; Faust, T. B.; Adams, H.; Harding, L. P.; Russo, L.; Clegg, W.; Ward, M. D. Octanuclear Cubic Coordination Cages. *J. Am. Chem. Soc.* **2008**, *130* (45), 15167–15175.

[273] Salles, A. G. Jr.; Zarra, S.; Turner, R. M.; Nitschke, J. R. A Self-Organizing Chemical Assembly Line. *J. Am. Chem. Soc.* **2013**, *135* (51), 19143–19146.

[274] Holloway, L. R.; Bogie, P. M.; Lyon, Y.; Ngai, C.; Miller, T. F.; Julian, R. R.; Hooley, R. J. Tandem Reactivity of a Self-Assembled Cage Catalyst with Endohedral Acid Groups. *J. Am. Chem. Soc.* **2018**, *140* (26), 8078–8081.

[275] Ngai, C.; Sanchez-Marsetti, C. M.; Harman, W. H.; Hooley, R. J. Supramolecular Catalysis of the oxa-Pictet-Spengler Reaction with an Endohedrally Functionalized Self-Assembled Cage Complex. *Angew. Chem. Int. Ed.* **2020**, *59* (52), 23505–23509.

[276] Meng, W.; Ronson, T. K.; Clegg, J. K.; Nitschke, J. R. Transformations within a Network of Cadmium Architectures. *Angew. Chem. Int. Ed.* **2013**, *52* (3), 1017–1021.

[277] Nicolaou, K. C.; Montagnon, T.; Baran, P. S.; Zhong, Y.-L. Iodine(V) Reagents in Organic Synthesis. Part 4. *o*-Iodoxybenzoic Acid as a Chemospecific Tool for Single Electron Transfer-Based Oxidation Processes. *J. Am. Chem. Soc.* **2002**, *124* (10), 2245–2258.

[278] Djerassi, Carl. Brominations with *N*-Bromosuccinimide and Related Compounds. The Wohl-Ziegler Reaction. *Chem. Rev.* **1948**, *43* (2), 271–317.

[279] Wijesinghe, C. A.; El-Khouly, M. E.; Zandler, M. E.; Fukuzumi, S.; D'Souza, F. A Charge-Stabilizing, Multimodular, Ferrocene-Bis(Triphenylamine)-Zinc-Porphyrin-Fullerene Polyad. *Chem. - Eur. J.* **2013**, *19* (29), 9629–9638.

[280] Nelson, T. D.; Crouch, R. D. Selective Deprotection of Silyl Ethers. *Synthesis* **1996**, *1996* (09), 1031–1069.

[281] Sasaki, S.; Citterio, D.; Ozawa, S.; Suzuki, K. Design and Synthesis of Preorganized Tripodal Fluororeceptors Based on Hydrogen Bonding of Thiourea Groups for Optical Phosphate Ion Sensing. *J. Chem. Soc., Perkin Trans. 2* **2001**, (12), 2309–2313.

[282] Borch, R. F.; Bernstein, M. D.; Durst, H. D. Cyanohydridoborate Anion as a Selective Reducing Agent. *J. Am. Chem. Soc.* **1971**, *93* (12), 2897–2904.

[283] Abdel-Magid, A. F.; Maryanoff, C. A.; Carson, K. G. Reductive Amination of Aldehydes and Ketones by Using Sodium Triacetoxyborohydride. *Tetrahedron Lett.* **1990**, *31* (39), 5595–5598.

[284] Abdel-Magid, A. F.; Carson, K. G.; Harris, B. D.; Maryanoff, C. A.; Shah, R. D. Reductive Amination of Aldehydes and Ketones with Sodium Triacetoxyborohydride. Studies on Direct and Indirect Reductive Amination Procedures[1]. *J. Org. Chem.* **1996**, *61* (11), 3849–3862.

[285] Šolomek, T.; Powers-Riggs, N. E.; Wu, Y.-L.; Young, R. M.; Krzyaniak, M. D.; Horwitz, N. E.; Wasielewski, M. R. Electron Hopping and Charge Separation within a Naphthalene-1,4:5,8-Bis(Dicarboximide) Chiral Covalent Organic Cage. *J. Am. Chem. Soc.* **2017**, *139* (9), 3348–3351.

[286] DeBlase, C. R.; Hernández-Burgos, K.; Rotter, J. M.; Fortman, D. J.; Abreu, D. dos S.; Timm, R. A.; Diógenes, I. C. N.; Kubota, L. T.; Abruña, H. D.; Dichtel, W. R. Cation-Dependent Stabilization of Electrogenerated Naphthalene Diimide Dianions in Porous Polymer Thin Films and Their Application to Electrical Energy Storage. *Angew. Chem. Int. Ed.* **2015**, *54* (45), 13225–13229.

[287] Frischmann, P. D.; Kunz, V.; Würthner, F. Bright Fluorescence and Host-Guest Sensing with a Nanoscale M_4L_6 Tetrahedron Accessed by Self-Assembly of Zinc–Imine Chelate Vertices and Perylene Bisimide Edges. *Angew. Chem. Int. Ed.* **2015**, *54* (25), 7285–7289.

[288] Jansze, S. M.; Cecot, G.; Wise, M. D.; Zhurov, K. O.; Ronson, T. K.; Castilla, A. M.; Finelli, A.; Pattison, P.; Solari, E.; Scopelliti, R.; Zelinskii, G. E.; Vologzhanina, A. V.; Voloshin, Y. Z.; Nitschke, J. R.; Severin, K. Ligand Aspect Ratio as a Decisive Factor for the Self-Assembly of Coordination Cages. *J. Am. Chem. Soc.* **2016**, *138* (6), 2046–2054.

[289] Shannon, R. D. Revised Effective Ionic Radii and Systematic Studies of Interatomic Distances in Halides and Chalcogenides. *Acta Crystallogr., Sect. A: Found. Adv.* **1976**, *32* (5), 751–767.

[290] Andersen, O. Chelation of Cadmium. *Environ. Health Perspect.* **1984**, *54*, 249–266.

[291] Yin, J.; Qu, H.; Zhang, K.; Luo, J.; Zhang, X.; Chi, C.; Wu, J. Electron-Deficient Triphenylene and Trinaphthylene Carboximides. *Org. Lett.* **2009**, *11* (14), 3028–3031.

[292] Kasai, Y.; Sakamoto, C.; Muroya, N.; Kato, S.; Nakamura, Y. Synthesis of [60]Fullerene-Containing [2]Rotaxanes Using Axle Molecules Bearing Donor Moiety. *Tetrahedron Lett.* **2011**, *52* (5), 623–625.

[293] Gabutti, S.; Knutzen, M.; Neuburger, M.; Schull, G.; Berndt, R.; Mayor, M. A Rigid Sublimable Naphthalenediimide Cyclophane as Model Compound for UHV STM Experiments. *Chem. Commun.* **2008**, (20), 2370–2372.

[294] Bao, B.; Yuwen, L.; Zhan, X.; Wang, L. Water-Soluble Hyperbranched Polyelectrolytes with High Fluorescence Quantum Yield: Facile Synthesis and Selective Chemosensor for Hg^{2+} and Cu^{2+} Ions. *J. Polym. Sci., Part A: Polym. Chem.* **2010**, *48* (15), 3431–3439.

[295] Castilla, A. M.; Ousaka, N.; Bilbeisi, R. A.; Valeri, E.; Ronson, T. K.; Nitschke, J. R. High-Fidelity Stereochemical Memory in a $Fe^{II}_4L_4$ Tetrahedral Capsule. *J. Am. Chem. Soc.* **2013**, *135* (47), 17999–18006.

[296] Albano, G.; Aronica, L. A.; Biver, T.; Detti, R.; Pucci, A. *Tris*-Ethynylphenyl-Amine Fluorophores: Synthesis, Characterisation and Test of Performances in Luminescent Solar Concentrators. *ChemistrySelect* **2018**, *3* (6), 1749–1754.

[297] Chen, Z.; Chen, M.; Yu, Y.; Wu, L. Robust Synthesis of Free-Standing and Thickness Controllable Conjugated Microporous Polymer Nanofilms. *Chem. Commun.* **2017**, *53* (12), 1989–1992.

[298] Jornet-Mollá, V.; Romero, F. M. Synthesis of Rigid Ethynyl-Bridged Polytopic Picolinate Ligands for MOF Applications. *Tetrahedron Lett.* **2015**, *56* (44), 6120–6122.

[299] Bloch, W. M.; Abe, Y.; Holstein, J. J.; Wandtke, C. M.; Dittrich, B.; Clever, G. H. Geometric Complementarity in Assembly and Guest Recognition of a Bent Heteroleptic *cis*-[$Pd_2\mathbf{L}^{\mathbf{A}}{}_2\mathbf{L}^{\mathbf{B}}{}_2$] Coordination Cage. *J. Am. Chem. Soc.* **2016**, *138* (41), 13750–13755.

[300] Yang, Y.; Ronson, T. K.; Lu, Z.; Zheng, J.; Vanthuyne, N.; Martinez, A.; Nitschke, J. R. A Curved Host and Second Guest Cooperatively Inhibit the Dynamic Motion of Corannulene. *Nat. Commun.* **2021**, *12* (1), 4079.

[301] Brynn Hibbert, D.; Thordarson, P. The Death of the Job Plot, Transparency, Open Science and Online Tools, Uncertainty Estimation Methods and Other Developments in Supramolecular Chemistry Data Analysis. *Chem. Commun.* **2016**, *52* (87), 12792–12805.

[302] Wu, D. H.; Chen, A. D.; Johnson, C. S. An Improved Diffusion-Ordered Spectroscopy Experiment Incorporating Bipolar-Gradient Pulses. *J. Magn. Reson., Ser. A* **1995**, *115* (2), 260–264.

[303] Smith, B. M.; Kubczyk, T. M.; Graham, A. E. Indium(III) Triflate Catalysed Transacetalisation Reactions of Diols and Triols under Solvent-Free Conditions. *Tetrahedron* **2012**, *68* (38), 7775–7781.

[304] Vacca, A.; Nativi, C.; Cacciarini, M.; Pergoli, R.; Roelens, S. A New Tripodal Receptor for Molecular Recognition of Monosaccharides. A Paradigm for Assessing Glycoside Binding Affinities and Selectivities by ^{1}H NMR Spectroscopy. *J. Am. Chem. Soc.* **2004**, *126* (50), 16456–16465.

[305] Danchura, W.; Schaefer, T.; Rowbotham, J. B.; Wood, D. J. Proton Magnetic Resonance Study of Conformational Equilibria of the Pyridinealdehydes in Solution. Comparison with Other Methods. *Can. J. Chem.* **1974**, *52* (23), 3986–3995.

[306] Osawa, T.; Kajitani, T.; Hashizume, D.; Ohsumi, H.; Sasaki, S.; Takata, M.; Koizumi, Y.; Saeki, A.; Seki, S.; Fukushima, T.; Aida, T. Wide-Range 2D Lattice Correlation Unveiled for Columnarly Assembled Triphenylene Hexacarboxylic Esters. *Angew. Chem. Int. Ed.* **2012**, *51* (32), 7990–7993.

[307] Kim, T.; Joo, S. H.; Gong, J.; Choi, S.; Min, J. H.; Kim, Y.; Lee, G.; Lee, E.; Park, S.; Kwak, S. K.; Lee, H.-S.; Kim, B.-S. Geomimetic Hydrothermal Synthesis of Polyimide-Based Covalent Organic Frameworks. *Angew. Chem. Int. Ed.* **2022**, *61* (4), e202113780.

[308] Köster, J. M.; Tiefenbacher, K. Elucidating the Importance of Hydrochloric Acid as a Cocatalyst for Resorcinarene-Capsule-Catalyzed Reactions. *ChemCatChem* **2018**, *10* (14), 2941–2944.

[309] Engelhard, D. M.; Freye, S.; Grohe, K.; John, M.; Clever, G. H. NMR-Based Structure Determination of an Intertwined Coordination Cage Resembling a Double Trefoil Knot. *Angew. Chem. Int. Ed.* **2012**, *51* (19), 4747–4750.

[310] Lim, J. Y. C.; Marques, I.; Félix, V.; Beer, P. D. Enantioselective Anion Recognition by Chiral Halogen-Bonding [2]Rotaxanes. *J. Am. Chem. Soc.* **2017**, *139* (35), 12228–12239.

[311] von Krbek, L. K. S.; Roberts, D. A.; Pilgrim, B. S.; Schalley, C. A.; Nitschke, J. R. Multivalent Crown Ether Receptors Enable Allosteric Regulation of Anion Exchange in an Fe_4L_6 Tetrahedron. *Angew. Chem. Int. Ed.* **2018**, *57* (43), 14121–14124.

[312] Yi, H.; Hu, P.; Snyder, S. A. Development and Elucidation of a Pd-Based Cyclization-Oxygenation Sequence for Natural Product Synthesis. *Angew. Chem. Int. Ed.* **2020**, *59* (7), 2674–2678.

[313] Tian, W.-F.; Hu, C.-H.; He, K.-H.; He, X.-Y.; Li, Y. Visible-Light Photoredox-Catalyzed Decarboxylative Alkylation of Heteroarenes Using Carboxylic Acids with Hydrogen Release. *Org. Lett.* **2019**, *21* (17), 6930–6935.

[314] Borowiecki, P.; Wińska, P.; Bretner, M.; Gizińska, M.; Koronkiewicz, M.; Staniszewska, M. Synthesis of Novel Proxyphylline Derivatives with Dual Anti-Candida Albicans and Anticancer Activity. *Eur. J. Med. Chem.* **2018**, *150*, 307–333.

[315] Tu, G.; Wang, D.; Yuan, C.; Zhang, J.; Zhao, Y. Palladium-Catalyzed Para-Selective Difluoromethylation of Arene Esters. *J. Org. Chem.* **2020**, *85* (16), 10740–10749.

[316] Zhang, C.; Feng, P.; Jiao, N. Cu-Catalyzed Esterification Reaction via Aerobic Oxygenation and C–C Bond Cleavage: An Approach to α-Ketoesters. *J. Am. Chem. Soc.* **2013**, *135* (40), 15257–15262.

[317] Guha, S.; Goodson, F. S.; Corson, L. J.; Saha, S. Boundaries of Anion/Naphthalenediimide Interactions: From Anion−π Interactions to Anion-Induced Charge-Transfer and Electron-Transfer Phenomena. *J. Am. Chem. Soc.* **2012**, *134* (33), 13679–13691.

[318] Huang, Y.-L.; Hung, W.-C.; Lai, C.-C.; Liu, Y.-H.; Peng, S.-M.; Chiu, S.-H. Using Acetate Anions To Induce Translational Isomerization in a Neutral Urea-Based Molecular Switch. *Angew. Chem. Int. Ed.* **2007**, *46* (35), 6629–6633.

[319] Thordarson, P. Determining Association Constants from Titration Experiments in Supramolecular Chemistry. *Chem. Soc. Rev.* **2011**, *40* (3), 1305–1323.

8 Bibliographic Data of Complete Publications

This chapter contains the bibliographic data of the publications included in this thesis.

A Water- and Base-Stable Iminopyridine-Based Cage That Can Bind Larger Organic Anions

Mattias Zenka,[a] Joachim Preinl,[a] Eric Pertermann,[b] Arne Lützen,[b] and Konrad Tiefenbacher*[a, c]

[a] Department of Chemistry, University of Basel, Mattenstrasse 24a, 4058 Basel, Switzerland

[b] Kekulé-Institut für Organische Chemie und Biochemie, Rheinische Friedrich-Wilhelms-Universität Bonn, 53121 Bonn, Germany

[c] Department of Biosystems Science and Engineering, ETH Zurich, Mattenstrasse 24, 4058 Basel, Switzerland

*Corresponding Author: konrad.tiefenbacher@unibas.ch

Originally published in: *Eur. J. Inorg. Chem.* **2023**, e202300110.

DOI: doi.org/10.1002/ejic.202300110

URL: https://chemistry-europe.onlinelibrary.wiley.com/doi/full/10.1002/ejic.202300110

9 Reprints and Reprint Permission

The manuscript published in European Journal of Inorganic Chemistry, Full Article was reproduced with the permission of John Wiley and Sons.

JOHN WILEY AND SONS LICENSE
TERMS AND CONDITIONS

Oct 17, 2023

This Agreement between University of Basel -- Mattias Zenka ("You") and John Wiley and Sons ("John Wiley and Sons") consists of your license details and the terms and conditions provided by John Wiley and Sons and Copyright Clearance Center.

License Number	5651470491656
License date	Oct 17, 2023
Licensed Content Publisher	John Wiley and Sons
Licensed Content Publication	European Journal of Inorganic Chemistry
Licensed Content Title	A Water- and Base-Stable Iminopyridine-Based Cage That Can Bind Larger Organic Anions
Licensed Content Author	Mattias Zenka, Joachim Preinl, Eric Pertermann, et al
Licensed Content Date	Mar 22, 2023
Licensed Content Volume	26
Licensed Content Issue	15
Licensed Content Pages	9
Type of use	Dissertation/Thesis
Requestor type	Author of this Wiley article
Format	Print and electronic
Portion	Full article
Will you be translating?	No
Title	Investigation of Positively Charged Supramolecular Cage Compounds towards Guest-Uptake and Catalysis
Institution name	University of Basel
Expected presentation date	Oct 2023
Order reference number	300119942
Requestor Location	Mattias Zenka Flurstraße 5 Freiburg, 79114 Germany Attn: University of Basel
Publisher Tax ID	EU826007151
Total	0.00 EUR

Check for updates

EurJIC
European Journal of Inorganic Chemistry

Research Article
doi.org/10.1002/ejic.202300110

Chemistry Europe
European Chemical Societies Publishing

www.eurjic.org

A Water- and Base-Stable Iminopyridine-Based Cage That Can Bind Larger Organic Anions

Mattias Zenka,[a] Joachim Preinl,[a] Eric Pertermann,[b] Arne Lützen,[b] and Konrad Tiefenbacher*[a, c]

Catalysis inside molecular cages and capsules has attracted an increasing amount of attention over the last decade. While many examples of the catalysis of reactions with cationic intermediates and transition states are known, those with anionic counterparts are scarce. One limiting factor is access to suitably sized cationic iminopyridine-based cages that are stable towards water and anionic/nucleophilic guest molecules. This study aimed at identifying such suitable cages. In this full paper, we describe the journey that finally led to the synthesis of a novel iminopyridine-based tetrahedron that can bind larger organic anions with binding constants of up to 850 M^{-1} in MeCN–d_3/H_2O = 9:1. Importantly, it also displays stability in basic aqueous acetonitrile. Surprisingly, investigations towards catalysis of reactions with anionic transition states did not indicate rate accelerations in the presence of the cage.

Introduction

Self-assembled molecular capsules and cages and their host-guest chemistry have been explored extensively over the past few decades. Potential applications range from chemical transport or separation[1–11] and molecular sensing[12–17] to the stabilization of reactive guests.[18–27] Moreover, catalysis has also been a major focus in self-assembled molecular capsules and cages.[28–49] Out of the reactions catalysed most examples feature cationic intermediates and transition states. Only a few examples of catalysis of reactions with anionic transition states in supramolecular cages are known.[50–56] Additionally, Matile and co-workers have demonstrated the application of anion-π interactions in the context of catalysis using aromatic naphthalenediimide (NDI) moieties in open, non-capsular systems.[57–60] Although supramolecular cages bearing such NDI structures have been reported,[61–65] anion-π catalysis has not yet been investigated within them to our knowledge. Cage I (Figure 1a) may be suitable for such catalysis as it features an overall charge of +8 that should additionally stabilize anionic intermediates and transition states via strong ion-ion interactions. The stabilization of charged ground states may be the decisive factor for catalysis as recent work for an anionic host has shown.[66] To our knowledge, no guest-uptake and stability studies with cage I have been reported; it was, however, shown that it reassembles to heteroleptic cages under appropriate conditions.[62]

Besides cage I, metal-ligand based cages in general should be very suitable for the stabilization of anionic intermediates, as they often feature a high net positive charge. Moreover, such cages can be rendered water-soluble to drive the binding of the guest via the hydrophobic effect.[67–72] A broad scope of water-soluble self-assembled iminopyridine complexes has been investigated by Nitschke and co-workers.[73] The solubility of the formed cages is mainly dictated by the counter anions. Two key features were elucidated: (1) the stability in a series of porphyrin-based iminopyridine assemblies was dependent on the metal ions used, following the trend $Ni^{II} > Fe^{II} > Co^{II} > Zn^{II} > Cd^{II}$. (2) Binding cooperativity around metal centers is increased by choosing chelating ligands like tris(2-aminoethyl)amine (TREN, Figure 1b) or tris(3-aminopropyl)amine (TRPN). This enabled the formation of water-stable structures even with Zn^{II} and Cd^{II} ions.[73] For example, the face-capped tetrahedron II was stable for months in D_2O at room temperature and only showed decomposition above 80 °C (Figure 1b). However, no guest uptake studies with the water-soluble derivative have been reported, so far. Its acetonitrile-soluble derivative, featuring triflimide counter anions, has been shown to bind small anions like ReO_4^-, PF_6^- or SbF_6^- exclusively[4] while no binding of neutral organic molecules was observed.

This work aimed to identify iminopyridine-based cages that are potentially suitable for the catalysis of reactions with anionic transition states/intermediates. Specifically, the cages should display (1) a size suitable for the encapsulation of larger anions

[a] M. Zenka, J. Preinl, Prof. Dr. K. Tiefenbacher
Department of Chemistry,
University of Basel
4058 Basel (Switzerland)
E-mail: konrad.tiefenbacher@unibas.ch
tkonrad@ethz.ch
https://nanocat.chemie.unibas.ch/en/
[b] Dr. E. Pertermann, Prof. Dr. A. Lützen
Kekulé-Institut für Organische Chemie und Biochemie,
Rheinische Friedrich-Wilhelms-Universität Bonn
53121 Bonn (Germany)
[c] Prof. Dr. K. Tiefenbacher
Department of Biosystems Science and Engineering,
ETH Zurich
4058 Basel (Switzerland)

Supporting information for this article is available on the WWW under https://doi.org/10.1002/ejic.202300110

EurJIC
European Journal of Inorganic Chemistry

Research Article
doi.org/10.1002/ejic.202300110

Chemistry Europe
European Chemical Societies Publishing

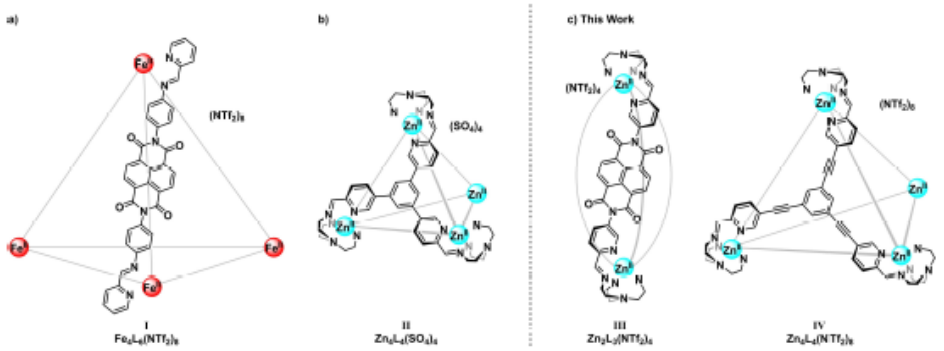

Figure 1. a) Literature-known Fe_4L_6 cage **I**. b) Literature-known Zn_4L_4 cage **II**. c) Newly synthesized Zn_2L_3 helicate **III** and Zn_4L_4 tetrahedron **IV**.

than cage **II** and (2) stability towards water and anionic guest molecules.

Results and Discussion

Initially, the focus was put on the known cage **I** as it features NDI units potentially stabilizing anionic guests and offers a large cavity. The synthesis of cage **I** was performed as described in literature via the subcomponent self-assembly method from $Fe(NTf_2)_2$, the corresponding NDI-based diamine ligand and 2-formylpyridine.[62] The edge-linked Fe_4L_6 tetrahedron **I** (Figure 1a) was obtained as a mixture of the *T*-, C_3- and the predominating S_4-symmetric diastereomers. With the cage in hands, we explored its stability towards water and bases in a series of titration experiments in (aqueous) acetonitrile. It was found that cage **I** did not tolerate $KHCO_3$ in aqueous acetonitrile at room temperature (Figure 2a). In these studies, a relatively high amount of water was chosen to ensure the solubility of the base in stock solutions and during the titration process. A precipitate was observed during base titration indicating the disassembly of the cage and the formation of insoluble subcomponents, signals of which almost disappeared in this solvent system due to lack of solubility (Figure 2a). Further titrations revealed that the cage even disassembled in the absence of base, as aldehyde signals (9.94 ppm) appeared even at low water content (SI, chapter 4.2.1).

In order to improve the stability of the iminopyridine metal complex, we decided to explore the multidentate TREN ligands. However, this required a functionality swap in the ligand subcomponents, as the NDI building block of cage **I** requires aldehyde capping units (Figure 2a). Starting with 1,4,5,8-naphthalenetetracarboxylic dianhydride (**1**), amine condensation followed by radical iodination and Kornblum oxidation in one pot furnished NDI building block **3** in moderate yields (Figure 3a). With **3** in hands, several conditions for cage formation were explored. Most metal triflimide ($M^{II}(NTf_2)_2$, M=Fe, Cd) and sulfate salts ($M^{II}SO_4$, M=Zn, Cd) investigated failed to produce defined self-assembled structures. Only the use of $Zn(NTf_2)_2$ enabled the formation of a defined assembly in the presence of dialdehyde **3** and TREN. However, instead of generating the initially expected tetrahedral cage, we observed Zn_2L_3 helicate **III** (Figure 3b) to form instead. Its formation required unusually high temperatures (120–150 °C) and was accompanied by undefined side-products as indicated by broad resonances in the crude ^{1}H NMR spectra. Good separation was achieved via size-exclusion chromatography followed by recrystallization, to yield helicate **III** in 22% isolated yield. A crystal of Zn_2L_3 helicate **III** suitable for X-ray analysis was obtained by slow diffusion of diethyl ether into an acetonitrile solution of cage **III**. The X-ray crystal structure of Zn_2L_3 helicate **III** shows preferential π-π-stacking between the NDI units (Figure 3c). Therefore, the helicate does not offer any cavity for guest encapsulation in the solid state anymore which is most likely also true in solution as the NDI protons show an unusually broad singlet in the ^{1}H NMR (Figure S18). Thus, no guest binding studies were performed with helicate **III**.

While the exact reason for the failure of obtaining a tetrahedron are difficult to elucidate, there are several factors that might be at play: (1) ligand **3** features a reduced aspect ratio (length-to-width ratio) compared to the ligand used for the construction of Fe_4L_6 tetrahedron **I**, a factor that is known to influence the geometry and the composition of coordination cages.[74,75] (2) The absence of bulky substituents on the NDI moiety might also facilitate the π-π-stacking between the ligands (Figure 3c). π-π-stacking was observed to influence the outcome of related self-assembly processes.[62] (3) The multidentate TREN ligand may additionally influence the self-assembly process, as a monodentate pyridine component was utilized in the formation of tetrahedron **I**.

Due to these setbacks with the NDI-based assemblies, we decided to explore alternative motifs. Driven by the desire to avoid helicate M_2L_3 formation, a panelling approach was explored. The use of a tritopic panel would exclude the formation of a helicate and should form face-capped tetrahedral structures.[12,76–85] However, the NDI unit is not amendable

EurJIC
European Journal of Inorganic Chemistry

Research Article
doi.org/10.1002/ejic.202300110

Chemistry Europe
European Chemical Societies Publishing

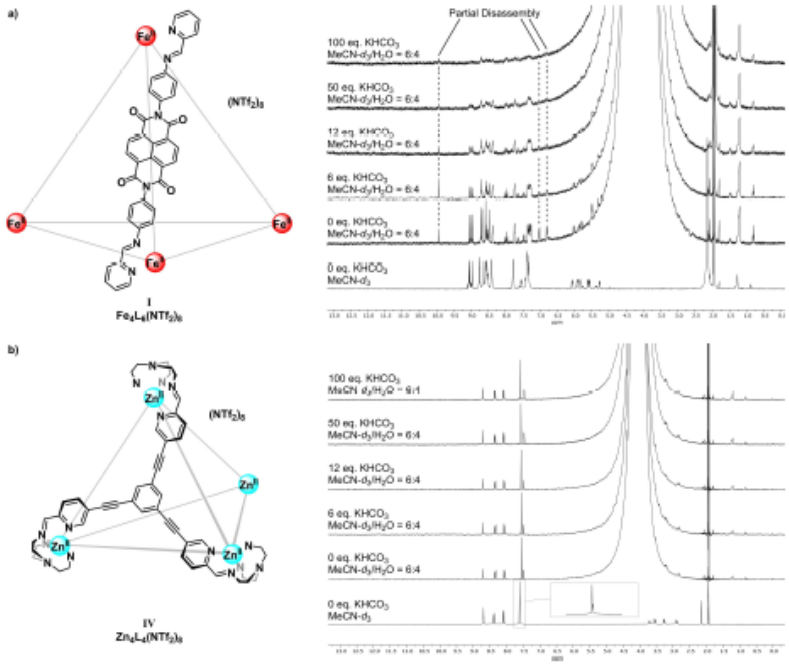

Figure 2. Base ($KHCO_3$) stability investigations of a) edge-linked tetrahedral Fe_4L_6 cage **I** and b) face-capped tetrahedral Zn_4L_4 cage **IV**. Cage concentration = 0.125 mM. MeCN–d_3/H_2O = 6 : 4 was used as the solvent system.

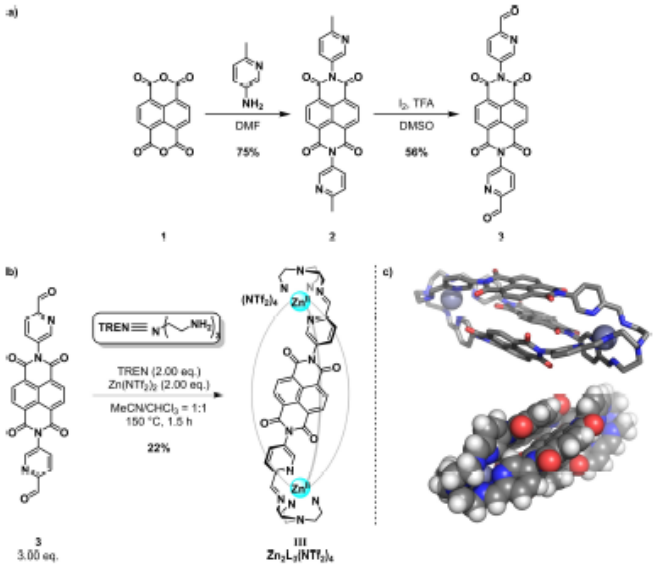

Figure 3. a) Synthesis of dialdehyde ligand **3**. b) Self-assembly of Zn_2L_3 helicate **III**. c) Crystal structure of Zn_2L_3 helicate **III**.

EurJIC
European Journal of Inorganic Chemistry

Research Article
doi.org/10.1002/ejic.202300110

Chemistry Europe
European Chemical Societies Publishing

for the formation of a symmetric tritopic ligand. Thus, it was decided to replace the π-acidic NDI surface with an electronically similarly polarized triphenylenetriimide (TPTI) scaffold (compound **7**, Figure 4), that may be capped with TREN. This ambitious plan was based on the known triphenylene hexacarboxylic acid **4** that can be accessed in three steps.[86,87] Trisanhydride **5** was obtained via exposure to neat thionyl chloride and was very poorly soluble across all organic solvents to the point where a mixture of acetonitrile-d_3 and HCl-saturated $CDCl_3$ (1:1) was needed to record a useful ^{13}C NMR spectrum at room temperature. Nevertheless, TPTI **6** was obtained stepwise by amide formation at 80 °C followed by imide condensation, again with thionyl chloride, in two steps. Direct imide condensation at 150 °C with the corresponding amine only led to complex mixtures. Unfortunately, all attempts of obtaining the oxidized aldehyde product **7** via a Kornblum oxidation failed, although aldehyde signals were detected in the NMR of the crude mixture. A variety of workup procedures was explored, without success. It was concluded that the product is not stable towards water during workup, making the approach not suitable for obtaining a stable cage.

Having failed in the construction of a novel cage that meets the requirements concerning water/base stability and size, a less ambitious path was pursued. We decided to modify the known Zn_4L_4 cage **II** (Figure 1b) as it was shown to be stable towards water and can easily be prepared in 3 steps.[73,88,89] To overcome the limiting cavity size of **II**, we decided to expand the panel via the insertion of acetylene units between the benzene core and the pyridyl ligands (**11**, Figure 5). Compound **11** was synthesized from 1,3,5-tribromobenzene (**8**) via Sonogashira coupling with TMS-acetylene to deliver the protected trialkyne **9**.[90] After deprotection,[91] trialkyne **10** was coupled in a second Sonogashira reaction with 5-bromopyridine-2-carbaldehyde, to deliver the tridentate ligand **11** in good yields.

Gratifyingly, the self-assembly between trialdehyde **11**, TREN, and $Zn(NTf_2)_2$ in acetonitrile/chloroform at 110 °C furnished Zn_4L_4 tetrahedron **IV** as a single diastereomer as indicated by the single set of resonances expected for the formation of the most symmetric tetrahedron with *T* point

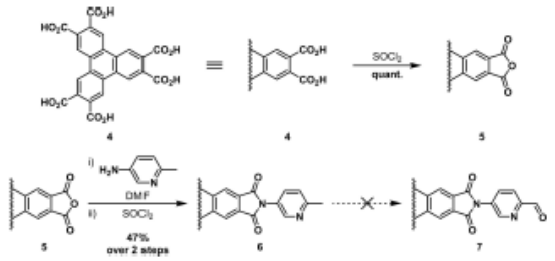

Figure 4. Synthesis of triphenylenetriimide (TPTI) **6**. Every transformation shown was performed globally.

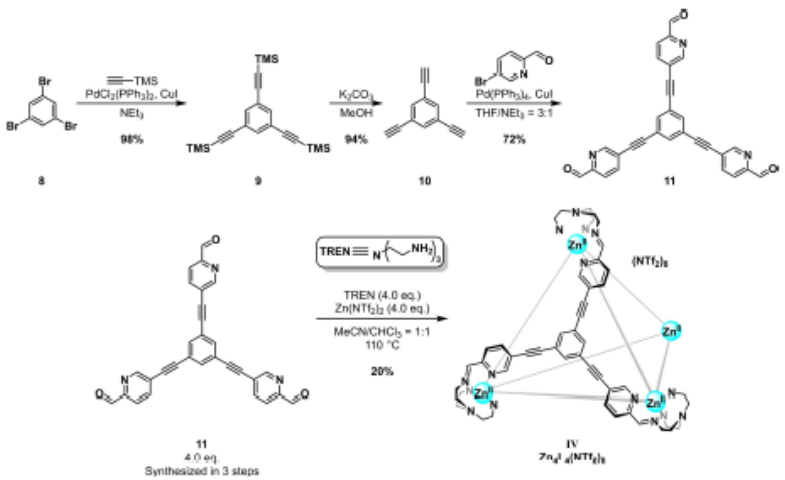

Figure 5. Synthesis of threefold symmetric ligand **11** over three steps (top). The self-assembly of tetrahedral Zn_4L_4 cage **IV** is depicted below.

EurJIC
European Journal of Inorganic Chemistry

Research Article
doi.org/10.1002/ejic.202300110

Chemistry Europe
European Chemical Societies Publishing

symmetry. The cage displays good solubility in polar aprotic solvents such as acetone, $MeNO_2$, and MeCN, while it does not dissolve in alkanes, alcohols, chlorinated solvents, and toluene or benzene. With triflimide as the counter anion, it is not water-soluble in comparison to its predecessor Zn_4L_4 sulfate cage **II** (Figure 1b), as the counter anion dictates the solubility. Interestingly, the corresponding sulfate derivative of cage **IV** was not accessible. Neither the use of metal sulfate $M^{II}SO_4$ (M=Ni, Co, Fe, Zn) salts in H_2O or H_2O/MeCN = 1:1 nor an anion exchange of the Zn_4L_4 triflimide cage, as reported previously by Nitschke et al.[73] for related cages were successful. According to ^{1}H NMR, the cage seemed to form initially after anion exchange but decomposed quickly in D_2O. The high binding cooperativity of the subcomponents seemed not to ensure stability in water as a water-soluble complex. It seems that the poor water solubility of the ligand prevents a stable cage formation. Similar observations have been reported before.[73]

With cage **IV** in hands, its properties were explored next. First, its water and base stability were examined. Base titration experiments were conducted, showing that triflimide cage **IV** remained stable against various bases (including 30 equiv. of $KHCO_3$, NEt_3, or *i*-Pr_2NEt) at temperatures of up to 60 °C in MeCN–d_3/H_2O = 6:4 (see Supporting Information, chapter 4.2.3). Figure 2b also shows the initial titration experiment with $KHCO_3$ at room temperature. The higher binding cooperativity from the subcomponents in comparison to Fe_4L_6 tetrahedron **I** (Figure 2a) increased cage stability so that after the addition of 100 equivalents of $KHCO_3$, the cage remained intact even after 18 h (see Supporting Information, chapter 4.2.2).

Subsequently, the binding properties were explored. This was especially of interest, as the original cage (triflimide derivative of Zn_4L_4 cage **II**, Figure 1b) was only able to bind small anions in acetonitrile.[4] Our goal was to bind larger organic molecules for potential applications in the catalysis of anionic reactions. The binding studies were performed in MeCN–d_3/H_2O = 9:1 to ensure good solubility of the cage as well as of the ionic guests explored. Due to the limited solubility of cage **IV**, guest uptake studies in purely aqueous solutions were not possible as it starts precipitating out of acetonitrile at around 55% water content. A series of neutral (**12**–**18**, Figure 6a) and anionic guests (**19**–**27**, Figure 6b) was explored. No significant shifts of the cage or guest signals was observed for the neutral guests. However, all ionic guests displayed some interactions in the fast binding regime on the ^{1}H chemical shift timescale. A series of titrations was performed to estimate the binding constants, which range from 40 to 850 M^{-1}.

In order to elucidate if indeed a guest uptake into the cage is taking place, or if this binding is rather an outside interaction with the charged vertices, control titrations were performed with the simple cationic model complex **V** (Figure 6c). It represents the charged vertex of cage **IV**, and thus was used in four-fold higher concentration as cage **IV** for the titration experiments. In general, the binding constants obtained with **V** are significantly lower than for Zn_4L_4 tetrahedron **IV**. While comparable for guests **19** and **20**, the cage shows much higher affinity for the anions of **21**–**24** while phosphate salts **25**–**27** showed even stronger binding to cage **IV**. Determining the binding constants of phosphate salts **25**–**27** with model

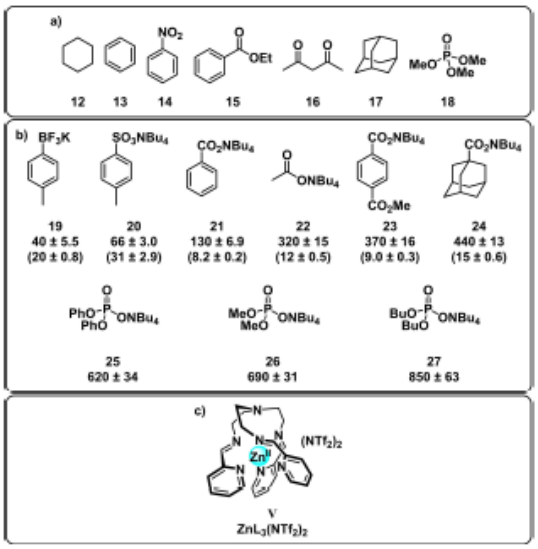

Figure 6. Guest screening for cage **IV**. a) Neutral guests **12**–**18** that showed no binding. b) Organic Salts **19**–**27** for which fast exchange was observed for the anionic component as determined by NMR spectroscopy in MeCN–d_3/H_2O = 9:1. Binding constants are shown for cage **IV**. For guests **19**–**24** the binding constants of the ZnL_3 complex **V** are shown in parentheses for comparison. c) Mononuclear ZnL_3 complex **V**.

EurJIC
European Journal of Inorganic Chemistry

Research Article
doi.org/10.1002/ejic.202300110

Chemistry Europe
European Chemical Societies Publishing

complex **V** was not possible due to solubility issues during the titration.

The best binding guests in this series turned out to be the phosphates **25**–**27**, potentially due to a good shape fit to the tetrahedral cage.[92,93] While the binding constants for diphenyl phosphate **25** and dimethyl phosphate **26** are similar, better binding was observed for dibutyl phosphate **27**. The more flexible butyl chains may enable a better shape fit than the phenyl and methyl groups of guests **25** and **26**.

Having finally access to a base-stable cationic cage with a sizable cavity, we explored the catalytic potential of cage **IV**. We chose four substrates and in total three different reaction types (Figure 7) with anionic transition states and intermediates under basic conditions: a) phosphate hydrolysis of trimethyl phosphate (**18**), b) ester hydrolysis of ethyl benzoate (**15**), c) decarboxylation of β-ketoacid **30** and d) ester hydrolysis of monocarboxylate mono methyl ester **23**. The reactions were run in MeCN–d_3/H_2O = 6:4 at different temperature profiles depending on the reaction rate at a substrate concentration of 20 mM in the presence of 10 mol-% of cage **IV** and 3 eq. of base (either $KHCO_3$, NEt_3, or *i*-Pr_2NEt). As control experiments, the respective background reactions without Zn_4L_4 cage **IV** were investigated as well. Durene was used as an internal standard to follow the reaction progress via ^{1}H NMR. Interestingly, in all four reactions explored the reaction rate slowed down in the presence of cage **IV**. Even though two neutral substrates (**18** and **15**) were used in this study that showed no significant uptake, it was assumed that even very little uptake into cage **IV** may lead to rate accelerations, as subsequent anionic transition states, as well as intermediates, should be stabilized inside the positively charged cage environment. A similar result was observed even when using the anionic substrates **30** and **23**. This was surprising to us since catalysis within metal-organic cages under basic conditions has previously been achieved.[51,55] The reduced conversion with cage **IV** in the case of the neutral substrates **15** and **18** might be a result of the failure of guest binding, combined with a local increase in hydroxide concentration around the cage, as observed for another cationic cage.[51] However, the failure of acceleration in the cases of the anionic substrates remains unknown.

Conclusion

This study aimed at identifying iminopyridine-based cages that are large enough for the encapsulation of organic anions and stable towards water and anionic/nucleophilic guest molecules. Although several approaches failed, this was achieved by the construction of the Zn_4L_4 tetrahedron **IV**. Its stability against water and bases is superior to alternative cages of similar size, as demonstrated by the comparison with the literature known Fe_4L_6 tetrahedron **I**. Triflimide cage **IV** proved to be stable

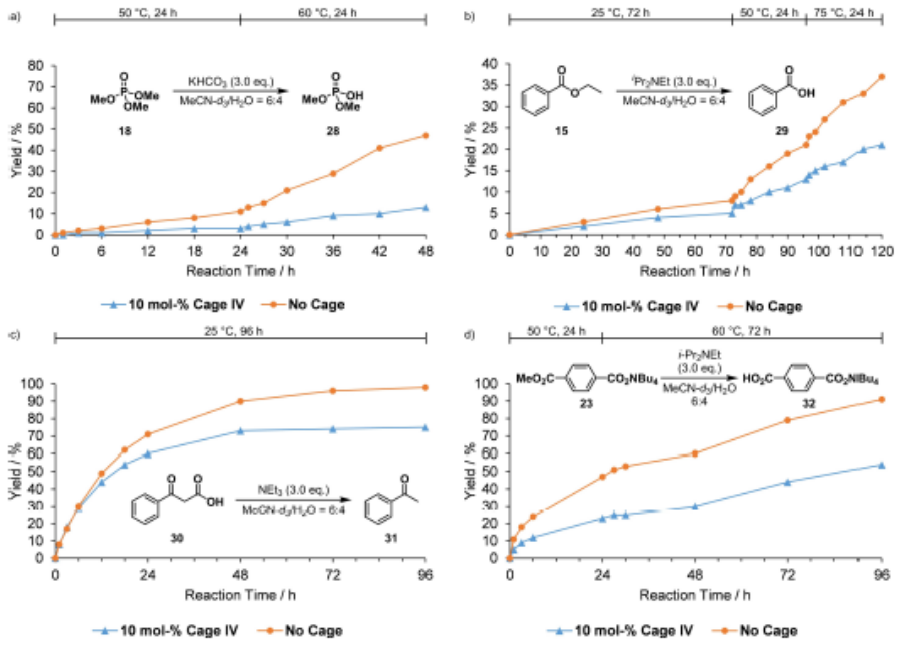

Figure 7. Catalysis experiments with cage **IV** utilizing neutral (a–b), and anionic substrates (c–d). Three different reaction types were investigated: a) phosphate hydrolysis, b) and d) ester hydrolysis, and c) decarboxylation of a β-ketoacid.

EurJIC
European Journal of Inorganic Chemistry

Research Article
doi.org/10.1002/ejic.202300110

Chemistry Europe
European Chemical Societies Publishing

against high amounts of water and even an excess of bases at elevated temperatures. Furthermore, cage **IV** proved suitable for the binding of larger organic anions with binding constants of up to 850 M^{-1} in MeCN–d_3/H_2O = 9:1 in a fast guest exchange regime on the ^{1}H chemical shift timescale. Intriguingly, investigations towards catalysis of reactions with anionic transition states showed a deceleration in the presence of cage **IV**. While the reduced conversion of the neutral substrates might be a result of the failure of guest binding, combined with a local increase in hydroxide concentration around the cage, the failure of acceleration in the cases of the anionic substrates remains unknown. This study demonstrates that the catalysis of reactions with anionic transition states remains a challenge.

Experimental Section

Reagents and Methods: All reactions were carried out under an atmosphere of dry argon as inert gas using standard Schlenk techniques and the glassware was heated out under high vacuum (10^{-2} mbar) using a heat gun at 500–600 °C unless stated otherwise. Reactions carried out at elevated temperatures were heated using oil baths.

Anhydrous $CHCl_3$ was purchased from Sigma-Aldrich. All other anhydrous solvents were purchased from Acros Organics and were used without prior purification. Solvents for extractions, chromatography, filtrations and non-anhydrous reactions were purchased from VWR as HPLC grade solvents and were used without prior purification. NMR solvents were purchased from Cambridge Isotope Laboratories and were used without prior purification. The anhydrous solvents $CHCl_3$, MeCN, THF and NEt_3 used in the reactions listed below were purged with dry argon gas for 30 min beforehand. All reagents used were purchased from commercial distributors (Acros, Alfa Aesar, Fluorochem, Sigma-Aldrich, TCI, VWR) and were used without prior purification. 1,3,5-triethynylbenzene (**10**) was prepared following literature procedures.[90,91]

DOSY NMR experiments were performed at 298 K on a Bruker Avance III HD four-channel NMR spectrometer operating at 600.13 MHz proton frequency. ^{1}H NMR spectra were recorded at 298 K and 500 MHz using a Bruker UltraShield 500 spectrometer. ^{13}C NMR spectra were recorded at 298 K and 151 MHz using a Bruker Avance III NMR spectrometer equipped with a cryogenic QCI-F probe. ^{19}F NMR spectra were recorded at 471 MHz on a Bruker UltraShield 500 spectrometer. Chemical shifts of ^{1}H NMR and ^{13}C NMR spectra are given in ppm by using residual solvent signals as references (DCM-d_2: 5.32 ppm and 53.84 ppm, respectively; MeCN-d_3: 1.94 ppm and 1.32 ppm, respectively); chemical shifts of ^{19}F NMR spectra are given in ppm, referenced to $CFCl_3$ (0.00 ppm) as internal standard. Coupling constants (J) are reported in Hertz (Hz). Standard abbreviations indicating multiplicity were used as follows: s (singlet), d (doublet), t (triplet), q (quartet), m (multiplet), m_c (centered multiplet), br. (broad). High resolution mass spectra were obtained using the electrospray ionization – time of flight (ESI-TOF) technique on a Bruker maXis 4G mass spectrometer. Infrared spectra were recorded on a Bruker Alpha spectrometer (attenuated total reflection, ATR). Only selected absorbances (ν_{max}) are reported. Standard abbreviations indicating signal intensity were used as follows: vs (very strong), s (strong), m (medium), w (weak), b (broad). Melting Points were recorded on a Büchi Melting Point M-565 apparatus using open capillary tubes. Size-Exclusion column chromatographic separations were performed with Bio-Beads S-X1 support resins from Bio-Rad (1 %cross-linkage, 40–80 µm bead size, 600–14000 MW exclusion range) using gravity flow. The beads were swollen overnight in DCM/MeCN = 7:3 and washed extensively via filtration before use with the same solvent system to remove baseline impurities.

Synthetic procedures for Zn_4L_4 cage IV

Synthesis of trialdehyde 11: A dried 100 mL round-bottom flask was charged with 1,3,5-triethynylbenzene (**10**, 751 mg, 5.00 mmol, 1.00 eq.), 5-bromopyridine-2-carbaldeyhde (3.07 g, 16.5 mmol, 3.30 eq.), $PdCl_2(PPh_3)_2$ (212 mg, 0.302 mmol, 6.04 mol-%) and copper(I)-iodide (60.4 mg, 0.317 mmol, 6.34 mol-%). Dry THF (45 mL) and dry NEt_3 (15 mL) were added and the reaction mixture was refluxed at 85 °C oil bath temperature for 3.5 h. The solvent was removed under reduced pressure and the crude product was suspended in acetone. The suspension was ultrasonicated, heated to reflux and subjected to hot filtration. The filtering cake was washed with excess hot acetone and a beige solid was collected. This hot filtration procedure was repeated once again with the beige solid residue. Trialdehyde **11** (1.78 g, 3.82 mmol, 76 %) was obtained as a beige powder and used without further purification. ^{1}H NMR (500 MHz, DCM-d_2): δ [ppm] = 10.07 (d, $^5J_{1,3}$ = 0.8 Hz, 3H, 1-H), 8.94 (dd, $^4J_{meta}$ = 2.0 Hz, $^5J_{para}$ = 0.8 Hz, 3H, 4-H), 8.03 (ddd, $^3J_{ortho}$ = 8.1 Hz, $^4J_{meta}$ = 2.0 Hz, $^5J_{3,1}$ = 0.8 Hz, 3H, 3-H), 7.96 (dd, $^3J_{ortho}$ = 8.1 Hz, $^5J_{para}$ = 0.9 Hz, 3H, 2-H), 7.83 (s, 3H, 5-H). ^{13}C NMR (151 MHz, DCM-d_2): δ [ppm] = 192.92, 152.97, 151.84, 139.98, 135.62, 124.29, 123.80, 121.24, 93.08, 87.57. IR (ATR): $\tilde{\nu}$ [cm^{-1}] = 3051 (m, C–$H_{arom.}$), 2822 (m, C–$H_{aldeh.}$), 2709 (w), 2207 (m), 1706 (vs, C=O), 1576 (s), 1553 (m), 1477 (w), 1416 (w), 1364 (m), 1289 (m), 1267 (w), 1206 (s), 1116 (m), 1019 (m), 928 (w), 878 (m), 842 (s), 726 (vs), 677 (m), 644 (m), 610 (m), 587 (m), 524 (w), 408 (s). HR-MS (pos. ESI) m/z calcd for $C_{30}H_{16}N_3O_3$: 466.1186 $[M+H]^+$; found: 466.1188. M.p.: Decomposition observed at 200 °C onwards.

Synthesis of Zn_4L_4 cage IV: A dried 350 mL pressure tube was charged with a stir bar, trialdehyde **11** (354 mg, 0.761 mmol, 4.00 eq.) and zinc(II) triflimide (476 mg, 0.761 mmol, 4.00 eq.). Dry MeCN (38 mL), dry $CHCl_3$ (38 mL) and tris(2-aminoethyl)amine (114 µL, 111 mg, 0.759 mmol, 3.99 eq.) were added and the mixture was ultrasonicated. The reaction mixture was heated to 110 °C oil bath temperature while stirring vigorously for 18 h. The mixture was then cooled to room temperature and filtered over a celite pad. The solvent was removed under reduced pressure and the residue re-dissolved in just enough MeCN (ca. 8 mL). The dark solution was diluted with excess Et_2O, and the suspension was centrifuged. The supernatant was decanted and the black residue (781 mg divided into 80–105 mg aliquots) was subjected to size-exclusion chromatography with 1 % crosslinked Bio-Beads SX-1 Support Resin (DCM/MeCN = 7:3, Column Dimensions: Diameter d = 4.5 cm, Height h = 34 cm, gravity-flow). Residual side-products and polymers were removed by crystallization via slow diffusion of Et_2O into an MeCN solution of the product mixture. The supernatant was removed and the crystals were dissolved in MeCN. Et_2O was added and the suspension was centrifuged. The supernatant was decanted, and the residue dried under high vacuum. Zn_4L_4 cage **IV** (180 mg, 0.0380 mmol, 20 %) was obtained as a microcrystalline amber solid. During crystallization, a polymer precipitate formed alongside the product crystals which did not readily dissolve back when adding MeCN to re-dissolve the crystals. ^{1}H NMR (500 MHz, MeCN-d_3): δ [ppm] = 8.69 (s, 12H, 1-H), 8.38 (dd, $^3J_{ortho}$ = 8.1 Hz, $^4J_{meta}$ = 2.0 Hz, 12H, 3-H), 8.09 (d, $^3J_{ortho}$ = 8.1 Hz, 12H, 2-H), 7.61 (s, 12H, 5-H), 7.60 (d, $^4J_{meta}$ = 2.0 Hz, 12H, 4-H), 3.77–3.63 (m, 12H, 6-H), 3.55 (dd, J = 11.3 Hz, J = 3.2 Hz, 12H, 6-H), 3.27 (dd, J = 13.7 Hz, J = 3.3 Hz, 12H, 7-H), 2.90 (ddd, J = 13.7 Hz, J = 13.7 Hz, J = 3.5 Hz, 12H, 7-H). ^{13}C NMR (151 MHz, MeCN-d_3): δ [ppm] = 164.1, 151.7, 146.7, 144.9, 136.2, 129.5, 125.8, 124.0, 120.9 (q, J = 321.0 Hz, CF_3), 94.7, 87.6, 57.6, 55.9. ^{19}F NMR (471 MHz, MeCN-d_3, $CFCl_3$ as int.

EurJIC
European Journal of Inorganic Chemistry

Research Article
doi.org/10.1002/ejic.202300110

Chemistry Europe
European Chemical Societies Publishing

Std.): δ [ppm] = −78.8. DOSY NMR (600 MHz, MeCN-d_3, 298 K): Diffusion coefficient $D = 4.59 \cdot 10^{-6}$ $cm^2 s^{-1}$. IR (ATR): $\tilde{\nu}$ [cm^{-1}] = 3071 (w, C–$H_{arom.}$), 2931 (w, C–$H_{aliph.}$), 2863 (w, C–$H_{aliph.}$), 2211 (w), 1656 (m), 1592 (m), 1558 (m), 1462 (w), 1450 (w), 1419 (w), 1345 (s), 1174 (vs), 1128 (vs), 1048 (vs), 965 (m), 936 (m), 878 (m), 849 (m), 787 (m), 759 (m), 738 (m), 652 (m), 598 (s), 569 (s), 506 (s), 464 (m), 415 (m). HR-MS (pos. ESI) *m/z* calcd for $C_{144}H_{108}N_{28}Zn_4$: 311.4551 $[M\text{-}8NTf_2]^{8+}$; found: 311.4563; calcd for $C_{146}H_{108}F_6N_{29}O_4S_2Zn_4$: 396.3650 $[M\text{-}7NTf_2]^{7+}$; found: 396.3666; calcd for $C_{148}H_{108}F_{12}N_{30}O_8S_4Zn_4$: 509.0787 $[M\text{-}6NTf_2]^{6+}$; found: 509.0805; calcd for $C_{150}H_{108}F_{18}N_{31}O_{12}S_6Zn_4$: 666.4787 $[M\text{-}5NTf_2]^{5+}$; found: 666.4798; calcd for $C_{152}H_{108}F_{24}N_{32}O_{16}S_8Zn_4$: 903.0778 $[M\text{-}4NTf_2]^{4+}$; found: 903.0790. M.p.: Decomposition observed at 250 °C onwards.

Deposition Number 2228123 (for **III**) contains the supplementary crystallographic data for this paper. These data are provided free of charge by the joint Cambridge Crystallographic Data Centre and Fachinformationszentrum Karlsruhe Access Structures service.

Acknowledgements

The generous support from the Swiss National Science Foundation (GrantSNF:200021_178714) is gratefully acknowledged. We thank Dr. Michael Pfeffer for HR-MS analysis. Open Access funding provided by Universität Basel.

Conflict of Interest

The authors declare no conflict of interest.

Data Availability Statement

The data that support the findings of this study are available in the supplementary material of this article.

Keywords: Cage compounds · Homogeneous catalysis · Host-guest systems · Iminopyridine ligands · Supramolecular chemistry

[1] C. L. D. Gibb, B. C. Gibb, *J. Am. Chem. Soc.* **2006**, *128*, 16498–16499.
[2] S. Löffler, J. Lübben, L. Krause, D. Stalke, B. Dittrich, G. H. Clever, *J. Am. Chem. Soc.* **2015**, *137*, 1060–1063.
[3] A. Garci, J.-P. Mbakidi, V. Chaleix, V. Sol, E. Orhan, B. Therrien, *Organometallics* **2015**, *34*, 4138–4146.
[4] A. M. Castilla, T. K. Ronson, J. R. Nitschke, *J. Am. Chem. Soc.* **2016**, *138*, 2342–2351.
[5] A. B. Grommet, J. R. Nitschke, *J. Am. Chem. Soc.* **2017**, *139*, 2176–2179.
[6] D. Zhang, T. K. Ronson, J. Mosquera, A. Martinez, J. R. Nitschke, *Angew. Chem. Int. Ed.* **2018**, *57*, 3717–3721; *Angew. Chem.* **2018**, *130*, 3779–3783.
[7] T. Grancha, A. Carné-Sánchez, L. Hernández-López, J. Albalad, I. Imaz, J. Juanhuix, D. Maspoch, *J. Am. Chem. Soc.* **2019**, *141*, 18349–18355.
[8] B.-N. T. Nguyen, A. B. Grommet, A. Tron, M. C. A. Georges, J. R. Nitschke, *Adv. Mater.* **2020**, *32*, 1907241.
[9] A. M. Antonio, K. J. Korman, G. P. A. Yap, E. D. Bloch, *Chem. Sci.* **2020**, *11*, 12540–12546.
[10] D. Zhang, T. K. Ronson, Y.-Q. Zou, J. R. Nitschke, *Nat. Rev. Chem.* **2021**, *5*, 168–182.
[11] B.-N. T. Nguyen, J. D. Thoburn, A. B. Grommet, D. J. Howe, T. K. Ronson, H. P. Ryan, J. L. Bolliger, J. R. Nitschke, *J. Am. Chem. Soc.* **2021**, *143*, 12175–12180.
[12] J. Wang, C. He, P. Wu, J. Wang, C. Duan, *J. Am. Chem. Soc.* **2011**, *133*, 12402–12405.
[13] Y. Jiao, J. Wang, P. Wu, L. Zhao, C. He, J. Zhang, C. Duan, *Chem. Eur. J.* **2014**, *20*, 2224–2231.
[14] M. Zhang, M. L. Saha, M. Wang, Z. Zhou, B. Song, C. Lu, X. Yan, X. Li, F. Huang, S. Yin, P. J. Stang, *J. Am. Chem. Soc.* **2017**, *139*, 5067–5074.
[15] X.-Z. Li, L.-P. Zhou, L.-L. Yan, D.-Q. Yuan, C.-S. Lin, Q.-F. Sun, *J. Am. Chem. Soc.* **2017**, *139*, 8237–8244.
[16] C.-L. Liu, R.-L. Zhang, C.-S. Lin, L.-P. Zhou, L.-X. Cai, J.-T. Kong, S.-Q. Yang, K.-L. Han, Q.-F. Sun, *J. Am. Chem. Soc.* **2017**, *139*, 12474–12479.
[17] Y. Sun, C. Chen, J. Liu, P. J. Stang, *Chem. Soc. Rev.* **2020**, *49*, 3889–3919.
[18] D. J. Cram, M. E. Tanner, R. Thomas, *Angew. Chem. Int. Ed.* **1991**, *30*, 1024–1027; *Angew. Chem.* **1991**, *103*, 1048–1051.
[19] R. Warmuth, *Angew. Chem. Int. Ed.* **1997**, *36*, 1347–1350; *Angew. Chem.* **1997**, *109*, 1406–1409.
[20] M. Ziegler, J. L. Brumaghim, K. N. Raymond, *Angew. Chem. Int. Ed.* **2000**, *39*, 4119–4121; *Angew. Chem.* **2000**, *112*, 4285–4287.
[21] R. Warmuth, M. A. Marvel, *Angew. Chem. Int. Ed.* **2000**, *39*, 1117–1119; *Angew. Chem.* **2000**, *112*, 1168–1171.
[22] M. Yoshizawa, T. Kusukawa, M. Fujita, K. Yamaguchi, *J. Am. Chem. Soc.* **2000**, *122*, 6311–6312.
[23] D. Fiedler, R. G. Bergman, K. N. Raymond, *Angew. Chem. Int. Ed.* **2006**, *45*, 745–748; *Angew. Chem.* **2006**, *118*, 759–762.
[24] V. M. Dong, D. Fiedler, B. Carl, R. G. Bergman, K. N. Raymond, *J. Am. Chem. Soc.* **2006**, *128*, 14464–14465.
[25] T. Iwasawa, R. J. Hooley, J. Rebek, *Science* **2007**, *317*, 493–496.
[26] P. Mal, B. Breiner, K. Rissanen, J. R. Nitschke, *Science* **2009**, *324*, 1697–1699.
[27] A. Galan, P. Ballester, *Chem. Soc. Rev.* **2016**, *45*, 1720–1737.
[28] M. Yoshizawa, J. K. Klosterman, M. Fujita, *Angew. Chem. Int. Ed.* **2009**, *48*, 3418–3438; *Angew. Chem.* **2009**, *121*, 3470–3490.
[29] M. J. Wiester, P. A. Ulmann, C. A. Mirkin, *Angew. Chem. Int. Ed.* **2011**, *50*, 114–137; *Angew. Chem.* **2011**, *123*, 118–142.
[30] M. Raynal, P. Ballester, A. Vidal-Ferran, P. W. N. M. van Leeuwen, *Chem. Soc. Rev.* **2014**, *43*, 1734–1787.
[31] S. Zarra, D. M. Wood, D. A. Roberts, J. R. Nitschke, *Chem. Soc. Rev.* **2015**, *44*, 419–432.
[32] C. J. Brown, F. D. Toste, R. G. Bergman, K. N. Raymond, *Chem. Rev.* **2015**, *115*, 3012–3035.
[33] L. J. Jongkind, X. Caumes, A. P. T. Hartendorp, J. N. H. Reek, *Acc. Chem. Res.* **2018**, *51*, 2115–2128.
[34] M. D. Ward, C. A. Hunter, N. H. Williams, *Acc. Chem. Res.* **2018**, *51*, 2073–2082.
[35] Q. Zhang, L. Catti, K. Tiefenbacher, *Acc. Chem. Res.* **2018**, *51*, 2107–2114.
[36] V. Mouarrawis, R. Plessius, J. I. van der Vlugt, J. N. H. Reek, *Front. Chem.* **2018**, *6*, 623.
[37] Y. Fang, J. A. Powell, E. Li, Q. Wang, Z. Perry, A. Kirchon, X. Yang, Z. Xiao, C. Zhu, L. Zhang, F. Huang, H.-C. Zhou, *Chem. Soc. Rev.* **2019**, *48*, 4707–4730.
[38] X. Li, J. Wu, C. He, Q. Meng, C. Duan, *Small* **2019**, *15*, 1804770.
[39] C. Tan, D. Chu, X. Tang, Y. Liu, W. Xuan, Y. Cui, *Chem. Eur. J.* **2019**, *25*, 662–672.
[40] C. Gaeta, C. Talotta, M. De Rosa, P. La Manna, A. Soriente, P. Neri, *Chem. Eur. J.* **2019**, *25*, 4899–4913.
[41] A. B. Grommet, M. Feller, R. Klajn, *Nat. Nanotechnol.* **2020**, *15*, 256–271.
[42] Y. Yu, J.-M. Yang, J. Rebek, *Chem* **2020**, *6*, 1265–1274.
[43] K. Wang, J. H. Jordan, X.-Y. Hu, L. Wang, *Angew. Chem. Int. Ed.* **2020**, *59*, 13712–13721; *Angew. Chem.* **2020**, *132*, 13816–13825.
[44] R. J. Hooley, *Synlett* **2020**, *31*, 1448–1463.
[45] M. Morimoto, S. M. Bierschenk, K. T. Xia, R. G. Bergman, K. N. Raymond, F. D. Toste, *Nat. Catal.* **2020**, *3*, 969–984.
[46] C. Gaeta, P. La Manna, M. De Rosa, A. Soriente, C. Talotta, P. Neri, *ChemCatChem* **2021**, *13*, 1638–1658.
[47] H. Takezawa, M. Fujita, *Bull. Chem. Soc. Jpn.* **2021**, *94*, 2351–2369.
[48] R. Saha, B. Mondal, P. S. Mukherjee, *Chem. Rev.* **2022**, *122*, 12244–12307.
[49] A. B. Solea, B. Suditttapong, C. G. P. Taylor, M. D. Ward, *Dalton Trans.* **2022**, *51*, 11277–11285.
[50] T. Murase, Y. Nishijima, M. Fujita, *J. Am. Chem. Soc.* **2012**, *134*, 162–164.
[51] W. Cullen, M. C. Misuraca, C. A. Hunter, N. H. Williams, M. D. Ward, *Nat. Chem.* **2016**, *8*, 231–236.
[52] W. Cullen, A. J. Metherell, A. B. Wragg, C. G. P. Taylor, N. H. Williams, M. D. Ward, *J. Am. Chem. Soc.* **2018**, *140*, 2821–2828.

EurJIC
European Journal of Inorganic Chemistry

Research Article
doi.org/10.1002/ejic.202300110

Chemistry Europe
European Chemical Societies Publishing

[53] C. G. P. Taylor, A. J. Metherell, S. P. Argent, F. M. Ashour, N. H. Williams, M. D. Ward, *Chem. Eur. J.* **2020**, *26*, 3065–3073.
[54] J. Wang, T. A. Young, F. Duarte, P. J. Lusby, *J. Am. Chem. Soc.* **2020**, *142*, 17743–17750.
[55] M. D. Ludden, C. G. P. Taylor, M. B. Tipping, J. S. Train, N. H. Williams, J. C. Dorrat, K. L. Tuck, M. D. Ward, *Chem. Sci.* **2021**, *12*, 14781–14791.
[56] K. Li, K. Wu, Y.-L. Lu, J. Guo, P. Hu, C.-Y. Su, *Angew. Chem. Int. Ed.* **2022**, *61*, e202114070.
[57] Y. Zhao, Y. Domoto, E. Orentas, C. Beuchat, D. Emery, J. Mareda, N. Sakai, S. Matile, *Angew. Chem. Int. Ed.* **2013**, *52*, 9940–9943; *Angew. Chem.* **2013**, *125*, 10124–10127.
[58] Y. Zhao, Y. Cotelle, L. Liu, J. López-Andarias, A.-B. Bornhof, M. Akamatsu, N. Sakai, S. Matile, *Acc. Chem. Res.* **2018**, *51*, 2255–2263.
[59] X. Zhang, X. Hao, L. Liu, A.-T. Pham, J. López-Andarias, A. Frontera, N. Sakai, S. Matile, *J. Am. Chem. Soc.* **2018**, *140*, 17867–17871.
[60] M. Paraja, X. Hao, S. Matile, *Angew. Chem. Int. Ed.* **2020**, *59*, 15093–15097; *Angew. Chem.* **2020**, *132*, 15205–15209.
[61] S. P. Black, A. R. Stefankiewicz, M. M. J. Smulders, D. Sattler, C. A. Schalley, J. R. Nitschke, J. K. M. Sanders, *Angew. Chem. Int. Ed.* **2013**, *52*, 5749–5752; *Angew. Chem.* **2013**, *125*, 5861–5864.
[62] T. K. Ronson, D. A. Roberts, S. P. Black, J. R. Nitschke, *J. Am. Chem. Soc.* **2015**, *137*, 14502–14512.
[63] S. P. Black, D. M. Wood, F. B. Schwarz, T. K. Ronson, J. J. Holstein, A. R. Stefankiewicz, C. A. Schalley, J. K. M. Sanders, J. R. Nitschke, *Chem. Sci.* **2016**, *7*, 2614–2620.
[64] Z. Lu, R. Lavendomme, O. Burghaus, J. R. Nitschke, *Angew. Chem. Int. Ed.* **2019**, *58*, 9073–9077; *Angew. Chem.* **2019**, *131*, 9171–9175.
[65] Z. Lu, T. K. Ronson, J. R. Nitschke, *Chem. Sci.* **2020**, *11*, 1097–1101.
[66] Q. N. N. Nguyen, K. T. Xia, Y. Zhang, N. Chen, M. Morimoto, X. Pei, Y. Ha, J. Guo, W. Yang, L.-P. Wang, R. G. Bergman, K. N. Raymond, F. D. Toste, D. J. Tantillo, *J. Am. Chem. Soc.* **2022**, *144*, 11413–11424.
[67] D. Chandler, *Nature* **2002**, *417*, 491–491.
[68] L. R. Pratt, A. Pohorille, *Chem. Rev.* **2002**, *102*, 2671–2692.
[69] D. Chandler, *Nature* **2005**, *437*, 640–647.
[70] S. Granick, S. C. Bae, *Science* **2008**, *322*, 1477–1478.
[71] F. Biedermann, W. M. Nau, H.-J. Schneider, *Angew. Chem. Int. Ed.* **2014**, *53*, 11158–11171; *Angew. Chem.* **2014**, *126*, 11338–11352.
[72] E. G. Percástegui, T. K. Ronson, J. R. Nitschke, *Chem. Rev.* **2020**, *120*, 13480–13544.
[73] E. G. Percástegui, J. Mosquera, T. K. Ronson, A. J. Plajer, M. Kieffer, J. R. Nitschke, *Chem. Sci.* **2019**, *10*, 2006–2018.
[74] S. M. Jansze, G. Cecot, M. D. Wise, K. O. Zhurov, T. K. Ronson, A. M. Castilla, A. Finelli, P. Pattison, E. Solari, R. Scopelliti, G. E. Zelinskii, A. V. Vologzhanina, Y. Z. Voloshin, J. R. Nitschke, K. Severin, *J. Am. Chem. Soc.* **2016**, *138*, 2046–2054.
[75] J. A. Davies, A. Tarzia, T. K. Ronson, F. Auras, K. E. Jelfs, J. R. Nitschke, *Angew. Chem. Int. Ed.* **2023**, *62*, e202217987.
[76] A. J. Amoroso, J. C. Jeffery, P. L. Jones, J. A. McCleverty, P. Thornton, M. D. Ward, *Angew. Chem. Int. Ed.* **1995**, *34*, 1443–1446; *Angew. Chem.* **1995**, *107*, 1577–1580.
[77] C. Brückner, R. E. Powers, K. N. Raymond, *Angew. Chem. Int. Ed.* **1998**, *37*, 1837–1839; *Angew. Chem.* **1998**, *110*, 1937–1940.
[78] D. L. Caulder, C. Brückner, R. E. Powers, S. König, T. N. Parac, J. A. Leary, K. N. Raymond, *J. Am. Chem. Soc.* **2001**, *123*, 8923–8938.
[79] R. W. Saalfrank, H. Glaser, B. Demleitner, F. Hampel, M. M. Chowdhry, V. Schünemann, A. X. Trautwein, G. B. M. Vaughan, R. Yeh, A. V. Davis, K. N. Raymond, *Chem. Eur. J.* **2002**, *8*, 493–497.
[80] M. Albrecht, I. Janser, J. Runsink, G. Raabe, P. Weis, R. Fröhlich, *Angew. Chem. Int. Ed.* **2004**, *43*, 6662–6666; *Angew. Chem.* **2004**, *116*, 6832–6836.
[81] M. Albrecht, I. Janser, R. Fröhlich, *Chem. Commun.* **2005**, 157–165.
[82] M. Albrecht, I. Janser, S. Burk, P. Weis, *Dalton Trans.* **2006**, 2875–2880.
[83] J. Hamacek, G. Bernardinelli, Y. Filinchuk, *Eur. J. Inorg. Chem.* **2008**, *2008*, 3419–3422.
[84] Y. Liu, Z. Lin, C. He, L. Zhao, C. Duan, *Dalton Trans.* **2010**, *39*, 11122–11125.
[85] R. A. Bilbeisi, J. K. Clegg, N. Elgrishi, X. de Hatten, M. Devillard, B. Breiner, P. Mal, J. R. Nitschke, *J. Am. Chem. Soc.* **2012**, *134*, 5110–5119.
[86] T. Osawa, T. Kajitani, D. Hashizume, H. Ohsumi, S. Sasaki, M. Takata, Y. Koizumi, A. Saeki, S. Seki, T. Fukushima, T. Aida, *Angew. Chem. Int. Ed.* **2012**, *51*, 7990–7993; *Angew. Chem.* **2012**, *124*, 8114–8117.
[87] T. Kim, S. H. Joo, J. Gong, S. Choi, J. H. Min, Y. Kim, G. Lee, E. Lee, S. Park, S. K. Kwak, H.-S. Lee, B.-S. Kim, *Angew. Chem. Int. Ed.* **2022**, *61*, e202113780.
[88] B. Bao, L. Yuwen, X. Zhan, L. Wang, *J. Polym. Sci. Part A* **2010**, *48*, 3431–3439.
[89] A. M. Castilla, N. Ousaka, R. A. Bilbeisi, E. Valeri, T. K. Ronson, J. R. Nitschke, *J. Am. Chem. Soc.* **2013**, *135*, 17999–18006.
[90] G. Albano, L. A. Aronica, T. Biver, R. Detti, A. Pucci, *ChemistrySelect* **2018**, *3*, 1749–1754.
[91] Z. Chen, M. Chen, Y. Yu, L. Wu, *Chem. Commun.* **2017**, *53*, 1989–1992.
[92] W. M. Bloch, Y. Abe, J. J. Holstein, C. M. Wandtke, B. Dittrich, G. H. Clever, *J. Am. Chem. Soc.* **2016**, *138*, 13750–13755.
[93] Y. Yang, T. K. Ronson, Z. Lu, J. Zheng, N. Vanthuyne, A. Martinez, J. R. Nitschke, *Nat. Commun.* **2021**, *12*, 4079.

Manuscript received: March 1, 2023
Revised manuscript received: March 9, 2023
Accepted manuscript online: March 9, 2023

RESEARCH ARTICLE

A novel iminopyridine-based Zn_4L_4 tetrahedral cage, synthesized in four steps, binds larger organic anions with binding constants of up to 850 M^{-1} in MeCN–d_3/H_2O = 9:1 and displays stability in basic aqueous acetonitrile. Surprisingly, investigations towards catalysis of reactions with anionic transition states did not indicate rate accelerations in the presence of the cage.

Iminopyridine-based Zn_4L_4 Tetrahedron

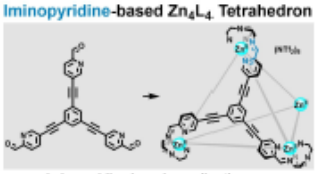

- new iminopyridine-based coordination cage
- stability in basic aqueous acetonitrile at higher T
- binding of larger organic anions

*M. Zenka, J. Preinl, Dr. E. Pertermann, Prof. Dr. A. Lützen, Prof. Dr. K. Tiefenbacher**